ENERGY, WATER, AND CARBON DIOXIDE FLUXES AT THE EARTH'S SURFACE

EDITED BY: Meghan F. Cronin, Carol Anne Clayson, Simon Josey, Petra Heil and Masao Ishii

PUBLISHED IN: Frontiers in Marine Science, Frontiers in Environmental Science and Frontiers in Earth Science

frontiers Research Topics

frontiers

ISSN 1664-8714
ISBN 978-2-83250-136-8
DOI 10.3389/978-2-83250-136-8

About Frontiers

Frontiers is more than just an open-access publisher of scholarly articles: it is a pioneering approach to the world of academia, radically improving the way scholarly research is managed. The grand vision of Frontiers is a world where all people have an equal opportunity to seek, share and generate knowledge. Frontiers provides immediate and permanent online open access to all its publications, but this alone is not enough to realize our grand goals.

Frontiers Journal Series

The Frontiers Journal Series is a multi-tier and interdisciplinary set of open-access, online journals, promising a paradigm shift from the current review, selection and dissemination processes in academic publishing. All Frontiers journals are driven by researchers for researchers; therefore, they constitute a service to the scholarly community. At the same time, the Frontiers Journal Series operates on a revolutionary invention, the tiered publishing system, initially addressing specific communities of scholars, and gradually climbing up to broader public understanding, thus serving the interests of the lay society, too.

Dedication to Quality

Each Frontiers article is a landmark of the highest quality, thanks to genuinely collaborative interactions between authors and review editors, who include some of the world's best academicians. Research must be certified by peers before entering a stream of knowledge that may eventually reach the public - and shape society; therefore, Frontiers only applies the most rigorous and unbiased reviews.
Frontiers revolutionizes research publishing by freely delivering the most outstanding research, evaluated with no bias from both the academic and social point of view. By applying the most advanced information technologies, Frontiers is catapulting scholarly publishing into a new generation.

What are Frontiers Research Topics?

Frontiers Research Topics are very popular trademarks of the Frontiers Journals Series: they are collections of at least ten articles, all centered on a particular subject. With their unique mix of varied contributions from Original Research to Review Articles, Frontiers Research Topics unify the most influential researchers, the latest key findings and historical advances in a hot research area! Find out more on how to host your own Frontiers Research Topic or contribute to one as an author by contacting the Frontiers Editorial Office: frontiersin.org/about/contact

ENERGY, WATER, AND CARBON DIOXIDE FLUXES AT THE EARTH'S SURFACE

Topic Editors:
Meghan F. Cronin, National Oceanic and Atmospheric Administration (NOAA), United States
Carol Anne Clayson, Woods Hole Oceanographic Institution, United States
Simon Josey, University of Southampton, United Kingdom
Petra Heil, Australian Antarctic Division, Australia
Masao Ishii, Meteorological Research Institute (MRI), Japan

Citation: Cronin, M. F., Clayson, C. A., Josey, S., Heil, P., Ishii, M., eds. (2022). Energy, Water, and Carbon Dioxide Fluxes at the Earth's Surface. Lausanne: Frontiers Media SA. doi: 10.3389/978-2-83250-136-8

Table of Contents

frontiers in Earth Science

ORIGINAL RESEARCH
published: 26 June 2020
doi: 10.3389/feart.2020.00245

Distinct Impacts of Land Use and Land Management on Summer Temperatures

Liang Chen[1,2]* *and Paul A. Dirmeyer*[2]

[1] Climate and Atmospheric Sciences Section, Illinois State Water Survey, Prairie Research Institute, University of Illinois at Urbana-Champaign, Champaign, IL, United States, [2] Center for Ocean-Land-Atmosphere Studies, George Mason University, Fairfax, VA, United States

Land use has been recognized as an important anthropogenic forcing of climate change in recent studies. However, climatic effects of land management practices have been little discussed and compared to land-use impacts. As land-atmosphere interactions via surface fluxes are particularly strong during the warm season, we investigate the impacts of historical land use and present irrigation practices on summer temperatures in the Northern Hemisphere using the most recent version of Community Earth System Model. Our results suggest that historical land use leads to an overall cooling in the middle latitudes and a warming in the tropics, and the sign and magnitude of the changes in temperature depend on the type of land cover change. On the other hand, summer irrigation leads to a significant cooling over many irrigated areas due to enhanced evapotranspiration, and the local cooling is comparable to and even stronger than the land-use effects. Both land use and irrigation can also significantly influence the intensity and frequency of hot extremes. Land use shows stronger impacts during the night through ground heat flux feedback, while irrigation shows stronger impacts during the day through latent heat flux feedback. Our comparison demonstrates the importance of irrigation in local and regional climate, highlighting the necessity of considering such land management practices in future assessments of regional climate change and climate mitigation.

Keywords: land use – land cover change, climate modeling, land-atmosphere interaction, irrigation, CESM2

OPEN ACCESS

Edited by:
Gert-Jan Steeneveld, Wageningen University and Research, Netherlands

Reviewed by:
Emanuel Dutra, University of Lisbon, Portugal
Stefan Hagemann, Helmholtz Centre for Materials and Coastal Research (HZG), Germany

***Correspondence:**
Liang Chen
liangch@illinois.edu

Specialty section:
This article was submitted to Atmospheric Science, a section of the journal Frontiers in Earth Science

Received: *05 March 2020*
Accepted: *04 June 2020*
Published: *26 June 2020*

Citation:
Chen L and Dirmeyer PA (2020) Distinct Impacts of Land Use and Land Management on Summer Temperatures. Front. Earth Sci. 8:245. doi: 10.3389/feart.2020.00245

INTRODUCTION

It is widely recognized that land use/land cover change (hereafter referred to simply as land use) affects the overlying atmosphere through land-atmosphere interactions, and thus modifies the local and broader-scale climate. The importance of land use in the climate system promoted the Coupled Model Intercomparison Project Phase 5 (CMIP5) to include land use forcing in its climate projections (Hurtt et al., 2011). Based on the CMIP5 simulations, many studies have been carried out to investigate the impacts of land use on climate (Brovkin et al., 2013; Kumar et al., 2013; Di Vittorio et al., 2014) and extreme events (Lejeune et al., 2017, 2018; Chen and Dirmeyer, 2018; Li et al., 2018). It is found that land use can have impacts comparable to increased greenhouse gasses or sea surface temperature variations for many climate variables (Avila et al., 2012; de Noblet-Ducoudré et al., 2012), and land-use forcing can be as important as other anthropogenic forcings

in explaining the historical changes in temperature extremes over the regions with extensive land use (Chen and Dirmeyer, 2018).

Besides land use, which usually refers to conversions from one land cover to another due to human activities, land management practices and their climatic impacts have drawn increasing attention recently (Luyssaert et al., 2014; Mahmood et al., 2014). As an important agricultural practice to maintain adequate soil moisture for stable crop production, irrigation not only modifies the surface water budget, but also affects the energy balance of the land surface, thereby altering the climate (Kueppers et al., 2007). For instance, irrigation can change surface partitioning of available energy between sensible and latent heat fluxes by allowing more evapotranspiration through increased soil moisture and larger vegetation coverage, potentially lowering near-surface temperatures over the irrigated areas.

Recent modeling studies have demonstrated the significant impacts of irrigation on near-surface climate and atmospheric circulation (e.g., Boucher et al., 2004; Kueppers et al., 2007; Lobell et al., 2009; Sacks et al., 2009; Lo and Famiglietti, 2013; Wei et al., 2013; Lu and Kueppers, 2015; de Vrese et al., 2016; Huang and Ullrich, 2016; Krakauer et al., 2016), especially the strong cooling effects on daytime temperatures or hot extremes. It is proposed that irrigation can be an effective way to mitigate the regional warming of hot extremes (Hirsch et al., 2017; Thiery et al., 2017). Studies based on satellite observations also indicate the substantial local cooling of irrigation (Ambika and Mishra, 2019; Chen and Dirmeyer, 2019b), and imply that the cooling effects may be underestimated by global climate models due to their coarse spatial resolutions (Sorooshian et al., 2011; Chen and Dirmeyer, 2019b).

Despite its fundamental importance in altering the regional climate, the full scope of land management has rarely been considered in recent climate assessment projects. For instance, CMIP5 did not include irrigation as a historical forcing (Kumar et al., 2013), and many of the participating Earth system models did not implement irrigation schemes in their land surface models (Singh et al., 2018). The project Land-Use and Climate, Identification of Robust Impacts (LUCID), for example, is mainly focused on the biogeophysical impacts of historical land use (de Noblet-Ducoudré et al., 2012). There are a few studies demonstrating the siginificance of irrigation compared to other land surface changes. For instance, the effects of irrigation on water vapor flows are equally as important as deforestation (Gordon et al., 2005); the cooling of irrigation is most pronounced compared to increased leaf area index and reduced tillage (Lobell et al., 2006). However, few studies have investigated the impacts of irrigation and its relative importance compared to historical land use in modifying local and regional temperatures.

With the goal of comparing these two types of land management, this study uses a state-of-the-art Earth system model, Community Earth System Model version 2 (CESM2), to investigate the separate impacts of land use and irrigation on summer temperatures and extreme heat events. We focus on boreal summer temperature because of the strong land-atmosphere interactions and high irrigation demands during the warm season, when these two land surface forcings should have the most profound climatic impacts and the greatest social implications.

METHODOLOGY

Land-Use Experiments in CESM2

The land-use experiments are conducted with CESM2, which is a coupled Earth System model composed of separate climate system components for atmosphere, ocean, land, sea ice and land ice. The major focus of this study is on the interactions between the land surface and atmosphere, so only the Community Atmosphere Model (CAM6) and Community Land Model (CLM5) components are used in our simulations (no interactive ocean or sea ice), with the component set F2000climo at a spatial resolution of $0.9° \times 1.25°$. The F2000climo component set allows climatology simulations with cyclic circa-year-2000 forcing, in which there are prescribed sea surface temperature (SST) and sea ice cover with a fixed CO_2 concentration of 367.0 ppm. Monthly mean climatology of SST and sea ice cover are derived from a merged product based on the monthly mean Hadley Center Sea Ice and SST dataset, version 1 (HadISST1), and version 2 of the NOAA weekly Optimum Interpolation SST (OISST2) analysis during the period 1995–2005 (Hurrell et al., 2008). Compared with the previous version of CLM, improvements are made in CLM5 to better represent soil and plant hydrology, snow density, carbon and nitrogen cycling and coupling, the representation of crops and human land management (Lawrence et al., 2019).

In CLM5, land surface heterogeneity is represented as a nested subgrid hierarchy, in which grid cells are composed of multiple land units (such as the vegetated unit and crop unit). The vegetated unit can be composed of different plant functional types (PFTs), and the crop unit can be composed of different crop functional types (CFTs). Land use is represented as the changes in percent PFTs and CFTs within a grid cell. In this study, two land-use experiments (*pre-industrial* and *present*) are carried out with prescribed pre-industrial and present land cover conditions (**Table 1**). The difference between *present* and *pre-industrial* can be considered as the impacts of historical land use. A two-tailed Student's t-test is conducted to assess the significance of the land-use induced difference. Details of the pre-industrial land cover can be found in Hurtt et al. (2006) and Lawrence et al. (2012), while the present land cover is derived from MODIS satellite data as described in Lawrence and Chase (2007).

Irrigation in CLM5

In the CLM5, there are a total of 31 managed crop types (Lawrence et al., 2018). Each crop type has rainfed and irrigated

TABLE 1 | Experimental design in CESM2.

Name	Land cover	Irrigation scheme
pre-industrial	pre-industrial (1850)	off
present	present (2015)	off
irrig	present (2015)	on

CFTs, which are placed on separate soil columns. The proportion of irrigated CFTs is based on a dataset of areas equipped for irrigation (Portmann et al., 2010), which is shown in **Figure 1D**. When irrigation is enabled, the model checks if the crops need irrigation in the first time step after 6 AM local time every day. If the crop leaf area is greater than zero and the available soil water is below a specified threshold, irrigation will be triggered. Irrigated water is removed from river water storage and applied directly to the ground surface. Details of the irrigation scheme in CLM5 can be found in Lawrence et al. (2018). To separate the impacts of land use and land management, an irrigation experiment, *irrig*, is carried out with the present land cover conditions (**Table 1**). Irrigation is not automatically activated in the *pre-industrial* and *present* experiments, so the difference between *irrig* and *present* can be considered as the effects of irrigation. A two-tailed Student's *t*-test is used to assess the significance of the irrigation induced difference.

Because the prognostic biogeochemical model is activated to estimate the vegetation phenology, land initial conditions for each experiment are obtained from a separate 700−year offline spin−up run, then each experiment is conducted for 60 years with output saved at three-hourly intervals.

Indices of Hot Extremes

Previous studies suggest that land use and irrigation have significant impacts on hot extremes (Avila et al., 2012; Pitman et al., 2012; Christidis et al., 2013; Hirsch et al., 2017; Thiery et al., 2017). Therefore, we assess the changes in four warm extreme temperature indices, listed and defined in **Table 2**, as recommended by the CCl/CLIVAR/JCOMM Expert Team on Climate Change Detection and Indices (ETCCDI; Alexander et al., 2006). These indices are based on daily maximum and minimum temperature and are developed to assess the intensity and frequency of extreme temperature events.

Additionally, to understand the mechanism of temperature responses to changes in land use and land management, other land surface variables (such as surface fluxes and radiation) are also included in our analysis. With the focus on daily minimum and maximum temperature, we identify the timing of daily maximum (minimum) land surface temperatures (T_s) based on three-hourly model output, and extract the corresponding surface fluxes and radiation when T_s reaches the daily maximum (minimum).

TABLE 2 | Temperature indices used in this study.

Index	definition	Unit
TXx	The warmest day of the year	K
TNx	The warmest night of the year	K
TX90p	Number of days when TX > 90th percentile	days
TN90p	Number of days when TN > 90th percentile	days

TX is daily maximum temperature, and TN is daily minimum temperature. Definitions of these indices can be found at http://etccdi.pacificclimate.org/list_27_indices.shtml (Karl et al., 1999; Peterson et al., 2001).

RESULTS

Historical Land Use and Irrigation Activities

Figures 1A–C shows the historical land cover change from pre-industrial to present day over the Northern Hemisphere. Deforestation has mainly occurred in the Midwest of the US, eastern Europe, India, eastern China, and in tropical areas such as Central America, Africa, and southeastern Asia. Most of the deforestation is driven by agricultural demand through cropland expansion in the middle latitudes, which has also led to grassland loss in such regions as the Great Plains, Eastern Europe, and India. Meanwhile, the conversion of cropland back into forest or grassland occurs in some regions of the northeastern US and western Europe. Grassland degradation (conversion of grassland into bare ground) is found in some regions of the Tibetan Plateau, which might be associated with over-stocking (Li et al., 2013).

Areas of the irrigated cropland are shown in **Figure 1D**. The irrigation systems are mainly distributed in northern India, eastern China, the Middle East, Southern Europe, the Central Valley in California, the North American Great Plains, and the Mississippi Embayment, according to Portmann et al. (2010). Based on the irrigation experiment, the total amount of irrigated water can be estimated in CLM5 (**Figure 2A**), which shows good agreement with observationally based estimates (Thiery et al., 2017), indicating that CESM2 is an appropriate tool to investigate the impact of irrigation (Huang and Ullrich, 2016; Thiery et al., 2017). Seven subregions with high irrigation rates are selected for regional analysis. We also identified the month with the highest irrigation rate (**Figure 2B**). Summertime peak irrigation occurs mostly in the middle latitudes, such as North America, the Mediterranean, and western/eastern Asia. In the tropics and regions that are influenced by monsoons (such as the East Asian Monsoon and North American Monsoon), the highest irrigation rate is mainly found in spring, which is the dry season prior to the onset monsoon rains. However, there is still a large amount of irrigated water applied during the summer in those regions, according to the irrigation algorithm in CLM5 (**Supplementary Figure S1**), exerting impacts on the surface climate then as well.

Changes in Temperature

Due to possible different responses of daytime temperature to deforestation at the land surface (T_s) and 2-m air (T_{2m}) reported in our previous work (Chen and Dirmeyer, 2019a), we present the results of T_s and T_{2m} separately (**Figure 3**). Historical deforestation leads to a significant daytime warming at the land surface (T_s) in the tropics, India, and the central US (**Figure 3A**). However, the change in daily maximum T_{2m} largely depends on the type of land use. Cooling effects on T_{2m} are found in parts of the central US, Central America and Columbia, where the major land use is the conversion of forest into cropland and grassland. For regions like India and Southeast Asia where forest and grassland are converted into cropland, there is increased daily maximum T_{2m}. In eastern Europe, the combined effects of deforestation and grassland conversion do

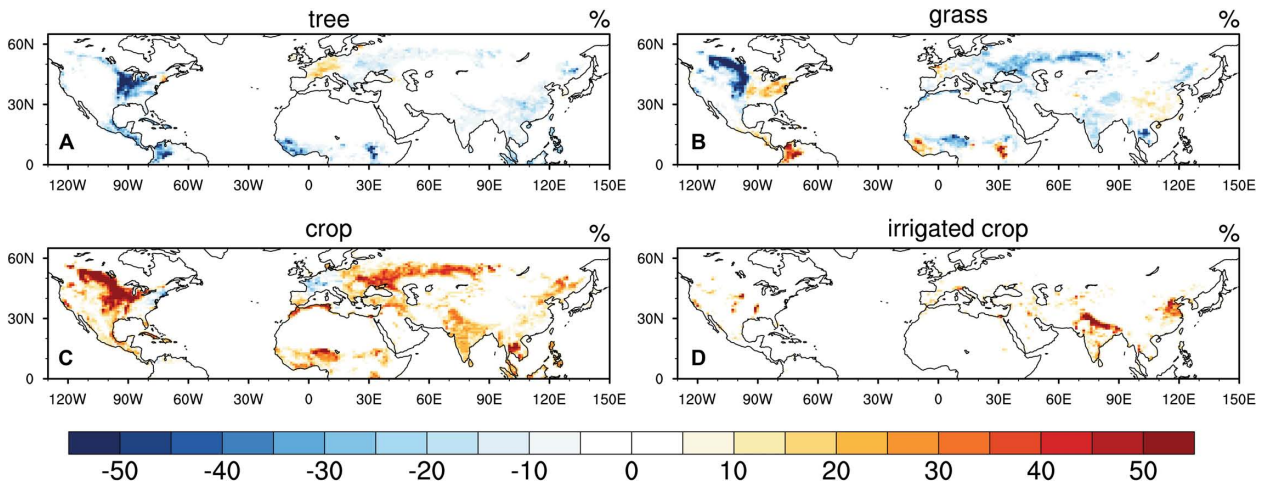

FIGURE 1 | Changes (% of each grid cell) in major plant functional types [PFTs: **(A)** tree, **(B)** grass, **(C)** crop] from pre-industrial to present day in the Northern Hemisphere, and areas (% of each grid cell) of the irrigated crop **(D)**.

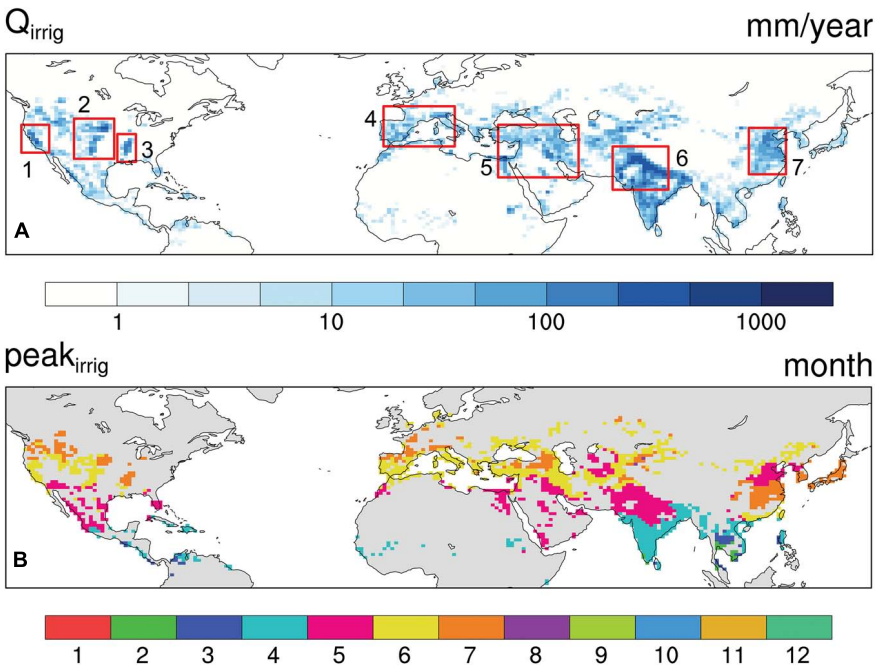

FIGURE 2 | Total amount of irrigated water (Q_{irrig} in mm/year) on a log scale **(A)** and the month with the highest irrigation rate **(B)**. The red boxes show the seven subregions: 1. California's Central Valley (CA), 2. the Great Plains (GP), 3. the Mississippi Embayment (MS), 4. Southern Europe (SE), 5. the Middle East (ME), 6. India (IN), and 7. Eastern China (EC).

not result in significant changes to either T_s or T_{2m}. In eastern China, although there is no significant change in daily maximum T_s, land use can significantly decrease daily maximum T_{2m}. Conversion of grassland into cropland over the Great Plains tends to substantially decrease both daily maximum T_s and T_{2m}. Additionally, grassland degradation in the Tibetan Plateau leads to significant warming.

During the night, there are consistent changes in T_s and T_{2m} (**Figures 3E,G**), which show a similar pattern to the changes in daily maximum T_s (**Figure 3A**). Significant cooling is found in the Great Plains and eastern Europe, while warming land surface and 2-m air are found in a majority of the deforested areas.

Irrigation activities can lead to a significant cooling at both the land surface and the 2-m air throughout the day, with greater changes in daytime temperatures. The cooling effects are more local, but comparable to (and even stronger than) the impacts of the historical land use. **Table 3** shows the regional changes in daily maximum and monthly mean T_{2m} and T_s due to historical

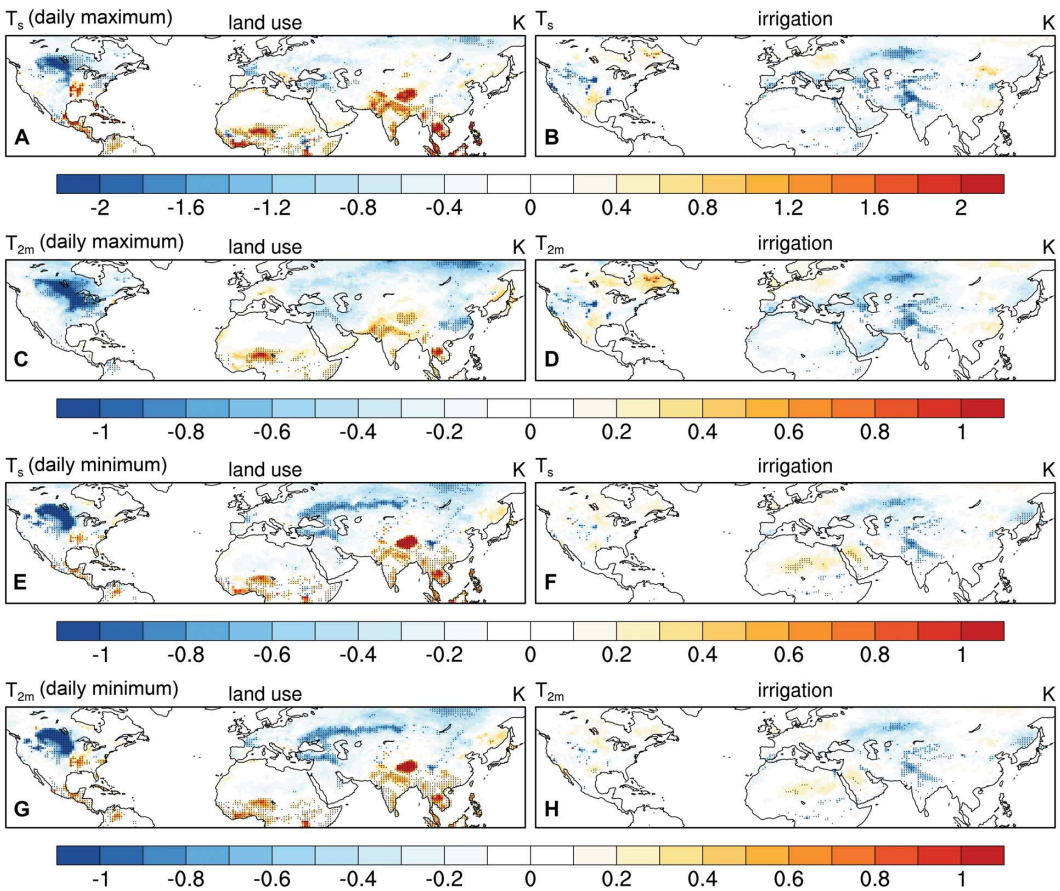

FIGURE 3 | Changes in summer daily maximum **(A–D)** and minimum **(E–H)** land surface temperature (T_s in K) and 2-m air temperature (T_{2m} in K) due to historical land use (left) and irrigation (right). Stippling indicates significance at the 95% confidence level.

TABLE 3 | Regional average temperature changes due to land use and irrigation in the irrigated grid cells (with total summertime irrigation greater than 30 mm) in seven sub-regions. Bold numbers indicate over half of the grid cells have statistically significant temperature changes at the 95% confidence level.

Sub-regions		CA	GP	MS	SE	ME	IN	EC
No. of grid cells		11	25	11	20	37	33	43
Q_{irrg} (mm)	irrigation	77.23	73.88	86.14	50.17	47.17	42.27	46.96
T_{2m} daytime(K)	land use	**−0.24**	**−0.73**	**−0.76**	−0.12	**−0.42**	**0.48**	−0.19
	irrigation	**−1**	**−0.81**	**−0.38**	−0.36	**−0.65**	**−0.51**	**−0.58**
T_s daytime (K)	land use	0.03	**−1.66**	**0.79**	−0.4	**−0.5**	**1.26**	0.27
	irrigation	**−2.12**	**−1.46**	**−0.88**	**−0.87**	**−1.29**	**−1.41**	**−0.95**
T_{2m} monthly (K)	land use	**−0.31**	**−0.8**	0.1	−0.14	**−0.46**	**0.48**	−0.01
	irrigation	**−0.8**	**−0.52**	−0.16	−0.23	**−0.48**	**−0.51**	**−0.49**
T_s monthly (K)	land use	−0.24	**−1.1**	**0.55**	−0.22	**−0.52**	**0.68**	0.13
	irrigation	**−1.19**	**−0.71**	−0.31	−0.4	**−0.7**	**−0.88**	**−0.61**

land use and irrigation in the irrigated regions, where land use usually also occurs during the historical period. For instance, the local cooling by irrigation can be up to 2.1 K on daily maximum T_s and 1.0 K on T_{2m} in California. In India, land use leads to significant land surface warming (about 1.3 K), while irrigation cools local temperature by 1.4 K. Only in the Mississippi Embayment and Great Plains does land use show greater impacts on daily maximum or monthly mean 2-m air than irrigation. In southern Europe, because of the mixed land use (both increased and decreased cropland) and relatively fewer areas with irrigation (**Figures 1C,D**), significant change is only manifested in the irrigation impacts on daily maximum T_s. There are also areas of warming away from the irrigated regions, which result from shifts in the general circulation driven by irrigation. Broader atmospheric effects are discussed further in section "Changes above the surface."

Changes in Surface Fluxes

To understand the mechanism of the temperature responses, we investigate the changes in the diurnal cycle of surface fluxes (**Figure 4** for daytime and **Figure 5** for nighttime). During the daytime, there is increased latent heat flux (LE) and decreased sensible heat flux (H) in the regions with the conversion of grassland to cropland (**Figure 4A**), such as the northern Great Plains, Eastern Europe, and northeastern China, where there is decreased T_s (**Figure 3A**). Increased LE is also found in the afforested regions, such as the northeastern US and western Europe, where there is a slight cooling at the land surface. In most areas of the tropics, deforestation leads to significantly decreased LE, suggesting the less evapotranspiration and consequently more H (**Figure 4C**) over the open land than the forest, resulting in a warming effect at the land surface (**Figure 3A**). However, in the United States Midwest, there is an evident decrease in H mainly due to decreased surface roughness after deforestation, which can explain the warming land surface but cooling of the air (**Figures 3A,C**).

Compared to LE and H, ground heat flux (G) responds to land use with relatively small magnitudes during the daytime. Therefore, its change is not a major factor influencing the daytime temperature change. Generally, deforestation leads to more heat flux stored in the ground, while afforestation or grassland conversion results in a reduction of heat entering the ground because of more surface available energy being used as latent heat flux. During nighttime, there is an upward ground heat flux. In other words, the heat stored in the soil layers during the daytime can feed back to the land surface and enter the lower atmosphere. Therefore, changes in G show opposite signs during the daytime and nighttime (**Figures 4E**, **5E**), and the nighttime T_s and T_{2m} (**Figures 3E,G**) are mainly determined by the changes in G.

Compared with land use, irrigation leads to consistently increased latent heat flux and decreased sensible heat flux throughout the day in the irrigated areas, especially in the Great Plains, California, and northwestern India (**Figures 5B,D**, **6B,D**). Reduced T_s and T_{2m} are mainly associated with the evaporative cooling of irrigation.

Changes Above the Surface

Land use and land management do not only modify the local land surface features; they are also able to influence the atmosphere and large-scale circulation. Therefore, the temperature changes (especially for T_{2m}) can also be associated with the atmospheric feedback to land use or land management. **Figure 6** shows the changes in summer total cloud cover and precipitation due to land use and irrigation. Land use leads to a significant increase in cloud cover and precipitation over the northern plains of North America and parts of eastern Europe, which corresponds to the cooling effects in those regions. A significant decrease in cloud cover and precipitation is found in northern India and tropical Africa, which corresponds to the land use-induced warming effects in those regions. Irrigation generally increases cloud cover in many regions, possibly due to enhanced local convective processes, but the significant increase in precipitation is only found in northwestern India and limited regions of the Great

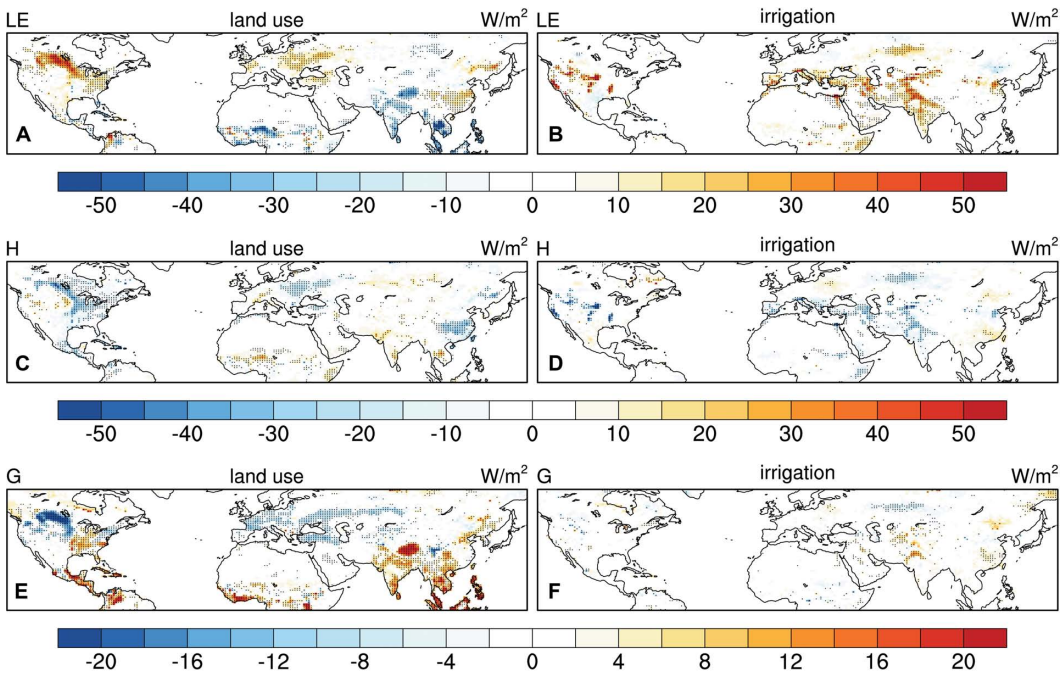

FIGURE 4 | Changes in summer daytime latent heat [LE in W/m^2, **(A,B)**], sensible heat [H in W/m^2, **(C,D)**], and ground heat [G in W/m^2, **(E,F)**] fluxes due to historical land use (left) and irrigation (right). Note that the scale of the label bar for G is different than those for LE and H. Stippling indicates significance at the 95% confidence level.

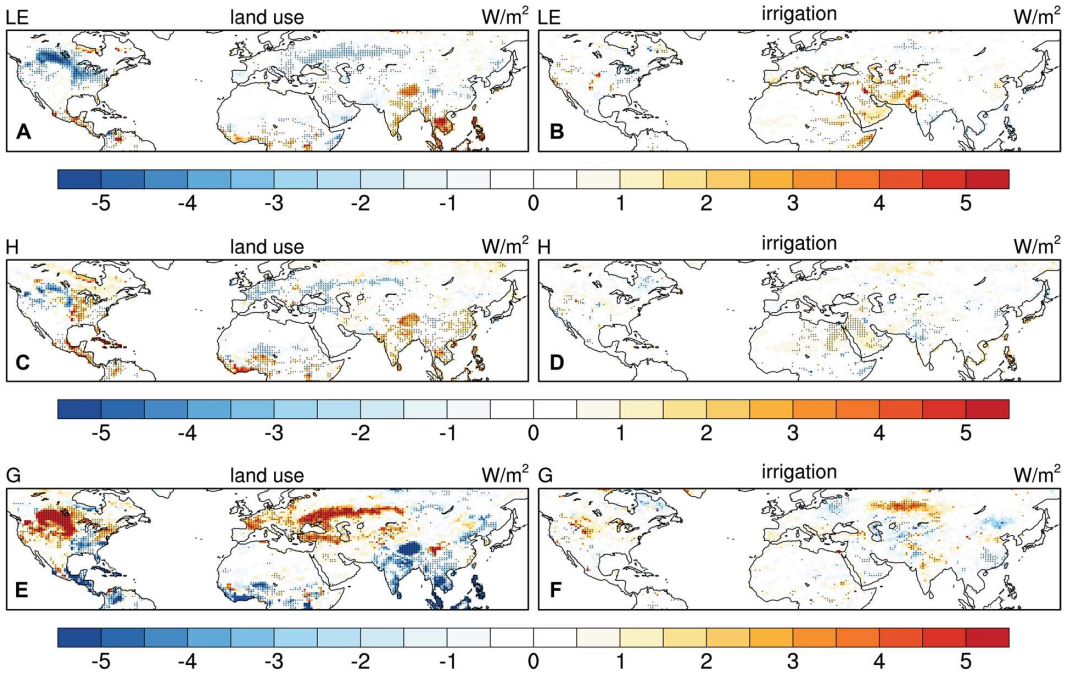

FIGURE 5 | Changes in summer nighttime latent heat [LE in W/m^2, **(A,B)**], sensible heat [H in W/m^2, **(C,D)**], and ground heat [G in W/m^2, **(E,F)**] fluxes due to historical land use (left) and irrigation (right). Stippling indicates significance at the 95% confidence level.

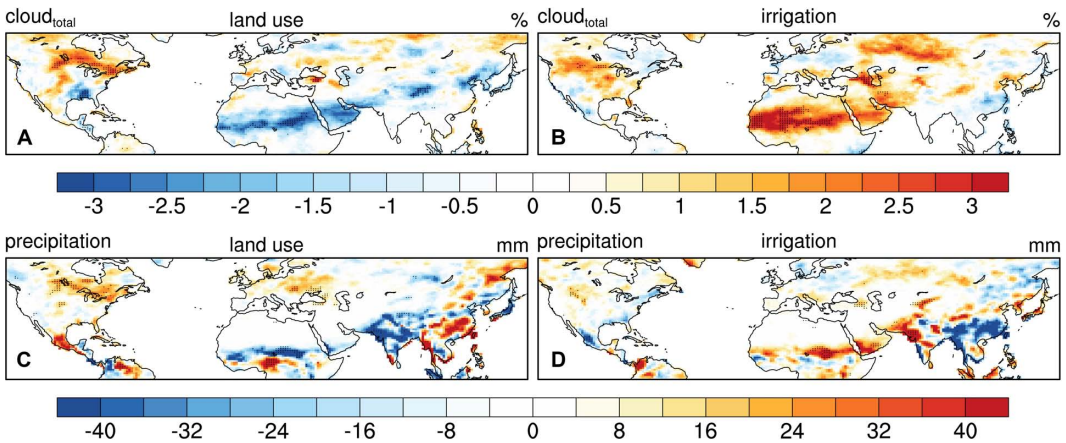

FIGURE 6 | Changes in summer monthly mean cloud cover [in %, **(A,B)**] and total precipitation [in mm, **(C,D)**] due to historical land use (left) and irrigation (right). Stippling indicates significance at the 95% confidence level.

Plains in the United States, which exhibit significant cooling effects of irrigation.

Although the changes in large-scale circulation and remote effects of land use/land management are not the scope of this study, the evident atmospheric feedback certainly demonstrates the impacts of land surface change on temperature through land-atmosphere interactions. For instance, the conversion of grassland into cropland in the northern plains of North America enhances evapotranspiration at the land surface, which exerts cooling effects based on the surface energy budget. On the other hand, higher evapotranspiration may lead to more cloud cover, which in turn decreases surface and near-surface temperature, and also potentially enhances precipitation, which further increases soil moisture and surface evapotranspiration.

Changes in Hot Extremes

We also examine the changes in hot extremes due to land use and land management (**Figure 7**). Generally, deforestation slightly reduces the intensity and frequency of hot events in middle latitudes during daytime, but leads to evidently more intense and frequent hot events during nighttime. The conversion of grassland into cropland, especially in the northern plains, shows

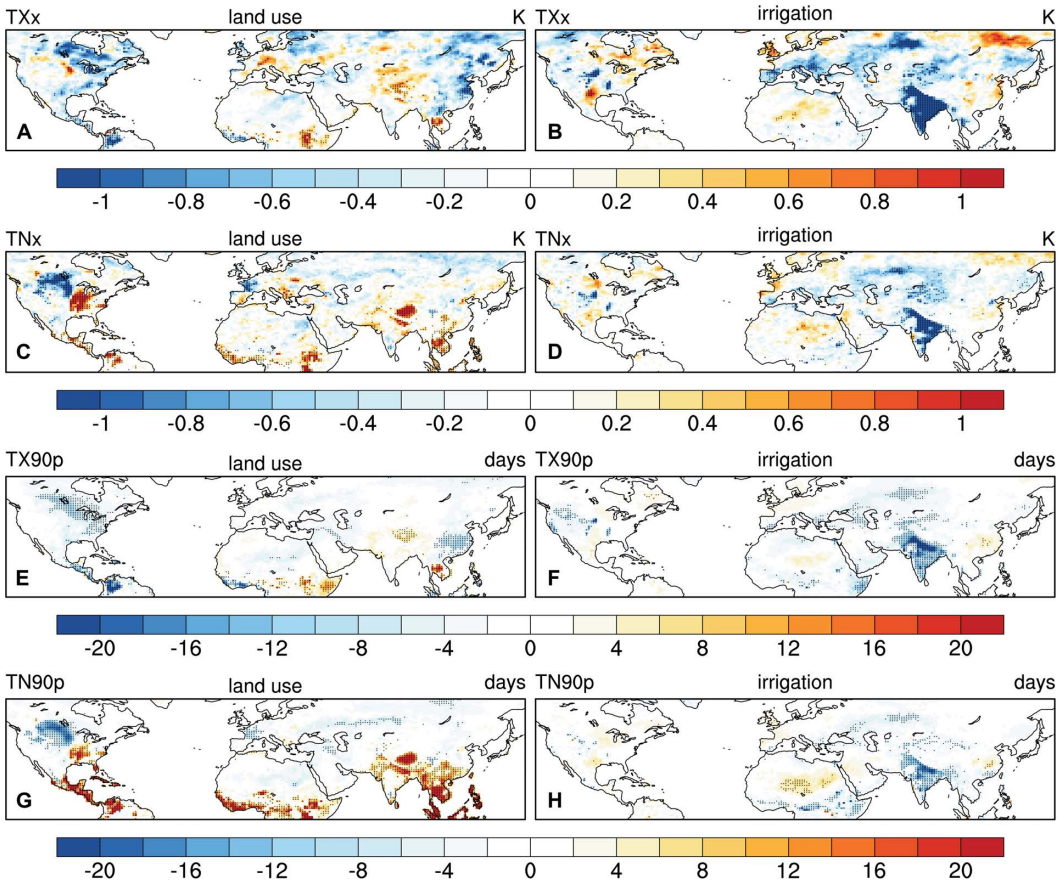

FIGURE 7 | Changes in warmest day [TXx in K, **(A,B)**], warmest night [TNx in K, **(C,D)**], number of warm days [TX90p in days, **(E,F)**] and number of warm nights [TN90p in days, **(G,H)**] due to historical land use (left) and irrigation (right). Stippling indicates significance at the 95% confidence level.

significantly reduced hot extremes. On the contrary, the impacts of irrigation on hot extremes are more evident during daytime. Significantly reduced hot extremes are found in the irrigated regions (except eastern China), where the irrigation-induced cooling can be stronger than the land-use impacts. It should be noted that maximum temperature in India occurs in late spring before the monsoon when there is a high irrigation demand. Therefore, strong cooling effects are found in this region, but are not manifested in the summertime temperature responses discussed in previous sections.

DISCUSSION AND CONCLUSION

This study presents a comparison between land use and irrigation with respect to their impacts on summer temperatures. Tropical deforestation shows an evident warming effect, especially at the land surface and during the nighttime. However, land-use impacts in the middle latitudes are dominated by the cooling effect of grassland conversion, while the extensive deforestation in the United States Midwest does not show strong impacts on local or regional temperature. A few caveats should be noted regarding the deforestation-temperature relationship. First, uncertainties still remain in current land surface models in representing the energy partitioning between latent and sensible heat flux (Chen et al., 2018; Cai et al., 2019). Unlike the observed decrease in ET after deforestation (Meier et al., 2018), the models suggest a slight increase in latent heat flux (**Figure 4A**), consequently exerting a cooling effect. Second, the model suggests a warmer land surface but cooler air mainly due to the decreased sensible heat flux after deforestation. The conversion of forest lands to agriculture reduces surface roughness and increases aerodynamic resistance, so the heat transfer becomes less efficient over the open land (Chen and Dirmeyer, 2019a). Consequently, less efficient turbulent heat exchange with the atmosphere leads to land surface warming (**Figure 3A**) but cooling of the lower-atmosphere (**Figure 3C**). The dominance of surface roughness (or aerodynamic resistance) in deforestation-induced biophysical effects has been documented in previous studies (Liao et al., 2018; Winckler et al., 2019a). The different responses in T_s and T_{2m} to deforestation are also found in another climate model (Winckler et al., 2019a). However, further assessments of land-use impacts on temperature are necessarily taken using multi-model experiments, such as The Land Use Model Intercomparison Project [LUMIP, (Lawrence et al., 2016)]. Furthermore, observation-based studies suggest

nighttime cooling (Schultz et al., 2017; Liao et al., 2018), which can be attributed to the decreased turbulence after deforestation and less heat aloft being brought to the surface (Lee et al., 2011). However, our results suggest nighttime warming of deforestation, which is mainly driven by the heat storage in the ground. Similar nighttime warming is also shown in other climate models (Vanden Broucke et al., 2015; Winckler et al., 2019b), suggesting ground heat flux and the nocturnal boundary layer need further attention in future model evaluation and development.

Meanwhile, a strong cooling effect is found in the irrigated areas, especially during the daytime and at the land surface. For instance, irrigation in California reduces daytime T_s by over 2 K. Such a cooling effect of irrigation is even greater than the land-use impacts in many regions (**Table 2**). Even though the irrigation-induced cooling is also confirmed through ground-based and satellite observations (Bonfils and Lobell, 2007; Lobell et al., 2008; Chen and Dirmeyer, 2019b), caution should be taken to interpret the simulated irrigation effects. The local cooling of irrigation can be even stronger if the model is run at a higher spatial resolution (Kueppers et al., 2007; Lobell et al., 2009; Sacks et al., 2009; Lo and Famiglietti, 2013; Lu and Kueppers, 2015; Huang and Ullrich, 2016; Chen and Dirmeyer, 2019b). For instance, there is up to 7 K of cooling due to irrigation over California based on a regional climate model (e.g., Kueppers et al., 2007), which highlights the impacts of irrigation at local or regional scales.

It also should be noted that uncertainties exist in current irrigation simulations. Observation-based studies suggest a nighttime warming in irrigated areas (Kanamaru and Kanamitsu, 2008; Chen and Jeong, 2018) because irrigation increases soil heat capacity (Kalnay and Cai, 2003) and thermal conductivity (Kanamaru and Kanamitsu, 2008), which allows more heat to be stored during daytime and released from the ground to the air during nighttime. Meanwhile, elevated moisture of the air would enhance downward longwave radiation, which would have a warming effect especially during night (Souri et al., 2020). In our results, although increased ground heat flux (implying more heat entered into the soil) is evident in the irrigated areas during daytime (**Figure 4F**), decreased ground heat flux (implying more heat released from the ground) is not found during nighttime (**Figure 5F**), and irrigation leads to a slight cooling in daily minimum temperature (**Figures 3F,H**). The issue with the simulated response of minimum temperature to irrigation has also been documented in other model-based studies (Kueppers et al., 2008; Huang and Ullrich, 2016). As ground heat flux is calculated from the residual of the surface energy balance in order to precisely conserve energy (Lawrence et al., 2018), the model bias may be associated with the uncertainties in surface flux parameterization in land surface models. The uncertainties in the representation of irrigation characteristics are also documented in other climate models, such as the Max Planck Institute for Meteorology's Earth System model (MPI-ESM), and regional climate models. The irrigation-induced temperature change can be highly related to the land-atmosphere coupling scheme used in the model, irrigation effectiveness, timing of irrigation (de Vrese and Hagemann, 2017). Kueppers et al. (2008) also found that the simulated effects of irrigation vary among different regional climate models due to different model physics and irrigation parameterizations. These factors should to considered in future assessments of irrigation impacts, and multiple-model approaches are necessary to further evaluate the uncertainties in the representation of irrigation in different Earth system models.

Additionally, there are possibly remote impacts of land use or irrigation on climate beyond the regions where the land use and land management occur. For instance, there are evident changes in temperature (**Figure 3**), evapotranspiration (**Figure 4**), cloud cover (**Figure 6**) in the northeast of Caspian Sea, although irrigation is only applied in the south of this region. Such a non-local effect of irrigation is also shown in previous studies using different climate models (e.g., Puma and Cook, 2010). Although many studies have discussed the remote effects of land use and land management (e.g., Wei et al., 2013; Badger and Dirmeyer, 2016; de Vrese et al., 2016; Swann et al., 2018), the detected remote effects can be influenced by many factors, such as the length of simulations (Swann et al., 2018), representation of ocean circulation (Badger and Dirmeyer, 2016; Krakauer et al., 2016), and model physics (de Vrese et al., 2016), which need further investigation in future studies.

Our results mainly present the climatic impacts of land use and land management during summer because of the strong land-atmosphere interactions and intensive agricultural practices in the warm season. We acknowledge land cover change also has significant impacts on temperature during winter, especially for boreal deforestation, which exerts a cooling effect through snow-albedo effects (Davin and de Noblet-Ducoudré, 2010); irrigation also occurs in winter in some regions and has the potential to alter temperature then (Chen and Jeong, 2018). **Supplementary Figure S2** shows a significant cooling in the deforested areas in the United States Midwest and Northern Plains and a significant warming effect of tropical deforestation during the boreal winter. However, no evident change in surface temperature is found in the irrigation regions in this study.

As the goal of this paper is to emphasize the relative importance of land management in regional climate (Thiery et al., 2017) and the implications in hot extreme adaptation under the background of global climate change (Hirsch et al., 2017), our results suggest that the local cooling effects of irrigation can be as strong as the land-use impacts during the boreal summer. As the cropland area is projected to continue growing in all the shared socioeconomic pathways (SSPs) in CMIP6 and about a half of the SSP scenarios suggest an increase in irrigated cropland area in the future (Lawrence et al., 2016), the importance of land management in local and regional climate will be amplified by potentially intensified irrigation activities under a warming climate. Additionally, considering the enhanced ET due to irrigation (**Figure 4B**), which can potentially raise wet-bulb temperatures (Kang and Eltahir, 2018), humidity should also be considered in future assessments of irrigation impacts on heat waves and their social impacts.

In summary, this study highlights the importance of irrigation in local and regional climate based on the experiments using the most recent version of CESM. It should be noted that other land management practices, such no-till farming

(Davin et al., 2014) or cover crops (Lombardozzi et al., 2018), may also have certain climatic consequences from the biogeophysical perspective through radiative processes. Also, there are many approaches to irrigation (e.g., surface irrigation, sprinklers including center-pivot irrigation, drip irrigation) drawing from both surface water and groundwater. Current models do not represent this variety, yet each has different potential effects on soil moisture and surface fluxes including evaporative cooling. Therefore, toward a comprehensive understanding of the climatic impacts of land management, different agricultural practices should be considered and compared when assessing regional-scale climate adaptation and mitigation (Lobell et al., 2006; Seneviratne et al., 2018).

DATA AVAILABILITY STATEMENT

The datasets generated for this study are available on request to the corresponding author.

AUTHOR CONTRIBUTIONS

LC and PD designed the study. LC performed the model simulations and the data analysis. Both authors contributed to the writing of the manuscript.

FUNDING

This study was supported by the National Science Foundation (AGS-1419445). LC was also supported by the Illinois State Water Survey, Prairie Research Institute at the University of Illinois in Urbana-Champaign.

ACKNOWLEDGMENTS

All views and opinions expressed do not necessarily reflect those of these institutions. We would like to acknowledge high-performance computing support from Cheyenne (doi: 10.5065/D6RX99HX) provided by NCAR's Computational and Information Systems Laboratory, sponsored by the National Science Foundation. The Community Earth System Model is freely available at http://www.cesm.ucar.edu/models/cesm2/. We also are grateful to the reviewers whose insightful comments helped improve our manuscript.

SUPPLEMENTARY MATERIAL

The Supplementary Material for this article can be found online at: https://www.frontiersin.org/articles/10.3389/feart.2020.00245/full#supplementary-material

REFERENCES

Alexander, L. V., Zhang, X., Peterson, T. C., Caesar, J., Gleason, B., Klein Tank, A. M. G., et al. (2006). Global observed changes in daily climate extremes of temperature and precipitation. *J. Geophys. Res.* 111, 1–22. doi: 10.1029/2005JD006290

Ambika, A. K., and Mishra, V. (2019). Observational evidence of irrigation influence on vegetation health and land surface temperature in India. *Geophys. Res. Lett.* 46, 13441–13451. doi: 10.1029/2019GL084367

Avila, F. B., Pitman, A. J., Donat, M. G., Alexander, L. V., and Abramowitz, G. (2012). Climate model simulated changes in temperature extremes due to land cover change. *J. Geophys. Res.* 117:D04108. doi: 10.1029/2011JD016382

Badger, A. M., and Dirmeyer, P. A. (2016). Diagnosing nonlinearities in the local and remote responses to partial Amazon deforestation. *J. Geophys. Res. Atmos.* 121, 9033–9047. doi: 10.1002/2015JD024013

Bonfils, C., and Lobell, D. (2007). Empirical evidence for a recent slowdown in irrigation-induced cooling. *Proc. Natl. Acad. Sci. U.S.A.* 104, 13582–13587. doi: 10.1073/pnas.0700144104

Boucher, O., Myhre, G., and Myhre, A. (2004). Direct human influence of irrigation on atmospheric water vapour and climate. *Clim. Dyn.* 22, 597–603. doi: 10.1007/s00382-004-0402-4

Brovkin, V., Boysen, L., Arora, V. K., Boisier, J. P., Cadule, P., Chini, L., et al. (2013). Effect of anthropogenic land-use and land-cover changes on climate and land carbon storage in CMIP5 projections for the twenty-first century. *J. Clim.* 26, 6859–6881. doi: 10.1175/JCLI-D-12-00623.1

Cai, X., Riley, W. J., Zhu, Q., Tang, J., Zeng, Z., Bisht, G., et al. (2019). Improving representation of deforestation effects on evapotranspiration in the E3SM land model. *J. Adv. Model. Earth Syst.* 11, 2412–2427. doi: 10.1029/2018MS001551

Chen, L., and Dirmeyer, P. A. (2018). The relative importance among anthropogenic forcings of land use/land cover change in affecting temperature extremes. *Clim. Dyn.* 52, 1–17. doi: 10.1007/s00382-018-4250-z

Chen, L., and Dirmeyer, P. A. (2019a). Differing responses of the diurnal cycle of land surface and air temperatures to deforestation. *J. Clim.* 32, 7067–7079. doi: 10.1175/JCLI-D-19-0002.1

Chen, L., and Dirmeyer, P. A. (2019b). Global observed and modelled impacts of irrigation on surface temperature. *Int. J. Climatol.* 39, 2587–2600. doi: 10.1002/joc.5973

Chen, L., Dirmeyer, P. A., Guo, Z., and Schultz, N. M. (2018). Pairing FLUXNET sites to validate model representations of land-use/land-cover change. *Hydrol. Earth Syst. Sci.* 22, 111–125. doi: 10.5194/hess-22-111-2018

Chen, X., and Jeong, S.-J. (2018). Irrigation enhances local warming with greater nocturnal warming effects than daytime cooling effects. *Environ. Res. Lett.* 13:024005. doi: 10.1088/1748-9326/aa9dea

Christidis, N., Stott, P. A., Hegerl, G. C., and Betts, R. A. (2013). The role of land use change in the recent warming of daily extreme temperatures. *Geophys. Res. Lett.* 40, 589–594. doi: 10.1002/grl.50159

Davin, E. L., and de Noblet-Ducoudré, N. (2010). Climatic impact of global-scale deforestation: radiative versus nonradiative processes. *J. Clim.* 23, 97–112. doi: 10.1175/2009JCLI3102.1

Davin, E. L., Seneviratne, S. I., Ciais, P., Olioso, A., and Wang, T. (2014). Preferential cooling of hot extremes from cropland albedo management. *Proc. Natl. Acad. Sci. U.S.A.* 111, 9757–9761. doi: 10.1073/pnas.1317323111

de Noblet-Ducoudré, N., Boisier, J.-P., Pitman, A., Bonan, G. B., Brovkin, V., Cruz, F., et al. (2012). Determining robust impacts of land-use-induced land cover changes on surface climate over North America and Eurasia: results from the First Set of LUCID experiments. *J. Clim.* 25, 3261–3281. doi: 10.1175/JCLI-D-11-00338.1

de Vrese, P., and Hagemann, S. (2017). Uncertainties in modelling the climate impact of irrigation. *Clim. Dyn.* 51, 1–16. doi: 10.1007/s00382-017-3996-z

de Vrese, P., Hagemann, S., and Claussen, M. (2016). Asian irrigation, African rain: remote impacts of irrigation. *Geophys. Res. Lett.* 43, 3737–3745. doi: 10.1002/2016GL068146

Di Vittorio, A. V., Chini, L. P., Bond-Lamberty, B., Mao, J., Shi, X., Truesdale, J., et al. (2014). From land use to land cover: restoring the afforestation signal in a coupled integrated assessment–earth system model and the implications for CMIP5 RCP simulations. *Biogeosciences* 11, 6435–6450. doi: 10.5194/bg-11-6435-2014

Gordon, L. J., Steffen, W., Jönsson, B. F., Folke, C., Falkenmark, M., and Johannessen, A. (2005). Human modification of global water vapor flows from the land surface. *Proc. Natl. Acad. Sci. U.S.A.* 102, 7612–7617. doi: 10.1073/pnas.0500208102

Hirsch, A. L., Wilhelm, M., Davin, E. L., Thiery, W., and Seneviratne, S. I. (2017). Can climate-effective land management reduce regional warming? *J. Geophys. Res. Atmos.* 122, 2269–2288. doi: 10.1002/2016JD026125

Huang, X., and Ullrich, P. A. (2016). Irrigation impacts on California's climate with the variable-resolution CESM. *J. Adv. Model. Earth Syst.* 8, 1151–1163. doi: 10.1002/2016MS000656

Hurrell, J. W., Hack, J. J., Shea, D., Caron, J. M., and Rosinski, J. (2008). A new sea surface temperature and sea ice boundary dataset for the community atmosphere model. *J. Clim.* 21, 5145–5153. doi: 10.1175/2008JCLI2292.1

Hurtt, G. C., Chini, L. P., Frolking, S., Betts, R. A., Feddema, J., Fischer, G., et al. (2011). Harmonization of land-use scenarios for the period 1500–2100: 600 years of global gridded annual land-use transitions, wood harvest, and resulting secondary lands. *Clim. Change* 109, 117–161. doi: 10.1007/s10584-011-0153-152

Hurtt, G. C., Frolking, S., Fearon, M. G., Moore, B., Shevliakova, E., Malyshev, S., et al. (2006). The underpinnings of land-use history: three centuries of global gridded land-use transitions, wood-harvest activity, and resulting secondary lands. *Glob. Change Biol.* 12, 1208–1229. doi: 10.1111/j.1365-2486.2006.01150.x

Kalnay, E., and Cai, M. (2003). Impact of urbanization and land-use change on climate. *Nature* 423, 528–531. doi: 10.1038/nature01675

Kanamaru, H., and Kanamitsu, M. (2008). Model Diagnosis of Nighttime Minimum Temperature Warming during Summer due to Irrigation in the California Central Valley. *J. Hydrometeor.* 9, 1061–1072. doi: 10.1175/2008JHM967.1

Kang, S., and Eltahir, E. A. B. (2018). North China Plain threatened by deadly heatwaves due to climate change and irrigation. *Nat. Commun.* 9:2894. doi: 10.1038/s41467-018-05252-y

Karl, T. R., Nicholls, N., and Ghazi, A. (1999). "CLIVAR/GCOS/WMO workshop on indices and indicators for climate extremes workshop summary," in *Weather and Climate Extremes*, eds T. R. Karl, N. Nicholls, and A. Ghazi (Dordrecht: Springer Netherlands), 3–7. doi: 10.1007/978-94-015-9265-9_2

Krakauer, N. Y., Puma, M. J., Cook, B. I., Gentine, P., and Nazarenko, L. (2016). Ocean–atmosphere interactions modulate irrigation's climate impacts. *Earth Syst. Dynam.* 7, 863–876. doi: 10.5194/esd-7-863-2016

Kueppers, L. M., Snyder, M. A., and Sloan, L. C. (2007). Irrigation cooling effect: regional climate forcing by land-use change. *Geophys. Res. Lett.* 34:L03703. doi: 10.1029/2006GL028679

Kueppers, L. M., Snyder, M. A., Sloan, L. C., Cayan, D., Jin, J., Kanamaru, H., et al. (2008). Seasonal temperature responses to land-use change in the western United States. *Glob. Planet. Change* 60, 250–264. doi: 10.1016/j.gloplacha.2007.03.005

Kumar, S., Dirmeyer, P. A., Merwade, V., DelSole, T., Adams, J. M., and Niyogi, D. (2013). Land use/cover change impacts in CMIP5 climate simulations: a new methodology and 21st century challenges. *J. Geophys. Res. Atmos.* 118, 6337–6353. doi: 10.1002/jgrd.50463

Lawrence, D., Fisher, R., Koven, C., Oleson, K., Swenson, S., and Vertenstein, M. (2018). *Technical Description of version 5.0 of the Community Land Model (CLM)*. Andhra Pradesh: National Center for Atmospheric Research.

Lawrence, D. M., Fisher, R. A., Koven, C. D., Oleson, K. W., Swenson, S. C., Bonan, G., et al. (2019). The Community Land Model version 5: description of new features, benchmarking, and impact of forcing uncertainty. *J. Adv. Model. Earth Syst.* 11, 4245–4287. doi: 10.1029/2018MS001583

Lawrence, D. M., Hurtt, G. C., Arneth, A., Brovkin, V., Calvin, K. V., Jones, A. D., et al. (2016). The Land Use Model Intercomparison Project (LUMIP) contribution to CMIP6: rationale and experimental design. *Geosci. Model Dev.* 9, 2973–2998. doi: 10.5194/gmd-9-2973-2016

Lawrence, P. J., and Chase, T. N. (2007). Representing a new MODIS consistent land surface in the Community Land Model (CLM 3.0). *J. Geophys. Res.* 112:G01023. doi: 10.1029/2006JG000168

Lawrence, P. J., Feddema, J. J., Bonan, G. B., Meehl, G. A., O'neill, B. C., Oleson, K. W., et al. (2012). Simulating the Biogeochemical and Biogeophysical Impacts of Transient Land Cover Change and Wood Harvest in the Community Climate System Model (CCSM4) from 1850 to 2100. *J. Clim.* 25, 3071–3095. doi: 10.1175/JCLI-D-11-00256.1

Lee, X., Goulden, M. L., Hollinger, D. Y., Barr, A., Black, T. A., Bohrer, G., et al. (2011). Observed increase in local cooling effect of deforestation at higher latitudes. *Nature* 479, 384–387. doi: 10.1038/nature10588

Lejeune, Q., Davin, E. L., Gudmundsson, L., Winckler, J., and Seneviratne, S. I. (2018). Historical deforestation locally increased the intensity of hot days in northern mid-latitudes. *Nat. Clim. Chang.* 8, 386–390. doi: 10.1038/s41558-018-0131-z

Lejeune, Q., Seneviratne, S. I., and Davin, E. L. (2017). Historical land-cover change impacts on climate: comparative assessment of LUCID and CMIP5 multimodel experiments. *J. Clim.* 30, 1439–1459. doi: 10.1175/JCLI-D-16-0213.1

Li, X., Chen, H., Wei, J., Hua, W., Sun, S., Ma, H., et al. (2018). Inconsistent responses of hot extremes to historical land use and cover change among the selected CMIP5 models. *J. Geophys. Res. Atmos.* 123, 3497–3512. doi: 10.1002/2017JD028161

Li, X. L., Gao, J., Brierley, G., Qiao, Y. M., Zhang, J., and Yang, Y. W. (2013). Rangeland degradation on the qinghai-tibet plateau: implications for rehabilitation. *Land Degrad. Dev.* 24, 72–80. doi: 10.1002/ldr.1108

Liao, W., Rigden, A. J., and Li, D. (2018). Attribution of local temperature response to deforestation. *J. Geophys. Res. Biogeosci.* 123, 1572–1587. doi: 10.1029/2018JG004401

Lo, M.-H., and Famiglietti, J. S. (2013). Irrigation in California's Central Valley strengthens the southwestern U.S. water cycle. *Geophys. Res. Lett.* 40, 301–306. doi: 10.1002/grl.50108

Lobell, D., Bala, G., Mirin, A., Phillips, T., Maxwell, R., and Rotman, D. (2009). Regional differences in the influence of irrigation on climate. *J. Clim.* 22, 2248–2255. doi: 10.1175/2008JCLI2703.1

Lobell, D. B., Bala, G., and Duffy, P. B. (2006). Biogeophysical impacts of cropland management changes on climate. *Geophys. Res. Lett.* 33: L06708. doi: 10.1029/2005GL025492

Lobell, D. B., Bonfils, C. J., Kueppers, L. M., and Snyder, M. A. (2008). Irrigation cooling effect on temperature and heat index extremes. *Geophys. Res. Lett.* 35:L09705. doi: 10.1029/2008GL034145

Lombardozzi, D. L., Bonan, G. B., Wieder, W., Grandy, A. S., Morris, C., and Lawrence, D. L. (2018). Cover crops may cause winter warming in snow-covered regions. *Geophys. Res. Lett.* 45:024005. doi: 10.1029/2018GL079000

Lu, Y., and Kueppers, L. (2015). Increased heat waves with loss of irrigation in the United States. *Environ. Res. Let.* 10:064010. doi: 10.1088/1748-9326/10/6/064010

Luyssaert, S., Jammet, M., Stoy, P., Estel, S., Pongratz, J., Ceschia, E., et al. (2014). Land management and land-cover change have impacts of similar magnitude on surface temperature. *Nat. Clim. Chang.* 4, 389–393. doi: 10.1038/nclimate2196

Mahmood, R., Pielke, R. A. Sr., Hubbard, K. G., Niyogi, D., Dirmeyer, P. A., et al. (2014). Land cover changes and their biogeophysical effects on climate. *Int. J. Climatol.* 34, 929–953. doi: 10.1002/joc.3736

Meier, R., Davin, E. L., Lejeune, Q., Hauser, M., Li, Y., Martens, B., et al. (2018). Evaluating and improving the Community Land Model's sensitivity to land cover. *Biogeosciences* 15, 4731–4757. doi: 10.5194/bg-15-4731-2018

Peterson, T. C., Folland, C., Gruza, G., Hogg, W., Mokssit, A., and Plummer, N. (2001). *Report on the Activities of the Working Group on Climate Change Detection and Related Rapporteurs 1998-2001*. Geneve: WMO.

Pitman, A. J., de Noblet-Ducoudré, N., Avila, F. B., Alexander, L. V., Boisier, J.-P., Brovkin, V., et al. (2012). Effects of land cover change on temperature and rainfall extremes in multi-model ensemble simulations. *Earth Syst. Dynam.* 3, 213–231. doi: 10.5194/esd-3-213-2012

Portmann, F. T., Siebert, S., and Döll, P. (2010). MIRCA2000-Global monthly irrigated and rainfed crop areas around the year 2000: a new high-resolution data set for agricultural and hydrological modeling. *Global Biogeochem. Cycles* 24:GB1011. doi: 10.1029/2008GB003435

Puma, M. J., and Cook, B. I. (2010). Effects of irrigation on global climate during the 20th century. *J. Geophys. Res.* 115:D16120. doi: 10.1029/2010JD014122

Sacks, W. J., Cook, B. I., Buenning, N., Levis, S., and Helkowski, J. H. (2009). Effects of global irrigation on the near-surface climate. *Clim. Dyn.* 33, 159–175. doi: 10.1007/s00382-008-0445-z

Schultz, N. M., Lawrence, P. J., and Lee, X. (2017). Global satellite data highlights the diurnal asymmetry of the surface temperature response to deforestation. *J. Geophys. Res. Biogeosci.* 122, 903–917. doi: 10.1002/2016JG003653

Seneviratne, S. I., Phipps, S. J., Pitman, A. J., Hirsch, A. L., Davin, E. L., Donat, M. G., et al. (2018). Land radiative management as contributor to regional-scale climate adaptation and mitigation. *Nat. Geosci.* 11, 88–96. doi: 10.1038/s41561-017-0057-5

Singh, D., McDermid, S. P., Cook, B. I., Puma, M. J., Nazarenko, L., and Kelley, M. (2018). Distinct influences of land cover and land management on seasonal climate. *J. Geophys. Res. Atmos.* 123, 12017–12039. doi: 10.1029/2018JD028874

Sorooshian, S., Li, J., Hsu, K., and Gao, X. (2011). How significant is the impact of irrigation on the local hydroclimate in California's Central Valley? Comparison of model results with ground and remote-sensing data. *J. Geophys. Res.* 116:D06107. doi: 10.1029/2010JD014775

Souri, A. H., Wang, H., González Abad, G., Liu, X., and Chance, K. (2020). Quantifying the impact of excess moisture from transpiration from crops on an extreme heat wave event in the midwestern U.S.: a top-down constraint from moderate resolution imaging spectroradiometer water vapor retrieval. *J. Geophys. Res. Atmos.* 125:e2019JD031941. doi: 10.1029/2019JD031941

Swann, A. L. S., Laguë, M. M., Garcia, E. S., Field, J. P., Breshears, D. D., Moore, D. J. P., et al. (2018). Continental-scale consequences of tree die-offs in North America: identifying where forest loss matters most. *Environ. Res. Lett.* 13:055014. doi: 10.1088/1748-9326/aaba0f

Thiery, W., Davin, E. L., Lawrence, D. M., Hirsch, A. L., Hauser, M., and Seneviratne, S. I. (2017). Present-day irrigation mitigates heat extremes. *J. Geophys. Res. Atmos.* 122, 1403–1422. doi: 10.1002/2016JD025740

Vanden Broucke, S., Luyssaert, S., Davin, E. L., Janssens, I., and Lipzig, N. (2015). New insights in the capability of climate models to simulate the impact of LUC based on temperature decomposition of paired site observations. *J. Geophys. Res. Atmos.* 120, 5417–5436. doi: 10.1002/2015JD023095

Wei, J., Dirmeyer, P. A., Wisser, D., Bosilovich, M. G., and Mocko, D. M. (2013). Where does the irrigation water go? an estimate of the contribution of irrigation to precipitation using MERRA. *J. Hydrometeor* 14, 275–289. doi: 10.1175/JHM-D-12-079.1

Winckler, J., Reick, C. H., Bright, R. M., and Pongratz, J. (2019a). Importance of surface roughness for the local biogeophysical effects of deforestation. *J. Geophys. Res. Atmos.* 124, 8605–8618. doi: 10.1029/2018JD030127

Winckler, J., Reick, C. H., Luyssaert, S., Cescatti, A., Stoy, P. C., Lejeune, Q., et al. (2019b). Different response of surface temperature and air temperature to deforestation in climate models. *Earth Syst. Dynam.* 10, 473–484. doi: 10.5194/esd-10-473-2019

Conflict of Interest: The authors declare that the research was conducted in the absence of any commercial or financial relationships that could be construed as a potential conflict of interest.

The reviewer ED declared a past co-authorship with one of the authors PD to the handling Editor.

frontiers in Marine Science

ORIGINAL RESEARCH
published: 31 August 2020
doi: 10.3389/fmars.2020.00712

Cardinal Buoys: An Opportunity for the Study of Air-Sea CO_2 Fluxes in Coastal Ecosystems

*Jean-Philippe Gac[1], Pierre Marrec[2], Thierry Cariou[1], Christophe Guillerm[3], Éric Macé[1], Marc Vernet[1] and Yann Bozec[1]**

[1] CNRS, Sorbonne Université, UMR 7144 AD2M, Station Biologique de Roscoff, Roscoff, France, [2] Graduate School of Oceanography, University of Rhode Island, Narragansett, RI, United States, [3] Division Technique INSU/CNRS, Technopôle Brest Iroise, Plouzané, France

From 2015 to 2019 we installed high-frequency (HF) sea surface temperature (SST), salinity, fluorescence, dissolved oxygen (DO) and partial pressure of CO_2 (pCO_2) sensors on a cardinal buoy of opportunity (ASTAN) at a coastal site in the southern Western English Channel (sWEC) highly influenced by tidal cycles. The sensors were calibrated against bimonthly discrete measurements performed at two long-term time series stations near the buoy, thus providing a robust multi-annual HF dataset. The tidal transport of a previously unidentified coastal water mass and an offshore water mass strongly impacted the daily and seasonal variability of pCO_2 and pH. The maximum tidal variability associated to spring tides (>7 m) during phytoplankton blooms represented up to 40% of the pCO_2 annual signal at ASTAN. At the same time, the daily variability of 0.12 pH units associated to this tidal transport was 6 times larger than the annual acidification trend observed in the area. A frequency/time analysis of the HF signal revealed the presence of a day/night cycle in the tidal signal. The diel biological cycle accounted for 9% of the annual pCO_2 amplitude during spring phytoplankton blooms. The duration and intensity of the biologically productive periods, characterized by large inter-annual variability, were the main drivers of pCO_2 dynamics. HF monitoring enabled us to accurately constrain, for the first-time, annual estimates of air-sea CO_2 exchanges in the nearshore tidally-influenced waters of the sWEC, which were a weak source to the atmosphere at 0.51 mol CO_2 m^{-2} yr^{-1}. This estimate, combined with previous studies, provided a full latitudinal representation of the WEC (from 48°75′ N to 50°25′ N) over multiple years for air-sea CO_2 fluxes in contrasted coastal ecosystems. The latitudinal comparison showed a clear gradient from a weak source of CO_2 in the tidal mixing region toward sinks of CO_2 in the stratified region with a seasonal thermal front separating these hydrographical provinces. In view of the fact that several continental shelf regions have been reported to have switched from sources to sinks of CO_2 in the last century, weak CO_2 sources in such tidal mixing areas could potentially become sinks of atmospheric CO_2 in coming decades.

Keywords: buoy of opportunity, high-frequency, tidal cycle, multi-annual, air-sea CO_2 exchanges, ocean acidification, coastal ecosystems

OPEN ACCESS

Edited by:
Masao Ishii, Meteorological Research Institute (MRI), Japan

Reviewed by:
Adrienne J. Sutton, Pacific Marine Environmental Laboratory (NOAA), United States
Shinya Kouketsu, Japan Agency for Marine-Earth Science and Technology (JAMSTEC), Japan

****Correspondence:***
Yann Bozec
bozec@sb-roscoff.fr

Specialty section:
This article was submitted to Ocean Observation, a section of the journal Frontiers in Marine Science

Received: *22 May 2020*
Accepted: *04 August 2020*
Published: *31 August 2020*

Citation:
Gac J-P, Marrec P, Cariou T, Guillerm C, Macé É, Vernet M and Bozec Y (2020) Cardinal Buoys: An Opportunity for the Study of Air-Sea CO_2 Fluxes in Coastal Ecosystems. Front. Mar. Sci. 7:712. doi: 10.3389/fmars.2020.00712

INTRODUCTION

The dynamics of the carbonate system in the ocean are complex and simultaneously controlled by physical, chemical, and biological processes (Zeebe and Wolf-Gladrow, 2001). As an interface between land, ocean, and atmosphere, coastal ecosystems are characterized by strong physical and biogeochemical heterogeneity, introducing further complexity into the coastal carbon cycle and carbonate system dynamics (Walsh, 1991; Gattuso et al., 1998; Muller-Karger et al., 2005). Despite representing only 7% of the global ocean, coastal ecosystems are a key component of the global carbon cycle because of their disproportionately high rates of primary production (10–30%) and organic matter remineralization (Walsh et al., 1988; de Haas et al., 2002; Bauer et al., 2013). The coastal ocean therefore exhibits enhanced air-sea CO_2 fluxes (FCO_2) compared to open oceans (Tsunogai et al., 1999; Thomas et al., 2004; Chen and Borges, 2009). According to the most recent estimates, during the 1998–2015 period coastal ecosystems were a global CO_2 sink of 0.20 ± 0.02 Pg C yr^{-1} compared to a net CO_2 sink of 1.7 ± 0.3 Pg C yr^{-1} for the open ocean (Roobaert et al., 2019). Coastal ecosystems account for 13% of the total CO_2 sink despite representing a much lower proportion of global ocean surface area (7%). In terms of anthropogenic CO_2 sink, coastal ecosystems represent 4.5% (Bourgeois et al., 2016) of the latest estimates of 2.6 ± 0.3 Pg C yr^{-1} for the 1994–2007 period (Gruber et al., 2019) and 2.6 ± 0.6 Pg C yr^{-1} for the last decade (Friedlingstein et al., 2019). Due to their proximity with human activities, coastal ecosystems are also particularly vulnerable to anthropogenic forcing such as eutrophication and ocean acidification (OA) (Borges and Gypens, 2010; Borges et al., 2010; Cai et al., 2011, 2017; Bauer et al., 2013). Coastal ecosystems can show extremes of OA hotspots due to the intrusion of acidified water with low saturation state Ω_{arag} (Feely et al., 2016, 2010; Chan et al., 2017; Fennel et al., 2019) or conversely constitute refuge with more stable pH (Chan et al., 2017).

In the context of climate change and continuous atmospheric CO_2 increase, unraveling CO_2 system dynamics and air-sea CO_2 fluxes in coastal ecosystems remains a major challenge (Laruelle et al., 2018). Long-term high-frequency (HF) monitoring of the carbonate system in coastal ecosystems is essential to distinguish natural variability from responses to anthropogenically induced changes at various temporal and spatial scales (Borges et al., 2010; Ciais et al., 2014). Extreme or short-scale events may affect mean estimates of coastal carbon fluxes, thus budgets based on short time-series of observations should seldom be viewed with caution (Salisbury et al., 2009). In the past decade, autonomous moorings and observing platforms considerably improved estimates of air-sea CO_2 fluxes at various time and spatial scales to better constrain carbon budgets in coastal ecosystems (Sutton et al., 2014; Xue et al., 2016; Reimer et al., 2017). Recent technical advances in terms of measurement of partial pressure of surface CO_2 (pCO_2) and pH (Sastri et al., 2019) mean that it is now possible to develop accurate long-term records of these parameters in nearshore ecosystems. Combining HF measurements of pH or pCO_2 with discrete carbonate system parameters (DIC/TA) can be a valuable tool for carbon cycle research based on autonomous moorings (Cullison Gray et al., 2011). This type of calibrated data could then potentially be included in large international databases such as the Surface Ocean CO_2 Atlas (SOCAT, Bakker et al., 2016).

A key challenge for the scientific community focusing on the coastal marine environment is to integrate observations of essential ocean variables for physical, biogeochemical, and biological processes on appropriate spatial and temporal scales, in a sustained and scientifically based manner (Farcy et al., 2019). The European projects JERICO and JERICO-Next (2010–2020) built an integrated and innovation-driven coastal research infrastructure for Europe, notably for the observation of the carbonate system parameters, based on Voluntary Observation Ships (VOS), long-term time series, and buoys of opportunity (Puillat et al., 2016; Farcy et al., 2019). From 2011 to 2015, a VOS program provided seasonal and latitudinal HF measurements across the Western English Channel (WEC), enabling first assessments of air-sea CO_2 fluxes (FCO_2) dynamics in the WEC and adjacent coastal seas (Marrec et al., 2013, 2014, 2015). As part of the French network for the monitoring of coastal environments (SOMLIT[1]), two long-term time-series in the WEC off Roscoff have been implemented to monitor carbonate parameters at SOMLIT-pier and SOMLIT-offshore stations. Sampling in this program is bimonthly and can therefore miss specific, short-term events occurring between scheduled sampling dates. In the framework of the national program COAST-HF (Coastal Ocean Observing System-High Frequency[2]), the cardinal buoy of opportunity "ASTAN," located halfway between the two SOMLIT sampling sites, was equipped with oceanographic and meteorological sensors to complete the discrete sampling.

This study describes the benefits and challenges of deploying and maintaining a HF autonomous coastal observation platform of opportunity. We report the results of 5 years of HF pCO_2 and ancillary data recorded at the ASTAN buoy and 5 years of low frequency monitoring of similar parameters at the SOMLIT-pier and SOMLIT-offshore sites. We examine the dynamics of sea surface pCO_2 and associated FCO_2 from tidal to inter-annual timescales. We identify the main factors controlling pCO_2 variability at short timescales using frequency analysis and quantify the impact of the tidal and diel cycles on CO_2 system dynamics. Ultimately, we place the annual FCO_2 data in a broader context to fully describe the latitudinal variability of FCO_2 throughout the WEC.

STUDY SITE

The WEC is part of the North-West European continental shelf, one of the world's largest temperate margins, and is a pathway between the North Atlantic and the North Sea. High salinity and relatively warm waters from the North Atlantic Drift flow eastward to the western Channel entrance (Salomon and Breton, 1993). The WEC is characterized by three distinct hydrographical

[1]http://somlit.epoc.u-bordeaux1.fr/
[2]http://coast-hf.fr

regimes: permanently well-mixed waters in the southern WEC (sWEC), seasonally stratified waters in the northern WEC (nWEC) and a frontal structure separating these hydrographical provinces (Pingree and Griffiths, 1978). The intense tidal streams permanently mix the water column from the bottom to the surface all year round in the sWEC, although weak and brief stratification can occur during summer, particularly during neap tides with low wind velocity (L'Helguen et al., 1996; Guilloux et al., 2013). Many rivers and estuaries discharge freshwater into the sWEC, with enhanced river influx during winter due to intense precipitation (Tréguer et al., 2014). These freshwater inputs release nutrient stocks into the marine environment (Meybeck et al., 2006; Dürr et al., 2011; Tréguer and De La Rocha, 2013) fueling spring phytoplankton blooms (e.g., Del Amo et al., 1997; Beucher et al., 2004) and maintaining substantial primary productivity in summer, when light is the limiting factor, not nutrients (Wafar et al., 1983).

The ASTAN buoy is a cardinal buoy of opportunity located 3.1 km offshore from Roscoff (48°44′55″ N; 3°57′40″ W, **Figure 1**), east of the Batz Island. The mean bathymetry is around 45 m. This location is characterized by strong tidal streams with a tidal range up to 8 m during spring tides. The weather conditions can be rough with frequent gusts of wind and storms making work at sea difficult, especially on a mooring. During winter storms, the swell and waves north of the Batz Island can reach 6–7 m high, but the mooring is somewhat protected by the island from swell from the North Atlantic Ocean.

Two low-frequency stations are present either side of the HF buoy (**Figure 1**), with SOMLIT-pier located south of the buoy (48:43′59″ N; 3:58′58″ W) and SOMLIT-offshore located north (48:46′49″ N; 3:58′14″ W). Despite their close proximity, these two stations are quite different. SOMLIT-pier is located very close to the coast, strongly influenced by coastal waters, with a particular hydrodynamic regime: a strong tidal range and a low water column (around 5 m). SOMLIT-offshore is characteristic of sWEC surface waters with a well-mixed water column (around 60 m), with the distance from the coast (3.5 km) limiting the impact of rainwater and river inflow.

MATERIALS AND METHODS

High-Frequency Measurements From the ASTAN Buoy

From 2015 to 2019, conductivity and temperature were recorded every 30 min using a SBE16 + (SeaBird, Inc.) instrument. A Cyclops7 fluorimeter (Turner Designs, Inc.) and a SBE43 sensor (Seabird, Inc.) measured at the same frequency Chl-a fluorescence and DO, respectively. The manufacturer accuracies were ± 0.005°C for the temperature sensor, 2% for oxygen saturation and 0.0005 S/m for conductivity. TBTO® anti-fouling cylinders and black Tygon® tubing were installed in the pumping circuit to prevent biofouling, which is a major issue for deployment of sensors in coastal water, with a critical period from May to September.

A Submersible Autonomous Moored Instrument for CO_2 (SAMI-CO_2, SunBurst Sensors) was installed from March 2015 to December 2019 to measure pCO_2 in seawater with a 1-h frequency. The SAMI-CO_2 sensor uses calibrated reagent-based colorimetry to measure the change in pH of the dye [bromothymol blue (BTB)]. The BTB is contained in a gas-permeable membrane that is exposed to the environment. The pH change is driven by diffusion of CO_2 across the membrane. The dye absorbance is recorded at two wavelengths, corresponding to the absorption peaks of acid/base forms of BTB. Blank measurements were performed regularly in distilled water for quality control. The accuracy of measurements reported by the manufacturer is ± 8 μatm (DeGrandpre et al., 1997). All sensors were recovered every 3 months for inspection, cleaning, battery checks and control of reagent levels.

Bimonthly Measurements at Fixed Stations SOMLIT-Pier and SOMLIT-Offshore

From March 2015 to December 2019, bimonthly sampling was performed at SOMLIT-pier and SOMLIT-offshore fixed stations (**Figure 1**) during neap tides and at high tide slack. CTD profiles were obtained with a Seabird SBE19 + with accuracies for temperature and computed salinity of 0.005°C and 0.002 respectively. Discrete seawater was sampled using 10 L Niskin bottle. Salinity measurements were performed by sampling seawater in glass bottles with a rubber seal and analyzed in the following months in a temperature regulated room with a portasal Guidline Salinometer at the SHOM (Service Hydrographique et Oceanographique de la Marine) with an accuracy of 0.002. For DO measurements seawater from the Niskin bottle was transferred into 280 mL brown glass bottles that were sealed with special caps to remove all air after addition of 1.7 mL of Winkler reagent I and II. Bottles were kept in the dark in a water bath and analyzed by the Winkler method using potentiometric end-point determination using a Metrohm titrator. The estimated accuracy of this method is 0.2 μM (Carpenter, 1965). For Chl-a measurements 500 ml of seawater were filtered through a GF/F (Whatman) glass filter under 0.2 bar vacuum. The filters were stored in a plastic tube at −20°C before analysis. The EPA (1997) extraction method was used in which Chl-a was extracted in a 90% acetone solution for a few hours at 4°C, followed by measurement of Chl-a concentration using a Turner AU10 fluorometer. Nutrient concentrations (PO_4^{3-} and SiO_4^-) were determined using an AA3 auto-analyzer (AXFLOW) following the method of Aminot and Kérouel (2007) with accuracies of 1 ng L^{-1} and 0.01 μg L^{-1} for PO_4^{3-} and SiO_4^-, respectively. During the same period, total alkalinity (TA), dissolved inorganic carbon (DIC) and pH were measured at SOMLIT-pier and SOMLIT-offshore stations. Seawater was sampled in 500 mL borosilicate glass bottles and poisoned with 50 μL of saturated $HgCl_2$. TA and the DIC were determined at the SNAPO (Service National d'Analyse des Paramètres Océaniques) using potentiometric analysis following the Edmond (1970) method and DOE (1994) with accuracies of 2.5 μmol kg^{-1} for both parameters (see Marrec et al., 2013 for details on this method). pH was determined using the same protocol as for the ASTAN buoy measurements (see below).

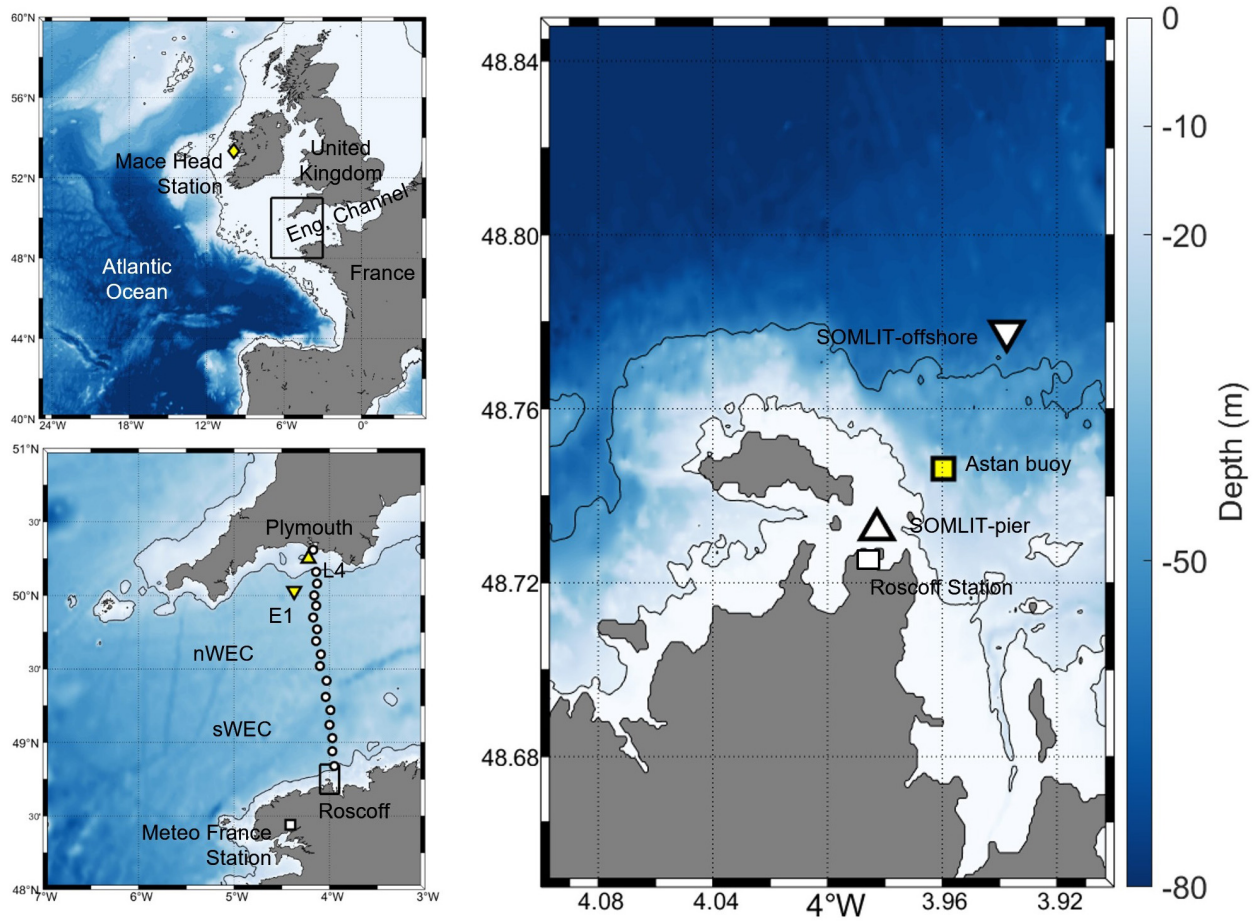

FIGURE 1 | (Right) Map and bathymetry (5 and 50 m isobaths) of the study area in the sWEC with the location of the ASTAN buoy (yellow square) with the two SOMLIT sampling sites: SOMLIT-pier (upward triangle) and SOMLIT-offshore (downward triangle) and the location of the Roscoff observatory. **(Top left)** Map and bathymetry (200 m isobath) of the North Atlantic Ocean with the location of the Mace Head atmospheric station, the black frame represents the WEC. **(Bottom left)** Map and bathymetry (50 m isobath) of the WEC with the Meteo France station (white square) for wind speed data, E1 (downward triangle), L4 (upward triangle) and FerryBox transect from Roscoff to Plymouth used in the comparison of FCO_2 in Section "Dynamics of FCO_2 in the WEC" and **Figure 10**.

From March 2017 to December 2019, additional sampling for pH and TA in the vicinity of the ASTAN buoy was performed every 2 weeks. 50 discrete samples for the determination of TA and pH were collected in 500 mL borosilicate glass bottles and poisoned with 50 µL of saturated $HgCl_2$. TA was determined from approximately 51 g of weighed sample at 25°C using a potentiometric titration with 0.1M HCl using a Titrino 847 plus Metrohm. The balance point was determined by the Gran method (Gran, 1952) according to the method of Haraldsson et al. (1997). The accuracy of this method is $\pm$ 2.1 µmol kg^{-1} (Millero, 2007) and was verified by Certified Reference Material (CRM 131) provided by A. Dickson (Scripps Institute of Oceanography, University of South California, San Diego, United States). pH was determined with an accuracy of 0.002 pH units by spectrophotometry (Perin-Elmer Lambda 11) at a controlled temperature of 25°C with the method of Clayton and Byrne (1993) and corrected by Chierici et al. (1999), using the sulfonephthaleindiprotic indicator of meta-CresolPurple (mCP).

Calculated Data

Dissolved Oxygen Saturation

Calculation of dissolved oxygen saturation (DO%) gives access to the impact of non-thermodynamical processes, such as biological production and respiration, on the variation of DO. The DO% was calculated from Eq. 1 using *in situ* temperature, salinity, and dissolved oxygen concentrations.

$$In\,C^* = A_1 + (\frac{A_2 \times T}{100}) + [A_3 \times \log(\frac{T}{100})]$$
$$+S \times [(B_1 + (B_2 \times \frac{T}{100}) + B_3 \times (\frac{T}{100})^2)]$$
$$DO\% = (\frac{DO}{C^*}) \times 100 \quad (1)$$

Where C^* is the concentration of DO at saturation, A and B coefficients are constants described in Weiss (1970), T is the SST (in K) and S the sea surface salinity (SSS).

Carbonate System Parameters

At the ASTAN buoy, we used the combination of TA, pH, SSS and SST as input parameters in the CO_2 chemical speciation model (CO_{2sys} Program, Pierrot et al., 2011). We used the equilibrium constants of CO_2 proposed by Mehrbach et al. (1973), refitted by Dickson and Millero (1987) on the total pH scale, as recommended by Dickson et al. (2007) and Orr et al. (2015), and including PO_4^{3-} and SiO_4^- concentrations. At SOMLIT-pier and SOMLIT-offshore, from January 2015 to April 2018, we used the combination of TA, DIC, SSS, SST, PO_4^{3-} and SiO_4^- concentrations, and from May 2018 to December 2019 we used the combination of pH, DIC, SSS, SST and PO_4^{3-} and SiO_4^- concentrations as input parameters in the model. We use the standard uncertainty propagation package updated by Orr et al. (2018) for comparison with current computations of uncertainty on the carbonate system parameters in the field of OA. The average uncertainty on pCO_{2calc} were estimated at 11 µatm for TA/pH, at 18 µatm for DIC/TA and at 8 µatm for pH/DIC. These uncertainties were in agreement with similar pCO_{2calc} computations using the propagation technique: 20 µatm for Shadwick et al. (2019) and 15 µatm for Kapsenberg et al. (2017) with DIC/TA as entry parameters.

To estimate pH variations from pCO_2 at the ASTAN buoy (pH_{calc}), we relied on 20 seasonal surveys performed in 2011, 2019 and 2020, when we collected more than 150 data points for TA and SSS covering the entire SSS gradient (0–35.5) in the Penzé and Morlaix rivers, the main sources of freshwater input at our study site. We combined these data with the 2016 discrete dataset marked by intense freshwater inputs at the ASTAN site with important rainfall (563 mm during that winter compared to 274 mm during 2019), and SSS varying from 34.50 to 35.50. We were able to establish a very robust relationship between TA and SSS (n = 236, r^2 = 0.98) with the following equation 2 (**Supplementary Figure S1**):

$$TA_{calc} = 50.4(\pm 0.5)^{*}SSS + 575(\pm 14) \quad (2)$$

We therefore estimated the HF pH with CO_{2sys} using the same parameters SST, SSS, pCO_2 and TA_{calc}. We compared the discrete pH values obtained in 2019 at the ASTAN buoy with the spectrophotometric technique [precision of 0.001 and bias of 0.005 pH units (Dickson et al., 2007)] to the pH_{calc} from the TA/SSS relationship (**Supplementary Figure S2**). From this comparison, we estimate the uncertainty on the pH_{calc} at 0.04.

Deconvolution of Thermal and Non-thermal Processes on pCO_2

The variability of surface pCO_2 caused by thermal and non-thermal processes was estimated from Takahashi et al. (1993, 2002). The method is based on the well-constrained temperature dependence of pCO_2 (4.23%°C^{-1}) (Takahashi et al., 1993). It helps to construct the thermally forced seasonal pCO_2 cycle (pCO_2^{therm}, Eq. 3) and remove the thermal effect from observed pCO_2 ($pCO_2^{non-therm}$, Eq. 4). We then were able to quantified the respective influence of δpCO_2^{therm} (pCO_2-$pCO_2^{non-therm}$) and $\delta pCO_2^{non-therm}$ (pCO_2-pCO_2^{therm}) on the pCO_2.

$$pCO_2^{therm} = pCO_{2,mean} \times e^{0.0423\times(T_{obs}-T_{mean})} \quad (3)$$

$$pCO_2^{non-therm} = pCO_{2,obs} \times e^{0.0423\times(T_{mean}-T_{obs})} \quad (4)$$

For HF data from the buoy, $pCO_{2,obs}$ and T_{obs} are the calibrated pCO_2 data (**Figure 2** and **Supplementary Figure S2**) from the SAMI-CO_2 and the SST measured at ASTAN, respectively. $pCO_{2,mean}$ is the mean sea surface pCO_2 (420 ± 50 µatm, n = 30788) and T_{mean} the annual average temperature (13.20 ± 2.09°C, n = 33442), calculated from the most complete HF dataset recorded in 2016 and 2019 (**Supplementary Table T1**). For bimonthly data, means were calculated from January 2015 to December 2019 based on the bimonthly dataset: $pCO_{2,obs}$ is the pCO_2 computed from TA/DIC and pH/DIC, with an annual mean of $pCO_{2,mean}$ = 410 ± 64 µatm (n = 109) at SOMLIT-pier and $pCO_{2,mean}$ = 436 ± 39 µatm (n = 119) at SOMLIT-offshore. The average temperature observed at SOMLIT-pier was T_{mean} = 13.17 ± 2.27°C (n = 119) and at SOMLIT-offshore was T_{mean} = 13.05 ± 2.04°C (n = 121) (**Supplementary Table T1**).

Air-Sea CO_2 Fluxes

Atmospheric pCO_2 (pCO_2^{air}) was calculated from the CO_2 molar fraction (xCO_2) from the Mace Head site (53°33′ N 9°00′ W, southern Ireland) (**Figure 1**) of the RAMCES network (Observatory Network for Greenhouse gases) and from the water vapor pressure (pH_2O) using the Weiss and Price (1980) equation. Atmospheric pressure (P_{atm}) was obtained from the weather station of the Roscoff Marine Station, and the wind data from the Guipavas meteorological station (48°26′36″ N, 4°24′42″ W, Météo France) (**Figure 1**). All data were recorded at hourly frequency and then allocated to the HF pCO_2 signal of the ASTAN buoy obtained every 30 min by linear interpolation, daily means were then assigned to discrete values of SOMLIT stations. FCO_2 (in mmol C m^{-2} d^{-1}, Eq. 5) at the air-sea interface was determined from the difference of pCO_2 between the surface seawater and the air (δpCO_2 = pCO_2-pCO_2^{air}), SST, SSS and wind speed.

$$FCO_2 = k \times \alpha \times \delta pCO_2 \quad (5)$$

Where k represents the gas transfer velocity (m s^{-1}) and α represents the solubility coefficient of CO_2 (mol atm^{-1} m^{-3}) calculated as in Weiss (1970). The exchange coefficient k (Eq. 6) was calculated according to the wind speed with the updated algorithm of Wanninkhof (2014) appropriate for regional to global flux estimates and high spatial and temporal resolution of wind products:

$$k = 0.251 \times u_{10}^2 \times \left(\frac{Sc}{660}\right)^{-0.5} \quad (6)$$

Where u_{10} represents the wind speed at 10 m height (m s^{-1}) and S_c the Schmidt number at *in situ* surface temperature, which varied from 770 to 1250.

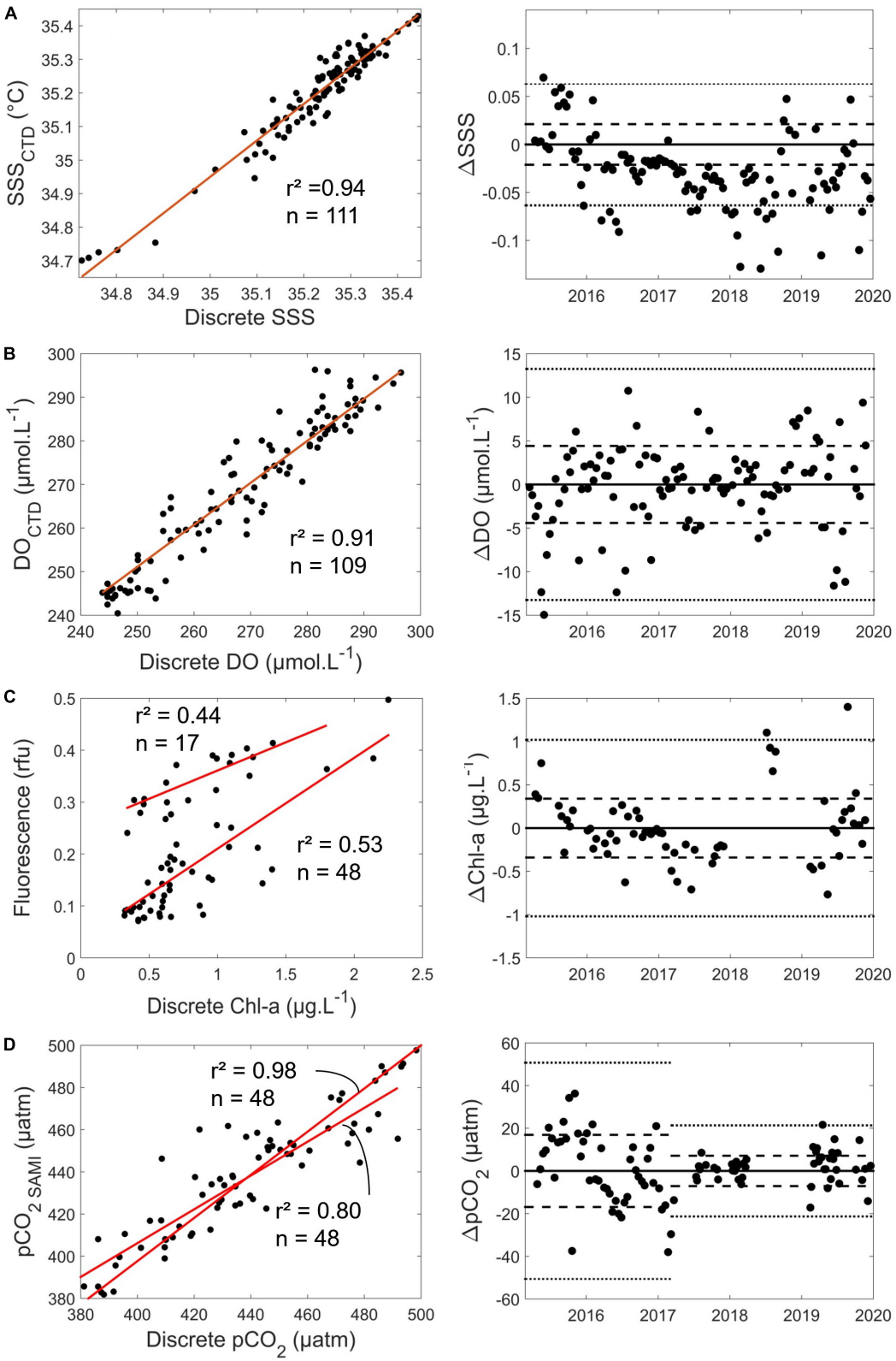

FIGURE 2 | Correlations between HF and discrete data for **(A)** SSS, **(B)** DO (µM), **(C)** Chl-a (µg L^{-1}), and **(D)** pCO_2 (µatm). Left plots show discrete measurements versus sensor values, with *n* the number of discrete measurements, red lines the linear regression between discrete and sensor measurements and associated r^2 values. The right plot shows the differences between sensor values and discrete measurements over time. Dashed lines represent standard deviation of the difference between sensor values and discrete measurements, and dotted lines represent three times the standard deviation.

Wavelet Analysis

To extract further information on our HF data, mathematical transformations were applied. In 2016 and 2019 the HF dataset covered a major part of the year, and all the studied parameters were measured simultaneously. Wavelet analyses were thus performed on SST, SSS, DO%, and $pCO_2^{non-therm}$ to identify the principal frequencies driving the variability of these parameters. Typically, Fourier transforms are used to quantify the constant periodic component in time series. This method is limited when the frequency content changes with time, as in the case of ecological time-series. To overcome these limitations, the wavelets analysis became the norm in environmental time-series analysis, and were used for example to analyze El Nino Southern oscillation (Goring and Bell, 1999) or to follow precipitations distributions (Santos and de Morais, 2013). Wavelet analysis maintain time and frequency localization in a signal analysis, decomposing a time-series into a time-frequency image. This image, generated as a power spectrum, provides simultaneous information on the amplitude of any periodic signals within the series, and on how this amplitude varies with time (Santos and de Morais, 2013). Our measurements were carried out at stations influenced by many factors, stationary or not (e.g., tidal range, currents, day–night cycle, marked seasons. . .). In the case of such HF analysis of an environmental signal the continuous wavelet transform (CWT) must be used and the Morlet wavelets are privileged to follow localized scales (Cazelles et al., 2008). The wavelets analysis is also suitable for the analysis of the relationship between two signals, and thus determining the links between each of the environmental variables studied. We used the cross-wavelets transforms to estimate the covariance between each pair of time-series as a function of frequency. The wavelet analyses were carried out from the Matlab package "wavelet-coherence" (Grinsted et al., 2004) on Matlab v2015b.

RESULTS

Reliability of the Dataset

From the 06/03/2015 to the 31/12/2019, SST from the Seabird SBE16 + of the ASTAN buoy and from SBE19 + used during discrete sampling at SOMLIT-offshore were very well-correlated (r^2 = 0.99, n = 99, standard deviation of the residuals < 0.1°C) (**Supplementary Figure S3**). We used the bimonthly discrete measurements of SSS, DO and Chl-a from the SOMLIT-offshore station to determine whether post-calibration of the corresponding sensors of the SBE16 + deployed at the ASTAN buoy was necessary. These samples were collected during high tide slack when the ASTAN and SOMLIT-offshore surface waters had similar biogeochemical properties according to our transect data. The SSS values were in good agreement with discrete salinity measurements with a 1:1 relationship (r^2 = 0.95, n = 111; standard deviation of the residuals < 0.02) (**Figure 2A**). Similarly, for DO the linear relationship between both measurements was close to 1:1 ($DO = 1.03*DO_{SBE43} - 6.7$, r^2 = 0.91, n = 109, standard deviation of the residuals < 4.4 μM) (**Figure 2B**). During the 5 years of study, the mean difference between discrete DO and DO measured by the SBE43 sensor was 0.31 μM. In light of these results, no corrections were applied to the HF SSS and DO. For Chl *a* two different fluorometers were used during the study, from March 2015 to June 2018 and from June 2018 to December 2019. During the first and second deployments, fluorescence (in relative fluorescence units, RFU) showed significant correlations with discrete Chl-a concentrations of (1) Fluorescence = 0.18*Chl-a + 0.04, r^2 = 0.52, n = 48 and (2) Fluorescence = 0.11*Chl-a + 0.25, r^2 = 0.43, n = 17, respectively (**Figure 2C**). Once the two different conversions between fluorescence and Chl-a measurements were performed, the standard deviation on the residuals was 0.34 μg L^{-1}. Conversion of *in situ* fluorescence into Chl-a concentrations has always been challenging, with fluorescence influenced by numerous factors: heterogeneity of the phytoplankton community structure across the year (Southward et al., 2005; Guilloux et al., 2013), phytoplankton taxonomy (Proctor and Roesler, 2010), cell size (Alpine and Cloern, 1985), pigment packing (Bricaud et al., 1983, 1995; Sosik et al., 1989; Sosik and Mitchell, 1991) and the effect of non-photochemical quenching (Xing et al., 2012). Despite these limitations, Chl-a concentrations remains a suitable proxy for phytoplankton biomass (Carberry et al., 2019). The standard deviations obtained on the residuals were close to those obtained with similar sensors on the Armorique Ferry Box between Roscoff and Plymouth (Marrec et al., 2014), therefore no further corrections were applied to the converted Chl *a* signal.

Maintenance of the SAMI-pCO_2 sensor was conducted at least every 3 months and more often during the productive period. Offsets between discrete pCO_2 estimates and SAMI-pCO_2 were detected each time. The offset remained stable during the deployment periods. For example, from the 13/07/2017 to the 31/08/2017, the mean difference between discrete measurements and the sensor was + 8.9 μatm, while from 02/10/2017 to 11/01/2018 it was −9.9 μatm. The pCO_2 values obtained from the sensor were corrected using measured offsets. From March 2015 to March 2017, we used the TA/DIC measurements at SOMLIT-offshore during high tide slack to compute pCO_2. The pCO_2 values obtained from the sensor were corrected from the measured offset, taking into account the average difference between SOMLIT-offshore and ASTAN buoy. Once the offset was corrected (**Figure 2D**), we obtained a 1:1 relationship between *in situ* pCO_2 computed from DIC/TA and pCO_2 values given by the SAMI-CO_2 (r^2 = 0.80, n = 48) with a standard deviation of the residuals of 16.9 μatm. From March 2017 to December 2019, to reduce errors linked to short time and space scales variability, discrete samples for the determination of pH and TA were taken very close to or directly from the buoy at the same depth than the SAMI sensor. We used this pH/TA combination to compute sea surface pCO_2 at the buoy since they provide accurate pCO_2 values (Millero, 2007). We obtained a better 1:1 relationship between *in situ* pCO_2 computed from pH and TA and pCO_2 values given by the SAMI-CO_2 (r^2 = 0.98, n = 48) with a standard deviation of the residuals of 7.1 μatm.

The percentage of environmental parameters acquired by each sensor had a mean success rate of 60% (**Table 1**). The SST and SSS mean ratios were most reliable due to the robustness of these sensors. SSTs measured concomitantly by the CTD and the SAMI-CO_2, were well-correlated (**Supplementary Figure S3B**).

TABLE 1 | Percentage of data acquired for each parameter measured at the ASTAN buoy from March 2015 to December 2019.

	SST	SSS	DO	Fluorescence	pCO_2
2015	67.7%	50.3%	37.8%	47.11%	47.2%
2016	91.0%	88.5%	88.7%	85.9%	60.8%
2017	74.0%	88.8%	57.3%	60.4%	13.2%
2018	75.0%	75.0%	60.1%	0%	25.4%
2019	68.2%	65.9%	35.7%	68.8%	74.5%

DO and fluorescence sensors were more sensitive to specific problems (e.g., biofouling) due to the substantial sensitivity of detection technologies used by theses sensors, which are based on polarography (SBE43) and optics (Cyclops C7), respectively. The SAMI-CO_2 was the most impacted sensor in terms of acquisition, principally due to frequent battery shortage, missing reagents, or problems with embedded electronics. With the installation of radio transmission during summer 2018, it was easier to detect breakdowns and therefore quickly undertake repairs. The percentage of data acquisition thus increased for all sensors from this point onwards.

Physical and Biogeochemical Variability of Coastal sWEC Waters

Variability of Physical Parameters

Sea surface temperature and SSS showed marked seasonality with cold and fresh water during winter and early spring, and warmer and more saline waters during summer and early fall (**Figures 3A,B**). SST ranged from 9.0°C during winter to 17.0°C during summer. Averaged seasonal SST at SOMLIT-pier was warmer than at SOMLIT-offshore during summer (15.89 ± 0.70°C, n = 31 vs. 15.34 ± 0.66°C, n = 31, p-value < 0.001), and colder during winter (10.44 ± 0.78°C, n = 36 vs. 10.75 ± 0.76°C, n = 37, p-value < 0.001) (**Supplementary Table T1**). The seasonal mean of SSS varied from ∼35.15 ± 0.13 in winter to ∼35.27 ± 0.13 in summer. SSS at SOMLIT-pier was significantly lower than at SOMLIT-offshore because of larger freshwater inputs during the winter with a mean difference of 0.30 (**Supplementary Table T1**). During summer SSS at both stations was in a similar range. At the ASTAN buoy, high-frequency SSS measurements indicated a variability of up to 0.70 within 24 h cycles in winter and up to 0.30 during summer. Interannually, the climatology was calculated from HF daily means of SST and SSS values over 5 years and SST followed a similar pattern between years, except in winter 2018 when the coldest SST was observed, with a 1.5°C difference compared to the 5-year average. SSS did not follow regular seasonality: in 2015 and 2017 SSS followed the 5-year average, with SSS values remaining above 35.0; while in 2016 and 2018, winter SSS decreased down to 34.80 and 34.50, respectively (**Figure 3B**).

Variability of Chl-a Concentrations and DO%

The SOMLIT-pier DO% and Chl-a were higher than SOMLIT-offshore values, with a mean difference around 2% and 0.05 μg L^{-1} in winter, and around 10% and 0.1 μg L^{-1} in summer. At ASTAN, the variations of HF DO% and converted Chl-a showed similar dynamics with high DO% > 110%, high Chl-a concentrations (>2 μg L^{-1}) during spring, and low Chl-a (<0.5 μg L^{-1}) concentrations associated with low DO values close to the equilibrium and/or undersaturated during fall/winter with a mean DO% of 98.2 ± 1.6% during winter and values below 93% in November (**Figures 3C,D** and **Supplementary Table T1**). The DO oversaturation generally lasted around 6 months, from April to September, and surface waters were close to equilibrium and/or undersaturated in DO for the rest of the year. High-frequency DO% data recorded at the ASTAN buoy were closer to the data observed at SOMLIT-offshore than at SOMLIT-pier. Both DO% and Chl-a were characterized by high variability when observed from HF measurements, particularly during spring and summer. DO% and Chl-a followed the same general pattern each year but differed temporally. For example DO oversaturation (DO% above 115%) and high Chl-a (5 μg L^{-1}) were observed in early spring (March) during 2015, but only during late spring (May) in 2018 (**Figures 3C,D**), when large riverine inputs marked by lower SSS values occurred.

Variability of pCO_2 and FCO_2

At SOMLIT-offshore and SOMLIT-pier, pCO_2 ranged from 295 to 507 μatm on an annual scale (**Figure 3E**). Minimum values (<350 μatm) were observed during spring and early summer, with pCO_2 values below atmospheric equilibrium (pCO_2^{air} ranging from 400 to 410 μatm). Maximum values (>450 μatm), above atmospheric equilibrium, were observed during fall and early winter (**Figure 3E**). Surface water CO_2 undersaturation relative to pCO_2^{air} lasted around 6 months, from April to September, while CO_2 oversaturation dominated the rest of the year, inversely related to DO%. During summer, pCO_2 at SOMLIT-offshore was higher than at the SOMLIT-pier (+ 65 μatm mean difference), while during winter we observed an opposite pattern (−23 μatm mean difference). HF pCO_2 was generally well-correlated to the low frequency data. However, during May 2016 and 2019 HF data indicated important drawdowns below 300 μatm (related to high Chl *a* values), which were not detected by the low frequency monitoring.

The annual amplitude of FCO_2 (**Figure 3F**) varied from −14 mmol C m^{-2} d^{-1} to + 26 mmol C m^{-2} d^{-1}. During winter, the fluxes were positive, with surface waters releasing CO_2 to the atmosphere, while the spring negative values revealed a strong absorption of atmospheric CO_2. During spring, atmospheric CO_2 absorption at the SOMLIT-pier was larger (−2.10 ± 1.80 mmol C m^{-2} d^{-1}, n = 29) than at SOMLIT-offshore (0.29 ± 1.00 mmol C m^{-2} d^{-1}, n = 31), with an average difference of 1.8 mmol C m^{-2} d^{-1} (**Supplementary Table T1**). During winter, the two stations acted rather similarly, with important CO_2 emissions to the atmosphere during the high wind speed periods (e.g., December 2015 and January 2018) (**Figure 3F**). The HF monitoring enabled the observation of important daily FCO_2 variations during the spring of 2015 and 2016. For example, during 2015 HF data revealed values down to −14 mmol C m^{-2} d^{-1}, compared to the FCO_2 computed from discrete sampling around −4 mmol C m^{-2} d^{-1}. Similar observations were made during winter 2015, 2016, 2017 and 2019 with, as in 2017, high HF FCO_2 values of 26 mmol C m^{-2} d^{-1} compared to values of 3 mmol C m^{-2} d^{-1} computed

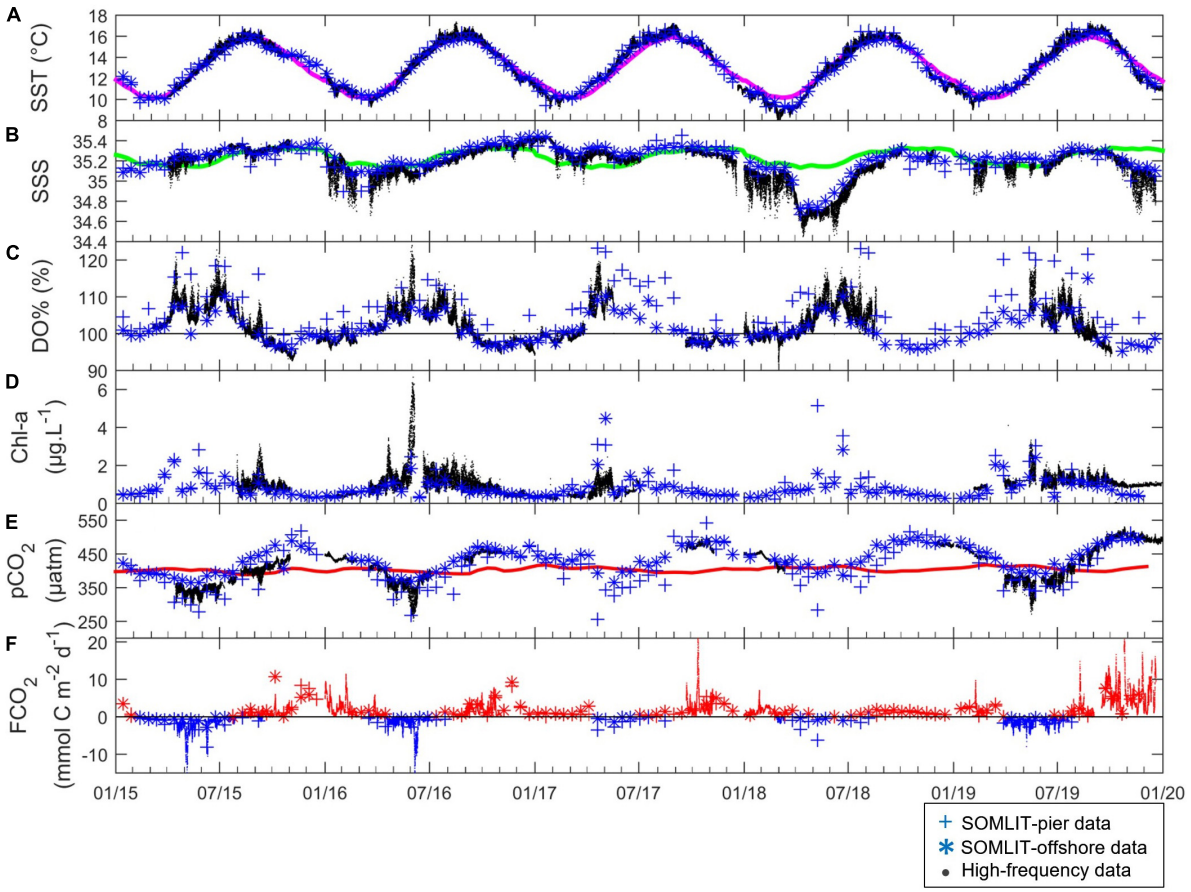

FIGURE 3 | (. in black) High-frequency, (+ in blue) SOMLIT-pier, and (* in blue) SOMLIT-offshore data of **(A)** SST (°C), **(B)** SSS, **(C)** DO% (%), **(D)** Chl-a (µg L^{-1}), **(E)** pCO_2 (µatm) and **(F)** FCO_2 (mmol C m^{-2} d^{-1}) from January 2015 to January 2020. Colored lines represent the climatology of **(A)** SST, **(B)** SSS, and the pCO_2^{atm} (µatm) on **(E)**. The black lines of **(C,F)** represent the atmospheric equilibrium of DO and CO_2, respectively. Negative FCO_2 (sink of atmospheric CO_2) values are represented in blue, and positive FCO_2 (source of CO_2 to the atmosphere) are in red.

from discrete sampling at the same time. Mean seasonal FCO_2 were relatively similar at the three stations during winter, with values between + 2.0 and +4.0 mmol C d^{-2} m^{-1} (**Figure 4**). The spatial difference was more marked during spring, when FCO_2 was negative at SOMLIT-pier (less than −2 mmol C m^{-2} d^{-1}) and at ASTAN buoy (around −1.6 mmol C m^{-2} d^{-1}), but close to equilibrium at SOMLIT-offshore (around −0.3 mmol C m^{-2} d^{-1}). During summer, SOMLIT-pier and ASTAN buoy had values close to atmospheric equilibrium, while SOMLIT-offshore surface waters released CO_2 at + 1.0 mmol C m^{-2} d^{-1}. During fall, all sites exhibited large emissions of CO_2 to the atmosphere with values between + 2 and + 6 mmol C m^{-2} d^{-1}.

Frequency Analysis

Frequency Study of the Physical Structure

Wavelet analyses were applied to the 2016 and 2019 HF SST and SSS data (**Figure 5A**) to identify the main frequencies of variability at the ASTAN buoy. The years 2016 and 2019 were used because the datasets were the most complete. For both years, the SST followed closely the climatology, while the SSS signal was more variable each year because of the high riverine variability but did not show extreme values as those recorded in 2018.

A 12 h cycle, representative of the tidal period of 0.5 day, clearly appeared on both wavelet analyses throughout the year: high variance values between the signal and the wavelets appeared, indicating more marked correlations during the summer period for SST and during winter for SSS. The diurnal cycle (period of 1 day) appeared weakly and episodically in the wavelet transformation of SST data. The crossed wavelets of SST and SSS highlighted the main periodicity of 0.5 days. At the 12 h frequency, we clearly observed a phase alternation, represented by the change of direction of the arrow, with a signal in phase from October to April, and shifted the rest of the year. The statistical analysis revealed very sharp phase changes and allowed precise pinpointing of the different physical characteristics of two water masses influencing HF measurements. For example, the first inversion started on April 10 during 2016, while the second inversion occurred on November 9 in 2016. Similar analysis for 2019 revealed an inversion on November 7 in 2019, remarkably close in terms of inter-annual variability. These results underline the potential of HF monitoring combined to wavelet analyses

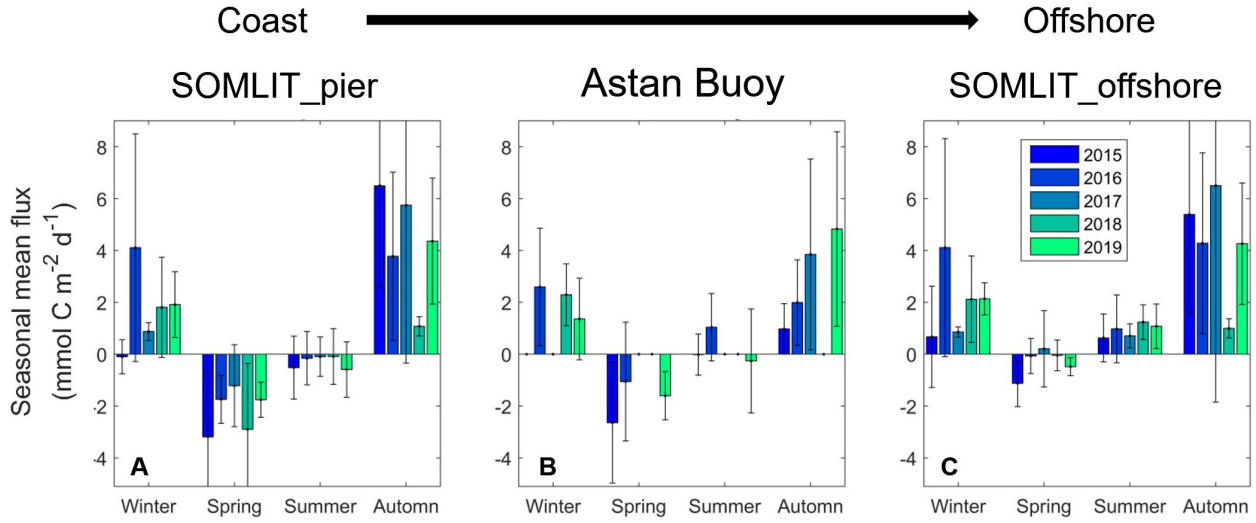

FIGURE 4 | Seasonal mean FCO_2 (mmol C m^{-2} d^{-1}) across a coast-to-offshore gradient at **(A)** SOMLIT-pier **(B)** ASTAN buoy, and **(C)** SOMLIT-offshore from 2015 to 2019. The high frequency means were established only for seasons with a number of observations n_{obs} > 1500, and for the bimonthly stations with a n_{obs} > 4. The error lines represent the standard deviation.

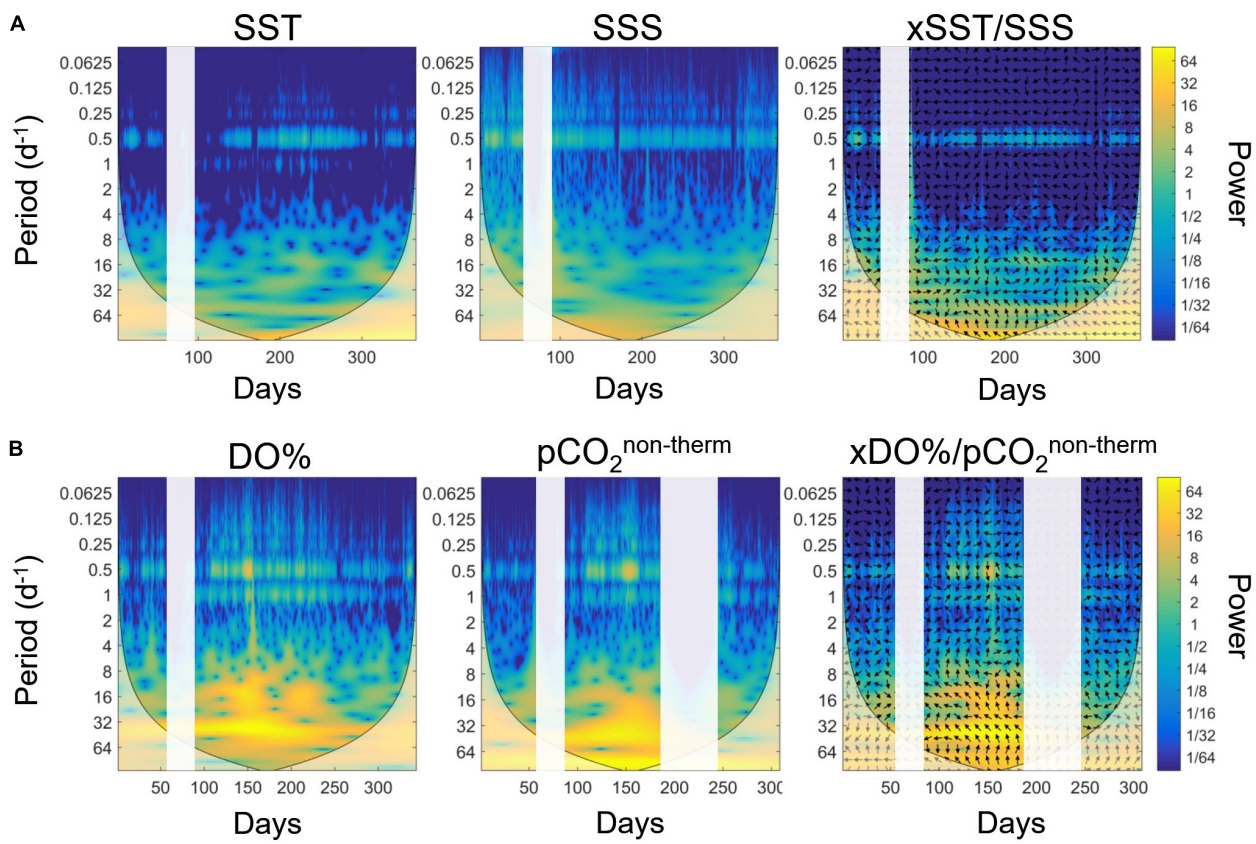

FIGURE 5 | Wavelet power spectrum based on the Morlet wavelets during the year 2016 for **(A)** SST (°C), SSS, and cross-wavelet spectrum between SST and SSS, and for **(B)** DO% (%), $pCO_2^{non-therm}$ (µatm) and cross-wavelet spectrum between DO% and $pCO_2^{non-therm}$. Time is expressed in day of the year. The color bars represent the power of the wavelet transform, in absolute squared value. A high power is represented in yellow. For the cross-wavelets spectrum, the arrows indicate if the signals are in phases (arrow pointing right) or in phase inversion (arrow pointing left). White bands represent a lack of data.

for following shifts in terms of physical regimes in complex nearshore ecosystems.

Frequency Study of Biogeochemical Parameters

Wavelet transformation for the biogeochemical parameters DO% and $pCO_2^{non-therm}$ (**Figure 5B**), representative of biological processes, revealed two characteristic frequencies of 0.5 and 1 days. These frequencies were more marked during summer compared to winter, with higher power. The cross-wavelet analysis revealed that these two frequencies were identical for both parameters underlying potential diel biological cycles in surface waters at the ASTAN buoy. However, the phases did not show any relevant pattern, and the cross wavelet between the biological and the physical parameters didn't bring more information (not shown). For the 12 h signal, we did not observe distinct regimes similar to those of SST and SSS. In winter, they seemed shifted, with DO% maximal when $pCO_2^{non-therm}$ decreased.

Short-Term Variability of Physical and Biogeochemical Parameters

Short-term variability of HF data recorded at the ASTAN buoy during two representatives 6-days periods in January 2016 and May 2016 is shown in **Figure 6**. From 05/01/2016 to 10/01/2016 (winter period, **Figure 6A**), SST ranged from 11 to 14°C, and SSS from 34.85 to 34.95. The SST and SSS varied following 12-h cycles: SST and SSS differences within a 6-h time frame ranged from 0.10 to 0.30°C for SST and from 0.03 to 0.40 for SSS. These two parameters followed the same pattern as the tidal ranges. During high tides SST and SSS reached their highest values, while during low tides minimum SST and SSS values were observed. Similarly, 6-h variation was observed for DO and pCO_2 (**Figure 6C**). DO ranged from 264 to 274 μM, and pCO_2 ranged from 443 to 457 μatm with a 6-h difference of around 7 μM and 13 μatm, respectively.

From 20/05/2016 to 25/05/2016 (spring period, **Figure 6B**), SST ranged from 15.80 to 17.20°C, and SSS from 35.18 to 35.25. We observed 6-h variations of SST around 0.40°C, and 6-h variations of SSS around 0.50. SSS followed the tidal variations, and SST was in the opposite phase; i.e., the phase shift highlighted by the wavelet analysis had occurred. DO and pCO_2 patterns were linked to the 12 h tidal cycle, as suggested by the wavelet analysis. During the bloom (**Figure 6D**), DO ranged from 277 to 290 μM, and pCO_2 from 347 to 379 μatm. 6-h variations were 8 μM for DO and 20 μatm for pCO_2. pCO_2 was correlated with the tidal pattern, while DO was in the opposite phase. These observations highlight the importance of the tidal cycle in daily variations of biogeochemical parameters at the ASTAN buoy.

DISCUSSION

Short-Scale Variability of the CO_2 System in Coastal sWEC

Discrete data, wavelet analysis and HF data described in Section "Short-Term Variability of Physical and Biogeochemical Parameters" highlighted the tidal transport of two distinct water masses: firstly a coastal water mass (CWM), unidentified in previous studies (Marrec, 2014), with properties corresponding to the SOMLIT-pier data and present at ASTAN during low tides; secondly an offshore water mass (OWM) corresponding to SOMLIT-offshore data and present at ASTAN during high tides. During the 5 years of observations, the CWM had lower SST during winter, higher SST during summer; and generally lower SSS (**Figures 3A,B**) (**Supplementary Table T1**) than the OWM. The phase inversion observed in November and April (**Figure 5**), which occurred every year, was the consequence of the opposite SST seasonality between the CWM and the OWM (lower SST in summer in OWM and lower SST in winter in CWM). The influence of tides on pCO_2 dynamics is prominent in estuarine ecosystems (De la Paz et al., 2007; Bozec et al., 2012; Oliveira et al., 2018), but has also been observed in various continental shelves of the world ocean (DeGrandpre et al., 1998; Hofmann et al., 2011; Horwitz et al., 2019). Several studies have reported the impact of the tidal cycle on pCO_2 over various European continental shelf provinces, for example in the nWEC (Litt et al., 2010), in the Bay of Brest (Bozec et al., 2011) or in the Cadiz Bay (Ribas-Ribas et al., 2011, 2013). Likewise, enhanced variability at 12-h periods of DO% and pCO_2 were associated to tidal levels and SST/SSS variations at ASTAN (**Figures 5**, **6**). Previous studies were limited to shorter periods of observation, spanning from 20 h to 4 months, with tidal amplitude lesser than 2 m (Litt et al., 2010; Ribas-Ribas et al., 2011, 2013) or to a semi-enclosed bay with limited tidal exchange with the adjacent open ocean (Bozec et al., 2011). During 5 years, we observed mean variations of DO% and pCO_2 around 10% and 15 μatm, respectively, during tidal cycles. The maximum tidal variability associated to spring tides (>7 m) during phytoplankton blooms (16% for DO% and 88 μatm for $pCO_2^{non-therm}$) represented up to 50 and 40% of the respective annual signals at ASTAN. These variabilities reflected the important tidal transport of the CWM and OWM in the coastal sWEC, distinctively revealed by HF monitoring at the ASTAN buoy.

In addition to the tidal variability of DO% and pCO_2 as a result of the presence of distinct water masses at ASTAN, HF monitoring of these biologically dependent variables should also present diurnal variability. During the day, the combination of photosynthesis and respiration is supposed to increase DO% and decrease $pCO_2^{non-therm}$, whereas during the night, respiration processes tend to decrease DO% and increase $pCO_2^{non-therm}$. Borges and Frankignoulle (2003) first revealed a combination of the tidal signal coupled with the biological diel cycle on pCO_2 variations in the English Channel. The impact of the diel cycle on DO%, $pCO_2^{non-therm}$ and FCO_2 had also been detected and quantified during the productive period in the nWEC (Marrec et al., 2014). In the adjacent Bay of Brest, HF data showed a maximum of DO% and a minimum of pCO_2 at dusk, and a maximum of pCO_2 and a minimum of DO% at dawn (Bozec et al., 2011). More recently, Liu et al. (2019) highlighted the superimposition of the diel biological signal on the pCO_2 tidal signal in a subtropical tidal estuary. In our case, the main difficulty was to extract the diurnal signal from the high tidal signal, which dominated the short-term variability of pCO_2, as also observed by Dai et al. (2009) in several

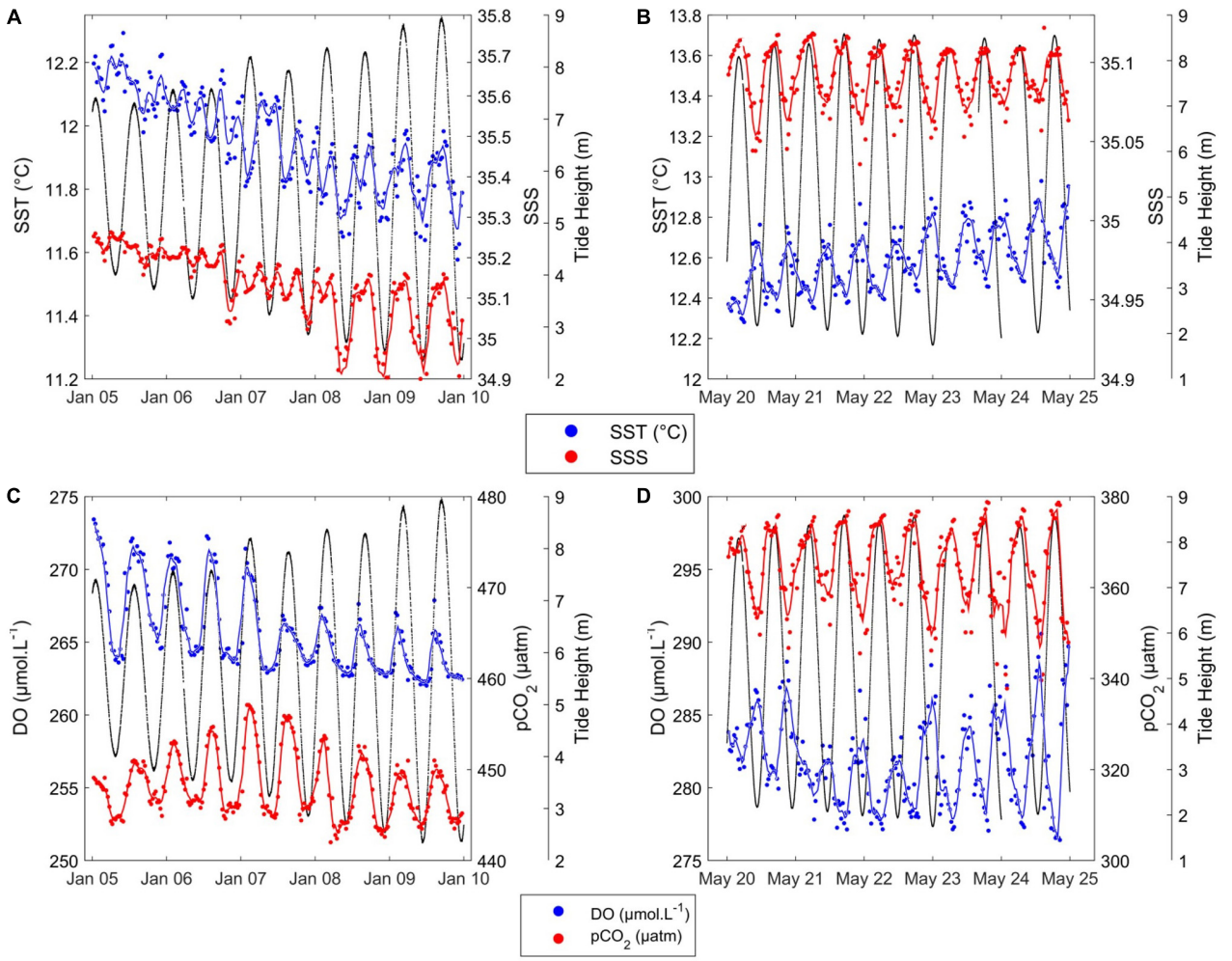

FIGURE 6 | Short-term variability of SST (°C) (blue) and SSS (red) during **(A)** winter, from 05/01/2016 to 10/01/2016, and **(B)** summer, from 20/05/2016 to 25/05/2016; and short-term variability of DO (µM) (blue) and pCO_2 (µatm) (red) during **(C)** winter and **(D)** summer. Black lines represent tidal height (m). Smooth lines in blue and red are obtained using a moving average filter with a 2-h span on the corresponding parameters.

ecosystems of the South China Sea. At the ASTAN site, the diel variability of DO% and $pCO_2^{non-therm}$ was indistinguishable due to the prevalence of the tidal signal (**Figure 6**). However, the wavelet analysis revealed a potential day/night cycle for DO% and $pCO_2^{non-therm}$ (**Figure 5**), with an important signal on a 24 h period. To estimate the effect of the biological diel cycle on these parameters, we separated the signal, keeping only the data at dusk and dawn according to PAR values measured at the buoy. The day–night differences for DO% and $pCO_2^{non-therm}$ clearly appeared during the productive period, when such differences were the most pronounced (**Figure 7**). The data revealed a diel biological cycle with maximum differences of + 5% for DO% and −22 µatm of $pCO_2^{non-therm}$ between dawn and dusk. A 10–15 day cycle appeared between day and night variability of DO% and $pCO_2^{non-therm}$, with more pronounced day–night differences at certain periods. This period was closely related to the time when the dawn/dusk cycle was in phase with the low/high tide cycle (data not shown), which means that similar water masses (CWM or OWM) were in vicinity of the ASTAN buoy at dusk and dawn. The annual mean difference of the day/night DO% was 0.6%, and 3 µatm for $pCO_2^{non-therm}$, remaining rather low compared to tidal variability. However, when considering the maximum wavelet amplitude of %DO and $pCO_2^{non-therm}$ during the bloom (Day ∼140 corresponding to May, **Figure 5**), the day/night signal accounted for 30% of the annual variation of DO% and for 9% of the annual variation of $pCO_2^{non-therm}$. As well as revealing the significant tidally induced variability of the pCO_2 signal, HF monitoring of coastal sWEC waters provided key information about the impact of the diel biological cycle on the CO_2 system.

Combining HF measurements of pH or pCO_2 with discrete carbonate system parameters (DIC/TA) can be a valuable tool for carbon cycle research based on autonomous mooring (Cullison Gray et al., 2011). Our robust TA/SSS relationship established in Section "Carbonate System Parameters" was concordant with similar relationships estimated in North Atlantic waters mixing

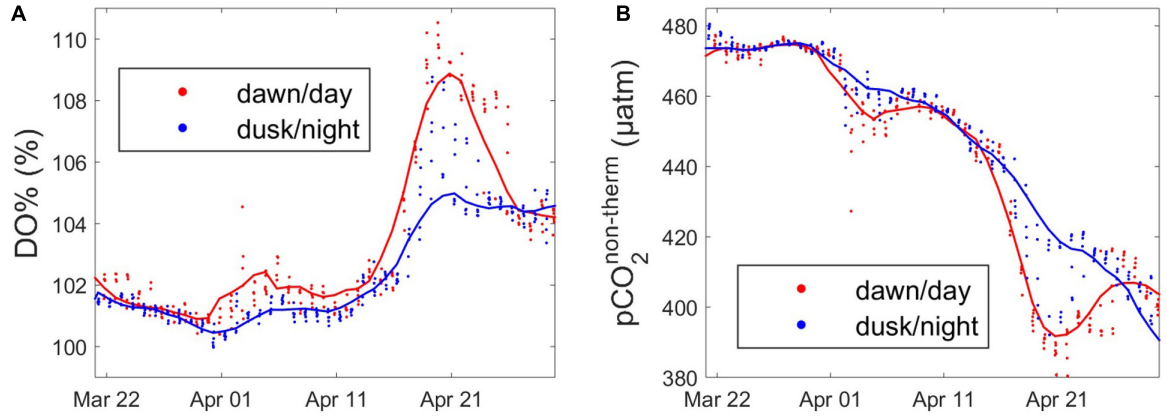

FIGURE 7 | Diurnal variability of **(A)** DO% (%) and **(B)** $pCO_2^{non-therm}$ (µatm) data extracted at dawn (red) and dusk (blue) ± 3 h during the productive period, from 22/03/2016 to 27/04/2016. Smooth lines in blue and red are obtained using a moving average filter with a 5-data span on the corresponding parameters.

with freshwater from non-limestone Irish rivers with similar TA end members (McGrath et al., 2016). We therefore estimated HF pH_{calc} for 2016, which varied from 8.00 during winter to 8.20 during summer (**Figure 8A**). These values were within the range of the *in situ* pH estimated between 7.97 and 8.35 by Marrec (2014) in the WEC and with pH values reported by McGrath et al. (2019) in Irish coastal waters (between 8.00 and 8.30). Unsurprisingly, pH_{calc} exhibited opposite dynamics to pCO_2 and was strongly related to the tidal signal. During spring/summer, low pH_{calc} values were observed at high tide and high pH_{calc} values at low tide, with 12-h variations up to 0.12 units (**Figure 8B**). The pH variability is particularly intense in coastal ecosystems (Ostle et al., 2016; Brodeur et al., 2019) resulting from various biogeochemical and physical processes (Waldbusser and Salisbury, 2014). In this study, most of the variability of pH_{calc} observed at the ASTAN site during spring likely resulted from tidal transport of the CWM and the OWM with contrasting biological and physical properties.

Hydes et al. (2011) reported long-term pH decrease of −0.002 to −0.004 pH unit yr^{-1} from 1995 to 2009 in the northwest European continental shelf, higher than in the Atlantic waters (Kitidis et al., 2017) and in the open ocean (Doney et al., 2009). At a daily time-scale, we observed variations up to 6 times greater than this regional annual acidification trend, and the seasonal variation was 10 times greater than the decadal change in the area. These strong variabilities are similar to the observations of McGrath et al. (2019) who reported, in similar coastal ecosystems in Ireland, a pH variability from 10 to 50 times greater than the decadal change linked to OA. Large changes of pCO_2 and pH were previously observed during short measurements period at fixed locations in various coastal ecosystems (Hofmann et al., 2011; Saderne et al., 2013). Intense changes in pH and saturation state Ω_{arag} have also been reported at coastal mooring sites in the California Current Ecosystem with natural variability overlapping with preindustrial conditions but also revealing critical OA conditions (Sutton et al., 2016). This variability has direct implications for calcifying species because variable pH exposure can affect organism response to OA (Vargas et al., 2017). Extremes decrease of Ω_{arag} have also been related to pteropods shell dissolution (Feely et al., 2016) and identified as a potential threat for the shellfish industry (Salisbury et al., 2008). Marine organisms in regions of persistent low pH might be locally adapted to OA (Sanford and Kelly, 2011; Pespeni et al., 2013). However, knowledge gaps about when and where corrosive conditions occur (Feely et al., 2016; Chan et al., 2017; Fennel et al., 2019) and how the timing of such conditions relates to key life stages (Legrand et al., 2017; Kapsenberg et al., 2018) still have to be filled to assess vulnerability to OA. Here we showed large daily changes in pH/pCO_2 but also DO/SST at the ASTAN mooring associated with the tidal transport of the CWM and the OWM in the nearshore area of the WEC over 5 years. These data can improve experimental design to evaluate organism response under real-world conditions by submitting these organisms to realistic variability in carbonate parameters (Chan et al., 2017) but also to varying DO and SST (Reum et al., 2016) instead of previous classical experimental designs (Noisette et al., 2016; Legrand et al., 2017) used in the WEC.

Seasonal and Interannual Control of pCO_2 in Coastal sWEC

Previous studies investigating the seasonal patterns of pCO_2 in the WEC indicated important physical and biological influence on carbonate cycling (Borges and Frankignoulle, 2003; Padin et al., 2007; Dumousseaud et al., 2010; Litt et al., 2010; Kitidis et al., 2012). With our 5 years of HF and discrete data we further investigated the seasonal and inter-annual variability of pCO_2 in the proximal area of the sWEC. Following the approach proposed by Takahashi et al. (1993, 2002), we discriminated the influence of thermal processes (pCO_2^{therm}) from non-thermal processes ($pCO_2^{non-therm}$) (**Figures 9A,B**) and we quantified the respective influence of δpCO_2^{therm} and $\delta pCO_2^{non-therm}$ on pCO_2 (**Figure 9C**).

The SST followed a rather regular pattern every year with limited inter-annual variations. Since pCO_2^{therm} is mainly influenced by temperature, we observed a variation of pCO_2^{therm}

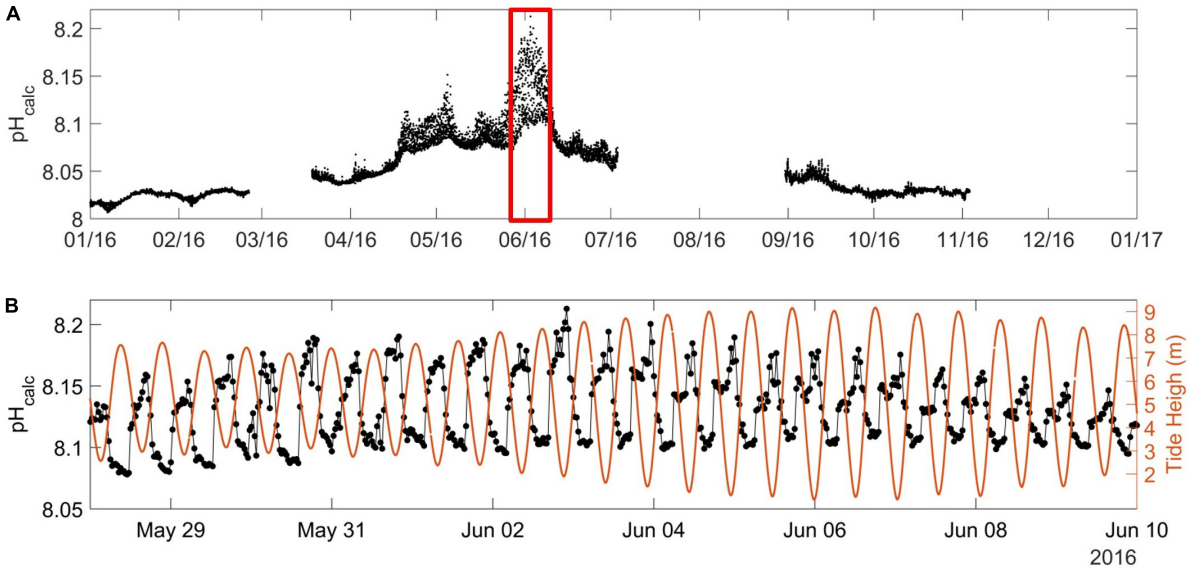

FIGURE 8 | (A) pH_{calc} (in pH units on the total scale at *in situ* SST) at the ASTAN buoy during the year 2016 as explained in Section "Carbonate System Parameters" with **(B)** emphasis on the spring short-term variability of pH_{calc} (black dot) and the water level [in meters (orange line)] from 28/05/2016 to 09/06/2016.

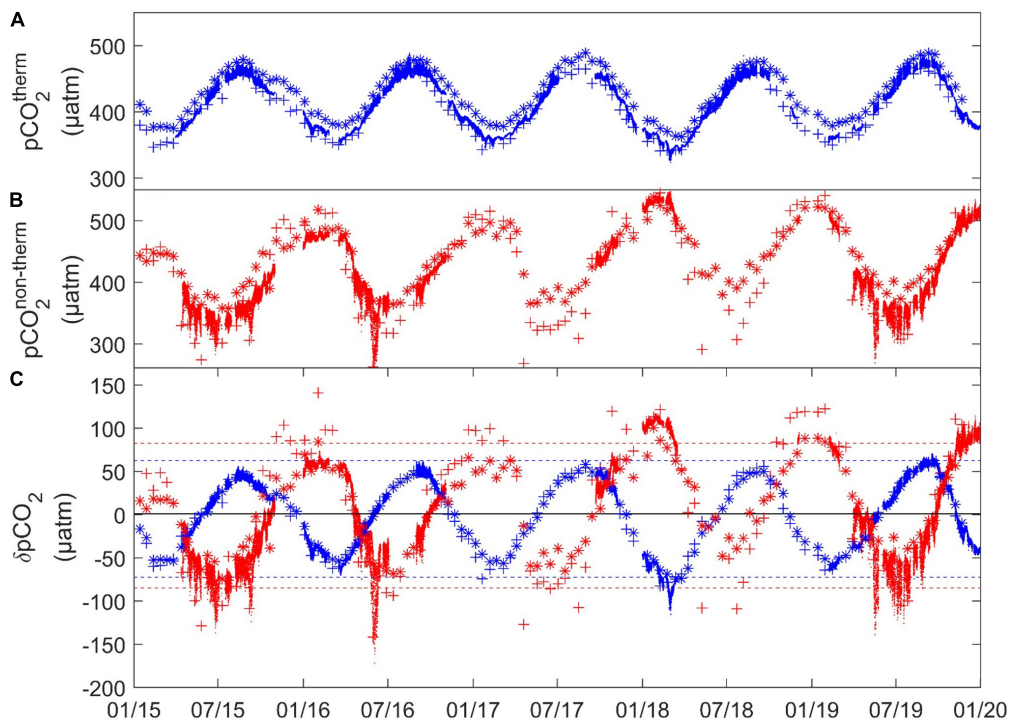

FIGURE 9 | (A) pCO_2^{therm} (blue), **(B)** $pCO_2^{non-therm}$ (red) **(C)** δpCO_2^{therm} = pCO_2-$pCO_2^{non-therm}$ (blue) and $\delta pCO_2^{non-therm}$ = pCO_2-pCO_2^{therm} (red) (all in µatm) for (.) High-frequency, (+) SOMLIT-pier, and (*) SOMLIT-offshore data. Dashed lines represent the maximum and minimum of the monthly mean of δpCO_2^{therm} (blue) and $\delta pCO_2^{non-therm}$ (red).

mirroring SST variations, varying from 325 to 490 µatm during winter and summer, respectively. δpCO_2^{therm} varied from + 67 µatm due to increasing SST during summer to −104 µatm due to decreasing SST during winter. In 2018, winter values diverged from the other years with lower SST (−1.5°C) compared to average values. Therefore, the lowest pCO_2^{therm} values (around 345 µatm) and a δpCO_2^{therm} of −104 µatm (20 µatm lower than the other years) were encountered that

year. It is worth noting that during the same period SSS largely diverged from the average with values as low as 34.60, only recorded by HF monitoring. The decrease of pCO_2 induced by thermal processes was counterbalanced by particularly high $pCO_2^{non-therm}$ values at this time (>500 µatm). The strong impact of non-thermal processes in winter 2018 might be related to intense riverine inputs, which brought a large amount of organic material. Besides this interannual variability, the 5-year dataset at the two discrete stations revealed spatial variability of the thermal effect on pCO_2. During winter, pCO_2^{therm} was lower at SOMLIT-pier (or CWM) compared to SOMLIT-offshore (or OWM), due to stronger cooling of nearshore waters during the winter regime. δpCO_2^{therm} revealed an impact 7 µatm higher of the SST cooling on pCO_2 in the CWM (**Supplementary Table T1**). During summer, after the shift from the winter to the summer regime, SST was higher at SOMLIT-pier than at SOMLIT-offshore. δpCO_2^{therm} showed that this higher SST was responsible for a potential increase of 5 µatm of pCO_2 in CWM compared to OWM (**Supplementary Table T1**).

Non-thermal effects on pCO_2, $pCO_2^{non-therm}$, are strongly influenced by biological production/respiration processes, but also by factors such as lateral advection, vertical mixing, air-sea CO_2 exchanges, dissolution/formation of $CaCO_3$, sediment/water-column interactions, or riverine inputs. However, this parameter remains a valuable and efficient approach to assess the impact of biological processes on pCO_2 variability (Thomas et al., 2005). Windspeed data (**Supplementary Figure S4**) showed a rather stable signal (higher values during winter's storms and lower values during spring/summer) throughout the 5 years of study, which did not induce large inter-annual $pCO_2^{non-therm}$ variability. The HF data showed a clear opposite dynamic between Chl-a-DO%, and the $pCO_2^{non-therm}$ signals both temporally and in terms of intensity. The opposite patterns indicated that $pCO_2^{non-therm}$ could reasonably be considered as an indicator to quantify the effect of biological processes on natural pCO_2 variability.

Spring in the sWEC is characterized by phytoplankton blooms between March and April fueled by the winter nutrient stock. The onset of spring phytoplankton blooms depends on light availability throughout the well-mixed water column (Wafar et al., 1983; L'Helguen et al., 1996). Surface waters, and the entire water column (except when weak and short stratification occurred), still exhibited relatively high Chl-a concentrations and oversaturated DO% along the summer since nutrient stocks (particularly nitrate) are rarely totally depleted because of the light limitation induced by strong mixing (Wafar et al., 1983; L'Helguen et al., 1996; Marrec, 2014). In fall, light availability becomes insufficient to support the substantial level of primary production required to maintain DO% oversaturation. Respiration and remineralization processes therefore become the main driver of pCO_2 variability, consuming DO, releasing CO_2, and driving the nutrient concentrations as in other temperate ecosystems of the northwest European continental shelf (Bozec et al., 2011; Marrec et al., 2013; Salt et al., 2016; Hartman et al., 2019). The biologically productive periods were accompanied by DO% > 100% and Chl-a concentrations > 1 µg L^{-1} from April to October every year, with oxygen saturation reaching values up to 120%. During winter the heterotrophic activity (respiration and remineralization of organic matter) dominated with much lower Chl-a and undersaturated DO%. $\delta pCO_2^{non-therm}$ showed a regular pattern driven by these production/respiration processes, with a strong coupling between the start/end of < 0 $\delta pCO_2^{non-therm}$ and > 100% DO% values, and proved to be a suitable indicator of the extent and duration of the productive period (**Figure 9C**).

Important interannual variability was observed with respect to the onset and end of the productive period, as indicated by the DO% and $\delta pCO_2^{non-therm}$ signals. In 2015, DO% started to be significantly higher than 100% in March, synchronized with an increase of Chl-a, and surface waters remained oversaturated in DO up to mid-September, while in 2018, the productive period started in May and ended in late August. 2018 was characterized by larger freshwater inputs (**Figure 3B**) due to heavy precipitations in late winter/early spring, and thus reduced light availability, associated with greater turbidity, which might have limited light penetration in the mixed water-column and thus delayed the start of the productive period. The $pCO_2^{non-therm}$ and $\delta pCO_2^{non-therm}$ signals followed similar dynamics. In 2015, $pCO_2^{non-therm}$ and $\delta pCO_2^{non-therm}$ started to decrease and to be negative, respectively, in April, whereas negative $\delta pCO_2^{non-therm}$ started to be observed in May in 2018. Positive $\delta pCO_2^{non-therm}$ values were observed from September in 2015 and from August in 2018. The decrease of $pCO_2^{non-therm}$ in spring can be particularly rapid, as in spring 2016 with a drawdown of around 250 µatm during a 2-month period (March–May), revealing a large consumption of pCO_2 by biological activity partly counteracted by the increasing SST and pCO_2^{therm} at the same period.

Spatial variability was visible from the discrete data, particularly in summer, when $pCO_2^{non-therm}$ was persistently lower at SOMLIT-pier (CWM) than at SOMLIT-offshore (OWM). During the productive period, seasonal minimal $\delta pCO_2^{non-therm}$ values lower than −100 µatm were observed in the CWM every year, while the $\delta pCO_2^{non-therm}$ signals never reached values below −70 µatm in the OWM. The shallower depth in the CMW favors light penetration, which can result in higher pelagic production (when nutrients are not depleted) compared to the deeper OWM. The role of benthic production processes on CO_2 variations is also important in proximal shallow areas (Hammond et al., 1999; Cai et al., 2000; Forja et al., 2004; Waldbusser and Salisbury, 2014; Oliveira et al., 2018). The low $\delta pCO_2^{non-therm}$ associated to CWM during the productive period might include both higher pelagic and benthic production, with a predominance of the latter. The tidal transport of the CWM over adjacent seagrass and macroalgae beds with high CO_2 consumption (Ouisse et al., 2011; Bordeyne et al., 2017) extended the biological productive period of the CWM to the benthic compartment. The $\delta pCO_2^{non-therm}$ seasonal mean difference of 30 µatm recorded between both stations was therefore a gross estimation of the benthic compartment production within the nearshore area. Similarly, a nearshore to offshore gradient was observed during fall and early winter. Values of $\delta pCO_2^{non-therm}$ in the CWM of 130 µatm were 40 µatm higher than in the OWM, the important benthic and pelagic remineralization in the

shallower CWM contributing to a larger increase of pCO_2. This increase was partly counteracted by the decreasing pCO_2^{therm} due to fall and winter SST cooling as discussed above.

Our data revealed a somewhat classical picture of pCO_2 control in temperate ecosystems with counteracting effects of thermodynamic and biological activity depending on the seasons (Thomas et al., 2005; Bozec et al., 2011). The combined 5-year HF and discrete data allowed for the first time the quantification of rather large interannual and spatial variability in the proximal surface waters of the sWEC. Non-thermal processes, that we assumed to be mainly controlled by biological activity, were the main driver of pCO_2 in the coastal sWEC, as shown by the larger amplitude, both during winter and summer, of $pCO_2^{non-therm}$ compared to pCO_2^{therm}. The interannual variability of pCO_2 depended mainly on the duration and the intensity of the productive period. The weak interannual variability in terms of SST limited its control over the 5 years of study on pCO_2 compared to production/respiration processes.

Dynamics of FCO_2 in the WEC

Our study provides FCO_2 estimates at daily, seasonal and annual time scales. One major limitation for estimating HF FCO_2 is the requirement to access HF atmospheric CO_2 data in the surrounding study area. Northcott et al. (2019) recently demonstrated the impact of higher atmospheric CO_2 transported by offshore winds from urban and agricultural land on FCO_2 estimates in Monterey Bay, California. This concern was also addressed by Wimart-Rousseau et al. (2020) in their study of FCO_2 in the vicinity of a highly urbanized area. Unfortunately, we did not have access to local HF atmospheric CO_2 data, so atmospheric xCO_2 data from the RAMCES network collected at the Mace Head site (53°33′ N 9°00′ W, southern Ireland) were used to calculate pCO_2^{atm}. The dominant onshore south-westerly winds and rather lowly urbanized surroundings in our study area mean that the Mace Head record should be representative of our study site. The use of local wind products from the nearby Guipavas weather station (**Supplementary Figure S4**) and of recent gas transfer velocity parametrization adapted to regional estimates (Wanninkhof, 2014) limited the error linked to different wind products in regional air-sea flux estimations (Roobaert et al., 2018). The impact of rain, extreme wind events and associated bubble entrainment, surface films or boundary layer stability (Wanninkhof et al., 2009 for a review) are factors inducing additional uncertainty into gas transfer velocity k, and therefore HF FCO_2 calculation, but remain particularly difficult to assess. The eddy covariance technique, as used by Yang et al. (2019) in the nWEC, can overcome most of these limitations inherent to gas transfer velocity parametrization, and presents some undeniable advantages for studying HF FCO_2. However, the use of *in situ* seawater pCO_2 sensor remained the most effective way to study pCO_2, examine its control, and simultaneously estimate air-sea CO_2 fluxes using widely used wind dependent gas transfer velocity parametrization.

The main benefit of HF data was to assess daily FCO_2 variability and capture extreme events such as high fluxes observed during winter or abrupt shifts and drawdown during spring. For example, during winter 2017 a HF FCO_2 of 26 mmol C m^{-2} d^{-1} was recorded at ASTAN compared to values of 3 mmol C m^{-2} d^{-1} computed from discrete values at the same time. During spring, as explained in Section "Seasonal and Interannual Control of pCO_2 in Coastal WEC," the large interannual variability of the intensity and trigger of spring blooms was responsible for variable spring drawdown in pCO_2, revealing sudden and strong inversions of the fluxes. For example, in March 2016 FCO_2 was on average positive with a monthly maximum of + 5.93 mmol C m^{-2} d^{-1} (03/27/16), and within a few days became negative, with a monthly minimum of −4.42 mmol C m^{-2} d^{-1} (04/19/16). This large daily variability should be taken into account when considering the spring average carbon sink for each year (with a mean estimate at −2.12 mmol C m^{-2} d^{-1}). With the method applied in Section "Short-Scale Variability of the CO_2 System in Coastal sWEC" we were able to separate the day/night signal during this period and found a mean difference of FCO_2 of −0.12 mmol m^{-2} d^{-1} due to the diel biological cycle. This estimation was understandably lower than the day–night difference estimated at −0.90 mmol m^{-2} d^{-1} for FCO_2 during spring in the stratified and more productive nWEC (Marrec et al., 2014). FCO_2 based on HF data provided relevant information on short-term variability, the main caveat of the cardinal buoy data being the significant loss of data, which hindered computation of mean seasonal averages.

The mean seasonal FCO_2 values for the three sites during the 5 years of study were compared to assess the seasonal and spatial variability of FCO_2 along a coastal/offshore gradient (**Figure 4**). FCO_2 computed from the HF data at ASTAN exhibited similar overall variability as FCO_2 obtained from discrete measurements at SOMLIT-pier (CWM) and at SOMLIT-offshore (OWM). Similar general patterns between HF and discrete data at the seasonal level have also been reported in recent studies (Shadwick et al., 2019). Regardless of sampling frequency and locations, the three studied sites acted as strong sources of CO_2 to the atmosphere during winter/fall. During spring, SOMLIT-pier and ASTAN acted as sinks of atmospheric CO_2, with higher CO_2 sink at SOMLIT-pier than at ASTAN, while fluxes computed at SOMLIT-offshore indicated exchanges near equilibrium. Summer was the only time of the year when significant differences in terms of flux intensity and direction were observed between the three sites. This time of the year corresponds to the shift from dominant production of organic matter by photosynthetic organisms toward dominant remineralization and respiration processes, which usually start earlier in the deeper well-mixed water column at SOMLIT-offshore. The 2015/2018 years were marked by large differences in terms of the date of onset and length of the productive period, which were poorly reflected in the mean seasonal spring and summer FCO_2. However, the following fall was marked by large differences in terms of emissions of CO_2 to the atmosphere, much lower in 2018 compared to 2015 when it was driven by high wind speeds (maximum monthly mean of 9.7 m s^{-1}). The mean wind speeds recorded during fall 2018 (4.6 m s^{-1}) were followed by lower than average wind speeds the following winter months (4.6 m s^{-1} compared to mean 5.2 m s^{-1}) (**Figure 3**), which still resulted in significant flux differences, driven this time by the

delayed remineralization period (**Figure 4**). This study confirms that seasonal variability of FCO_2 in this part of the NE European continental shelf is controlled by complex interactions between high/low wind speeds, production/respiration of organic matter and winter cooling (Kitidis et al., 2019).

On an annual basis, given the dominant impact of the tidal cycle at ASTAN, it seemed particularly interesting to assess the proximal coastal/offshore gradient of FCO_2 from the buoy data only. In 2016/2019 the HF dataset was sufficiently complete to attempt an estimation of annual FCO_2 in the CMW and OMW based on tidal separation of the HF signal. We separated the dataset according to high tides (>8 m) and low tides (<2.5 m), as previously explained. The annual mean FCO_2 over 2016/2019 was estimated at 0.37 mol C m^{-2} yr^{-1} for the CMW and 0.65 mol C m^{-2} yr^{-1} for the OWM (**Figure 10**). The mean HF FCO_2 of 0.51 mol C m^{-2} yr^{-1} for 2016/2019 at the ASTAN buoy was obviously within the range of FCO_2 in the CWM and OWM. FCO_2 computed at ASTAN comprised both the tidal and diurnal signals and was therefore representative of nearshore surface waters in the sWEC. Comparison of these HF budget with the annual mean budget for 2016/2019 based on discrete sampling at SOMLIT-pier (0.35 mol C m^{-2} yr^{-1}) and SOMLIT-offshore (0.62 mol C m^{-2} yr^{-1}), which we assumed representative of the CWM and OWM, respectively, revealed very similar values. Here, the arbitrary separation of the HF data according to tide levels provided coherent results with discrete samples collected at noon during neap tides at both SOMLIT stations. We were able to estimate FCO_2 in the CWM and OWM with the ASTAN mooring, which underly the great potential of cardinal buoys to capture the dynamic of FCO_2 in nearshore tidal ecosystems. It is worth noting that CO_2 emissions at SOMLIT-offshore (averaged over the 5-year period) showed a similar trend but lower values than emissions computed from 2011 to 2013 at the same site (**Figure 10**), with an atmospheric CO_2 increase of + 9 to + 15 μatm recorded between the studies. These new estimates in nearshore waters of the sWEC over a 5-year period combined with previous studies provided a full latitudinal representation over multiple years for FCO_2 in the WEC (**Figures 1**, **10**). This is particularly relevant since proximal areas are currently excluded from global estimates in the coastal ocean (Bourgeois et al., 2016). The latitudinal comparison showed a clear gradient from a weak source of CO_2 in the tidal mixing areas toward sinks of CO_2 in the stratified regions less influenced by tidal mixing in agreement with recent global modeling studies (Laruelle et al., 2018). Interestingly, in the tidal mixing ecosystems the sources increased from nearshore to offshore waters, whereas in stratified ecosystems the sink increased toward nearshore waters. Andersson and Mackenzie (2004) first suggested that shelves may have turned from a CO_2 source in the preindustrial time to a sink at present and that the CO_2 uptake rate would increase with time. More recently Cai (2011) and Bauer et al. (2013) suggested an increasing global shelf CO_2 sink with time as a result of the atmospheric pCO_2 increase. The latest SOCAT data confirm this trend with a slower pCO_2 increase in shelf waters compared to atmospheric pCO_2 that could increase the air-sea gradient and thus the uptake of atmospheric CO_2 in the decades to come, although high spatial variability in air–sea fluxes is to be expected across shelf regions (Laruelle et al., 2018). This is particularly significant for the sWEC, which is a weak source of CO_2 and could potentially become a sink of CO_2 in the coming decades.

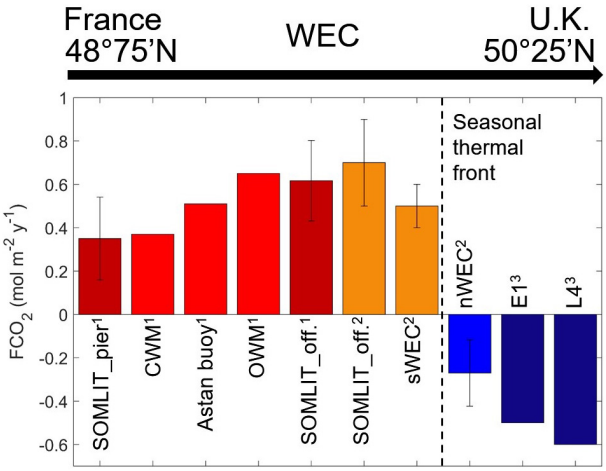

FIGURE 10 | Annual mean FCO_2 (mol C m^{-2} y^{-1}) across the WEC at discrete stations SOMLIT-pier and SOMLIT-offshore for the 2015–2019 period (dark red), in the CMW, OMW and at ASTAN based on HF data from 2016 and 2019 (red) from this study[1]; at SOMLIT-offshore (orange), in the sWEC (orange) and nWEC (blue) for the period 2011–2013 from Marrec (2014)[2]; and at discrete stations E1 and L4 (dark blue) for the period 2007–2010 from Kitidis et al. (2012)[3].

CONCLUSION

The recent OceanObs 2019 conference highlighted the need for innovative and sustained coastal observatories (Farcy et al., 2019) notably for the study of FCO_2. In the last decade, the emergence of new high-performance pH and pCO_2 sensors has been extremely valuable for the investigation of OA and FCO_2 (Sastri et al., 2019). Here, the implementation of a cardinal buoy of opportunity equipped with such novel sensors into an existing network of time-series and Ferrybox monitoring programs provided a robust multiple year assessment of FCO_2 and also pH variability in a temperate coastal ecosystem. This is particularly relevant on a socio-economical level since nearshore ecosystems host large stocks of shellfish species sensitive to ongoing ocean acidification. Numerous cardinal buoys are present in the global coastal ocean to direct traffic, particularly along rocky shores with large tidal ranges. These buoys of opportunity can be equipped with meteorological and oceanographic sensors and transmit data daily to the shore, thus providing real-time data for the study of coastal ecosystems under climate change. This network of buoys therefore has significant potential to be exploited for efficient, low cost observation of coastal ecosystems.

DATA AVAILABILITY STATEMENT

Discrete data are available at: http://somlit-db.epoc.u-bordeaux1.fr/bdd.php?serie=ST&sm=3 (accessed date 14 August 2020).

AUTHOR CONTRIBUTIONS

J-PG collected, analyzed, processed and interpreted the data, and wrote the first version of the manuscript. PM provided scientific discussion, new ideas on the interpretation of the results, and contributed to writing the manuscript. TC initiated the collaboration on the Cardinal buoy. TC, CG, ÉM, and MV configured the data acquisition system on the buoy, calibrated and cleaned the sensors, collected data in the field, analyzed discrete samples in the laboratory and processed the data. YB designed the study, led the research, interpreted the data, wrote the manuscript, and managed the project. All authors contributed to the article and approved the submitted version.

FUNDING

This work was funded by the CNRS through INSU [COAST HF, SOMLIT, project CHANNEL (LEFE/CYBER)] and INEE, by the "Conseil Général du Finistère" (CD29) and by the "Region Bretagne" (program ARED, project Hi-Tech). Part of this work was supported by the JERICO-NEXT project from the European Union's Horizon 2020 Research and Innovation Program under grant agreement no. 654410. YB is P.I. of the CHANNEL and Hi-Tech projects and associate researcher (CRCN) at CNRS. J-PG holds a Ph.D. grant from the Region Bretagne and Sorbonne University (ED129).

ACKNOWLEDGMENTS

We thank the "Service des Phares et Balises" for providing access to the ASTAN buoy and the "Service Mer" of the SBR for their valuable support during sampling at sea. We thank the SNAPOCO2 for DIC/TA analysis and M. Ramonet for providing the atmospheric CO_2 data from the RAMCES network (Observatory Network for Greenhouse gases). G. Charia (Ifremer) provided valuable help with the wavelet frequency analysis. We thank the SOMLIT (Service d'Obervation du Milieu LIToral) network for providing oceanographic data at the SOMLIT sites and help during fieldwork. We thank A. Durand and E. Collin for their help during field campaign on the Penzé river. We are grateful to the Menden-Deuer lab (URI-GSO) and A. C. Baudoux for constructive collaboration and scientific discussions during finalization of the manuscript. We thank I. Probert for correcting the revised manuscript and the two reviewers whose comments greatly improved the quality of the manuscript. In memory of FB.

SUPPLEMENTARY MATERIAL

The Supplementary Material for this article can be found online at: https://www.frontiersin.org/articles/10.3389/fmars.2020.00712/full#supplementary-material

REFERENCES

Alpine, A. E., and Cloern, J. E. (1985). Differences in *in vivo* fluorescence yield between three phytoplankton size classes. *J. Plankton Res.* 7, 381–390. doi: 10.1093/plankt/7.3.381

Aminot, A., and Kérouel, R. (2007). *Dosage Automatique des Nutriments dans les Eaux Marines: Méthodes en Flux Continu*. Brest: Ifremer.

Andersson, A. J., and Mackenzie, F. T. (2004). Shallow-water oceans: a source or sink of atmospheric CO2? *Front. Ecol. Environ.* 2:348–353.

Bakker, D. C., Pfeil, B., Landa, C. S., Metzl, N., O'Brien, K. M., Olsen, A., et al. (2016). A multi-decade record of high-quality fCO2 data in version 3 of the Surface Ocean CO2 Atlas (SOCAT). *Earth Syst. Sci. Data* 8, 383–413.

Bauer, J. E., Cai, W. J., Raymond, P. A., Bianchi, T. S., Hopkinson, C. S., and Regnier, P. A. (2013). The changing carbon cycle of the coastal ocean. *Nature* 504, 61–70. doi: 10.1038/nature12857

Beucher, C., Treguer, P., Corvaisier, R., Hapette, A. M., and Elskens, M. (2004). Production and dissolution of biosilica, and changing microphytoplankton dominance in the Bay of Brest (France). *Mar. Ecol. Prog. Ser.* 267, 57–69. doi: 10.3354/meps267057

Bordeyne, F., Migné, A., and Davoult, D. (2017). Variation of fucoid community metabolism during the tidal cycle: insights from *in situ* measurements of seasonal carbon fluxes during emersion and immersion. *Limnol. Oceanogr.* 62, 2418–2430. doi: 10.1002/lno.10574

Borges, A. V., Alin, S. R., Chavez, F. P., Vlahos, P., Johnson, K. S., Holt, J. T., et al. (2010). "A global sea surface carbon observing system: inorganic and organic carbon dynamics in coastal oceans," in *Proceedings of OceanObs'09: Sustained Ocean Observations and Information for Society*, Vol. 2, (Paris: European Space Agency), 67–88. doi: 10.5270/OceanObs09.cwp.07

Borges, A. V., and Frankignoulle, M. (2003). Distribution of surface carbon dioxide and air sea exchange in the English Channel and adjacent areas. *J. Geophys. Res. Oceans* 108:3140. doi: 10.1029/2000JC000571

Borges, A. V., and Gypens, N. (2010). Carbonate chemistry in the coastal zone responds more strongly to eutrophication than ocean acidification. *Limnol. Oceanogr.* 55, 346–353.

Bourgeois, T., Orr, J. C., Resplandy, L., Terhaar, J., Ethé, C., Gehlen, M., et al. (2016). Coastal-ocean uptake of anthropogenic carbon. *Biogeosciences* 13, 4167–4185. doi: 10.5194/bg-13-4167-2016

Bozec, Y., Cariou, T., Macé, E., Morin, P., Thuillier, D., and Vernet, M. (2012). Seasonal dynamics of air-sea CO2 fluxes in the inner and outer Loire estuary (NW Europe). *Estuar. Coast. Shelf Sci.* 100, 58–71.

Bozec, Y., Merlivat, L., Baudoux, A. C., Beaumont, L., Blain, S., Bucciarelli, E., et al. (2011). Diurnal to inter-annual dynamics of pCO2 recorded by a CARIOCA sensor in a temperate coastal ecosystem (2003–2009). *Mar. Chem.* 126, 13–26. doi: 10.1016/j.marchem.2011.03.003

Bricaud, A., Babin, M., Morel, A., and Claustre, H. (1995). Variability in the chlorophyll-specific absorption coefficients of natural phytoplankton: analysis and parameterization. *J. Geophys. Res. Oceans* 100, 13321–13332. doi: 10.1029/95JC00463

Bricaud, A., Morel, A., and Prieur, L. (1983). Optical efficiency factors of some phytoplankters 1. *Limnol. Oceanogr.* 28, 816–832. doi: 10.4319/lo.1983.28.5.0816

Brodeur, J. R., Chen, B., Su, J., Xu, Y. Y., Hussain, N., Scaboo, K. M., et al. (2019). Chesapeake Bay inorganic carbon: spatial distribution and seasonal variability. *Front. Mar. Sci.* 6:99. doi: 10.3389/fmars.2019.00099

Cai, W.-J. (2011). Estuarine and coastal ocean carbon paradox: CO2 sinks or sites of terrestrial carbon incineration? *Annu. Rev. Mar. Sci.* 3, 123–145.

Cai, W. J., Hu, X., Huang, W. J., Murrell, M. C., Lehrter, J. C., Lohrenz, S. E., et al. (2011). Acidification of subsurface coastal waters enhanced by eutrophication. *Nat. Geosci.* 4, 766–770. doi: 10.1038/ngeo1297

Cai, W.-J., Huang, W.-J., Luther, G. W., Pierrot, D., Li, M., Testa, J., et al. (2017). Redox reactions and weak buffering capacity lead to acidification in the Chesapeake Bay. *Nat. Commun.* 8:369. doi: 10.1038/s-017-00417-7

Cai, W. J., Wiebe, W. J., Wang, Y., and Sheldon, J. E. (2000). Intertidal marsh as a source of dissolved inorganic carbon and a sink of nitrate in the Satilla River-estuarine complex in the southeastern US. *Limnol. Oceanogr.* 45, 1743–1752. doi: 10.4319/lo.2000.45.8.1743

Carberry, L., Roesler, C., and et Drapeau, S. (2019). Correcting in situ chlorophyll fluorescence time-series observations for nonphotochemical quenching and

tidal variability reveals nonconservative phytoplankton variability in coastal waters. *Limnol. Oceanogr. Methods* 17, 462–473. doi: 10.1002/lom3.10325

Carpenter, J. H. (1965). The accuracy of the winkler method for dissolved oxygen analyisis. *Limnol. Oceanogr.* 10, 135–140.

Cazelles, B., Chavez, M., Berteaux, D., Ménard, F., Vik, J. O., Jenouvrier, S., et al. (2008). Wavelet analysis of ecological time series. *Oecologia* 156, 287–304. doi: 10.1007/s00442-008-0993-2

Chan, F., Barth, J. A., Blanchette, C. A., Byrne, R. H., Chavez, F., Cheriton, O., et al. (2017). Persistent spatial structuring of coastal ocean acidification in the California Current System. *Sci. Rep.* 7:2526. doi: 10.1038/s41598-017-02777-y

Chen, C. T. A., and Borges, A. V. (2009). Reconciling opposing views on carbon cycling in the coastal ocean: continental shelves as sinks and near-shore ecosystems as sources of atmospheric CO2. *Deep Sea Res. Part II Top. Stud. Oceanogr.* 56, 578–590.

Chierici, M., Fransson, A., and Anderson, L. G. (1999). Influence of m-cresol purple indicator additions on the pH of seawater samples: correction factors evaluated from a chemical speciation model. *Mar. Chem.* 65, 281–290. doi: 10.1016/S0304-4203(99)00020-1

Ciais, P., Sabine, C., Bala, G., Bopp, L., Brovkin, V., Canadell, J., et al. (2014). "Carbon and other biogeochemical cycles," in *Climate change 2013: the physical Science Basis. Contribution of Working Group I to the Fifth Assessment Report of the Intergovernmental Panel on Climate Change*, eds T. F. Stocker, D. Qin, G.-K. Plattner, M. Tignor, S. K. Allen, et al. (Cambridge: Cambridge University Press), 465–570.

Clayton, T. D., and Byrne, R. H. (1993). Spectrophotometric seawater pH measurements: total hydrogen ion concentration scale calibration of m-cresol purple and at-sea results. *Deep Sea Res. Part I Oceanogr. Res. Pap.* 40, 2115–2129. doi: 10.1016/0967-0637(93)90048-8

Cullison Gray, S. E., DeGrandpre, M. D., Moore, T. S., Martz, T. R., Friederich, G. E., and Johnson, K. S. (2011). Applications of in situ pH measurements for inorganic carbon calculations. *Mar. Chem.* 125, 82–90. doi: 10.1016/j.marchem.2011.02.005

Dai, M., Lu, Z., Zhai, W., Chen, B., Cao, Z., Zhou, K., et al. (2009). Diurnal variations of surface seawater pCO2 in contrasting coastal environments. *Limnol. Oceanogr.* 54, 735–745. doi: 10.4319/lo.2009.54.3.0735

DeGrandpre, M. D., Hammar, T. R., Wallace, D. W., and Wirick, C. D. (1997). Simultaneous mooring-based measurements of seawater CO2 and O2 off Cape Hatteras, North Carolina. *Limnol. Oceanogr.* 42, 21–28. doi: 10.4319/lo.1997.42.1.0021

DeGrandpre, M. D., Hammar, T. R., and Wirick, C. D. (1998). Short-term pCO_2 and O_2 dynamics in California coastal waters. *Deep Sea Res. Part II: Top. Stud. Oceanogr.* 45, 1557–1575. doi: 10.1016/S0967-0645(98)80006-4

de Haas, H., van Weering, T. C., and de Stigter, H. (2002). Organic carbon in shelf seas: sinks or sources, processes and products. *Cont. Shelf Res.* 22, 691–717. doi: 10.1016/S0278-4343(01)00093-0

De la Paz, M., Gómez-Parra, A., and Forja, J. (2007). Inorganic carbon dynamic and air–water CO2 exchange in the Guadalquivir Estuary (SW Iberian Peninsula). *J. Mar. Syst.* 68, 265–277. doi: 10.1016/j.jmarsys.2006.11.011

Del Amo, Y., Quéguiner, B., Tréguer, P., Breton, H., and Lampert, L. (1997). Impacts of high-nitrate freshwater inputs on macrotidal ecosystems. II. Specific role of the silicic acid pump in the year-round dominance of diatoms in the Bay of Brest (France). *Mar. Ecol. Prog. Ser.* 161, 225–237. doi: 10.3354/meps161225

Dickson, A. G., and Millero, F. J. (1987). A comparison of the equilibrium constants for the dissociation of carbonic acid in seawater media. *Deep Sea Res. Part A Oceanogr. Res. Pap.* 34, 1733–1743. doi: 10.1016/0198-0149(87)90021-5

Dickson, A. G., Sabine, C. L., and Christian, J. R. (eds) (2007). *Guide to Best Practices for Ocean CO2 Measurements. North Pacific Marine Science Organization, 176*. Available online at: www.nodc.noaa.gov/ocads/oceans/Handbook_2007.html (accessed July 17, 2020).

DOE (1994). *Handbook of Methods for Analysis of the Various Parameters of the Carbon Dioxide System in Sea Water, Version 2*. Available online at: https://core.ac.uk/download/pdf/98639593.pdf doi: 10.2172/10107773 (accessed July 17, 2020).

Doney, S. C., Fabry, V. J., Feely, R. A., and Kleypas, J. A. (2009). Ocean acidification: the other CO2 problem. *Annu. Rev. Mar. Sci.* 1, 169–192. doi: 10.1146/annurev.marine.010908.163834

Dumousseaud, C., Achterberg, E. P., Tyrrell, T., Charalampopoulou, A., Schuster, U., Hartman, M., et al. (2010). Contrasting effects of temperature and winter mixing on the seasonal and inter-annual variability of the carbonate system in the Northeast Atlantic, Ocean. *Biogeosciences* 7, 1481–1492. doi: 10.5194/bg-7-1481-2010

Dürr, H. H., Meybeck, M., Hartmann, J., Laruelle, G. G., and Roubeix, V. (2011). Global spatial distribution of natural riverine silica inputs to the coastal zone. *Biogeosciences* 8, 597–620. doi: 10.5194/bg-8-597-2011

Edmond, J. M. (1970). High precision determination of titration alkalinity and total carbon dioxide content of sea water by potentiometric titration. *Deep Sea Res. Oceanogr. Abstr.* 17, 737–750. doi: 10.1016/0011-7471(70)90038-0

Farcy, P., Durand, D., Charria, G., Painting, S. J., Collingridge, K., Grémare, A. J., et al. (2019). Towards a European Coastal Observing Network to provide better answer to science and to societal challenges; the JERICO/JERICO-NEXT Research Infrastructure. *Front. Mar. Sci.* 6:529. doi: 10.3389/fmars.2019.00529

Feely, R. A., Alin, S., Carter, B., Bednaršek, N., Hales, B., Chan, F., et al. (2016). Chemical and biological impacts of ocean acidification along the west coast of North America. *Estuar. Coast. Shelf Sci.* 183, 260–270. doi: 10.1016/j.ecss.2016.08.043

Feely, R. A., Alin, S. R., Newton, J., Sabine, C. L., Warner, M., Devol, A., et al. (2010). The combined effects of ocean acidification, mixing, and respiration on pH and carbonate saturation in an urbanized estuary. *Estuar. Coast. Shelf Sci.* 88, 442–449. doi: 10.1016/j.ecss.2010.05.004

Fennel, K., Alin, S., Barbero, L., Evans, W., Bourgeois, T., Cooley, S., et al. (2019). Carbon cycling in the North American coastal ocean: a synthesis. *Biogeosciences* 16, 1281–1304.

Forja, J. M., Ortega, T., DelValls, T. A., and Gómez-Parra, A. (2004). Benthic fluxes of inorganic carbon in shallow coastal ecosystems of the Iberian Peninsula. *Mar. Chem.* 85, 141–156. doi: 10.1016/j.marchem.2003.09.007

Friedlingstein, P., Jones, M., O'sullivan, M., Andrew, R., Hauck, J., Peters, G. et al. (2019). Global carbon budget 2019. *Earth Syst. Sci. Data* 11, 1783–1838. doi: 10.5194/essd-11-1783-2019

Gattuso, J. P., Frankignoulle, M., and Wollast, R. (1998). Carbon and carbonate metabolism in coastal aquatic ecosystems. *Annu. Rev. Ecol. Syst.* 29, 405–434. doi: 10.1146/annurev.ecolsys.29.1.405

Goring, D. G., and Bell, R. G. (1999). El Niño and decadal effects on sea-level variability in northern New Zealand: a wavelet analysis. *N. Z. J. Mar. Freshw. Res.* 33, 587–598. doi: 10.1080/00288330.1999.9516902

Gran, G. (1952). Determination of the equivalence point in potentiometric titrations. Part II. *Analyst* 77, 661–671.

Grinsted, A., Moore, J. C., and Jevrejeva, S. (2004). Application of the cross wavelet transform and wavelet coherence to geophysical time series. *Nonlinear Process. Geophys.* 11, 561–566.

Gruber, N., Clement, D., Carter, B. R., Feely, R. A., Van Heuven, S., Hoppema, M., et al. (2019). The oceanic sink for anthropogenic CO2 from 1994 to 2007. *Science* 363, 1193–1199. doi: 10.1126/science.aau5153

Guilloux, L., Rigaut-Jalabert, F., Jouenne, F., Ristori, S., Viprey, M., Not, F., et al. (2013). An annotated checklist of Marine Phytoplankton taxa at the SOMLIT-Astan time series off Roscoff (Western English Channel, France): data collected from 2000 to 2010. *Cah. Biol. Mar.* 54, 247–256.

Hammond, D. E., Giordani, P., Berelson, W. M., and Poletti, R. (1999). Diagenesis of carbon and nutrients and benthic exchange in sediments of the Northern Adriatic Sea. *Mar. Chem.* 66, 53–79. doi: 10.1016/S0304-4203(99)00024-9

Haraldsson, C., Anderson, L. G., Hassellöv, M., Hulth, S., and Olsson, K. (1997). Rapid, high-precision potentiometric titration of alkalinity in ocean and sediment pore waters. *Deep Sea Res. Part I Oceanogr. Res. Pap.* 44, 2031–2044. doi: 10.1016/S0967-0637(97)00088-5

Hartman, S. E., Humphreys, M. P., Kivimäe, C., Woodward, E. M. S., Kitidis, V., McGrath, T., et al. (2019). Seasonality and spatial heterogeneity of the surface ocean carbonate system in the northwest European continental shelf. *Prog. Oceanogr.* 177:101909. doi: 10.1016/j.pocean.2018.02.005

Hofmann, G. E., Smith, J. E., Johnson, K. S., Send, U., Levin, L. A., Micheli, F., et al. (2011). High-frequency dynamics of ocean pH: a multi-ecosystem comparison. *PLoS One* 6:e28983. doi: 10.1371/journal.pone.0028983

Horwitz, R. M., Hay, A. E., Burt, W. J., Cheel, R. A., Salisbury, J., and Thomas, H. (2019). High-frequency variability of CO2 in Grand Passage, Bay of Fundy, Nova Scotia. *Biogeosciences* 16, 605–616.

Hydes, D. J., Hartman, S. E., Hartman, M. C., Jiang, Z., Hardman-Mountford, N., Artioli, Y., et al. (2011). *DEFRApH, Tech. rep. DEFRA Contract ME4133 "DEFRApH Monitoring Project"*. Southampton: National Oceanography Centre Southampton, 53.

Kapsenberg, L., Alliouane, S., Gazeau, F., Mousseau, L., and Gattuso, J.-P. (2017). Coastal ocean acidification and increasing total alkalinity in the northwestern Mediterranean Sea. *Ocean Sci.* 13, 411–426. doi: 10.5194/os-13-411-2017

Kapsenberg, L., Miglioli, A., Bitter, M. C., Tambutté, E., Dumollard, R., and Gattuso, J. P. (2018). Ocean pH fluctuations affect mussel larvae at key developmental transitions. *Proc. R. Soc. B* 285:20182381. doi: 10.1098/rspb.2018.2381

Kitidis, V., Brown, I., Hardman-Mountford, N., and Lefèvre, N. (2017). Surface ocean carbon dioxide during the Atlantic Meridional Transect (1995–2013); evidence of ocean acidification. *Prog. Oceanogr.* 158, 65–75. doi: 10.1016/j.pocean.2016.08.005

Kitidis, V., Hardman-Mountford, N. J., Litt, E., Brown, I., Cummings, D., Hartman, S., et al. (2012). Seasonal dynamics of the carbonate system in the Western English Channel. *Cont. Shelf Res.* 42, 30–40. doi: 10.1016/j.csr.2012.04.012

Kitidis, V., Shutler, J. D., Ashton, I., Warren, M., Brown, I., Findlay, H., et al. (2019). Winter weather controls net influx of atmospheric CO2 on the north-west European shelf. *Sci. Rep.* 9:20153. doi: 10.1038/s41598-019-56363-5

Laruelle, G. G., Cai, W. J., Hu, X., Gruber, N., Mackenzie, F. T., and Regnier, P. (2018). Continental shelves as a variable but increasing global sink for atmospheric carbon dioxide. *Nat. Commun.* 9:454. doi: 10.1038/s41467-017-02738-z

Legrand, E., Riera, P., Lutier, M., Coudret, J., Grall, J., and Martin, S. (2017). Species interactions can shift the response of a maerl bed community to ocean acidification and warming. *Biogeosciences* 14, 5359–5376. doi: 10.5194/bg-14-5359-2017

L'Helguen, S., Madec, C., and Le Corre, P. (1996). Nitrogen uptake in permanently well-mixed temperate coastal waters. *Estuar. Coast. Shelf Sci.* 42, 803–818. doi: 10.1006/ecss.1996.0051

Litt, E. J., Hardman-Mountford, N. J., Blackford, J. C., Mitchelson-Jacob, G., Goodman, A., Moore, G. F., et al. (2010). Biological control of pCO2 at station L4 in the Western English Channel over 3 years. *J. Plankton Res.* 32, 621–629. doi: 10.1093/plankt/fbp133

Liu, Q., Dong, X., Chen, J., Guo, X., Zhang, Z., Xu, Y., et al. (2019). Diurnal to interannual variability of sea surface pCO2 and its controls in a turbid tidal-driven nearshore system in the vicinity of the East China Sea based on buoy observations. *Mar. Chem.* 216:103690. doi: 10.1016/j.marchem.2019.103690

Marrec, P. (2014). *Dynamics of the Carbonate System and Air-Sea CO2 Fluxes in Western European Shelf Waters: A Multi-Scale Approach*. Paris: Sorbonnes Université.

Marrec, P., Cariou, T., Collin, E., Durand, A., Latimier, M., Macé, E., et al. (2013). Seasonal and latitudinal variability of the CO2 system in the western English Channel based on Voluntary Observing Ship (VOS) measurements. *Mar. Chem.* 155, 29–41. doi: 10.1016/j.marchem.2013.05.014

Marrec, P., Cariou, T., Latimier, M., Macé, E., Morin, P., Vernet, M., et al. (2014). Spatio-temporal dynamics of biogeochemical processes and air–sea CO2 fluxes in the Western English Channel based on two years of FerryBox deployment. *J. Mar. Syst.* 140, 26–38. doi: 10.1016/j.jmarsys.2014.05.010

Marrec, P., Cariou, T., Macé, É., Morin, P., Salt, L. A., Vernet, M., et al. (2015). Dynamics of air-sea CO2 fluxes in the northwestern European shelf based on voluntary observing ship and satellite observations. *Biogeosciences* 12, 5371–5391. doi: 10.5194/bg-12-5371-2015

McGrath, T., McGovern, E., Cave, R. R., and Kivimäe, C. (2016). The inorganic carbon chemistry in coastal and shelf waters around Ireland. *Estuaries Coasts* 39, 27–39. doi: 10.1007/s12237-015-9950-6

McGrath, T., McGovern, E., Gregory, C., and Cave, R. R. (2019). Local drivers of the seasonal carbonate cycle across four contrasting coastal systems. *Reg. Stud. Mar. Sci.* 30:100733. doi: 10.1016/j.rsma.2019.100733

Mehrbach, C., Culberson, C. H., Hawley, J. E., and Pytkowicx, R. M. (1973). Measurement of the apparent dissociation constants of carbonic acid in seawater at atmospheric pressure 1. *Limnol. Oceanogr.* 18, 897–907. doi: 10.4319/lo.1973.18.6.0897

Meybeck, M., Dürr, H. H., and Vörösmarty, C. J. (2006). Global coastal segmentation and its river catchment contributors: a new look at land-ocean linkage. *Glob. Biogeochem. Cycles* 20:W07517. doi: 10.1029/2005GB002540

Millero, F. J. (2007). The marine inorganic carbon cycle. *Chem. Rev.* 107, 308–341. doi: 10.1021/cr0503557

Muller-Karger, F. E., Varela, R., Thunell, R., Luerssen, R., Hu, C., and Walsh, J. J. (2005). The importance of continental margins in the global carbon cycle. *Geophys. Res. Lett.* 32:L01602.

Noisette, F., Bordeyne, F., Davoult, D., and Martin, S. (2016). Assessing the physiological responses of *Crepidula fornicata*to predicted ocean acidification and warming conditions. *Limnol. Oceanogr.* 61, 430–444. doi: 10.1002/lno.10225

Northcott, D., Sevadjian, J., Sancho-Gallegos, D. A., Wahl, C., Friederich, J., and Chavez, F. P. (2019). Impacts of urban carbon dioxide emissions on sea-air flux and ocean acidification in nearshore waters. *PLoS One* 14:e0214403. doi: 10.1371/journal.pone.0214403

Oliveira, A. P., Pilar-Fonseca, T., Cabeçadas, G., and Mateus, M. (2018). Local variability of CO2 partial pressure in a mid-latitude mesotidal estuarine system (Tagus Estuary, Portugal). *Geosciences* 8:460. doi: 10.3390/geosciences8120460

Orr, J. C., Epitalon, J.-M., Dickson, A., and Gattuso, J.-P. (2018). Routine uncertainty propagation for the marine carbon dioxide system. *Mar. Chem.* 207, 84–107. doi: 10.1016/j.marchem.2018.10.006

Orr, J. C., Epitalon, J.-M., and Gattuso, J.-P. (2015). Comparison of ten packages that compute ocean carbonate chemistry. *Biogeosciences* 12, 1483–1510. doi: 10.5194/bg-12-1483-2015

Ostle, C., Willliamson, P., Artioli, Y., Bakker, D. C., Birchenough, S. N. R., Davis, C. E., et al. (2016). *Carbon Dioxide and Ocean Acidification Observations in UK Waters: Synthesis Report with a Focus on 2010–2015*. Available online at: www.researchgate.net/publication/304324178_Carbon_dioxide_and_ocean_acidification_observations_in_UK_waters_Synthesis_report_with_a_focus_on_2010_-_2015?channel=doi&linkId=576be75d08aead4e3add04a1&showFulltext=true (accessed July 17, 2020).

Ouisse, V., Migné, A., and Davoult, D. (2011). Community-level carbon flux variability over a tidal cycle in *Zostera marina* and *Z. noltii* beds. *Mar. Ecol. Prog. Ser.* 437, 79–87. doi: 10.3354/meps09274

Padin, X. A., Vázquez-Rodríquez, M., Ríos, A. F., and Pérez, F. F. (2007). Surface CO2 measurements in the English Channel and Southern Bight of North Sea using voluntary observing ships. *J. Mar. Syst.* 66, 297–308. doi: 10.1016/j.jmarsys.2006.05.011

Pespeni, M. H., Chan, F., Menge, B. A., and Palumbi, S. R. (2013). Signs of adaptation to local pH conditions across an environmental mosaic in the California Current Ecosystem. *Integr. Comp. Biol.* 53, 857–870. doi: 10.1093/icb/ict094

Pierrot, D., Wallace, D., Lewis, E., Pierrot, D., Lewis, E., Wallace, R., et al. (2011). *MS Excel Program Developed for CO2 System Calculations*. Oak Ridge, TN: Oak Ridge National Laboratory. doi: 10.3334/CDIAC/otg.CO2SYS_XLS_CDIAC105a

Pingree, R. D., and Griffiths, D. K. (1978). Tidal fronts on the shelf seas around the British Isles. *J. Geophys. Res. Oceans* 83, 4615–4622. doi: 10.1029/JC083iC09p04615

Proctor, C. W., and Roesler, C. S. (2010). New insights on obtaining phytoplankton concentration and composition from in situ multispectral Chlorophyll fluorescence. *Limnol. Oceanogr. Methods* 8, 695–708. doi: 10.4319/lom.2010.8.0695

Puillat, I., Farcy, P., Durand, D., Karlson, B., Petihakis, G., Seppala, J., et al. (2016). Progress in marine science supported by European joint coastal observation systems: the JERICO-RI research infrastructure. *J. Mar. Syst.* 162, 1–3.

Reimer, J. J., Cai, W.-J., Xue, L., Vargas, R., Noakes, S., Hu, X., et al. (2017). Time series pCO2 at a coastal mooring: internal consistency, seasonal cycles, and interannual variability. *Cont. Shelf Res.* 145, 95–108. doi: 10.1016/j.csr.2017.06.022

Reum, J. C., Alin, S. R., Harvey, C. J., Bednaršek, N., Evans, W., Feely, R. A., et al. (2016). Interpretation and design of ocean acidification experiments in upwelling systems in the context of carbonate chemistry co-variation with temperature and oxygen. *ICES J. Mar. Sci.* 73, 582–595. doi: 10.1093/icesjms/fsu231

Ribas-Ribas, M., Anfuso, E., Gómez-Parra, A., and Forja, J. M. (2013). Tidal and seasonal carbon and nutrient dynamics of the Guadalquivir estuary and the Bay of Cádiz (SW Iberian Peninsula). *Biogeosciences* 10, 4481–4491. doi: 10.5194/bg-10-4481-2013

Ribas-Ribas, M., Gómez-Parra, A., and Forja, J. M. (2011). Air–sea CO2 fluxes in the north-eastern shelf of the Gulf of Cádiz (southwest Iberian Peninsula). *Mar. Chem.* 123, 56–66. doi: 10.1016/j.marchem.2010.09.005

Roobaert, A., Laruelle, G., Landschützer, P., and Régnier, P. (2018). Uncertainty in the global oceanic CO2 uptake induced by wind forcing: quantification and spatial analysis. *Biogeosciences* 15, 1701–1720. doi: 10.5194/bg-15-1701-2018

Roobaert, A., Laruelle, G. G., Landschützer, P., Gruber, N., Chou, L., and Regnier, P. (2019). The spatiotemporal dynamics of the sources and sinks of CO2 in the global coastal ocean. *Glob. Biogeochem. Cycles* 33, 1693–1714. doi: 10.1029/2019GB006239

Saderne, V., Fietzek, P., and Herman, P. M. J. (2013). Extreme variations of pCO2 and pH in a macrophyte meadow of the Baltic Sea in summer: evidence of the effect of photosynthesis and local upwelling. *PLoS One* 8:e62689. doi: 10.1371/journal.pone.0062689

Salisbury, J., Green, M., Hunt, C., and Campbell, J. (2008). Coastal acidification by rivers: A threat to shellfish? *EOS* 89, 513–528. doi: 10.1029/2008EO500001

Salisbury, J., Vandemark, D., Hunt, C., Campbell, J., Jonsson, B., Mahadevan, A., et al. (2009). Episodic riverine influence on surface DIC in the coastal Gulf of Maine. *Estuar. Coast. Shelf Sci.* 82, 108–118.

Salomon, J. C., and Breton, M. (1993). An atlas of long-term currents in the Channel. *Oceanol. Acta* 16, 439–448.

Salt, L. A., Beaumont, L., Blain, S., Bucciarelli, E., Grossteffan, E., Guillot, A., et al. (2016). The annual and seasonal variability of the carbonate system in the Bay of Brest (Northwest Atlantic Shelf, 2008–2014). *Mar. Chem.* 187, 1–15. doi: 10.1016/j.marchem.2016.09.003

Sanford, E., and Kelly, M. W. (2011). Local adaptation in marine invertebrates. *Annu. Rev. Mar. Sci.* 3, 509–535. doi: 10.1146/annurev-marine-120709-142756

Santos, C. A. G., and de Morais, B. S. (2013). Identification of precipitation zones within São Francisco River basin (Brazil) by global wavelet power spectra. *Hydrol. Sci. J.* 58, 789–796. doi: 10.1080/02626667.2013.778412

Sastri, A., Christian, J. R., Achterberg, E. P., Atamanchuk, D., Buck, J. J. H., Bresnahan, P. J., et al. (2019). Perspectives on in situ sensors for ocean acidification research. *Front. Mar. Sci.* 6:653. doi: 10.3389/fmars.2019.00653

Shadwick, E. H., Friedrichs, M. A., Najjar, R. G., De Meo, O. A., Friedman, J. R., Da, F., et al. (2019). High-frequency CO2 system variability over the winter-to-spring transition in a coastal plain estuary. *J. Geophys. Res. Oceans* 124, 7626–7642. doi: 10.1029/2019JC015246

Sosik, H. M., Chisholm, S. W., and Olson, R. J. (1989). Chlorophyll fluorescence from single cells: interpretation of flow cytometric signals. *Limnol. Oceanogr.* 34, 1749–1761. doi: 10.4319/lo.1989.34.8.1749

Sosik, H. M., and Mitchell, B. G. (1991). Absorption, fluorescence, and quantum yield for growth in nitrogen-limited Dunaliellatertiolecta. *Limnol. Oceanogr.* 36, 910–921. doi: 10.4319/lo.1991.36.5.0910

Southward, A. J., Langmead, O., Hardman-Mountford, N. J., Aiken, J., Boalch, G. T., Dando, P. R., et al. (2005). Long-term oceanographic and ecological research in the Western English Channel. *Adv. Mar. Biol.* 47, 1–105. doi: 10.1016/s0065-2881(04)47001-1

Sutton, A. J., Sabine, C. L., Feely, R. A., Cai, W.-J., Cronin, M. F., McPhaden, M. J., et al. (2016). Using present-day observations to detect when anthropogenic change forces surface ocean carbonate chemistry outside preindustrial bounds. *Biogeosciences* 13, 5065–5083. doi: 10.5194/bg-13-5065-2016

Sutton, A. J., Sabine, C. L., Maenner-Jones, S., Lawrence-Slavas, N., Meinig, C., Feely, R. A., et al. (2014). A high-frequency atmospheric and seawater pCO2 data set from 14 open ocean sites using a moored autonomous system. *Earth Sys. Sci. Data* 6, 353–366. doi: 10.5194/essd-6-353-2014

Takahashi, T., Olafsson, J., Goddard, J. G., Chipman, D. W., and Sutherland, S. C. (1993). Seasonal variation of CO2 and nutrients in the high-latitude surface oceans: a comparative study. *Glob. Biogeochem. Cycles* 7, 843–878. doi: 10.1029/93GB02263

Takahashi, T., Sutherland, S. C., Sweeney, C., Poisson, A., Metzl, N., Tilbrook, B., et al. (2002). Global sea–air CO2 flux based on climatological surface ocean pCO2, and seasonal biological and temperature effects. *Deep Sea Res. Part II Top. Stud. Oceanogr.* 49, 1601–1622. doi: 10.1016/S0967-0645(02)00003-6

Thomas, C. D., Cameron, A., Green, R. E., Bakkenes, M., Beaumont, L. J., Collingham, Y. C., et al. (2004). Extinction risk from climate change. *Nature* 427, 145–148. doi: 10.1038/nature02121

Thomas, H., Bozec, Y., de Baar, H. J., Borges, A., and Schiettecatte, L. S. (2005). Controls of the surface water partial pressure of CO2 in the North Sea. *Biogeosciences* 2, 323–334. doi: 10.5194/bg-2-323-2005

Tréguer, P., Goberville, E., Barrier, N., l'Helguen, S., Morin, P., Bozec, Y., et al. (2014). Large and local-scale influences on physical and chemical characteristics of coastal waters of Western Europe during winter. *J. Mar. Syst.* 139, 79–90. doi: 10.1016/j.jmarsys.2014.05.019

Tréguer, P. J., and De La Rocha, C. L. (2013). The world ocean silica cycle. *Annu. Rev. Mar. Sci.* 5, 477–501. doi: 10.1146/annurev-marine-121211-172346

Tsunogai, S., Watanabe, S., and Sato, T. (1999). Is there a "continental shelf pump" for the absorption of atmospheric CO2? *Tellus B* 51, 701–712. doi: 10.3402/tellusb.v51i3.16468

Vargas, C. A., Lagos, N. A., Lardies, M. A., Duarte, C., Manríquez, P. H., Aguilera, V. M., et al. (2017). Species-specific responses to ocean acidification should account for local adaptation and adaptive plasticity. *Nat. Ecol. Evol.* 1:0084. doi: 10.1038/s41559-017-0084

Wafar, M. V. M., Le Corre, P., and Birrien, J. L. (1983). Nutrients and primary production in permanently well-mixed temperate coastal waters. *Estuar. Coast. Shelf Sci.* 17, 431–446. doi: 10.1016/0272-7714(83)90128-2

Waldbusser, G. G., and Salisbury, J. E. (2014). Ocean acidification in the coastal zone from an organism's perspective: multiple system parameters, frequency domains, and habitats. *Annu. Rev. Mar. Sci.* 6, 221–247. doi: 10.1146/annurev-marine-121211-172238

Walsh, J. J. (1991). Importance of continental margins in the marine biogeochemical cycling of carbon and nitrogen. *Nature* 350, 53–55. doi: 10.1038/350053a0

Walsh, J. J., Biscaye, P. E., and Csanady, G. T. (1988). The 1983–1984 shelf edge exchange processes (SEEP)—I experiment: hypotheses and highlights. *Cont. Shelf Res.* 8, 435–456. doi: 10.1016/0278-4343(88)90063-5

Wanninkhof, R. (2014). Relationship between wind speed and gas exchange over the ocean revisited. *Limnol. Oceanogr. Methods* 12, 351–362. doi: 10.4319/lom.2014.12.351

Wanninkhof, R., Asher, W. E., Ho, D. T., Sweeney, C., and McGillis, W. R. (2009). Advances in quantifying air-sea gas exchanges and environmental forcings. *Annu. Rev. Mar. Sci.* 1, 213–244. doi: 10.1146/annurev.marine.010908.163742

Weiss, R. F. (1970). The solubility of nitrogen, oxygen and argon in water and seawater. *Deep Sea Res. Oceanogr. Abstr.* 17, 721–735. doi: 10.1016/0011-7471(70)90037-9

Weiss, R. F., and Price, B. A. (1980). Nitrous oxide solubility in water and seawater. *Mar. Chem.* 8, 347–359. doi: 10.1016/0304-4203(80)90024-9

Wimart-Rousseau, C., Lajaunie-Salla, K., Marrec, P., Wagener, T., Raimbault, P., Lagadec, V., et al. (2020). Temporal variability of the carbonate system and air-sea CO2 exchanges in a Mediterranean human-impacted coastal site. *Estuar. Coast. Shelf Sci.* 236:106641. doi: 10.1016/j.ecss.2020.106641

Xing, X., Claustre, H., Blain, S., d'Ortenzio, F., Antoine, D., Ras, J., et al. (2012). Quenching correction for in vivo chlorophyll fluorescence acquired by autonomous platforms: a case study with instrumented elephant seals in the Kerguelen region (Southern Ocean). *Limnol. Oceanogr. Methods* 10, 483–495. doi: 10.4319/lom.2012.10.483

Xue, L., Cai, W.-J., Hu, X., Sabine, C., Jones, S., Sutton, A. J., et al. (2016). Sea surface carbon dioxide at the Georgia time series site (2006–2007): air–sea flux and controlling processes. *Prog. Oceanogr.* 140, 14–26. doi: 10.1016/j.pocean.2015.09.008

Yang, M., Bell, T. G., Brown, I. J., Fishwick, J., Kitidis, V., Nightingale, P. D., et al. (2019). Insights from year-long measurements of air-water CH4 and CO2 exchange in a coastal environment. *Biogeosciences* 16, 961–978. doi: 10.5194/bg-16-961-2019

Zeebe, R. E., and Wolf-Gladrow, D. (2001). *CO2 in Seawater: Equilibrium, Kinetics, Isotopes (No. 65)*. Houston, TX: Gulf Professional Publishing.

Conflict of Interest: The authors declare that the research was conducted in the absence of any commercial or financial relationships that could be construed as a potential conflict of interest.

frontiers in Marine Science

ORIGINAL RESEARCH
published: 27 October 2020
doi: 10.3389/fmars.2020.571720

Consistency and Challenges in the Ocean Carbon Sink Estimate for the Global Carbon Budget

Judith Hauck[1], Moritz Zeising[1], Corinne Le Quéré[2,3], Nicolas Gruber[4], Dorothee C. E. Bakker[2], Laurent Bopp[5], Thi Tuyet Trang Chau[6], Özgür Gürses[1], Tatiana Ilyina[7], Peter Landschützer[7], Andrew Lenton[8,9,10], Laure Resplandy[11], Christian Rödenbeck[12], Jörg Schwinger[13] and Roland Séférian[14]*

[1] Alfred-Wegener-Institut, Helmholtz-Zentrum für Polar und Meeresforschung, Bremerhaven, Germany, [2] School of Environmental Sciences, University of East Anglia, Norwich, United Kingdom, [3] Tyndall Center for Climate Change Research, University of East Anglia, Norwich, United Kingdom, [4] Institute of Biogeochemistry and Pollutant Dynamics, Eidgenössische Technische Hochschule Zurich (ETH Zurich), Zürich, Switzerland, [5] Laboratoire de Météorologie Dynamique, Institut Pierre-Simon Laplace, Centre National de la Recherche Scientifique, Ecole Normale Supérieure, Université PSL, Sorbonne Université, Ecole Polytechnique, Paris, France, [6] Laboratoire des Sciences du Climat et de l'Environnement, LSCE/IPSL, Paris, France, [7] The Ocean in the Earth System, Max Planck Institute for Meteorology, Hamburg, Germany, [8] Commonwealth Scientific and Industrial Research Organisation (CSIRO) Oceans and Atmosphere, Hobart, TAS, Australia, [9] Australian Antarctic Program Partnership, Institute for Marine and Antarctic Studies, University of Tasmania, Hobart, TAS, Australia, [10] Center for Southern Hemisphere Oceans Research, Hobart, TAS, Australia, [11] Department of Geosciences, Princeton Environmental Institute, Princeton University, Princeton, NJ, United States, [12] Biogeochemical Signals, Max Planck Institute for Biogeochemistry, Jena, Germany, [13] NORCE Norwegian Research Centre, Bjerknes Centre for Climate Research, Bergen, Norway, [14] CNRM, Université de Toulouse, Météo-France, CNRS, Toulouse, France*

OPEN ACCESS

Edited by:
Masao Ishii, Meteorological Research Institute (MRI), Japan

Reviewed by:
Rik Wanninkhof, National Oceanic and Atmospheric Administration (NOAA), United States
Shinya Kouketsu, Japan Agency for Marine-Earth Science and Technology (JAMSTEC), Japan

***Correspondence:**
Judith Hauck
judith.hauck@awi.de

Specialty section:
This article was submitted to Ocean Observation, a section of the journal Frontiers in Marine Science

Received: *11 June 2020*
Accepted: *27 August 2020*
Published: *27 October 2020*

Citation:
Hauck J, Zeising M, Le Quéré C, Gruber N, Bakker DCE, Bopp L, Chau TTT, Gürses Ö, Ilyina T, Landschützer P, Lenton A, Resplandy L, Rödenbeck C, Schwinger J and Séférian R (2020) Consistency and Challenges in the Ocean Carbon Sink Estimate for the Global Carbon Budget. Front. Mar. Sci. 7:571720. doi: 10.3389/fmars.2020.571720

Based on the 2019 assessment of the Global Carbon Project, the ocean took up on average, 2.5 ± 0.6 PgC yr^{-1} or 23 ± 5% of the total anthropogenic CO_2 emissions over the decade 2009–2018. This sink estimate is based on simulation results from global ocean biogeochemical models (GOBMs) and is compared to data-products based on observations of surface ocean pCO_2 (partial pressure of CO_2) accounting for the outgassing of river-derived CO_2. Here we evaluate the GOBM simulations by comparing the simulated surface ocean pCO_2 to observations. Based on this comparison, the simulations are well-suited for quantifying the global ocean carbon sink on the time-scale of the annual mean and its multi-decadal trend (RMSE <20 μatm), as well as on the time-scale of multi-year variability (RMSE <10 μatm), despite the large model-data mismatch on the seasonal time-scale (RMSE of 20–80 μatm). Biases in GOBMs have a small effect on the global mean ocean sink (0.05 PgC yr^{-1}), but need to be addressed to improve the regional budgets and model-data comparison. Accounting for non-mapped areas in the data-products reduces their spread as measured by the standard deviation by a third. There is growing evidence and consistency among methods with regard to the patterns of the multi-year variability of the ocean carbon sink, with a global stagnation in the 1990s and an extra-tropical strengthening in the 2000s. GOBMs and data-products point consistently to a shift from a tropical CO_2 source to a CO_2 sink in recent years. On average, the GOBMs reveal less variations in the sink than the data-based products. Despite the reasonable simulation of surface ocean pCO_2 by the GOBMs, there are discrepancies between the resulting sink estimate from GOBMs and data-products. These discrepancies are within the uncertainty of the river flux adjustment, increase over time, and largely stem from the Southern Ocean. Progress in our understanding

of the global ocean carbon sink necessitates significant advancement in modeling and observing the Southern Ocean carbon sink including (i) a game-changing increase in high-quality pCO_2 observations, and (ii) a critical re-evaluation of the regional river flux adjustment.

Keywords: ocean carbon uptake, anthropogenic CO_2, ocean carbon cycle model evaluation, riverine carbon flux, variability of the ocean carbon sink, seasonal cycle

1. INTRODUCTION

The Global Carbon Project provides annual budgets of the anthropogenic perturbations to the global carbon cycle. It assesses CO_2 emissions from burning of fossil fuels, cement production and land-use change as well as the evolution of the ocean and land carbon sinks, and of the atmospheric CO_2 inventory. The Global Carbon Project has published annual updates of the Global Carbon Budget (GCB) since 2007 (Canadell et al., 2007; Le Quéré et al., 2009) with more detailed documentations since 2013 (e.g., Le Quéré et al., 2013, 2014; Friedlingstein et al., 2019).

Fossil fuel CO_2 emissions reached 10.0 PgC yr^{-1} in 2018, but the fraction of the CO_2 remaining in the atmosphere has been remarkably stable at 45% on average since 1958. Land and ocean have sequestered 29 ± 5 and 23 ± 5%, respectively, of total fossil and land-use change emissions over the last decade, 2009–2018 (Friedlingstein et al., 2019). The ocean figures prominently in the Global Carbon Budget by having sequestered 25% of cumulative CO_2 emissions since 1850. Over the same period, the land has sequestered 30% of cumulative emissions, but has also released a comparable amount of CO_2 by land-use change emissions (Friedlingstein et al., 2019).

The ocean carbon sink (S_{OCEAN}) has been estimated from global ocean biogeochemical models (GOBMs) since the start of the GCB activity. Initially, the land sink was calculated from the balance of the CO_2 emissions, the increase in the atmospheric inventory and the flux into the ocean (Le Quéré et al., 2013). Due to the decisive role of the ocean sink estimate for the calculated land sink, the ocean models were scaled to the mean ocean anthropogenic carbon sink for the 1990s of 2.2 ± 0.4 PgC yr^{-1} as estimated by the IPCC based on three selected methods after examination of seven independent observational-based methods (Denman et al., 2007). Hence, the GOBMs were only used to estimate the year-to-year change around the mean 1990s anthropogenic carbon sink. Since 2017, the land sink is estimated independently, based on Dynamic Global Vegetation Models (DGVMs), and the GOBMs are not scaled anymore to the 1990s sink (Le Quéré et al., 2018b). This change in methodology has reduced the ocean carbon sink estimate in the GCB by roughly 0.2 PgC yr^{-1} and the independence of land and ocean sink estimates allowed for the introduction of the budget imbalance (B_{IM}) in the Global Carbon Budget. The B_{IM} quantifies the gap between the best estimates of emissions and sinks, and hence reflects limitations in our understanding of the global carbon cycle. The B_{IM} is 0.4 PgC yr^{-1} or 4% of CO_2 emissions for the decade 2009–2018 and could either be due to overestimated emissions or underestimated sinks. The uncertainties in the sinks (land and/or ocean) are more likely to play an important role for the B_{IM} given that it has the same magnitude now as in the 1960s, when the emissions were a lot smaller.

The estimate of the mean S_{OCEAN} and its year-to-year variability is discussed in comparison with ocean carbon sink estimates from data-based pCO_2 mapping methods, which are referred to as pCO_2-based data-products in the GCB or data-products in short. The mapping methods use statistical interpolation or neural network regression to map the global sea-surface pCO_2 field based on pCO_2 measurements from the Surface Ocean CO_2 Atlas (SOCAT, Bakker et al., 2016) and other environmental data-sets (Rödenbeck et al., 2015). Despite SOCATv2019 containing more than 25 million observations, they cover only a tiny fraction of the spatio-temporal pCO_2 field (on the order of 2% of the monthly 1 × 1° pixels in 1982–2018). The spatial and temporal autocorrelation of the pCO_2 field around the data locations, with a global median spatial autocorrelation length of 400 ± 250 km (Jones et al., 2012), suggests that the observations also include information about a larger region than the actual sampling site and hence the implicitly observed ocean area is substantially larger than 2%. Nevertheless, the sparsity of the observations and their highly uneven coverage in space and time remain a major challenge. In order to upscale these scarce observations to a globally gridded product, the mapping methods make use of a range of assumptions and input data sets (Rödenbeck et al., 2015).

GOBMs and mapping methods approach the estimation of the ocean carbon sink from opposite sides. The GOBMs simulate the carbon transport with large-scale ocean circulation and resolve carbon source and sink processes on large spatial and temporal scales. The GOBMs thereby constrain the air-sea CO_2 flux by the transport of carbon into the ocean interior, which is also the controlling factor of ocean carbon uptake in the real world. When carbon is transported from the surface mixed layer into the ocean interior, more CO_2 can be taken up at the surface. The air-sea CO_2 flux in GOBMs therefore depends strongly on the simulated large-scale ocean circulation. In contrast, the data-products are based on statistical tools to map scarce pCO_2 observations and derive the ocean sink with the use of gas-exchange parameterizations. They are more closely linked to observations, but their estimated air-sea CO_2 flux depends strongly on uncertainties in the gas-exchange parameterization (e.g., Wanninkhof, 2014; Woolf et al., 2019) and gridded wind products, and there is no constraint from the ocean interior perspective. Ocean inversion and data-assimilated models that combine the process understanding of the GOBMs and are tied

to observations are becoming available, but are so far limited to estimating the (decadal) mean ocean sink, annual estimates for the last 10 years, and/or regional estimates (e.g., Mikaloff Fletcher et al., 2006; Verdy and Mazloff, 2017; DeVries et al., 2019).

As the estimates of S_{OCEAN} are not tied to an observational estimate any more since the GCB 2017, an accurate simulation of the mean ocean carbon sink by the models has become more important. Model evaluation was introduced in 2018 (Le Quéré et al., 2018a, Figure B1) as a single mismatch metric between surface ocean pCO_2 (partial pressure of CO_2) observations from the Surface Ocean CO_2 Atlas (SOCAT, Bakker et al., 2016). A thorough documentation of the strengths and weaknesses of the CO_2 source and sink characteristics modeled by the GOBMs used in the GCB has been lacking thus far. In this study, we aim to assess the performance and spread of the GOBMs with respect to simulations of surface pCO_2 and air-sea CO_2 exchange, on different time-scales (preindustrial mean; historical: monthly, annual including the trend, and multi-year variability), document the effects of recent changes in methodology in the GCB 2019 ocean carbon sink estimate, and highlight consistencies and challenges across GOBMs and data-based pCO_2 mapping methods.

2. METHODS

2.1. Definition of Air-Sea CO_2 Fluxes

The contemporary air-sea CO_2 flux (F_{net}) can be decomposed into multiple terms:

$$F_{net} = F_{ant,ss} + F_{ant,ns} + F_{nat,ss} + F_{nat,ns} + F_{riv,ss} + F_{riv,ns} \quad (1)$$

where the subscript *ant* denotes anthropogenic, *nat* natural, *riv* rivers, *ss* steady state, and *ns* denotes non-steady state. Anthropogenic refers to the direct effect of atmospheric CO_2 increase only. The annotation *steady state* stands for fluxes in a constant or preindustrial climate and *non-steady state* for climate change and natural climate variability effects on the respective flux. Based on the assumption that ocean and atmosphere were in equilibrium in preindustrial times, the global total of $F_{nat,ss}$ is supposed to be zero, although regional fluxes are different from zero. The steady-state preindustrial state, i.e., the sum of $F_{nat,ss}$ and $F_{riv,ss}$, is characterized by net outgassing of CO_2.

The ocean sink S_{OCEAN} as defined in the GCB accounts for a subset of terms in F_{net}. This is motivated to capture those terms directly influenced by anthropogenic perturbations, including climate change, but also comprises climate variability:

$$S_{OCEAN} = F_{ant,ss} + F_{ant,ns} + F_{nat,ns} \quad (2)$$

with $F_{ant,ss}$ being the flux in response to the atmospheric CO_2 increase only, $F_{ant,ns}$ the effect of climate change and variability on $F_{ant,ss}$, and $F_{nat,ns}$ being the effect of climate change and variability on the natural CO_2 flux. Note that this definition of the ocean carbon sink S_{OCEAN} in the GCB is different from the definition of the "anthropogenic CO_2 sink" referred to as the change in ocean carbon content only due to the direct effect of increasing CO_2 concentration in the atmosphere ($F_{ant,ss}$ + $F_{ant,ns}$), often used in the observational ocean carbon cycle community (e.g., Gruber et al., 2019).

The steady-state river flux, $F_{riv,ss}$, i.e., the ocean outgassing due to carbon transport from land to sea, is estimated to be between 0.45 ± 0.18 PgC yr^{-1} (Jacobson et al., 2007) and 0.78 ± 0.41 PgC yr^{-1} (Resplandy et al., 2018). The steady-state outgassing of riverine carbon reflects the balance between the input into the ocean of inorganic and organic carbon by rivers and the burial of inorganic and organic carbon in the oceanic sediments (Sarmiento and Sundquist, 1992). Riverine carbon is transported to the open ocean in the form of particulate or dissolved organic carbon and subsequently remineralized to inorganic carbon, which can be exchanged with the atmosphere. In the pre-industrial state, the riverine outgassing is considered to occur in the open ocean with the coastal ocean being neither a source nor a sink for CO_2 (Regnier et al., 2013). We thus consider that the underrepresentation of coastal data points in SOCAT and hence in the data-based products does not justify omitting the river flux adjustment.

The non-steady state river flux component, $F_{riv,ns}$, consists of anthropogenic perturbations of river fluxes and natural variability. These non-steady state components should conceptually be included in the GCB, but are not accounted for due to a lack of annually resolved and regularly updated estimates. The organic carbon export from terrestrial ecosystems into aquatic systems has increased by 1.0 ± 0.5 PgC yr^{-1} since pre-industrial times (Regnier et al., 2013). This exported carbon is partly respired in the land-ocean aquatic continuum (freshwaters, estuaries, coastal areas), partly buried in sediments, and to a smaller extent transferred to the open ocean (Regnier et al., 2013).

2.2. Global Ocean Biogeochemistry Models Contributing to the Global Carbon Budget

The Global Ocean Biogeochemical Models used in the GCB are general ocean circulation models with coupled ocean biogeochemistry. The nine contributing models in GCB2019 are NEMO-PlankTOM5 (Buitenhuis et al., 2013), MICOM-HAMOCC (NorESM-OC, Schwinger et al., 2016), MPIOM-HAMOCC6 (Paulsen et al., 2017), NEMO3.6-PISCESv2-gas (CNRM, Berthet et al., 2019), CSIRO (Law et al., 2017), MITgcm-REcoM2 (Hauck et al., 2018), MOM6-COBALT (Princeton, Adcroft et al., 2019), CESM-ETHZ (Doney et al., 2009), and NEMO-PISCES (IPSL, Aumont et al., 2015). A detailed overview table of model spin-up, initial conditions and forcing can be found as Table A2 in Friedlingstein et al. (2019). Here, we only summarize the main features. The GOBMs use a fixed resolution in longitude of between 0.5 and 2° and eight out of the nine models use a varying resolution in latitude between 0.17 and 2° (see Table A2 in Friedlingstein et al., 2019). The number of depth levels varies between 30 and 75. The models are spun-up with varying spin-up procedures for a period ranging from 28 to 1,000 years. All models except for MPI initialize from alkalinity and pre-industrial dissolved inorganic carbon (DIC) fields from either GLODAPv1 (Key et al., 2004) or GLODAPv2 (Lauvset et al., 2016). MPI initializes from a uniform distribution

followed by a long spin-up (several 1,000 years). The time-step of the models varies between 15 and 96 min and CO_2 flux and surface pCO_2 are saved with a monthly frequency (**Supplementary Table 2**).

Here, we add FESOM-REcoM to this suite of GOBMs, which will replace MITgcm-REcoM in future releases of the GCB. It consists of the biogeochemical model REcoM2 (Hauck et al., 2013, 2018; Schourup-Kristensen et al., 2014) coupled to the finite element ocean circulation model FESOM-1.4 (Wang et al., 2014). The model previously described by Schourup-Kristensen et al. (2014, 2018) has been updated to use the mocsy2.0 routines for carbonate chemistry including water vapor correction (Orr and Epitalon, 2015), the photodamage parameterization by Álvarez et al. (2018), and the dust fields from Albani et al. (2014) as surface forcing for iron. River fluxes of carbon and nutrients are switched off to comply with the GCB protocol. The multi-resolution mesh configuration is based on a coarse mesh with a global nominal resolution of 1°, which is increased to about 25 km north of 50°N and to about 1/3° in the equatorial belt, and is also moderately refined along the coasts (REF mesh in Sidorenko et al., 2015; Rackow et al., 2018). The simulation shown here is the second cycle of JRA-55-do forcing 1958–2017. Alkalinity and preindustrial DIC are initialized from GLODAPv2 (Lauvset et al., 2016). In the following, we include FESOM-REcoM in all analyses, and give total budget numbers with and without FESOM-REcoM to document the effects of methodological changes on the GCB2019 ocean sink estimate exactly as in Friedlingstein et al. (2019).

The GOBMs are forced with atmospheric reanalysis data sets and observed atmospheric CO_2 concentration. As the model simulations are updated once a year for the latest calendar year, only atmospheric reanalysis data sets that are regularly updated within few months can be used. Five out of the ten models are forced with either JRA-55 or JRA55-do (Kobayashi et al., 2015; Tsujino et al., 2018, CSIRO, MITgcm-REcoM, FESOM-REcoM, MOM6-COBALT, CESM-ETHZ, IPSL), two models are forced with NCEP/NCAR-R1 (Kalnay et al., 1996, MPIOM-HAMOCC and NEMO-PlankTOM5) and two models use NCEP/NCAR-R1 with CORE-II corrections (CNRM and NorESM). CORE-II (Yeager and Large, 2008) and ERA-20C (Poli et al., 2013) forcing data sets are used for the spin-up by single groups.

The monthly atmospheric CO_2 mixing ratio (xCO_2, in ppm, including the seasonal cycle) is an average of Mauna Loa and South Pole stations for the 1958–1979 period and of multiple stations with well-mixed background air thereafter (Ballantyne et al., 2012; Dlugokencky and Tans, 2019). Data prior to March 1958 are estimated with a cubic spline fit to ice core data from Joos and Spahni (2008). As the seasonality in this global time-series is dominated by the northern hemisphere land, some modeling groups (CNRM, IPSL) derive an annual mean xCO_2 from the provided monthly fields to avoid an out-of phase seasonal cycle in the southern hemisphere. The provided atmospheric xCO_2 is converted to pCO_2 by accounting for atmospheric sea-level pressure p_{atm} (CESM-ETH, NEMO-PlankTOM5, MOM6-COBALT, IPSL, FESOM-REcoM, CSIRO) or with a constant sea-level pressure (CNRM: 1,000 hPa, NorESM: 1013.25 hPa). Two models use xCO_2 without conversion to pCO_2 (MITgcm-REcoM, MPI, **Table 1**). Five models (CNRM, NEMO-PlankTOM5, MOM6-COBALT, IPSL, FESOM-REcoM) further take into account the water vapor pressure (pH_2O) correction as

$$pCO_2 = xCO_2 \cdot \left(p_{atm} - pH_2O\right) \quad (3)$$

The GOBMs do not consider river fluxes of carbon, alkalinity and nutrients into the ocean in the versions used here (MITgcm-REcoM, FESOM-REcoM, NorESM-OC, MPIOM-HAMOCC6, CSIRO) or their river fluxes are approximately balanced by burial in sediments (NEMO-PlankTOM5, IPSL, Princeton, CESM-ETHZ). In this case, these river fluxes do not induce a river-driven net sea-to-air CO_2 flux. Only in CNRM is the burial substantially larger than the lateral inflow of carbon into the ocean (**Table 1**).

TABLE 1 | Specifications of Global Ocean Biogeochemical Models: River carbon input, net burial and conversion from xCO_2 (ppm) to pCO_2 (μatm) using atmospheric sea-level pressure p_{atm} and water vapor correction.

Model	River C (PgC yr^{-1})	Burial (PgC yr^{-1})	p_{atm}	Water vapor correction
MITgcm-REcoM	0	0	No	No
MPI	0	0	No	No
CESM-ETH	0.33	0.25	Yes	No
CNRM	0.61	0.94	Fixed at 1,000 hPa	Yes
CSIRO	0	0	Yes	No
NorESM	0	0	Fixed at 1013.25 hPa	No
PlankTOM	0.72	0.72	Yes	Yes
MOM6-COBALT	0.11	0.18	Yes	Yes
IPSL	0.61	0.59	Yes	Yes
FESOM-REcoM	0	0	Yes	Yes

2.2.1. GOBM Simulations and Analysis

Two simulations are performed by each modeling group. Simulation A is designed to reproduce the interannual variability and trend in the ocean carbon uptake in response to changes in both atmospheric CO_2 and climate. Simulation A is forced with interannual varying atmospheric forcing and increasing atmospheric CO_2. This is the contemporary CO_2 flux simulation and it includes the following terms:

$$F_{simA} = F_{ant,ss} + F_{ant,ns} + F_{nat,ss} + F_{nat,ns} + F_{drift+bias} \quad (4)$$

Simulation B is a control simulation with constant atmospheric forcing (normal year or repeated year forcing) and constant preindustrial atmospheric CO_2 (modeling groups use either 278 or 284 ppm). It represents the natural steady-state flux plus any flux due to bias and drift:

$$F_{simB} = F_{nat,ss} + F_{drift+bias} \quad (5)$$

All models except CNRM and IPSL use a climatology or single year forcing for simulation B. Simulation B of CNRM is forced

by cycling over the first 10 years of the NCEP/NCAR-R1 forcing. IPSL instead contributed a simulation with constant atmospheric CO_2 and interannual varying atmospheric forcing that corresponds to $F_{nat,ss} + F_{nat,ns} + F_{drift+bias}$.

In order to derive S_{OCEAN} from the model simulations, we subtract the annual time-series of simulation B from the annual time-series of simulation A for all models that used single year or climatological forcing for their simulation B. Assuming that $F_{drift+bias}$ is the same in simulations A and B, we thereby correct for any model drift. Further, this difference also removes the $F_{nat,ss}$, which is often a major source of biases. Simulations B of IPSL and CNRM have to be treated differently due to their different protocols. For these models, we fit a linear trend to the simulation B and subtract this linear trend from simulation A. This approach assures that the interannual variability is not removed from IPSL simulation A. It will also remove a potential trend in $F_{nat,ns}$, which tends to be substantially smaller than the trend in $F_{ant,ss}$, but is still of potential interest in the context of decadal variability in the ocean carbon sink.

Modeling groups submit global and regional annual time-series of the ocean carbon sink integrated from their native model grids. This procedure avoids errors in the integrated carbon sink due to interpolation. These data are used for all time-series figures. Three regions are considered: north (>30°N), tropics (30°S-30°N) and south (<30°S). Further, gridded fields of pCO_2 and air-sea CO_2 flux on a 1x1 degree grid are used for model evaluation. The regional CO_2 fluxes are not corrected for bias and drift of the control simulation, as the assumption of zero $F_{nat,ss}$ only holds on the global level. The submitted time-series and gridded fields for simulation A and B are published in the data repository Pangaea (Hauck et al., 2020).

2.3. Data-Based pCO_2 Mapping Methods

Three mapping methods are used here: the MPI-SOMFFN (Landschützer et al., 2016), the Jena-MLS (Rödenbeck et al., 2014), and the CMEMS (Denvil-Sommer et al., 2019) methods. The products are regularly updated, now covering the period 1982–2018 (Jena-MLS, MPI-SOMFFN) or 1985-2018 (CMEMS). All methods are based on SOCATv2019 surface ocean fugacity of CO_2 (pCO_2 corrected for the non-ideal behavior of the gas) as input data set, which is an update of SOCAT version 3 (Bakker et al., 2016). CMEMS used only two thirds of the SOCATv2019 data for training the method and the rest for validation. We refer to the resulting data sets as pCO_2-based data-products. From these gridded pCO_2 products, the contributing groups calculated the air-sea CO_2 flux using their own methods, and integrated their global and regional ocean carbon sink estimates over their native grids to provide the resulting air-sea CO_2 flux time-series. MPI-SOMFFN and CMEMS use the global monthly atmospheric xCO_2 time-series. Jena-MLS uses the spatially and temporally explicit xCO2 boundary conditions from the Jena Carbo Scope atmospheric inversion (Rödenbeck et al., 2018). All methods convert xCO_2 to pCO_2 using sea-level pressure and the water vapor correction. All three mapping methods use a quadratic gas-exchange formulation ($k \cdot U^2 \cdot (Sc/660)^{-0.5}$) with the transfer coefficient k scaled to match a global mean transfer rate of 16 cm/h (Wanninkhof, 1992; Naegler, 2009) and the Schmidt number Sc estimated with a third-order polynomial fit of sea surface temperature. The mapping methods use different wind speed products [Jena-MLS: NCEP/NCAR-R1 (Kalnay et al., 1996), MPI-SOMFFN: ERA-INTERIM (Dee et al., 2011), CMEMS: ERA5 (Hersbach et al., 2020; Simmons et al., 2020)] for the calculation of the CO_2 flux (**Supplementary Table 1**). Gridded fields of pCO_2 and air-sea CO_2 flux were submitted for the evaluation, where MPI-SOMFFN and CMEMS submitted monthly 1 × 1° fields. The daily 4 × 5° Jena-MLS fields were regridded to monthly 1 × 1° fields using nearest neighbor interpolation with the griddata function from the python SciPy module. The submitted time-series and gridded fields are published in the data repository Pangaea (Hauck et al., 2020).

The data-products are based on contemporary sea surface pCO_2 observations and thus estimate F_{net} (see Equation 1). In order to compare them with the S_{OCEAN} estimate, they have to be adjusted for the riverine flux $F_{riv,ss}$ (using 0.78 ± 0.41 PgC yr^{-1}, Resplandy et al., 2018). The riverine adjustment is attributed to three latitudinal bands using the spatial distribution of Aumont et al. (2001) with the caveat that the regional boundaries are defined at 20°N and 20°S as opposed to the latitudinal boundaries of 30°N/S used in the GCB otherwise. This results in additive river flux adjustment terms of $F_{riv,ss}$ of 0.20 PgC yr^{-1} (north), 0.19 PgC yr^{-1} (tropics), and 0.38 PgC yr^{-1} (south).

2.4. Area Weighting

GOBMs and mapping methods all cover different amounts of ocean surface area. To close the Global Carbon Budget with CO_2 sources and sinks, the total ocean area has to be considered. Hence, the total ocean area covered by each GOBM and mapping method on their native grids was requested and compared to the global ocean area of 361,900,000 km^2 from ETOPO1 (Amante and Eakins, 2009; Eakins and Sharman, 2010).

The ocean area covered by the ocean models range between 352,050,000 km^2 for MITgcm-REcoM which excludes the Arctic north of 80°N to 365,980,000 km^2 for MPI. The ocean models hence cover 97.3–101.1% of the global ocean area. These differences in ocean coverage originate from the grid specifications in coastal regions, besides the missing Arctic and Mediterranean Sea in MITgcm-REcoM. As none of the models resolves coastal processes explicitly, we scale the annual time-series of the total ocean carbon sink by the ratio of the ETOPO1 global ocean area (Amante and Eakins, 2009; Eakins and Sharman, 2010) to the modeled ocean area.

The covered ocean area ranges from 88.9% of the global ETOPO1 ocean area in two data-products (MPI-SOMFFN and CMEMS) to 101.4% in the Jena-MLS. The non-mapped ocean area in MPI-SOMFFN and CMEMS are located all along the coasts and in marginal seas, including the Mediterranean Sea and the Arctic Ocean. We apply the same area-scaling procedure to the data-products as to the models to yield a consistent estimate of the global ocean carbon sink.

The areal correction is not applied to the regional fluxes due to the lack of information on area coverage per region. The effects of this area-correction or its omission are described and discussed in sections 3.2 and 4.5.

Global and regional time-series of GOBMs and data-products after area weighting but without river flux adjustment are archived in ICOS (Global Carbon Project, 2019).

2.5. Quantification of Temporal Variability

To quantify agreement of GOBMs and mapping methods on the multi-year variability of the GCB ocean sink estimate, we define four distinct periods. We chose the years 1992, 2001, and 2011 as boundaries for the four phases following Landschützer et al. (2015). These years also mark cusps in the ensemble mean of data-products, most pronounced in the Southern Ocean. We tested the trend significance within these multi-year periods from start year to end year with a Mann-Kendall test using the python module pyMannKendall (Hussain and Mahmud, 2019).

Furthermore, we calculate the amplitude of interannual variability (AIAV, Rödenbeck et al., 2015) as the temporal standard deviation of the air-sea CO_2 exchange derived from the gridded fields as follows: (1) air-sea CO_2 exchange filtered for water depth exceeding 400 m (not subsampled for SOCAT sampling sites), (2) spatially-integrated, (3) 12-months running mean filter applied, and (4) detrended. Our AIAV calculation differs from Rödenbeck et al. (2015) only by the detrending which is used to separate out the variability from the trend. It differs from the AIAV shown in Friedlingstein et al. (2019) by the detrending and also by the time period considered (1992–2018), which is shorter but has a larger data density.

2.6. Evaluation Metrics

We use the gridded pCO_2 fields for model evaluation on which we apply two filters. First, we follow Rödenbeck et al. (2015) by using only open ocean data points where water depth exceeds 400 m (thereby excluding 8% of the ocean area). Second, we subsample data-points from models and mapping methods for which there is a matching fCO_2 (fugacity of CO_2) value from the binned SOCATv2019 product (gridded, on a monthly 1 $\times$ 1° resolution; Bakker et al., 2016), which we refer to as pCO_2 in the following. The fugacity of CO_2 is 3–4‰ smaller than the partial pressure of CO_2 (Zeebe and Wolf-Gladrow, 2001). We acknowledge the importance of this distinction in the observational community, but consider it negligible for the model evaluation.

We generate global and regional monthly mean pCO_2 time-series by averaging over all subsampled pCO_2 data points in a given region. All data points are weighted equally. Monthly correlation coefficient and root mean squared error (RMSE) between simulated and observed pCO_2 are calculated from the subsampled data sets before calculating the spatial average. Statistics are calculated for the period 1992–2018, due to the limited data availability of surface pCO_2 observations prior to 1992 (Bakker et al., 2016).

Annual time-series are calculated from the monthly mean *subsampled* time-series after integration over regions. Annual RMSE and correlation coefficient are calculated from these time-series, contrary to the monthly statistics. We consider this to be more robust than to calculate the annual mean at each pixel given the data sparsity. Hence, the annual metrics are to be interpreted as a measure of the misfit on the large regional or global spatial scale and on the multi-year time-scale (mean and trend). RMSE and correlation coefficient were additionally calculated from detrended annual mean time-series to separate out the mismatch of interannual variability on large spatial scales. For the GOBMs and data-products, a second annual time-series is calculated from the *full* data set to distinguish "true" variability from a potentially biased variability stemming from the sparse and inhomogeneous sampling.

The pCO_2 mismatch is calculated as simulated or mapped pCO_2 minus SOCAT pCO_2 at each data-point of the subsampled data set. It is then spatially averaged into a monthly time-series and temporally averaged into an annual time-series. The mean bias is calculated as the average of the annual mean mismatch.

TABLE 2 | Global bias and drift of annual air-sea CO_2 flux in control simulation of individual Global Ocean Biogeochemical Models. The drift is calculated as a linear fit to the full annual time-series 1959–2018.

Model	Bias (PgC yr^{-1})	Drift (PgC yr^{-2})
MITgcm-REcoM	−0.07	−0.0015
MPI	0.09	0.00022
CESM-ETH	0.14	−0.0012
CNRM	0.31*	−0.0017*
CSIRO	−0.21	0.0034
NorESM	−0.01	0.00049
PlankTOM	−0.05	−0.0026
MOM6-COBALT	0.37	−0.0020
IPSL	0.19	−0.0024
FESOM-REcoM	0.19	0.0026

An updated simulation with CNRM with repeated 1948 forcing yields slightly lower bias (0.26) and drift (−0.0003).

3. RESULTS

3.1. Control Simulation—Global and Regional CO_2 Flux

The ten GOBMs simulate a preindustrial ocean carbon sink $F_{nat,ss}$ + $F_{drift+bias}$ (simulation B) between −0.21 to 0.37 PgC yr^{-1} with a mean of 0.1 PgC yr^{-1} (0.08 PgC yr^{-1} without FESOM as in Friedlingstein et al., 2019, a positive number indicates a flux into the ocean; **Table 2**, **Figure 1**). It follows from the definition of $F_{nat,ss}$ = 0, that any deviation of CO_2 flux in simulation B from zero is considered a model bias. The drift of CO_2 flux in the control simulations varies between −0.0026 and 0.0034 PgC yr^{-2} and is thus small compared to the trend of CO_2 flux in the historical simulation. The smallest drifts are found in two models with long spin-up (1,000 years, NorESM and MPI). CNRM and IPSL show more variability due to their forcing choices. FESOM-REcoM falls within the range of the other GOBMs with a positive bias and drift (**Table 2**).

The strong positive bias in CNRM can be explained by the burial flux which is larger than the river carbon input and leads to a CO_2 flux into the ocean in the preindustrial state. The burial is also larger than the river input in MOM6-COBALT, but not large enough to explain the bias of 0.37 PgC yr^{-1}. Other positive

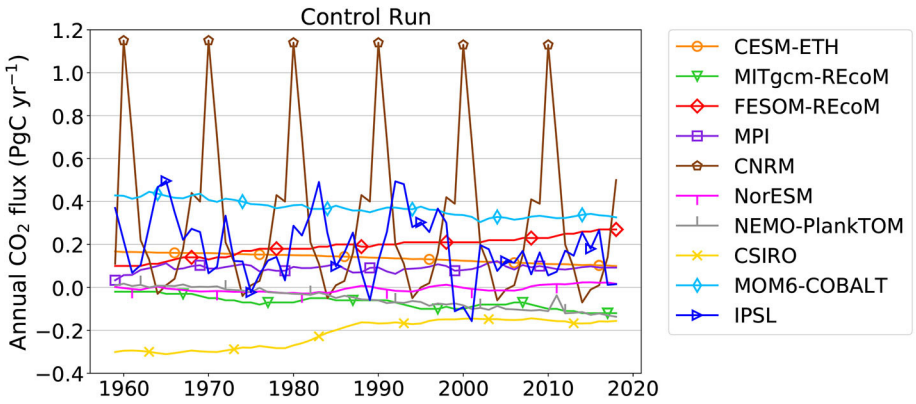

FIGURE 1 | Annual air-sea CO_2 flux in control simulation (simulation B) of individual Global Ocean Biogeochemical Models. This is equivalent to $F_{simB} = F_{nat,ss} + F_{drift+bias}$ (Equation 5), where any flux different from zero is considered a bias and any temporal change in the control simulation is considered a drift. Positive: CO_2 flux into the ocean.

or negative biases cannot be explained by an imbalance of burial and river fluxes.

There are substantial natural CO_2 fluxes into and out of the ocean on a regional level that have previously been assessed using ocean inversions and ocean models (Mikaloff Fletcher et al., 2007). All GOBMs reproduce the natural CO_2 outgassing flux in the tropics, particularly the large flux to the atmosphere in the equatorial Pacific (**Figure 2**). There is less agreement on the relative contributions to natural CO_2 outgassing in the tropical Indian Ocean vs. the tropical Atlantic with a slightly larger contribution from the tropical Atlantic in MPI, NorESM, CSIRO, CESM-ETH, MOM6-COBALT, and FESOM-REcoM as in Mikaloff Fletcher et al. (2007). NEMO-PlankTOM simulates a much larger outgassing in the tropical Indian Ocean, whereas MITgcm-REcoM has close to zero flux and CNRM even a slight CO_2 uptake in the tropical Indian Ocean.

There are differences between the models on the relative contributions of certain regions also in the northern extra-tropics, where the inversion showed the strongest CO_2 uptake in the low- and mid-latitude North Pacific, followed by the low- and mid-latitude North Atlantic and then high-latitudes (north of 49°N). This pattern is only reproduced by NorESM. Other models (MPI, CSIRO, CNRM, CESM-ETH, MOM6-COBALT, FESOM-REcoM) simulate a larger uptake in the high-latitudes than in the low- and mid-latitude North Atlantic. NEMO-PlankTOM5 and MITgcm-REcoM exhibit a small net outgassing signal in the low- and mid-latitude North Pacific or the low- and mid-latitude North Atlantic, respectively.

In the southern extra-tropics, the inversion exhibited CO_2 uptake with the strongest signal in the South Pacific, followed by the Southern Indian Ocean and the South Atlantic. This pattern is reproduced by NEMO-PlankTOM, CSIRO and CESM-ETH. Other models found a stronger CO_2 sink in the Southern Indian Ocean than in the Southern Pacific Ocean (NorESM, CNRM, MOM6-COBALT). In contrast, MPI and MITgcm-REcoM show weak outgassing signals in the South Pacific or South Atlantic, respectively. FESOM-REcoM produces a net zero flux in the South Pacific.

Previously identified discrepancies between ocean models and the ocean inversion estimates on the natural CO_2 flux prevail in the Southern Ocean (Mikaloff Fletcher et al., 2007, models: roughly zero flux, ocean inversion: outgassing). MPI and MITgcm-REcoM models have no net natural CO_2 outgassing in the regions 44–58°S or south of 58°S, all other models have net outgassing in at least one of these regions. The total natural CO_2 outgassing signal in the Southern Ocean is smaller in all models than in the ocean inversion.

3.2. Historical Simulation—Global CO_2 Flux

Since models are not scaled to the observational constraint of the 1990s anymore, their bias and drift as determined with the control simulation has to be subtracted to satisfy our definition of S_{OCEAN}. The mean correction applied in the GCB2019 (Friedlingstein et al., 2019) varies between −0.36 and +0.16 PgC yr^{-1} when averaged over the 1990s and the multi-model mean CO_2 flux is thereby reduced by 0.07 PgC yr^{-1}. The correction leads to a larger model spread with a standard deviation of 0.27 PgC yr^{-1}. Similar reductions and larger spreads of the ensemble mean CO_2 flux result for other time periods, e.g., a reduction of 0.06 and 0.05 PgC yr^{-1} for the 2000s and the period 2009–2018, respectively (**Table 3**).

To close the Global Carbon Budget, the total ocean area has to be considered, and we scale all GOBMs to the same global ocean area. This has a small effect on the ocean carbon sink estimate with corrections of −0.02 PgC yr^{-1} for the MPI model to +0.05 PgC yr^{-1} for MITgcm-REcoM, when averaged over the 1990s. The multi-model mean increases by 0.01, 0.01, and 0.02 PgC yr^{-1} when averaged over the 1990s, 2000s, and 2009–2018, respectively (**Table 3**). The model spread is further enlarged as the CO_2 flux in the MPI model which has already the lowest ocean carbon sink, is further reduced and the CO_2 flux in the two models with the largest ocean carbon sink (CSIRO, NorESM) is further increased.

Taken together, the bias-correction and area-weighting reduce the multi-model mean ocean carbon sink estimate slightly and increase the model spread (**Table 3**). All models are within the

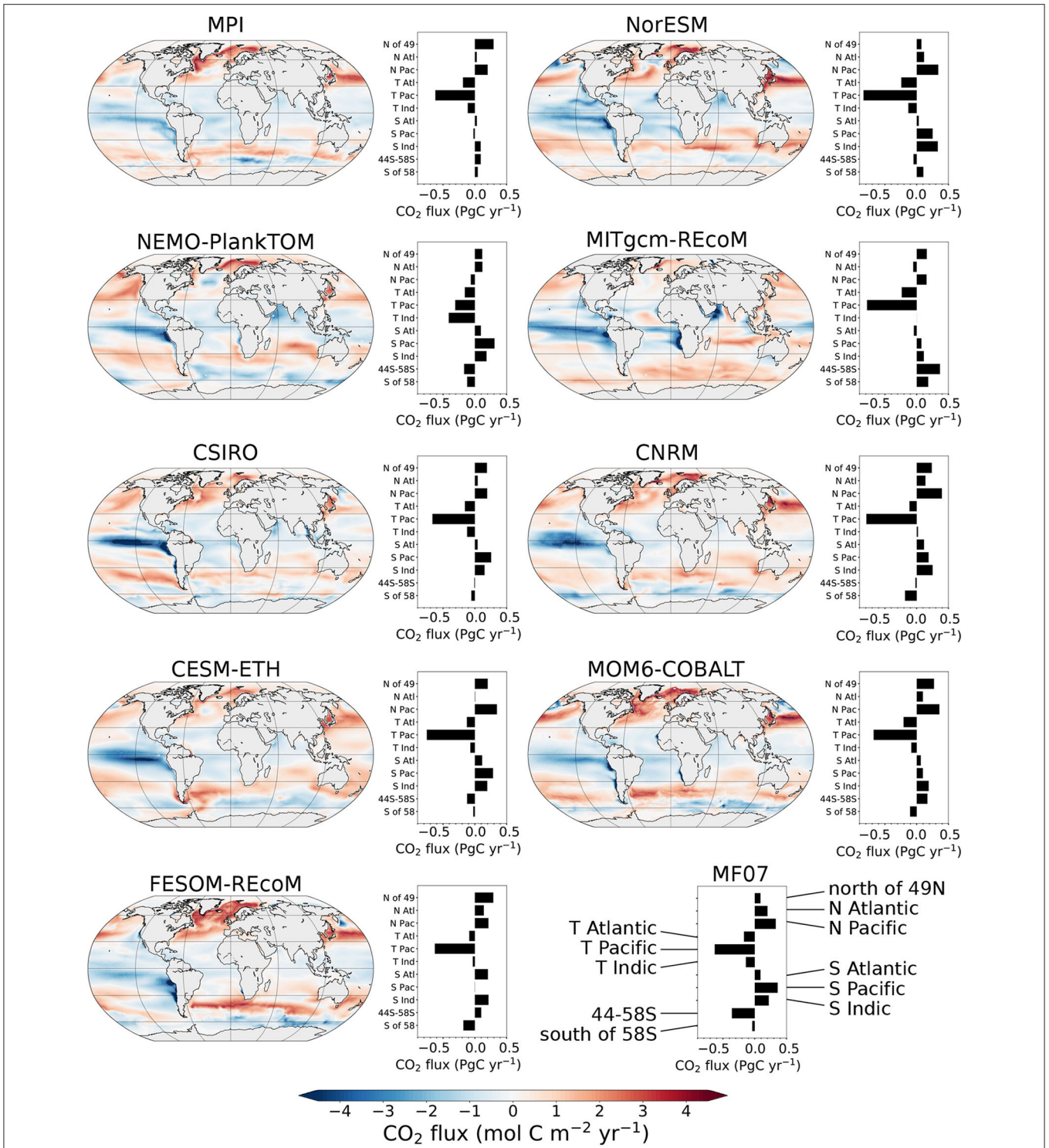

FIGURE 2 | Natural air-sea CO_2 flux in individual Global Ocean Biogeochemical Models as derived from control simulation B. The air-sea CO_2 flux is averaged over the last 10 years of the control simulation. The bar plots exhibit integrated air-sea CO_2 fluxes over the regions used in Mikaloff Fletcher et al. (2007). The lower right bar plot shows the ocean inversion results from Mikaloff Fletcher et al. (2007, MF07). Positive numbers indicate a flux into the ocean.

observational constraint of anthropogenic ocean CO_2 uptake for the 1990s of 2.2 ± 0.6 PgC yr^{-1} before and after applying these corrections. This observational constraint is based on an assessment taking into account indirect observations with seven different methodologies (Denman et al., 2007). These methods include the observed atmospheric O_2/N_2 concentration trends

TABLE 3 | Ensemble mean and standard deviation of air-sea CO_2 flux before and after applying corrections.

Method	Ensemble mean ± std (PgC yr^{-1})		
	1990s	2000s	2009–2018
GLOBAL OCEAN BIOGEOCHEMISTRY MODELS			
Simulation A	2.03 ± 0.20	2.21 ± 0.21	2.55 ± 0.24
Sim A, bias-corrected	1.96 ± 0.27	2.15 ± 0.28	2.50 ± 0.31
Sim A, bias-corrected and area-weighted	1.97 ± 0.30	2.17 ± 0.31	2.52 ± 0.34
Sim A, bias-corrected and area-weighted (incl FESOM-REcoM)	1.99 ± 0.25	2.17 ± 0.26	2.52 ± 0.29
DATA-PRODUCTS			
Raw (F_{net})	1.44 ± 0.26	1.55 ± 0.20	2.15 ± 0.16
Area-weighted F_{net}	1.54 ± 0.18	1.66 ± 0.14	2.31 ± 0.10
Area-weighted and river adjustment applied (S_{OCEAN})	2.32 ± 0.18	2.44 ± 0.14	3.09 ± 0.10

Note that the first three rows are for nine models as in Friedlingstein et al. (2019) and the fourth row is for 10 models including FESOM-REcoM. The river adjustment is 0.78 PgC yr^{-1} (Resplandy et al., 2018).

(Manning and Keeling, 2006; Keeling and Manning, 2014), an ocean inversion method constrained by ocean biogeochemistry data (Mikaloff Fletcher et al., 2006), and a method based on chlorofluorocarbons (McNeil et al., 2003). In the GCB, the confidence interval was adjusted to 90% to avoid rejecting models that may be outliers but are still plausible (2.2 ± 0.6 PgC yr^{-1}, Friedlingstein et al., 2019).

The spread in the covered ocean area is larger in the data-products than in the GOBMs and area-scaling has a pronounced effect on their ocean carbon sink estimate. The area-scaling changes the 1990s ocean carbon sink by +0.15, −0.02, and +0.18 PgC yr^{-1} in MPI-SOMFFN, Jena-MLS, and CMEMS, respectively. The ensemble mean increases by 0.10 PgC yr^{-1} and the standard deviation is substantially reduced from 0.26 to 0.18 PgC yr^{-1} (**Table 3**). The area-weighting effect increases over time to 0.16 PgC yr^{-1} over the period 2009–2018. The standard deviation of the data-products decreases over time, but is still reduced by a third through area-weighting in the decade 2009–18.

The ocean carbon sink estimate from data-products is the contemporary CO_2 flux, hence an adjustment for the preindustrial CO_2 outgassing due to river carbon flux has to be applied to comply with S_{OCEAN}. The river flux adjustment of 0.78 ± 0.41 PgC yr^{-1} (Resplandy et al., 2018) to the data-products results in a larger ocean carbon uptake compared to the GOBMs. The data-products mean of 2.32 ± 0.18 PgC yr^{-1} (±1 standard deviation) of the 1990s falls within the observational constraint for the 1990s. The discrepancy between model and data-based estimates varies between 0.35 PgC yr^{-1} in the 1990s and 0.27 PgC yr^{-1} in the 2000s, to 0.57 PgC yr^{-1} in 2009–2018, and 0.82 PgC yr^{-1} in the last year 2018. The uncertainty in the river flux adjustment of ±0.41 PgC yr^{-1} (Resplandy et al., 2018) can explain a large part of the mean discrepancy. Due to a backlog in submissions to the SOCAT database, the total amount of observations used to constrain the last year has a third less observations (1.3 million observations in 2019 and 2 million observations in 2018) than in previous years. Therefore, 2018 also shows quite a remarkable spread between the mapping methods.

The models generally simulate an enhanced CO_2 uptake during El Niño events, though not all models show a response to all strong and very strong El Niño events (e.g., NorESM and MPI El Niño 1997/98, **Figure 3** lower panel). Models and data-products show the same patterns of variability, but differences exist in the mean S_{OCEAN} and in the decadal trends. This is particularly pronounced since 2005, but also applies to earlier decades 1980–2000 (**Figure 3**). While the uncertainty in the river flux adjustment can account for a large part of the mean discrepancy, it cannot explain the difference in trends since 2005. The discrepancy in trends could only be explained through the riverine term by a reduced riverine outgassing over time, which would mean a reduced river carbon inflow into the ocean under the assumption of a constant ratio of river carbon inflow to riverine outgassing. There is, however, no indication of a decreased river transport of carbon into the ocean (Regnier et al., 2013).

3.3. Historical Simulation: Regional CO_2 Flux

Separating the global S_{OCEAN} into large-scale regional bands reveals substantial differences in our understanding of the mean ocean carbon sink and its variability. In the tropics, GOBMs and data-products agree well on the mean of S_{OCEAN} and its variability (**Figure 4**). Models simulate a mean uptake of 0.01 PgC yr^{-1} in 2018 with a spread from outgassing of 0.16 PgC yr^{-1} in NEMO-PlankTOM to an uptake of 0.32 PgC yr^{-1} in CNRM. The data-products agree on a small tropical CO_2 sink of 0.04–0.19 PgC yr^{-1}. The ensemble of data-products and GOBMs agree that the tropics are in the process of turning from a CO_2 source to a CO_2 sink. The first occurrence of the tropical CO_2 sink was in 2015 in the data-product ensemble and in 2014 in the GOBM ensemble.

In the north, GOBMs simulate a CO_2 sink of 0.85–1.45 PgC yr^{-1} in 2018. Seven models and all data-products fall within an envelope of 1.15–1.45 PgC yr^{-1}. The CO_2 sink in the MITgcm-REcoM set-up without the Arctic and CESM are lower with 0.89 and 0.85 PgC yr^{-1}, respectively, and stagnate

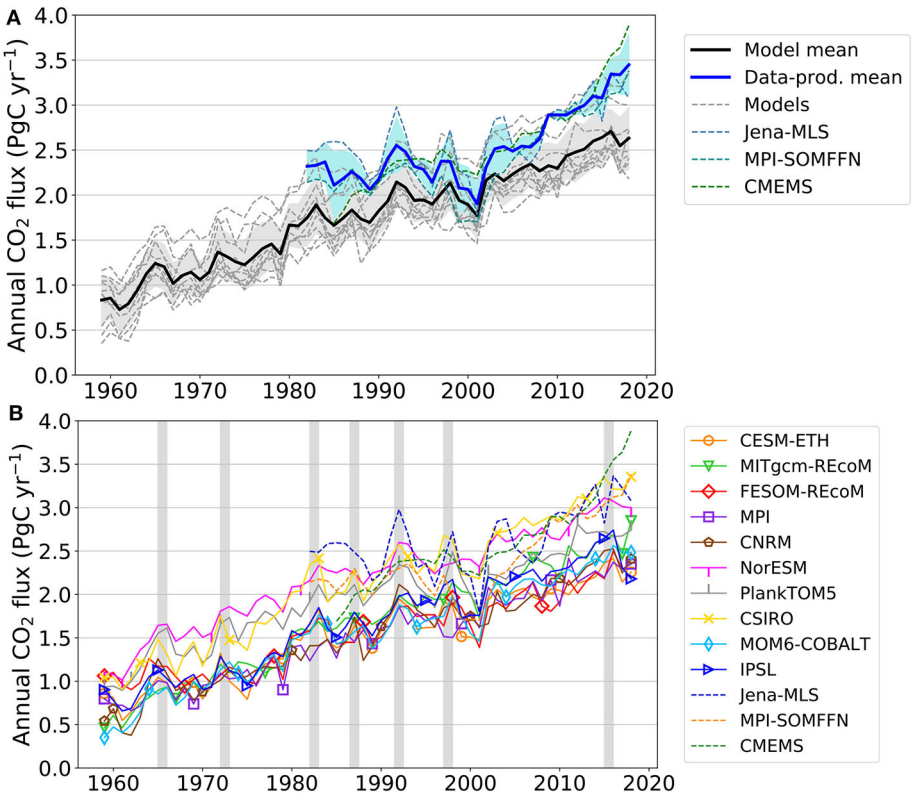

FIGURE 3 | Annual air-sea CO_2 flux from Global Ocean Biogeochemistry Models (GOBMs) and data-products used in the Global Carbon Budget 2019, after applying bias and area-corrections and river flux adjustment of 0.78 PgC yr^{-1} (Resplandy et al., 2018). **(A)** Mean of model ensemble and data-product ensemble as thick lines, individual models and data-products as thin dashed lines. **(B)** Individual models and data-products in color. Gray bars indicate strong and very strong El Niño events with the extended Multivariate ENSO index (MEI) being above 1.5 for at least 3 months in a row (Wolter and Timlin, 2011). Positive numbers indicate a flux into the ocean.

since 2000. The data-product ensemble mean yields a CO_2 sink lower than the model ensemble mean by 0.1–0.2 PgC yr^{-1} between 1985 and 2001 and good agreement since 2005.

The largest model spread occurs in the Southern Ocean with the models simulating a CO_2 sink between 1.11 PgC yr^{-1} (CNRM) and 1.84 PgC yr^{-1} (CSIRO) in 2018. Six models fall in an envelope of 1.16–1.50 PgC yr^{-1}. One model (CNRM) is lower than the multi-model mean by about 0.3 PgC yr^{-1} throughout the entire period, although it comes closer in 2018 with a simulated sink of 1.11 PgC yr^{-1}. Two models are higher with NorESM simulating higher CO_2 uptake by about 0.3 PgC yr^{-1} throughout the entire period with 1.78 PgC yr^{-1} in 2018 and CSIRO branching off the other models in 1980 to reach 1.84 PgC yr^{-1} in 2018. The data-products have the largest temporal variability and different patterns of interannual variability in the south and result in CO_2 uptake estimated between 1.67 and 2.09 PgC yr^{-1} in 2018, after river flux adjustments. The data-product mean is higher by 0.3 PgC yr^{-1} than the model ensemble mean. The only exception is the early 2000s where the data-product mean comes close to the model ensemble mean due to the low CO_2 sink in the MPI-SOMFFN product in the late 1990s and early 2000s. The Jena-MLS exhibits similar variability but on a higher mean level and the CMEMS and the GOBMs show weaker internannual and multi-year variability.

The ocean carbon sink in FESOM-REcoM is close to the multi model mean globally and in the tropics. The simulated ocean carbon uptake in the north is at the high end of the simulated range, clustering with the CNRM, NorESM, MOM6-COBALT, and IPSL models. In the south, FESOM-REcoM is in the lower range of simulated carbon uptake, but still on average 0.24 PgC yr^{-1} above CNRM.

3.4. Historical Simulation: Multi-Year Variability of CO_2 Flux

All models and data-products show a slower growth or stagnation of the ocean sink in the 1990s and a reinforcement in the 2000s (**Figure 3**). Here, we test the consistency of multi-year variability of the ocean carbon sink among the GOBMs and the data-products in the three regions (**Figure 5**). We use the term multi-year variability to describe variability on a time-scale longer than interannual variability (1–3 years), but not strictly restricted to a decade (decadal variability, DeVries et al., 2019).

In the data-products, phase I (1985–1992) is characterized by a positive trend in the south ($p = 0.013$) and no significant trends in the tropics and the north. The significant trend for the south

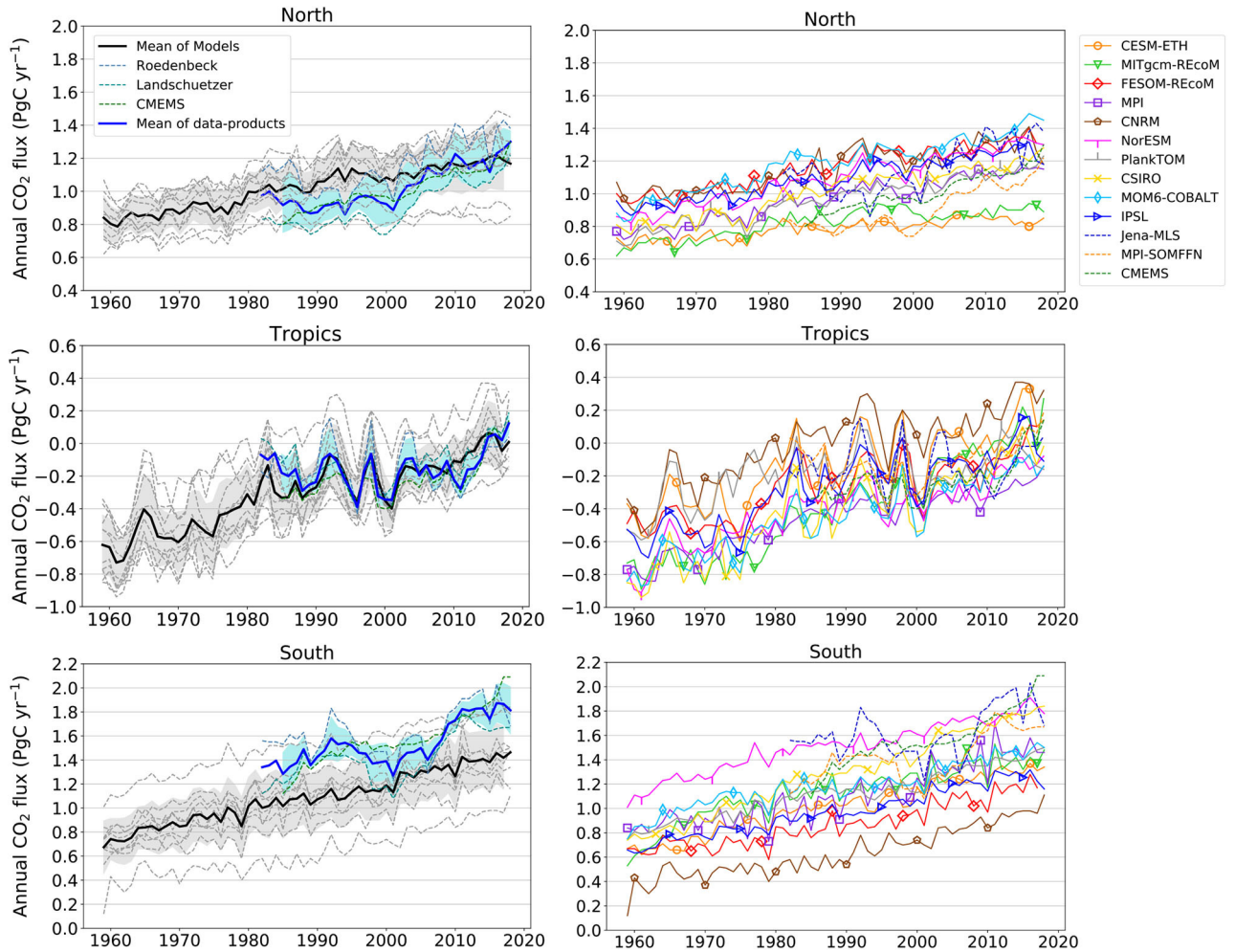

FIGURE 4 | Annual air-sea CO_2 flux integrated over the regions North (north of 30°N, top), Tropics (30°S-30°N, center), South (south of 30°S, bottom). These time-series are taken from the historical simulation A and are not corrected for biases or covered area. Note the different scales for different regions. Horizontal lines have the same distance in all subfigures (0.2 PgC yr^{-1}). Positive: CO_2 flux into the ocean. Left: Ensemble mean of Global Ocean Biogeochemical Models and data-products. Individual models in gray. Right: Individual models and data-products color coded.

in the data-products does not coincide with a significant trend in the models. The model ensemble mean also suggests a positive trend in the tropics, although with less certainty (p = 0.036). It is noteworthy that there is least confidence in data-products in phase I due to lower data availability, and the highest confidence in phases III and IV.

In phase II (1992–2001), the trend in the south is reversed (p = 0.001) in the data-product ensemble, and is zero in the north and in the tropics. The model ensemble mean also suggests a negative trend in the tropics, although with less certainty (p = 0.032). The significant trend for the south in the data-products does not coincide with a significant trend in the models. Although there are discrepancies on whether or not the ocean carbon sink was decreasing, GOBMs and data-products agree remarkably well on the slow-down or stagnation of the ocean carbon sink in phase II (1992–2001) with no GOBM or data-product exhibiting a significantly increasing trend. All GOBMs and data-products agree on the absence of a significant trend in the north.

Phase III (2001–2011) is again characterized by a sign reversal and strong positive trend in the south (p = 0.006) in the data-product ensemble mean, accompanied by a positive trend in the north (p = 0.006) and no trend in the tropics with a remarkable agreement of all data-products. The model ensemble mean agrees with positive trends of CO_2 flux in the north (p = 0.008) and south (p = 0.020).

Finally, in phase IV (2011–2018) the data-product ensemble mean exhibits a positive trend in the tropics (p = 0.004), which is however only matched by one GOBM out of the full ensemble. The ensemble means of data-products or GOBMs indicate no significant trend in the north and south, although few individual GOBMs and data-products do so. Phase IV is shorter than the other phases and therefore potentially less conclusive.

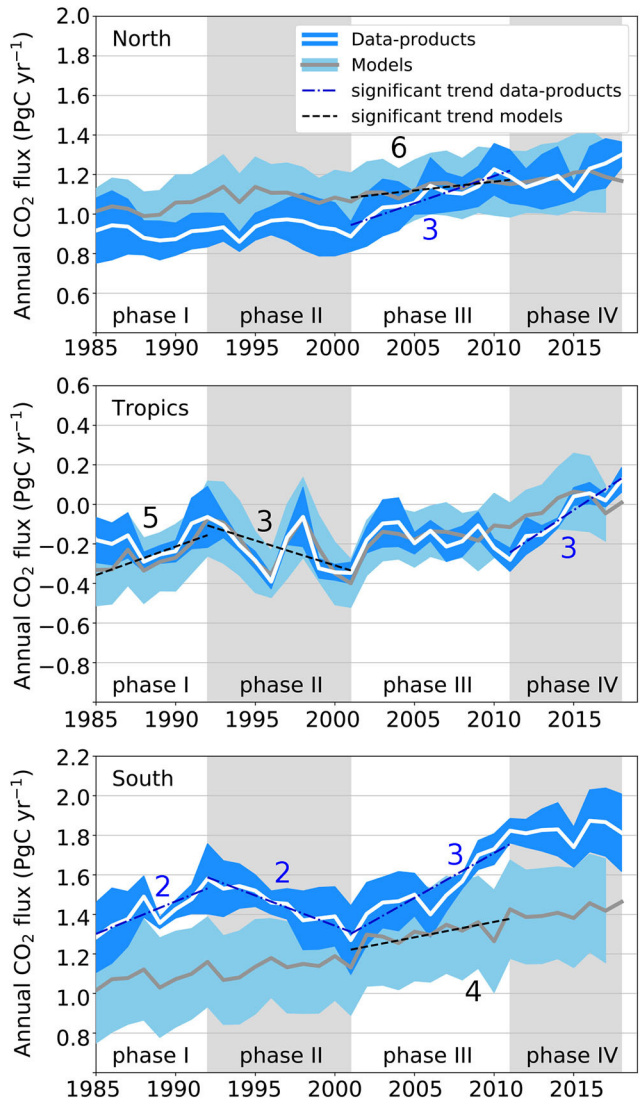

FIGURE 5 | Multi-year variability of regional air-sea CO_2 flux with agreement among methods on no significant or a decreasing trend in phase II and an increasing trend in the extratropics in phase III. Shown are the average and standard deviation of annual CO_2 flux for the ensemble of data-products and the ensemble of Global Ocean Biogeochemical Models (GOBMs) in the north (top), tropics (center) and south (bottom). Broken lines represent significant trend over that time-period. Numbers indicate the number of individual data-products and GOBMs that agree on the significant trend and are only given if the trend of the ensemble average is also significant. Note the different scales for different regions. Horizontal lines have the same distance in all subfigures (0.2 PgC yr^{-1}). Positive: CO_2 flux into the ocean.

While models and data-products agree on the large-scale (quasi-)decadal variability (**Figure 5**), the strength of the interannual variability and its hot spots differ largely (**Figures 6**, **7** y-axis). Among the data-products, MPI-SOMFFN and CMEMS show similar patterns of variability with the largest amplitude of interannual variability per pixel in the subpolar regions of all basins and the equatorial Pacific (**Figure 6**). The same spatial pattern although generally higher variability is visible in the Jena-MLS product. The data-products generally distribute the variability roughly equally between these regions. In the model suite, only MOM6-COBALT and MITgcm-REcoM distribute the variability similarly among these regions, although in MITgcm-REcoM the variability is not limited to these regions. Some models place most of the variability in the tropical Pacific (CSIRO, PlankTOM, CESM-ETH, NorESM), in other models the northern subpolar regions and the equatorial Pacific are dominant regions of variability (FESOM-REcoM, IPSL and CNRM). MPI exhibits strong variability in the Southern Ocean and the North Atlantic.

The amplitude of interannual variability (AIAV) of the global and regional CO_2 flux time-series of GOBMs and data-products is summarized in **Figure 7** (y-axis). The interannual variability as reproduced by GOBMs and data-products fall into similar ranges in the north (0.02–0.08 PgC yr^{-1}) and in the tropics (0.05–0.16 PgC yr^{-1}). There is disagreement among GOBMs and data-products on the AIAV in the south with the data-products varying between 0.08 and 0.18 PgC yr^{-1} while all GOBMs are below 0.1 PgC yr^{-1}.

3.5. Historical Simulation: Model and Data Comparison

Model evaluation was introduced as a single mismatch metric using monthly surface ocean pCO_2 observations from the Surface Ocean CO_2 Atlas (SOCAT, Bakker et al., 2016) in Le Quéré et al. (2018a, their Figure B1). Here, we show a detailed model-data comparison for models and data-products with the SOCAT pCO_2 data set on three time-scales: (i) monthly, (ii) annual + trend, and (iii) multi-year variability. The latter is the approach most closely quantifying interannual to multi-year variability, and therefore, we argue, the most appropriate metric for the Global Carbon Budget, with the aim to quantify the mean S_{OCEAN} and the deviation from previous years (i.e., multi-year variability).

Annual time-series of subsampled pCO_2 from GOBMs and data-products are compared to SOCATv2019 for the ensemble mean of the GOBMs and data-products (**Figure 8** with statistics on annual + trend time-scale), and for all individual models and data-products in the Appendix (**Supplementary Figures 3–15**). The data-products follow the SOCAT pCO_2 closely, with the best agreement in the tropics (RMSE = 2.0 μatm, r = 0.991, **Figure 8**), followed by the north (RMSE = 4.0 μatm, r = 0.985), and slightly lower agreement in the south (RMSE = 5.5 μatm, r = 0.968). As expected, the average of the subsampled pCO_2 of the data-products deviates from the average of the fully gridded product. It is, however, remarkable, that this difference is smallest in the north and largest in the south, confirming that data coverage is best in the north and sampled pCO_2 can represent the entire area reasonably well. In the tropics and the south, larger differences between subsampled mean pCO_2 and average over the full domain suggest that data coverage is insufficient to adequately represent these large areas.

The subsampled GOBM pCO_2 captures the variability of SOCAT pCO_2 remarkably well (**Figure 8**), given that SOCAT pCO_2 is an independent data set for the models. The model ensemble mean shows the highest correlation in the tropics

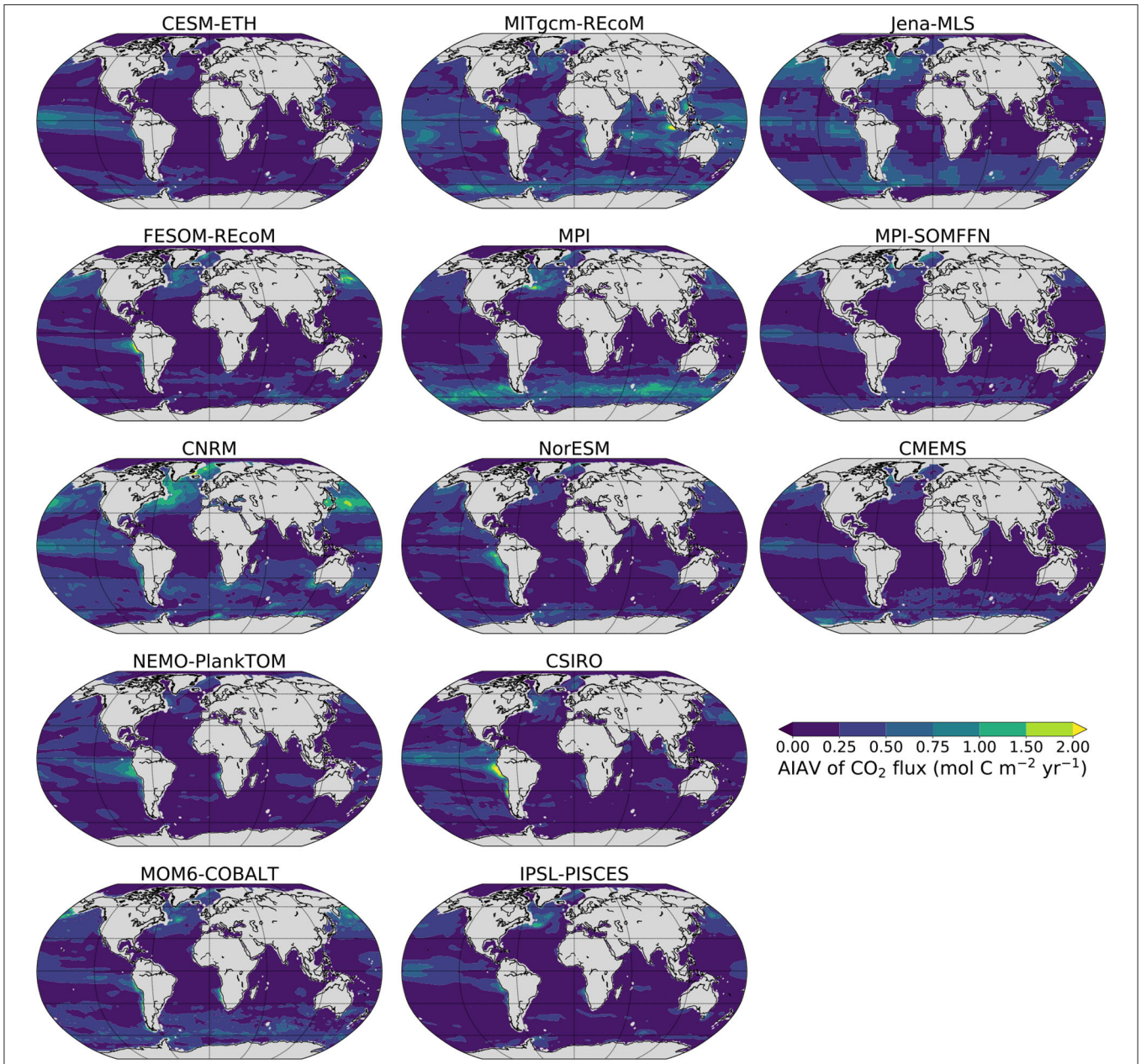

FIGURE 6 | Spatially resolved amplitude of interannual variability (AIAV) of annual air-sea CO_2 flux calculated as the standard deviation of the detrended annual CO_2 flux for all GOBMs and data-products.

(r = 0.963), but the lowest RMSE in the north (5.1 μatm). While the high correlation in the tropics indicates that the variability is well-captured, the RMSE is higher here as the water vapor correction, which is not included in some models, has a stronger effect at higher temperatures (see discussion on mean bias below). It is noteworthy that the mismatch between modeled and observed pCO_2 in the south is lower since 1999. Similar to the data-products, the difference between subsampled and full domain average pCO_2 is largest in the south.

In the following, we will show that the RMSE in comparison with SOCAT pCO_2 time-series is smaller on the relevant time-scale of multi-year variability (GOBMs: <10 μatm, data-products: <5 μatm, **Figure 9**) than on the time-scale annual + trend (GOBMs: <20 μatm, data-products: <7 μatm) and substantially smaller than on the monthly time-scale (GOBMs: 20–80 μatm, data-products: <20 μatm).

The monthly means of modeled surface ocean pCO_2 cover a large range of simulated realizations, from smaller (e.g., PlankTOM, north, **Supplementary Figure 6**) to larger seasonal

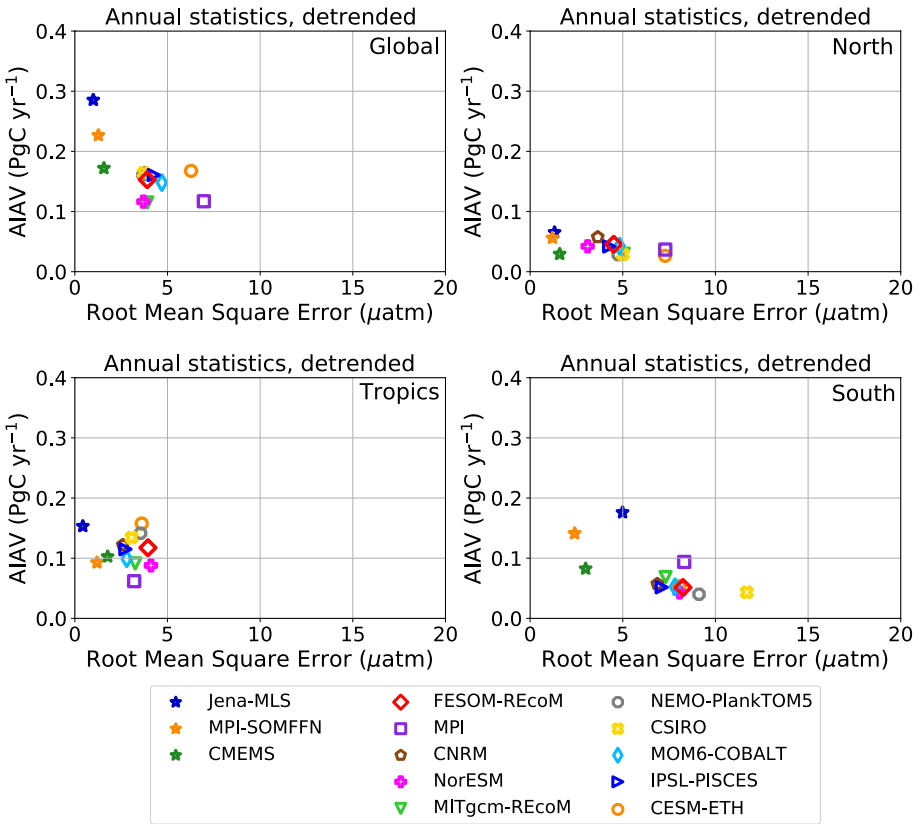

FIGURE 7 | Summary figure of temporal variability (y-axis) and model-data mismatch (x-axis). Mismatch of simulated or mapped pCO_2 and observed sea surface pCO_2 for the period 1992–2018 on the time-scale of multi-year variability and amplitude of interannual variability (AIAV) of CO_2 flux. x-axis: RMSE of spatially-averaged detrended annual time-series. y-axis: amplitude of interannual variability, defined as the standard deviation of the detrended annual time-series of air-sea CO_2 flux. These statistics are shown globally, and regionally for north, tropics, and south as indicated in the figure panels.

cycles (e.g., MPI, south, **Supplementary Figure 4**) compared to the observations, pointing to model deficiencies in representing the seasonal cycle correctly, especially in the Southern Ocean (Kessler and Tjiputra, 2016; Mongwe et al., 2016, 2018). Most models exhibit larger variability than in the observations on a monthly basis. This is mirrored in correlations of modeled and observed monthly pCO_2 ranging from 0.2 to 0.8 and the RMSE from 20 to 80 μatm (**Figure 9A** and **Supplementary Figure 1**). The data-products are inter- and extrapolations of SOCAT data, and hence have higher correlation coefficients and lower RMSEs than the GOBMs. However, they also have RMSEs of 15–20 μatm (see also Gregor et al., 2019) and correlation coefficients of 0.8–1.0 with lower correlation values in the southern and northern extratropics (**Figure 9A**, **Supplementary Figures 1, 3–15** for individual models and data-products). Comparison on monthly time-scales is a common approach to measure misfit between estimated and observed pCO_2 (e.g., Le Quéré et al., 2018a; Friedlingstein et al., 2019; Gregor et al., 2019).

On the time-scale annual + trend, correlations for annual time-series are between 0.8 and 1 for all models, except in the Southern Ocean with values down to 0.6 (**Figure 9B** and **Supplementary Figure 1**). Despite all models having similarly high correlation values, the RMSEs range between 4 and 20 μatm. Data-products have correlation coefficients close to 1 and RMSE lower than 4 μatm. As the pCO_2 signal on the annual + trend time-scale is dominated by the continuous atmospheric CO_2 increase, we conclude that models and data-products capture the climate trend of increasing surface pCO_2 reasonably well.

Finally, on the time-scale of interannual and multi-year variability (statistics of detrended annual time-series, **Figures 7**, **9C**, and **Supplementary Figure 2**), RMSEs between GOBMs and SOCAT are small (globally: 3.5–7 μatm); with the lowest mismatch in the tropics (2–4 μatm), and the largest mismatch in the south (6.5–9.5 μatm). On this time-scale, correlation coefficients are generally higher for GOBMs with lower RMSE, with highest correlation coefficients in the tropics (0.5–0.9) and lower in the extratropics (0.2–0.9 in the north and 0.2–0.8 in the south). The data-products are by design closer to the observations and have RMSEs below 2 μatm, except in the Southern Ocean with RMSEs up to 5 μatm, and correlation coefficients of above 0.8 in the south and above 0.9 elsewhere. The data-products cluster closely together in the north, with a wider

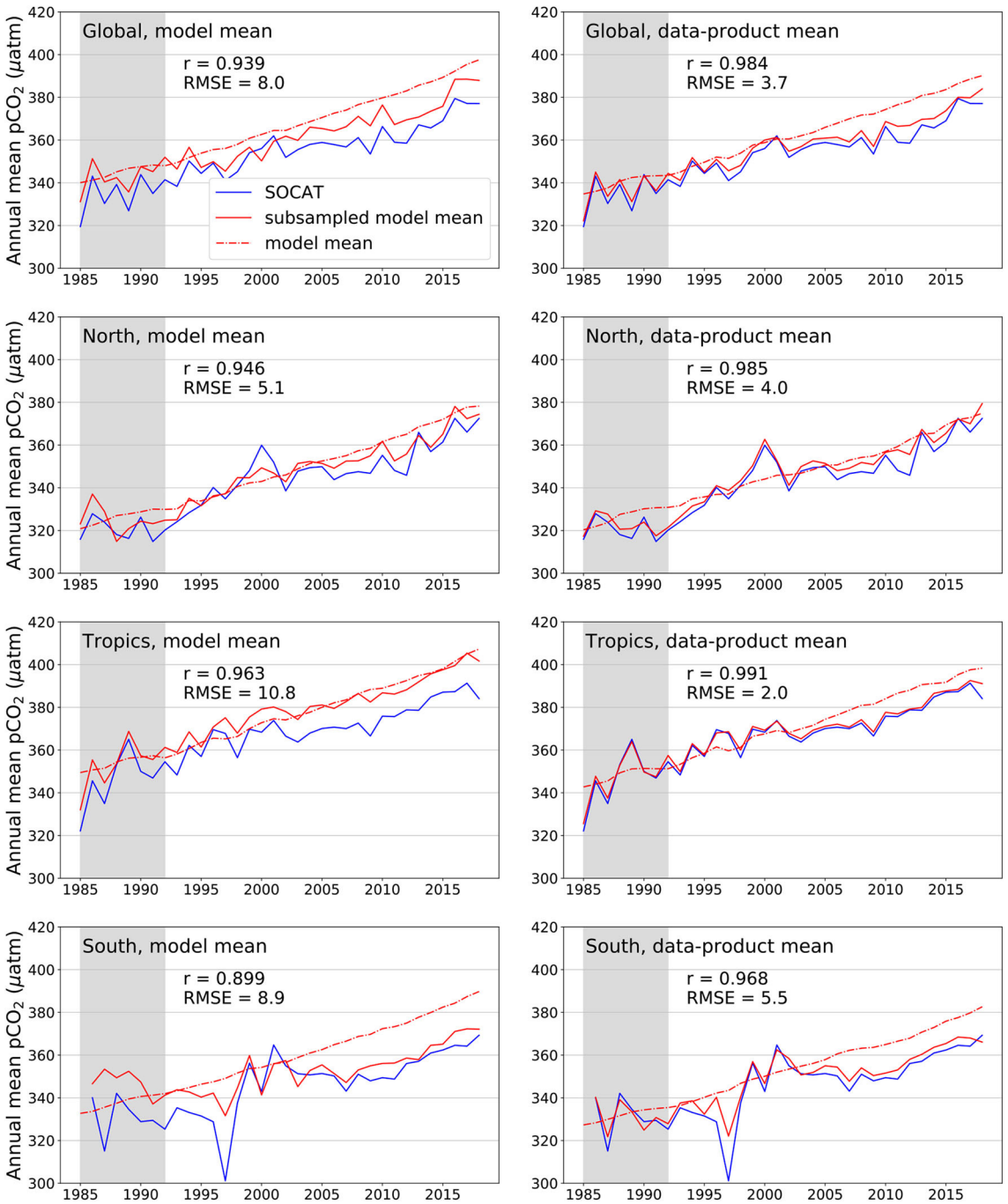

FIGURE 8 | Comparison between annual sea-surface pCO_2 from SOCATv2019 (Bakker et al., 2016) and the model ensemble mean (left) or data-product ensemble mean (right) globally (top), and in the different regions North, Tropics, South as indicated in the figures. Red solid line shows model or data-product mean from subsampled models/data-products at SOCAT sampling sites. Broken lines indicate the area-weighted average from the full models (not subsampled). Correlation coefficient r and Root Mean Squared Error RMSE are calculated from the annual time-series 1992–2018, i.e., the white area in the figures. These figures are shown for all models and data-products separately in the **Supplementary Material**.

range in the tropics and the south; again suggesting that data-availability can constrain the data-products better in the north than elsewhere.

The mean bias (**Figure 9D**, x-axis) is a measure of how well the models capture the mean pCO_2. It ranges between −1 and +15 μatm globally and up to 20 μatm in the tropics. Some models

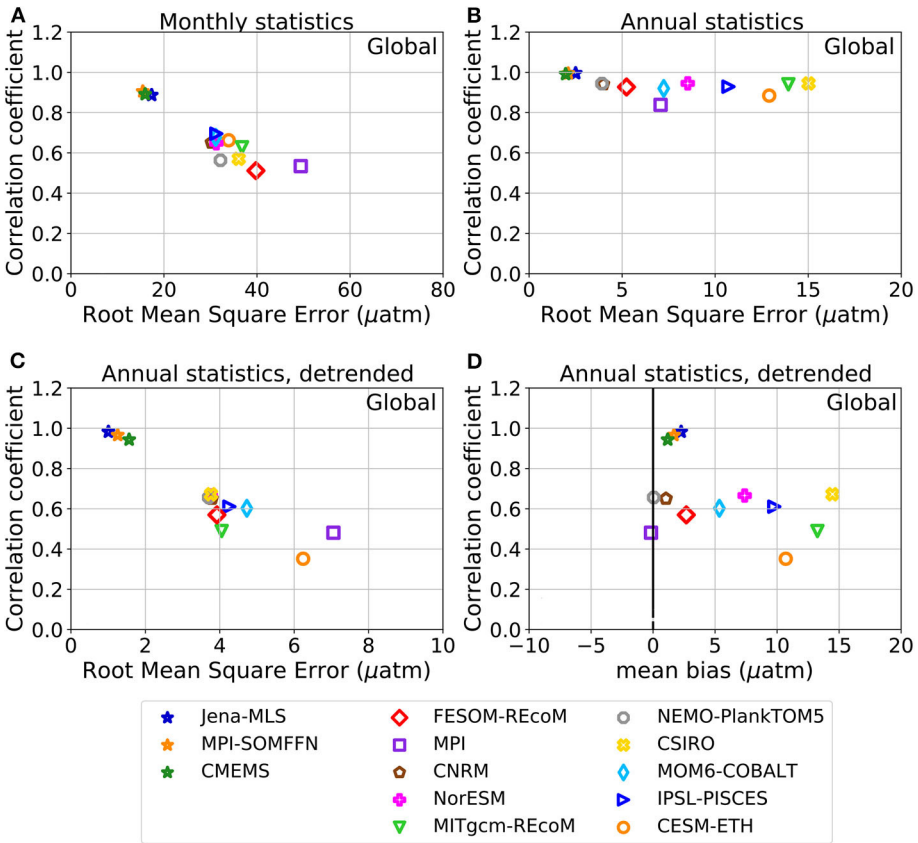

FIGURE 9 | Mismatch of simulated or mapped pCO_2 and observed sea surface pCO_2 for the period 1992–2018 on different time-scales: **(A)** monthly, **(B)** annual + trend as derived from annual statistics, **(C)** multi-year variability as derived from detrended annual statistics, **(D)** long term mean. **(A–C)** Display the mismatch as RMSE and correlation coefficient. In **(D)** the mean bias is plotted against the correlation coefficient. Global figures are shown here, regional figures (north, tropics, south) are displayed in the **Supplementary Material**. Note the different scales on the x-axis.

show a consistent positive bias as expected from the missing water vapor correction. The water vapor correction would reduce the modeled pCO_2 by 2 μatm at 0°C and by 15 μatm at 30°C. Including the water vapor correction in all models would substantially reduce the bias and would therefore allow for more detailed interpretation of model biases, e.g., in comparison to the regional CO_2 flux in the preindustrial control simulation. The mean bias of the data-products is always positive and small by design with a maximum of 5 μatm in the south.

4. DISCUSSION

The ocean mitigates climate change by sequestering anthropogenic CO_2. A high-quality assessment of the ocean carbon sink is critical for assessing changes in the contemporary carbon cycle and to robustly project its evolution into the future. Sudden changes in the ocean carbon sink would immediately affect the allowable emissions for limiting global warming to well below 2°C. Furthermore, reliable quantification of the ocean carbon sink is also an important constraint on the land carbon sink estimate when combined with accurately reported emissions. The latter contributes 60–90% of the observed decadal variability in the natural carbon sinks (DeVries et al., 2019), but cannot be directly observed.

The ocean carbon cycle community is blessed with an annually-updated global compilation of quality-controlled surface ocean pCO_2 observations (the Surface Ocean CO_2 Atlas, SOCAT, Bakker et al., 2016), which can be used to derive the ocean carbon sink and to evaluate global ocean biogeochemical models (GOBMs). The ocean carbon sink can be assessed currently within <2 years delay through ocean surface pCO_2 observations combined with mapping methods and additional data sets and parameterizations, and by global ocean biogeochemical models. We demonstrated that these different tools agree reasonably well when enough high-quality observations are available. It has to be noted though, that the discrepancy between GOBMs and data-products is increasing over time, being larger in 2018 than in any year before.

The biggest discrepancies exist in the Southern Ocean, where model biases are largest and high-quality ship-board measurements are scarce and biased toward summer. Novel autonomous methods are starting to fill data gaps, e.g., pH sensors on biogeochemical Argo floats in the Southern Ocean

(Bushinsky et al., 2019), but the uncertainty of calculated pCO_2 from pH sensors is higher than from direct pCO_2 observations (Williams et al., 2017). A global-scale high-quality ocean pCO_2 observation network combining traditional and novel observation systems is needed to improve the accuracy of the ocean carbon sink from observations.

4.1. The Mean Ocean Carbon Sink

The GOBMs best estimate for the mean ocean carbon sink is 2.1 $\pm$ 0.5 PgC yr^{-1} between 1994 and 2007, which is 0.5 PgC yr^{-1} lower than a recent anthropogenic carbon estimate of 2.6 $\pm$ 0.3 PgC yr^{-1} based on ocean interior observations (Gruber et al., 2019). The two estimates overlap within the given uncertainties. More importantly, the 2.6 $\pm$ 0.3 PgC yr^{-1} in Gruber et al. (2019) is equivalent to the geochemical increase in ocean inorganic carbon or $F_{ant,ss}$ + $F_{ant,ns}$ (Clement and Gruber, 2018). Gruber et al. (2019), however, also estimate outgassing of natural carbon, $F_{nat,ns}$, to be -0.4 ± 0.24 PgC yr^{-1} over the same period. This is based on the difference of the net flux from a data-product (Landschützer et al., 2016) adjusted for riverine outgassing (i.e., F_{ant} + F_{nat} = F_{net} − F_{riv}) and two estimates of temporally-resolved F_{ant} [transient steady state scaled Landschützer et al. (2016) and ocean inversion Mikaloff Fletcher et al., 2006]. Hence, in order to compare the same conceptual S_{OCEAN} flux ($F_{ant,ss}$ + $F_{ant,ns}$ +$F_{nat,ns}$, Equation 2), the GOBM's S_{OCEAN} estimate has to be compared with the sum of Gruber's F_{ant} and $F_{nat,ns}$ fluxes; and the resulting 2.2 $\pm$ 0.4 PgC yr^{-1} are in good agreement with the numbers presented here and in the GCB releases (Friedlingstein et al., 2019). It is not a circular argument to use Gruber's F_{ant} plus $F_{nat,ns}$ to compare to the GOBMs which are independent of both the F_{ant} and $F_{nat,ss}$ estimates in Gruber et al. (2019). There would be some circularity when comparing to the data-based products, which is not done here.

On a regional level, global ocean biogeochemical models and data-products agree reasonably well on the mean ocean carbon sink in the tropics and in the northern extratropics. An exception to that is the offset between 1985 and 2003 in the northern extratropics. The better agreement since the early 2000s coincides with a large increase in number of (global) observations from 400,000 to 1,300,000 observations between 2003 and 2006 (Bakker et al., 2016), and a jump from a few hundred to a few thousand observations in the North Atlantic in 2002 (Lebehot et al., 2019). There is substantial disagreement on the mean ocean carbon sink in the Southern Ocean between GOBMs and data-products. This offset might be related to the high uncertainty of the river-flux adjustment, to an overestimate of the ocean carbon sink based on SOCAT observations due to a sampling bias or to model biases. Bushinsky et al. (2019) demonstrated that adding biogeochemical Argo floats to the input data set for two of the three mapping methods used here, reduces the Southern Ocean carbon sink by 0.39–0.75 PgC yr^{-1} south of 35°S due to added winter-time data with previously underrepresented outgassing of CO_2. However, a systematic bias of 4 μatm well within the float pCO_2 uncertainty of around 11 μatm (Williams et al., 2017) would half the impact of the additional data from floats (Bushinsky et al., 2019). The global river flux adjustment (Resplandy et al., 2018) is distributed across the ocean based on one ocean circulation model study (Aumont et al., 2001). How much CO_2 outgasses in which ocean region depends on model assumptions, such as the remineralization time-scale of organic carbon and the burial. Further sensitivity studies on the effect of model assumptions are needed to constrain the regional river flux adjustments better.

4.2. Multi-Year Variability of the Ocean Carbon Sink

There is growing evidence for a multi-year variability of the ocean carbon sink with remarkable consistency among data-products and GOBMs on a global stagnation of the ocean carbon sink in the period 1992–2001 and an extra-tropical strengthening between 2001 and 2011 (**Figure 5**, Rödenbeck et al., 2015; Landschützer et al., 2016; DeVries et al., 2019; McKinley et al., 2020). Explanations for this multi-year variability range from the ocean's response to changes in atmospheric circulation (Le Quéré et al., 2007; Landschützer et al., 2015; Keppler and Landschützer, 2019), especially the variations in the upper ocean overturning (DeVries et al., 2017) to external forcing through surface cooling associated with volcanic eruptions and variations in atmospheric CO_2 growth rate (McKinley et al., 2020). The mapping methods and an ocean inverse model suggest that the GOBMs underestimate the magnitude of the multi-year variability (DeVries et al., 2019). Cooling due to volcanic eruptions and variations in atmospheric growth rate are included in the model forcing and the ocean circulation's response to climate variability is part of the model dynamics. Which of the two is the dominant factor is not distinguished in our analysis.

In the most recent period since 2011, all data-products yield a strong increasing trend of S_{OCEAN} in the tropics. This is not reproduced by the GOBMs, even though they generally represent the same amplitude of interannual variability (AIAV) as the data-products (**Figure 7**). In the northern extra-tropics, the AIAV of the data-products is smallest of all regions (<0.08 PgC yr^{-1}), but nevertheless varies by a factor of two between the data-products. The GOBMs fall within the same range. In the southern extratropics, the magnitude of the variability is by no means understood, with a large range of AIAV among data-products and GOBMs.

4.3. Lessons Learned From pCO_2 Data Mismatch

The pCO_2 data mismatch has to be interpreted in the context of high spatial and temporal ocean pCO_2 variability. The 1998–2011 mean pCO_2 varies spatially between 280 μatm in the high-latitude North Atlantic and North Pacific to over 440 μatm in the equatorial Pacific (Landschützer et al., 2014). Seasonal and interannual variability of surface pCO_2 can be 100 μatm or more (Wanninkhof et al., 2013). The zonal mean ΔpCO_2, i.e., the difference between surface ocean pCO_2 and atmospheric pCO_2 ranges from 40 μatm just south of the equator (outgassing) to -20 μatm at 40° of both hemispheres and -60 μatm (uptake) in the northern high latitudes (Wanninkhof et al., 2013). The global mean ΔpCO_2 varied only between -2 to +1 μatm between 1990 to 2009 according to Wanninkhof et al. (2013) and between

−3 to 1 μatm from 1982 to 2000 and have since then increased to −6 μatm in the MPI-SOMFFN data-product used here (not shown). Over the same period, the global mean CO_2 flux has always been into the ocean and has not changed sign in the same product. This illustrates that the global mean ΔpCO_2 is dominated by the large areas in the tropics whereas the CO_2 flux is dominated by the subpolar regions with the highest wind speeds. We conclude from this context, that it is difficult to quantify an uncertainty of the CO_2 flux based on the pCO_2 bias or RMSE, but that it is encouraging that the GOBMs show only slightly weaker correlation with the SOCAT pCO_2 (0.94 globally) than the data-products (0.98) indicating that interannual and multi-year changes are captured reasonably well (**Figure 8**).

The detailed comparison of mapped and simulated pCO_2 with SOCAT data at sampling locations reveals that there is no relation between the RMSE or bias of the GOBM or data-product with the magnitude of temporal variability (**Figure 7**). We can therefore not constrain the "true" multi-year variability by choosing models with lower pCO_2 biases. Our analysis further assesses the fidelity of the GOBMs and data-products on different time-scales. While GOBMs have clear weaknesses on resolving the seasonal cycle (**Figure 7A**, **Supplementary Figures 1, 3–15**, Kessler and Tjiputra, 2016; Mongwe et al., 2016, 2018), they capture the pCO_2 on annual + trend time-scale reasonably well, and even better on the time-scale of multi-year variability (**Figures 7**, **9**, and **Supplementary Figure 2**). We argue that the detrended annual statistic is more informative for the evaluation of annual estimates of S_{OCEAN} with the aim to robustly estimate the mean S_{OCEAN} and multi-year variability. The monthly statistics, which are most commonly used to evaluate GOBMs and data-products (Rödenbeck et al., 2015; Friedlingstein et al., 2019; Gregor et al., 2019) quantify to a large extent the representation of the seasonal cycle. Based on our analysis of model-data mismatch, we conclude that misrepresentations of the seasonal cycle in GOBMs have little effect on the global annual estimate of S_{OCEAN}. Yet, they illustrate the weaknesses of GOBMs to represent the underlying mechanisms correctly, which questions their ability to produce robust projections into the future.

4.4. Constraints on the Regional CO_2 Flux

Some models are clear outliers in the regional S_{OCEAN} time-series, e.g., CESM and MITgcm show the lowest S_{OCEAN} in the north, CNRM shows the highest flux in the tropics, and CNRM and NorESM exhibit a very low and very high S_{OCEAN} in the south, respectively. These models simulate very similar RMSEs and correlation coefficients in comparison to SOCAT pCO_2 as the other GOBMs and hence the regional fluxes cannot be constrained by the pCO_2 mismatch. In fact, CNRM shows the lowest RMSE in the south and in the tropics, but this assessment is hampered by the large global S_{OCEAN} bias in CNRM.

Similarly, the regionally resolved comparison of the preindustrial control air-sea CO_2 flux with ocean inversion estimates (Mikaloff Fletcher et al., 2007) is not conclusive on which models are more realistic than others, e.g., there is no obvious explanation for the low S_{OCEAN} in CESM in the north to be found in the preindustrial air-sea CO_2 flux in CESM in this region. However, a few impressions can be noted. MITgcm and MPI have clear issues with no net CO_2 outgassing in the preindustrial Southern Ocean. Models with a high CO_2 uptake in the north show this also in the preindustrial simulation (NorESM, CNRM, MOM6-COBALT, FESOM-REcoM), indicating that the model set-up and parameter choices lead to a vigorous overturning in the north. CNRM and FESOM-REcoM, which simulate the lowest historical S_{OCEAN} in the south, are the models with the strongest preindustrial outgassing south of 58°S, but still lower than in Mikaloff Fletcher et al. (2007).

4.5. Changes in Methodology in GCB2019

GOBMs have biases and they drift, which can be quantified with a control simulation that is required for the GCB since 2019 (Friedlingstein et al., 2019). The global ocean carbon sink estimate for the GCB can be corrected for model bias and drift and the effect of this correction is small on the ensemble global mean sink as some GOBMs have positive and others negative biases. Regional and subregional biases are, however, not quantified and cannot be corrected for as the assumption of net zero steady state natural flux only holds globally. Therefore, regional estimates of S_{OCEAN} are associated with a higher uncertainty and uncorrected gridded fields from historical model simulation A are used for model evaluation. This introduces an inconsistency between adjusted global estimates for S_{OCEAN} on the one hand and unadjusted regional S_{OCEAN} estimates and model evaluation on the other hand. Model simulations with reduced global biases are desirable for a more robust model-data comparison and reduced uncertainty of regional ocean carbon sink estimates.

Two of the mapping methods represent <90% of the global ocean area. This results from unmapped areas all along the coast lines, the Mediterranean and other marginal seas, including the Arctic Ocean. This mirrors the poor data coverage in some marginal seas (Mediterranean Sea, Canadian archipelago, Chinese Sea, Malaysian Archipelago) and in the Arctic Ocean. Thus, ideally, these gaps would be closed by data collection or data sharing for these regions, as well as mapping. This correction is on the order of 0.1–0.15 PgC yr^{-1} and is considered conservative as it is smaller than the estimate for the Arctic Ocean of 0.12 ± 0.06 PgC yr^{-1} (Schuster et al., 2013) and the global coastal ocean carbon sink of 0.2 PgC yr^{-1} (Roobaert et al., 2019), which, however, overlaps partly with the area covered by the global data-products (37% of the area in the coastal product is already represented in the global product of Landschützer et al., 2016) and by the Arctic Ocean. This simple approach uses the maximally covered area of the data-products, i.e., regions which are mapped in some months of the year are not filled (e.g., parts of the Southern Ocean which are mapped in summer but not in winter). While this approach might tend to overestimate the flux in the permanently ice-covered parts of the Arctic Ocean, the region north of 80°N covers only 1% of the global ocean area. The area correction is dominated by the coastal ocean, which has a similar flux density as the open ocean (0.39 mol C $m^{-2}yr^{-1}$ coastal south of 60°N vs. 0.35 mol C $mr^{-2}yr^{-1}$ globally Wanninkhof et al., 2013; Roobaert et al., 2019). The simplistic area-scaling approach to fill data gaps is hence considered conservative, also in comparison to the

60% higher area correction from a time-resolved gap-filling using ocean models (McKinley et al., 2020).

While the effect of the area correction on the mean ocean carbon sink is small (0.1–0.15 PgC yr^{-1}) compared to the uncertainties, e.g., from the river flux adjustment ($\pm$0.41 PgC yr^{-1}; Resplandy et al., 2018) or the gas-exchange calculation ($\pm$0.6 PgC yr^{-1}; Woolf et al., 2019), the spread between data-products can be reduced by a third when taking the area-correction into account and is thus considered an important correction.

4.6. Strengths, Weaknesses, and Ways Forward

Both approaches have uncertainties, and both have strengths and weaknesses. An ensemble of GOBMs is a robust tool to estimate the global ocean mean carbon sink and anthropogenic trends, with their spread likely being driven by differences in the strength of the simulated overturning circulation (e.g., Doney et al., 2004; Goris et al., 2018). Large-scale multi-year variability is driven by the interplay of external forcing and ocean circulation (McKinley et al., 2020). The smaller the spatial and temporal scale of interest, the more important it becomes that the GOBMs simulate the delicate interplay between physical and biological processes appropriately. The seasonal cycle is a testbed for how well GOBMs reproduce these interactions, and most GOBMs fail to reproduce the seasonal cycle of air-sea CO_2 flux satisfyingly, especially in the Southern Ocean (**Figure 9**, **Supplementary Figure 1**, Kessler and Tjiputra, 2016; Mongwe et al., 2016, 2018). Data-products, in turn, are closely tied to surface ocean observations, which carry imprints of temporal and spatial variability. Their key strength is therefore the assessment of interannual and multi-year variability, particularly in regions with high data densities.

We see potential for improvement in all contributions to the ocean carbon sink estimate: (1) Extending and sustaining the high-quality surface ocean observing network is pivotal to reduce uncertainty in the data products obtained with mapping methods from surface pCO_2 observations, especially in data-poor regions; (2) mapping methods should represent the full global ocean including coastal areas, marginal seas and the Arctic and work toward including data from novel observation platforms, such as biogeochemical Argo floats and saildrones, which is to date still hampered by lower accuracy for pCO_2 data from novel platforms; (3) a robust understanding of river carbon, alkalinity and nutrient input into the ocean and of the partitioning of river carbon fluxes in burial and carbon outgassing and its regional distribution is critically needed. A spatially-resolved field of river-induced effects on surface pCO_2 by current generation ocean biogeochemical models along with sensitivities to assumptions, e.g., on remineralization time-scale would be highly desirable to take riverine fluxes into account for the assessment of model-data mismatch; (4) GOBMs are to reduce bias and drift for a more robust regional assessment and model evaluation. Further model improvement is needed to reduce the model-data mismatch, particularly in the high latitudes; including the water vapor correction in all models is a simple but crucial step to allow for interpretation of other model biases; (5) and finally, remaining discrepancies in multi-year variability from data-products and GOBMs remain to be resolved.

DATA AVAILABILITY STATEMENT

The datasets analyzed in this study are available under the following links: the global and regional time-series of the ocean sink analyzed for this study can be found in ICOS: https://doi.org/10.18160/GCP-2019. Gridded fields, raw time-series, and FESOM-REcoM output is available under https://doi.pangaea.de/10.1594/PANGAEA.920753.

AUTHOR CONTRIBUTIONS

JH designed the study and wrote the manuscript. MZ and JH analyzed the data and produced the figures. JH, CL, NG, DB, LB, TC, ÖG, TI, PL, AL, LR, CR, JS, and RS contributed data or model output. All authors commented on the manuscript.

FUNDING

This research has received funding from the Helmholtz Young Investigator Group Marine Carbon and Ecosystem Feedbacks in the Earth System (MarESys), grant number VH-NG-1301, the European Union's Horizon 2020 research and innovation programme under grant agreement nos. 820989 (COMFORT), 821003 (4C), and 730944 (RINGO). CL received funding from the UK Natural Environment Research Council SONATA project (no. NE/P021417/1). LB received funding from the ANR project SOBUMS (ANR-16-CE01-0014) and from the Chanel Research Chair. LR gratefully acknowledged the support of the Sloan Foundation Research Fellowship program. JS acknowledged funding from the Research Council of Norway through project INES (270061) and HPC resources provided by the National Infrastructure for HPC and Data Storage in Norway, UNINETT Sigma2 (nn/ns2980k).

ACKNOWLEDGMENTS

The Surface Ocean CO_2 Atlas (SOCAT) is an international effort, endorsed by the International Ocean Carbon Coordination Project (IOCCP), the Surface Ocean Lower Atmosphere Study (SOLAS) and the Integrated Marine Biosphere Research (IMBeR) program, to deliver a uniformly quality-controlled surface ocean CO_2 database. The many researchers and funding agencies responsible for the collection of data and quality control are thanked for their contributions to SOCAT. We thank Amanda Fay and Marion Gehlen for discussions on technical aspects of the ocean carbon sink estimate and its evaluation and two reviewers for their constructive comments. JH thanks Cara Nissen and Hanna Ewen for their contributions to the plotting scripts.

SUPPLEMENTARY MATERIAL

The Supplementary Material for this article can be found online at: https://www.frontiersin.org/articles/10.3389/fmars.2020.571720/full#supplementary-material

REFERENCES

Adcroft, A., Anderson, W., Balaji, V., Blanton, C., Bushuk, M., Dufour, C. O., et al. (2019). The GFDL global ocean and sea ice model OM4.0: model description and simulation features. *J. Adv. Model. Earth Syst.* 11, 3167–3211. doi: 10.1029/2019MS001726

Albani, S., Mahowald, N. M., Perry, A. T., Scanza, R. A., Zender, C. S., Heavens, N. G., et al. (2014). Improved dust representation in the community atmosphere model. *J. Adv. Model. Earth Syst.* 6, 541–570. doi: 10.1002/2013MS000279

Álvarez, E., Thoms, S., and Völker, C. (2018). Chlorophyll to carbon ratio derived from a global ecosystem model with photodamage. *Glob. Biogeochem. Cycles* 32, 799–816. doi: 10.1029/2017GB005850

Amante, C., and Eakins, B. W. (2009). *ETOPO1 1 Arc-Minute Global Relief Model: Procedures, Data Sources and Analysis*. NOAA Technical Memorandum NESDIS, NGDC-24. Amante, C., and Eakins, B. W. (2009). *ETOPO1 1 Arc-Minute Global Relief Model: Procedures, Data Sources and Analysis.* NOAA Technical Memorandum NESDIS NGDC-24. Washington, DC: National Geophysical Data Center, NOAA. doi: 10.7289/V5C8276M

Aumont, O., Ethé, C., Tagliabue, A., Bopp, L., and Gehlen, M. (2015). PISCES-v2: an ocean biogeochemical model for carbon and ecosystem studies. *Geosci. Model Dev.* 8, 2465–2513. doi: 10.5194/gmd-8-2465-2015

Aumont, O., Orr, J. C., Monfray, P., Ludwig, W., Amiotte-Suchet, P., and Probst, J.-L. (2001). Riverine-driven interhemispheric transport of carbon. *Glob. Biogeochem. Cycles* 15, 393–405. doi: 10.1029/1999GB001238

Bakker, D. C. E., Pfeil, B., Landa, C. S., Metzl, N., O'Brien, K. M., Olsen, A., et al. (2016). A multi-decade record of high-quality fCO_2 data in version 3 of the surface ocean CO_2 Atlas (SOCAT). *Earth Syst. Sci. Data* 8, 383–413. doi: 10.5194/essd-8-383-2016

Ballantyne, A., Alden, C., Miller, J., Tans, P., and White, J. (2012). Increase in observed net carbon dioxide uptake by land and oceans during the past 50 years. *Nature* 488, 70–72. doi: 10.1038/nature11299

Berthet, S., Séférian, R., Bricaud, C., Chevallier, M., Voldoire, A., and Ethé, C. (2019). Evaluation of an online grid-coarsening algorithm in a global Eddy-admitting ocean biogeochemical model. *J. Adv. Model. Earth Syst.* 11, 1759–1783. doi: 10.1029/2019MS001644

Buitenhuis, E. T., Hashioka, T., and Le Quere, C. (2013). Combined constraints on global ocean primary production using observations and models. *Glob. Biogeochem. Cycles* 27, 847–858. doi: 10.1002/gbc.20074

Bushinsky, S. M., Landschützer, P., Rödenbeck, C., Gray, A. R., Baker, D., Mazloff, M. R., et al. (2019). Reassessing Southern Ocean air-sea CO_2 flux estimates with the addition of biogeochemical float observations. *Glob. Biogeochem. Cycles* 33, 1370–1388. doi: 10.1029/2019GB006176

Canadell, J. G., Le Quéré, C., Raupach, M. R., Field, C. B., Buitenhuis, E. T., Ciais, P., et al. (2007). Contributions to accelerating atmospheric CO_2 growth from economic activity, carbon intensity, and efficiency of natural sinks. *Proc. Natl. Acad. Sci. U.S.A.* 104, 18866–18870. doi: 10.1073/pnas.0702737104

Clement, D., and Gruber, N. (2018). The eMLR(C*) method to determine decadal changes in the global ocean storage of anthropogenic CO_2. *Glob. Biogeochem. Cycles* 32, 654–679. doi: 10.1002/2017GB005819

Dee, D. P., Uppala, S. M., Simmons, A. J., Berrisford, P., Poli, P., Kobayashi, S., et al. (2011). The ERA-Interim reanalysis: configuration and performance of the data assimilation system. *Q. J. R. Meteorol. Soc.* 137, 553–597. doi: 10.1002/qj.828

Denman, K. L., Brasseur, G., Chidthaisong, A., Ciais, P., Cox, P. M., Dickinson, R. E., et al. (2007). "Couplings between changes in the climate system and biogeochemistry," in *Climate Change 2007: The Physical Science Basis. Contribution of Working Group I to the Fourth Assessment Report of the Intergovernmental Panel on Climate Change*, eds S. Solomon, D. Qin, M. Manning, M. Marquis, K. Averyt, M. M. B. Tignor, et al. (Cambridge; New York, NY: Cambridge University Press), 499–587.

Denvil-Sommer, A., Gehlen, M., Vrac, M., and Mejia, C. (2019). LSCE-FFNN-v1: a two-step neural network model for the reconstruction of surface ocean pCO_2 over the global ocean. *Geosci. Model Dev.* 12, 2091–2105. doi: 10.5194/gmd-12-2091-2019

DeVries, T., Holzer, M., and Primeau, F. (2017). Recent increase in oceanic carbon uptake driven by weaker upper-ocean overturning. *Nature* 542, 215–218. doi: 10.1038/nature21068

DeVries, T., Le Quéré, C., Andrews, O., Berthet, S., Hauck, J., Ilyina, T., et al. (2019). Decadal trends in the ocean carbon sink. *Proc. Natl. Acad. Sci. U.S.A.* 116, 11646–11651. doi: 10.1073/pnas.1900371116

Dlugokencky, E. and Tans, P. (2019). *Trends in Atmospheric Carbon Dioxide.* Boulder, CO: National Oceanic & Atmospheric Administration, Earth System Research Laboratory (NOAA/ESRL). Available online at: http://www.esrl.noaa.gov/gmd/ccgg/trends/global.html (accessed November 3, 2019).

Doney, S. C., Lima, I., Feely, R. A., Glover, D. M., Lindsay, K., Mahowald, N., et al. (2009). Mechanisms governing interannual variability in upper-ocean inorganic carbon system and air-sea CO_2 fluxes: physical climate and atmospheric dust. *Deep Sea Res. II Top. Stud. Oceanogr.* 56, 640–655. doi: 10.1016/j.dsr2.2008.12.006

Doney, S. C., Lindsay, K., Caldeira, K., Campin, J.-M., Drange, H., Dutay, J.-C., et al. (2004). Evaluating global ocean carbon models: the importance of realistic physics. *Glob. Biogeochem. Cycles* 18, GB3017. doi: 10.1029/2003GB002150

Eakins, B. W. and Sharman, G. F. (2010). *Volumes of the World's Oceans from ETOPO1.* Washington, DC: NOAA National Geophysical Data Center. Available online at: http://www.ngdc.noaa.gov/mgg/global/etopo1_ocean_volumes.html (accessed September 27, 2019).

Friedlingstein, P., Jones, M. W., O'Sullivan, M., Andrew, R. M., Hauck, J., Peters, G. P., et al. (2019). Global carbon budget 2019. *Earth Syst. Sci. Data* 11, 1783–1838. doi: 10.5194/essd-11-1783-2019

Global Carbon Project (2019). *Supplemental Data of Global Carbon Budget 2019 (Version 1.0)*. Global Carbon Project, ICOS. Available online at: https://doi.org/10.18160/gcp-2019

Goris, N., Tjiputra, J. F., Olsen, A., Schwinger, J., Lauvset, S. K., and Jeansson, E. (2018). Constraining projection-based estimates of the future North Atlantic carbon uptake. *J. Clim.* 31, 3959–3978. doi: 10.1175/JCLI-D-17-0564.1

Gregor, L., Lebehot, A. D., Kok, S., and Scheel Monteiro, P. M. (2019). A comparative assessment of the uncertainties of global surface ocean CO_2 estimates using a machine-learning ensemble (CSIR-ML6 version 2019a)-have we hit the wall? *Geosci. Model Dev.* 12, 5113–5136. doi: 10.5194/gmd-12-5113-2019

Gruber, N., Clement, D., Carter, B. R., Feely, R. A., van Heuven, S., Hoppema, M., et al. (2019). The oceanic sink for anthropogenic co_2 from 1994 to 2007. *Science* 363, 1193–1199. doi: 10.1126/science.aau5153

Hauck, J., Lenton, A., Langlais, C., and Matear, R. (2018). The fate of carbon and nutrients exported out of the Southern Ocean. *Glob. Biogeochem. Cycles* 32, 1556–1573. doi: 10.1029/2018GB005977

Hauck, J., Völker, C., Wang, T., Hoppema, M., Losch, M., and Wolf-Gladrow, D. A. (2013). Seasonally different carbon flux changes in the Southern Ocean in response to the southern annular mode. *Glob. Biogeochem. Cycles* 27, 1236–1245. doi: 10.1002/2013GB004600

Hauck, J., Zeising, M., Le Quéré, C., Gruber, N., Bakker, D. C. E., Bopp, L., et al. (2020). *The Ocean Carbon Sink Estimate in the Global Carbon Budget 2019.* PANGAEA. Available online at: https://doi.org/10.1594/PANGAEA.920753

Hersbach, H., Bell, B., Berrisford, P., Hirahara, S., Horányi, A., Muñoz-Sabater, J., et al. (2020). The ERA5 global reanalysis. *Q. J. R. Meteorol. Soc.* 146, 1999–2049. doi: 10.1002/qj.3803

Hussain, M., and Mahmud, I. (2019). pyMannKendall: a python package for non parametric Mann Kendall family of trend tests. *J. Open Source Softw.* 4:1556. doi: 10.21105/joss.01556

Jacobson, A. R., Fletcher, S. E. M., Gruber, N., Sarmiento, J. L., and Gloor, M. (2007). A joint atmosphere-ocean inversion for surface fluxes of carbon dioxide: 2. Regional results. *Glob. Biogeochem. Cycles* 21, GB1020. doi: 10.1029/2006GB002703

Jones, S. D., Le Quéré, C., and Rödenbeck, C. (2012). Autocorrelation characteristics of surface ocean pCO_2 and air-sea CO_2 fluxes. *Glob. Biogeochem. Cycles* 26, GB2042. doi: 10.1029/2010GB004017

Joos, F., and Spahni, R. (2008). Rates of change in natural and anthropogenic radiative forcing over the past 20,000 years. *Proc. Natl. Acad. Sci. U.S.A.* 105, 1425–1430. doi: 10.1073/pnas.0707386105

Kalnay, E., Kanamitsu, M., Kistler, R., Collins, W., Deaven, D., Gandin, L., et al. (1996). The NCEP/NCAR 40-year reanalysis project. *Bull. Am. Meteorol. Soc.* 77, 437–471. doi: 10.1175/1520-0477(1996)077<0437:TNYRP>2.0.CO;2

Keeling, R. F., and Manning, A. C. (2014). "Studies of recent changes in atmospheric O_2 content," in *Treatise on Geochemistry*, Vol. 5,

eds H. D. Holland and K. K. Turekian (Oxford: Elsevier), 385–404. doi: 10.1016/B978-0-08-095975-7.00420-4

Keppler, L., and Landschützer, P. (2019). Regional wind variability modulates the Southern Ocean carbon sink. *Sci. Rep.* 9:7384. doi: 10.1038/s41598-019-43826-y

Kessler, A., and Tjiputra, J. (2016). The Southern Ocean as a constraint to reduce uncertainty in future ocean carbon sinks. *Earth Syst. Dyn.* 7, 295–312. doi: 10.5194/esd-7-295-2016

Key, R., Kozyr, A., Sabine, C., Lee, K., Wanninkhof, R., Bullister, J., et al. (2004). A global ocean carbon climatology: results from Global Data Analysis Project (GLODAP). *Glob. Biogeochem. Cycles* 18, GB4031. doi: 10.1029/2004GB002247

Kobayashi, S., Ota, Y., Harada, Y., Ebita, A., Moriya, M., Onoda, H., et al. (2015). The JRA-55 reanalysis: general specifications and basic characteristics. *J. Meteorol. Soc. Jpn.* 93, 5–48. doi: 10.2151/jmsj.2015-001

Landschützer, P., Gruber, N., and Bakker, D. C. E. (2016). Decadal variations and trends of the global ocean carbon sink. *Glob. Biogeochem. Cycles* 30, 1396–1417. doi: 10.1002/2015GB005359

Landschützer, P., Gruber, N., Bakker, D. C. E., and Schuster, U. (2014). Recent variability of the global ocean carbon sink. *Glob. Biogeochem. Cycles* 28, 927–949. doi: 10.1002/2014GB004853

Landschützer, P., Gruber, N., Haumann, A., Rödenbeck, C., Bakker, D. C. E., van Heuven, S., et al. (2015). The reinvigoration of the Southern Ocean carbon sink. *Science* 349, 1221–1224. doi: 10.1126/science.aab2620

Lauvset, S. K., Key, R. M., Olsen, A., van Heuven, S., Velo, A., Lin, X., et al. (2016). A new global interior ocean mapped climatology: the 1 degrees × 1 degrees GLODAP version 2. *Earth Syst. Sci. Data* 8, 325–340. doi: 10.5194/essd-8-325-2016

Law, R. M., Ziehn, T., Matear, R. J., Lenton, A., Chamberlain, M. A., Stevens, L. E., et al. (2017). The carbon cycle in the Australian Community Climate and Earth System Simulator (ACCESS-ESM1)–part 1: model description and pre-industrial simulation. *Geosci. Model Dev.* 10, 2567–2590. doi: 10.5194/gmd-10-2567-2017

Le Quéré, C., Andres, R. J., Boden, T., Conway, T., Houghton, R. A., House, J. I., et al. (2013). The global carbon budget 1959–2011. *Earth Syst. Sci. Data* 5, 165–185. doi: 10.5194/essd-5-165-2013

Le Quéré, C., Andrew, R. M., Friedlingstein, P., Sitch, S., Hauck, J., Pongratz, J., et al. (2018a). Global carbon budget 2018. *Earth Syst. Sci. Data* 10, 2141–2194. doi: 10.5194/essd-10-2141-2018

Le Quéré, C., Andrew, R. M., Friedlingstein, P., Sitch, S., Pongratz, J., Manning, A. C., et al. (2018b). Global carbon budget 2017. *Earth Syst. Sci. Data* 10, 405–448. doi: 10.5194/essd-10-405-2018

Le Quéré, C., Peters, G. P., Andres, R. J., Andrew, R. M., Boden, T. A., Ciais, P., et al. (2014). Global carbon budget 2013. *Earth Syst. Sci. Data* 6, 235–263. doi: 10.5194/essd-6-235-2014

Le Quéré, C., Raupach, M., Canadell, J., and Marland, G. (2009). Trends in the sources and sinks of carbon dioxide. *Nat. Geosci.* 2, 831–836. doi: 10.1038/ngeo689

Le Quéré, C., Rödenbeck, C., Buitenhuis, E. T., Conway, T. J., Langenfelds, R., Gomez, A., et al. (2007). Saturation of the Southern Ocean CO_2 sink due to recent climate change. *Science* 316, 1735–1738. doi: 10.1126/science.1136188

Lebehot, A. D., Halloran, P. R., Watson, A. J., McNeall, D., Ford, D. A., Landschützer, P., et al. (2019). Reconciling observation and model trends in North Atlantic surface CO_2. *Glob. Biogeochem. Cycles* 33, 1204–1222. doi: 10.1029/2019GB006186

Manning, A., and Keeling, R. (2006). Global oceanic and land biotic carbon sinks from the Scripps atmospheric oxygen flask sampling network. *Tellus B* 58, 95–116. doi: 10.1111/j.1600-0889.2006.00175.x

McKinley, G. A., Fay, A. R., Eddebbar, Y. A., Gloege, L., and Lovenduski, N. S. (2020). External forcing explains recent decadal variability of the ocean carbon sink. *AGU Adv.* 1:e2019AV000149. doi: 10.1029/2019AV000149

McNeil, B., Matear, R., Key, R., Bullister, J., and Sarmiento, J. (2003). Anthropogenic CO_2 uptake by the ocean based on the global chlorofluorocarbon data set. *Science* 299, 235–239. doi: 10.1126/science.1077429

Mikaloff Fletcher, S., Gruber, N., Jacobson, A., Doney, S., Dutkiewicz, S., Gerber, M., et al. (2006). Inverse estimates of anthropogenic CO_2 uptake, transport, and storage by the ocean. *Glob. Biogeochem. Cycles* 20, GB2002. doi: 10.1029/2005GB002530

Mikaloff Fletcher, S. E., Gruber, N., Jacobson, A. R., Gloor, M., Doney, S. C., Dutkiewicz, S., et al. (2007). Inverse estimates of the oceanic sources and sinks of natural CO_2 and the implied oceanic carbon transport. *Global Biogeochemical Cycles* 21, GB1010. doi: 10.1029/2006GB002751

Mongwe, N. P., Chang, N., and Monteiro, P. M. (2016). The seasonal cycle as a mode to diagnose biases in modelled CO_2 fluxes in the Southern Ocean. *Ocean Model.* 106, 90–103. doi: 10.1016/j.ocemod.2016.09.006

Mongwe, N. P., Vichi, M., and Monteiro, P. M. S. (2018). The seasonal cycle of pCO_2 and CO_2 fluxes in the Southern Ocean: diagnosing anomalies in CMIP5 earth system models. *Biogeosciences* 15, 2851–2872. doi: 10.5194/bg-15-2851-2018

Naegler, T. (2009). Reconciliation of excess ^{1}4C-constrained global CO_2 piston velocity estimates. *Tellus B* 61, 372–384. doi: 10.1111/j.1600-0889.2008.00408.x

Orr, J. C., and Epitalon, J.-M. (2015). Improved routines to model the ocean carbonate system: mocsy 2.0. *Geosci. Model Dev.* 8, 485–499. doi: 10.5194/gmd-8-485-2015

Paulsen, H., Ilyina, T., Six, K. D., and Stemmler, I. (2017). Incorporating a prognostic representation of marine nitrogen fixers into the global ocean biogeochemical model HAMOCC. *J. Adv. Model. Earth Syst.* 9, 438–464. doi: 10.1002/2016MS000737

Poli, P., Hersbach, H., Tan, D., Dee, D., Thepaut, J.-N., Simmons, A., et al. (2013). *ERA Report Series Number 14: The Data Assimilation System and Initial Performance Evaluation of the ECMWF Pilot Reanalysis of the 20th-Century Assimilating Surface Observations Only (ERA-20C).* Reading: European Centre for Medium-Range Weather Forecasts.

Rackow, T., Goessling, H. F., Jung, T., Sidorenko, D., Semmler, T., Barbi, D., et al. (2018). Towards multi-resolution global climate modeling with ECHAM6-FESOM. Part II: climate variability. *Clim. Dyn.* 50, 2369–2394. doi: 10.1007/s00382-016-3192-6

Regnier, P., Friedlingstein, P., Ciais, P., Mackenzie, F. T., Gruber, N., Janssens, I. A., et al. (2013). Anthropogenic perturbation of the carbon fluxes from land to ocean. *Nat. Geosci.* 6, 597–607. doi: 10.1038/ngeo1830

Resplandy, L., Keeling, R. F., Roedenbeck, C., Stephens, B. B., Khatiwala, S., Rodgers, K. B., et al. (2018). Revision of global carbon fluxes based on a reassessment of oceanic and riverine carbon transport. *Nat. Geosci.* 11, 504–509. doi: 10.1038/s41561-018-0151-3

Rödenbeck, C., Bakker, D. C. E., Gruber, N., Iida, Y., Jacobson, A. R., Jones, S., et al. (2015). Data-based estimates of the ocean carbon sink variability first–results of the surface ocean pCO_2 mapping intercomparison (SOCOM). *Biogeosciences* 12, 7251–7278. doi: 10.5194/bg-12-7251-2015

Rödenbeck, C., Bakker, D. C. E., Metzl, N., Olsen, A., Sabine, C., Cassar, N., et al. (2014). Interannual sea-air CO_2 flux variability from an observation-driven ocean mixed-layer scheme. *Biogeosciences* 11, 4599–4613. doi: 10.5194/bg-11-4599-2014

Rödenbeck, C., Zaehle, S., Keeling, R., and Heimann, M. (2018). How does the terrestrial carbon exchange respond to inter-annual climatic variations? A quantification based on atmospheric CO_2 data. *Biogeosciences* 15, 2481–2498. doi: 10.5194/bg-15-2481-2018

Roobaert, A., Laruelle, G. G., Landschützer, P., Gruber, N., Chou, L., and Regnier, P. (2019). The spatiotemporal dynamics of the sources and sinks of CO_2 in the global coastal ocean. *Glob. Biogeochem. Cycles* 33, 1693–1714. doi: 10.1029/2019GB006239

Sarmiento, J. L., and Sundquist, E. (1992). Revised budget for the oceanic uptake of anthropogenic carbon dioxide. *Nature* 356, 589–593. doi: 10.1038/356589a0

Schourup-Kristensen, V., Sidorenko, D., Wolf-Gladrow, D. A., and Völker, C. (2014). A skill assessment of the biogeochemical model REcoM2 coupled to the finite element sea ice-ocean model (FESOM 1.3). *Geosci. Model Dev.* 7, 2769–2802. doi: 10.5194/gmd-7-2769-2014

Schourup-Kristensen, V., Wekerle, C., Wolf-Gladrow, D. A., and Völker, C. (2018). Arctic Ocean biogeochemistry in the high resolution FESOM 1.4-REcoM2 model. *Prog. Oceanogr.* 168, 65–81. doi: 10.1016/j.pocean.2018.09.006

Schuster, U., McKinley, G. A., Bates, N., Chevallier, F., Doney, S. C., Fay, A. R., et al. (2013). An assessment of the Atlantic and Arctic sea-air CO_2 fluxes, 1990–2009. *Biogeosciences* 10, 607–627. doi: 10.5194/bg-10-607-2013

Schwinger, J., Goris, N., Tjiputra, J. F., Kriest, I., Bentsen, M., Bethke, I., et al. (2016). Evaluation of NorESM-OC (versions 1 and 1.2), the ocean carbon-cycle

stand-alone configuration of the Norwegian Earth System Model (NorESM1). *Geosci. Model Dev.* 9, 2589–2622. doi: 10.5194/gmd-9-2589-2016

Sidorenko, D., Rackow, T., Jung, T., Semmler, T., Barbi, D., Danilov, S., et al. (2015). Towards multi-resolution global climate modeling with ECHAM6-FESOM. Part I: model formulation and mean climate. *Clim. Dyn.* 44, 757–780. doi: 10.1007/s00382-014-2290-6

Simmons, A. J., Soci, C., Nicolas, J., Bell, B., Berrisford, P., Dragani, R., et al. (2020). *Global Stratospheric Temperature Bias and Other Stratospheric Aspects of ERA5 and ERA5.1.* Technical Memorandum 859. Reading: ECMWF.

Tsujino, H., Urakawa, S., Nakano, H., Small, R. J., Kim, W. M., Yeager, S. G., et al. (2018). JRA-55 based surface dataset for driving ocean-sea-ice models (JRA55-do). *Ocean Model.* 130:79–139. doi: 10.1016/j.ocemod.2018.07.002

Verdy, A., and Mazloff, M. R. (2017). A data assimilating model for estimating Southern Ocean biogeochemistry. *J. Geophys. Res. Oceans* 122, 6968–6988. doi: 10.1002/2016JC012650

Wang, Q., Danilov, S., Sidorenko, D., Timmermann, R., Wekerle, C., Wang, X., et al. (2014). The finite element sea ice-ocean model (FESOM) v.1.4: formulation of an ocean general circulation model. *Geosci. Model Dev.* 7, 663–693. doi: 10.5194/gmd-7-663-2014

Wanninkhof, R. (1992). Relationship between wind speed and gas exchange over the ocean. *J. Geophys. Res. Oceans* 97, 7373–7382. doi: 10.1029/92JC00188

Wanninkhof, R. (2014). Relationship between wind speed and gas exchange over the ocean revisited. *Limnol. Oceanogr. Methods* 12, 351–362. doi: 10.4319/lom.2014.12.351

Wanninkhof, R., Park, G.-H., Takahashi, T., Sweeney, C., Feely, R., Nojiri, Y., et al. (2013). Global ocean carbon uptake: magnitude, variability and trends. *Biogeosciences* 10, 1983–2000. doi: 10.5194/bg-10-1983-2013

Williams, N. L., Juranek, L. W., Feely, R. A., Johnson, K. S., Sarmiento, J. L., Talley, L. D., et al. (2017). Calculating surface ocean pCO_2 from biogeochemical Argo floats equipped with pH: an uncertainty analysis. *Glob. Biogeochem. Cycles* 31, 591–604. doi: 10.1002/2016GB005541

Wolter, K., and Timlin, M. S. (2011). El Niño/southern oscillation behaviour since 1871 as diagnosed in an extended multivariate ENSO index (MEI.ext). *Int. J. Climatol.* 31, 1074–1087. doi: 10.1002/joc.2336

Woolf, D., Shutler, J., Goddijn-Murphy, L., Watson, A., Chapron, B., Nightingale, P., et al. (2019). Key uncertainties in the recent air-sea flux of CO_2. *Glob. Biogeochem. Cycles* 33, 1548–1563. doi: 10.1029/2018GB006041

Yeager, S. G., and Large, W. G. (2008). *CORE.2 Global Air-Sea Flux Dataset*. Research Data Archive at the National Center for Atmospheric Research, Computational and Information Systems Laboratory.

Zeebe, R., and Wolf-Gladrow, D. (2001). *CO_2 in Seawater: Equilibrium, Kinetics, Isotopes,* Vol. 65. Amsterdam: Elsevier.

Conflict of Interest: The authors declare that the research was conducted in the absence of any commercial or financial relationships that could be construed as a potential conflict of interest.

The handling editor declared a past co-authorship with one of the authors NG.

frontiers in Environmental Science

ORIGINAL RESEARCH
published: 09 December 2020
doi: 10.3389/fenvs.2020.609254

Evaluation of the FLake Model in ERA5 for Lake Champlain

Alan K. Betts[1]*, *Daniel Reid*[2] and *Caitlin Crossett*[2]

[1] Atmospheric Research, Pittsford, VT, United States, [2] Vermont EPSCoR, University of Vermont, Burlington, VT, United States

Global model reanalyses of temperature and radiation are used for many purposes because of their spatial and temporal homogeneity. However, they use sub-models for lakes that are smaller than the model grid. This paper compares the simplified small-lake model, known as FLake, used in the European Centre global reanalysis known as ERA5, with observations made in and near Lake Champlain in northern Vermont. Lake Champlain is a challenging test for the ERA5 FLake model. The lake, which extends over several grid cells, is the lowest region at 30 m above sea level within complex mountain topography. The smoothing of the adjacent mountain topography means that the ERA5 grid cells containing the lake have higher mean elevations then 30 m, and this contributes to a small cool bias in FLake mid-summer temperatures. The seasonal cycle of FLake temperatures has a sharper peak than the observed lake temperatures. In winter, lake temperatures are close to 3°C, while the 30 m deep FLake mixed layer (ML) is near freezing. In May and June, FLake maintains a deep ML, while lake profiles are generally strongly stratified with peak temperatures near the surface several degrees above the model ML. One possible contributing reason is that inflowing river temperatures that are not considered by FLake are as much as 5°C above the lake surface temperature from April to June. The lake does develop a ML structure as it cools from the temperature peak in August, but the FLake ML cools faster and grows deeper in fall. We conclude that the vertical mixing in the FLake ML is stronger than the vertical mixing in Lake Champlain.

Keywords: reanalysis, FLake model, lake-atmosphere coupling, Lake Champlain, seasonal cycle

OPEN ACCESS

Edited by:
Paul A. Dirmeyer, George Mason University, United States

Reviewed by:
Wim Thiery, Vrije University Brussel, Belgium
Laura Rontu, Finnish Meteorological Institute, Finland
Patrick Le Moigne, National Center for Meteorological Research (CNRM, Meteo-France), France

***Correspondence:**
Alan K. Betts
akbetts@aol.com
orcid.org/0000-0003-2749-5333

Specialty section:
This article was submitted to Interdisciplinary Climate Studies, a section of the journal Frontiers in Environmental Science

Received: *22 September 2020*
Accepted: *16 November 2020*
Published: *09 December 2020*

Citation:
Betts AK, Reid D and Crossett C (2020) Evaluation of the FLake Model in ERA5 for Lake Champlain. Front. Environ. Sci. 8:609254. doi: 10.3389/fenvs.2020.609254

KEY POINTS

- Higher mean elevations in ERA5, from smoothing the adjacent mountain topography, contribute to a small cool bias in FLake mid-summer temperatures.
- Inflow of warmer river water contributes to observed lake stratification as the lake warms.
- The seasonal cycle of FLake temperatures has a sharper summer peak than observed.
- The vertical mixing driving the FLake ML is stronger than the vertical mixing in Lake Champlain.

INTRODUCTION

This paper will compare *in-situ* data for Lake Champlain, which is bordered by the states of Vermont and New York and the province of Quebec, with the sub-grid-scale lake model FLake (Mironov, 2008; Dutra et al., 2010; Mironov et al., 2010) used in the current reanalysis from the European Center for Medium-Range Weather Forecasts (ECMWF), known as ERA5 (C3S: Copernicus Climate Change Service, 2017). Exchanges of energy and water differ greatly for land

and water surfaces, and at the land-ocean boundary. Global models explicitly handle this transition using a land-sea grid-box fraction. Over land, both large lakes that are resolved by the model grid, and the large numbers of unresolved smaller lakes are modeled in ERA5 using the one-dimensional FLake model to compute the diurnal and seasonal cycle of lake temperature profiles, and the contribution to the mean grid-box surface fluxes. This study will focus on Lake Champlain, but small lakes are extensive over the continents. For example, Canada has about 31000 small lakes with areas between 1 and 100 km^2 which substantially impact surface temperature (Verseghy and MacKay, 2017).

The broader context is a University of Vermont project called Basin Resilience to Extreme Events (BREE), funded by the National Science Foundation to understand the ecohydrology and economic impacts of the lake as climate and extreme events change. Already toxic blooms of blue-green algae in summer contaminate the shallow lake waters near the urban area of Burlington Vermont, impacting local health and tourism (Isles et al., 2015). In the broad context, the BREE project is developing an integrated assessment model for the Lake Champlain region (Zia et al., 2016) with an atmospheric model (Huang et al., 2019) driving a lake circulation model, coupled to a biogeochemistry model (e.g., Isles et al., 2017), and to land-use and governance issues (Bitterman and Koliba, 2020; Doran et al., 2020).

This study however, which started as a BREE student summer project by the second author (DR), has a limited scope. We compare the simplified 1-D FLake model from ERA5 with surface and profile measurements for two sites on Lake Champlain that are available for several years.

REANALYSIS AND OBSERVATIONS

ERA5 Domain and Observation Sites

The operational ECMWF analysis-forecast system is under continual development with significant upgrades typically twice a year. For historic reanalysis a frozen version of the model is used. This paper uses the latest reanalysis, ERA5, based on model cycle Cy41r2, which was introduced operationally in 2016. Extensive details of the representation of physical processes, including the surface parameterization and parameter tables, are available in Hersbach et al. (2020) and Cy41r2 (2016). Here we give a very brief overview.

The land-surface model in ERA5, known as HTESSEL (Balsamo et al., 2009, 2011), represents each grid-box in terms of the fraction of eight tiles, one of which is FLake for sub-grid-scale lakes (Mironov et al., 2010). Note that the tiles at the interface of the soil-atmosphere are in energy and hydrological contact with one single atmospheric profile above and one single soil profile below. Each grid-box is divided into eight fractions: two vegetated fractions (high and low vegetation without snow), one bare soil fraction, three snow/ice fractions (snow on bare ground/low vegetation, high vegetation with snow beneath, and lake-ice), and two water fractions (interception reservoir, and sub-grid-lakes which have a specific sub-model (FLake, described in next section). The distinction between low and high vegetation is particularly important for snow, because exposed snow has a high albedo, whereas, a canopy with snow underneath has a low albedo (Betts and Ball, 1997; Betts et al., 2001). The vegetation characteristics in ERA5 are defined by fractional cover and the type of the dominant high and low vegetation, which are based on the Global Land Cover Characterization (GLCC) data set derived from 1 km AVHRR (Advanced Very High Resolution Radiometer) satellite observations (Loveland et al., 2000). For each vegetation type, Leaf Area Index (LAI) has an annual cycle, which comes from a satellite-derived monthly climatology (Boussetta et al., 2011) and which modulates evapotranspiration.

We use ERA5 grid-boxes that are 0.25 × 0.25 degrees, corresponding to about 27.8 km in latitude and 20 km in longitude at 44°N, and therefore, an area of about 550 km^2. Lakes with an area >1% grid-box cover are represented by FLake, but they are aggregated to a single lake tile, which communicates with the single grid scale atmospheric profile.

Figure 1A shows the mean topography of the 0.25 degree ERA5 grid as a square pattern, showing the north-south chain of the Green Mountains in central Vermont to the east of Lake Champlain, and the higher Adirondack mountains to the west in New York. ERA5 also represents the sub-grid-scale orography (not shown) to improve estimates of the surface stress. The New York-Vermont border runs through the lake (black line) north to the Canadian border at 45°N.

Figure 1B shows the ERA5 grid-boxes which are rectangular in geographic coordinates, superimposed on a map of the sites where there are observations around Lake Champlain for comparison. This paper is a direct comparison of the ERA5 FLake tile model data and the ERA5 grid-mean data with observational data, primarily from the Diamond Island (green diamond) and Colchester Reef (red triangle) sites. We will use ERA5 data from 2012 to 2017. Recent work over the central Canadian Prairies (Betts et al., 2019) showed that the near-surface air temperature bias in ERA5 is small, typically $< \pm 1$°C for the April to October warm season with no snow. This is much less than the earlier reanalysis known as ERA-Interim (Betts and Beljaars, 2017).

ERA5 FLake Tile Model

The representation of inland water bodies (lakes, reservoirs, rivers, and coastal waters) is important in order to account for the thermal inertia effects, albedo and roughness characteristics of open water and to account for phase change during freezing/melting. This is simulated in ERA5 by the Fresh-water Lake model FLake [Mironov (2008), Mironov et al. (2010)], which was chosen for its intermediate complexity, particularly adapted for numerical weather prediction and climate applications. Moreover, FLake benefits from a large research community effort, contributing to validation and development [FLake (2017)]. Its use and evaluation as the tile representing sub-grid-scale lakes in the ECMWF HTESSEL land surface model (Balsamo et al., 2009, 2012) is discussed in Dutra et al. (2010) and Balsamo (2013).

The FLake model was developed to predict the surface temperature in small lakes of various depths on time scales from a few hour to a year, specifically for numerical weather prediction. Key parameters are lake fraction and lake depth

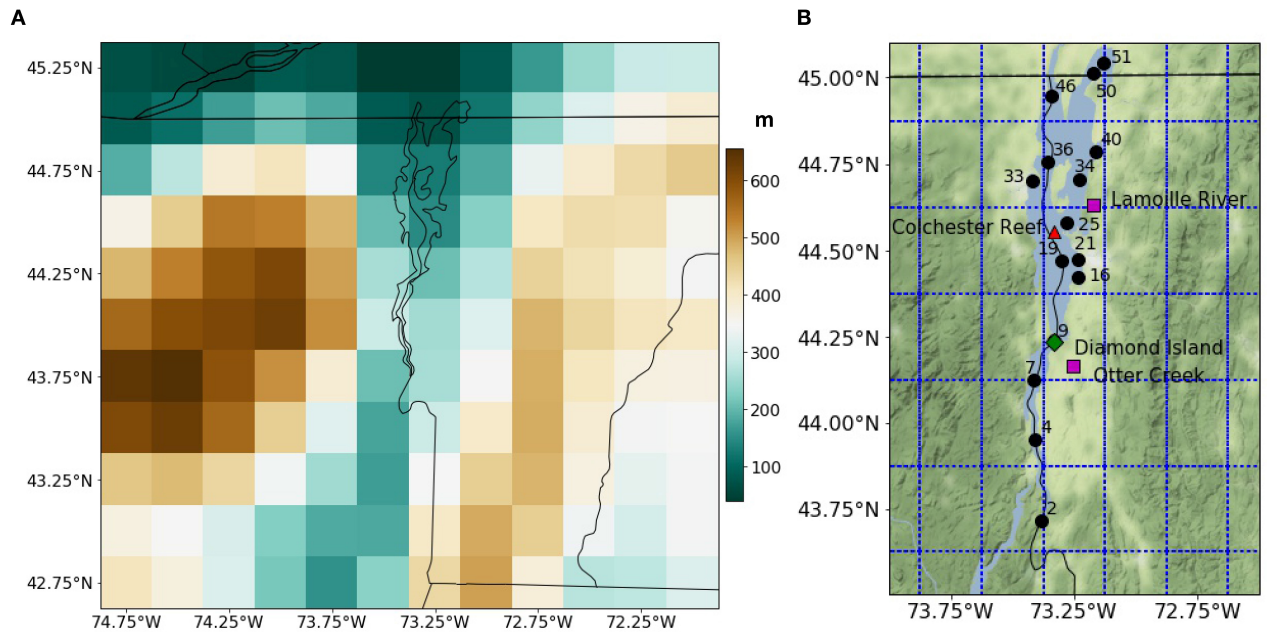

FIGURE 1 | (A) ERA5 $(0.25°)^2$ grid for larger domain showing model grid mean topography and **(B)** Lake Champlain observation sites with ERA5 grid boxes superimposed. The green diamond and red triangle mark our main observation sites: Diamond Island and Colchester reef.

which are mapped from global datasets—see Chapter 11.11 in Cy41r2 (2016). The global lake depth and coverage datasets were developed by Kourzeneva (2010), Kourzeneva et al. (2012), and Choulga et al. (2014). The FLake model is based on a two-layer parameterization of the lake temperature profile, with an upper mixed layer (ML) above the stratified lake thermocline extending down to lake bottom. These are described using the concept of self-similarity for the evolving temperature profile. **Figure 2A** is a schematic of this parameterization, adapted from Mironov (2008). The model is forced at the surface by the wind at the lowest model level, as well as by temperature, humidity and precipitation and the shortwave and longwave radiation; and it adjusts to a new equilibrium profile on timescales of a few hour. Full details are available in Chapter 8.8 in Cy41r2 (2016). The key parameters are ML Temperature (MLT) and ML Depth (MLD); Bottom layer temperature (BLT), and a profile shape factor for the lower layer. ERA5 provides hourly data, which we have integrated to UTC (Universal Time) daily means. Observations made in Eastern Standard Time (EST) will be converted to the same time-base: UTC=EST+5. Our climate analysis begins with daily and monthly timescales, which are longer than the FLake adjustment time.

Figure 2B shows the tight coupling on daily timescales ($R^2 \approx 0.95$) between ML temperature and ML depth for August 2015 and 2016 for the ERA5 grid-box centered on 44.25°N, −73.25°W. August has the most linear structure because it is near the time of maximum temperature, and 2016 (a warmer summer than 2015) has a slightly warmer and deeper ML.

METHODS

Observations

We compare observations and ERA5 for the seasonal cycle of lake temperature (T_{water}) and air temperature (T_{air}) for 2 key sites run by the Forest Ecosystem Monitoring Cooperative (FEMC, 2019). Diamond Island (green diamond in **Figure 1B**) at 44.237°N, 73.333°W has 15-min observations for 2012–2017, including T_{water} at 3 m depth, and T_{air} at 42.6 m above mean sea-level (MSL) (see Duncan and Waite, 2017). The mean elevation of Lake Champlain is 29.9 m (98ft) MSL, with a typical annual variation that can be as large as ±1 m. We compare the Diamond Island data with the ERA5 grid-box centered at 44.25°N, −73.25°W which has a mean elevation of 208.3 m MSL. For this grid-box the ERA5 lake cover is 4% and the lake depth is 48.6 m: the FLake model limits lake depth to 50 m. Lake temperature profiles to a depth of 85 m for the Otter Creek Segment (OCS) near Diamond Island are available about 10 times a year for 2012–2017 from the Vermont Department of Environmental Conservation Lake Monitoring Program (VTDEC, 2019). Inflowing river temperatures for the Otter Creek (OCRT, 2019) are also available about 10 times a year for the same period, except there is no data for 2014.

Colchester Reef at 44.555°N, 73.329°W (red triangle in **Figure 1B**: FEMC, 2019) also has 15-min T_{water} at 3 m depth and T_{air} at 47.1 m MSL for 2015–2017, which we will compare with the ERA5 grid-box centered at 44.5°N, −73.25°W, which has a mean elevation of 148.4 m MSL. For this grid-box the ERA5 lake cover is 14% and the lake depth is 33.8 m, but we have no comparison lake profile data.

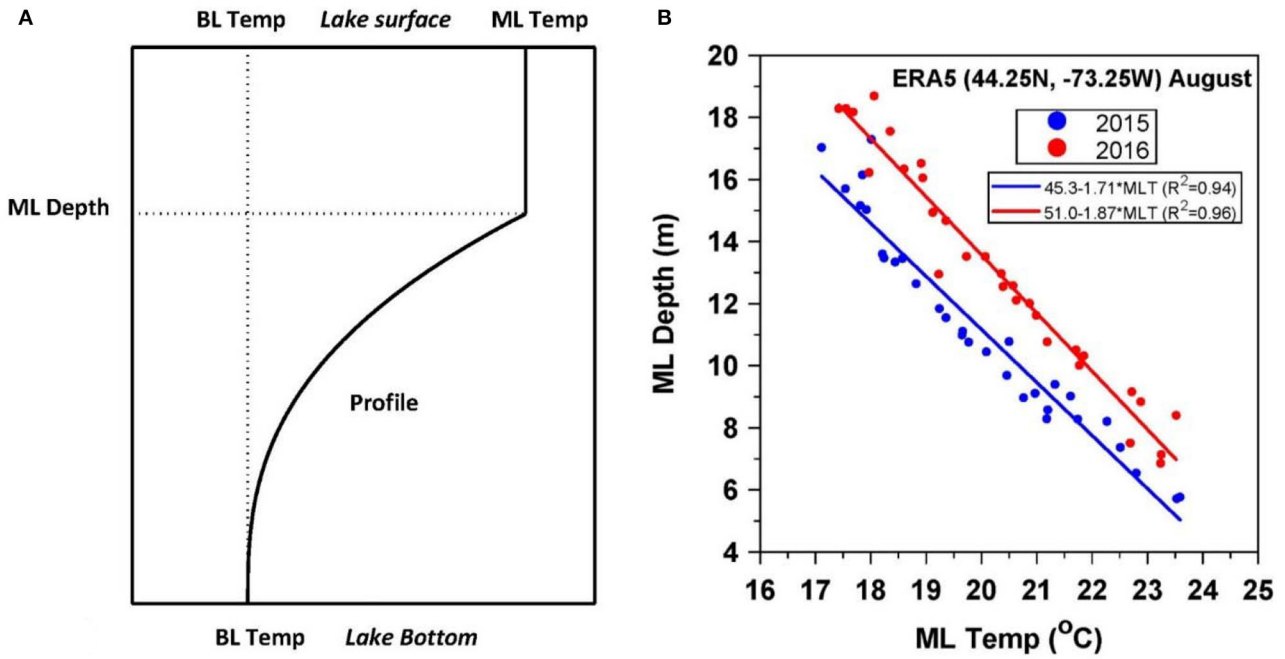

FIGURE 2 | (A) Idealized self-similar profile in the FLake model and **(B)** Tight coupling on daily timescales between ML temperature and ML depth in August.

ERA5 Processing

The hourly ERA5 data was accessed at quarter degree resolution from the Copernicus Climate Data Store (C3S: Copernicus Climate Change Service, 2017). We used the 6–18 h short-term forecasts that are initialized from the 0 and 12 UTC analyses. This resolves the diurnal cycle well and removes the initial spin-up in the first 6 h of the forecast (Betts et al., 2019). These short-range forecasts are close to the analyzed large-scale flow, but they already contain any systematic errors in the land surface model (Haiden et al., 2016).

For the seasonal cycle, the ERA5 hourly grid point data were reduced to daily means in UTC days. The observations are 15 m means, and from these we also computed daily (UTC) and monthly means.

RESULTS

Air and Water Temperature Comparison

We will directly compare the seasonal cycle of air and water temperature between ERA5 and FLake and the observations. There are some issues. The mean height of the surface of Lake Champlain (above MSL) is 29.9 m. In times of major flood, like Tropical Storm Irene in 2011, it rose above 31 m. Lake Champlain at 30 m elevation is surrounded by higher terrain shown in **Figure 1A**. The Adirondack Mountains to the west have many peaks above 1,200 m, and the Green Mountains to the east have peaks above 1,000 m. The ERA5 native resolution of 31 km (sampled at a quarter degree) smooths the topography. For example, Mount Marcy is in the gridbox at 44°N, 74°W, only 40 km west of the lake, with a peak elevation above 1,500 m, while this ERA5 grid-box has a mean elevation around 600 m. The smoothed ERA5 topography does not represent the mountain peaks, nor the smaller hills that surround the lake. As a result, all the ERA5 grid-boxes that include parts of the lake have mean elevations higher than 30 m; and this height difference increases southward.

FLake is a simplified model with a specified fixed lake area and depth for each grid-box. There is no water flow or water balance equation, so the transfer of heat and water by rivers and lake circulations are not represented.

Figure 3 compares the mean annual cycle of T_{air}, and T_{water} (at 3 m below the mean lake surface) for 2012–2017 for Diamond Island and 2015–2017 for Colchester Reef, with the ERA5 2-m mean air temperature ($T2_m$) and the FLake model MLT on the corresponding ERA5 grid-boxes. The right-hand-scale shows the mean seasonal cycle of the FLake MLD, which is constrained by the specified model lake depths, which are 48.6 m and 33.8 m for the southern and northern grid-boxes.

The Diamond Island air temperature (**Figure 3A**) is warmer than ERA5 by 1.1±0.3°C in the warm season (April to September) and 1.6±0.4°C for the cold season (October to March). The elevation difference between model topography and measured air temperature (at 42.6 m MSL, 12.7 m above the lake) is 165.7 m, and a nominal correction for this elevation difference, using the standard atmosphere lapse rate of -6.5 °Ckm^{-1}, is 1.1°C, comparable to the warm season bias. However, it should be noted that the model 2-m temperatures are computed to represent synoptic measurements above a grass plot, while the observations are on a small island tower at 12.7 m above the lake surface. In addition, we are averaging over day and night with

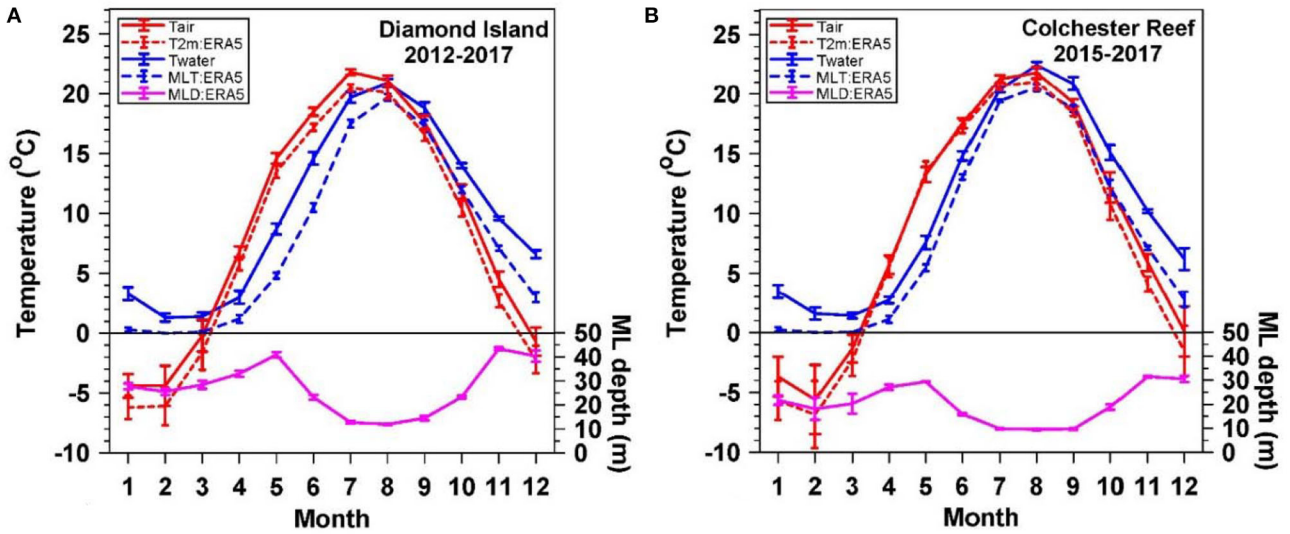

FIGURE 3 | (A) Mean annual cycle of T_{air}, $T2_m$, T_{water}, MLT, and MLD for Diamond Island and **(B)** Colchester Reef (right).

substantially different boundary layers. The Colchester Reef air temperature (**Figure 3B**) is warmer than ERA5 by 0.4 ± 0.5°C in the warm season and 1.5 ± 0.5°C for the cold season. In April and May the two air temperature are very close. The elevation difference between model topography of 148.4 m for this grid-box at 44.5°N and the sensor height of 47.1 m MSL is 101 m; giving a nominal correction using the standard atmosphere lapse rate of 0.66°C, which is comparable to the summer bias.

The measured water temperatures for Diamond Island (left) are warmer than the FLake MLT. The difference is largest in May and June (4.1 ± 0.8°C), smallest at the peak lake temperatures in August (1.2 ± 0.2°C), and the difference is again large in December and January (3.3 ± 0.8°C). Only at the peak in August is the difference in lake temperatures the same as the difference in air temperatures, which is likely connected to the higher elevation of the ERA5 grid-box above the lake.

In winter, the Diamond Island water temperatures at 3 m depth remain above freezing. In contrast the FLake MLT falls to 0°C in January and stays at 0°C through March with a surface ice thickness in February and March that ranges from 20 to 76 cm. This same unrealistic 0°C ML with the FLake model was seen in an earlier study of Sparkling Lake in northern Wisconsin, which was part of the Lake Model Intercomparison Project (Stepanenko et al., 2010). For Lake Champlain, the two coldest winters are 2014 and 2015, when the FLake model has the thickest February-March ice layer (66 and 76 cm, respectively) and Lake Champlain froze over on February 12 and 14, respectively. For the other four warmer winters the FLake ice depth was between 20 and 37 cm, and Lake Champlain did not freeze over.

The warming of the FLake MLT from its frozen state is slow in spring, but we also see the lake ML cools faster in the fall than the Diamond Island water temperatures. For the grid-point to the north including Colchester Reef, MLT rises faster in spring and falls a little faster in fall. This is related to the smaller specified depth in the lake model. As a result, in May and June the difference between measured T_{water} and MLT is (1.9 ± 1.2°C) (smaller than for Diamond Island), with the smallest difference in July (1.0 ± 0.6°C) and a similar large difference in December and January (3.3 ± 0.8°C). These lake temperature comparisons near Diamond Island are discussed further in the next section.

Seasonal Comparison With Otter Creek Segment Profiles

Profiles of lake temperature with depth are made at several locations on Lake Champlain. The Otter Creek Segment (OCS) profiles down to 85 m are close to Diamond Island. **Figure 4A** shows the mean temperature profiles for 2012–2017, binned in 4 m ranges of depth down to 50 m, from May to October. Two late April profiles (from 2010 and 2013) show almost constant temperatures in the range 3.5–3.8°C with depth, just below the temperature of maximum density of water (3.98°C). The lake warms from the surface in May, June and July (red curves), reaching its maximum temperature in August (heavy black line) and then cooling in September and October (blue curves). We show only monthly mean profiles, which are 6-year averages, because the data is heterogeneous. There are typically only 2 profiles in May and as many as 4 profiles in August; and profiles are on different days in different years. During the warming phase, there is a strong stratification with depth in the mean, as well as in most individual profiles (see next section), with no suggestion of a ML. However, after August as the lake is cooled from the surface, these mean profiles show the development of a ML, which is also seen in individual profiles. There is no cold season profile data.

Figure 4B is the Diamond Island comparison just for water temperatures. It shows the annual cycle of the ERA5 MLT and also BLT (bottom layer temperature at 48.6 m depth), along with the Diamond Island T_{water} at 3 m below the surface. From the

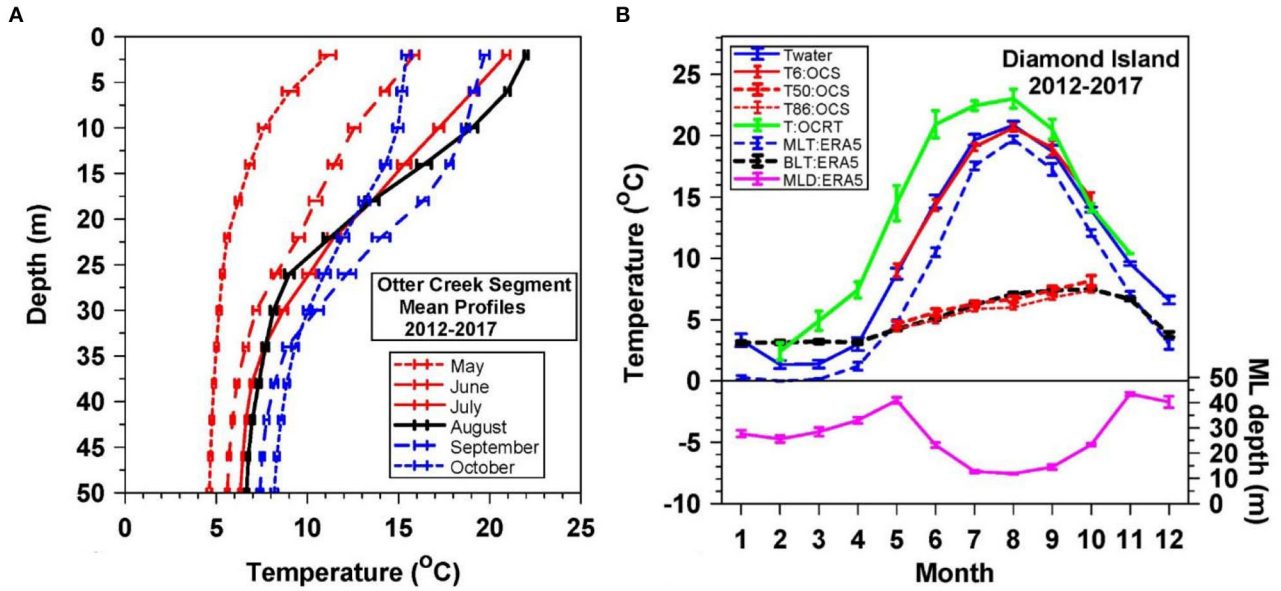

FIGURE 4 | (A) Mean monthly temperature profiles with depth for Otter Creek Segment and **(B)** seasonal cycle of ERA5 ML depth, ERA5 water temperatures and different observations at different depths.

profiles in the left panel, May to October Otter Creek Segment means have been calculated. T6:OCS is the mean for the near-surface layers down to 12 m. The close agreement between T_{water} (fully sampled at 15 min) and T6:OCS (sampled only a few times a month) is encouraging. Lake Champlain for the Otter Creek segment is much deeper than 50 m, and the OCS profiles go as deep as 90 m. So we also show the 50 m comparison of T50:OCS, which corresponds to the depth of ERA5 BLT, as well as T86:OCS, an 86 m-mean at lake bottom. It is clear there is consistency between the BLT and the poorly sampled deep layer OCS temperatures from May to October. In winter, the BLT is close to 3°C. The temperature, T:OCRT (in green), comes from another dataset for the Otter Creek river temperatures (OCRT, 2019) measured shortly before the river enters Lake Champlain. The annual sampling is poor, the scatter is large and there is no data for 2014. However, these temperatures of the inflowing nearby river are around 5°C warmer in spring than the Diamond Island T_{water}.

It is clear that the ERA5 MLT is cooler than the near-surface lake observations. In mid-summer the small differences of order 1°C are probably connected to cooler air temperatures of the ERA5 grid-box which has a mean elevation over 170 m above the elevation of Lake Champlain. However, MLT is 4°C cooler than Diamond Island T_{water} in May and June. As discussed in the previous section, the FLake MLT falls to 0°C in January and stays at 0°C through March with a surface ice layer. As ML depth increases to a peak in May, MLT rises much slower than T_{water} and T6:OCS. The OCS mean profile observations show that Lake Champlain is strongly stratified in Spring. It does not have the ML that is imposed in the FLake model. The T_{water} observations in winter and the few T6:OCS in April (not shown) suggest the lake is close to maximum density near 3°C. Stepanenko et al. (2010) noted this same behavior and suggested that vertical mixing was too strong in Spring in FLake and two other models. In the fall, the ERA5 ML reaches almost the full FLake model depth in November, which then cools through 3°C, typically in mid-December.

A separate issue is that FLake cannot represent the rivers that run into Lake Champlain year-round. The warmer river inflow in Spring contributes to the stratification of the lake (Morrill et al., 2005), as suggested by the higher Otter Creek river temperatures T:OCRT shown in **Figure 4B**.

The next section illustrates the seasonal differences between the ERA5 and the OCS profiles for a single year: May to October 2016.

ERA5-Otter Creek Segment 2016 Profile Comparisons

Figure 5 compares the ERA5 (44.25° N, 73.25° W) temperature-depth profiles (dashed) with the Otter Creek Segment (OCS) profiles (solid) down to 50 m for the same dates in 2016 to illustrate differences between the warming and the cooling period, and the differences between the FLake ML and observations. The plots again show that ERA5 tends to underestimate the temperature of the lake especially in the spring and late fall. **Figure 5A** shows that the measured OCS profiles in late May are strongly stratified in the first 10 m. In contrast, ERA5 has deep cold ML down to 40 m. The model ML profile, which was at 0°C into March, reaches 2°C on April 22, and climbs roughly 1°C every 10 days, reaching 5°C on May 24. The OCS profiles are all stratified in June and July as well, with one exception, June 14, which shows a 23 m deep ML after a few days with strong winds. At depths of 40-50 m the observed profiles and ERA5 agree well.

Figure 5B compares daily profiles from the peak lake surface temperature in August through the cooling period in September

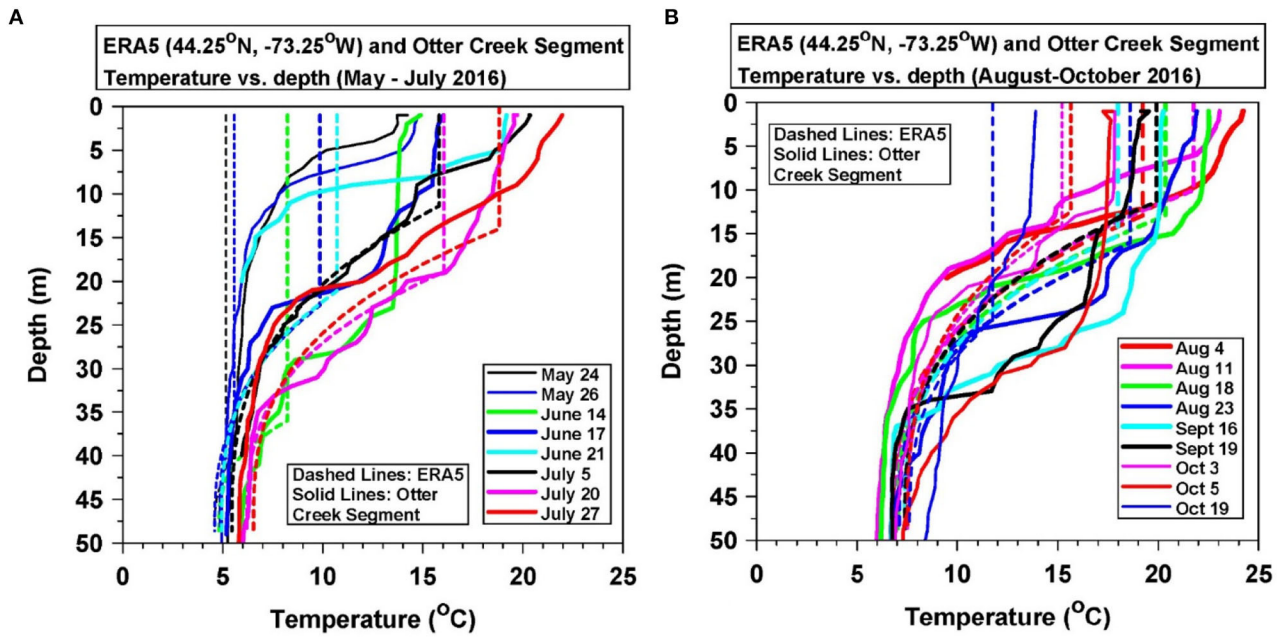

FIGURE 5 | (A) Comparison of temperature depth profiles between ERA5 (dashed) and Otter Creek Segment (solid) for the same dates: May to July and **(B)** August to October.

and October. During the cooling period, most of the OCS profiles show a ML, so the agreement with ERA5 is better, although the OCS profiles are mostly warmer than the ERA5 profiles. As mentioned earlier this may be partially due to the higher elevation of the lake surface in ERA5 (198 m above Lake Champlain), and warmer temperatures in inflowing rivers may play a role in August. After October when we have no profiles, **Figure 4B** shows that the deep ERA5 ML continues to cool faster than the Diamond Island water temperatures, as it cools toward 0°C in mid-winter.

DISCUSSION AND CONCLUSIONS

Lake Champlain is a challenging test for the ERA5 FLake model in ERA5 where the native resolution of ERA5 is 31 km, which we have sampled at a quarter degree. The lake is the lowest region at 30 m MSL within complex mountain topography (**Figure 1A**) and extends over several grid cells. For the Colchester Reef and Diamond Island sites, where we have extensive comparison data, the mean ERA5 grid-box elevations are above the lake surface by 118 m and 178 m, respectively. This contributes to mean near-surface air temperatures in ERA5 that are cooler than observations of order 1°C. We compared the seasonal cycle of grid-box air temperature and lake temperature from FLake with a range of observations. The FLake model gives reasonable peak summer temperatures, consistent with the higher mean elevation and cooler air temperatures for the ERA5 grid boxes.

However, the seasonal cycle of FLake temperatures has a sharper peak than observed lake temperatures. In winter, lake temperatures are close to 3°C not far below the temperature of maximum density, while the deep FLake ML cools to 0°C in February and March with a surface ice cover ranging from 20 to 76 cm thickness in warm and cold years respectively,. The recovery from this deep cold ML is slow in spring. In May and June, while FLake maintains a deep ML, the lake profiles are generally strongly stratified with peak temperatures near the surface several degrees above the model ML. One possible contribution is that inflowing river temperatures that are not considered by FLake are as much as 5°C above the lake surface temperature from April to June. The lake does develop a ML structure as it cools from the temperature peak in August. However, the FLake ML cools faster and grows deeper in fall as the model lake returns to a deep near-freezing mixed layer in winter. For the Diamond Island site comparison, the model lake bottom temperatures at 48.6 m correspond closely to observed lake temperatures at 50 m from May to October.

Our conclusion is that the vertical mixing in the FLake ML is stronger than the vertical mixing in Lake Champlain. Higher spatial resolution would reduce the small cool bias in FLake mid-summer temperatures associated with the high bias of the ERA5 grid-box elevations from the smoothing of the adjacent mountain topography. Choulga et al. (2019) are working on improving the resolution of both the orography and the depth topography of the lake.

DATA AVAILABILITY STATEMENT

The ERA5 reanalysis data are available from the Copernicus data store at: https://cds.climate.copernicus.eu/cdsapp#!/dataset/reanalysis-era5-single-levels?tab=form; The Diamond Island

dataset is available from Duncan and Waite (2017). The Colchester Reef dataset is available from FEMC (2019). The Otter Creek Profiles are available from VTDEC (2019). The Otter Creek River Temperatures are available from OCRT (2019).

AUTHOR CONTRIBUTIONS

Conceptualization, analysis, writing, and editing: AB. Analysis, writing, and review: DR. Data curation, supervision, and review: CC. All authors contributed to the article and approved the submitted version.

FUNDING

This work was supported by the EPSCoR National Science Foundation Grant No. OIA-1556770 to the University of Vermont.

ACKNOWLEDGMENTS

We are grateful to the many observers who made and evaluated the Lake Champlain observations; to J. Duncan and C. Waite from the Forest Ecosystem Monitoring Cooperative for their guidance, and to Angela Shambaugh from the VT DEC Lake water quality monitoring program.

REFERENCES

Balsamo, G. (2013). Interactive lakes in the integrated forecasting system. *ECMWF Newsletter* 137, 30–34. doi: 10.21957/rffv1gir

Balsamo, G., Boussetta, S., Dutra, E., Beljaars, A., Viterbo, P., and den Hurk, B. V. (2011). Evolution of land-surface processes in the IFS. *ECMWF Newsletter* 127, 12–22.

Balsamo, G., Salgado, R., Dutra, E., Boussetta, S., Stockdale, T., and Potes, M. (2012). On the contribution of lakes in predicting near-surface temperature in a global weather forecasting model. *Tellus A Dyn. Meteorol. Oceanogr*. 64:15829. doi: 10.3402/tellusa.v64i0.15829

Balsamo, G., Viterbo, P., Beljaars, A., van den Hurk, B., Hirschi, M., Betts, A. K., et al. (2009). A revised hydrology for the ECMWF model: verification from field site to terrestrial water storage and impact in the integrated forecast system. *J. Hydrometeorol.* 10, 623–643. doi: 10.1175/2008JHM1068.1

Betts, A., Viterbo, P., Beljaars, A. C. M., and Van den Hurk, B. J. J. M. (2001). Impact of BOREAS on the ECMWF forecast model. *J. Geophys. Res.* 106, 33593–33604. doi: 10.1029/2001JD900056

Betts, A. K., and Ball, J. H. (1997). Albedo over the boreal forest. *J. Geophys. Res.* 102, 28901–28910. doi: 10.1029/96JD03876

Betts, A. K., and Beljaars, A. C. M. (2017). Analysis of near-surface biases in ERA-interim over the canadian prairies. *J. Adv. Model Earth Syst*. 9, 2158–2173. doi: 10.1002/2017MS001025

Betts, A. K., Chan, D. Z., and Desjardins, R. L. (2019). Near-surface biases in ERA5 over the canadian prairies. *Front. Environ. Sci*. 7:129. doi: 10.3389/fenvs.2019.00129

Bitterman, P., and Koliba, C. J. (2020). Modeling alternative collaborative governance network designs: an agent-based model of water governance in the lake champlain basin, Vermont. *J. Public Adm. Res Theory* 30, 636–655. doi: 10.1093/jopart/muaa013

Boussetta, S., Balsamo, G., Beljaars, A., Kral, T., and Jarlan, L. (2011). Impact of a satellite-derived leaf area index monthly climatology in a global numerical neather prediction model. *ECMWF Tech. Memo.* 640:28. doi: 10.21957/h7n0ilfkp

C3S: Copernicus Climate Change Service (2017). *Search ERA5: Fifth Generation of ECMWF Atmospheric Reanalyses of the Global Climate. Copernicus Climate Change Service Climate Data Store* (CDS). Available online at: https://cds.climate.copernicus.eu/cdsapp#!/home (accessed March, 2019).

Choulga, M., Kourzeneva, E., Balsamo, G., Boussetta, S., and Wedi, N. (2019). Upgraded global mapping information for earth system modelling: an application to surface water depth at the ECMWF. *Hydrol. Earth Syst. Sci*. 23, 4051–4076. doi: 10.5194/hess-23-4051-2019

Choulga, M., Kourzeneva, E., Zakharova, E., and Doganovsky, A. (2014). Estimation of the mean depth of boreal lakes for use in numericalweather prediction and climate modelling. *Tellus A Dyn. Meteorol. Oceanogr*. 66:21295. doi: 10.3402/tellusa.v66.21295

Cy41r2 (2016). *Part IV, Physical Processes, Chapters 3 and 8; Part II, Data Assimilation, Chapter 9.* Available online at: https://www.ecmwf.int/en/publications/search/?solrsort=sort_label%20asc&secondary_title=%22IFS%20Documentation%20CY41R2%22 (accessed November, 2020).

Doran, E. M. B., Zia, A., Hurley, S., Tsai, Y.-S., Koliba, C. J., Adair, C. E., et al. (2020). Social-psychological determinants of farmer intention to adopt nutrient best management practices: implications for resilient adaptation to climate change. *J Environ. Manage* 276:111304. doi: 10.1016/j.jenvman.2020.111304

Duncan, J., and Waite, C. (2017). *Quality-Controlled Diamond Island Meteorological Data.* FEMC. Available online at: https://www.uvm.edu/femc/data/archive/project/diamond-island-meteorological-monitoring/dataset/diamond-island-meteorological-monitoring-final (accessed November, 2020).

Dutra, E., Stepanenko, V. M., Balsamo, G., Viterbo, P., Miranda, P. M. A., Mironov, D., et al. (2010). An offline study of the impact of lakes on the performance of the ECMWF surface scheme. *Boreal Env. Res.* 15, 100–112.

FEMC (2019). *Colchester Reef Meteorological Monitoring.* VMC. Available online at: https://www.uvm.edu/femc/data/archive/project/colchester-reef-meteorological-monitoring-38-m (accessed November, 2020)

FLake (2017). Available online at: http://www.flake.igb-berlin.de/ (accessed November, 2020).

Haiden, T., Janousek, M., Bidlot, J., Ferranti, L., Prates, F., Vitart, F., et al. (2016). Evaluation of ECMWF forecasts, Including the 2016 Resolution upgrade. *ECMWF. Tech. Memo*. 792, 1–53.

Hersbach, H., Bell, B., Berrisford, P., Hirahara, S., Horányi, A., Muñoz-Sabater, J., et al. (2020). The ERA5 global reanalysis. *Q. J. R. Meteorol. Soc*. 146, 1999–2049. doi: 10.1002/qj.3803

Huang, H., Winter, J. M., Osterberg, E. C., Hanrahan, J., Bruyere, C. L., Clemins, P. J., et al. (2019). Simulating precipitation and temperature in the lake champlain basin using a regional climate model: limitations and uncertainties. *Clim. Dyn*. 54, 69–84. doi: 10.1007/s00382-019-04987-8

Isles, P. D. F., Giles, C. D., Gearhart, T. A., Xu, Y., Druschel, G. K., and Schroth, A. W. (2015). Dynamic internal drivers of a historically severe cyanobacteria bloom in lake champlain revealed through comprehensive monitoring. *J. Gt. Lakes Res*. (Lake Champlain) 41, 818–829. doi: 10.1016/j.jglr.2015.06.006

Isles, P. D. F., Xu, Y., Stockwell, J. D., and Schroth, A. W. (2017). Climate-driven changes in energy and mass inputs systematically alter nutrient concentration and stoichiometry in deep and shallow regions of Lake Champlain. *Biogeochemistry* doi: 10.1007/s10533-017-0327-8

Kourzeneva, E. (2010). External data for lake parameterization in numerical weather prediction and climate modelling. *Boreal Env. Res*. 15, 165–177.

Kourzeneva, E., Asensio, H., Martin, E., and Faroux, S. (2012). Global gridded dataset of lake coverage and lake depth for use in nu-merical weather prediction and climate modelling. *Tellus A Dyn. Meteorol. Oceanogr*. 64:15640. doi: 10.3402/tellusa.v64i0.15640

Loveland, T. R., Reed, B. C., Brown, J. F., Ohlen, D. O., Zhu, Z., Youing, L., et al. (2000). Development of a global land cover characteristics database and IGB6 DISCover from the 1 km AVHRR data. *Int. J. Remote Sens.* 21, 1303–1330. doi: 10.1080/014311600210191

Mironov, D., Heise, E., Kourzeneva, E., Ritter, B., Schneider, N., and Terzhevik, A. (2010). Implementation of the lake parameterisation scheme Flake

into the numerical weather prediction model COSMO. *Boreal Env. Res.* 15, 218–230.

Mironov, D. V. (2008). *Parameterization of Lakes in Numerical Weather Prediction. Description of a Lake Model.* COSMO Technical Report, No.11. Deutscher Wetterdienst.

Morrill, J. C., Bales, R. C., and Conklin, M. H. (2005). Estimating stream temperature from air temperature: implications for future water quality. *J. Environ. Eng.* 131, 1–26. doi: 10.1061/(ASCE)0733-9372(2005)131:1(139)

OCRT (2019). *Tributary Monitoring*. Available online at: https://anrweb.vermont.gov/DEC/_DEC/TributaryResults.aspx (accessed November, 2020).

Stepanenko, V. M., Goyette, S., Martynov, A., Perroud, M., Fang, X., and Mironov, D. (2010). First steps of a lake model intercomparison project: lakeMIP. *Boreal Env. Res.* 15, 191–202.

Verseghy, D. L., and MacKay, M. D. (2017). Offline implementation and evaluation of the canadian small lake model with the canadian land surface scheme over Western Canada. *J. Hydromet.* 18, 1563–1582.. doi: 10.1175/JHM-D-16-0272.1

VTDEC (2019). *Lake Champlain Long-term Monitoring Multi-Probe Sonde Profiles*. Available online at: https://anrweb.vt.gov/DEC/_DEC/MultiProbeSonde.aspx (accessed November, 2020).

Zia, A., Bomblies, A., Schroth, A. W., Koliba, C., Isles, P. D. F., Tsai, Y. S., et al. (2016). Coupled impacts of climate and land use change across a river-lake continuum: insights from an integrated assessment model of Lake Champlain's Missisquoi Basin, 2000-2040. *Environ. Res. Lett*. 11:114026. doi: 10.1088/1748-9326/11/11/114026

Conflict of Interest: The authors declare that the research was conducted in the absence of any commercial or financial relationships that could be construed as a potential conflict of interest.

frontiers in Marine Science

ORIGINAL RESEARCH
published: 15 January 2021
doi: 10.3389/fmars.2020.612842

The Annual Cycle of Air-Sea Fluxes in the Northwest Tropical Atlantic

Sebastien P. Bigorre and Albert J. Plueddemann*

Upper Ocean Processes Group, Woods Hole Oceanographic Institution, Woods Hole, MA, United States

In this article we analyze 11 years of near-surface meteorology using observations from an open-ocean surface mooring located in the Northwestern Tropical Atlantic (51°W, 15°N). Air-sea fluxes of heat, freshwater, and momentum are derived from these observations using the Coupled Ocean–Atmosphere Response Experiment (COARE) bulk parameterization. Using this dataset, we compute a climatology of the annual cycle of near-surface meteorological conditions and air-sea fluxes. These *in situ* data are then compared with three reanalyses: the National Centers for Environmental Prediction-Department of Energy [NCEP-DOE (hereafter referred to as NCEP-2)], the European Centre for Medium-Range Weather Forecasts (ECMWF) Interim and the Modern-Era Retrospective analysis for Research and Applications, version 2 (MERRA-2) reanalyses. Products from the Clouds and the Earth's Radiant Energy System (CERES) and the Tropical Rainfall Measuring Mission (TRMM) are also used for comparison. We identify the agreements and characterize the discrepancies in the annual cycles of meteorological variables and the different components of air-sea heat fluxes (latent, sensible, shortwave, and longwave radiation). Recomputing the reanalyses fluxes by applying the COARE algorithm to the reanalyses meteorological variables results in better agreement with the *in situ* fluxes than using the reanalyses fluxes directly. However, the radiative fluxes (longwave and shortwave) from some of the reanalyses show significant discrepancies when compared with the *in situ* measurements. Longwave radiation from MERRA-2 is biased high (too much oceanic heat loss), and NCEP-2 longwave does not correlate to *in situ* observations and other reanalyses. Shortwave radiation from NCEP-2 is biased low in winter and does not track the observed variability in summer. The discrepancies in radiative fluxes versus *in situ* fluxes are explored, and the potential regional implications are discussed using maps of satellite and reanalyses products, including radiation and cloud cover.

Keywords: annual cycle, surface meteorology, air-sea fluxes, tropical, Atlantic

OPEN ACCESS

Edited by:
Simon Josey,
University of Southampton,
United Kingdom

Reviewed by:
Benjamin Rabe,
Alfred Wegener Institute Helmholtz Centre for Polar and Marine Research (AWI), Germany
Manuel Bensi,
National Institute of Oceanography and Experimental Geophysics (OGS), Italy

****Correspondence:***
Sebastien P. Bigorre
sbigorre@whoi.edu

Specialty section:
This article was submitted to Physical Oceanography, a section of the journal Frontiers in Marine Science

Received: *30 September 2020*
Accepted: *14 December 2020*
Published: *15 January 2021*

Citation:
Bigorre SP and Plueddemann AJ (2021) The Annual Cycle of Air-Sea Fluxes in the Northwest Tropical Atlantic. Front. Mar. Sci. 7:612842. doi: 10.3389/fmars.2020.612842

INTRODUCTION

The northwest tropical Atlantic hosts a multitude of air-sea interaction phenomena that impact the climate, ecosystem and society on a wide array of temporal and spatial scales. Numerous hurricanes are created or intensified there, due to high sea surface temperature (SST) and low wind shear (Wang et al., 2006). Oceanic barriers layers in the Northwest Tropical Atlantic are the thickest in the world (Mignot et al., 2012) and contain subsurface heat anomalies that intensify hurricanes (Balaguru et al., 2012). Anomalies

of the meridional migration of the Intertropical Convergence Zone (ITCZ) lead to interannual to decadal variability of SST's meridional gradient ("dipole mode") which are linked to droughts in Northern Brazil and the Sahel region (Servain et al., 1999). The trade winds converge in the region, giving rise to the Hadley circulation, which then feeds the atmospheric meridional heat transport from Equator to poles. The Gulf of Mexico, Caribbean Sea, and Northwest Tropical Atlantic form the Atlantic Warm Pool (AWP). Anomalous ascent in the upper troposphere above the AWP leads to an anomalous Hadley-type circulation, with interhemispheric exchange and anomalous subsidence in the Southeast Pacific (Wang et al., 2010). The westward trade winds also carry aerosols from Sub-Saharan Africa (Weinzierl et al., 2017), which affect albedo, cloud nucleation, and fertilization in the ocean and Amazonian forest (Bristow et al., 2010).

One of the most prominent features of the regional climate is the ITCZ, where the trade winds from the Northern and Southern hemispheres converge. Precipitation has a meridional maximum at the ITCZ (Chiang et al., 2002), which is surrounded by a large cloud cover that influences Earth's albedo and the regional radiative forcing. The ITCZ has a latitudinal extent of about 5°and is located near, although slightly north of the Equator over most of the ocean basins. Waliser and Gautier (1993) used 17 years of visible and infrared satellite observations to infer the climatology of cloud convection associated with the ITCZ. Their study indicates that in the Atlantic ocean, the mean ITCZ is centered near 6° N, but moves meridionally from near the Equator in February–March to 10° N in August through October when the convection also increases in intensity. Servain et al. (1999) showed that the northward migration of the ITCZ influences not only the seasonal cycles but also inter-annual modes of variability. Using a 9 years record of satellite precipitation data from Tropical Rainfall Measuring Mission (2001–2009), we computed a monthly climatology. This Tropical Rainfall Measuring Mission (TRMM) climatology is shown in **Figure 1** as maps of the daily precipitation accumulation in the Northwest Tropical Atlantic in April and October. The Northwest Tropical Atlantic Station (NTAS) site is free of the ITCZ influence in April, but notably impacted by the northern edge of the ITCZ in October, with expected precipitation of 3–5 mm/day.

To circumvent the scarcity of observations in the ocean, air-sea interaction studies often rely on Numerical Weather Prediction (NWP) products such as reanalyses. Reanalyses blend model forecasts with observations that are assimilated in a physically consistent manner in order to produce gridded datasets (Dee et al., 2011; Gelaro et al., 2017). For each reanalysis, the assimilation scheme, including the forecast model, remains the same. Reanalyses are therefore often used for climate studies. Comparison between reanalyses and independent datasets is valuable to detect and quantify the uncertainties or possible biases in the reanalyses but also to complement limited available observations. Note that NTAS data is withheld from assimilation in forecast models. Since NTAS is located in a region with otherwise sparse data, the NTAS dataset provides an opportunity to test the performance of reanalyses in the region. In this study we compare *in situ* data from the NTAS buoy with three commonly used reanalyses: the NCEP-DOE (hereafter referred to as NCEP-2), the European Centre for Medium-Range Weather Forecasts (ECMWF) Interim and the Modern-Era Retrospective analysis for Research and Applications, version 2 (MERRA-2).

The self-consistency of reanalysis products is of significant benefit, but different products do not always give consistent descriptions of climate phenomena or agree with observations, pointing to the need for an assessment of errors and their effects on climate simulations. For example, Brunke et al. (2011) compared meteorological variables and air-sea fluxes from 11 Numerical Weather Prediction products (six reanalyses, four satellite based analyses and one hybrid product) to *in situ* observations collected during 12 cruises in the tropics and mid-latitudes. They found that MERRA reanalysis performed best among all products, with small biases in latent and specific heat, and momentum fluxes, and small standard deviation error. In comparison, ECMWF Re-Ananalysis Interim (ERA-Interim), and NCEP-2 were among a group with larger standard deviation errors compared to *in situ* fluxes. Some of the errors were attributed to bulk variables, and some to residual effects (model, assimilation, and bulk algorithm). Wen et al. (2017) analyzed the sensitivity of an ocean general circulation model (OGCM) forced with NCEP-2 and NCEP Climate Forecast System Reanalysis (CFSR). They showed that different zonal wind stress and wind stress curl between the two reanalyses lead to different biases in the subsurface ocean in the outer tropical Atlantic. Comparison between the OGCM simulations and *in situ* observations at the PIRATA mooring at (38°W, 15°N), indicated a warm bias of 4°C below 150 m when using the NCEP-2 forcing. Comparison with satellite SST indicated that discrepancies in surface flux caused cold (warm) SST biases in NCEP-2 (CFSR) in the central-eastern tropical Atlantic. The authors concluded that more *in situ* observations were crucial around the North Equatorial current and near the Caribbean Sea.

In this article, we use 11 years of *in situ* observations to describe the mean and seasonal cycle of near surface meteorology and air-sea fluxes in the northwest tropical Atlantic. This method provides insight into important climate timescales with well-known physics. This dataset is then compared to estimates from reanalyses; discrepancies are characterized using time series and spatial maps. The paper is organized as follows: section "Materials and Methods" presents the *in situ* data and the reanalyses; section "Results" presents the results of the comparison, section "Discussion" discusses the results and their relevance to the regional tropical Atlantic, section "Summary and Conclusion" summarizes and concludes.

MATERIALS AND METHODS

In situ Meteorology and Fluxes

The NTAS is an open ocean (5,000 m water depth) surface mooring with a nominal location of 51°W, 15°N, roughly 1,000 km east of Martinique in the lesser Antilles. It is north of the Equatorial currents system, but in the trade wind system. From September through November the site is influenced by

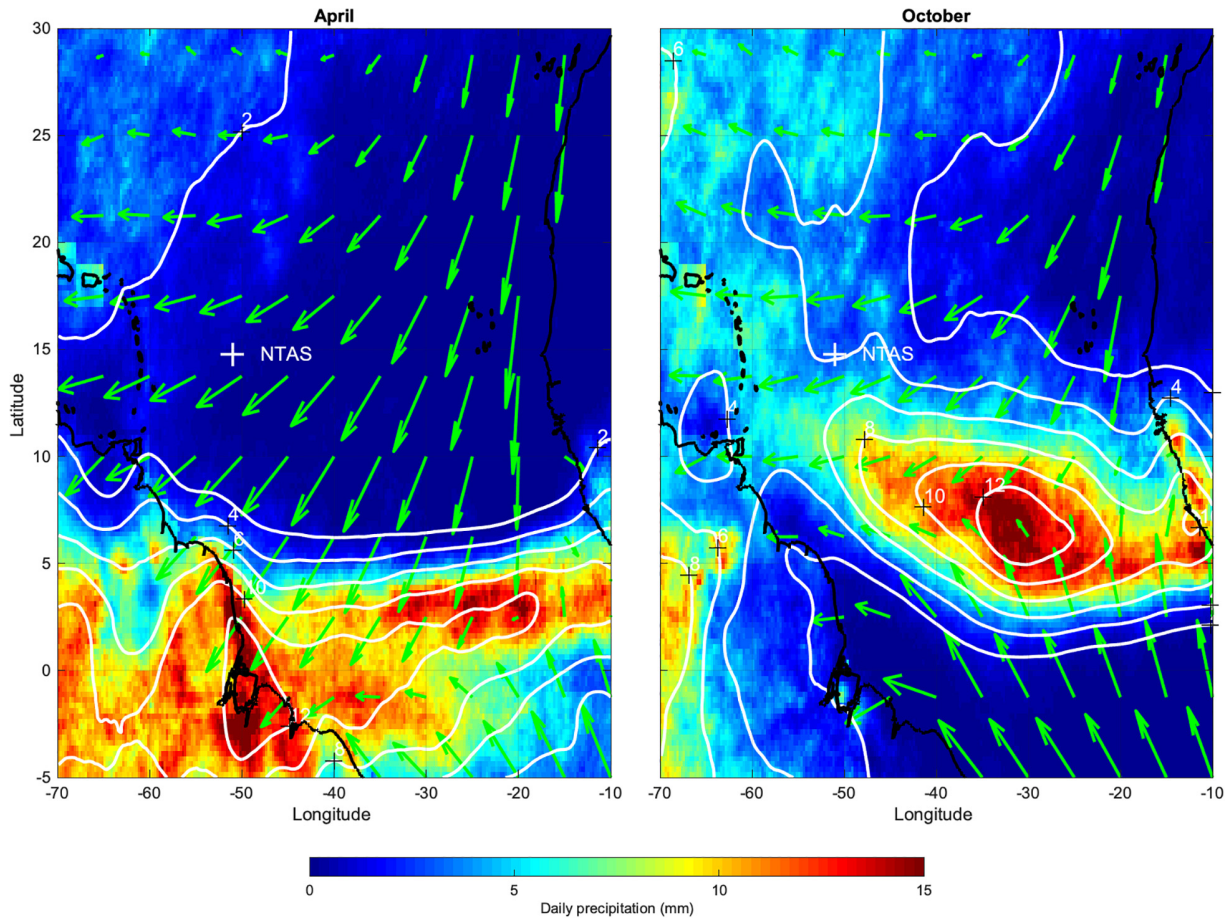

FIGURE 1 | Tropical Rainfall Measuring Mission daily precipitation accumulation (mm) in color shading and white isolines every 2 mm (label locations denoted by black crosses): averages for April (left) and October (right) during period 2002 to 2011. Green arrows are 10-m wind vectors, averages for same months, using Seawinds data from 2000 to 2012. White cross indicates the NTAS buoy location near 51°W, 15°N. Coastlines in black lines.

the ITCZ (**Figure 1**). The NTAS mooring is an air-sea flux site and an Ocean Reference Station (Cronin et al., 2012) within the OceanSITES network[1] maintained by the Upper Ocean Processes Group at the Woods Hole Oceanographic Institution. The *in situ* data collected at NTAS are not distributed to the Global Telecommunications System (GTS) and withheld from data assimilation into the reanalysis models. The *in situ* NTAS observations are therefore a truly independent dataset that can be used to evaluate reanalyses and help improve their physical models and assimilation schemes. The work presented here offers such an evaluation and suggests some possible leads for improvement. In addition, Josey et al. (2014) showed that data assimilation of mooring observations can sometimes create non-realistic local anomalies in reanalyses.

Mooring turn-arounds (recovery and replacement with a refurbished system) are conducted at nominal annual intervals to ensure that data are collected from freshly calibrated instrumentation. For each turn-around, the replacement mooring is deployed typically a day or more before recovery of the existing mooring to ensure overlap of the observations and validation of the data. The new and existing moorings are deployed near two fixed nominal sites that are 11 km from each other. Comparison of buoy data during the period of overlap, along with shipboard measurements meteorology and conductivity-temperature-depth (CTD) profiles, in combination with pre- and post-deployment calibrations, allow the identification and correction of errors and drifts on both moorings (Bigorre and Galbraith, 2018). Using corrected data from the first through eleventh NTAS deployments (NTAS 1–NTAS 11) we create an 11-year contiguous record for analysis (April 1, 2001 until March 31, 2012). Note that there was no overlap between the third and fourth deployments; the 2 days gap was filled by repeating data from the last day of NTAS 3 to first day of NTAS 4.

The NTAS buoys are outfitted with two sets of Air-Sea Interaction METeorology (ASIMET) instrumentation (Hosom et al., 1995) that measure: air temperature (ATMP) and relative humidity (HRH), wind speed (WSPD) and direction (WDIR), barometric pressure (BPR), precipitation (PRC), downward longwave (LWR) and downward shortwave (SWR) radiations, and sea surface temperature (SST). ASIMET measurements are made at roughly 3 m above the sea surface; SST is measured about

[1]http://www.oceansites.org

0.8 m below the air-sea interface. The raw observations are either single or multiple samples during each minute; when multiple samples are taken, they are averaged to produce a 1-min record.

The accuracy of the ASIMET data has been characterized using comparisons with measurements from ships, fixed platforms and satellites (Colbo and Weller, 2009; Bigorre et al., 2013; Weller, 2018; Schlundt et al., 2020), as well as Computational Fluid Dynamics simulations (Emond et al., 2012). Colbo and Weller, 2009 describe the accuracy of ASIMET measurements at NTAS and from similar moorings in trade winds regions. The ASIMET measurement errors are summarized in **Table 1**, which includes recent improvements on error characterization. Typical sources of errors include sensor drift, solar heating (air temperature and humidity), platform motion and flow distortion. Drifts are evaluated using post-calibrations and field validations (Bigorre and Galbraith, 2018). Solar heating may induce high temperature bias during the day in low wind conditions (Anderson and Baumgartner, 1998). Using data from a mooring deployed in the Gulf Stream, where high winds and currents induced significant platform motion and tilt, Bigorre et al. (2013) showed that the total wind speed error could reach up to 10% of the true wind in these extreme conditions. Schlundt et al. (2020) compared satellite and ASIMET wind measurements from other Ocean Reference Stations in the trade winds regions, including NTAS, and observed that wind speed discrepancies were less than 5% and consistent with flow distortion from CFD simulations (Emond et al., 2012). An empirical correction to the flow distortion exists that reduces the wind speed error to 5% of the true wind (Bigorre et al., 2013; Schlundt et al., 2020). This correction was not implemented here, as the flow distortion and platform motion errors are small at NTAS and do not impact our conclusions. However, the present work does use wind velocity relative to the water surface, thanks to the near-surface current meter deployed under the NTAS buoy that provides a proxy for surface current. Platform motion also influences radiation measurements. The ASIMET 1-min shortwave measurements are an average over six samples taken 10 s apart, which decreases the tilt error. Longwave measurements are a snapshot at the end of each minute, but are also less sensitive to tilts since radiation in the infrared band is more diffuse than the shortwave signal.

The ASIMET meteorological 1-min data are hourly averaged and input in the version 3.0 of the COARE bulk flux algorithm (Fairall et al., 1996, 2003; henceforth COARE-3). COARE-3 is a bulk algorithm for air-sea fluxes that was initially calibrated with datasets from tropical regions and later extended to extra-tropical regions with mid-range winds. The COARE algorithm includes a physical model of the upper-ocean thermal evolution (warm-layer and cool skin), based on the diurnal cycle of the heat fluxes. This allows for the conversion of SST from its bulk measurement below the surface to its skin value at the air-sea interface. Through an iterative procedure, better estimates of the air-sea heat fluxes can then be computed. For example, while the downward component of longwave radiation ($Q_{L\downarrow}$) is measured by ASIMET, the upward component of longwave ($Q_{L\uparrow}$) is computed as the product of seawater emissivity (0.97) with the Stefan-Boltzmann constant (5.67 10^{-8} W m^{-2} K^{-4}) and the fourth power of the skin SST. The difference ($Q_{L\downarrow}$–$Q_{L\uparrow}$) is the net longwave radiation flux Q_L. The upward component of shortwave ($Q_{S\uparrow}$) is computed using a daily average albedo of 0.055, so that the net shortwave radiation flux Q_S = 0.945 $Q_{S\downarrow}$, where $Q_{S\downarrow}$ is the downward shortwave flux measured by ASIMET. Since some of the reanalyses used in this work provide only Q_S and Q_L, the comparison with ASIMET will focus on the net radiative fluxes.

TABLE 1 | ASIMET measurement errors for daily averages on the NTAS buoy.

Measurement	Errors and Biases
Specific humidity (g kg^{-1})	Total: 0.4 g kg^{-1}
Air temperature (°C)	Total: 0.1 (°C)
Wind speed (ms^{-1})	Flow distortion: < 4% Tilt: < 4% Total: 8% or 0.4 m s^{-1}
Wind direction (deg)	Compass accuracy: 5 (deg) Flow distortion: 5 (deg) Total: 10 (deg)
Bulk SST (°C)	Accuracy: 8 10^{-4} (°C) Flow distortion (high bias): < 0.1 (°C) Total: 0.1 (°C)
Barometric pressure (mb)	Accuracy: 0.083 (mb) Drift: 0.11 (mb) Total: 0.2 (mb)
Precipitation rate (mm hr^{-1})	Flow distortion (low bias): < 10%
Incoming longwave (Wm^{-2})	Accuracy: 3.1 (W $m^{-2)}$ Tilt: < 5% Total: 4 (W m^{-2})
Incoming shortwave (Wm^{-2})	Accuracy: 1.5 (W m^{-2}) Tilt: < 5% Calibration low bias: < 5% Total: 6 (W m^{-2})
Latent heat flux (W m^{-2})	12 W m^{-2}
Sensible heat flux (W m^{-2})	2.5 W m^{-2}
Net heat flux (W m^{-2})	15.5 W m^{-2}
Momentum flux (N m^{-2})	0.01 N m^{-2} or 14%

In addition to Q_S and Q_L, the COARE algorithm also computes the turbulent fluxes of sensible heat (Q_B), latent heat (Q_H), and wind stress (τ). Together, these provide the net fluxes of heat, momentum and freshwater exchanged between the atmosphere and ocean. Here we use the oceanographic convention, with positive fluxes being downward (e.g., positive net heat flux warms the ocean). COARE is also used to adjust the meteorological variables (wind speed, air temperature, and humidity) to a standard height of 10 m. The *in situ* observations are adjusted from their original measurement height (about 3 m above sea level), as well as reanalysis data when necessary (e.g., air temperature and humidity in NCEP-2 and ERA-Interim are valid at 2 m). It is the ASIMET and reanalyses values adjusted to 10 m that are presented in section "Results."

The errors associated with ASIMET measurements in the trade wind region have been documented by Colbo and Weller (2009) using the first two deployments at NTAS, as well as the first three deployments at a site in southeast Pacific, off Chile. These authors note that the daily and annual errors are reduced by averaging compared to the instantaneous errors. The ASIMET measurements of air temperature and relative humidity are collocated and the errors induced by radiative heating are partially anti-correlated, leading to a reduced error in specific humidity (Anderson and Baumgartner, 1998). Colbo and Weller (2009) estimated the annual biases for net radiation fluxes (downward minus upward components) were mostly from the errors in the downward components, which were one order of magnitude larger than errors in skin temperature and albedo. The ASIMET errors discussed by Colbo and Weller

(2009) are reproduced in **Table 1**, with the updated wind speed error.

The turbulent flux errors were computed by adding a random noise to the meteorological variables, which were then input into the COARE algorithm. The random noise was modeled with a normal distribution (zero mean, standard deviation from **Table 1**). Each derived turbulent flux therefore included a random contribution, whose standard deviation was used to quantify its associated measurement error. These errors are reported in **Table 1** and are 12 (2.5) W m^{-2} for latent (sensible) and 0.01 N m^{-2} for the momentum flux. The error for the total (turbulent plus radiative) net heat flux is 15 W m^{-2}.

To compare *in situ* ASIMET data with the reanalyses and satellite observations, all variables were daily averaged. The annual cycle was then computed by averaging together the 11 members of the 11-year record. We use the median of each 11-member ensemble to decrease the impact of outliers.

Reanalyses Products

The National Centers for Environmental Prediction (NCEP) produces the NCEP-DOE reanalysis, often referred to as NCEP-2 (Kanamitsu et al., 2002); it is an updated version of the initial NCEP-NCAR (NCEP-1) reanalysis but uses the same 210 km horizontal resolution with 28 vertical levels and outputs data at 6 h intervals. Some of the corrections include reduction of the albedo over the ocean [from unrealistically large values in NCEP-1 (around 0.15) to values of 0.06–0.07], better orography representation (especially in Amazonian basin), and improved parameterizations (addition of non-local vertical diffusion scheme to avoid undesirable vertical eddy flux convergence of heat, moisture, and momentum within the planetary boundary layer; better shortwave radiation scheme that reduced surface insolation).

The National Aeronautics and Space Administration (NASA) produces the Modern-Era Retrospective Analysis for Research and Applications (MERRA). The MERRA-2 forecast model is run on 72 layers with 50 km × 50 km spatial resolution but output is produced on 0.625° × 0.5° longitude-by-latitude grid. The atmospheric model has a time step of 30 min for its physics parameterization, although the dynamics time step is considerably shorter (Rienecker et al., 2008). MERRA-2 improves on MERRA (Molod et al., 2015; Bosilovich et al., 2016; Gelaro et al., 2017) through assimilation of additional data, such as aerosols, and upgrades of parameterizations in the forecast model (e.g., background gravity wave drag, relationship between the ocean surface stress and the ocean roughness). Details and evaluation of the forecast model in MERRA-2 are presented in Molod et al. (2015). In MERRA-2, SST is from the daily 1/4° resolution data from National Oceanic and Atmospheric Administration (NOAA) Optimal Interpolation Sea Surface Temperature (OISST) (Reynolds et al., 2007) from 1982 through March 2006; and daily 1/20° resolution data from Operational Surface Temperature and Ice Analysis (OSTIA) (Donlon et al., 2012) from April 2006 onward. After January 2003, the NOAA OISST product is a blended product between infrared Advanced Very High Resolution Radiometer (AVHRR) and microwave Advanced Microwave Scanning Radiometer – Earth Observing System (AMSR-E), while prior to that date the data is from AVHRR only.

ERA-Interim's atmospheric model has a 30 min time step, uses 60 layers in the vertical and 79 km horizontal resolution for surface fields (Dee et al., 2011). Compared to its predecessor ERA-40, the ERA-Interim reanalysis benefited from a better cloud scheme, which increased convection and improved atmospheric stability, wind in the tropical band and timing of precipitation events. Other modifications included a moist-boundary layer scheme, which increased stratocumulus cover in upwelling regions, orographic and surface roughness effects, and the impact of salinity on humidity at the ocean surface. This led to decrease in tropical ocean total cloud cover, and increase in land cloud cover, especially high clouds (Dee et al., 2011). For dates between 1981 and 2001/12, ERA-Interim used the same SST input data as ERA-40 (two-dimensional variational interpolation analysis of the most recent 24-h buoy and ship data, and satellite-retrieved SST data with bias removed). According to Fiorino (2004), the NCEP 2DVAR SST product (Reynolds and Smith, 1994) is very similar to the operational product OISST.v2 (Reynolds et al., 2002), except in eastern equatorial regions, western boundary currents and high latitudes, and the latter SST product was actually used in ERA from 2001/07 to 2001/12. Starting in 2002/01, a switch was made to data used in the ECMWF operational forecasting system, beginning with the daily operational NCEP product, and after 2009 to data from the OSTIA product (Donlon et al., 2012).

Gridded reanalyses data were extracted for a region between 10°W and 70°W and 2°N to 35°N, which encompasses the tropical/subtropical North Atlantic. Wider areas were used for some satellite products, such as cloud cover, to encompass the Equatorial region. For each reanalysis, data was extracted from the gridpoint nearest to the center between the two nominal NTAS sites, namely 50.9°W, 14.8°N. Distance from the selected gridpoint and the NTAS center is 2.5, 37, and 67 km for ERA-Interim, MERRA2, and NCEP2, respectively. These reanalyses provide meteorological variables similar to the ones measured by the ASIMET sensors, but at model standard heights (10 m or 2 m, typically). The reanalyses also provide air-sea fluxes that are derived from models using different surface layer parameterization schemes that can depart from the COARE-3 algorithm. To enable a comparison between the datasets from ASIMET, MERRA-2, ERA-Interim and NCEP-2 and which are available with temporal resolutions of 1 min, 1, 3, and 6 h, respectively, the data were averaged to daily values.

Satellite Remote Sensing

The clouds and the earth's radiant energy system (CERES) sensors on satellite platforms Terra and Aqua provide top of the atmosphere radiance fluxes. Kato et al. (2013) adjusted the CERES fluxes using cloud measurements from MODIS and other geostationary satellites, as well as aerosols transport models, and air temperature and humidity profiles from the Goddard Earth Observing System (GEOS-5.4.1) Data Assimilation System reanalysis. The resulting energy balanced and filled (EBAF) CERES fluxes show better agreement with *in situ* surface stations, compared to initial CERES surface fluxes. Monthly 1°×1°

surface radiance fluxes from CERES EBAF Edition 4.0 are used in this article.

The TRMM product used in this paper is from the multi-satellite precipitation analysis (TMPA), namely the 3B42 version 7 (Huffman et al., 2007), with daily resolution on a grid 0.25°×0.25°. Behrangi et al. (2012) use 3 years of data (2007–2009) to compare CloudSat, which has better sensitivity to light rain, and show good agreement with TRMM estimates in the tropics.

The MODerate resolution Imaging Spectroradiometer (MODIS) sensor, equipped with 36 spectral channels from the visible into the infrared frequency range, started operation aboard the Earth Observing System – Terra (EOS-Terra) and Earth Observing System – Aqua (EOS-Aqua) satellites since 2000 and 2002, respectively. The MODIS data used here is from Collection 6.1 EOS-TERRA MODIS Atmosphere Level-3 data of MOD08 (Platnick et al., 2017). The cloud mask fraction from this dataset results from a two-tiered averaging processing: the ratio of pixels with clouds sampled at 1 km to the total number of pixels are first averaged in boxes 5 × 5 km; the 5 km regions are then averaged in each 1°×1° L3 output grid box. The cloud mask cloud fraction is based on daytime and night time samples.

RESULTS

Surface meteorological variables from *in situ* ASIMET measurements at NTAS tend to agree well with estimates from reanalyses and satellite products at nearby grid points. This converging tendency is encouraging, and provides support for the efforts of the observational, modeling and remote sensing communities. It also bears support to the value of *in situ* observations, as a reference for measurements in terms of quality and temporal resolution. We describe in the following sections the comparison of the surface meteorological observations and fluxes between the different datasets used here, and point out the levels of (dis)agreements between them.

Surface Meteorology

Figure 2 show the annual cycle of the near-surface meteorology at NTAS. The annual cycle was computed as the median from the eleven members ensemble that the 11-year long dataset covers. The annual averages are computed as the arithmetic mean over this annual cycle and shown to the right of each annual cycle plot. The annual cycle is dominated by the cold and warm seasons, in boreal winter and summer, respectively. Air temperature at 10 m (ATMP) is minimum (∼25°C) in February and maximum (∼28°C) in September. SST shows an annual cycle comparable to ATMP, albeit delayed by about 2 weeks in winter. SST is warmer than ATMP all year long, but the difference reaches a maximum above 0.6°C in the winter and fall, and a minimum of 0.3°C in June. The annual cycle of specific humidity is also analogous to ATMP, with a minimum (14 g kg^{-1}) in February and maximum (18 g kg^{-1}) in September. The precipitation rate is minimum (near 0.015 mm hr^{-1}) from February to June, then increases to its annual maximum (0.1 mm hr^{-1}) in late September, and tapers off in the fall.

The annual cycle of WSPD and BPR is dominated by the stalling of the trade winds in the fall when both WSPD and BPR reach their annual minima (6 m s^{-1} and 1013 mb, respectively), concurrent with the northernmost position of the ITCZ and its closest approach to NTAS. WSPD and BPR have an annual double maximum. The first maximum is in February with peak values reaching 8 m s^{-1} and 1016 mb, respectively, and the second one is in July, with slightly lower (higher) values for WSPD (BPR). Wind direction (not shown) remains mostly easterly with a small northerly component during the year. The annual range of variability is only about 10°, going from 250° T in January and February to 260° T in May, then back down to 253° in August, peaking at 262° T in November (the oceanographic convention is used here: wind is blowing toward the stated directions).

The annual cycle of the surface state atmospheric variables in the reanalyses generally match the ASIMET data, albeit with some notable biases. Compared to the ASIMET estimates, the fall ATMP is warmer in NCEP-2 and colder in MERRA-2. However, for the annual averages the differences are comparable to the ASIMET error. ERA-Interim has a persistent cold bias (annual averaged bias is -0.4°C) that is larger than the ASIMET error and consistent with the cold bias found by Brunke et al. (2011). The winter minimum of ATMP is reached in early March in NCEP-2 and MERRA-2, delayed compared to the late February minimum observed in ASIMET and ERA-Interim.

The annual average SST in NCEP-2 agrees well with ASIMET, whereas MERRA-2 and ERA-Interim are slightly colder (∼0.1 to 0.2°C). All three reanalyses show the winter minimum of SST in early March, delayed compared to the ASIMET minimum in late February. NCEP-2 and ERA-Interim SST show the winter minimum delayed by about a week from the ATMP minimum, consistent with ASIMET, whereas MERRA-2 shows the SST minimum leading ATMP by about 5 days.

Compared to ASIMET, the air specific humidity is dryer in MERRA-2 and ERA-Interim and wetter in NCEP-2. The MERRA-2 specific humidity tracks ASIMET throughout the year, within the ASIMET measurement error. ERA-Interim is similar to MERRA-2, except with an enhanced dry bias in the fall and winter. The NCEP-2 wet bias is enhanced in late winter and early spring, reaching up to 1 g kg^{-1} during February-March. The wet bias for NCEP-2 is consistent with the results of Brunke et al. (2011), however, the seasonal dry bias in ERA-Interim is distinct.

Wind speeds for MERRA-2 and ERA-Interim agree well with the *in situ* values; discrepancies are small compared to the expected ASIMET error. In contrast, the NCEP-2 wind speed is biased high by 0.7 m s^{-1} on average or about 10% of the wind speed. The discrepancy increases to 12% in winter and is lower (6%) in summer. Brunke et al. (2011) also found a high bias in the NCEP-2 wind speed.

The annual cycle of barometric pressure is similar to ASIMET for both ERA-Interim and NCEP-2, although biased low by about 0.2 and 0.5 mb, respectively. Note that the MERRA-2 reanalysis product does not provide surface pressure, so discrepancies could not be assessed; instead, ASIMET pressure data were

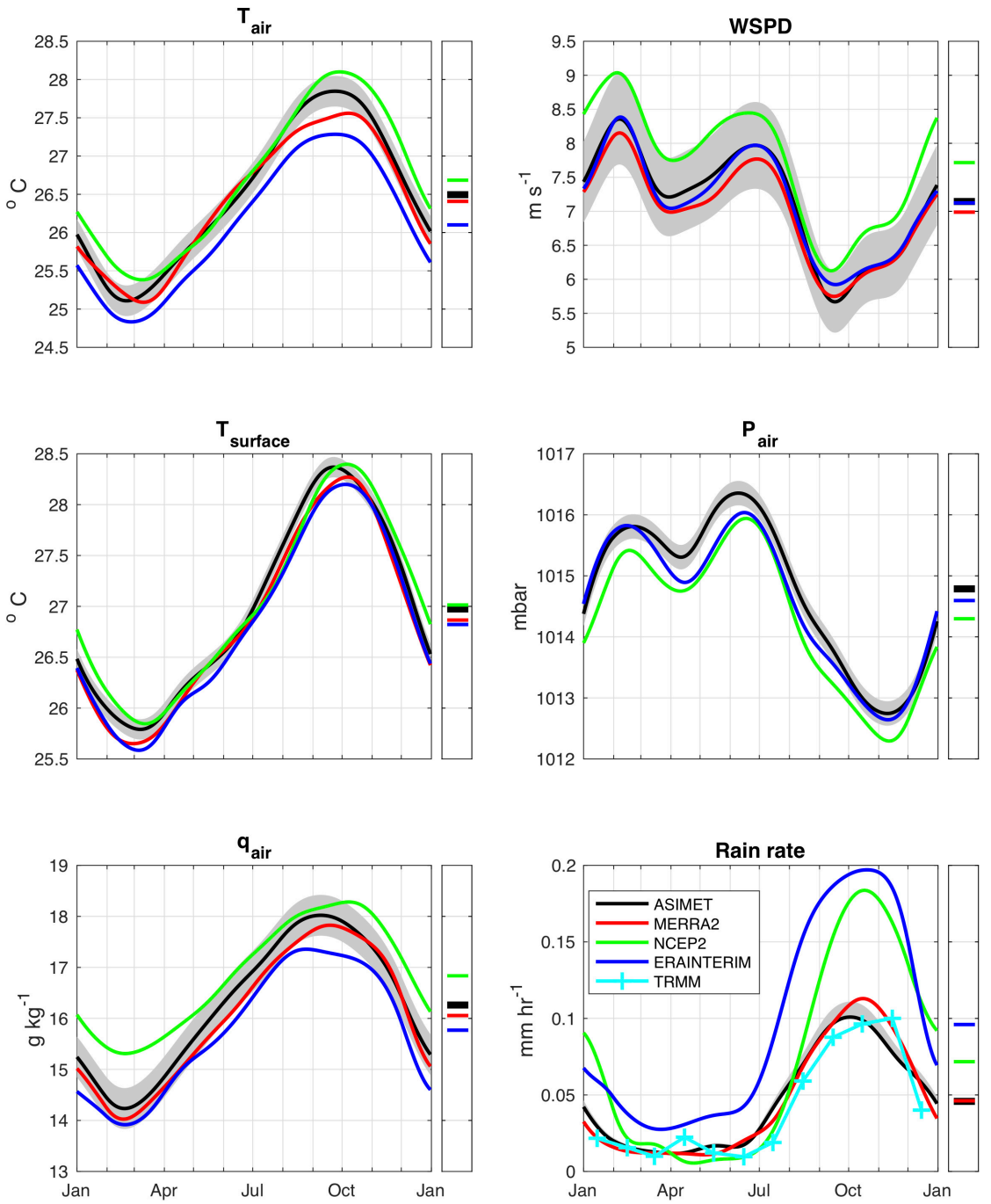

FIGURE 2 | Time-series of annual cycle of near surface meteorology at NTAS location, and annual averages on the right. From left to right, top to bottom: air temperature at 10 m, wind speed at 10 m, skin sea surface temperature, barometric pressure, specific humidity at 10 m, rain rate. Gray shading indicates error associated with ASIMET measurements on the NTAS buoy. ASIMET (black), MERRA-2 (red), NCEP-2 (green), ERA-Interim (blue). Based on daily data from April 1, 2001 through March 31, 2012.

used when computing fluxes with the COARE-3 algorithm and MERRA-2 data.

Although the ASIMET RM Young self-siphoning rain gauges may under-estimate rainfall by 10% (e.g., Serra et al., 2001; Colbo and Weller, 2009), the *in situ* rain rate agrees well with the Tropical Rainfall Measuring Mission satellite estimate. The MERRA-2 rain rate shows relatively good agreement (±20%) with both ASIMET and TRMM. The rain rate from NCEP-2 shows good agreement with ASIMET in spring and summer (February–August), but is

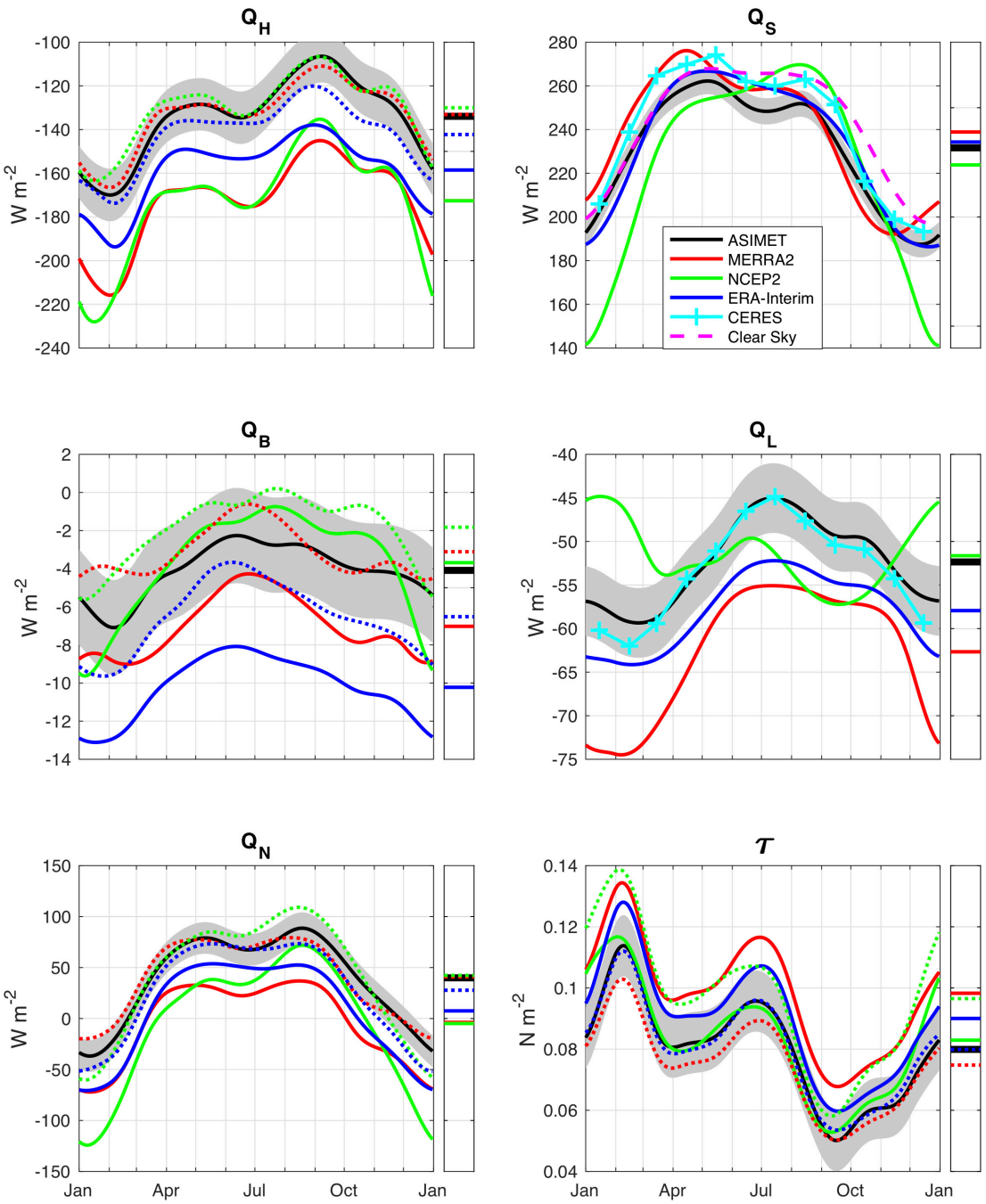

FIGURE 3 | Time-series of annual cycle of air-sea bulk fluxes at NTAS location, and annual averages on the right. Positive values mean heat input into the ocean. From left to right, top to bottom: latent heat, net shortwave radiation, sensible heat, net longwave radiation, net heat, wind stress. Gray shading indicates error associated with ASIMET measurements on the NTAS buoy. ASIMET (black), MERRA-2 (red), NCEP-2 (green), ERA-Interim (blue). Solid (dotted) lines denote native (hybrid) reanalyses fluxes. Based on daily data from April 1, 2001 through March 31, 2012.

significantly higher in September–November when the ITCZ extends north. The ERA-Interim rain rate is consistently biased high by ∼100%, and is the only product that shows a noticeable bias compared to ASIMET during the "dry season" (February–June). A histogram of rain rate (not shown) for the whole record shows that ERA-Interim has more low rain events compared to ASIMET and the reanalyses used in this study. This result is consistent with Dee et al. (2011), who show that ERA-Interim exhibits about 1 mm day^{-1} more rain compared to Global Precipitation Climatology Project (GPCP) in the Northwest Tropical Atlantic.

Air-Sea Fluxes

The annual cycle of air-sea fluxes from ASIMET and reanalyses are shown in **Figure 3**. Note that the sensible heat flux associated with precipitation (Fairall et al., 1996) is small (peaks slightly below 0.3 W m^{-2} in October) and is neglected in the current work. The ASIMET turbulent heat fluxes (Q_H, Q_B) show a maximum oceanic heat loss in winter when wind stress is the strongest. The turbulent heat flux is dominated by latent heat loss (-134 W m^{-2}) and the sensible heat flux is much smaller (-4 W m^{-2}). The net longwave flux Q_L is negative all year long and has a maximum heat loss in winter. The net shortwave radiative flux Q_S is positive all year long, with a minimum in winter and double maximum in April and August. The net heat flux Q_N is therefore negative in winter (ocean heat loss) and positive in summer (ocean heat gain). The climatological annual average of the ASIMET net heat flux is over 40 W m^{-2}, indicating that on average the ocean gains heat at the air-sea interface at NTAS. The surface heat gain is from net shortwave radiation, which is partly compensated by heat loss through latent heat and net longwave radiation. The net balance between annual averages of heat flux components is $Q_N = Q_S + Q_L - Q_H - Q_B = 232 - 52 - 134 - 4 = 42$ Wm^{-2}.

The air-sea turbulent fluxes of heat and momentum provided by the reanalyses (hereafter native fluxes) exhibit an annual cycle similar to the ASIMET *in situ* estimates. However, there are noticeable biases. The reanalyses native fluxes overestimate the turbulent heat loss ($Q_H + Q_B$) during the whole annual cycle when compared to the ASIMET estimate. Latent heat loss Q_H is biased 15 to 28% high across the three reanalyses used here. The ERA-Interim bias is minimum in winter. Sensible heat flux is overestimated by 75 and 150% in MERRA-2 and ERA-Interim, respectively. These discrepancies are larger than the 10% error associated with the COARE-3 bulk flux algorithm. The annual average of Q_B in NCEP-2 aligns with the ASIMET estimate, but Q_B in NCEP-2 is higher (lower) than ASIMET in winter (summer). The annual net heat input Q_N, is biased low in all three reanalyses (near zero), compared to the oceanic heat gain (42 W m^{-2}) estimated by ASIMET.

Most of the net heat flux bias can be explained by the overestimate (25 to 38 W m^{-2}) of latent heat loss in the reanalyses native fluxes (**Table 2**). Since the surface meteorology shows relatively good agreement (**Figure 2**), we therefore investigate whether the biases in Q_N are caused by a difference in the bulk formulation used in the reanalyses compared to the COARE algorithm used on the ASIMET *in situ* data. To do so, we follow Smith et al. (2001) and compute "hybrid" reanalyses air-sea fluxes, using the meteorological variables provided by each reanalysis and the same bulk algorithm as the ASIMET estimates. The common bulk algorithm used here is COARE-3.

The hybrid flux estimates (dotted lines in **Figure 3**) show a dramatic impact for latent heat flux. All three reanalyses hybrid Q_H agree with the ASIMET estimates (generally within the error bar) throughout the annual cycle, and the annual means differ by less than 10 W m^{-2}. The improvement in the hybrid latent heat flux cannot be explained by biases in the meteorological bulk variables for two reasons. Firstly, all three reanalyses improve and the meteorological variables in MERRA-2 and ERA-Interim showed very little biases compared to the ASIMET *in situ* measurements. Secondly, the wet bias in NCEP-2 (0.5 g kg^{-1}) reduces the vertical gradient in humidity and therefore Q_H, by 10% or 10 W m^{-2} in the region near NTAS (the winter bias is roughly twice that amount). However, the high bias in wind speed in NCEP-2 increases bulk fluxes, so biases in humidity and wind speed compensate each other when computing Q_H. Therefore, the correcting factor for the latent heat flux Q_H must be the transfer coefficient (Dalton number).

The small, but significant overestimates of Q_B for MERRA-2 and ERA-Interim are reduced in the native fluxes, reducing biases by about 50%. However, Q_B in NCEP-2 deteriorates slightly in the hybrid formulation, where a low bias of about 2 W m^{-2} is introduced. This low bias is opposite to what is expected from the high bias in wind speed in NCEP-2, and again points to the transfer coefficient as the likely contributor. Although the sensible heat flux is much smaller than the latent heat flux (4 W m^{-2} compared to 136 W m^{-2} for the ASIMET yearly averages), its contribution to the atmospheric buoyancy flux is important for convection phenomena.

The native wind stresses in ERA-Interim and MERRA-2 are consistently higher than the ASIMET estimate despite relatively good agreement in wind speed. The high bias is significant (larger than the ASIMET error) for MERRA-2. However, both ERA-Interim and MERRA-2 hybrid stresses are in good agreement with ASIMET. Interestingly, the NCEP-2 native wind stress agrees with ASIMET despite the high bias in native wind speed. When the NCEP-2 hybrid stress is computed from native wind, it shows a ∼20% high bias. Whether the native wind speed (ERA-Interim, MERRA-2) or stress (NCEP-2) agrees better with the *in situ* observations may depend on what wind data (speed or stress) are assimilated in the reanalyses, and the algorithms used to convert between speed and stress.

The introduction of a common bulk algorithm better reconciles the reanalyses turbulent heat fluxes with the ASIMET estimates and reduces the discrepancies in net heat flux. However, there remain important seasonal differences in Q_S and Q_L that motivate examination of the annual cycle of radiative fluxes, which we focus on below.

The ASIMET net shortwave radiation Q_S shows a distinct seasonal cycle with a minimum near 190 W m^{-2} in winter and double maxima near 260 W m^{-2} in April–May and 250 W m^{-2} in August. The structure of the ASIMET annual cycle in Q_S matches the Clouds and the Earth's Radiant Energy System (CERES) satellite data remarkably well, although the CERES net shortwave is about 10 W m^{-2} higher. Since the NTAS site lies south of the Tropic of Cancer, two shortwave peaks might be expected, but the clear-sky shortwave (dashed line in **Figure 3**) shows a much less pronounced trough than ASIMET. This suggests that seasonal cloud cover plays a role in the warm season Q_S variability. All three reanalyses show a double maximum of net shortwave in the warm season, although it is hardly noticeable in ERA-Interim and the relative height of the peaks is reversed in NCEP-2. Another notable departure of NCEP-2 Q_S from ASIMET is a significant low bias (20% or 40–50 W/m^2) in winter.

TABLE 2 | Averages over 11 years record of air-sea fluxes and surface meteorological values (directly given by reanalyses, and adjusted to common standard heights using COARE 3.0).

	Q_B (W m^{-2})	Q_H (W m^{-2})	Q_S (W m^{-2})	Q_L (W m^{-2})	Q_N (W m^{-2})	Stress (N m^{-2})	WSPD (m s^{-1})	q_a (g kg^{-1})	t_{air} (°C)	t_{skin} (°C)
ASIMET	−3.9	−133.5	231.5	−52.4	41.7	0.079	6.55	16.74	26.64	27.28
MERRA2	−7.0	−171.5	238.2	−62.4	−2.6	0.098	6.93	15.99	26.36	27.05
NCEP2	−4.0	−170.6	223.8	−51.9	−2.8	0.082	7.72	17.43	26.86	27.24
ERA	−10.3	−158.4	234.1	−57.9	7.5	0.09	7.07	16.4	26.3	27.13
ASIMET + COARE3	−3.9	−133.5	231.5	−52.4	41.7	0.079	7.04	16.34	26.55	27.05
MERRA2 + COARE3	−3.1	−132.5	238.2	−61.0	41.6	0.075	6.91	15.99	26.36	26.81
NCEP2 + COARE3	−2.1	−129.3	225.4	−49.0	45.1	0.096	7.7	16.89	26.77	27.05
ERA + COARE3	−6.3	−142.5	233.2	−55.3	29.1	0.079	7.05	15.83	26.16	26.89

Net longwave radiation Q_L is negative all year in all products, and the ocean loses more heat than it receives in the infrared band. The annual cycle of downward longwave (not shown), as measured by ASIMET, tracks the air temperature, with a winter (summer) minimum (maximum) around 390 W m^{-2} (420 W m^{-2}). The ASIMET Q_L (**Figure 3**) is maximum in summer (-45 W m^{-2}) and minimum in winter (-60 W m^{-2}) with an annual mean of -52 W m^{-2}. The structure of the ASIMET annual cycle in Q_L matches the CERES satellite data. ERA-Interim Q_L tracks ASIMET during the whole annual cycle, albeit with a consistent bias of about 5 W m^{-2}. MERRA-2 has a more significant bias (10–15 W m^{-2}) and more pronounced seasonal variability. The NCEP-2 annual mean Q_L is the closest to ASIMET, but its annual cycle is not correlated to ASIMET, CERES or the other reanalyses MERRA-2 and ERA-Interim. We will see in the section "Discussion" that this discrepancy is a regional effect and appears to be related to the discrepancy in NCEP-2 net shortwave Q_S noted above.

DISCUSSION

We have compared ASIMET *in situ* observations at NTAS with reanalyses gridded data. For each reanalysis, we presented here the data from the gridpoint closest to NTAS location. Using data from the next closest gridpoints surrounding the NTAS location did not introduce discrepancies larger than the ASIMET measurement errors, even for the data set with the coarser resolution (NCEP-2). We also looked, for each air-sea interaction variables discussed in this work, at the correlation between the NTAS gridpoint and other gridpoints. The correlation maps (not shown) indicate that the NTAS location is representative of a large domain in the northwest tropical Atlantic. For longwave radiation and wind speed, the domain with high correlation ($>$0.8) around NTAS is smaller but still extends almost 1000 and 2000 km in the meridional and longitudinal directions, respectively. The near-surface state variables from the NTAS buoy match those from reanalyses with minor discrepancies, and precipitation and humidity were among the variables that differed from observations. In addition, there were significant discrepancies in the radiation fields. This suggests that relationships among atmospheric water vapor, cloud cover, and radiation should be explored. In order to apply the findings in a regional context, we consider spatial maps from the reanalyses compared to satellite remote sensing products.

In boreal winter, downward shortwave radiation is low in NCEP-2 compared to CERES and MERRA-2, in a large domain encompassing the western North Tropical Atlantic region (**Figure 4**), whereas downward longwave radiation is high (**Figure 5**). **Figures 6**, **7** show the difference in the climatological for the winter and summer seasons between the reanalyses (MERRA-2 and NCEP-2) and CERES observations. In NCEP-2, most of the north tropical Atlantic shows this winter low bias in downward shortwave radiation and high bias in downward longwave radiation. Although these biases disappear north of the ITCZ in the boreal summer, they emerge to the south of the ITCZ.

MERRA-2 does not show significant biases in downward shortwave radiation in the north tropical Atlantic, except for low values in summer in and north of the Caribbean Sea. Compared to CERES, downward longwave radiation is low in MERRA-2 across the whole north tropical Atlantic in winter, and in the central north tropical Atlantic (including the NTAS region) in the summer.

The radiation biases between reanalyses and satellite data described above are similar to the discrepancies with the ASIMET *in situ* observations at NTAS, shown in **Figure 3**. In winter, NCEP-2 also shows a wet bias at NTAS. The intensification of humidity and radiation biases in winter in NCEP-2 is not seen in MERRA-2 or ERA-Interim. Atmospheric water vapor can absorb longwave radiation and participate in cloud formation, which in turn impact shortwave radiation. It is therefore possible that the humidity and radiation biases in NCEP-2 are not fortuitous but rather indicate a characteristic of its modeled hydrological cycle. Due to radiation absorption, integrated water vapor, and downward longwave radiation are related. Most of the absorption occurs in the first 1000 m above the surface in cloud free conditions (Ruckstuhl et al., 2007). Specific humidity being a good proxy for integrated water vapor, we looked at the relationship between downward longwave radiation and specific humidity (**Figure 8**). A clear relationship is visible in the ASIMET *in situ* data, which is fitted to a power law and is in good agreement with similar observations by Ruckstuhl et al. (2007). A similar relationship and power law fit is exhibited using the ERA-Interim and MERRA-2 data. The goodness-of-fit R^2 is 0.67, 0.77 and 0.69 in ASIMET, MERRA-2, and ERA-Interim, respectively. All datasets show a correlation (0.82, 0.88,

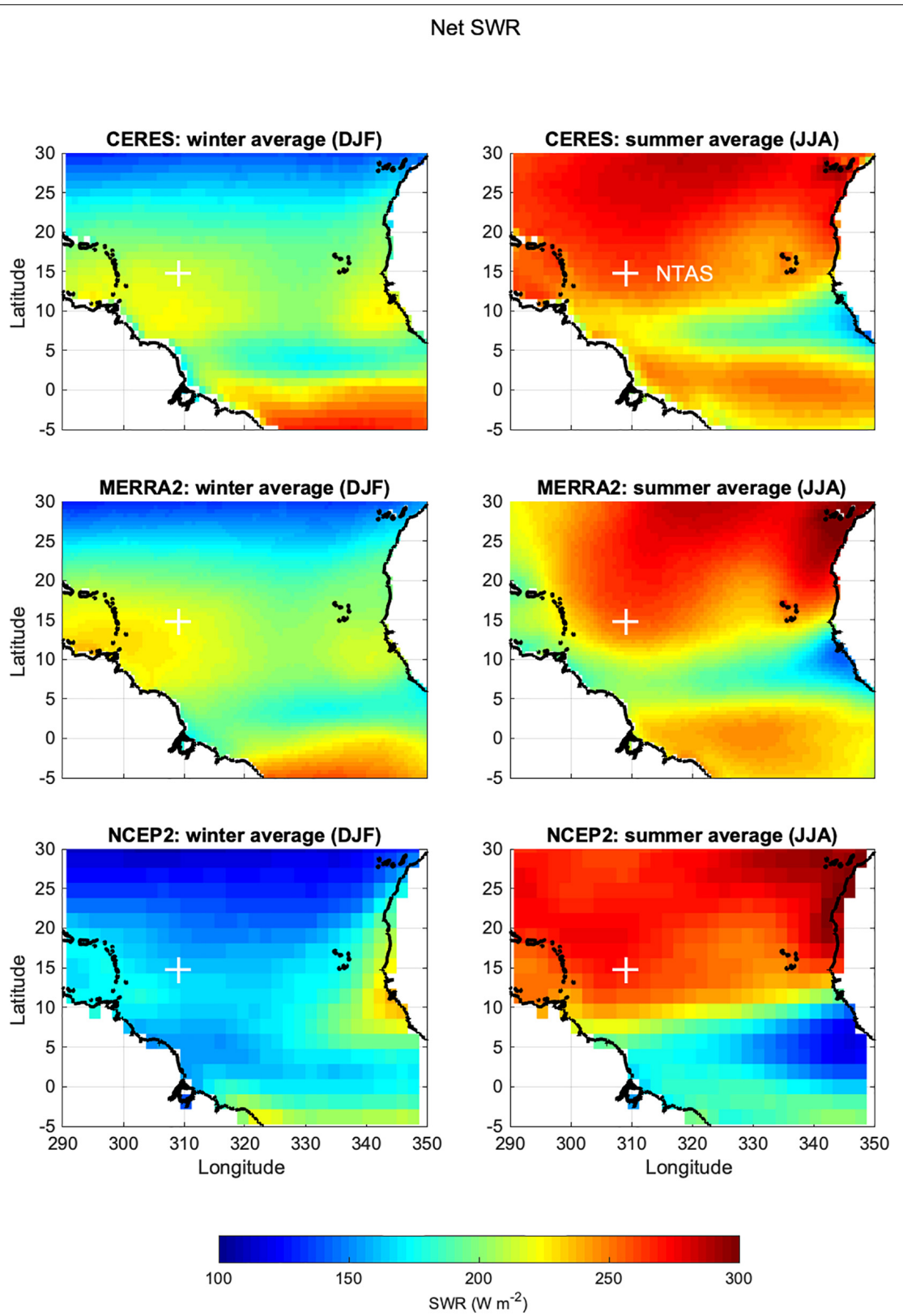

FIGURE 4 | Maps of seasonal climatology from years 2002 to 2011 in the tropical Atlantic: net shortwave radiation flux at the surface (in W m^{-2}), during boreal winter months (left) and summer (right). CERES (top row), MERRA-2 (middle row) and NCEP-2 (bottom row).

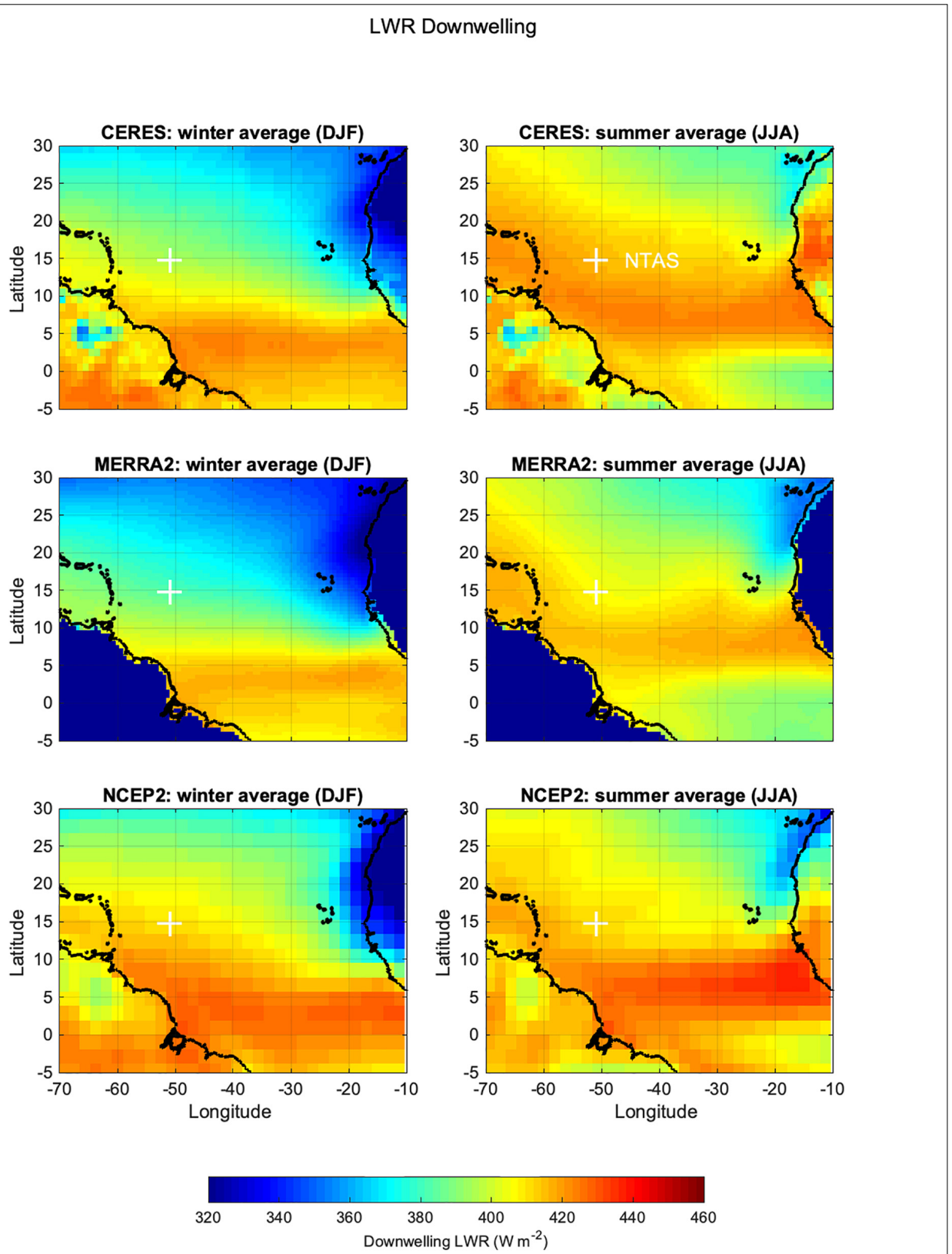

FIGURE 5 | Maps of seasonal climatology from years 2002 to 2011 in the tropical Atlantic: net downward longwave radiation flux at the surface (in W m^{-2}), during boreal winter months (left) and summer (right). CERES (top row), MERRA-2 (middle row) and NCEP-2 (bottom row).

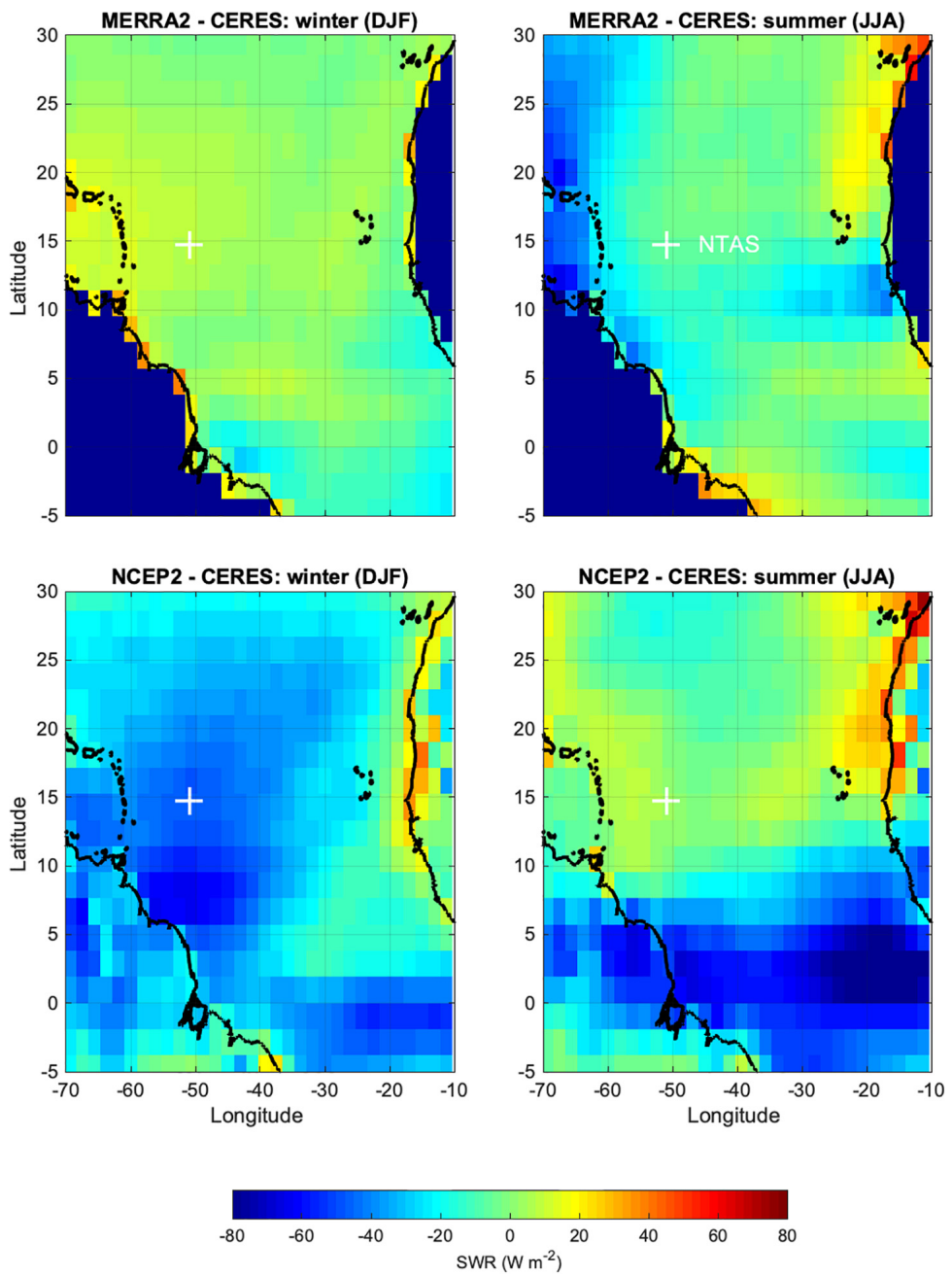

FIGURE 6 | Differences of climatological seasonal averages of shortwave radiation. Left: winter (DJF), right: summer (JJA). Top MERRA-2 minus CERES, bottom: NCEP-2 minus CERES. MERRA-2 and CERES were interpolated to the NCEP-2 spatial grid.

0.83, respectively), between longwave radiation and humidity, significant at $p < 0.01$. NCEP-2 data also shows a significant, although weaker correlation (0.42), with a larger data scatter and a noticeable difference in the resulting power law fit ($R^2 = 0.17$). The data used in **Figure 8** are for all sky conditions, but the same relationship is seen when differentiating between cloudy and clear-sky conditions (not shown). Note that ERA-Interim shows a strong relationship between downward longwave radiation and specific humidity, LWR(q), despite a small dry bias. This indicates that the presence of a strong LWR(q) relationship, and not

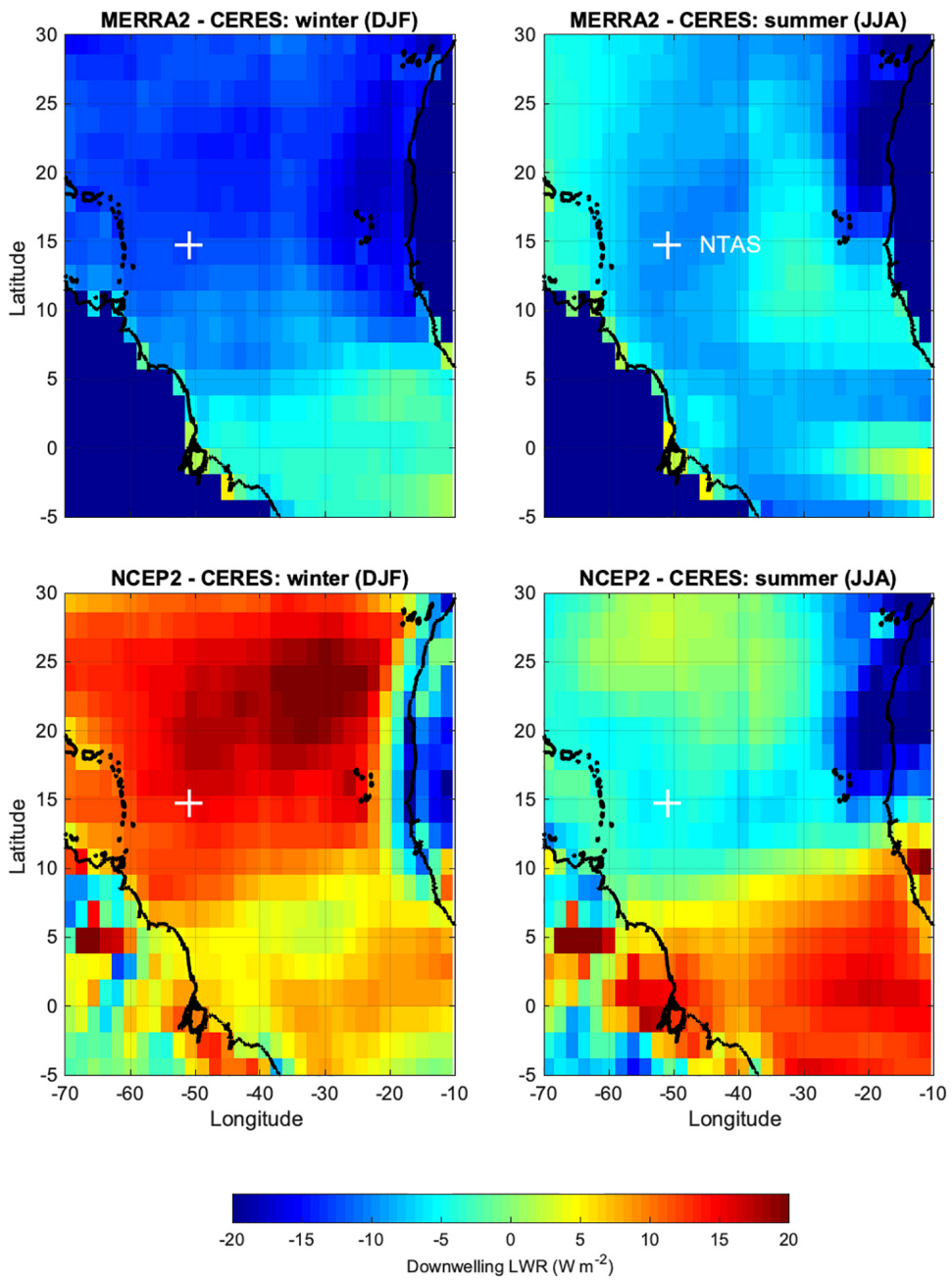

FIGURE 7 | Differences of climatological seasonal averages of downward longwave radiation. Left: winter (DJF), right: summer (JJA). Top MERRA-2 minus CERES, bottom: NCEP-2 minus CERES. MERRA-2 and CERES were interpolated to the NCEP-2 spatial grid.

necessarily its details, may be used as a self-sufficient diagnostic tool to evaluate the quality of downward longwave radiation in reanalyses, independent of observations.

The surface radiation fields and humidity are also related through cloud cover. Cloud fraction maps from MODIS show a local minimum in winter in a large domain around NTAS (**Figure 9**). This region with sparse cloud coverage coincides with a local maximum shortwave input area in winter in both MERRA-2 and CERES (**Figure 4**). In contrast, in NCEP-2 the same region has high cloud coverage and low downward shortwave radiation in winter. In spring and summer, MODIS cloud data shows that the ITCZ encroaches on the region

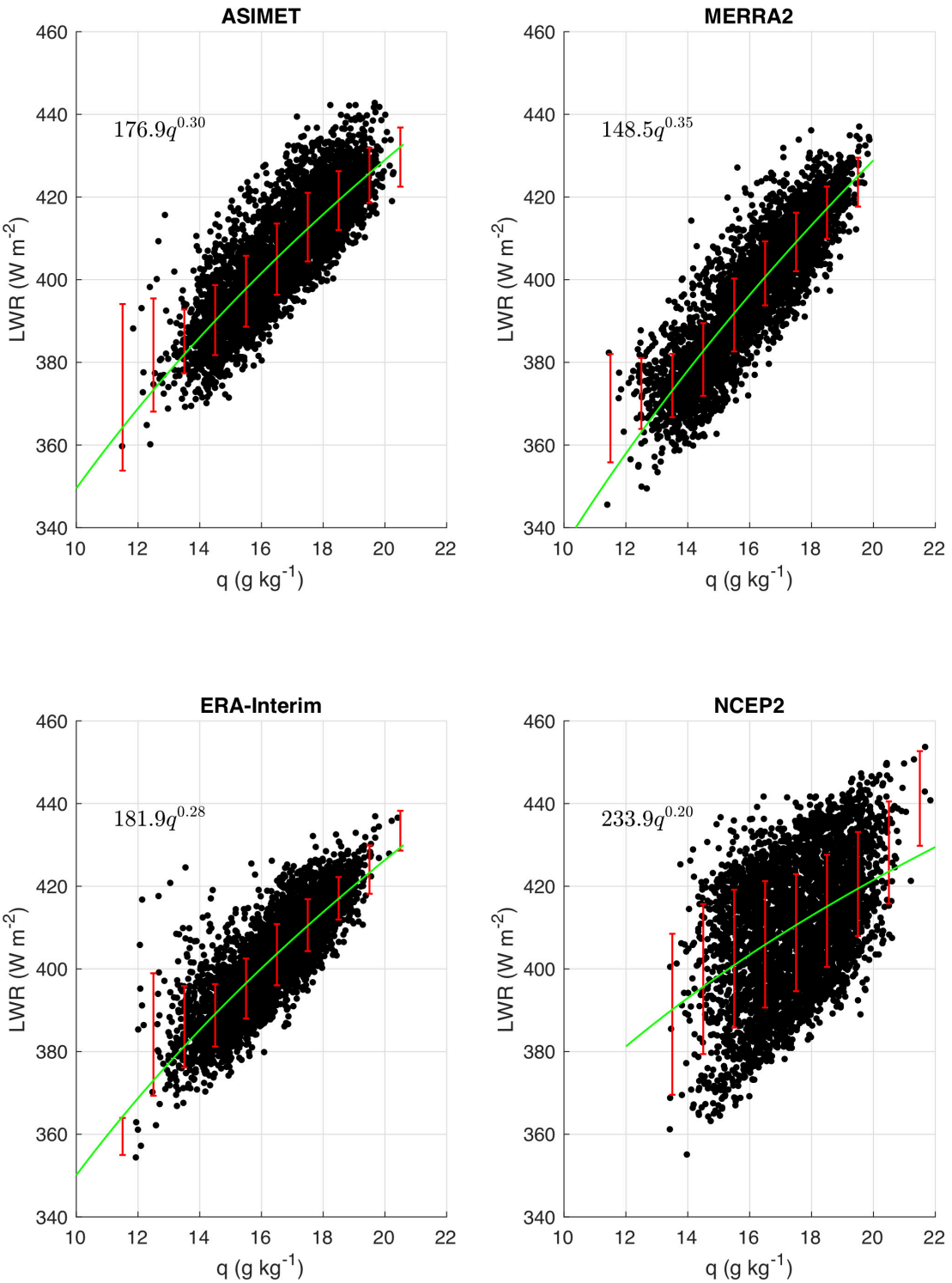

FIGURE 8 | Scatter plots of downward longwave radiation vs. specific humidity using daily averages between 2002 and 2012 (black dots). Power law fits to the daily values (green lines and annotations). Mean and one standard deviation in 1 g kg^{-1} bins (red lines).

surrounding NTAS from the south and east. In comparison, the summer cloud cover around the ITCZ is much weaker in NCEP-2, so that NTAS is located in a region with minimal cloud cover. These differences in NCEP-2 cloud cover in winter and summer are consistent with NCEP-2 anomalous annual cycle of shortwave radiation at NTAS in **Figure 3**. The MODIS

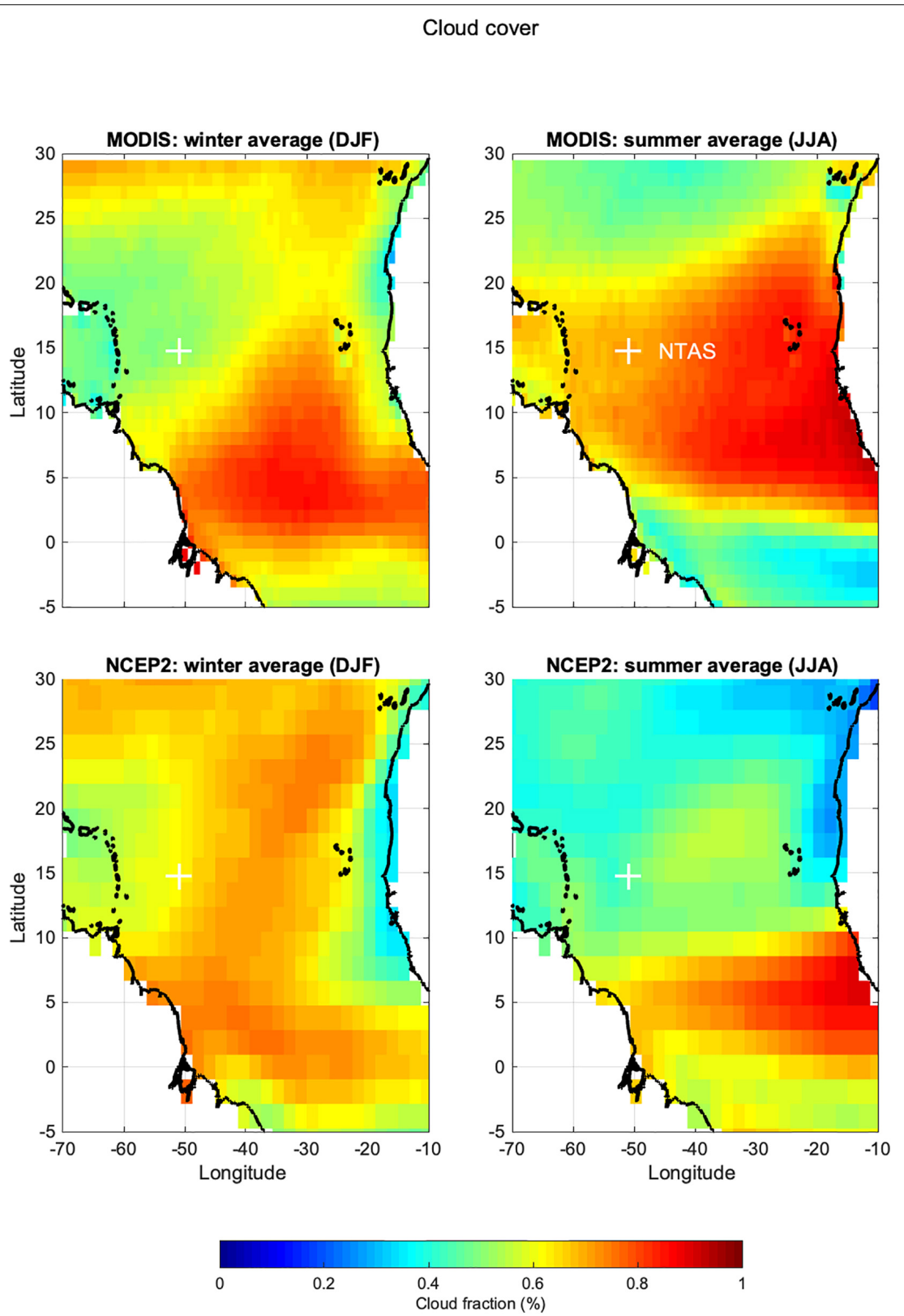

FIGURE 9 | Maps of season averaged cloud fraction from MODIS and NCEP2. Winter (DJF) and summer averages based on daily data from years 2002 through 2012. Magenta cross denotes NTAS location.

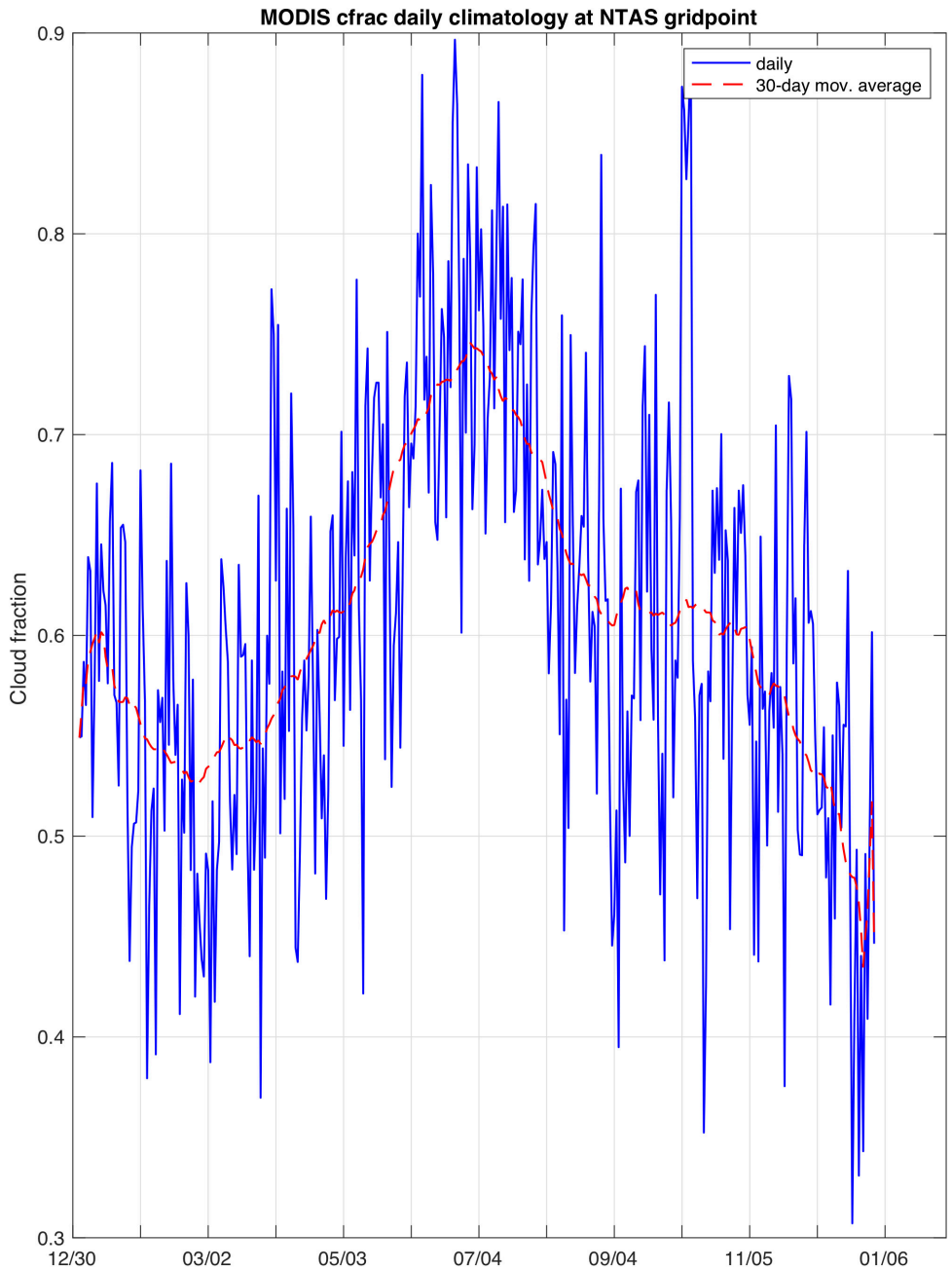

FIGURE 10 | Daily cloud fraction at NTAS, based on MODIS data for period 2001 to 2012.

cloud fraction extracted at NTAS peaks in July (**Figure 10**), which coincides with the summer local minimum of downward shortwave radiation seen in the *in situ* ASIMET data. The all sky downward shortwave radiation measured at NTAS is low in July, although the clear-sky theoretical value does not show such a minimum (**Figure 3**). This indicates that the variability of cloud cover and solar radiation are related in the seasonal and intra-seasonal in the NTAS region. Moreover, NCEP-2 cloud cover and shortwave radiation also co-vary consistently with each other, but not with the observations.

SUMMARY AND CONCLUSION

We evaluated here the seasonal cycle of near surface meteorology in the Northwest Tropical Atlantic region using long term *in situ* observations from the NTAS oceanic surface mooring. We compared three commonly used reanalyses, NCEP-2, MERRA-2, and ERA-Interim, to the *in situ* observations and analyzed the strengths and weaknesses of each.

Most surface meteorological variables observed with the ASIMET instrumentation at NTAS are reproduced well by the

three reanalyses MERRA-2, ERA-Interim, and NCEP-2. Minor discrepancies included high (low) seasonal biases in NCEP-2 (ERA-Interim) specific humidity, a high bias in NCEP-2 wind speed (albeit not reflected in the stress) and high biases in NCEP-2 and ERA-Interim precipitation. Precipitation from the Tropical Rainfall Measuring Mission satellite sensor agreed well with the ASIMET *in situ* measurements at NTAS. More notable were discrepancies in radiative fluxes. Although measurements of net longwave and shortwave radiations are similar between ASIMET and CERES remote sensing, three issues were found when comparing ASIMET to reanalyses: (1) longwave radiation in MERRA-2 is biased low by 10 to 15 W m^{-2} and this bias is present in most of the tropical Atlantic, (2) downward shortwave radiation in NCEP-2 is biased low (50 W m^{-2}) in the boreal winter, and departs from other datasets in summer, (3) the annual cycle of downward longwave in NCEP-2 does not show an annual cycle consistent with the *in situ* data.

The native fluxes provided by the reanalyses underestimate the net ocean heat gain. However, when re-computed with the same bulk algorithm (COARE-3) and using meteorological variables from the reanalyses, these hybrid fluxes agree relatively well with the *in situ* estimates. The 11-year mean fluxes are within 10 W m^{-2}. The net ocean heat gain based on COARE-3 is between 30 and 45 W m^{-2}.

Of particular concern are the biases in the radiative fluxes observed in NCEP-2 and MERRA-2. These biases exist in large domains of the tropical Atlantic and vary during the year. The seasonal variability and spatial structure of NCEP-2 longwave and shortwave errors are consistent with its anomalous cloud cover compared to MODIS cloud cover data. NCEP-2 underestimates downward shortwave in winter. MERRA-2 underestimate net longwave radiation at NTAS and in most of the north tropical Atlantic. The source of this bias deserves attention as it could be related to clouds or aerosols, which are important parameters for climate studies. Moreover, longwave being responsible for most of the radiative forcing associated with global warming it is important for reanalyses to reproduce accurate representations on basin scales like the tropical Atlantic. We suggest that the presence of a strong LWR(q) relationship be used as a validation check for downward longwave radiation in reanalyses datasets. Similarly, departure of shortwave radiation from the clear-sky background can also be useful to detect erroneous patterns in cloud cover.

As Wen et al. (2017) showed, the impact of 50 W m^{-2} error in ocean heating at the air-sea interface leads to SST anomalies of order 0.5°C in the north tropical Atlantic. Since SST is a controlling factor for atmospheric convection and hurricane development, care must be taken into using accurate air-sea heat fluxes in this region. Wen et al. (2017) also showed that inaccuracies in wind stress forcing lead to deep heat anomalies and biases in the mixed layer depth. The north tropical Atlantic is a place of intricate air-sea interaction phenomena, such as ocean barrier layers that store heat, modify the upper ocean stratification and are controlled by a subtle balance between air-sea fluxes, and freshwater input. Careful use of reanalyses is therefore warranted in studies of the north tropical Atlantic region.

DATA AVAILABILITY STATEMENT

The datasets presented in this study can be found in online repositories. The names of the repository/repositories and accession number(s) can be found below: The NTAS meteorological data from each deployment, as well as concatenated, continuous time series of meteorological variables and air-sea fluxes, are available from the Upper Ocean Processes Group website (uop.whoi.edu) and from the OceanSITES Global Data Assembly Centers (GDACs). The US OceanSITES GDAC is served by the National Data Buoy Center (https://dods.ndbc.noaa.gov/oceansites).

AUTHOR CONTRIBUTIONS

SB and AP led seagoing operations contributing to the 11-year observational record, contributed to all stages of manuscript conceptualization and development, and contributed equally to manuscript review and editing. SB led the data analysis efforts and manuscript writing. Both authors contributed to the article and approved the submitted version.

FUNDING

The NTAS project was funded by the Global Ocean Monitoring and Observing Program of the National Oceanic and Atmospheric Administration (CPO FundRef number 100007298), through the Cooperative Institute for the North Atlantic Region (CINAR) under Cooperative Agreement NA14OAR4320158.

ACKNOWLEDGMENTS

We acknowledge the sustained, multi-decadal effort of the Upper Ocean Processes Group, on shore and at sea, to provide high quality time series data from open ocean moorings. NCEP/DOE 2 Reanalysis data provided by the NOAA/OAR/ESRL PSD, Boulder, CO, United States (http://www.esrl.noaa.gov/psd/). MERRA-2 data obtained from the Goddard Earth Sciences (GES) Data and Information Services Center (DISC) (http://disc.sci.gsfc.nasa.gov/mdisc/). MODIS data was kindly provided in netCDF file format by Stefan Kern from the Integrated Climate Data Center (ICDC), CEN, University of Hamburg, Hamburg, Germany, icdc.cen.uni-hamburg.de. Original MODIS collection 6.1 cloud parameter data (http://dx.doi.org/10.5067/MODIS/MOD08_D3.061) provided in hdf format by https://ladsweb.modaps.eosdis.nasa.gov/. The 10-m wind vectors shown in **Figure 1** are from the Blended Sea Winds dataset (Zhang et al., 2006).

REFERENCES

Anderson, S. P., and Baumgartner, M. F. (1998). Radiative heating errors in naturally ventilated air temperature measurements made from buoys. *J. Atmosph. Ocean. Technol.* 15, 157–173. doi: 10.1175/1520-0426(1998)015<0157:rheinv>2.0.co;2

Balaguru, K., Chang, P., Saravanan, R., Leung, L. R., Xu, Z., Li, M., et al. (2012). Ocean barrier layers' effect on tropical cyclone intensification. *Proc. Natl Acad. Sci. U.S.A.* 109, 14343–14347. doi: 10.1073/pnas.1201364109

Behrangi, A., Lebsock, M., Wong, S., and Lambrigtsen, B. (2012). On the quantification of oceanic rainfall using spaceborne sensors. *J. Geophys. Res.* 117:D20105. doi: 10.1029/2012JD017979

Bigorre, S., and Galbraith, N. (2018). "Sensor performance and data quality control," in *Observing the Oceans in Real Time*, eds R. Venkatesan, A. Tandon, E. D'Asaro, and M. A. Atmanand (Cham: Springer), 243–261. doi: 10.1007/978-3-319-66493-4_12

Bigorre, S. P., Weller, R. A., Edson, J. B., and Ware, J. D. (2013). A Surface Mooring for Air–Sea Interaction Research in the Gulf Stream. *Part II: Analysis of the Observations and Their Accuracies*. *J. Atmosph. Ocean. Technol.* 30, 450–469. doi: 10.1175/jtech-d-12-00078.1

Bosilovich, M. G., Lucchesi, R., and Suarez, M. (2016). MERRA-2: file specification. *GMAO Office Note* 9:73.

Bristow, C. S., Hudson-Edwards, K. A., and Chappell, A. (2010). Fertilizing the Amazon and equatorial Atlantic with West African dust. *Geophys. Res. Lett.* 37:L14807.

Brunke, M. A., Wang, Z., Zeng, X., Bosilovich, M., and Shie, C.-L. (2011). An assessment of the uncertainties in ocean surface turbulent fluxes in 11 reanalysis, satellite-derived, and combined global datasets. *J. Clim.* 24, 5469–5493. doi: 10.1175/2011jcli4223.1

Chiang, J. C. H., Kushnir, Y., and Giannini, A. (2002). Deconstructing Atlantic Intertropical Convergence Zone variability: influence of the local cross-equatorial sea surface temperature gradient and remote forcing from the eastern equatorial Pacific. *J. Geophys. Res.* 107, ACL 3-1-ACL 3-19. doi: 10.1029/2000JD000307

Colbo, K., and Weller, R. A. (2009). The accuracy of the IMET sensor package in the subtropics. *J. Atmosph. Ocean. Technol.* 9, 1867–1890. doi: 10.1175/2009jtecho667.1

Cronin, M. F., Weller, R. A., Lampitt, R. S., and Send, U. (2012). "Ocean Reference Stations," in *Earth Observations*, eds R. B. Rustam and S. E. Salahova (London: IntechOpen), doi: 10.5772/27423

Dee, D. P., Uppala, S. M., Simmons, A. J., Berrisford, P., Poli, P., Kobayashi, S., et al. (2011). The ERA-Interim reanalysis: configuration and performance of the data assimilation system. *Q. J. R. Meteorol. Soc.* 137, 553–597. doi: 10.1002/qj.828

Donlon, C. J., Martin, M., Stark, J., Roberts-Jones, J., Fiedler, E., and Wimmer, W. (2012). The operational sea surface temperature and sea ice analysis (OSTIA) system. *Remote Sens. Environ.* 116, 140–158. doi: 10.1016/j.rse.2010.10.017

Emond, M., Vandemark, D., Forsythe, J., Plueddemann, A. J., and Farrar, J. T. (2012). Flow distortion investigation of wind velocity perturbations for two ocean meteorological platforms. *Woods Hole Oceanogr. Institut. Tech. Rep.* 201:66.

Fairall, C. W., Bradley, E. F., Hare, J., Grachev, A., and Edson, J. (2003). Bulk parameterization of air-sea fluxes: updates and verification for the COARE algorithm. *J. Clim.* 16, 571–591. doi: 10.1175/1520-0442(2003)016<0571:bpoasf>2.0.co;2

Fairall, C. W., Bradley, E. F., Rogers, D. P., Edson, J. B., and Young, G. S. (1996). Bulk parameterization of air–sea fluxes for tropical ocean-global atmosphere coupled-ocean atmosphere response experiment. *J. Geophys. Res.* 101, 3734–3764.

Fiorino, M. (2004). *A Multi-Decadal Daily Sea Surface Temperature and Sea Ice Concentration Data Set for the ERA-40 Reanalysis*'. ERA-40 Project Report Series No. 12. Reading: ECMWF.

Gelaro, R., McCarty, W., Suárez, M. J., Todling, R., Molod, A., Takacs, L., et al. (2017). The modern-era retrospective analysis for research and applications, version 2 (MERRA-2). *J. Clim.* 30, 5419–5454. doi: 10.1175/JCLI-D-16-0758.1

Hosom, D. S., Weller, R. A., Payne, R. E., and Prada, K. E. (1995). The IMET (Improved Meteorology) ship and buoy systems. *J. Atmosph. Ocean. Technol.* 12, 527–540. doi: 10.1175/1520-0426(1995)012<0527:timsab>2.0.co;2

Huffman, G. J., Adler, R. F., Bolvin, D. T., Gu, G., Nelkin, E. J., Bowman, K. P., et al. (2007). The TRMM multi-satellite precipitation analysis: quasi-global, multi-year, combined-sensor precipitation estimates at fine scale. *J. Hydrometeorol.* 8, 38–55. doi: 10.1175/jhm560.1

Josey, S. A., Yu, L., Gulev, S., Jin, X., Tilinina, N., Barnier, B., et al. (2014). Unexpected impacts of the Tropical Pacific array on reanalysis surface meteorology and heat fluxes. *Geophys. Res. Lett.* 41, 6213–6220. doi: 10.1002/2014GL061302

Kanamitsu, M., Ebisuzaki, W., Woollen, J., Yang, S.-K., Hnilo, J. J., Fiorino, M., et al. (2002). NCEP-DOE AMIP-II Reanalysis (R-2). *Bull. Am. Meteorol. Soc.* 83, 1631–1644. doi: 10.1175/BAMS-83-11-1631

Kato, S., Loeb, N. G., Rose, F. G., Doelling, D. R., Rutan, D. A., Caldwell, T. E., et al. (2013). Surface irradiances consistent with CERES-derived top-of-atmosphere shortwave and longwave irradiances. *J. Clim.* 26, 2719–2740. doi: 10.1175/JCLI-D-12-00436.1

Mignot, J., Lazar, A., and Lacarra, M. (2012). On the formation of barrier layers and associated vertical temperature inversions: a focus on the northwestern tropical Atlantic. *J. Geophys. Res.* 117:C02010. doi: 10.1029/2011JC007435

Molod, A., Takacs, L., Suarez, M., and Bacmeister, J. (2015). Development of the GEOS-5 atmospheric general circulation model: evolution from MERRA to MERRA2. *Geosci. Model Dev.* 8, 1339–1356. doi: 10.5194/gmd-8-1339-2015

Platnick, S., King, M., and Hubanks, P. (2017). MODIS Atmosphere L3 Daily Product. *NASA MODIS Adaptive Processing System*, Goddard Space Flight Center. doi: 10.5067/MODIS/MOD08_D3.061

Reynolds, R. W., Rayner, N. A., Smith, T. M., Stokes, D. C., and Wang, W. (2002). An improved in situ and satellite SST analysis for climate. *J. Clim.* 15, 1609–1625. doi: 10.1175/1520-0442(2002)015<1609:aiisas>2.0.co;2

Reynolds, R. W., and Smith, T. M. (1994). Improved global sea surface temperature analyses using optimum interpolation. *J. Clim.* 7, 929–948. doi: 10.1175/1520-0442(1994)007<0929:igssta>2.0.co;2

Reynolds, R. W., Smith, T. M., Liu, C., Chelton, D. B., Casey, K. S., and Schlax, M. G. (2007). Daily high-resolution-blended analyses for sea surface temperature. *J. Clim.* 20, 5473–5496. doi: 10.1175/2007JCLI1824.1

Rienecker, M. M., Suarez, M. J., Todling, R., Bacmeister, J., Takacs, L., and Liu, H.-C. (2008). The GEOS-5 Data Assimilation System—Documentation of versions 5.0.1, 5.1.0, and 5.2.0. *Tech. Rep. Ser. Global Model. Data Assimil.* 27, 118.

Ruckstuhl, C., Philipona, R., Morland, J., and Ohmura, A. (2007). Observed relationship between surface specific humidity, integrated water vapor, and longwave downward radiation at different altitudes. *J. Geophys. Res.* 112:D03302. doi: 10.1029/2006JD007850

Schlundt, M., Farrar, J. T., Bigorre, S. P., Plueddeman, A. J., and Weller, R. A. (2020). Accuracy of wind observations from open-ocean buoys: correction for flow distortion. *J. Atmosph. Ocean. Technol.* 37, 687–703. doi: 10.1175/jtech-d-19-0132.1

Serra, Y. L., A'Hearn, P., Freitag, H. P., and McPhaden, M. J. (2001). ATLAS self-siphoning rain gauge error estimates. *J. Atmospher. Ocean. Technol.* 18, 1989–2002. doi: 10.1175/1520-0426(2001)018<1989:assrge>2.0.co;2

Servain, J., Wainer, I., McCreary, J. P. Jr., and Dessier, A. (1999). Relationship between the equatorial and meridional modes of climatic variability in the tropical Atlantic. *Geophys. Res. Lett.* 26, 485–488. doi: 10.1029/1999GL900014

Smith, S. R., Legler, D. M., and Verzone, K. V. (2001). Quantifying uncertainties in NCEP reanalyses using high-quality research vessel observations. *J. Clim.* 14, 4062–4072. doi: 10.1175/1520-0442(2001)014<4062:quinru>2.0.co;2

Waliser, D. E., and Gautier, C. (1993). A satellite-derived climatology of the ITCZ. *J. Clim.* 6, 2162–2174. doi: 10.1175/1520-0442(1993)006<2162:asdcot>2.0.co;2

Wang, C., Enfield, D. B., Lee, S., and Landsea, C. W. (2006). Influences of the atlantic warm pool on western hemisphere summer rainfall and atlantic hurricanes. *J. Clim.* 19, 3011–3028. doi: 10.1175/JCLI3770.1

Wang, C., Lee, S., and Mechoso, C. R. (2010). Interhemispheric influence of the atlantic warm pool on the southeastern pacific. *J. Clim.* 23, 404–418. doi: 10.1175/2009JCLI3127.1

Weinzierl, B., Ansmann, A., Prospero, J. M., Althausen, D., Benker, N., Chouza, F., et al. (2017). The Saharan Aerosol Long-range Transport and Aerosol-Cloud-Interaction Experiment (SALTRACE): overview and selected

highlights. *Bull. Am. Meteorol. Soc.* 98, 1427–1451. doi: 10.1175/BAMSD-15-00142.1

Weller, R. A. (2018). "Observing Surface Meteorology and Air-Sea Fluxes," in *Observing the Oceans in Real Time*, eds R. Venkatesan, A. Tandon, E. D'Asaro, and M. A. Atmanand (Cham: Springer), doi: 10.1007/978-3-319-66493-4_2

Wen, C., Xue, Y., Kumar, A., Behringer, D., and Yu, L. (2017). How do uncertainties in NCEP R2 and CFSR surface fluxes impact tropical ocean simulations? *Clim. Dyn.* 49, 3327–3344. doi: 10.1007/s00382-016-3516-6

Zhang, H.-M., Bates, J. J., and Reynolds, R. W. (2006). Assessment of composite global sampling: Sea surface wind speed. *Geophys. Res. Lett.* 33:L17714.

Conflict of Interest: The authors declare that the research was conducted in the absence of any commercial or financial relationships that could be construed as a potential conflict of interest.

frontiers in Marine Science

ORIGINAL RESEARCH
published: 05 February 2021
doi: 10.3389/fmars.2021.612361

Advances in the Estimation of Global Surface Net Heat Flux Based on Satellite Observation: J-OFURO3 V1.1

Hiroyuki Tomita[1], Kunio Kutsuwada[2], Masahisa Kubota[3] and Tsutomu Hihara[4]*

[1] Institute for Space-Earth Environmental Research, Nagoya University, Nagoya, Japan, [2] School of Marine Science and Technology, Tokai University, Shizuoka, Japan, [3] Institute of Ocean Research and Development, Tokai University, Shizuoka, Japan, [4] System and Planning Division, Japan Fisheries Information Service Center, Tokyo, Japan

OPEN ACCESS

Edited by:
Carol Anne Clayson, Woods Hole Oceanographic Institution, United States

Reviewed by:
Zhongxiang Zhao, University of Washington, United States
Lei Zhou, Shanghai Jiao Tong University, China
Jason Roberts, National Aeronautics and Space Administration (NASA), United States

***Correspondence:**
Hiroyuki Tomita
tomita@isee.nagoya-u.ac.jp

Specialty section:
This article was submitted to Physical Oceanography, a section of the journal Frontiers in Marine Science

Received: *30 September 2020*
Accepted: *05 January 2021*
Published: *05 February 2021*

Citation:
Tomita H, Kutsuwada K, Kubota M and Hihara T (2021) Advances in the Estimation of Global Surface Net Heat Flux Based on Satellite Observation: J-OFURO3 V1.1. Front. Mar. Sci. 8:612361. doi: 10.3389/fmars.2021.612361

The reliability of surface net heat flux data obtained from the latest satellite-based estimation [the third-generation Japanese Ocean Flux Data Sets with Use of Remote Sensing Observations (J-OFURO3, V1.1)] was investigated. Three metrics were utilized: (1) the global long-term (30 years) mean for 1988–2017, (2) the local accuracy evaluation based on comparison with observations recorded at buoys located at 11 global oceanic points with varying climatological characteristics, and (3) the physical consistency with the freshwater balance related to the global water cycle. The globally averaged value of the surface net heat flux of J-OFURO3 was $-22.2\,W\,m^{-2}$, which is largely imbalanced to heat the ocean surface. This imbalance was due to the turbulent heat flux being smaller than the net downward surface radiation. On the other hand, compared with the local buoy observations, the average difference was $-5.8\,W\,m^{-2}$, indicating good agreement. These results indicate a paradox of the global surface net heat flux. In relation to the global water cycle, the balance between surface latent heat flux (ocean evaporation) and precipitation was estimated to be almost 0 when river runoff from the land was taken into consideration. The reliability of the estimation of the latent heat flux was reconciled by two different methods. Systematic ocean-heating biases by surface sensible heat flux (SHF) and long wave radiation were identified. The bias in the SHF was globally persistent and especially large in the mid- and high latitudes. The correction of the bias has an impact on improving the global mean net heat flux by $+5.5\,W\,m^{-2}$. Furthermore, since J-OFURO3 SHF has low data coverage in high-latitudes areas containing sea ice, its impact on global net heat flux was assessed using the latest atmospheric reanalysis product. When including the sea ice region, the globally averaged value of SHF was approximately 1.4 times larger. In addition to the bias correction mentioned above, when assuming that the global ocean average of J3 SHF is 1.4 times larger, the net heat flux value changes to the improved value ($-11.3\,W\,m^{-2}$), which is approximately half the original value ($-22.2\,W\,m^{-2}$).

Keywords: air-sea interaction, air-sea heat flux, satellite-remote sensing, J-OFURO, buoy

INTRODUCTION

Surface net heat flux, defined as the total heat exchange between the atmosphere and oceans, affects both atmospheric and oceanic processes. In addition, the surface net heat flux determines the actual state of atmospheric-ocean interaction and the climate system. Therefore, the surface net heat flux is an essential climate variable (ECV) and an essential observational variable (EOV). Accurate and observational estimations are required globally (Cronin et al., 2019). Global estimates based on observations are necessary to understand long-term climate change and related responses, in addition to validating climate model results. Consequently, estimating surface net heat flux using satellite observations and improvements are of vital importance.

Several efforts have been made to estimate based on satellite observations (e.g., Pinker et al., 2014) and the data products are available, but how reliable is the satellite estimation of surface net heat flux? This question is not self-evident. This is because the satellite-based surface net heat flux estimation is obtained by combining the output of the turbulent flux estimation and the radiation flux estimation, which are being promoted as separate research projects. Although each product has been previously evaluated in several studies (e.g., Andersson et al., 2011; Rutan et al., 2015; Bentamy et al., 2017), there are few studies related to net heat flux. Therefore, it must be evaluated as a surface net heat flux.

A recent study evaluated the estimation of the surface net heat flux resulting from ocean reanalysis as well as atmospheric reanalysis and satellite-based estimations (Valdivieso et al., 2017). The results showed that the ocean reanalysis gave close to 0 for the global mean surface net heat flux, while the atmospheric reanalysis and satellite-based estimates indicated that the global mean had a bias of heating the ocean. In addition, a comparison with observations from local buoys indicates that the satellite-based estimation was in good agreement, but ocean reanalysis estimates had a bias of cooling the ocean.

Yu (2019) reported that modifying the bulk equation of the turbulent heat fluxes improved the global heat balance in satellite-based estimations (OAFlux-HR). However, it was indicated that a large physical inconsistency regarding freshwater balance occurs when using the modified equation.

These two studies highlight the "paradox" of surface net heat flux estimations. This occurs because of the poor agreement between the global heat balance and the local accuracy in addition to similar inconsistencies between the heat and freshwater balances.

In this study, the latest satellite-derived surface net heat flux dataset, J-OFURO3 (Tomita et al., 2019) is evaluated using the following three metrics: (1) the long-term (30 years) mean, (2) local accuracy, and (3) physical consistency. In addition, the advancement in the satellite data will be estimated by comparing the current data with the previous generation dataset, J-OFURO2 (Tomita et al., 2010). The number of buoys used for comparison has also increased from those in past studies because of the inclusion of buoys in mid- and high-latitude areas. Through these efforts, the state of the latest satellite-based surface net heat flux estimations is better understood. Finally, suggestions for future improvements are provided.

Abbreviations: AMI, Active Microwave Instrument; AMSR-E, Advanced Microwave Scanning Radiometer—Earth observing system; ASCAT, Advanced Scatterometer; CFSR, NCEP Climate Forecast System Reanalysis (Xue et al., 2011); CGLORS 05V3, Ocean reanalysis at the Centro Euro-Mediterraneo sui Cambiamenti Climatici (CMCC) (Storto et al., 2014); CORE.2, Common Ocean Reference Experiment Version 2, known as the flux product of Large and Yeager (2009); ECCO v4, The Estimating the Circulation and Climate of the Ocean (https://www.ecco-group.org); ECDA, Ensemble Coupled Data Assimilation; ERA Interim, European Center for Medium-Range Weather Forecasts Reanalysis-Interim (Dee et al., 2011); ERA5, European Center for Medium-Range Weather Forecasts Reanalysis-5 (Hersbach et al., 2020); ERS, European Space Agency (ESA) Remote-Sensing Satellite; GECCO2, The German contribution of the Estimating the Circulation and Climate of the Ocean project (ECCO); GLORYS2 v1 and v3, Ocean reanalysis at Mercator Ocean: https://www.mercator-ocean.fr/en/science-publications/glorys/; GloSea5, UK Met Office Global Seasonal Forecasting System version 5 (Scaife et al., 2014; MacLachlan et al., 2015); GODAS, NCEP Global Ocean Data Assimilation System; HOAPS, Hamburg Ocean Atmosphere Parameters and Fluxes from Satellite data (Andersson et al., 2011, 2017); ISCCP, International Satellite Cloud Climatology Project; J-OFURO, Japanese Ocean Flux Data Sets with Use of Remote Sensing Observations (Tomita et al., 2019); JRA-55, the Japanese 55-year Reanalysis (Kobayashi et al., 2015); MERRA, Modern-Era Retrospective analysis for Research and Applications; MOVE-C, Multivariate Ocean Variational Estimation System–Coupled Version Reanalysis; NCEP-R2, NCEP-DOE AMIP-II reanalysis (Kanamitsu et al., 2002); NOC, National Oceanography Center; OAFlux, Objectively Analyzed Air-sea Fluxes (Yu and Weller, 2007); ORA-IP, Ocean Reanalysis Intercomparison Project (Balmaseda et al., 2015); ORAS4, ECMWF operational ocean reanalysis (Balmaseda et al., 2013); OSCAT, Oceansat-2 Scatterometer; PEODAS, Predictive Ocean Atmosphere Model for Australia (POAMA) Ensemble Ocean Data Assimilation System (Yin et al., 2011); SSMI, Special Sensor Microwave Imager; SSMIS, Special Sensor Microwave Imager/Sounder; TMI, Tropical Rainfall Measurement Mission (TRMM) Microwave Imager; TOA CERES/ERAi DIV, The hybrid product of CERES and ERA-Interim (Liu et al., 2015); UR025.3 and 025.4, University of Reading global ocean reanalysis.

MATERIALS AND METHODS

Satellite-Derived Air-Sea Heat Flux Datasets

J-OFURO (https://j-ofuro.isee.nagoya-u.ac.jp) is a research project on estimating surface heat, momentum, and freshwater fluxes based on satellite remote-sensing observations. The project also provides the global dataset for the research community. Although the first dataset (Kubota et al., 2002) did not cover the entire global region, the second-generation dataset, J-OFURO2 (Tomita et al., 2010) provided global surface net heat flux data for 1988–2008, with their own turbulent heat flux estimation and surface radiations obtained from ISCCP (Rossow and Schiffer, 1991). From here, we refer to the J-OFURO2 dataset as J2.

The third-generation dataset: J-OFURO3 (Tomita et al., 2019) was first released as V1.0 for 1988–2013. The J-OFURO3 is characterized by the use of multi-satellite, multi-microwave sensors, and the state-of-the-arts estimation algorithm (e.g., Tomita et al., 2018). During the data period of 1988–2013, data from the satellite microwave radiometer sensors: SSMI/SSMIS series, TMI, AMSR-E, and AMSR2 were used to estimate atmospheric specific humidity, which is essential for estimating latent heat flux. In addition to above microwave radiometers, data from microwave scatterometers: ERS AMI series, QuikSCAT, ASCAT, and OSCAT series were used to estimate ocean surface

winds. In addition to these estimates of surface specific humidity and surface winds, using ensembles obtained from 12 types of global SST products including satellite observation data and surface air temperature data obtained from atmospheric reanalysis data, the turbulent heat fluxes were calculated. J-OFURO3 provides a global net heat flux using its own surface turbulent heat flux estimates and surface radiation flux estimates utilizing ISCCP FD and CERES SYN1D (Doelling et al., 2013, 2016; Loeb et al., 2018). Please note that the J3 upward long wave radiation flux has been recalculated using J-OFURO3′s ensemble sea surface temperature data for consistency with other fluxes in J-OFURO3. This procedure is also the same as that of J2, despite the sea surface temperature data being different. Furthermore, J-OFURO3 calculates the evaporation from the ocean surface based on the J-OFURO3 surface latent heat flux and provides data on the freshwater flux in combination with the data for precipitation obtained from GPCP (Adler et al., 2003, version 2.3). These data were also used to confirm the consistency of the surface heat flux with the hydrological cycle. More details on J-OFURO3 V1.0 can be found in Tomita et al. (2019) and the official data documentation (Tomita, 2017).

The latest version, J-OFURO3 V1.1 with some updates including source data version updates, minor algorithm changes, and extended data periods covering 30 years for 1988–2017 have been released. For surface radiation data in V1.0, we found a temporal discontinuity in 2000. This temporal discontinuity is caused by changing input source data (i.e., from ISCCP to CERES products). Therefore, in the V1.1 we adjusted the radiations of ISCCP to CERES, assuming CERES is well calibrated. From here, we refer to the J-OFURO3 V1.1 dataset as J3.

The surface net heat flux (NHF) is calculated as the sum of the following components: net shortwave radiation (SWR), net long wave radiation (LWR), surface latent heat flux (LHF), and sensible heat flux (SHF), that is, NHF = SWR + LWR + LHF + SHF. In this study, all heat fluxes assumed to be positive when they are directed upward, away from the ocean surface to the atmosphere.

In this study, evaluation of J3 for 1988–2017 was the main focus, but to confirm the progress from J2, a comparison for 1988–2008 was also conducted. For J2, the monthly data of the 1-degree grid was used, and for J3, the monthly data of the 0.25-degree grid was used.

Furthermore, we have used another satellite-based product for comparison, namely: HOAPS-4.0 (Andersson et al., 2017). HOAPS is characterized by the unique development of both precipitation and evaporation (LHF) using SSMI and SSMIS series observations. The EUMETSAT Satellite Application Facility on Climate Monitoring (CM SAF) provides monthly global data from July 1987 to December 2014, with a spatial resolution of 0.5.

Calculation of Global Long-Term Average

Because the satellite-derived air-sea net heat flux datasets used in this study are gridded data, the globally averaged value is indicated as the area-weighted average value obtained from the data of each original grid size. The "global" means the region 0-360E, 90S-90N. However, it should be noted that the J2 and J3 data do not include data over land and sea ice areas. The global long-term average is calculated by the arithmetic mean over time after calculating the global area-weighted average.

In situ Observation Data

Buoy data were used to obtain the sea truth of the surface net heat flux. To obtain the surface net heat flux, the buoy measurements must provide a dataset of all components to estimate surface heat fluxes. Although there are few such buoys having sensors for radiation measurement, there are 11 in the global oceans that capture varying climatological characteristics (**Figure 1**, **Table 1**). These buoys are part of the following observation networks: ocean climate stations and the global tropical moored buoy array in NOAA/PMEL, the Ocean Reference Stations in the WHOI. The KEO, PAPA, and NTAS buoys are in the North Pacific region, and three TAO buoys (McPhaden et al., 1998) are in the tropical Pacific Ocean. There are two RAMA buoys (McPhaden et al., 2009) in the Indian Ocean. The PIRATA (Servain et al., 1998) and WHOTS buoys are in the Atlantic Ocean. STRATUS (Weller, 2015) is the only buoy in the Southern Hemisphere. The Southern Ocean Flux Station (SOFS, Schulz et al., 2012) and Agulhas Return Current (ARC) buoys are located in the Southern Hemisphere, but because they do not provide sufficient observational data, they were excluded from the main comparison of this study.

The four surface heat flux components (SWR, LWR, LHF, and SHF) were calculated from the hourly observation data of each buoy. Subsequently, the daily average values were derived after the flux calculations. Furthermore, the monthly averaged value was calculated from the daily averaged value of the flux data. The NHF was calculated from the monthly average value, and if any components were missing, all the components were set as the missing values.

The flux calculation was performed according to the method described by Tomita et al. (2010). The net SWR was calculated from the observed downward SWR according to Equation (1):

$$SWR = -\downarrow SWR\,(1-\alpha) \tag{1}$$

where α is the surface albedo, and the climatological monthly mean values on each grid obtained from the ISCCP have been used in this study. The net LWR was calculated from the observed downward LWR and the calculated upward LWR value from the sea surface temperature (SST) according to Equations (2) and (3),

$$LWR = \uparrow LWR - \downarrow LWR \tag{2}$$

$$\uparrow LWR = (\varepsilon\,\sigma\,SST^4 + (1-\varepsilon)\downarrow LWR) \tag{3}$$

where ε is the emissivity at the ocean surface, set as 0.984 following Konda et al. (1994), and σ is the Stefan–Boltzmann constant (5.679×10^{-8} W m^{-2} K^{-4}).

For the LHF and SHF, the bulk flux calculation algorithm, COARE 3.0 (Fairall et al., 2003) was used. The input parameters required in the flux calculation using the algorithm are air temperature, humidity, winds, SST, and sea level pressure. For all parameters, the observed values at each buoy were used. The algorithm also requires the observation height of each parameter.

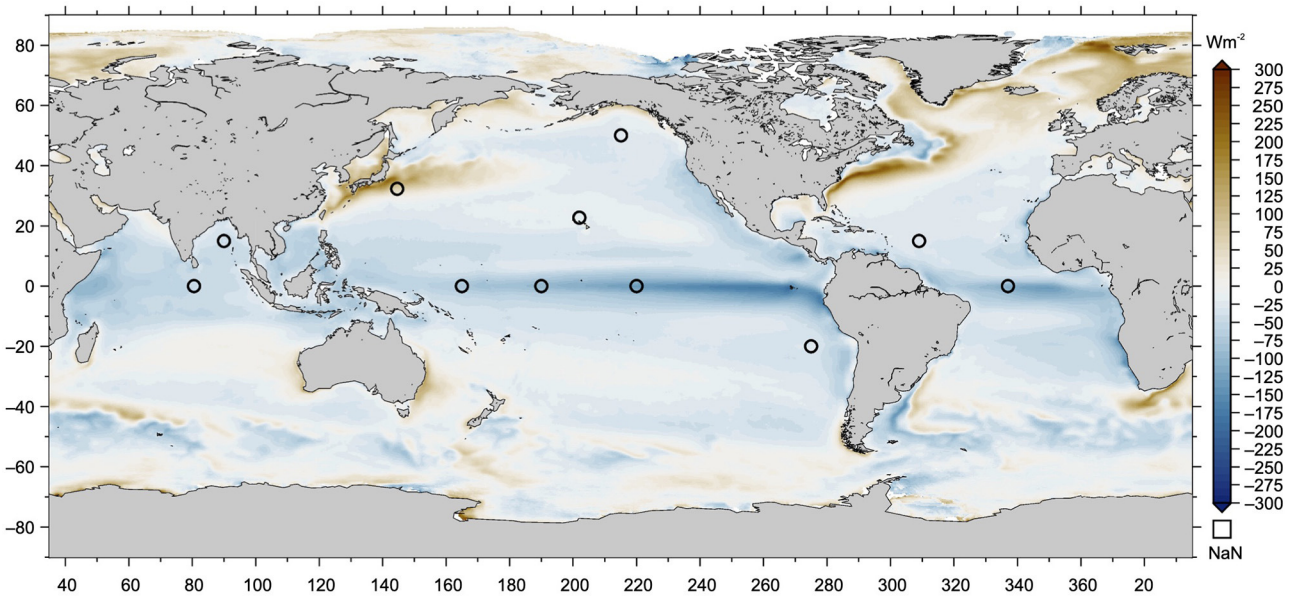

FIGURE 1 | Long-term (30 years) average of global surface net heat flux obtained from J-OFURO3 V1.1 monthly data for 1988–2017. Positive values are upward heat flux. Unit in W m^{-2}. Locations of 11 buoys used in comparison are indicated as black circles.

The observation height information for each buoy listed in **Supplementary Table 1** was used. For the SST, a skin/warm layer correction was not conducted.

The accuracy of the data on surface net heat flux obtained from *in situ* buoys is estimated to be 8 W/m^2 on average (Colbo and Weller, 2009; Cronin et al., 2019), while the values are slightly higher on a daily scale. For each flux component, the long-term averaged accuracy for SWR, LWR, LHF, and SHF are estimated 5.0, 3.9, 1.5, and 5.0 W/m^2, respectively. It can also be confirmed that the mid-latitude buoys (KEO) almost exhibit the same range (Tomita et al., 2010).

Comparison

The buoy data are point values while the satellite data are gridded. Therefore, we compared the values on gridded satellite data that include the locations of the buoys with the values calculated from the buoy measurements. All comparisons were conducted monthly. The statistics: bias, RMS, and correlation coefficient, r, were calculated for each flux component using the following equations:

$$bias = \frac{1}{n}\sum_{l=1}^{n}(s_l - b_l)$$

$$RMS = \sqrt{\sum_{l=1}^{n}\frac{(s_l - b_l - bias)^2}{n}}$$

$$r = \frac{\sum_{l=1}^{n}(s_l-\bar{s})(b_l-\bar{b})}{\sqrt{\sum_{l=1}^{n}(s_l-\bar{s})^2\sum_{l=1}^{n}(b_l-\bar{b})^2}}$$

where s and b are the satellite gridded value and buoy point value, respectively, and n is the number of monthly data at each buoy (see **Table 1**). It should be noted that the RMS is defined as a form in which the bias is removed from the difference between s and b (Taylor, 2001). All statistics values are available as **Supplementary Data**.

RESULTS

Global Long-Term Mean

Figure 1 shows the distribution of the long-term (1988–2017) mean for the global NHF obtained from J3. The figure represents the climatological features of the distribution for the NHF. In the tropical zone, a net heat flux exists from the atmosphere to the ocean, and in mid- and high-latitudes, there is a net heat flux from the ocean to the atmosphere.

Examining regional features, there is a larger heat flux from the atmosphere to the ocean in the eastern tropical Pacific and at the equator. These areas contain upwelling ocean currents. In addition, there is large net heat flux from the ocean to the atmosphere at the western boundary current region for both hemispheres. Moreover, there is a strong flux contrast corresponding to the ocean fronts in these areas.

The global long-term average value calculated from J3 is -22.2 W m^{-2}. This indicates that the net heat flow is to the ocean surface. Although the characteristics of the qualitative distribution are not significantly different from common knowledge, this value is more than one order of magnitude larger from the viewpoint of global surface heat balance (NHF $\rightarrow$ 0).

The results are similar when compared with the global average value obtained from the previous generation dataset (J2). J2 data

TABLE 1 | Summary of buoy observation data used for the comparison with J-OFURO3.

	Site name	Location	Start date	End date	*N*	Framework	Provider
1	KEO	32.3N, 144.6E	2004/6/17	2018/12/31	105	OCS*	NOAA/PMEL
2	PAPA	50.1N, 144.9W	2007/6/9	2018/12/31	108	OCS*	NOAA/PMEL
3	TAO/TRITON	0N, 165E	2006/7/13	2017/9/8	63	GTMBA†	NOAA/PMEL
4		0N, 170W	2006/6/25	2018/10/29	49	GTMBA†	NOAA/PMEL
5		0N, 140W	2006/9/16	2018/12/31	76	GTMBA†	NOAA/PMEL
6	PIRATA	0N, 23W	2007/5/26	2014/7/6	46	GTMBA†	NOAA/PMEL
7	RAMA	0N, 80.5E	2008/8/10	2014/8/17	35	GTMBA†	NOAA/PMEL
8		15N, 90E	2008/10/20	2016/5/21	50	GTMBA†	NOAA/PMEL
9	WHOTS	22.75N, 158W	2008/8/14	2018/9/24	152	ORS§	WHOI
10	STRATUS	20S, 85W	2000/10/8	2018/4/7	192	ORS§	WHOI
11	NTAS	15N, 51W	2001/3/31	2018/6/11	187	ORS§	WHOI

N indicates the number of valid monthly means.
**https://www.pmel.noaa.gov/ocs/.*
†*https://www.pmel.noaa.gov/gtmba/.*
§*http://uop.whoi.edu/ReferenceDataSets/index.html.*
End date is based on the data availability by 2018/12/31.

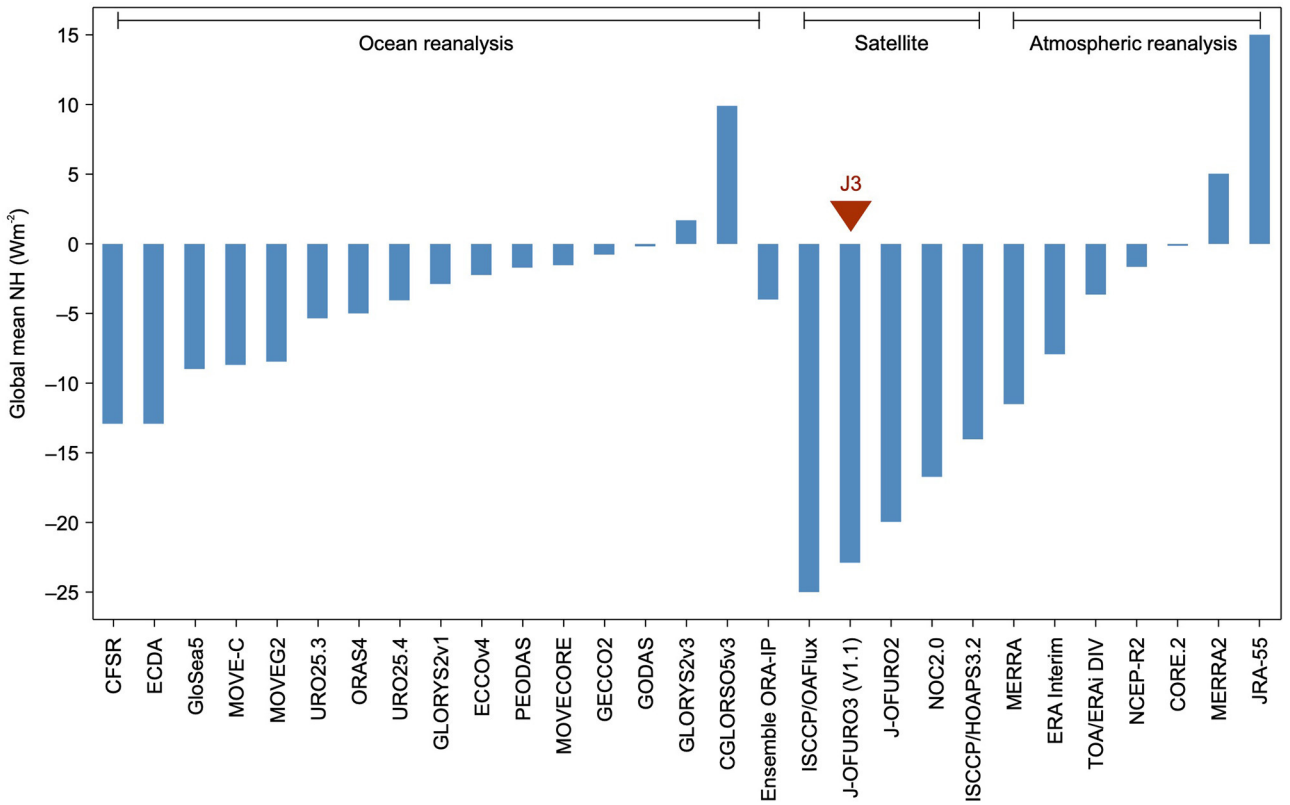

FIGURE 2 | Comparison of global long-term averages among various estimates. The values (except for f J-OFURO2 and J-OFURO3) were drawn from Valdivieso et al. (2017). Positive values are upward heat flux. Almost all estimates are indicating ocean heating. Please also see the list of abbreviations of each dataset name and reference.

are only available for 1988–2008. The average values for J2 and J3 in 1988–2008 were 22.2 and 23.2 W m^{-2}, respectively.

Figure 2 shows the average values of the global NHF obtained by various estimation approaches. Except for the values of J2 and J3, the values are shown by Valdivieso et al. (2017). From this figure, with a few exceptions, the global long-term average of NHF tends to indicate a net heat flux to the ocean for most methodologies. Most satellite-based estimates, including J2 and J3, show greater ocean heating than those shown in ocean reanalysis estimates.

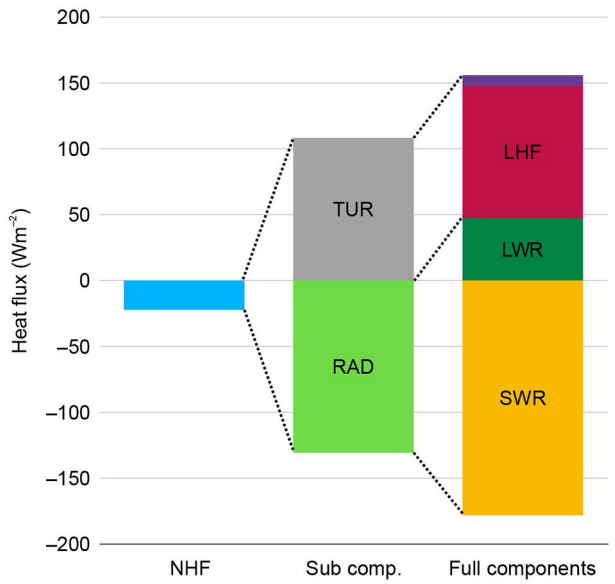

FIGURE 3 | Balance of each component for the global long-term average of J-OFURO3 for the surface net heat flux (NHF). The balance for the turbulent heat flux (TUR) and the net surface radiation (RAD), in addition to the full components: the net shortwave radiation (SWR), the net long wave radiation (LWR), the latent heat flux (LHF), and the sensible heat flux (SHF) are shown.

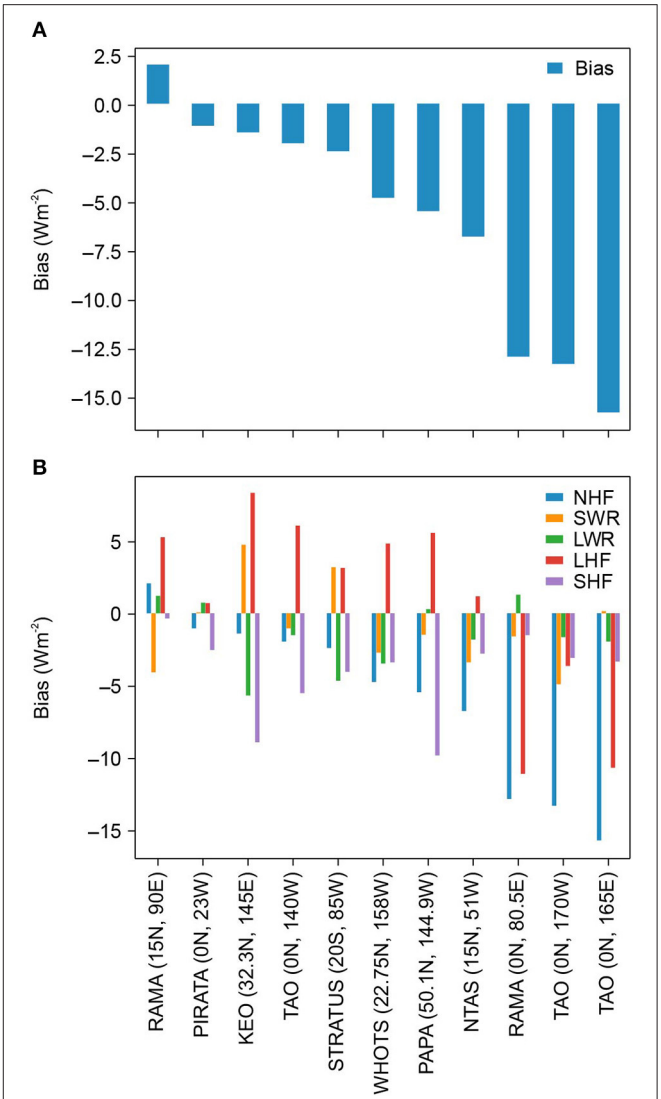

FIGURE 4 | Biases (J-OFURO3 minus buoys) of the surface heat fluxes at each buoy site for **(A)** the surface net heat flux (NHF) and **(B)** components. The comparison results are based on 1,063 monthly means from 11 sites.

Figure 3 shows the balance among components that consist of NHF. In J3, the turbulent flux is smaller than the net radiation, resulting in an NHF of -22.2 W m^{-2}.

Comparison With Buoys

Figure 4 shows the bias between the J3 estimates and buoy observations. At all buoy points except RAMA (15N, 90E), the bias is negative, indicating a significant ocean heating bias in J3. In particular, large negative biases were found in buoys in the western tropical Pacific (0N, 165E), central tropical Pacific (0N, 170W), and central tropical Indian Ocean (0N, 80.5E). The overall averaged bias is -5.8 W m^{-2}, and the averaged bias at mid-high latitudes excluding buoys in the tropical zone is -3.1 W m^{-2}, which shows good agreement.

There are cases in which the positive and negative biases of each component cancel each other out (**Figure 4B**). For example, at KEO, SW, and LH show positive biases, while LW and SH show negative biases. The sum of absolute biases of the components is 27.6 W m^{-2}, which is significantly larger than the absolute NHF bias of 1.5 W m^{-2}. Similar canceling out of biases was seen in Stratus, RAMA (15N, 90E), and TAO (0N, 140W).

Unexpectedly, **Figure 4B** indicates that the SH bias is always negative for these data, while biases of the other components show both negative and positive biases depending on the buoy locations. A comparison using more comprehensive global buoy data that can calculate turbulent heat flux confirms these negative SH biases, especially over the open ocean area (Tomita et al., 2019). The influence of SH biases on the global long-term mean of NHF is discussed in the "Discussion" section.

In addition, a pattern of characteristic bias was also observed in the LW. Relatively large negative biases in LW were found in the KEO, STRATUS, and WHOTS buoys located in the subtropics and mid-latitudes. The negative LW biases were relatively small at buoys in the tropics. The KEO and STRATUS buoy networks correspond to areas that have significant cloudiness consisting of low-level clouds.

The same comparisons were made using both J2 and J3 data for the period up to 2008. An improvement from the previous generation data was confirmed. **Figure 5** shows the bias, RMS, and the correlation for the NHF for J2 and J3. From the data in this figure, significant improvements in statistics from J2 were confirmed. At most buoy points, the RMS and correlation coefficients are improved. For the bias, on average, the absolute bias of J3 is slightly higher than that of J2. However, J2 has a small

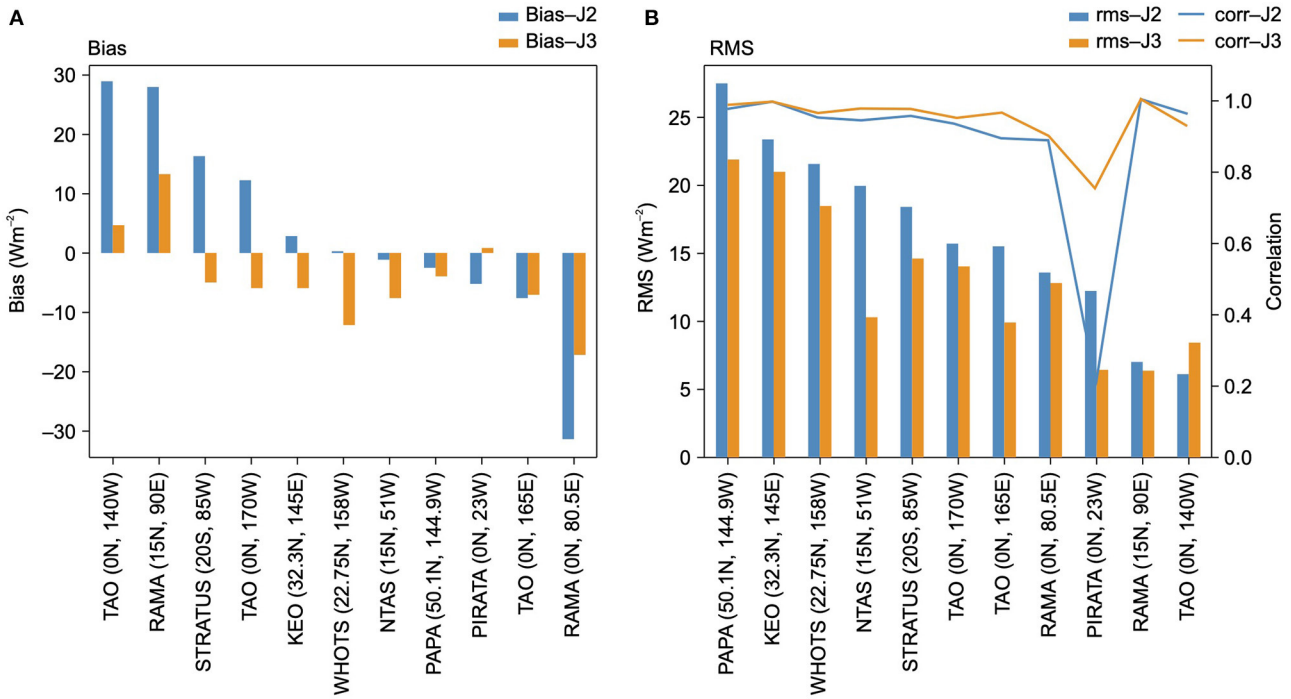

FIGURE 5 | Advances in comparative statistics of the **(A)** bias, **(B)** RMS, and correlation coefficient of surface net heat flux (NHF) for J-OFURO2 (J2) and J-OFURO3 V1.1 (J3). Note that the buoys are listed in different orders in **(A)** and **(B)**.

bias due to canceling out of the large positive and large negative biases. Such large positive and negative biases were improved in J3, while a slight negative bias was observed.

Consistency With Freshwater Flux

The LHF, which is one of the surface heat flux components, is proportional to the evaporation rate from the ocean surface and is a part of the freshwater flux as a counterpart for precipitation. Therefore, by checking the consistency between the latent heat flux (evaporation) and the surface freshwater balance one can evaluate the surface heat balance from a different perspective.

In general, the global ocean freshwater flux defined as (evaporation minus precipitation) is positive because a significant amount of water evaporates from the ocean. The evaporated water is transported to land by atmospheric advection, mainly in the form of water vapor. On a long-term average, the changes in atmosphere disappear and the net positive freshwater flux over the ocean is balanced by the runoff of river water from the continent into the ocean (i.e., freshwater flux–runoff = 0).

The global long-term mean value of ocean evaporation in J3 was 3.4 mm/day, while the precipitation over the ocean obtained from GPCP V2.3 was 3.0 mm/day. Therefore, the global long-term mean of freshwater flux was calculated as 0.4 mm per day. The result showed a good balance after considering the runoff from land. Various estimates have been obtained by studies on river runoff. These values range from approximately 0.27 to 0.34 mm/day (Schlosser and Houser, 2007). More recent studies estimate river runoff as 0.29 (Ghiggi et al., 2019) and 0.31 (Wilkinson et al., 2014) mm/day. According to these previous studies, if we assume a value of 0.3 mm/day of river runoff, the freshwater balance estimated from J3, GPCP, and the river runoff is 0.1 mm/day, which is a reasonable result. An improvement was confirmed compared to the estimation using J-OFURO2 (Iwasaki et al., 2014).

Although there are various global precipitation datasets (Kidd and Huffman, 2011), GPCP is used as the standard dataset in numerous studies (e.g., Andersson et al., 2011; Tapiador et al., 2017; Yu, 2019; Gutenstein et al., 2021). However, most studies suggest that much of the uncertainty in water balance lies in precipitation products as well as evaporation. To confirm the differences in the results that depend on the satellite products, we reconfirmed the results using another satellite precipitation/evaporation product, HOAPS-4.0. Consequently, it was confirmed that the long-term mean precipitation of HOAPS-4.0 for 1988–2014 (2.9 mm/day) was slightly smaller than that of GPCP V2.3 for the same period (3.0 mm/day). For evaporation, the long-term mean HOAPS-4.0 value for 1988–2014 was 3.4 mm/day. Therefore, the global ocean freshwater flux value (0.5 mm/day) was slightly higher than that estimated by J3 (0.4 mm/day, for 1988–2014), while being sufficiently comparable.

DISCUSSION

The global long-term mean value of the NHF from the J3 data was consistent with the previous generation data. The tendency of ocean heating is similar to other estimates such as satellite and ocean reanalysis. However, its value was large in magnitude, $-22.2\,W\,m^{-2}$, indicating a significant negative imbalance. In contrast, by comparison with local 11 buoys, the average bias

was found to be $-5.8\,W\,m^{-2}$ and the negative largest value of $-15.7\,W\,m^{-2}$ was found at buoy in the western tropical Pacific. Therefore, the relationship between the global mean value of J3 and the local bias was inconsistent, and the paradox of surface heat flux was confirmed. In previous studies (Pinker et al., 2017; Valdivieso et al., 2017), several tropical and subtropical buoys data (Stratus) were used for the evaluation of surface net heat flux. In contrast, for this study, the comparison was performed using more buoy data which included mid-high latitude buoys (KEO and PAPA). These data contained longer time series, and the paradox was confirmed. The cause is discussed in the following text.

In contrast to the excessively large negative imbalance for the NHF in the global long-term mean, the globally averaged ocean surface freshwater flux estimated by surface latent heat flux (evaporation) in J3, GPCP, and runoff was almost 0. This result was consistent with a previous estimate (Trenberth et al., 2007). Because the sum of these independently estimated components was close to 0, J3 the LHF is considered to be very reliable. Therefore, the cause of the imbalance might be other than the LHF. The comparison of the J3 LHF with more comprehensive global buoys (**Figure 6A**) revealed that the total bias was fairly small ($<1\,W\,m^{-2}$) while there are some regional biases. This fact also strongly suggests that the cause of the excessively large global long-term mean imbalance of NHF is likely to be other than LHF.

In contrast to the LHF, the J3 SHF had a persistent bias. As shown in the Results (Section "Comparison with Buoys"), the SHF showed negative biases in the comparisons with all of the 11 buoys. Negative biases were also confirmed by comparison with more comprehensive buoy observations (**Figure 6B**). There are negative biases in almost all open ocean areas except for the coastal area, and a larger negative bias occurs especially in mid-high latitudes (Tomita et al., 2019). **Figure 7** shows the bias of the SHF as a function of latitude. In order to investigate the effect of this SHF bias characteristic on the global averaged value, this bias was corrected by using a fitting curve and the global averaged value was recalculated. The global long-term mean value of the SHF without bias correction was $+8.1\,W\,m^{-2}$, while the global long-term average value after bias correction was $13.3\,W\,m^{-2}$. This bias correction has an impact of improving the global mean of the NHF by $+5.5\,W\,m^{-2}$, but a large imbalance of $-16.7\,W\,m^{-2}$ still remains. However, the number of buoy observations on which this bias correction was based does not completely cover global oceans (as seen in **Figure 6B**). It is necessary to consider a more robust correction method in the future. As shown in **Figure 7B**, the cause of this SHF bias is in the air temperature. The J3 uses atmospheric reanalysis data instead of satellite retrieval for air temperature estimation, and it is desirable to refer to better air temperature estimates or develop a satellite-based retrieval method in the future.

Furthermore, the data coverage of J3 SHF over high-latitudes is small. In the presence of sea ice, J3 cannot calculate the turbulent heat flux; therefore, the estimation of turbulent heat flux over regions with sea ice is overlooked. In a simple test performed using ERA5 (Hersbach et al., 2020), which has complete global coverage, the global ocean average value is approximately 30% smaller than the original ERA5 value when the sea ice area is excluded for simulating the coverage of J3. When including the sea ice region, the global ocean average SHF value is approximately 1.4 times larger. This is a reasonable result considering the large air–sea temperature difference (i.e., large SHF) with sea ice at high latitudes. The same test for LHF does not give the same result. In the case of LHF, the value corresponding to the sea ice region does not have a large influence on the global ocean averages, and by including the sea ice region, the global averaged value decreases slightly. In addition to the bias correction mentioned above, when assuming that the global ocean average of J3 SHF is approximately 1.4 times larger, the NHF value changes to the improved value ($-11.3\,W/m^2$), which is approximately half the original value ($-22.2\,W/m^2$). This indicates the limits of microwave satellite-based flux products such as J3 and the importance of considering the value of SHF over the sea ice region in the global ocean heat balance.

The LWR also had a notable bias characteristic. The LWR bias was relatively small in the tropics, while it was comparatively large in the subtropics and mid-latitudes. For example, the largest biases were found in the KEO and Stratus data. These were -5.7 and $-4.7\,W\,m^{-2}$, respectively. A detailed comparison was performed to investigate the cause in detail. **Figure 8** shows the bias in the upward and downward components of the long wave radiation described by Equation (2). As shown in Equation (3), the upward component of the LWR is not completely independent of the downward component, but the bias shows small negative values ($<1\,W\,m^{-2}$). The major factor of the LWR bias is the downward component. Validation of the downward LWR assessments was performed using more comprehensive buoy observations (Rutan et al., 2015; Kato et al., 2018). Our results are consistent with their results, indicating that the bias is $<5\,W\,m^{-2}$; however, the spatial characteristics of the error have never been investigated thoroughly.

The buoy locations of Stratus and KEO are known as oceanic areas frequently covered by low-level clouds (e.g., Klein and Hartmann, 1993). In contrast, for the high latitude area of the North Pacific, PAPA, which is also characterized by low-level clouds, the downward LWR shows a good agreement. A more detailed investigation of the bias and the relationship with clouds, air temperature, and sea surface temperature will be needed better understand this phenomenon.

In the above, we discussed the possibility of large biases outside the 11 buoys (which showed relatively good agreement on the global heat balance). As another possibility, we discuss the effect of the difference due to the bulk formula and the associated calculation method on the global heat balance. In general, the selection of a bulk formula has a major influence on the estimation of the global turbulent heat and momentum fluxes. Based on a comparative study (Brunke et al., 2003; Iwasaki et al., 2010), COARE 3.0 is used in J3 and other satellite products. Brodeau et al. (2017) estimated that changes in the bulk formula will affect the global heat balance by 10%, and the use of different bulk formulae may significantly change the global heat balance. However, it is necessary to pay attention to consistency with other physics by changing the bulk formula. Yu (2019) confirmed that although the global heat balance was improved by changing the bulk formula, the change in LH caused a freshwater imbalance.

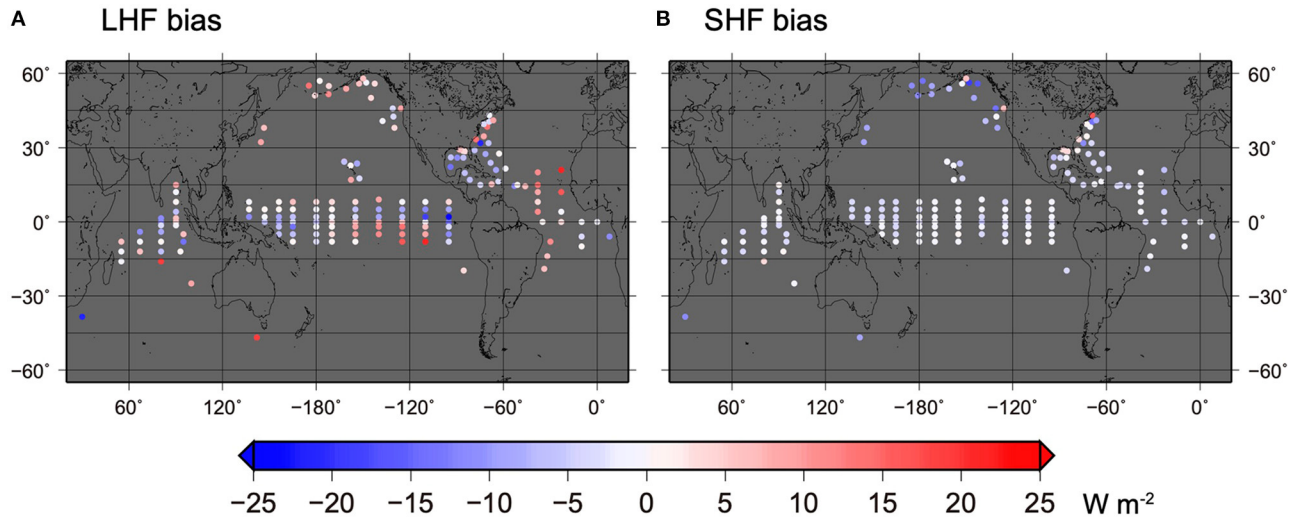

FIGURE 6 | Biases (J-OFURO3 V1.1 minus buoy) of **(A)** latent heat flux (LHF) and **(B)** sensible heat flux (SHF). The biases in this figure were calculated from global buoy data used in the J-OFURO3 Quality Check System (Tomita and Hihara, 2017).

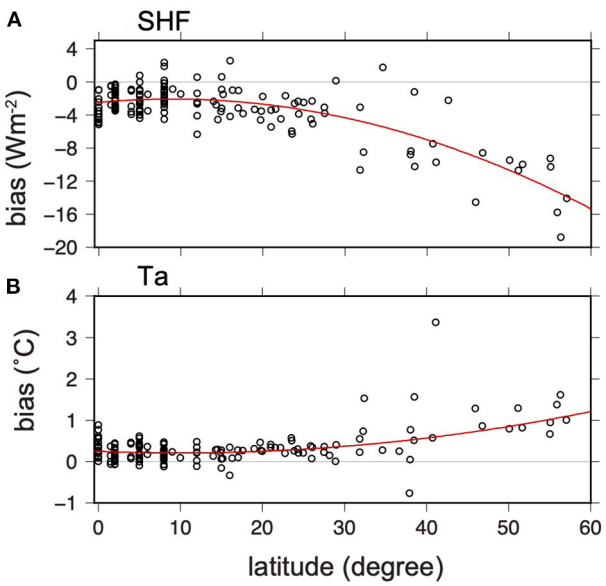

FIGURE 7 | Biases (J-OFURO3 V1.1 minus buoy) of **(A)** surface sensible heat flux (SHF) and **(B)** air temperature (Ta) as a function of latitudes. The solid lines show 2nd order polynormal fitting curves. The biases in this figure were calculated from global buoy data used in the J-OFURO3 Quality Check System (Tomita and Hihara, 2017). Note that the data in near coastal region (the distance from coastline < 200 km) were removed in this comparison.

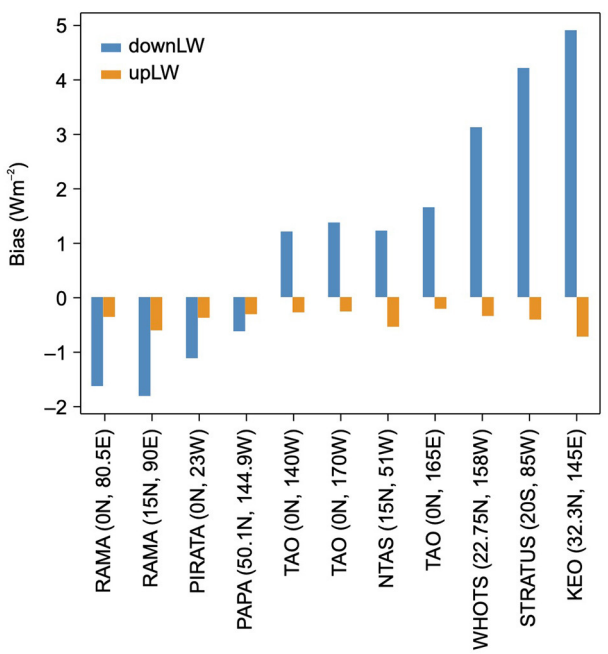

FIGURE 8 | Biases (J-OFURO3 minus buoy) of downward and upward components of the long wave radiations.

Similar results are expected for J3. Improvements in the bulk formula for turbulent heat fluxes are needed, while maintaining consistency with other physics.

In this study, we focused on the long-term mean surface net heat flux. The daily satellite-derived data set is very useful for analyzing the flux variation over time-scales varying from several days to inter-annual or decades. This type of analysis was not in the scope of this research. Weller (2015) showed that precise and long-term buoy observation revealed long-term flux trends. It will be useful for the verification of satellite data in the future. However, the number of buoys will still be small to understand the overall characteristics of these fluctuations.

In general, the uncertainty of precipitation and evaporation from the ocean is a major challenge in understanding of the water cycle. Improving satellite-based products should address this challenge. In this study, the state-of-the-art satellite-based products, J-OFURO3 (Tomita et al., 2019) and HOAPS-4.0 (Andersson et al., 2017), were confirmed to be consistent with each other in the estimation of freshwater flux, which confirms

the improvement of satellite products. Estimating and providing uncertainty information is also important. An approach that combines satellite and ocean observations with the estimation of atmospheric energy transport derived from atmospheric reanalysis data is also a powerful tool to better estimate global surface fluxes (e.g., Liu et al., 2015, 2017; Carton et al., 2018). In the future, it will be necessary to combine multiple approaches, while improving satellite products by their comparison with such approaches.

DATA AVAILABILITY STATEMENT

Publicly available datasets were analyzed in this study. This data can be found here: The J-OFURO3 V1.1 dataset analyzed for this study can be found in the DIAS, and APDRC (https://doi.org/10.20783/DIAS.612); the GPCP precipitation data for this study can be found at https://psl.noaa.gov/data/gridded/data.gpcp.html; the satellite-derived surface radiation data for this study can be found at CERES: https://ceres.larc.nasa.gov/data/ and ISCCP: https://isccp.giss.nasa.gov/products/onlineData.html; the HOAPS data for this study can be found at https://wui.cmsaf.eu/safira/action/viewDoiDetails?acronym=HOAPS_V002; and the surface moored buoy data for this study can be found at NOAA PMEL: https://www.pmel.noaa.gov/ocs/, https://www.pmel.noaa.gov/gtmba/ and WHOI: http://uop.whoi.edu/ReferenceDataSets/index.html.

AUTHOR CONTRIBUTIONS

HT designed the study, led the research, interpreted the data, wrote the manuscript, and managed the project. HT analyzed global satellite-based surface heat flux datasets. KK, TH, and HT collected *in situ* buoy observation data and calculated surface heat fluxes. KK and HT compared satellite estimates with buoy observations. TH contributed some useful scripts for this study. All authors contributed to improving the manuscript.

FUNDING

This work was supported by JSPS KAKENHI Grant Numbers JP18H03726, JP26287114, JP18H03737, and JP19H05696. The Japan Aerospace Exploration Agency (JAXA), Institute for Space-Earth Environmental Research of Nagoya University, and the Institute of Oceanic Research and Development of Tokai University (Grants # 2018–5 and 2019–5) also partly support this research.

ACKNOWLEDGMENTS

GPCP precipitation data provided by the NOAA/OAR/ESRL PSL, Boulder, Colorado, USA, from their website at https://psl.noaa.gov/. Satellite-derived surface radiation data were provided by the projects NASA CERES and ISCCP. HOAPS data provided by EUMETSAT CM SAF. Surface moored buoy data were provided by NOAA PMEL and WHOI.

SUPPLEMENTARY MATERIAL

The Supplementary Material for this article can be found online at: https://www.frontiersin.org/articles/10.3389/fmars.2021.612361/full#supplementary-material

REFERENCES

Adler, R. F., Huffman, G. J., Chang, A., Ferraro, R., Xie, P., Janowiak, J., et al. (2003). The version 2 global precipitation climatology project (GPCP) monthly precipitation analysis (1979-present). *J. Hydrometeor.* 4,1147–1167. doi: 10.1175/1525-7541(2003)004<1147:TVGPCP>2.0.CO;2

Andersson, A., Graw, K., Schroder, M., Fennig, K., Liman, J., Bakan, S., et al. (2017). *Hamburg Ocean Atmosphere Parameters and Fluxes from Satellite Data—HOAPS 4.0, Satellite Application Facility on Climate Monitoring*, Data set. doi: 10.5676/EUM_SAF_CM/HOAPS/V002

Andersson, A., Klepp, C., Fennig, K., Bakan, S., Grassl, H., and Schulz, J. (2011). Evaluation of HOAPS-3 ocean surface freshwater flux components. *J. Appl. Meterol. Climatol.* 50, 379–398. doi: 10.1175/2010JAMC2341.1

Balmaseda, M. A., Hernandez, F., Storto, A., Palmer, M. D., Alves, O., Shi, L., et al. (2015). The ocean reanalyses intercomparison project (ORA-IP). *J. Oper. Oceanogr.* 8, s80–s97. doi: 10.1080/1755876X.2015.1022329

Balmaseda, M. A., Mogensen, K., and Weaver, A., T. (2013). Evaluation of the ECMWF ocean reanalysis system ORAS4. *Quart. J. R. Meterol. Soc.* 139, 1132–1161. doi: 10.1002/qj.2063

Bentamy, A., Piollé, J. F., Grouazel, A., Danielson, R., Gulev, S., and Paul, F. (2017). Review and assessment of latent and sensible heat flux accuracy over the global oceans. *Remote Sens. Environ.* 201,196–218. doi: 10.1016/j.rse.2017.08.016

Brodeau, L., Barnier, B., Gulev, S. K., and Woods, C. (2017). Climatologically significant effects of some approximations in the bulk parameterizations of turbulent air–sea fluxes. *J. Phys. Oceanogr.* 47, 5–28. doi: 10.1175/JPO-D-16-0169.1

Brunke, M. A., Fairall, C. W., Zeng, X., Eymard, L., and Curry, J. A. (2003). Which bulk aerodynamic algorithms are least problematic in computing ocean surface turbulent fluxes? *J. Clim.* 16, 619–635. doi: 10.1175/1520-0442(2003)016<0619:WBAAAL>2.0.CO;2

Carton, J. A., Chepurin, G. A., Chen, L., and Grodsky, S. A. (2018). Improved global net surface heat flux. *J. Geophys. Res. Oceans* 123, 3144–3163. doi: 10.1002/2017JC013137

Colbo, K., and Weller, R. A. (2009). Accuracy of the IMET sensor package in the subtropics. *J. Atmos. Ocean. Technol.* 26, 1867–1890. doi: 10.1175/2009JTECHO667.1

Cronin, M. G., Gentemann, C. L., Edson, J., Ueki, I., Bourassa, M., Brown, S., et al. (2019). Air-sea fluxes with a focus on heat and momentum. *Front. Mar. Sci* 6:430. doi: 10.3389/fmars.2019.00430

Dee, D. P., Uppala, S. M., Simmons, A. J., Berrisford, P., Poli, P., Kobayashi, P. S., et al. (2011). The ERA-Interim reanalysis: configuration and performance of the data assimilation system. *Quart. J. R. Meterol. Soc.* 137, 553–597. doi: 10.1002/qj.828

Doelling, D. R., Loeb, N. G., Keyes, D. F., Nordeen, M. L., Morstad, D., Nguyen, C., et al. (2013). Geostationary enhanced temporal interpolation for CERES flux products. *J. Atmos. Ocean. Technol.* 30, 1072–1090. doi: 10.1175/JTECH-D-12-00136.1

Doelling, D. R., Sun, M., Nguyen, L. T., Nordeen, M. L., Haney, C. O., Keyes, D. F., et al. (2016). Advances in geostationary-derived longwave fluxes for the CERES Synoptic (SYN1deg) product. *J. Atmos. Ocean. Technol.* 33, 503–521. doi: 10.1175/JTECH-D-15-0147.1

Fairall, C. W., Bradley, E. F., Hare, J. E., Grachev, A. A., and Edson, J. B. (2003). Bulk parameterization of air-sea fluxes: updates and verification for the COARE algorithm. *J. Clim.* 16, 571–591.

Ghiggi, G., Humphrey, V., Seneviratne, S. I., and Gudmundsson, L. (2019). GRUN: an observation-based global gridded runoff dataset from 1902 to 2014. *Earth Syst. Sci. Data* 11, 1655–1674, doi: 10.5194/essd-11-1655-2019

Gutenstein, M., Fennig, K., Schröder, M., Trent, T., Bakan, S., Roberts, J. B., et al. (2021). Intercomparison of freshwater fluxes over ocean and investigations into

water budget closure. *Hydrol. Earth Syst. Sci.* 25, 121–146. doi: 10.5194/hess-20 20-317

Hersbach, H., Bell, B., Berrisford, P., Hirahara, S., Horányi, A., Muñoz-Sabater, J., et al. (2020). The ERA5 global reanalysis. *Quart. J. R. Meterol. Soc.*146, 1999–2049. doi: 10.1002/qj.3803

Iwasaki, S., Kubota, M., and Tomita, H. (2010). Evaluation of bulk method for satellite-derived latent heat flux. *J. Geophys. Res.* 115:C07007. doi: 10.1029/2010JC006175

Iwasaki, S., Kubota, M., and Watabe, T. (2014). Assessment of various global freshwater flux products for the global ice-free oceans. *Remote Sens. Environ.* 140, 549–561. doi: 10.1016/j.rse.2013.09.026

Kanamitsu, M., Ebitsuzaki, W., Woolen, J., Yang, S. K., Hnilo, J. J., Fiorino, M., et al. (2002). NCEP-DOE AMIP-II reanalysis (R-2). *Bull. Am. Meterol. Soc.* 83, 1631–1643. doi: 10.1175/BAMS-83-11-1631(2002)083<1631:NAR>2.3.CO;2

Kato, S., Rose, F. G., Rutan, D. A., Thorsen, T. J., Loeb, N. G., Doelling, D. R., et al. (2018). Surface irradiances of Edition 4.0 clouds and the earth's radiant energy system (CERES) energy balanced and filled (EBAF) data product. *J. Clim.* 31, 4501–4527. doi: 10.1175/JCLI-D-17-0523.1

Kidd, C., and Huffman, G. (2011). Global precipitation measurement. *Meterol. Appl.* 18, 334–353. doi: 10.1002/met.284

Klein, S. A., and Hartmann, D. L. (1993). The seasonal cycle of low stratiform clouds. *J. Clim.* 6, 1587–1606. doi: 10.1175/1520-0442(1993)006<1587:TSCOLS>2.0.CO;2

Kobayashi, S., Ota, Y., Harada, Y., Ebita, A., Moriya, M., Onoda, H., et al. (2015). The JRA-55 reanalysis: general specifications and basic characteristics. *J. Meterol. Soc. Jpn.* 93, 5–48. doi: 10.2151/jmsj.2015-001

Konda, M., Imasato, N., Nishi, K., and Toda, T. (1994). Measurement of the sea surface emissivity. *J. Oceanogr.* 50, 17–30. doi: 10.1007/BF02233853

Kubota, M., Iwasaka, N., Kizu, S., Konda, M., Kutsuwada, K. (2002). Japanese ocean flux data sets with use of remote sensing observations (J-OFURO). *J. Oceanogr.* 58, 213–225. doi: 10.1023/A:1015845321836

Large, W. G., and Yeager, S. G. (2009). The global climatology of an interannually varying air–sea flux data set. *Clim. Dyn.* 33, 341–364. doi: 10.1007/s00382-008-0441-3

Liu, C., Allan, R. P., Berrisford, P., Mayer, M., Hyder, P., Loeb, N., et al. (2015). Combining satellite observations and reanalysis energy transports to estimate global net surface energy fluxes 1985–2012. *J. Geophys. Res. Atmos.*120, 9374–9389. doi: 10.1002/2015JD023264

Liu, C., Allan, R. P., Berrisford, P., Mayer, M., Hyder, P., Loeb, N., et al. (2017). Evaluation of satellite and reanalysis-based global net surface energy flux and uncertainty estimates. *J. Geophys. Res. Atmos.* 122, 6250–6272. doi: 10.1002/2017JD026616

Loeb, N. G., Su, W., Doelling, D. R., Wong, T., Minnis, P., Thomas, S., et al. (2018). Earth's top-of-atmosphere radiation budget. *Compr. Remote Sen.* 5, 67–84. doi: 10.1016/B978-0-12-409548-9.10367-7

MacLachlan, C., Arribas, A., Peterson, K. A., Maidens, A., Fereday, D. A., Scaife, A., et al. (2015). Description of GloSea5: the Met Office high resolution seasonal forecast system. *Quart. J. R. Meterol. Soc.* 141, 1072–1084. doi: 10.1002/qj.2396

McPhaden, M., Busalacchi, A., Cheney, R., Donguy, J.-R., Gage, K., Halpern, D., et al. (1998). The tropical ocean global atmosphere observing system: a decade of progress. *J. Geophys. Res.* 103:14169–14240. doi: 10.1029/97JC02906

McPhaden, M. J., Meyers, G., Ando, K., Masumoto, Y., Murty, V. S. N., Ravichandran, M., et al. (2009). RAMA: the research moored array for African–Asian–Australian monsoon analysis and prediction. *Bull. Am. Meterol. Soc.* 90, 459–480. doi: 10.1175/2008BAMS2608.1

Pinker, R. T., Bentamy, A., Katsaros, K. B., Ma, Y., and Li, C. (2014). Estimates of net heat fluxes over the Atlantic Ocean. *J. Geophys. Res. Oceans* 119, 410–427. doi: 10.1002/2013JC009386

Pinker, R. T., Bentamy, A., Zhang, B., Chen, W., and Ma, Y. (2017). The net energy budget at the ocean-atmosphere interface of the "Cold Tongue" region. *J. Geophys. Res. Oceans* 122, 5502–5521. doi: 10.1002/2016JC012581

Rossow, W. B., and Schiffer, R. A. (1991). ISCCP cloud data products. *Bull. Am. Meterol. Soc.* 71, 2–20. doi: 10.1175/1520-0477(1991)072<0002:ICDP>2.0.CO;2

Rutan, D. A., Kato, S., Doelling, D. R., Rose, F. G., Nguyen, L. T., Caldwell, T. E., et al. (2015). CERES Synoptic product: methodology and validation of surface radiant flux. *J. Atmos. Oceanic Technol.* 32, 1121–1143. doi: 10.1175/JTECH-D-14-00165.1

Scaife, A. A., Arribas, A., Blockley, E., Brookshaw, A., Clark, R. T., Dunstone, N., et al. (2014). Skilful long range prediction of European and North American winters. *Geophys. Res. Lett.* 41, 2514–2519. doi: 10.1002/2014GL059637

Schlosser, C. A., and Houser, P. R. (2007). Assessing a satellite-era perspective of the global water cycle. *Clim. J.* 20, 1316–1338. doi: 10.1175/JCLI4057.1

Schulz, E. W., Josey, S. A., and Verein, R. (2012). First air-sea flux mooring measurements in the Southern Ocean. *Geophys. Res. Lett.* 39:L16606. doi: 10.1029/2012GL052290

Servain, J., Busalacchi, A. J., McPhaden, M. J., Moura, A. D., Reverdin, G., Vianna, M., et al. (1998). A pilot research moored array in the Tropical Atlantic (PIRATA). *Bull. Am. Meterol Soc.* 79, 2019–2031. doi: 10.1175/1520-0477(1998)079<2019:APRMAI>2.0.CO;2

Storto, A., Masina, S., and Dobricic, S. (2014). Estimation and impact of nonuniform horizontal correlation length scales for global ocean physical analyses. *J. Atmos. Ocean. Technol.* 31, 2330–2349. doi: 10.1175/JTECH-D-14-00042.1

Tapiador, F. J., Navarro, A., Levizzani, V., García-Ortega, E., Huffman, G. J., Kidd, C., et al. (2017). Global precipitation measurements for validating climate models. *Atmos. Res.*197, 1–20. doi: 10.1016/j.atmosres.2017.06.021

Taylor, K. E. (2001). Summarizing multiple aspects of model performance in a single diagram. *J. Geophys. Res. Atmos.* 106, 7183–7192. doi: 10.1029/2000JD900719

Tomita, H. (2017). J-OFURO3 data set detailed document, J-OFURO3 official document, J-OFURO3_DOC_002 (V1.1E). doi: 10.18999/27183

Tomita, H., and Hihara, T. (2017). Quality check system for J-OFURO3, J-OFURO3 official document, J-OFURO3_DOC_006, V1.0E. doi: 10.18999/27211

Tomita, H., Hihara, T., Kako, S., Kubota, M., and Kutsuwada, K. (2019). An introduction to J-OFURO3, a third-generation Japanese ocean flux data set using remote-sensing observations. *J. Oceanogr.* 75, 171–194. doi: 10.1007/s10872-018-0493-x

Tomita, H., Hihara, T., and Kubota, M. (2018). Improved satellite estimation of near-surface humidity using vertical water vapor profile information. *Geophys. Res. Lett.* 45, 899–906. doi: 10.1002/2017GL076384

Tomita, H., Kubota, M., Cronin, M. F., Iwasaki, S., Konda, M., and Ichikawa, H. (2010). An assessment of surface heat fluxes from J-OFURO2 at the KEO and JKEO sites. *J. Geophys. Res.* 115:C03018. doi: 10.1029/2009JC005545

Trenberth, K. E., Smith, L., Qian, T., Dai, A., and Fasullo, J. (2007). Estimates of the global water budget and its annual cycle using observational and model data. *J. Hydrometeor.* 8, 758–769. doi: 10.1175/JHM600.1

Valdivieso, M., Haines, K., Balmaseda, M., Chang, Y.-S., Drevillon, M., Ferry, N., et al. (2017). An assessment of air–sea heat fluxes from ocean and coupled reanalyses. *Clim. Dyn.* 49, 983–1008. doi: 10.1007/s00382-015-2843-3

Weller, R. A. (2015): Variability and trends in surface meteorology and air–sea fluxes at a site off Northern Chile. *Clim. J.* 28, 3004–3023. doi: 10.1175/JCLI-D-14-00591.1

Wilkinson, K., von Zabern, M., and Scherzer, S. (2014). *Global Freshwater Fluxes Into the World Oceans*. GRDC Report Series, UDATA Umweltschutz und Datenanalyse, Neustadt, 44, 9pp.

Xue, Y., Huang, B., Hu, Z.-Z., Kumar, A., Wen, C., Behringer, D., Nadiga, S. (2011). An assessment of oceanic variability in the NCEP climate forecast system reanalysis. *Clim Dyn.* 37, 2511–2539. doi: 10.1007/s00382-010-0954-4

Yin, Y., Alves, O., and Oke, P. (2011). An ensemble ocean data assimilation system for seasonal prediction. *Mon. Weather Rev.* 139, 786–808. doi: 10.1175/2010MWR3419.1

Yu, L. (2019). Global air–sea fluxes of heat, fresh water, and momentum: energy budget closure and unanswered questions. *Annu. Rev. Mar. Sci.* 11, 227–248. doi: 10.1146/annurev-marine-010816-060704

Yu, L., and Weller, R. A. (2007). Objectively analyzed air–sea heat fluxes for the global ice-free oceans (1981–2005). *Bull. Am. Meterol. Soc.* 88, 527–540. doi: 10.1175/BAMS-88-4-527

Conflict of Interest: The authors declare that the research was conducted in the absence of any commercial or financial relationships that could be construed as a potential conflict of interest.

frontiers in Marine Science

ORIGINAL RESEARCH
published: 22 March 2021
doi: 10.3389/fmars.2021.636881

Quantifying the Atmospheric CO_2 Forcing Effect on Surface Ocean pCO_2 in the North Pacific Subtropical Gyre in the Past Two Decades

Shuangling Chen[1], Adrienne J. Sutton[2], Chuanmin Hu[3] and Fei Chai[1,4]*

[1] State Key Laboratory of Satellite Ocean Environment Dynamics, Second Institute of Oceanography, Ministry of Natural Resources, Hangzhou, China, [2] National Oceanic and Atmospheric Admistration (NOAA) Pacific Marine Environmental Laboratory, Seattle, WA, United States, [3] College of Marine Science, University of South Florida, Tampa, FL, United States, [4] School of Marine Sciences, University of Maine, Orono, ME, United States

Despite the well-recognized importance in understanding the long term impact of anthropogenic release of atmospheric CO_2 (its partial pressure named as pCO_2air) on surface seawater pCO_2 (pCO_2sw), it has been difficult to quantify the trends or changing rates of pCO_2sw driven by increasing atmospheric CO_2 forcing ($pCO_2sw^{atm\_forced}$) due to its combination with the natural variability of pCO_2sw ($pCO_2sw^{nat\_forced}$) and the requirement of long time series data records. Here, using a novel satellite-based pCO_2sw model with inputs of ocean color and other ancillary data between 2002 and 2019, we address this challenge for a mooring station at the Hawaii Ocean Time-series Station in the North Pacific subtropical gyre. Specifically, using the developed pCO_2sw model, we differentiated and separately quantified the interannual-decadal trends of $pCO_2sw^{nat\_forced}$ and $pCO_2sw^{atm\_forced}$. Between 2002 and 2019, both pCO_2sw and pCO_2air show significant increases at rates of 1.7 ± 0.1 μatm yr^{-1} and 2.2 ± 0.1 μatm yr^{-1}, respectively. Correspondingly, the changing rate in $pCO_2sw^{nat\_forced}$ is mainly driven by large scale forcing such as Pacific Decadal Oscillation, with a negative rate (-0.5 ± 0.2 μatm yr^{-1}) and a positive rate (0.6 ± 0.3 μatm yr^{-1}) before and after 2013. The $pCO_2sw^{atm\_forced}$ shows a smaller increasing rate of 1.4 ± 0.1 μatm yr^{-1} than that of the modeled pCO_2sw, varying in different time intervals in response to the variations in atmospheric pCO_2. The findings of decoupled trends in $pCO_2sw^{atm\_forced}$ and $pCO_2sw^{nat\_forced}$ highlight the necessity to differentiate the two toward a better understanding of the long term oceanic absorption of anthropogenic CO_2 and the anthropogenic impact on the changing surface ocean carbonic chemistry.

Keywords: surface pCO_2, remote sensing, anthropogenic CO_2, sea surface temperature, North Pacific

OPEN ACCESS

Edited by:
Masao Ishii, Meteorological Research Institute (MRI), Japan

Reviewed by:
Nicolas Metzl, Centre National de la Recherche Scientifique (CNRS), France
Shin-ichiro Nakaoka, National Institute for Environmental Studies (NIES), Japan

****Correspondence:***
Shuangling Chen
slchen19@126.com;
slchen@sio.org.cn

Specialty section:
This article was submitted to Ocean Observation, a section of the journal Frontiers in Marine Science

Received: *02 December 2020*
Accepted: *01 March 2021*
Published: *22 March 2021*

Citation:
Chen S, Sutton AJ, Hu C and Chai F (2021) Quantifying the Atmospheric CO_2 Forcing Effect on Surface Ocean pCO_2 in the North Pacific Subtropical Gyre in the Past Two Decades. Front. Mar. Sci. 8:636881. doi: 10.3389/fmars.2021.636881

INTRODUCTION

Since industrialization, the global ocean has been a major sink of the increasing atmospheric CO_2, absorbing ~25% of anthropogenic CO_2 in recent years (Sabine et al., 2004a; Friedlingstein et al., 2019; Gruber et al., 2019). On one hand, the continuous ocean sink of atmospheric CO_2 (its partial pressure is named as pCO_2air) is changing ocean carbonic chemistry and the ocean carbon cycle

(Borges et al., 2005; Cai et al., 2006; Fujii et al., 2009; Landshützer et al., 2013; Wanninkhof et al., 2013; Xiu and Chai, 2014). On the other hand, the resulting ocean acidification has great potential to degrade marine ecosystems and marine biota, particularly the calcifying organisms such as shellfish and corals (Widdicombe and Spicer, 2008; Doney, 2010; Fabricius et al., 2011; Dickinson et al., 2012; Chan and Connolly, 2013; Davis et al., 2017). Both impacts are closely related to the sustainable development of the marine biota and ecology. Therefore, the anthropogenic effect on surface seawater carbonic chemistry and the potential of the ocean in absorbing anthropogenic CO_2 in the changing world are pressing concerns of the environmental research community.

At present, the study on anthropogenic CO_2 at the sea surface is quite limited. Instead, there are many studies on anthropogenic CO_2 in the ocean interior. The anthropogenic CO_2 stored in the ocean exists in various forms of carbon, originating from the cumulative CO_2 emissions from human activities (e.g., fossil fuel combustion, cement production, etc.) since the beginning of the Industrial Revolution. Several chemical and isotopic tracer approaches have been attempted to estimate the size of this pool of anthropogenic CO_2 (e.g., Sabine et al., 2002, 2004b; Lee et al., 2003; Quay et al., 2017; Gruber et al., 2019). However, due to the sparse measurements of chemical tracers in space and time, there is still significant uncertainty in the long-term accumulation rates of anthropogenic CO_2 and the potential of the ocean in continued absorption of anthropogenic CO_2, making it important to investigate the anthropogenic CO_2 variabilities at the sea surface.

One approach for tracking changes in surface pCO_2sw is through the collection of autonomous underway and mooring observations over the global ocean (e.g., Surface Ocean CO_2 Atlas (SOCAT, Bakker et al., 2016; Sutton et al., 2019). Many studies focused on the overall variabilities in surface pCO_2sw and CO_2 flux (e.g., Rödenbeck et al., 2015; Landshützer et al., 2016, 2019; Gregor et al., 2019; Denvil-Sommer et al., 2019; Iida et al., 2020 among others). However, because of the absence of isotope tracers in the autonomous observing systems of surface pCO_2sw, it is very challenging to estimate how much anthropogenic CO_2 emissions is driving measured pCO_2sw. Alternatively, it is known that surface pCO_2sw is affected by both increasing atmospheric CO_2 forcing (mainly caused by anthropogenic CO_2 emissions) and natural oceanic forcing (e.g., driven by oceanic physical and biogeochemical dynamics) (Fennel et al., 2008; Ikawa et al., 2013; Xue et al., 2016). The effect of atmospheric CO_2 forcing on surface pCO_2sw (named as $pCO_2sw^{atm\_forced}$ hereafter) actually refers to the changes of surface pCO_2sw driven by the increase of atmospheric CO_2. Since the increase of atmospheric CO_2 is due to anthropogenic emissions, the changing rates of $pCO_2sw^{atm\_forced}$ in the past decades can be used to infer the interannual-decadal variations of the anthropogenic signals in surface pCO_2sw. Yet the $pCO_2sw^{atm\_forced}$ should be differentiated from the total observed pCO_2sw because of the combination of the natural variability in surface pCO_2sw ($pCO_2sw^{nat\_forced}$). Here $pCO_2sw^{nat\_forced}$ refers to the remaining pCO_2sw component without atmospheric CO_2 forcing effect, which could be influenced by different physical and biogeochemical processes in the ocean, including the biological activities (i.e., photosynthesis and respiration), ocean warming driven by climate change and anthropogenic CO_2 emissions, and ocean mixing, etc. The effect of all these different processes was regarded as the overall natural oceanic forcing effect on surface pCO_2sw, It should be clarified that, although we regard all these different oceanic processes to be natural, their changes can still not be completely due to "natural" forcing because these changes in 2002–2019 inherently and implicitly contain atmospheric forcing.

Long time data records are needed to quantify the interannual-decadal trends of $pCO_2sw^{atm\_forced}$ and $pCO_2sw^{nat\_forced}$ in the ocean. Indeed, Sutton et al. (2019) analyzed the time scale of trend detection using 40 autonomous mooring time series of total observed surface pCO_2sw over the globe, and found that anthropogenic trend detection requires a minimum 8 and 16 years of data records for the sites studies in open ocean and coastal regions, respectively. However, the current global time series observation network of surface pCO_2sw just starts to approach these time scales, which has made it difficult to track the atmospheric forcing effect for most oceanic environments where the moorings are deployed. Several recent studies attempted to examine the anthropogenic trend in pCO_2sw based on underway measurements in the past decades (Takahashi et al., 2009, 2014; McKinley et al., 2011). For example, Takahashi et al. (2009, 2014) found that pCO_2sw is increasing at varying rates of $1.2 \pm 0.5 \sim 2.1 \pm 0.5$ μatm yr^{-1} in different ocean basins. However, the ship-based measurements are quite limited in both spatial and temporal coverage, leading to many uncertainties in the derived rates. More importantly, these rates are not exactly referring to the atmospheric forcing rates of surface pCO_2sw, because of the combination of natural variability (i.e., $pCO_2sw^{nat\_forced}$) as mentioned above and the difficulty to differentiate and quantify both $pCO_2sw^{atm\_forced}$ and $pCO_2sw^{nat\_forced}$ using *in situ* observations of surface pCO_2sw alone.

When combined with *in situ* surface pCO_2sw observations, satellite remote sensing has become an important tool for synoptic estimation of surface pCO_2sw (e.g., Lohrenz et al., 2010, 2018; Hales et al., 2012; Signorini et al., 2013; Bai et al., 2015; Chen et al., 2019). Without a spectroscopic method for direct measurements of surface pCO_2sw from space, it is possible to develop satellite-based pCO_2sw models through correlations with other related environmental variables. A satellite-based surface pCO_2sw model also makes it possible to differentiate $pCO_2sw^{atm\_forced}$ from $pCO_2sw^{nat\_forced}$. Indeed, satellite data accumulated in the past 20 years show great potential to quantify the interannual-decadal trends of the atmospheric forcing effect on pCO_2sw. However, the past remote sensing studies mainly focused on the retrieval of seasonal surface pCO_2sw (e.g., Lefèvre et al., 2005; Chierici et al., 2009; Zhu et al., 2009; Borges et al., 2010; Jo et al., 2012; Tao et al., 2012; Marrec et al., 2015; Parard et al., 2015; Le et al., 2019), and are quite limited in predicting interannual variability because of their insufficient parameterization of increasing atmospheric CO_2 forcing (Shadwick et al., 2010; Chen et al., 2019). Therefore, the satellite-based pCO_2sw algorithms need to be refined to

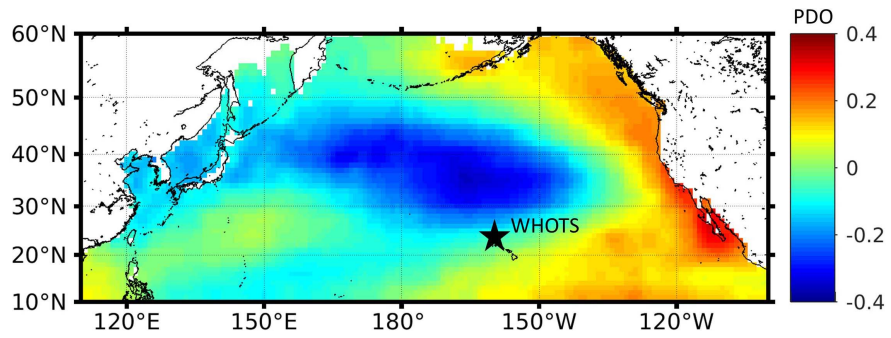

FIGURE 1 | The geolocation of the study site WHOTS (annotated in black star), and the general climate mode of the North Pacific in terms of PDO based on the HadISST data set (Rayner et al., 2003) for the period 1870–2019.

enable their capabilities in assessing the interannual trends of $pCO_2sw^{atm\_forced}$ and $pCO_2sw^{nat\_forced}$.

The Woods Hole Oceanographic Institution Hawaii Ocean Time-series Station (WHOTS) near Hawaii in the North Pacific Subtropical Gyre (NPSG) maintains high resolution surface pCO_2sw observations. It provides an important open ocean reference for Hawaiian coral reefs (Dore et al., 2003; Sutton et al., 2017; Terlouw et al., 2019), thus is important to know the interannual-decadal trends of the atmospheric forcing effect on surface pCO_2sw for a better understanding of the long-term ocean acidification and oceanic absorption of anthropogenic CO_2. The WHOTS station was selected mainly because it has sufficient field data records for anthropogenic trend detection as mentioned above. WHOTS is located at station ALOHA (A Long-term Oligotrophic Habitat Assessment) (Karl and Church, 2018) in the NPSG (**Figure 1**), under the large-scale climate forcing of Pacific Decadal Oscillation (PDO). Several published studies investigated the interannual variability of the upper ocean carbon cycle at this station (Dore et al., 2003, 2009; Keeling et al., 2004; Palevsky and Quay, 2017). For example, based on a 14-year time series (1988–2002) at ALOHA, Brix et al. (2004) found that surface pCO_2sw and isotopic $^{13}C/^{12}C$ showed long-term increase and decrease (yet no rates were provided), respectively, and they attributed it to the uptake of isotopically light anthropogenic CO_2 from the atmosphere. Using the same data time series of pCO_2sw at ALOHA, Dore et al. (2003) found that the significant decrease in CO_2 sink in 1989–2001 was driven by the climate variability in salinity (Lukas and Santiago-Mandujano, 2008). Later based on a longer data record of 19 years (1988–2007) at ALOHA, Dore et al. (2009) presented a pCO_2sw increasing rate of 1.88 μatm yr^{-1}. In contrast, with a synthesis of 35 years of observations in the North Pacific, Takahashi et al. (2006) found the interannual-decadal change in surface pCO_2sw is mostly correlated with the increases of sea surface temperature (SST) and anthropogenic CO_2. Therefore, it is necessary to further investigate the effects of both anthropogenic CO_2 emissions and the climate-driven natural variability in the ocean on surface pCO_2sw. However, to date, no studies have differentiated these two forcing effects.

Considering the importance of addressing this knowledge gap to promote our understanding of the ocean capability in absorbing anthropogenic CO_2 in the long run, here we for the first time differentiate the atmospheric forcing and natural forcing effects on surface pCO_2sw, that's, $pCO_2sw^{atm\_forced}$ and $pCO_2sw^{nat\_forced}$, based on a novel satellite-based pCO_2sw model developed in this study. Specifically, the objectives of this study include: (1) develop a satellite-based surface pCO_2sw model at WHOTS, which should be able to capture the interannual-decadal variabilities in pCO_2sw and differentiate $pCO_2sw^{atm\_forced}$ and $pCO_2sw^{nat\_forced}$, and (2) quantify the interannual-decadal trends of both terms in the past 2 decades, and understand its implications for ocean acidification and long term oceanic uptake of anthropogenic CO_2. Although the study was conducted at the WHOTS station, the findings in this study may provide insight on the interannual-decadal trends of pCO_2sw driven by atmospheric and natural forcing effects, respectively, in other global subtropical open ocean regions. More importantly, the approach developed in this study can be extended to other regions with sufficient data available.

DATA AND METHODS

Data

The WHOTS station (22.7°N, 158°W) is located in the subtropical oligotrophic region of the North Pacific and is operated by the Woods Hole Oceanographic Institution (WHOI). Field data time series [including surface pCO_2sw, and pCO_2air, SST, and sea surface salinity (SSS)] at this station collected between 2004 and 2018 at led by NOAA's Pacific Marine Environmental Laboratory and were obtained from the National Centers for Environmental information (NCEI)[1] (Sutton et al., 2012). Specifically, the pCO_2 data were measured by a non-dispersive infrared gas analyzer (LI-COR™, model LI-820), which has a sampling frequency of every 3 h, with an accuracy of 2 μatm (or better) (Sutton et al., 2014; Sabine et al., 2020). Surface pCO_2sw data were collected at a water depth of <0.5 m, and the pCO_2air data were collected at 1.2 m above the sea surface. SST and SSS were obtained from a CTD (SBE16) integrated in the autonomous CO_2 mooring system. The details of data collection, processing, and quality control can be found

[1]https://www.nodc.noaa.gov/ocads/oceans/Moorings/

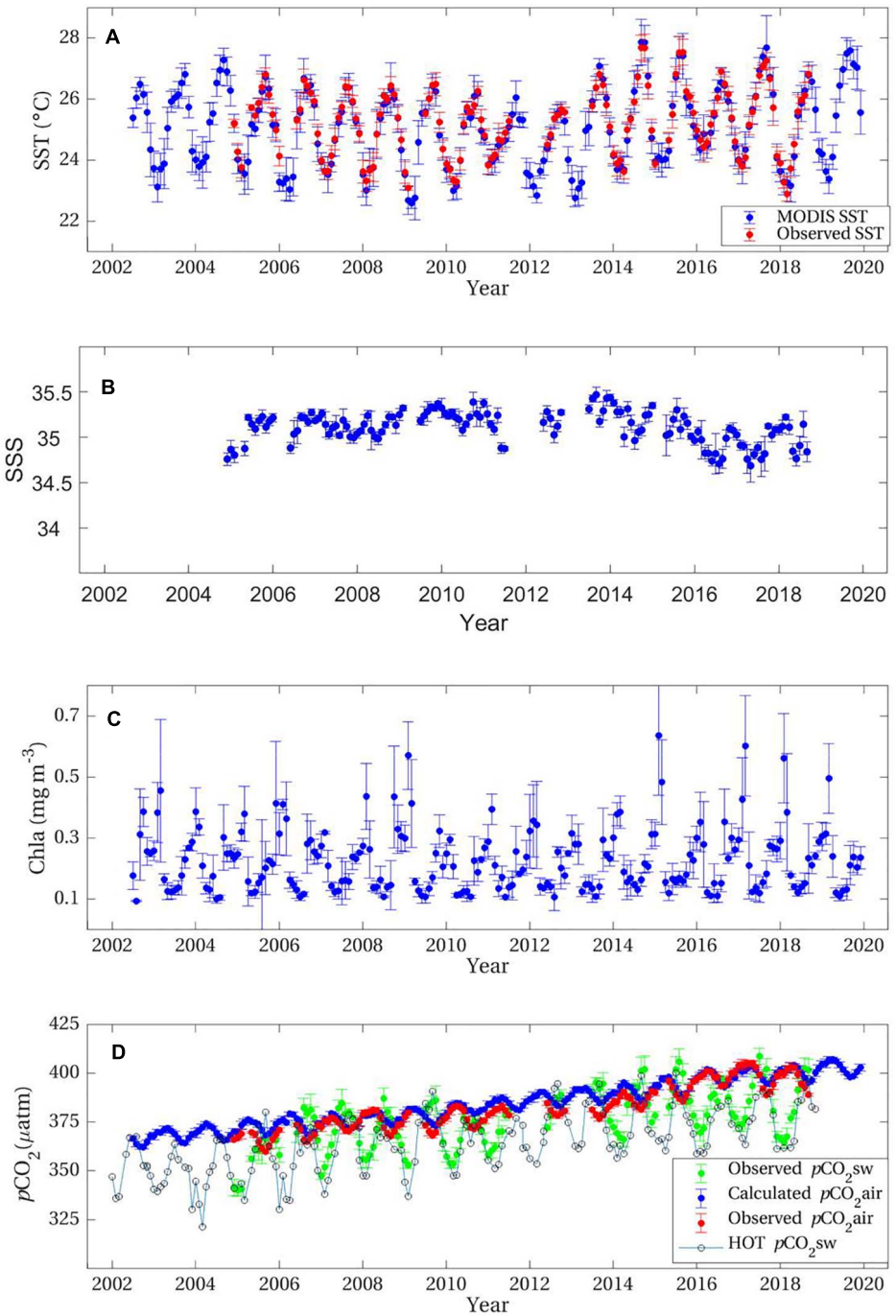

FIGURE 2 | Interannual variations of the monthly SST **(A)**, SSS **(B)**, Chla **(C)**, pCO_2air, and pCO_2sw **(D)** at the WHOTS station in the period of 2002–2019. Note that the ship-based monthly pCO_2sw time series at HOT calculated from DIC and TA measurements was overlaid in **(D)** for reference, and the calculated pCO_2air in **(D)** is based on the data of atmospheric CO_2 measured at MLO.

in Sutton et al. (2014). These data were binned to daily time series to remove the diurnal variations (i.e., 0.4∼3.4 μatm), which are not considered in this study. The data time series were then averaged at monthly scales as presented in in **Figures 2A,B,D**. The Hawaii Ocean Time-series (HOT) program also maintains ship-based monthly sampling of surface pCO_2sw calculated from dissolved inorganic carbon (DIC) and total alkalinity (TA) at this location (**Figure 2D**). We chose to use the high-frequency data from the WHOTS buoy mainly to assure that there are sufficient data available to develop the machine learning pCO_2sw model and the monthly averages of the modeled pCO_2sw should have lower bias than the monthly observed pCO_2sw at HOT.

NASA standard daily SST (**Figure 2A**) and 8 day Chlorophyll-a (Chla, mg m^{-3}) (**Figure 2C**) Level-3 data products (version R2018.0) covering the study region for the period of July 2002–December 2019 with a spatial resolution of ∼4 km were downloaded from the NASA Goddard Space Flight Center (GSFC)[2]. These Level-3 data products were derived from measurements by the Moderate Resolution Imaging Spectroradiometer (MODIS) on the Aqua satellite.

Clearly there are lots of data gaps in the field measurements (e.g., SST, pCO_2air, pCO_2sw, **Figures 2A,C**). Full record of SST is obtained from MODIS. For a full data record of pCO_2air at WHOTS between 2002 and 2019, daily time series of atmospheric xCO_2 (in unit of ppm) at Mauna Loa Observatory (MLO) in Hawaii between 2002 and 2019 were obtained from the NOAA ESRL Global Monitoring Laboratory (2019), and this data was regarded as the atmospheric xCO_2 at WHOTS over the study period considering the close distance between Mauna Loa and WHOTS. To calculate the corresponding pCO_2air at WHOTS from the atmospheric xCO_2 following the standard operating procedures (Weiss, 1974; Dickson et al., 2007), ancillary daily data of sea surface air pressure (in unit of atm) and specific humidity (in unit of%) were obtained from the National Centers for Environmental Prediction (NCEP), with a spatial resolution of 2.5°. The derived pCO_2air (**Figure 2D**) together with the MODIS data (**Figures 2A,C**) were used to estimate pCO_2sw between 2002 and 2019 based on the developed pCO_2sw model. It should be clarified that, for broader impact, one main reason in choosing MODIS SST and NCEP ancillary data instead of other *in situ* data at the WHOTS mooring was to demonstrate our model capability in dealing with the uncertainties in each parameter, particularly when extending our method to other locations or regions where field measurements could be limited.

Methods

Surface pCO_2sw is mainly controlled by four oceanic processes – the thermodynamic effect, biological activity, physical mixing, and air-sea CO_2 exchange (Fennel et al., 2008; Ikawa et al., 2013; Xue et al., 2016). Accordingly, satellite-derived variables of SST, SSS, and Chla are commonly used to estimate surface pCO_2sw from remote sensing in past studies (Olsen et al., 2004; Ono et al., 2004; Lohrenz and Cai, 2006; Sarma et al., 2006; Lohrenz et al., 2010, 2018; Nakaoka et al., 2013; Chen et al., 2016, 2017, 2019). However, these algorithms are quite limited in capturing the long-term trend in pCO_2sw, mainly because of the insufficient parameterization of the anthropogenic or atmospheric CO_2 forcing effect on pCO_2sw. Feely et al. (2006), and Landshützer et al. (2013, 2016) have investigated the interannual and decadal variations of pCO_2sw and CO_2 flux under the anthropogenic CO_2 forcing, yet to better quantify this effect, further studies are needed to differentiate the warming effect of SST from the atmospheric effect on surface pCO_2sw and quantify both effects separately.

Dore et al. (2003) found that the significant increase of pCO_2sw at ALOHA in 1989–2001 was mainly caused by the increase of SSS due to excess evaporation over this period, suggesting that the physical changes in the subtropical North Pacific may affect the ocean biogeochemistry including surface pCO_2sw. Yet in this study, SSS was found to have little effect on pCO_2sw (R = 0.102 at $p > 0.05$, which explains 1% nges in pCO_2sw) at the WHOTS station over the period of 2004∼2018, as also found by Sutton et al. (2017) which shows a small effect (<5%) of salinity changes on pCO_2sw increase. The SMOS satellite maintains the longest SSS data record since 2009 (Font et al., 2009, 2013), however, a comparison between the field SSS and SMOS-derived SSS shows a very large uncertainty of 1.1 for SSS ranging between 34.5 and 35.5 at WHOTS. As such, SSS was not used in the model. The mixed layer depth (MLD) could drive the interannual dynamics of surface pH at ALOHA (Dore et al., 2009), yet considering the lack of MLD data from remote sensing and the covariations of SST and MLD dynamics, we chose to use SST alone to indicate the effect of warming and mixing on surface pCO_2sw. Therefore, the inputs of the satellite pCO_2sw algorithm included observed SST and pCO_2air, and concurrent MODIS-derived Chla, as well as Julian day (Jday) normalized sinusoidally to "tune" the seasonal cycles of pCO_2sw (Friedrich and Oschlies, 2009; Signorini et al., 2013; Chen et al., 2016, 2017), and the output was modeled pCO_2sw (Eq. 1). In total, there were 3074 matched data samples between 2004 and 2017. Within this dataset, data samples collected in 2016 (N = 311) were kept for independent validation considering its near full coverage in each month (other years do not); the remaining were randomly divided into two groups: one for model training (N = 1,934), and the other for model validation (N = 829).

Various approaches have been used to model pCO_2sw from remote sensing, such as polynomial regression, mechanistic semi-analytical approach, machine-learning approaches (Friedrich and Oschlies, 2009; Jo et al., 2012; Landshützer et al., 2013; Bai et al., 2015; Moussa et al., 2016; Lohrenz et al., 2018). Chen et al. (2019) did extensive comparisons of these approaches and found that, the Random Forest based Regression Ensemble (RFRE) was the most robust one in modeling pCO_2sw. Therefore, this approach was used in this study with model parameters locally tuned for the WHOTS station (Eq. 1). RFRE is one type of machine learning technique, which ensembles many weighted regression trees to implement the random forest algorithm (Breiman, 1996, 2001; James et al., 2013) in Matlab (R2017a). For better model generalization, the RFRE takes advantage of each regression tree via bootstrap aggregation (or bagging) (Breiman, 1996; James et al., 2013) in model parameterization. In the model training phase, the ensemble regression trees grow independently on a drawn bootstrap replica of the training dataset. That's, each regression tree can randomly select a subset of predictors at each split and can involve many splits in the algorithm. This manipulation greatly reduces the correlations among the developed regression trees, resulting in improved independency among the regression trees. The mean square error was used as loss function to adjust the model performance in each iteration. Briefly, there are two important parameters to define the RFRE model structure: the minimum leaf size and the number of regression trees. Leaf size refers to the number of data samples used in each node of a regression tree, and its minimum thus determines the splits and depth of a regression tree. By trial

[2]https://oceancolor.gsfc.nasa.gov/

and error, these two parameters were optimized to be 8 and 28, respectively. With these settings, the RFRE model became stable and had the best model statistics, thus it was used to predict pCO_2sw. See Chen et al. (2019) for more details of the RFRE approach.

$$Modeled\ pCO_2sw = f_{RFRE}[SST, log_{10}(Chla), pCO_2air, cos(2\pi \times Jday/365)] \quad (1)$$

Standard statistical measures, including root mean square difference (RMSD, both absolute and relative), coefficient of determination (R^2), mean bias (MB), mean ratio (MR), unbiased percent difference (UPD), and mean relative difference (MRD) (Barnes and Hu, 2015), were used to quantify the accuracy of the modeled pCO_2sw.

We varied SST, Chla, and pCO_2air by ± 1°C, and ± 20%, and ± 5 μatm, respectively, to examine the sensitivity of the model to changes in each variable. The changes are based on the uncertainties in the MODIS-derived SST and Chla (Gregg and Casey, 2004; Mélin et al., 2007; Hu et al., 2009) as well as on the seasonal variations in pCO_2air.

The modeled pCO_2sw is the sum of $pCO_2sw^{atm\_forced}$ and $pCO_2sw^{nat\_forced}$. Just as its name implies, the $pCO_2sw^{nat\_forced}$ refers to the pCO_2sw without atmospheric CO_2 forcing, thus based on the model developed following Eq. 1, the $pCO_2sw^{nat\_forced}$ was calculated by assuming that the pCO_2air remained at the same level as in in the start year (i.e., 2002) of the study period (Eq. 2). The $pCO_2sw^{atm\_forced}$ was defined as the difference between the modeled pCO_2sw (Eq. 1) and $pCO_2sw^{nat\_forced}$ (Eq. 3). To quantify the natural forcing effect, the net atmospheric CO_2 forcing effect over the study period (2002–2017) remained at exactly zero by keeping the pCO_2air values in the model at the same level as in 2002. By doing so, both the derived $pCO_2sw^{nat\_forced}$ and $pCO_2sw^{atm\_forced}$ are relative quantities to the year of 2002, which should be higher than those derived by referring to pre-industrialization. However, either referring to 2002 or other years only affects the absolute values of these quantities, and they would affect the changing rates of trends in both $pCO_2sw^{nat\_forced}$ and $pCO_2sw^{atm\_forced}$ in the past two decades that we are interested in.

$$pCO_2sw^{nat\_forced} = f_{RFRE}[SST, log_{10}(Chla), pCO_2air_{@2002}, cos(2\pi \times Jday/365)] \quad (2)$$

where the $pCO_2air_{@2002}$ means the pCO_2air data in 2002–2019 remained at the same level as in 2002 by assuming that there is no additional atmospheric effect referred to 2002.

$$pCO_2sw^{atmp\_forced} = pCO_2sw - pCO_2sw^{nat\_forced} \quad (3)$$

Trends in pCO_2sw, $pCO_2sw^{atm\_forced}$, $pCO_2sw^{nat\_forced}$, pCO_2air, SST, and Chla were quantified based on their monthly anomalies, which were derived by subtracting the monthly climatologies from the monthly averages between 2002 and 2019 using least-square technique.

RESULTS

Figure 3 shows the performance of the RFRE-based pCO_2sw algorithm in both model training and validation. Clearly, most of the data pairs of the observed and modeled pCO_2sw followed closely along the 1:1 line, with a RMSD of 2.2 μatm (0.6%) and R^2 of 0.98. The additional independent validation (**Figure 4**) using the data time series in 2016 also shows good consistency between the observed pCO_2sw and modeled pCO_2sw, with a RMSD of 4.3 μatm (1.1%) and R^2 of 0.87.

The RFRE model is more sensitive to changes in SST and pCO_2air than to changes in Chla (**Figure 5**). Statistically, with + 1°C (-1°C) added to SST, the modeled pCO_2sw was higher (lower) than the original pCO_2sw, with RMSD of 9.7 μatm (2.6%) [8.0 μatm (2.1%)], R^2 of 0.89 (0.93), and MB of 8.5 μatm (-6.8 μatm). The resulting pCO_2sw shows slight underestimation and overestimation in cases of 20% increase and 20% decrease in Chla, with MB of 1.3 and −1.3 μatm, respectively. With + 5 μatm in pCO_2air, the new pCO_2sw was estimated higher than the original pCO_2sw, with RMSD of 5.7 μatm (1.6%), R^2 of 0.90, and MB of 3.7 μatm. With −5 μatm in pCO_2air, the new pCO_2sw was

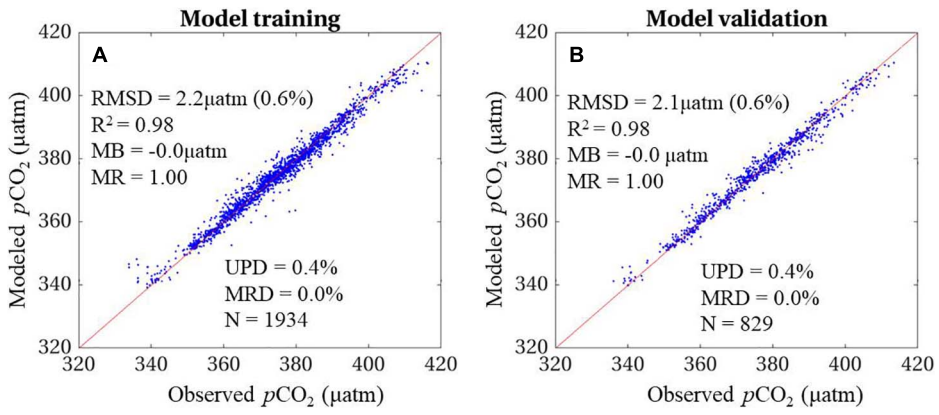

FIGURE 3 | The RFRE model performance in estimating surface pCO_2sw in both model training **(A)** and model validation **(B)**.

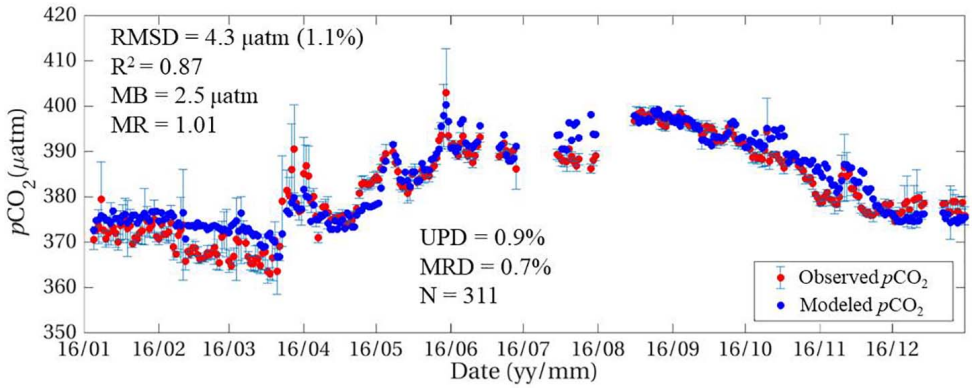

FIGURE 4 | The RFRE model performance in reconstructing the surface pCO_2sw data time series in 2016, in comparison with the corresponding mooring-observed surface pCO_2sw. Note that none of the field observations in 2016 was used in the model development. The error bar represents one standard deviation of the diurnal changes of pCO_2sw time series.

underestimated compared to the original pCO_2sw with RMSD of 6.1 µatm (1.6%), R^2 of 0.89 and MB of −4.2 µ atm.

In the North Pacific subtropical gyre at the WHOTS station, time series of pCO_2sw between 2002 and 2019 was obtained using this RRFE-based pCO_2sw algorithm, with good consistency to the observed pCO_2sw in the overlapped time periods (**Figure 6**). Overall, the pCO_2sw follows the same seasonal pattern as SST from high values in summer to low values in winter, with a seasonal magnitude of ∼50 µatm, in the opposite phase of pCO_2air (**Figure 6**). In addition, the pCO_2sw was lower than the pCO_2air most of the time over the years, suggesting a continuous CO_2 flux from the atmosphere to the ocean.

Both pCO_2sw and pCO_2air show significant increase between 2002 and 2019 (**Figure 6**). After removing the seasonality signals, statistically, the pCO_2sw had a mean rate of 1.7 ± 0.1 µatm yr^{-1} (R^2 = 0.80, at $p < 0.05$), lower than the rate of pCO_2air (2.2 ± 0.1 µatm yr^{-1}, R^2 = 0.99, at $p < 0.05$), as shown in **Figure 7**. The $pCO_2sw^{nat\_forced}$ shows a significant increasing rate of 0.2 ± 0.1 µatm yr^{-1} (R^2 = 0.07, at $p < 0.05$) on average in the study period. In contrast, the $pCO_2sw^{atm\_forced}$, which is just driven by the atmospheric CO_2 forcing, had a mean rate of 1.4 ± 0.1 µatm yr^{-1} (R^2 = 0.84, at $p < 0.05$), but tended to plateau since 2016. Indeed, the pCO_2sw without the thermodynamic effect (i.e., pCO_2nonT, Chen and Hu, 2019) had similar interannual patterns as pCO_{2ant} at a mean rate of 1.2 ± 0.1 µatm yr^{-1}. Correspondingly, the Chla time series did not show any trends over the years while the SST was increasing at an overall rate of 0.03 ± 0.01°C yr^{-1} (R^2 = 0.07, at $p < 0.05$). This warming trend could be influencing the $pCO_{2natural}$ trend.

Clearly, there are some visible trends (e.g., <10 years) particularly in SST and $pCO_2sw^{nat\_forced}$ different from those over the 20-year time frame (**Figure 7**). To further investigate the trends in each variable, we quantified the rates of each for a variety of periods starting between 2002 and 2015, ending between 2006 and 2019, with durations ranging from 5 to 18 years (**Figure 8**). It is found that, at confidence level of >95%, the SST had a negative and positive rate of −0.1 ± 0.02°C yr^{-1} and 0.1 ± 0.05°C yr^{-1} for periods ending in ≤2013 and >2013, respectively (**Figure 8A**). Again, the Chla did not show any trend over the years. Correspondingly, $pCO_2sw^{nat\_forced}$ shows a very similar pattern as the rates in SST, with a negative rate of −0.5 ± 0.2 µatm yr^{-1} for periods ending in ≤2013, and a positive rate of 0.6 ± 0.3 µatm yr^{-1} for periods ending in >2013. The anthropogenic forcing on atmospheric pCO_2 tends to accelerate over the study period consistent with the published studies (Canadell et al., 2007), with a rate of 1.7 ± 0.1 µatm yr^{-1} for periods ending in ≤2011, and a rate of 2.3 ± 0.2 µatm yr^{-1} for periods ending in beyond 2011, and the acceleration is getting even stronger (2.4 ± 0.1 µatm yr^{-1}) after 2016. As a result, the pCO_2sw shows a lower rate (1.5 ± 0.4 µatm yr^{-1}) for periods starting in 2002–2005, ending in 2006–2019; a higher rate (2.2 ± 0.3 µatm yr^{-1}) for periods starting in 2006–2013, ending in 2010–2017; and a lower rate (1.5 ± 0.4 µatm yr^{-1}) again for periods starting in 2006–2013, ending in 2018–2019. Correspondingly, the $pCO_2sw^{atm\_forced}$ shows similar but significantly weaken signals (at $p < 0.05$) in these three time frames, with rates of 1.6 ± 0.3 µatm yr^{-1}, 1.8 ± 0.5µatm yr^{-1}, and 0.9 ± 0.5 µatm yr^{-1}, respectively.

DISCUSSION

Model Uncertainty

The satellite-based RFRE pCO_2sw model developed in this study had a RMSD of 4.3 µatm (1.1%), significantly smaller than most of the published pCO_2sw algorithms in open ocean waters (Olsen et al., 2004; Feely et al., 2006; Nakaoka et al., 2013; Moussa et al., 2016). This uncertainty is reasonably acceptable considering the diurnal variations (i.e., 0.4∼3.4 µatm) in surface pCO_2sw at WHOTS.

The sensitivity of the pCO_2sw model to each input variable indicates not only the model's capacity in tolerating the uncertainty of each variable, but also the model's response to real changes in each variable. Specifically, the positive feedback of modeled pCO_2sw to changes in SST are consistent with the thermodynamic effect on pCO_2sw (increased SST leads to

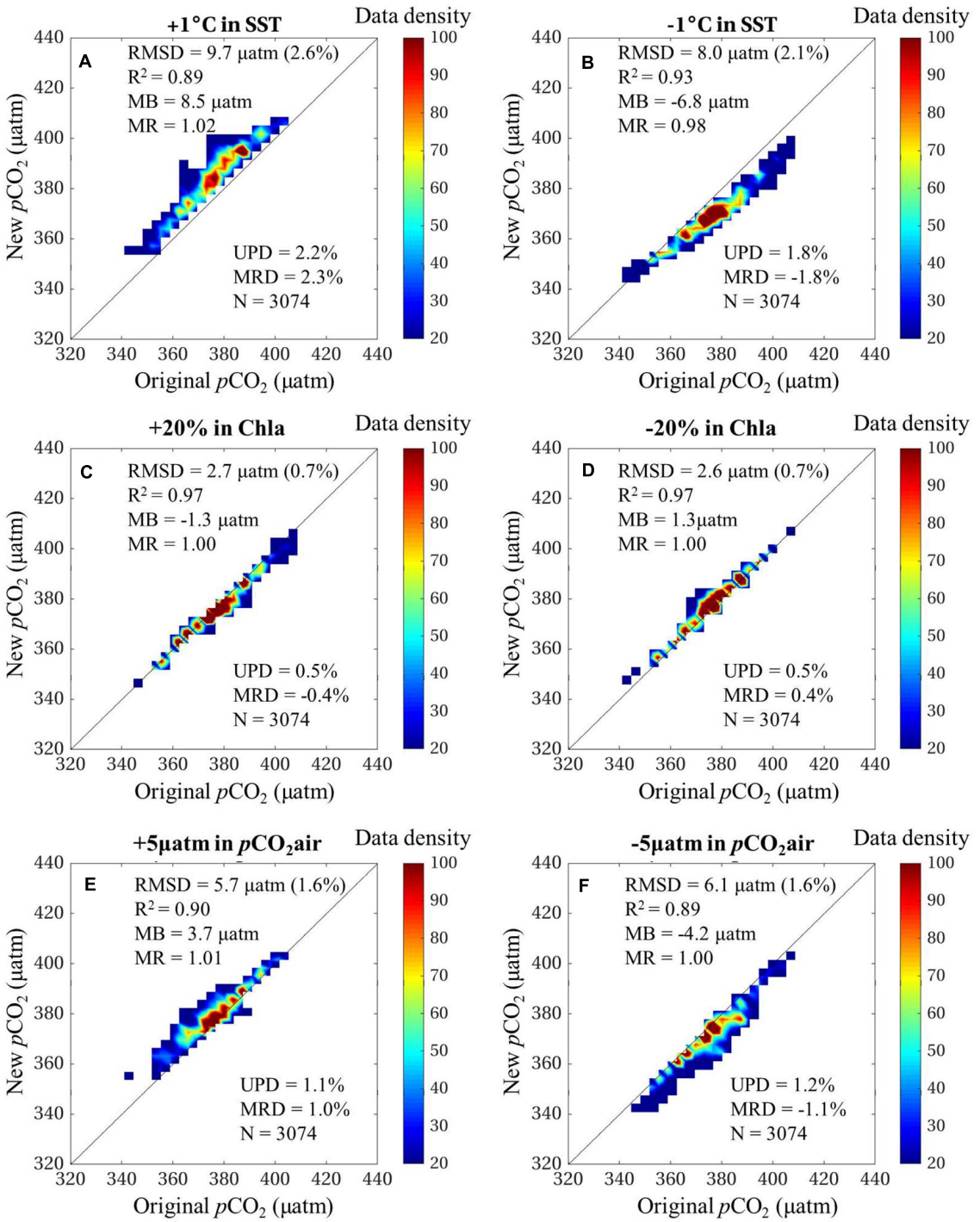

FIGURE 5 | Sensitivity of the RFRE pCO_2sw algorithm to uncertainties in satellite-derived SST **(A,B)** and Chla **(C,D)** and to the natural variability of pCO_2air **(E,F)**.

an increase in pCO_2sw and vice versa). The negative response of the pCO_2sw model to Chla suggests that the increase (decrease) in Chla indicates stronger (weaker) biological uptake of oceanic CO_2, therefore, the resulting modeled pCO_2sw was lower (higher) than without the Chla perturbation. Although the Chla level at the WHOTS station is consistently low (**Figure 2C**), the sensitivity analysis here suggests the necessity of including Chla in the model to better modulate the seasonal variations of surface pCO_2sw. Yet it should be noted that, Chla is only a proxy to indicate the overall biological activities that could affect surface pCO_2sw. Although there is no visible change in surface Chla, still there could be possible changes in the phytoplankton

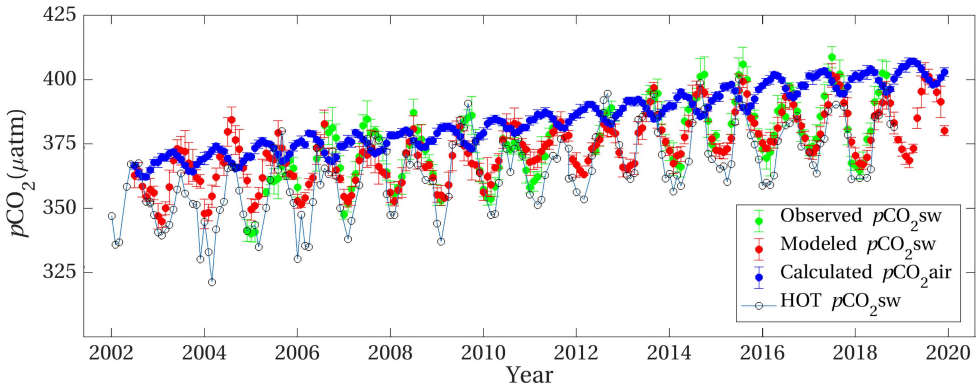

FIGURE 6 | Modeled pCO_2sw in the full time period between 2002 and 2019, in comparison with the mooring-observed surface pCO_2sw and calculated pCO_2air at WHOTS. Note that the calculated pCO_2air is based on the data of atmospheric CO_2 measured at MLO.

community and net community production. The insignificant responses of the pCO_2sw model to the 20% change in Chla suggest the model is insensitive to uncertainties in the satellite Chla. For the same reason, the biological uptake of CO_2 tends to have a quite limited effect on pCO_2sw in the oligotrophic ocean, consistent with previous studies (Chen and Hu, 2019). For regions where satellite Chla is not available due to severe cloud coverage (e.g., some tropical and high latitude zones), a first examination of the Chla effect on surface pCO_2sw using field observations (if there are) is suggested to determine the potential bias that would be resulted in pCO_2sw if Chla is not included in the model. The changes of pCO_2air directly affect the gradient between pCO_2air and pCO_2sw, which drives the air-sea CO_2 exchange, thus, it is reasonable to see a positive response of the pCO_2sw model to changes in pCO_2air. The resulting increase (MB = 3.7 μatm) in pCO_2sw was slightly weaker than the assigned increase of 5 μatm in pCO_2air, which may be due to the ocean's increasing Revelle Factor and reduced buffering capacity of seawater (Fassbender et al., 2017).

Interannual Changes of pCO_2sw Driven by Natural and Atmospheric Forcing

In response to the accelerating rates of pCO_2air, the modeled surface pCO_2sw shows different rates at various time intervals. Specifically, the 5 year pCO_2sw trends we derived for the periods of 2007–2011, 2008–2012, and 2009–2013 are high at rates of 2.5, 2.1, and 2.5 μatm yr^{-1}, respectively, which are higher than the relatively low rates in period of 2003–2007 visually interpreted from Figure 1 in Dore et al. (2009). To further examine the trends in pCO_2sw, we analyzed the ship-based monthly pCO_2sw datasets at ALOHA from HOT program (used in Dore et al., 2009). Indeed, the 5 year HOT-based pCO_2sw trends starting in 2007–2008 did show low values, but these low values are insignificant at $p > 0.05$, yet no such statistics was available in Dore et al. (2009). For the 5 year pCO_2sw trend starting in 2009, the HOT-based pCO_2sw and our modeled pCO_2sw show close trends of 2.5 and 2.2 μatm yr^{-1}, respectively, at $p < 0.05$. Meanwhile, the overall trend we detected in surface pCO_2sw (i.e., 1.7 $\pm$ 0.1μatm yr^{-1}) in period of 2002–2019 was a bit smaller than that (i.e., 1.88 μatm yr^{-1}) in period of 1988–2007 found in Dore et al. (2009) and that (i.e., 2.4 μatm yr^{-1}) in period of 2003–2014 presented in Sutton et al. (2017). This could be reasonable considering the different physical and biogeochemical dynamics on decadal time scales and the acceleration of ocean acidification in the western North Pacific (Ono et al., 2019). Besides, it should be noted that the ship-based monthly pCO_2sw dataset is derived from measurements of DIC and TA collected approximately once a month to compose this monthly dataset. In contrast, our monthly pCO_2sw is based on the daily modeled pCO_2sw and is validated thoroughly with daily-averaged *in situ* measurements at WHOTS. Therefore, the trends in the modeled pCO_2sw we derived here should be reliable with high confidence. Also, the mooring measures pCO_2sw at surface of <0.5 m, while the ship-based HOT data were based on the mean measurements within 0–30 m, which could be another potential source for the discrepancy. In the North Pacific subtropical gyre (represented by the WHOTS station), the interannual changes of surface pCO_2sw is mainly driven by both SST and pCO_2air (**Figures 7**, **8** and **Table 1**), consistent with the published studies (Takahashi et al., 2006). Despite the little impact of SSS on pCO_2sw shown in our study period (2002–2019), a further experiment with SSS added into our model was conducted. It shows that the inclusion of SSS did not result in any significant difference in the modeled pCO_2sw and $pCO_2sw^{nat\_forced}$. Considering the important impact of SSS on pCO_2sw in 1989–2007 presented in Dore et al. (2003), it seems that the effect of SSS depends on the specific study periods. Here we prefer to exclude SSS from our model mainly considering the large error (i.e., 1.1) in the SMOS SSS at present. With more accurate SSS data available from satellites in the future, it could be possible to include SSS to better model the variations of pCO_2sw, particularly the effect of rainfall minus precipitation on pCO_2sw in any time periods. However, most of the published studies directly regarded the interannual trend of pCO_2sw as the trend of anthropogenic pCO_2sw. It should be noted that the anthropogenic pCO_2sw refers to the pCO_2sw impacted by atmospheric CO_2 increases, thus most of the reported anthropogenic trend of pCO_2sw actually refers to

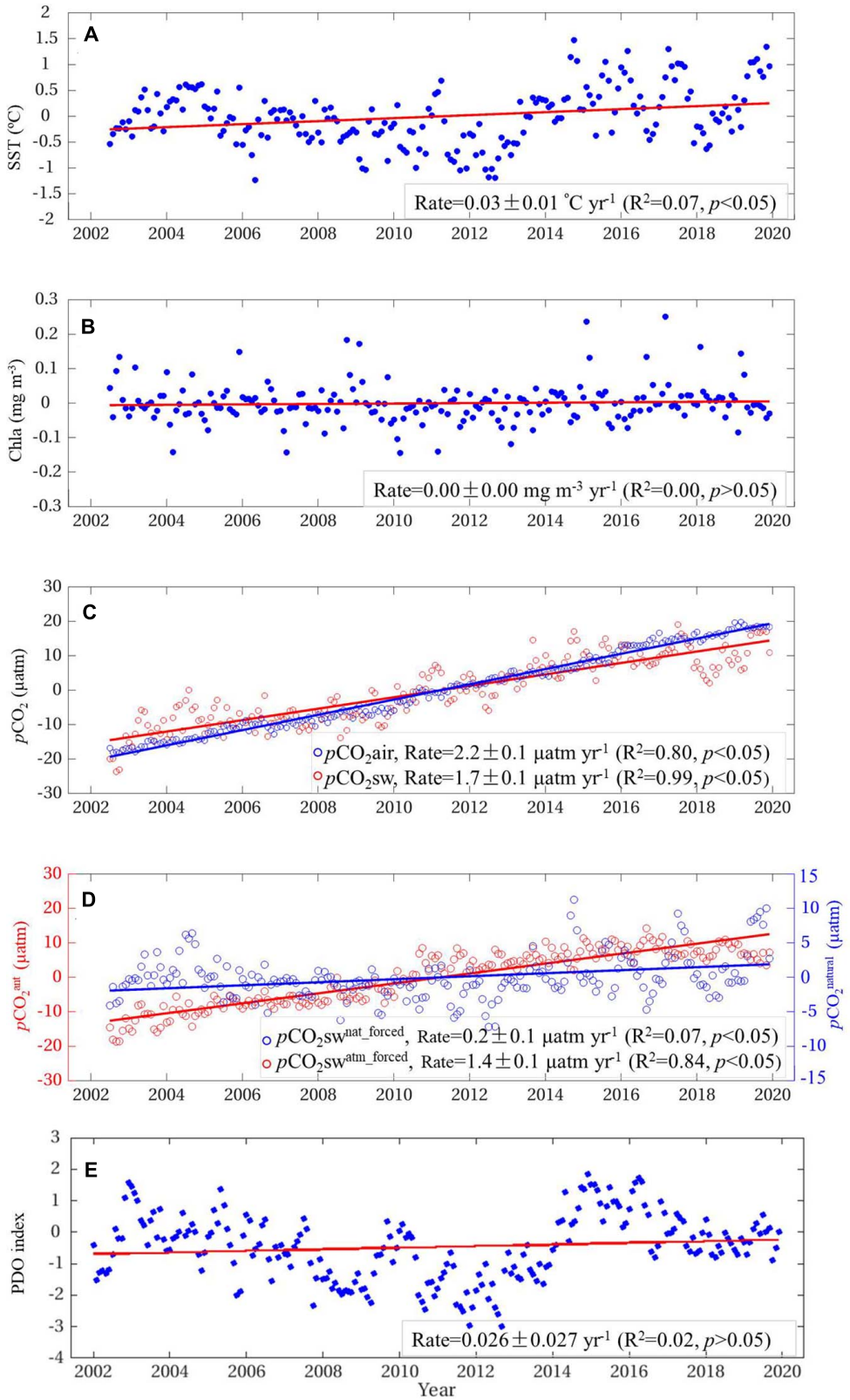

FIGURE 7 | Interannual variations of the monthly anomalies in SST **(A)**, Chla **(B)**, pCO_2air and modeled pCO_2sw **(C)**, modeled $pCO_2sw^{nat\_forced}$ and $pCO_2sw^{atm\_forced}$ **(D)**, and PDO index **(E)** in the period of 2002–2019.

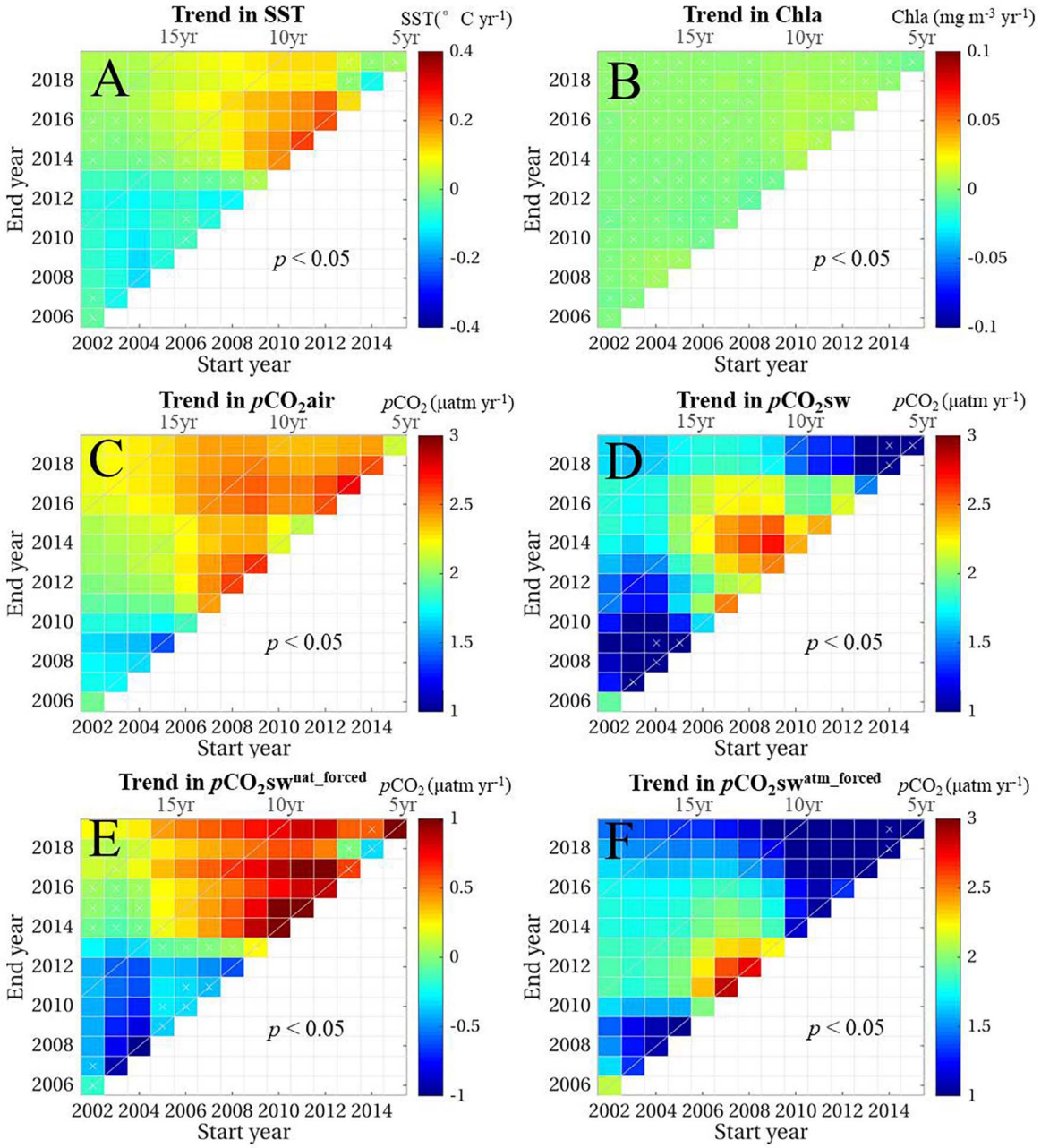

FIGURE 8 | Interannual changing rates of SST **(A)**, Chla **(B)**, pCO_2air **(C)**, modeled pCO_2sw **(D)**, modeled $pCO_2sw^{nat\_forced}$ **(E)**, and $pCO_2sw^{atm\_forced}$ **(F)** for a variety of periods starting between 2002 and 2015, and ending between 2006 and 2019 at Station WHOTS. The X-axis and Y-axis represent the start year and end year, respectively, of each rate analyzed. The diagonal lines (i.e., 5, 10, and 15 years) indicate the length of trend periods. A white cross is superposed on the plot when the p value was >0.05.

the total rate of pCO_2sw (Takahashi et al., 2009, 2014; McKinley et al., 2011; Sutton et al., 2019), which also includes the natural variability of pCO_2sw driven by the general oceanic processes (e.g., thermodynamics, ocean mixing, biological activities).

In this study, both the natural and atmospheric CO_2 forcing effects on pCO_2sw were separately quantified. The rates in $pCO_2sw^{nat\_forced}$ over the study period follow a similar pattern as those in SST with a correlation coefficient (R) of 0.82, indicating that the interannual trend signals in $pCO_2sw^{nat\_forced}$ are mainly driven by SST, at least over the study period of 2002–2019. The cooling characteristics in SST between 2002 and 2012 resulted in a significant negative rate in $pCO_2sw^{nat\_forced}$, and the warming effect since 2013, which were also reported in previous studies (Sutton et al., 2017; Terlouw et al., 2019), leads to a significant positive rate in $pCO_2sw^{nat\_forced}$. In addition to the global warming effect on SST, the interannual SST dynamics could also be attributed to the changes in MLD because of the ocean mixing effect on SST. As such, the interannual variations

in $pCO_2sw^{nat\_forced}$ could also be driven by the MLD changes, and more DIC enriched waters would be entrained into the surface when MLD deepens and SST decreases (Dore et al., 2009). Overall, it seems that the rate of $pCO_2sw^{nat\_forced}$ tends to correspond to decadal oscillations in SST between cooling and warming periods associated with PDO (Yasunaka et al., 2014; Newman et al., 2016; Landshützer et al., 2019). Indeed, the interannual PDO (**Figure 7E**) shows very similar variation patterns to the SST (**Figure 7A**) with a significant correlation of $R = 0.53$ (**Table 1**). Specifically, the PDO decreased progressively from 2004 to 2012, was low in 2011–2012, reached a maximum in 2015, and then decreased from 2015 to 2019. As a result, the $pCO_2sw^{nat\_forced}$ also shows a significant correlation ($R = 0.41$, see **Table 1**) with PDO, suggesting the large scale climate forcing also contribute to the natural oceanic forcing effect on surface pCO_2sw.

With the exclusion of $pCO_2sw^{nat\_forced}$, the $pCO_2sw^{atm\_forced}$ rates were significantly smaller than the corresponding pCO_2sw rates in various time intervals (**Figure 8**). Although $pCO_2sw^{atm\_forced}$ is mainly driven by the oceanic uptake of increasing atmospheric CO_2 ($R = 0.91$), it shows distinctively different patterns in changing rates from that of the pCO_2air over various time intervals in 2002–2019. This different response of $pCO_2sw^{atm\_forced}$ toward pCO_2air seems mainly caused by the buffering effect of dissolved CO_2 in seawater (Egleston et al., 2010). However, for the tendency of $pCO_2sw^{atm\_forced}$ to plateau after 2016, there could be several potential explanations depending on the condition of air-sea CO_2 fluxes. Specifically, it would be reasonable to observe a plateau signal in $pCO_2sw^{atm\_forced}$ if there is little change in air-sea CO_2 fluxes after 2016; yet if the dissolved CO_2 keeps increasing after 2016, the little response in $pCO_2sw^{atm\_forced}$ would tend to suggest that a larger fraction of dissolved CO_2 stays in forms of other carbonate species (i.e., HCO_{3-}, CO_{32-}), significantly lowering the Revelle factor and enhancing the ocean's buffering capacity in recent years; and if there is a decrease in air-sea CO_2 fluxes after 2016, it would be likely that a fration of bicarbonate and carbonate species are converted to dissolved CO_2, which would lower the ocean's buffering capacity and promote ocean acidification. Xue and Cai (2020) found that TA minus DIC can be used as a proxy for deciphering ocean acidification. Here using the ship-based monthly TA and DIC data in the study period, we found a significant decreasing trend in TA minus DIC over the years (**Figure 9A**), which suggests a strong ocean acidification in the study period. However, the changing rates of TA minus DIC is distinctively higher in recent years since 2014 (**Figure 9B**), suggesting a stronger ocean acidification and weaker buffering capacity in the past few years. Indeed, ocean acidification has shifted the carbonate chemistry speciation and lowered the $CaCO_3$ saturation state (Orr et al., 2005; Doney et al., 2009; Krug et al., 2011), yet further studies are needed to investigate and quantify the changing patterns of the air-sea CO_2 flux and the carbonate species over the past decades. In general, the oceanic uptake of anthropogenic CO_2 is resulting in more rapid changes in carbonic chemistry in the surface ocean and accelerating ocean acidification (Feely et al., 2009; Ono et al., 2019), yet a revisit of such phenomenon is needed when more satellite/field data are available in the coming years.

Implications

Long time series data are required to investigate the anthropogenic effect on surface pCO_2sw. However, the field data are always limited in both spatial and temporal coverage. For example, few of the 40 global pCO_2sw mooring stations have data coverage of >10 years (Sutton et al., 2019), and the global field pCO_2sw database (i.e., SOCAT or LDEO, Bakker et al., 2016; Takahashi et al., 2019), although greatly accumulated in recent years, still has data gaps in some regions and at some time intervals. More importantly, it is impossible or difficult to separate the $pCO_2sw^{atm\_forced}$ and $pCO_2sw^{nat\_forced}$ signals apart based on purely field measurements to better quantify the anthropogenic forcing impact on surface pCO_2sw. Instead, with the related environmental variables observed from satellites, surface pCO_2sw models using satellite data and other ancillary data can be developed and applied to the full satellite data record over the past ∼20 years. Besides, SSS measurements from SMOS and SMAP satellite have been available since 2009 and 2015, respectively, with longer and accurate data records available, the interannual and decadal trends in surface pCO_2sw as well as the natural forcing and atmospheric CO_2 forcing components can be further studied. The recovered long time series of pCO_2sw can be used to quantify both $pCO_2sw^{atm\_forced}$ and $pCO_2sw^{nat\_forced}$ accordingly. The findings of decoupled changing rates in $pCO_2sw^{atm\_forced}$ and $pCO_2sw^{nat\_forced}$ in this study highlight the necessity of differentiating the two, in order to have a better understanding of the long term oceanic absorption of anthropogenic CO_2 and its buffering capacity in the long term. Therefore, this study sets a template for future study to examine both natural and anthropogenic or atmospheric CO_2 forcing effects on pCO_2sw in various oceanic systems over the past

TABLE 1 | Correlation coefficients among the monthly anomalies of pCO_2sw, $pCO_2sw^{nat\_forced}$, $pCO_2sw^{atm\_forced}$, SST, Chla, pCO_2air, and PDO index, with insignificant correlation (i.e., $p > 0.05$) annotated in italic.

Correlation coef.	pCO_2sw	$pCO_2sw^{nat\_forced}$	$pCO_2sw^{atm\_forced}$	SST	Chla	pCO_2air	PDO index
pCO_2sw	1	/	/	/	/	/	/
$pCO_2sw^{nat\_forced}$	0.54	1	/	/	/	/	/
$pCO_2sw^{atm\_forced}$	0.89	*0.11*	1	/	/	/	/
SST	0.52	0.82	0.18	1	/	/	/
Chla	*-0.04*	*-0.13*	*0.02*	*-0.03*	1	–	/
pCO_2air	0.89	0.26	0.91	0.27	*0.06*	1	/
PDO index	0.19	0.41	*0.01*	0.53	*0.06*	*0.12*	1

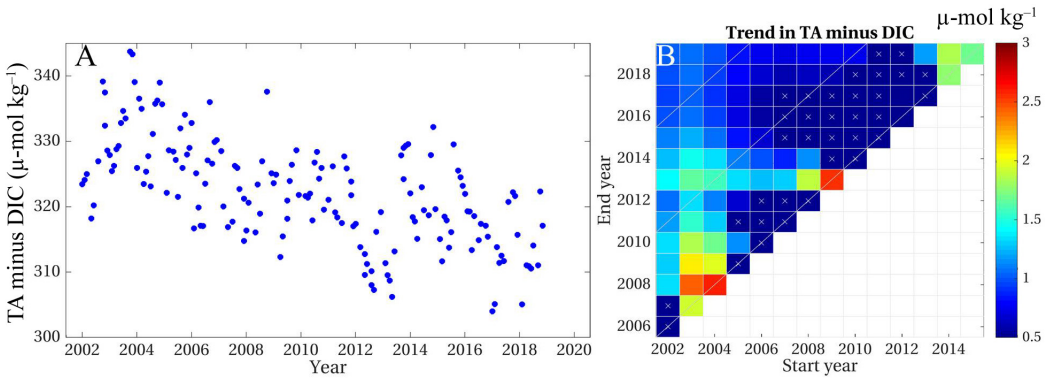

FIGURE 9 | The interannual variations of the monthly anomalies in TA minus DIC, which was a proxy of ocean acidification, based on the ship-based monthly TA and DIC measurements at ALOHA in surface waters **(A)**, and the corresponding interannual changing rates for a variety of periods starting between 2002 and 2015, and ending between 2006 and 2019 **(B)**. In **(B)**, the X-axis and Y-axis represent the start year and end year, respectively, of each rate analyzed, the diagonal lines (i.e., 5, 10, and 15 years) indicate the length of trend periods, and a white cross is superposed on the plot when the *p*-value was >0.05.

decades, toward an improved understanding of anthropogenic forcing on surface pCO_2sw.

Specifically, the pCO_2sw in the North Pacific subtropical gyre shows various increase rates in response to the increasing pCO_2air between 2002 and 2019. The accelerating increase rates in pCO_2air and the weaker rates in pCO_2sw indicate stronger gradients between pCO_2air and pCO_2sw, which implies an accelerated oceanic CO_2 uptake and ocean acidification. If the warming effect continues following the decadal pattern in SST in recent years since 2010, a steady rate of $\sim 0.8 \pm 0.1$ μatm yr^{-1} in $pCO_2sw^{nat\_forced}$ (see **Figure 8E**) would be expected in the coming few years. The weaker rate in $pCO_2sw^{atm\_forced}$ in recent years in response to the accelerating rate in pCO_2air implies a lower ocean buffering capacity leading to more rapidly changing oceanic carbon chemistry and ocean acidification, yet further study in this field is needed to promote our knowledge and understanding.

Based on observations at WHOTS, the present work demonstrated the necessity in differentiating the atmospheric forcing and natural forcing effects on surface pCO_2sw, and show unprecedented information on their interannual-decadal trends over both short and long time scales. The WHOTS station is located in the North Pacific Subtropical Gyre, therefore, the results and findings should be referential to understand the overall surface pCO_2sw dynamics for a broader impact of the ocean in absorbing anthropogenic CO_2, particularly under both anthropogenic CO_2 forcing and natural oceanic forcing (Henson et al., 2016).

More importantly, the pCO_2sw model was developed using satellite-derived environmental data and other ancillary data, thus the model is capable to tolerate the uncertainties involved in each variable as demonstrated in the sensitivity analysis. This is of great importance and significance to locations or areas where very limited data are available. Specifically, with these limited field observations of surface pCO_2sw, it would be possible to develop a surface pCO_2sw model with related environmental variables from satellite and ancillary data from NCEP to differentiate the two forcing effects following Eqs 1 and 2. With nearly 20 years of satellite data records, it would be straightforward to extend the current study to other oceanic regions to investigate the interannual-decadal surface pCO_2sw dynamics by differentiating the atmospheric forcing and natural forcing effects toward a better understanding of the ocean in absorbing anthropogenic CO_2 and its impact on the surface ocean carbonate chemistry.

CONCLUSION

The rate of anthropogenic or atmospheric CO_2 forcing pCO_2sw in surface seawater has been difficult to characterize because of the interaction of natural variability in pCO_2sw and the requirement of long time series data records. In this study, we show that a remote sensing algorithm applied to the WHOTS station in the North Pacific subtropical gyre can reveal the interannual-decadal variability of surface pCO_2sw between 2002 and 2019. Such an ability enables the separation of atmospheric CO_2 forced pCO_2sw ($pCO_2sw^{atm\_forced}$) from natural variability in pCO_2sw ($pCO_2sw^{nat\_forced}$). We believe that this is the first time such atmospheric CO_2 forced pCO_2sw and natural oceanic processes driven pCO_2sw are mathematically differentiated and their interannual-decadal changing rates are statistically quantified. Results show unprecedented information on their interannual-decadal rates over both short and long time scales at the WHOTS site. With the availability of ocean color data and other ancillary data globally, it is straightforward to extend the current study to other oceanic regions.

DATA AVAILABILITY STATEMENT

Publicly available datasets were analyzed in this study. This data can be found here: The WHOTS mooring dataset analyzed in this study is available at National Centers for Environmental information (NCEI) under https://www.nodc.noaa.gov/ocads/oceans/Moorings/. The MODIS ocean color data are available at the NASA Goddard Space Flight Center (GSFC) https://oceancolor.gsfc.nasa.gov/. The atmospheric xCO2 data at

Mauna Loa is available at the NOAA ESRL Global Monitoring Laboratory under https://www.esrl.noaa.gov/gmd/dv/data/index.php.

AUTHOR CONTRIBUTIONS

SC designed the study, processed, analyzed the data, and wrote the manuscript. AS contributed the mooring data and main concept definition. CH and FC contributed data analysis and manuscript writing. All authors commented on the manuscript.

FUNDING

This work was supported by the National Natural Science Foundation of China (NSFC) projects (42030708, 41906159, and 41730536). The pCO_2 observations at WHOTS were supported by the Office of Oceanic and Atmospheric Research of the NOAA, U.S. Department of Commerce, including resources from the Global Ocean Monitoring and Observation program.

ACKNOWLEDGMENTS

We gratefully acknowledge the support of National Natural Science Foundation of China (NSFC) and the contribution of NOAA PMEL. The MODIS data were maintained by the NASA Goddard Space Flight Center, the daily xCO_2 data was provided by the NOAA's Global Monitoring Laboratory. We thank NASA and NOAA for providing these data. This is PMEL contribution #5131.

REFERENCES

Bakker, D. C., Pfeil, B., Landa, C. S., Metzl, N., O'Brien, K. M., Olsen, A., et al. (2016). A multi-decade record of high-quality fCO_2 data in version 3 of the surface ocean CO2 Atlas (SOCAT). *Earth Syst. Sci. Data* 8, 383–413. doi: 10.5194/essd-8-383-2016

Bai, Y., Cai, W. J., He, X., Zhai, W., Pan, D., Dai, M., et al. (2015). A mechanistic semi-analytical method for remotely sensing sea surface pCO_2 in river-dominated coastal oceans: a case study from the East China Sea. *J. Geophysical Res. Oceans* 120, 2331–2349. doi: 10.1002/2014JC010632

Barnes, B. B., and Hu, C. (2015). Cross-sensor continuity of satellite-derived water clarity in the Gulf of Mexico: insights into temporal aliasing and implications for long-term water clarity assessment. *IEEE Trans. Geosci. Remote Sens.* 53, 1761–1772. doi: 10.1109/TGRS.2014.2348713

Borges, A. V., Delille, B., and Frankignoulle, M. (2005). Budgeting sinks and sources of CO_2 in the coastal ocean: diversity of ecosystems counts. *Geophys. Res. Lett.* 32:L14601. doi: 10.1029/2005GL023053

Borges, A., Ruddick, K., Lacroix, G., Nechad, B., Astoreca, R., Rousseau, V., et al. (2010). *Estimating pCO_2 from Remote Sensing in the Belgian Coastal Zone*. Paris: ESA Special Publication, 686.

Breiman, L. (1996). Bagging predictors. *Mach. Learn.* 24, 123–140. doi: 10.1007/BF00058655

Breiman, L. (2001). Random forests. *Mach. Learn.* 45, 5–32. doi: 10.1023/A:1010933404324

Brix, H., Gruber, N., and Keeling, C. D. (2004). Interannual variability of the upper ocean carbon cycle at station ALOHA near hawaii. *Global Biogeochem. Cycles* 18:GB4019. doi: 10.1029/2004GB002245

Cai, W. J., Dai, M., and Wang, Y. (2006). Air-sea exchange of carbon dioxide in ocean margins: a province-based synthesis. *Geophys. Res. Lett.* 33:L12603. doi: 10.1029/2006GL026219

Canadell, J. G., Le Quéré, C., Raupach, M. R., Field, C. B., Buitenhuis, E. T., Ciais, P., et al. (2007). Contributions to accelerating atmospheric CO2 growth from economic activity, carbon intensity, and efficiency of natural sinks. *Proc. Natil. Acad. Sci.* 104, 18866–18870. doi: 10.1073/pnas.0702737104

Chan, N. C. S., and Connolly, S. R. (2013). Sensitivity of coral calcification to ocean acidification: a meta-analysis. *Global Change Biol.* 19, 282–290. doi: 10.1111/gcb.12011

Chen, S., Hu, C., Byrne, R. H., Robbins, L. L., and Yang, B. (2016). Remote estimation of surface pCO_2 on the West Florida shelf. *Cont. Shelf Res.* 128, 10–25. doi: 10.1016/j.csr.2016.09.004

Chen, S., Hu, C., Cai, W. J., and Yang, B. (2017). Estimating surface pCO_2 in the northern Gulf of Mexico: which remote sensing model to use? *Cont. Shelf Res.* 151, 94–110. doi: 10.1016/j.csr.2017.10.013

Chen, S., Hu, C., Barnes, B. B., Wanninkhof, R., Cai, W. J., Barbero, L., et al. (2019). A machine learning approach to estimate surface ocean pCO2 from satellite measurements. *Remote sens. Environ.* 228, 203–226. doi: 10.1016/j.rse.2019.04.019

Chen, S., and Hu, C. (2019). Environmental controls of surface water pCO_2 in different coastal environments: observations from marine buoys. *Cont. Shelf Res.* 183, 73–86. doi: 10.1016/j.csr.2019.06.007

Chierici, M., Olsen, A., Johannessen, T., Trinañes, J., and Wanninkhof, R. (2009). Algorithms to estimate the carbon dioxide uptake in the northern North Atlantic using shipboard observations, satellite and ocean analysis data. *Deep-Sea Res. II Top. Stud. Oceanogr.* 56, 630–639. doi: 10.1016/j.dsr2.2008.12.014

Davis, C. V., Rivest, E. B., Hill, T. M., Gaylord, B., Russell, A. D., and Sanford, E. (2017). Ocean acidification compromises a planktic calcifier with implications for global carbon cycling. *Sci. Rep.* 7:2225. doi: 10.1038/s41598-017-01530-9

Denvil-Sommer, A., Gehlen, M., Vrac, M., and Mejia, C. (2019). LSCE-FFNN-v1: a two-step neural network model for the reconstruction of surface ocean pCO 2 over the global ocean. *Geosci. Model Dev.* 12, 2091–2105. doi: 10.5194/gmd-12-2091-2019

Dickinson, G. H., Ivanina, A. V., Matoo, O. B., Portner, H. O., Lannig, G., Bock, C., et al. (2012). Interactive effects of salinity and elevated CO_2 levels on juvenile eastern oysters. *Crassostrea virginica. J. Exp. Biol.* 215, 29–43. doi: 10.1242/jeb.061481

Dickson, A. G., Sabine, C. L., and Christian, J. R. (eds) (2007). *Guide to Best Practices for Ocean CO_2 Measurements*. Sidney: North Pacific Marine Science Organization, 176.

Doney, S. C., Fabry, V. J., Feely, R. A., and Kleypas, J. A. (2009). Ocean acidification: the other CO_2 problem. *Ann. Rev. Mar. Sci.* 1, 169–192. doi: 10.1146/annurev.marine.010908.163834

Dore, J. E., Lukas, R., Sadler, D. W., and Karl, D. M. (2003). Climate-driven changes to the atmospheric CO_2 sink in the subtropical North Pacific Ocean. *Nature* 424, 754–757. doi: 10.1038/nature01885

Dore, J. E., Lukas, R., Sadler, D. W., Church, M. J., and Karl, D. M. (2009). Physical and biogeochemical modulation of ocean acidification in the central North Pacific. *Proc. Natl. Acad. Sci.* 106, 12235–12240. doi: 10.1073/pnas.0906044106

Doney, S. C. (2010). The growing human footprint on coastal and open-ocean biogeochemistry. *Science* 328, 1512–1516. doi: 10.1126/science.1185198

Egleston, E. S., Sabine, C. L., and Morel, F. M. (2010). Revelle revisited: buffer factors that quantify the response of ocean chemistry to changes in DIC and alkalinity. *Global Biogeochem. Cycles* 24:GB1002. doi: 10.1029/2008GB003407

Fabricius, K. E., Langdon, C., Uthicke, S., Humphrey, C., Noonan, S., De'ath, G., et al. (2011). Losers and winners in coral reefs acclimatized to elevated carbon dioxide concentrations. *Nat. Clim. Change* 1, 165–169. doi: 10.1038/nclimate1122

Fassbender, A. J., Sabine, C. L., and Palevsky, H. I. (2017). Nonuniform ocean acidification and attenuation of the ocean carbon sink. *Geophys. Res. Lett.* 44, 8404–8413. doi: 10.1002/2017GL074389

Feely, R. A., Takahashi, T., Wanninkhof, R., and McPhaden, M. J. (2006). Decadal variability of the air-sea CO_2 fluxes in the equatorial Pacific Ocean. *J. Geophys. Res. Oceans* 111:C08S90. doi: 10.1029/2005JC003129

Feely, R. A., Orr, J., Fabry, V. J., Kleypas, J. A., Sabine, C. L., and Langdon, C. (2009). "Present and future changes in seawater chemistry due to ocean acidification," in *Geophysical Monograph Series*, eds B. J. McPherson and E. T. Sundquist (Washington, DC: American Geophysical Union), 175–188. doi: 10.1029/2005GM000337

Fennel, K., Wilkin, J., Previdi, M., and Najjar, R. (2008). Denitrification effects on air-sea CO_2 flux in the coastal ocean: simulations for the northwest North Atlantic. *Geophys. Res. Lett.* 35:L24608. doi: 10.1029/2008GL036147

Font, J., Camps, A., Borges, A., Martín-Neira, M., Boutin, J., Reul, N., et al. (2009). SMOS: the challenging sea surface salinity measurement from space. *Proc. IEEE* 98, 649–665. doi: 10.1109/JPROC.2009.2033096

Font, J., Boutin, J., Reul, N., Spurgeon, P., Ballabrera-Poy, J., Chuprin, A., et al. (2013). SMOS first data analysis for sea surface salinity determination. *Int. J. Remote Sens.* 34, 3654–3670. doi: 10.1080/01431161.2012.716541

Friedlingstein, P., Jones, M., O'sullivan, M., Andrew, R. M., Hauck, J., Peters, G. P., et al. (2019). Global carbon budget 2019. *Earth Syst. Sci. Data* 11, 1783–1838. doi: 10.5194/essd-11-1783-2019

Friedrich, T., and Oschlies, A. (2009). Neural network-based estimates of North Atlantic surface pCO_2 from satellite data: a methodological study. *J. Geophys. Res. Oceans* 114:C03020. doi: 10.1029/2007JC004646

Fujii, M., Chai, F., Shi, L., Inoue, H. Y., and Ishii, M. (2009). Seasonal and interannual variability of oceanic carbon cycling in the western and central tropical-subtropical pacific: a physical-biogeochemical modeling study. *J. oceanogr.* 65, 689–701. doi: 10.1007/s10872-009-0060-6

Gregg, W. W., and Casey, N. W. (2004). Global and regional evaluation of the SeaWiFS chlorophyll data set. *Remote Sens. Environ.* 93, 463–479. doi: 10.1016/j.rse.2003.12.012

Gregor, L., Lebehot, A. D., Kok, S., and Scheel Monteiro, P. M. (2019). A comparative assessment of the uncertainties of global surface ocean CO_2 estimates using a machine-learning ensemble (CSIR-ML6 version 2019a)–have we hit the wall? *Geosci. Model Dev.* 12, 5113–5136. doi: 10.5194/gmd-12-5113-2019

Gruber, N., Clement, D., Carter, B. R., Feely, R. A., Van Heuven, S., Hoppema, M., et al. (2019). The oceanic sink for anthropogenic CO2 from 1994 to 2007. *Science* 363, 1193–1199. doi: 10.1126/science.aau5153

Hales, B., Strutton, P. G., Saraceno, M., Letelier, R., Takahashi, T., Feely, R., et al. (2012). Satellite-based prediction of pCO2 in coastal waters of the eastern North Pacific. *Progr. Oceanogr.* 103, 1–15. doi: 10.1016/j.pocean.2012.03.001

Henson, S. A., Beaulieu, C., and Lampitt, R. (2016). Observing climate change trends in ocean biogeochemistry: when and where. *Global change biol.* 22, 1561–1571. doi: 10.1111/gcb.13152

Hu, C., Muller-Karger, F., Murch, B., Myhre, D., Taylor, J., Luerssen, R., et al. (2009). Building an automated integrated observing system to detect sea surface temperature anomaly events in the Florida keys. *IEEE Trans. Geosci. Remote Sens.* 47, 2071–2084. doi: 10.1109/TGRS.2009.2024992

Iida, Y., Takatani, Y., Kojima, A., and Ishii, M. (2020). Global trends of ocean CO_2 sink and ocean acidification: an observation-based reconstruction of surface ocean inorganic carbon variables. *J. Oceanogr.* 77, 323–358. doi: 10.1007/s10872-020-00571-5

Ikawa, H., Faloona, I., Kochendorfer, J., Paw, U., and Oechel, W. C. (2013). Air–sea exchange of CO_2 at a Northern California coastal site along the california current upwelling system. *Biogeosciences* 10, 4419–4432. doi: 10.5194/bg-10-4419-2013

James, G., Witten, D., Hastie, T., and Tibshirani, R. (2013). *Tree-Based Methods, an Introduction to Statistical Learning*, Vol. 112. New York, NY: Springer, 303–328. doi: 10.1007/978-1-4614-7138-7_8

Jo, Y. H., Dai, M., Zhai, W., Yan, X. H., and Shang, S. (2012). On the variations of sea surface pCO_2 in the northern South China Sea: a remote sensing based neural network approach. *J. Geophys. Res. Oceans* 117:C08022. doi: 10.1029/2011JC007745

Karl, D. M., and Church, M. J. (2018). Station ALOHA: a gathering place for discovery, education,and scientific collaboration. *Limnol. Oceanogr. Bull.* 28, 10–12. doi: 10.1002/lob.10285

Keeling, C. D., Brix, H., and Gruber, N. (2004). Seasonal and long−term dynamics of the upper ocean carbon cycle at station ALOHA near hawaii. *Global Biogeochem. Cycles* 18:GB4006. doi: 10.1029/2004GB002227

Krug, S., Schulz, K., and Riebesell, U. (2011). Effects of changes in carbonate chemistry speciation on Coccolithus braarudii: a discussion of coccolithophorid sensitivities. *Biogeosciences (BG)* 8, 771–777. doi: 10.5194/bg-8-771-2011

Landshützer, P., Gruber, N., Bakker, D. C. E., Schuster, U., Nakaoka, S., Payne, M. R., et al. (2013). A neural network-based estimate of the seasonal to inter-annual variability of the Atlantic Ocean carbon sink. *Biogeosciences* 10, 7793–7815. doi: 10.5194/bg-10-7793-2013

Landshützer, P., Gruber, N., and Bakker, D. C. (2016). Decadal variations and trends of the global ocean carbon sink. *Global Biogeochem. Cycles* 30, 1396–1417. doi: 10.1002/2015GB005359

Landshützer, P., Ilyina, T., and Lovenduski, N. S. (2019). Detecting regional modes of variability in observation−based surface ocean pCO_2. *Geophys. Res. Lett.* 46, 2670–2679. doi: 10.1029/2018GL081756

Le, C., Gao, Y., Cai, W. J., Lehrter, J. C., Bai, Y., and Jiang, Z. P. (2019). Estimating summer sea surface pCO2 on a river-dominated continental shelf using a satellite-based semi-mechanistic model. *Remote Sens. Environ.* 225, 115–126. doi: 10.1016/j.rse.2019.02.023

Lee, K., Choi, S. D., Park, G. H., Wanninkhof, R., Peng, T. H., Key, R. M., et al. (2003). An updated anthropogenic CO_2 inventory in the Atlantic Ocean. *Global Biogeochem. Cycles* 17:1116. doi: 10.1029/2003GB002067

Lefèvre, N., Watson, A. J., and Watson, A. R. (2005). A comparison of multiple regression and neural network techniques for mapping in situ pCO_2 data. *Tellus B* 57, 375–384. doi: 10.1111/j.1600-0889.2005.00164.x

Lohrenz, S. E., and Cai, W. J. (2006). Satellite ocean color assessment of air-sea fluxes of CO_2 in a river-dominated coastal margin. *Geophys. Res. Lett.* 33, L01601. doi: 10.1029/2005GL023942

Lohrenz, S. E., Cai, W. J., Chen, F., Chen, X., and Tuel, M. (2010). Seasonal variability in air-sea fluxes of CO_2 in a river-influenced coastal margin. *J. Geophys. Res. Oceans* 115:C10034. doi: 10.1029/2009JC005608

Lohrenz, S. E., Cai, W. J., Chakraborty, S., Huang, W. J., Guo, X., He, R., et al. (2018). Satellite estimation of coastal pCO_2 and air-sea flux of carbon dioxide in the northern Gulf of Mexico. *Remote Sens. Environ.* 207, 71–83. doi: 10.1016/j.rse.2017.12.039

Lukas, R., and Santiago-Mandujano, F. (2008). Interannual to interdecadal salinity variations observed near hawaii: local and remote forcing by surface freshwater fluxes. *Oceanography* 21, 46–55. doi: 10.5670/oceanog.2008.66

Marrec, P., Cariou, T., Macé, É, Morin, P., Salt, L. A., Vernet, M., et al. (2015). Dynamics of air-sea CO 2 fluxes in the northwestern European shelf based on voluntary observing ship and satellite observations. *Biogeosciences* 12, 5371–5391. doi: 10.5194/bg-12-5371-2015

McKinley, G. A., Fay, A. R., Takahashi, T., and Metzl, N. (2011). Convergence of atmospheric and North Atlantic carbon dioxide trends on multidecadal timescales. *Nat. Geosci.* 4, 606–610. doi: 10.1038/ngeo1193

Mélin, F., Zibordi, G., and Berthon, J. F. (2007). Assessment of satellite ocean color products at a coastal site. *Remote Sens. Environ.* 110, 192–215. doi: 10.1016/j.rse.2007.02.026

Moussa, H., Benallal, M. A., Goyet, C., and Lefèvre, N. (2016). Satellite-derived CO_2 fugacity in surface seawater of the tropical Atlantic Ocean using a feedforward neural network. *Int. J. Remote Sens.* 37, 580–598. doi: 10.1080/01431161.2015.1131872

Nakaoka, S., Telszewski, M., Nojiri, Y., Yasunaka, S., Miyazaki, C., Mukai, H., et al. (2013). Estimating temporal and spatial variation of ocean surface pCO_2 in the North Pacific using a self-organizing map neural network technique. *Biogeosciences* 10, 6093–6106. doi: 10.5194/bg-10-6093-2013

Newman, M., Alexander, M. A., Ault, T. R., Cobb, K. M., Deser, C., Di Lorenzo, E., et al. (2016). The pacific decadal oscillation, revisited. *J Clim.* 29, 4399–4427. doi: 10.1175/JCLI-D-15-0508.1

NOAA ESRL Global Monitoring Laboratory (2019). "updated annually." in *Atmospheric Carbon Dioxide Dry Air Mole Fractions from Quasi-Continuous Measurements at Mauna Loa, Hawaii, Barrow, Alaska, American Samoa and South Pole, Version 2020-04*. eds K. W. Thoning, A. Crotwell, and D. R. Kitzis (Boulder, CO: National Oceanic and Atmospheric Administration),

Olsen, A., Triñanes, J. A., and Wanninkhof, R. (2004). Sea–air flux of CO_2 in the caribbean sea estimated using in situ and remote sensing data. *Remote Sens. Environ.* 89, 309–325. doi: 10.1016/j.rse.2003.10.011

Ono, T., Saino, T., Kurita, N., and Sasaki, K. (2004). Basin-scale extrapolation of shipboard pCO_2 data by using satellite SST and Chl a. *Int. J. Remote Sens.* 25, 3803–3815. doi: 10.1080/01431160310001657515

Ono, T., Kosugi, N., Toyama, K., Tsujino, H., Kojima, A., Enyo, K., et al. (2019). Acceleration of Ocean Acidification in the Western North Pacific. *Geophys. Res. Lett.* 46, 13161–13169. doi: 10.1029/2019GL085121

Orr, J. C., Fabry, V. J., Aumont, O., Bopp, L., Doney, S. C., Feely, R. A., et al. (2005). Anthropogenic ocean acidification over the twenty-first century and its impact on calcifying organisms. *Nature* 437, 681–686. doi: 10.1038/nature04095

Palevsky, H. I., and Quay, P. D. (2017). Influence of biological carbon export on ocean carbon uptake over the annual cycle across the North Pacific ocean. *Global Biogeochem. Cycles* 31, 81–95. doi: 10.1002/2016GB005527

Parard, G., Charantonis, A. A., and Rutgerson, A. (2015). Remote sensing the sea surface CO_2 of the Baltic Sea using the SOMLO methodology. *Biogeosciences* 12, 3369–3384. doi: 10.5194/bg-12-3369-2015

Quay, P., Sonnerup, R., Munro, D., and Sweeney, C. (2017). Anthropogenic CO_2 accumulation and uptake rates in the Pacific Ocean based on changes in the $^{13}C/^{12}C$ of dissolved inorganic carbon. *Global Biogeochem. Cycles* 31, 59–80. doi: 10.1002/2016GB005460

Rayner, N. A. A., Parker, D. E., Horton, E. B., Folland, C. K., Alexander, L. V., Rowell, D. P., et al. (2003). Global analyses of sea surface temperature, sea ice, and night marine air temperature since the late nineteenth century. *J. Geophys. Res. Atmos.* 108:4407. doi: 10.1029/2002JD002670

Rödenbeck, C., Bakker, D. C., Gruber, N., Iida, Y., Jacobson, A. R., Jones, S., et al. (2015). Data-based estimates of the ocean carbon sink variability–first results of the Surface Ocean pCO_2 mapping intercomparison (SOCOM). *Biogeosciences* 12, 7251–7278. doi: 10.5194/bg-12-7251-2015

Sabine, C. L., Feely, R. A., Key, R. M., Bullister, J. L., Millero, F. J., Lee, K., et al. (2002). Distribution of anthropogenic CO_2 in the Pacific Ocean. *Global Biogeochem. Cycles* 16, 30–31. doi: 10.1029/2001GB001639

Sabine, C. L., Feely, R. A., Gruber, N., Key, R. M., Lee, K., Bullister, J. L., et al. (2004a). The oceanic sink for anthropogenic CO_2. *Science* 305, 367–371. doi: 10.1126/science.1097403

Sabine, C. L., Feely, R. A., Watanabe, Y. W., and Lamb, M. (2004b). Temporal evolution of the North Pacific CO_2 uptake rate. *J. Oceanogr.* 60, 5–15. doi: 10.1023/B:JOCE.0000038315.23875.ae

Sabine, C., Sutton, A., McCabe, K., Lawrence-Slavas, N., Alin, S., Feely, R., et al. (2020). Evaluation of a new carbon dioxide system for autonomous surface vehicles. *J. Atmos. Ocean. Technol.* 37, 1305–1317. doi: 10.1175/JTECH-D-20-0010.1

Sarma, V. V. S. S., Saino, T., Sasaoka, K., Nojiri, Y., Ono, T., Ishii, M., et al. (2006). Basin-scale pCO_2 distribution using satellite sea surface temperature, Chl a, and climatological salinity in the North Pacific in spring and summer. *Glob. Biogeochem. Cycles* 20: GB3005. doi: 10.1029/2005GB002594

Signorini, S. R., Mannino, A., Najjar, R. G., Friedrichs, M. A., Cai, W. J., Salisbury, J., et al. (2013). Surface ocean pCO_2 seasonality and sea-air CO_2 flux estimates for the North American east coast. *J. Geophys. Res. Oceans* 118, 5439–5460. doi: 10.1002/jgrc.20369

Shadwick, E. H., Thomas, H., Comeau, A., Craig, S. E., Hunt, C. W., and Salisbury, J. E. (2010). Air-Sea CO_2 fluxes on the scotian shelf: seasonal to multi-annual variability. *Biogeosciences* 7, 3851–3867. doi: 10.5194/bg-7-3851-2010

Sutton, A. J., Sabine, C. L., Dietrich, C., Maenner Jones, S., Musielewicz, S., Bott, R., et al. (2012). *High-Resolution Ocean and Atmosphere Pco2 Time-Series Measurements From Mooring Whots_158w_23n North Pacific Ocean (Ncei Accession 0100080). [Data in 2004-2017]*. Washington, D.C: NOAA, doi: 10.3334/CDIAC/otg.TSM_WHOTS

Sutton, A. J., Sabine, C. L., Maenner-Jones, S., Lawrence-Slavas, N., Meinig, C., Feely, R. A., et al. (2014). A high-frequency atmospheric and seawater pCO_2 data set from 14 open-ocean sites using a moored autonomous system. *Earth Syst. Sci. Data* 6, 353–366. doi: 10.5194/essd-6-353-2014

Sutton, A. J., Wanninkhof, R., Sabine, C. L., Feely, R. A., Cronin, M. F., and Weller, R. A. (2017). Variability and trends in surface seawater pCO_2 and CO_2 flux in the Pacific Ocean. *Geophys. Res. Lett.* 44, 5627–5636. doi: 10.1002/2017GL073814

Sutton, A. J., Feely, R. A., Maenner-Jones, S., Musielwicz, S., Osborne, J., Dietrich, C., et al. (2019). Autonomous seawater pCO_2 and pH time series from 40 surface buoys and the emergence of anthropogenic trends. *Earth System Sci. Data* 11, 421–439. doi: 10.5194/essd-11-421-2019

Takahashi, T., Sutherland, S. C., Feely, R. A., and Wanninkhof, R. (2006). Decadal change of the surface water pCO_2 in the North Pacific: a synthesis of 35 years of observations. *J. Geophys. Res. Oceans* 111:C07S05. doi: 10.1029/2005JC003074

Takahashi, T., Sutherland, S. C., Wanninkhof, R., Sweeney, C., Feely, R. A., and Baar, H. (2009). Climatological mean and decadal change in surface ocean pCO2, and net sea–air CO_2 flux over the global oceans. *Deep Sea Res. II Top. Stud. Oceanogr.* 56, 554–577. doi: 10.1016/j.dsr2.2008.12.009

Takahashi, T., Sutherland, S. C., Chipman, D. W., Goddard, J. G., Ho, C., Newberger, T., et al. (2014). Climatological distributions of pH, pCO_2, total CO_2, alkalinity, and $CaCO_3$ saturation in the global surface ocean, and temporal changes at selected locations. *Mar. Chem.* 164, 95–125. doi: 10.1016/j.marchem.2014.06.004

Takahashi, T., Sutherland, S. C., and Kozyr, A. (2019). *Global Ocean Surface Water Partial Pressure of CO2 Database: Measurements Performed During 1957-2018 (LDEO Database Version 2018) (NCEI Accession 0160492). Version 7.7*. Washington, D.C: NOAA ,

Tao, Z., Qin, B., Li, Z., and Yang, X. (2012). Satellite observations of the partial pressure of carbon dioxide in the surface water of the huanghai sea and the bohai sea. *Acta Oceanol. Sin.* 31, 67–73. doi: 10.1007/s13131-012-0207-y

Terlouw, G. J., Knor, L. A., De Carlo, E. H., Drupp, P. S., Mackenzie, F. T., Li, Y. H., et al. (2019). Hawaii coastal seawater CO_2 network: a statistical evaluation of a decade of observations on tropical coral reefs. *Front. Mar. Sci.* 6:226. doi: 10.3389/fmars.2019.00226

Wanninkhof, R., Park, G. H., Takahashi, T., Sweeney, C., Feely, R. A., Nojiri, Y., et al. (2013). Global ocean carbon uptake: magnitude. *Variability Trends.Biogeosci.* 10, 1983–2000. doi: 10.5194/bg-10-1983-2013

Weiss, R. F. (1974). . Carbon dioxide in water and seawater: the solubility of a non-ideal gas. *Mar. Chem.* 2, 203–215. doi: 10.1016/0304-4203(74)90015-2

Widdicombe, S., and Spicer, J. I. (2008). Predicting the impact of ocean acidification on benthic biodiversity: what can animal physiology tell us? *J. Exp. Mar. Biol. Ecol.* 366, 187–197. doi: 10.1016/j.jembe.2008.07.024

Xiu, P., and Chai, F. (2014). Variability of oceanic carbon cycle in the North Pacific from seasonal to decadal scales. *J. Geophys. Res. Oceans* 119, 5270–5288. doi: 10.1002/2013JC009505

Xue, L., Cai, W. J., Hu, X., Sabine, C., Jones, S., Sutton, A. J., et al. (2016). Sea surface carbon dioxide at the Georgia time series site (2006–2007): air–sea flux and controlling processes. *Prog. Oceanogr.* 140, 14–26. doi: 10.1016/j.pocean.2015.09.008

Xue, L., and Cai, W. J. (2020). Total alkalinity minus dissolved inorganic carbon as a proxy for deciphering ocean acidification mechanisms. *Mar. Chem.* 222:103791. doi: 10.1016/j.marchem.2020.103791

Yasunaka, S., Nojiri, Y., Nakaoka, S. I., Ono, T., Mukai, H., and Usui, N. (2014). North Pacific dissolved inorganic carbon variations related to the Pacific decadal oscillation. *Geophys. Res. Lett.* 41, 1005–1011. doi: 10.1002/2013GL058987

Zhu, Y., Shang, S., Zhai, W., and Dai, M. (2009). Satellite-derived surface water pCO_2 and air–sea CO_2 fluxes in the northern South China sea in summer. *Prog. Nat. Sci.* 19, 775–779. doi: 10.1016/j.pnsc.2008.09.004

Conflict of Interest: The authors declare that the research was conducted in the absence of any commercial or financial relationships that could be construed as a potential conflict of interest.

frontiers in Marine Science

ORIGINAL RESEARCH
published: 04 May 2021
doi: 10.3389/fmars.2021.642804

Ocean Surface Flux Algorithm Effects on Earth System Model Energy and Water Cycles

J. E. Jack Reeves Eyre[1*†], *Xubin Zeng*[1] *and Kai Zhang*[2]

[1] *Department of Hydrology and Atmospheric Sciences, University of Arizona, Tucson, AZ, United States,* [2] *Pacific Northwest National Laboratory, Richland, WA, United States*

Earth system models parameterize ocean surface fluxes of heat, moisture, and momentum with empirical bulk flux algorithms, which introduce biases and uncertainties into simulations. We investigate the atmosphere and ocean model sensitivity to algorithm choice in the Energy Exascale Earth System Model (E3SM). Flux differences between algorithms are larger in atmosphere simulations (where wind speeds can vary) than ocean simulations (where wind speeds are fixed by forcing data). Surface flux changes lead to global scale changes in the energy and water cycles, notably including ocean heat uptake and global mean precipitation rates. Compared to the control algorithm, both COARE and University of Arizona (UA) algorithms reduce global mean precipitation and top of atmosphere radiative biases. Further, UA may slightly reduce biases in ocean meridional heat transport. We speculate that changes seen here, especially in the ocean, could be even larger in coupled simulations.

Keywords: earth system modeling, ocean-atmosphere interactions, boundary layer turbulence, upper ocean processes, climate dynamics

OPEN ACCESS

Edited by:
Simon Josey,
National Oceanography Centre,
United Kingdom

Reviewed by:
Adam Thomas Devlin,
The Chinese University of Hong Kong,
China
Shijian Hu,
Institute of Oceanology (CAS), China
Shawn R. Smith,
Florida State University, United States

****Correspondence:***
J. E. Jack Reeves Eyre
jack.reeveseyre@gmail.com

†Present address:
J. E. Jack Reeves Eyre,
Cooperative Institute for Climate,
Ocean and Ecosystem Studies,
University of Washington, Seattle, WA,
United States

Specialty section:
This article was submitted to
Physical Oceanography,
a section of the journal
Frontiers in Marine Science

Received: *16 December 2020*
Accepted: *26 March 2021*
Published: *04 May 2021*

Citation:
Reeves Eyre JEJ, Zeng X and Zhang K
(2021) Ocean Surface Flux Algorithm
Effects on Earth System Model Energy
and Water Cycles.
Front. Mar. Sci. 8:642804.
doi: 10.3389/fmars.2021.642804

1. INTRODUCTION

Ocean surface fluxes of heat, moisture, and momentum control the ocean's impact on weather and climate. Despite many years of field studies, data set development and parameterization improvements, available data sets still do not close the surface energy budget (L'Ecuyer et al., 2015) and uncertainties in fluxes are too large to detect trends (Rhein et al., 2013). The methods used to calculate ocean surface turbulent fluxes are a significant contributor to surface energy budget uncertainties. While the methodological contribution to *observational* products has been acknowledged and fairly well-explored (e.g., Yu, 2019), the contribution to the spread of Earth system models is not well-understood. In this study we use atmosphere and ocean model simulations to quantify how sensitive model results are to surface flux algorithm design.

The methods used to calculate ocean surface turbulent fluxes in numerical models and global observational products rely on bulk flux algorithms. These algorithms use "bulk" quantities—sea surface temperature (SST) and near-surface values of air temperature, humidity, and wind speed—which are easier to measure than direct measurements of fluxes (e.g., Edson et al., 1998), and can be measured by remote sensing platforms. Bulk algorithms have been compared by Zeng et al. (1998), Brunke et al. (2002, 2003), and Brodeau et al. (2016), among others. While these studies are valuable for understanding how different aspects of algorithm design affect surface flux estimates, they have one limitation when it comes to understanding impacts on model results: they are based on comparison of fluxes using pre-specified bulk variables. Thus, the differences in fluxes do not

feed back onto the bulk variables. Therefore, such studies do not allow us to fully understand the changes that result when the algorithms are used in ocean and atmosphere general circulation models, in which case the flux differences do result in changes in the bulk variables. Understanding these feedbacks is key to assessing the full model sensitivity to algorithm choice.

A number of past studies give strong evidence suggesting that model sensitivity to ocean surface flux calculation is significant and important. Looking at the atmospheric response, Harrop et al. (2018) found that tropical Pacific precipitation biases in the Energy Exascale Earth System Model (E3SM) are reduced by including the effects of convective wind gustiness in flux calculations. Large and Caron (2015), building on the work of Zeng and Beljaars (2005), showed that parameterizing diurnal variation of SST in a global atmosphere model can affect net ocean surface heat flux and precipitation. Polichtchouk and Shepherd (2016) showed that the effects of changing the ocean surface roughness formulation in a global model are apparent across the globe and through the full depth of the troposphere. Compared to atmosphere models, the sensitivity of ocean models to surface flux algorithms is comparatively unexplored. However, it has been shown (Holdsworth and Myers, 2015; Kostov et al., 2019) that surface heat flux specification is important for simulating the Atlantic Meridional Overturning Circulation (AMOC). These studies provide motivation for asking what other aspects of ocean model behavior may be sensitive to surface flux algorithm choice.

Given the wide ranging aspects of model climate (i.e., the main features of the simulated Earth system) that are affected by flux calculation methods, and the large number of studies that compare bulk flux algorithms using pre-specified bulk variable data, it is surprising that there are not more studies investigating the consequences of bulk flux algorithm choice in global models—especially in ocean models. We aim to fill this gap, and identify three major aims in doing so:

1. Identify regions where differences between fluxes are largest. This will assist developers of parameterizations to understand uncertainties and identify strengths and weaknesses. Given the uncertainties in observation-based flux data sets (Găinuşă-Bogdan et al., 2015), it is difficult to identify a "least biased" parameterization. Instead we aim to identify where the differences between algorithms are significant, based on the what might be expected from internannual and longer term variability. Regions with significant differences can then be prioritized for more detailed regional process studies and analysis of structural differences in the algorithms.
2. Understand how the choice of test methodology (atmosphere vs. ocean simulations) affects the apparent outcome. Due to their different forcing data requirements, atmosphere and ocean simulations allow different amounts of flux-bulk variable feedback. Strobach et al. (2018) showed that inclusion or exclusion of such feedbacks has a large impact on ocean model simulations, and similar issues likely affect atmosphere-only simulations. Thus, our work will help modelers and parameterization developers to understand how the choice of testing framework may influence results.
3. Explore which other aspects of model climate are affected, to help model developers understand how surface flux parameterization may influence the perceived biases of the overlying atmosphere and/or underlying ocean model(s). Based on the studies mentioned above, we expect differences in precipitation, large-scale atmospheric circulation, and possibly in deep water formation at high latitudes. However, changes in other quantities and/or regions are possible.

The structure of this paper is as follows: section 2 summarizes the bulk flux algorithms, model simulations and observational data; section 3 presents results—of both surface fluxes and other aspects of model climate; section 4 includes further discussion and summarizes our findings.

2. DATA AND METHODS

2.1. Bulk Flux Algorithms

Exchanges of heat, moisture and momentum between atmosphere and ocean are calculated in global models using bulk flux algorithms. These algorithms parameterize turbulent fluxes based on bulk quantities: sea surface temperature (SST), near-surface air temperature and humidity, and near-surface wind speed. Bulk flux algorithms have sound theoretical foundations in Monin-Obukhov similarity theory. However, many aspects of the algorithms are empirical, relying on constants and functional forms estimated from (a relatively small number of) ship- and buoy-based observational campaigns. The general form of the flux algorithms can be expressed as:

$$\vec{\tau} = \rho C_D(\vec{U}_z - \vec{U}_s)U_B \tag{1}$$

$$Q_H = \rho c_p C_H(\theta_z - \theta_s)U_B \tag{2}$$

$$Q_E = \rho L_v C_E(q_z - q_s)U_B \tag{3}$$

where $\vec{\tau}$ is the wind stress, Q_H is the sensible heat flux, and Q_E is the latent heat flux. The main differences between algorithms lie in the calculation of the transfer coefficients C_D, C_E, and C_H, but there are also differences in U_B (which may simply be the wind speed or may have a modification due to boundary layer eddies or convective gustiness), and even in the calculation of q_s (surface specific humidity) and L_v (latent heat of vaporization). Other terms appearing in the equations are ρ (air density), c_p (specific heat capacity of air), θ (potential temperature), q (specific humidity), and $\vec{U}$ (wind velocity). Subscript z refers to a value at height z in the atmosphere (in our case, the height of the lowest atmosphere model level), while subscript s refers to the value at the ocean surface. The sign conventions employed mean that $\vec{\tau}$ is the force exerted on the ocean by the wind, and positive values of Q_H and Q_E correspond to heat gain by the ocean. The coefficients C_D, C_E, and C_H have two main dependencies: stability (turbulence is enhanced in unstable conditions) and surface roughness (the ocean surface becomes rougher at higher wind speeds). Many researchers have proposed different formulations for these coefficients, and the differences in their formulations are responsible for some of the differences between algorithms. In addition, several seemingly more trivial issues (e.g., reduction of surface specific humidity due to ocean

salinity; use of constant air density) can strongly affect flux calculations (Brodeau et al., 2016). This study uses three bulk flux algorithms: they are described in detail in the references given, but here (and in **Table 1**) we summarize some of their key features and differences.

The first, which we refer to as "control," is the algorithm used in the Energy Exascale Earth System Model version 1 (E3SMv1 Golaz et al., 2019). It is based on the work of Large and Pond (1981, 1982) and Large and Yeager (2004, 2009). The algorithm uses two stability classes—stable and unstable. The roughness length for momentum varies with wind speed. The roughness length for heat takes one of two constant values depending on stability, while that for moisture uses a single constant for all stability cases. Surface specific humidity is calculated with a simple formula based on temperature only and accounts for reduction due to ocean salinity.

The University of Arizona algorithm (Zeng et al., 1998), which we refer to as "UA," uses four stability cases (strongly stable, weakly stable, weakly unstable, and very unstable). Roughness lengths for momentum, heat and moisture are continuously varying functions of wind speed. Surface specific humidity uses a more accurate formula than the control algorithm, based on temperature and surface pressure. Again, the reduction due to ocean salinity is accounted for. Similarly, UA uses a temperature-dependent function for L_v, while the other two algorithms use a single constant. Finally, UA includes a gustiness factor due to large boundary layer eddies in unstable conditions, which increases fluxes in unstable, low wind conditions.

The third algorithm is based on the COARE (Coupled Ocean Atmosphere Response Experiment) version 3.0 algorithm (Fairall et al., 2003) which we refer to as simply "COARE." This uses three stability cases (stable, weakly unstable and strongly unstable) and roughness length functions are similar to the UA algorithm. Surface humidity calculation uses the same method as the control algorithm. COARE, like UA, includes a gustiness factor to account for increased fluxes in unstable, low wind conditions. The correction of sea surface temperature due to cool skin and diurnal warm layer effects available in COARE are not used.

2.2. Model Experiments

We test model sensitivity to ocean surface flux algorithm in a "standard resolution" version of E3SM similar to version 1 used in Golaz et al. (2019). The components of E3SM include atmosphere, land, ocean, sea ice, land ice, and river routing models. The atmosphere and land model horizontal resolutions are $\sim 1^\circ$ and the ocean and sea ice model horizontal resolutions are $\sim$50 km. The tests performed for this study fall into two categories: one uses active atmosphere and land model components, with sea surface temperature and sea ice distribution pre-specified (this configuration is referred to as an atmosphere run); the other uses active ocean and sea ice components, with near-surface meteorology and river discharge pre-specified (this configuration is referred to as an ocean run). The ocean and sea ice data used in the atmosphere runs is based on a repeating year representative of observations in the year 2000. The atmosphere and river discharge data used in the ocean runs is from the JRA55-do data set (Tsujino et al., 2018)—a version of the JRA-55 reanalysis adjusted to make it more suitable for forcing ocean models.

For each configuration (atmosphere and ocean), three simulations are performed—one with each of the algorithms. The atmosphere runs are 6 years long and analysis is based on the final 5 years. The ocean runs are 10 years long and the first year is disregarded when calculating climatologies but is used for some time series analysis. The ocean runs were originally intended to be the same length as the atmosphere runs, but we took advantage of an opportunity to extend them. Longer model runs would have been valuable, particularly for the ocean model, which can take hundreds to thousands of years to reach equilibrium (Li et al., 2013; Petersen et al., 2019). However, computing resources did not allow for such an ambitious investigation and we feel that the present simulations can still provide a valuable perspective on the degree of sensitivity compared to other model developments (e.g., tuning of parameterizations).

To understand how much of the observed differences between model runs may be due to internal climate variability, we use the E3SM v1 pre-industrial control run (produced for phase 6 of

TABLE 1 | Bulk flux algorithm overview.

Algorithm	Stability classes and functions	Roughness lengths
Control	Stable (D74); Unstable (D74)	Momentum: wind dependent. Heat, water: constants
UA	Very stable (Holtslag et al., 1990); Stable (D74); Unstable (D74); Very unstable (Kader and Yaglom, 1990)	Momentum: Smith (1988), constant Charnock parameter. Heat, water: Brutsaert (1982).
COARE	Stable (Beljaars and Holtslag, 1991); Unstable (D74); Very unstable (Fairall et al., 1996b)	Momentum: Smith (1988), variable Charnock parameter. Heat, water: Fairall et al. (2003)

Algorithm	Surface humidity dependence	L_v dependence	Gustiness	Cool skin	Diurnal warm-layer	References
Control	T	Constant	No	No	No	Large and Pond, 1981, 1982; Large and Yeager, 2004
UA	T, p	T	Boundary layer free convection	No	No	Zeng et al., 1998
COARE	T	Constant	Boundary layer free convection	No	No	Fairall et al., 1996b, 2003

Further details, e.g., constants, are given in the cited publications. D74 refers to the widely-used stability function formulation described in and advocated by Dyer (1974), although earlier publications described parts of this formulation.

the Coupled Model Intercomparison Project [CMIP6]). We use the final 100 years of the run (model years 401–500) to quantify internal variability.

When analyzing spatial fields, all variables are interpolated onto a common 1° latitude-longitude grid. Heat fluxes and precipitation are interpolated using an integral-conservative method, while wind stress and sea surface height are bilinearly interpolated. We used interpolation tools and several other data processing tools from the netCDF Operators package (Zender, 2020). Global averages are calculated on native model grids.

2.3. Observational Data

Most of the analysis presented here is based on the above model runs, but a few observational data sets are used to contextualize the results. We deem uncertainties in global gridded ocean flux products to be too large to use them for the basis of ranking the flux algorithms (Găinuşă-Bogdan et al., 2015; Yu, 2019). However, we use one such product, OAflux (Yu et al., 2006; Yu and Weller, 2007), to ascertain how the estimated internal variability of E3SM compares with observed variability in the real world. Precipitation from the atmosphere simulations is compared with 1981−2010 long-term averages from GPCP (Global Precipitation Climatology Project; Adler et al., 2003, 2018), a satellite-gauge merged observational data set. Global top of atmosphere (TOA) radiation measurements from the Clouds and the Earth's Radiant Energy System (CERES) mission are used to assess the atmosphere simulations: we use version 4.1 of the energy balanced and filled (EBAF) monthly means (Loeb et al., 2018; Doelling, 2019).

3. RESULTS

We first look at the differences in ocean surface fluxes between model simulations, before looking at the effects on other aspects of model climate in the ocean and atmosphere.

3.1. Surface Flux Changes

Changes in latent heat flux are shown in **Figure 1**. It is immediately clear that there are differences in sensitivity between atmosphere (left column) and ocean (right column) simulations. The magnitudes of differences are generally larger for atmosphere simulations than for ocean simulations and the spatial patterns differ. However, because the atmosphere simulations have both large positive and large negative differences, there is significant cancellation when considering the global means (**Table 2**). The sensitivity as shown by the global means therefore ends up being

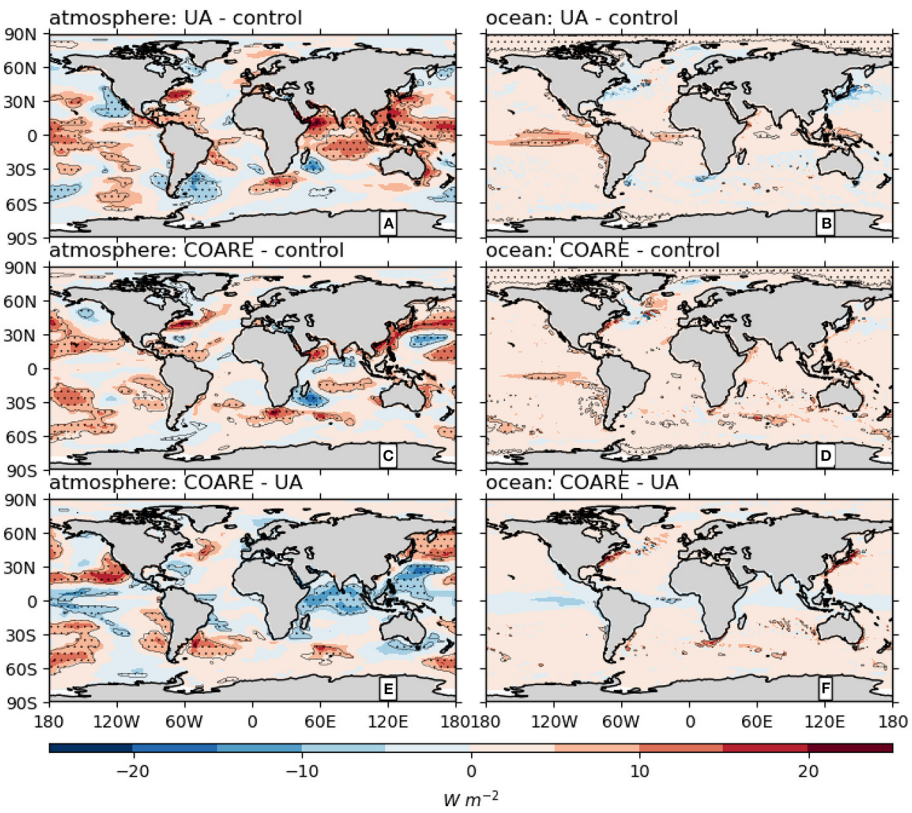

FIGURE 1 | Differences in annual mean latent heat flux climatology between simulations with different bulk flux algorithms. The atmosphere and ocean simulation results are shown in left and right panels, respectively. Stippling designates regions where the absolute value of the difference is larger than the interannual standard deviation from the E3SMv1 pre-industrial control run (shown in **Supplementary Figure 2**).

TABLE 2 | Long-term annual mean surface flux components from atmosphere and ocean simulations, averaged over global oceans.

		Control	UA	COARE
Q_E $(W\ m^{-2})$	atmo	–107.04	–104.32	–104.43
	ocn	–98.35	–96.64	–95.49
Evaporation $(mm\ day^{-1})$	atmo	3.70	3.68	3.61
	ocn	3.39	3.41	3.30
Q_H $(W\ m^{-2})$	atmo	–13.72	–13.63	–14.36
	ocn	–14.13	–14.40	–14.32
$R_{s,net}$ $(W\ m^{-2})$	atmo	171.3	171.6	172.6
	ocn	169.3	169.2	169.3
$R_{l,down}$ $(W\ m^{-2})$	atmo	360.6	360.3	358.6
	ocn	339.0	338.9	339.2
$R_{l,up}$ $(W\ m^{-2})$	atmo	–409.1	–409.4	–409.3
	ocn	–393.2	–393.5	–394.6
Q_{net} $(W\ m^{-2})$	atmo	1.70	4.45	3.02
	ocn	2.60	3.63	4.04

The sign convention for heat fluxes is positive into the ocean (i.e., positive values warm the ocean). Evaporation is positive by definition. The flux components shown are latent heat flux Q_E; sensible heat flux Q_H; net shortwave radiation $R_{s,net}$; downward longwave radiation $R_{l,down}$; upward longwave $R_{l,up}$ and net surface heat flux $Q_{net} = R_{s,net} + R_{l,up} + R_{l,down} + Q_E + Q_H$.

more consistent between atmosphere and ocean tests [e.g., (*UA* − *control*) is positive for both atmosphere and ocean].

At this point we pause to note that the global means in **Table 2** also show latent heat fluxes are of larger magnitude (i.e., more evaporation) in the atmosphere runs than in the ocean runs. However, the physical significance of this fact is doubtful, as the values are likely to be strongly affected by the forcing data sets (**Figure 2** and **Supplementary Figure 1**) and initial conditions, and may even reflect differences introduced by masking and interpolating from different model grids. We therefore do not dwell further on quantitative comparisons between ocean and atmosphere simulations.

Considering the spatial patterns of latent heat flux differences in **Figure 1**, a few regions stand out that have similar patterns of sensitivity in both the atmosphere and ocean runs. Examples include the Southern Ocean (e.g., around 50°S, 180°E) in *COARE* − *control*, and the eastern tropical Pacific (around 5°S, 120°W) in *UA*−*control*. Several other regions, however, have opposite changes in the atmosphere and ocean runs. For example, around the Gulf Stream at 35°N, 60°W (a region of large evaporation and therefore negative values in the sign convention of **Figure 1**) in the *UA*−*control* atmosphere comparison, UA has a positive change (less evaporation) relative to control, while in the *UA*−*control* ocean comparison, UA has a negative change (more evaporation). Other regions with opposite changes

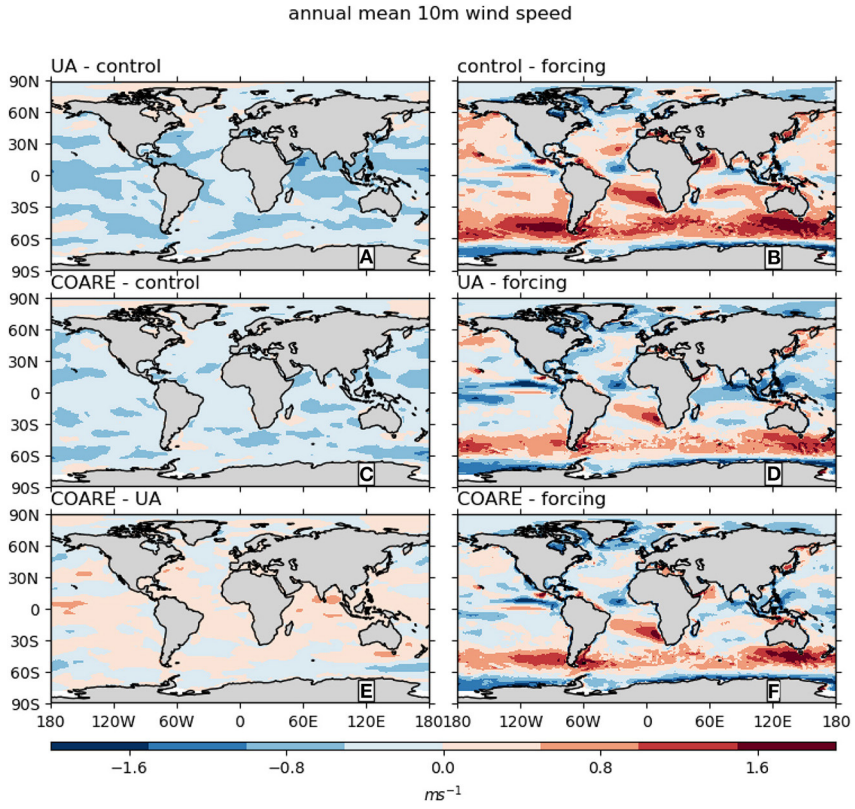

FIGURE 2 | Annual mean 10-m wind speed difference between (left column) pairs of atmosphere model runs and (right column) atmosphere model runs and forcing data used in ocean model runs. The same observation-based wind forcing is used for all three ocean model runs.

between atmosphere and ocean runs include parts of the North Atlantic Current (40°N, 50°W) and eastern tropical Pacific (5°S, 120°W) in *COARE − control*, and the Kuroshio (35°N, 140°E) and Agulhas (35°S, 15°E) currents in *UA−control*.

The regional inconsistencies between atmosphere and ocean simulations bring into question the robustness and significance of the differences shown. We argue below that some of the inconsistency between ocean and atmosphere sensitivity tests arises because the different test methods probe different aspects of the bulk flux algorithms. In the meantime, to address the question of significance, we compare the magnitude of changes to the interannual standard deviation of latent heat flux from the E3SMv1 pre-industrial control run (stippling in **Figure 1**). In the atmosphere sensitivity tests, large areas of the world's oceans exhibit significant changes. For the ocean tests, however, only a small fraction of ocean areas has significant changes. The chosen significance threshold (E3SMv1 interannual standard deviation) has similar patterns and magnitudes as the interannual standard deviation from the OAflux observational product (**Supplementary Figure 2**). An alternative significance threshold can be calculated as the range (maximum minus minimum) of 5-year means from the E3SM control run and from OAflux. This results in a larger threshold (**Supplementary Figure 2**), and therefore would lead to smaller areas of significant changes in **Figure 1**.

Evaporation differences (**Table 2**) largely reflect differences in latent heat flux. Thus, global mean evaporation is generally larger in control than in UA or COARE. However, one slight complication in this is that UA uses a temperature-dependent value for the latent heat of evaporation (L_v in Equation 3) while control and COARE both use a single constant. This accounts for the fact that UA has the largest evaporation in the ocean simulations, despite have a smaller magnitude of latent heat flux than control.

Compared to latent heat flux, sensible heat flux (**Figure 3**) shows greater consistency between sensitivity in atmosphere and ocean simulations. Taking the *UA−control* comparisons, for example, both the atmosphere and ocean simulations show negative changes across much of the tropics and subtropics and positive changes in parts of the Southern Ocean and North Atlantic. That being said, there are still clear differences. For example, tropical changes for *UA−control* are smaller (and generally not significant) in the atmosphere tests but are significant in the ocean tests.

Comparing across algorithms, we see that similarity between UA and COARE runs is generally greater for sensible heat flux than for latent heat flux (especially in the ocean simulations). This can be seen by noting that **Figures 3A,C** are quite similar and, to an even greater extent, **Figures 3B,D** are similar. Relative to this, the pairwise comparisons (A vs. C; B vs. D) in **Figure 1** show less

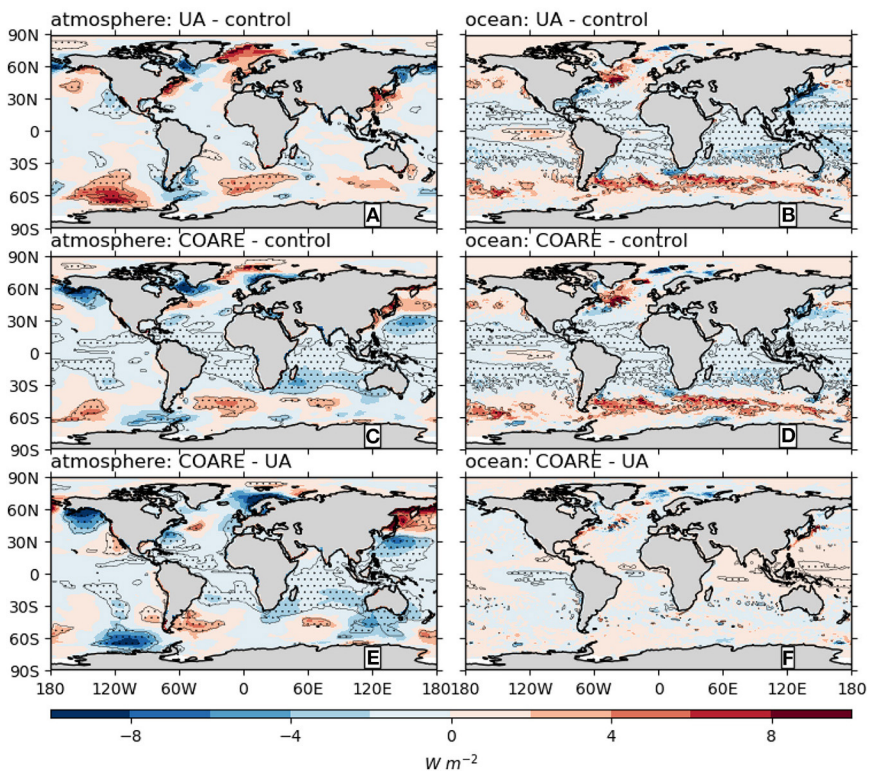

FIGURE 3 | Differences in annual mean sensible heat flux climatology between simulations with different bulk flux algorithms. The atmosphere and ocean simulation results are shown in left and right panels, respectively. Stippling designates regions where the absolute value of the difference is larger than the interannual standard deviation from the E3SMv1 pre-industrial control run. Note that the color scale is different from that in **Figure 1**.

similarity. This is in line with the finding of Brunke et al. (2011) who showed that, in observational flux products, latent heat flux uncertainties were dominated by algorithm differences, but sensible heat flux and wind stress uncertainties were dominated by bulk variable differences.

Despite the similarities in patterns of sensible heat flux differences shown in **Figure 3**, the global averages do not paint a clear picture. For example, in the atmosphere runs COARE has the largest magnitude, while in the ocean runs, UA has the largest magnitude. As a further example, for control and UA, the ocean simulations have larger magnitude sensible heat fluxes than for the atmosphere simulations, while for COARE, the atmosphere simulation has the larger magnitude. It should be noted that the *differences* in sensible heat flux between algorithms can be the same order of magnitude as differences in latent heat fluxes, even though the sensible fluxes themselves are an order of magnitude smaller.

By changing the sensible and latent heat fluxes, bulk flux algorithms can directly change the ocean surface net heat flux. Further *indirect* net heat flux changes are possible due to changes in radiation fluxes. In the ocean simulations, SST changes affect upward long wave radiation, though downward long wave and short wave are both specified by the forcing. In the atmosphere simulations, temperature, cloud, and humidity changes affect downward long wave and short wave radiation, though the upward long wave is specified by the forcing (Note that small differences occur in the forcing-specified fields in **Table 2** due to sea ice differences). These indirect radiation changes are of similar magnitudes to the latent and sensible heat flux differences. The combined impact of changes in all heat flux components are relatively large, in a relative sense. For example, the UA atmosphere simulation Q_{net} is more than double that of the control atmosphere simulation, and the COARE ocean simulation Q_{net} is more than 50% greater than that of the control ocean simulation. The effects of these changes on the atmosphere and ocean model climate are discussed in the following subsections.

We turn next to wind stress sensitivity. For zonal wind stress (**Figure 4**), ocean and atmosphere tests produce qualitatively similar results. There are, however, differences in the magnitude of changes (especially in midlatitudes) and some regions where sensitivity is of opposite sign in the atmosphere and ocean simulations (mostly in the Southern Ocean, e.g., at 45°S, 0°E). The effects of UA and COARE, relative to the control algorithm, are similar in the ocean simulations: relative to control both UA and COARE cause increased eastward wind stress in midlatitudes and increased westward wind stress in the tropics. Note that this essentially corresponds to UA and COARE giving a larger wind stress than control for any particular wind speed. While the same general pattern holds for the atmosphere simulations, the

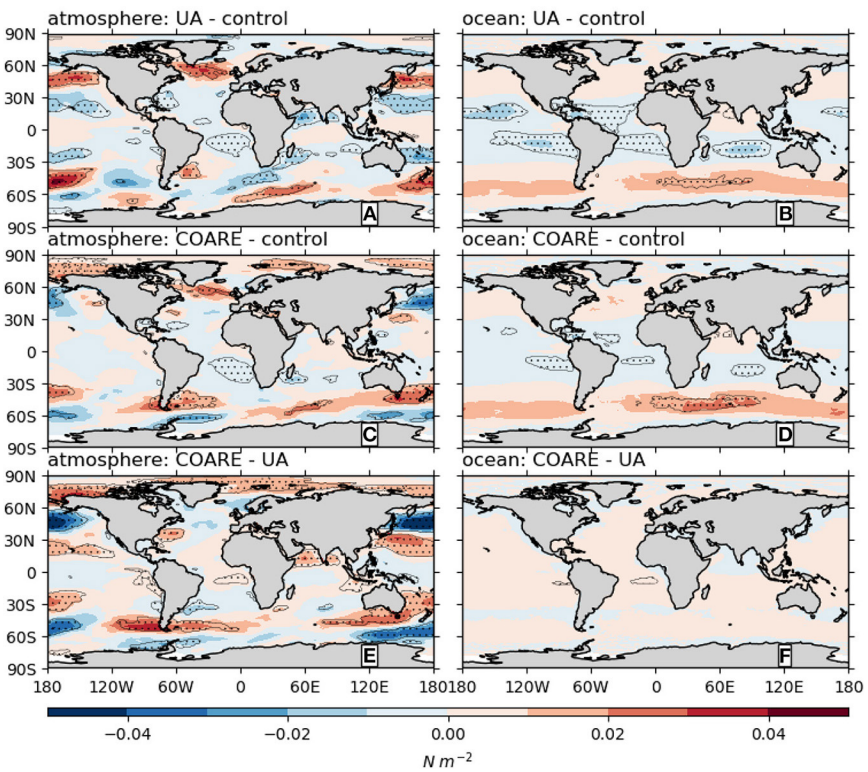

FIGURE 4 | Differences in annual mean zonal wind stress climatology between simulations with different bulk flux algorithms. The atmosphere and ocean simulation results are shown in left and right panels, respectively. Stippling designates regions where the absolute value of the difference is larger than the interannual standard deviation from the E3SMv1 pre-industrial control run.

COARE − UA atmosphere comparison reveals that their patterns are subtly different enough to result in significant differences.

Finally, for meridional wind stress (**Figure 5**) ocean and atmosphere tests produce very different results: in atmosphere tests, most of the regions with significant differences are in midlatitudes, while in ocean tests, the significant differences are almost entirely equatorward of 30°. Nonetheless, a few regions show consistent changes across both ocean and atmosphere tests. For example, in the UA-control comparisons, several subtropical marine stratocumulus regions (off the coasts of California, Chile, Namibia, Western Australia) have consistent changes between atmosphere and ocean simulations. The same holds to a lesser degree for the COARE-control comparisons.

3.2. Atmosphere Model Sensitivity

The analysis above is mostly concerned with the changes that occur *at the ocean surface* when using different bulk flux algorithms. We next consider what changes occur in the atmosphere model. We start with precipitation, as this is one of the most important outputs of Earth system models and previous studies (Brunke et al., 2008; Harrop et al., 2018) have demonstrated sensitivity to ocean surface flux parameterization methods.

Figure 6 shows that the precipitation changes induced by the change of flux algorithm have a rather noisy pattern. In general, the largest differences occur in the tropics, where the largest precipitation amounts occur. Some coherent regions of changes occur in and around the Intertropical Convergence Zone (ITCZ) and in monsoon regions (south and southeast Asia, west Africa). In the case of the Asian monsoon systems, the precipitation changes are likely related to moisture source evaporation reductions (for UA and COARE relative to control) in the Arabian Sea, Bay of Bengal, South, and East China Seas (Pathak et al., 2017; Hu et al., 2021), despite the likelihood of accompanying circulation changes (Harrop et al., 2019). In the case of the West African monsoon, the picture is less clear due to the presence of evaporation decreases in the Gulf of Guinea (∼0°N, 0°E) and increases in the tropical North Atlantic around 10°N, 20°W (for UA and COARE relative to control). We conjecture that the West African westerly jet (Lélé et al., 2015; Liu et al., 2020) can provide a causal link between the tropical North Atlantic evaporation changes and Sahelian precipitation changes, but this merits further investigation.

Regional precipitation changes further poleward consist of a patchwork of small (though significant) precipitation changes, without any obvious pattern. This may be because precipitation changes in these regions occur due to differences

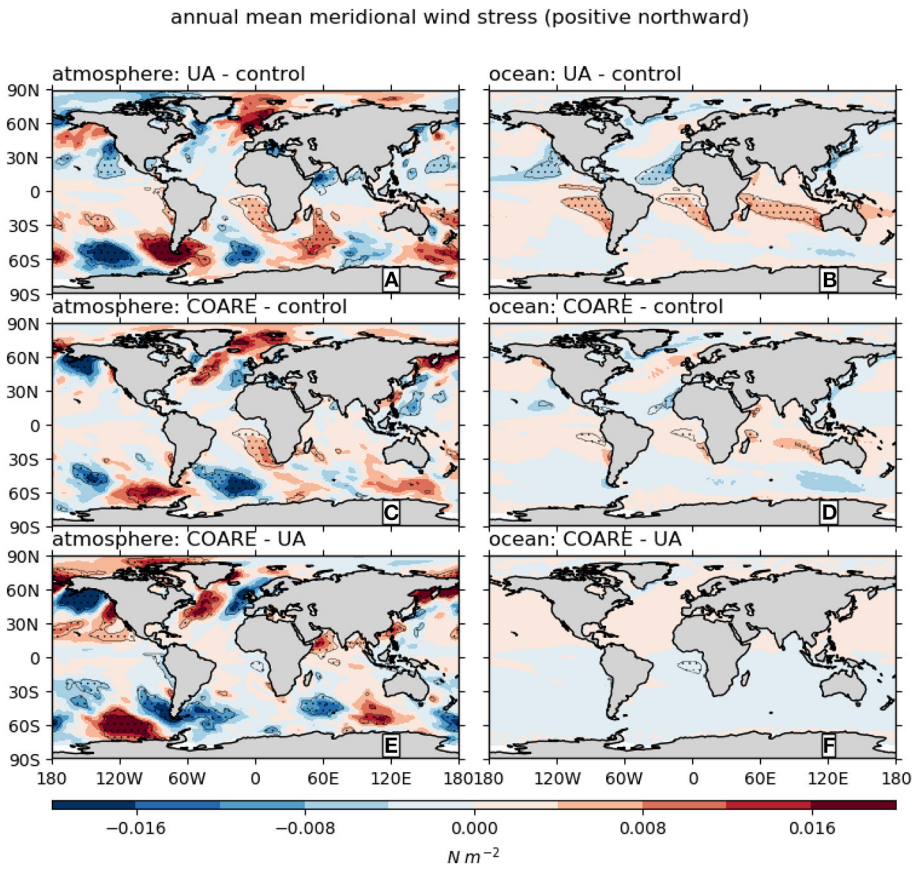

FIGURE 5 | Differences in annual mean meridional wind stress climatology between simulations with different bulk flux algorithms. The atmosphere and ocean simulation results are shown in left and right panels, respectively. Stippling designates regions where the absolute value of the difference is larger than the interannual standard deviation from the E3SMv1 pre-industrial control run. Note that the color scale is different from that in **Figure 4**.

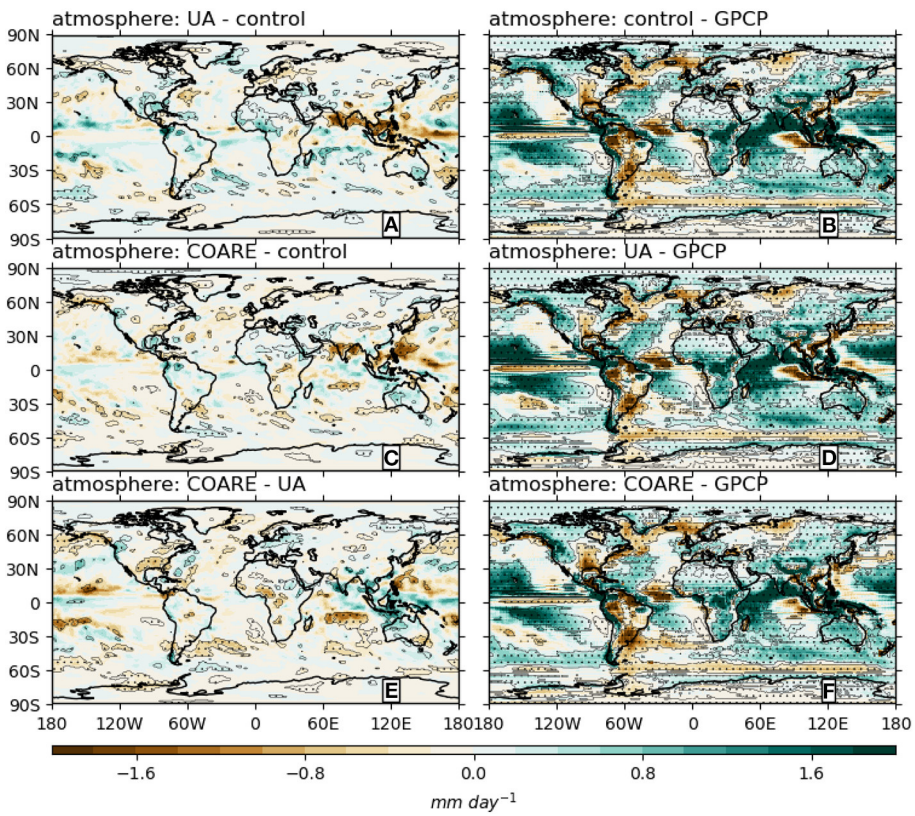

FIGURE 6 | Differences in annual mean precipitation climatology between simulations with different bulk flux algorithms (left column) and annual mean precipitation biases relative to GPCP (right column). Stippling designates regions where the absolute value of the difference is larger than the interannual standard deviation from the E3SMv1 pre-industrial control run.

in both circulation and moisture source region evaporation, with different processes dominating in different seasons. Seasonal analyses (not shown) support this to some extent. For example, summer precipitation in UA and COARE, relative to control, show a dipole with less precipitation in northwest Europe and more in the Iberian peninsula. Such a dipole has been linked to Atlantic multi-decadal Gulf Stream SST variability (e.g., Palter, 2015) so it is possible that the algorithm-induced Gulf Stream heat flux changes in our study have the same effect as the multidecadal SST variability-induced heat flux changes seen in observations. Meanwhile, in winter, a different and roughly opposite precipitation change occurs — wetter over the United Kingdom and drier in southwest Europe. A similar pattern occurs in the northwest Pacific between Alaska and California. Observational evidence (e.g., Wills et al., 2016; Wills and Thompson, 2018) suggests that these changes could be caused by circulation changes related to Gulf Stream and Kuroshio heat flux changes, but more detailed study is needed to better understand this.

Also shown in **Figure 6** are biases relative to the GPCP long-term mean. The biases are generally larger than the differences between simulations, and therefore have very similar patterns for all three atmosphere simulations. While the spatial patterns of biases do not offer a clear differentiation between algorithms, the global mean statistics do. For the global mean bias, COARE has the lowest (+0.32 $mm\ day^{-1}$), followed by UA (+0.37 $mm\ day^{-1}$) then control (+0.38 $mm\ day^{-1}$). For the root mean square error (RMSE), COARE again has the lowest (0.98 $mm\ day^{-1}$), while control and UA have very similar values (1.02 $mm\ day^{-1}$). These global annual mean figures obscure more nuanced regional and seasonal patterns, making selection of a "best" algorithm even more challenging.

The largest precipitation biases in **Figure 6** occur in the tropics, and especially in the warm pool of the Indian and Pacific oceans. This region is examined more closely in **Figure 7**, which shows distinct patterns of zonal mean bias in different seasons. All seasons share the feature that the model simulations generally have an exaggerated double maximum compared to GPCP. This is a widespread and long-standing problem in Earth system models (e.g., Zhang et al., 2015) and so it is interesting to note that algorithm choice makes some notable differences. In particular, UA has a markedly lower bias north of the equator in boreal summer (JJA) and COARE has the most realistic results in boreal spring (MAM). However, no single algorithm has the best results in all seasons. This point is reinforced by the precipitation RMSE for this sub-region: UA has the lowest in JJA and SON; COARE has the lowest in MAM; control has the lowest in DJF.

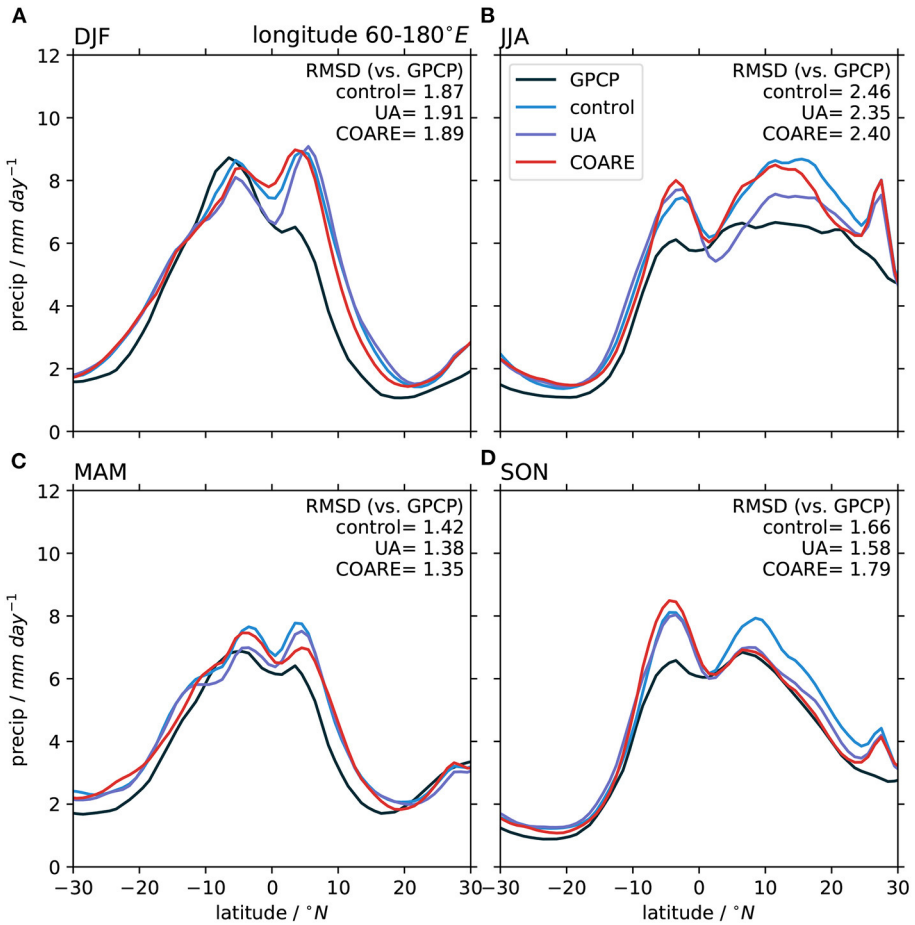

FIGURE 7 | Zonal mean, seasonal mean precipitation from the three atmosphere simulations and GPCP observational data: **(A)** December to February; **(B)** June to August; **(C)** March to May; **(D)** September to November. The zonal sector considered is 60°E to 180°E. GPCP data were bilinearly interpolated to the same 1° grid as the other data before calculating. Text in each panel shows the area-weighted root mean square difference, in mm day^{-1}, between each model and the GPCP data, calculated from gridded data rather than from the zonal means.

TABLE 3 | Long-term annual mean near-surface meteorology from atmosphere simulations, averaged over global oceans, unless otherwise indicated.

	Control	UA	COARE
Precip (*mm day*$^{-1}$)	3.33	3.31	3.24
Precip (*global*)[a]	3.08	3.07	3.01
T_{2m} (°*C*)	16.63	16.55	16.46
q_{2m} (*g kg*$^{-1}$)	11.09	11.02	10.81
U_{10m} (*m s*$^{-1}$)	7.52	7.14	7.20
($T_{2m} - T_s$) (°*C*)	−1.05	−1.12	−1.18

Variables are total precipitation; 2-m air temperature T_{2m}; 2-m specific humidity q_{2m}; 10-m wind speed U_{10m}; and difference between T_{2m} and surface temperature T_S.
[a] *For land and ocean combined.*

Table 3 shows that, relative to control, both UA and COARE have lower global (land and ocean combined) mean precipitation. This is in line with the evaporation changes shown in **Table 2**, demonstrating that, at least in a global sense, there is a general balance between evaporation and precipitation changes.

We next look at other aspects of near surface meteorology affected by choice of bulk flux algorithm, bearing in mind that the method of forcing the atmosphere model with specified sea surface temperatures strongly constrains some fields. Mean 2 m air temperature over the oceans is highest in control, followed by UA, with COARE the lowest. The differences at first glance appear modest ($< \ 0.2°C$ between control and COARE), but when reformulated as a difference between surface and 2 m temperature (also shown in **Table 3**), they seem somewhat more significant. The same is true of 2 m specific humidity: the absolute values appear similar but, considering that the differences arise just 2 m above surfaces of identical temperature, the size of the differences is more surprising. Finally, and arguably most importantly, the 10 m wind speed is reduced in both UA and COARE compared to control. This result is significant as it suggests that some of the atmosphere simulation flux changes, discussed above, occur due to changes in wind speed rather than changes in stability and roughness formulations.

Other changes in model climate higher in the atmosphere also occur. We briefly mention a few (and refer to relevant

figures in the **Supplementary Material**). Coherent patterns of zonal wind changes occur throughout the full depth of the troposphere (**Supplementary Figures 3, 4**). These changes bear some resemblance to changes induced by a decrease in surface roughness in Polichtchouk and Shepherd (2016), though in our case the changes are smaller and mostly limited to the winter hemisphere. The global mean temperatures at several different pressure levels (**Supplementary Figures 5, 6**) are reduced in both UA and COARE, relative to control. We suggest that this is a result of the net heat flux changes, though this interpretation is slightly complicated by net heat flux changes over land, which we do not consider here. Likewise, we suggest that changes in precipitable water (reduced in UA and COARE, relative to control; not shown) are due to reduced ocean evaporation in UA and COARE.

There are also differences in certain metrics that govern model simulations of variability and climate change. Arguably most important is the net top-of-atmosphere (TOA) radiation. Control has the smallest, at $+0.58$ W m^{-2}, followed by UA ($+1.05$ W m^{-2}) then COARE ($+1.54$ W m^{-2}). While the absolute values from our relatively short sensitivity tests may not be especially meaningful due to large internannual variability (e.g., Loeb et al., 2018), the differences are important, especially considering the magnitude of biases seen in Golaz et al. (2019) who reported TOA imbalance smaller than observed in both the coupled (model minus observations = -0.54 W m^{-2}) and AMIP (model minus observations = -0.71 W m^{-2}) simulations. Noting that those simulations used the control algorithm, and based on the differences between the three algorithms, UA therefore does best at correcting this bias, while COARE slightly overshoots. The differences arise from a combination of changes in clouds and clear-sky longwave emission.

High quality satellite observations from CERES-EBAF v4.1 data allow calculation of mean biases and root-mean-square differences (RMSD) for several TOA radiation quantities (**Table 4**). In most quantities, UA is intermediate between COARE and control. This means that the smallest bias usually occurs with control (e.g., TOA net longwave) or COARE (e.g., TOA net shortwave). This does, however, conceal a number of more complicated regional biases. For example, compared to control, COARE seems to reduce the mean bias in net cloud radiative effect, but part of this improvement comes from COARE's *increased* bias in subtropical stratocumulus shortwave cloud forcing. Similarly, we see that UA has the smallest net cloud forcing RMSD, despite the fact that COARE has the smallest net cloud forcing mean bias. We also note, in reference to the above discussion of net TOA radiation, that UA has the smallest bias and RMSD in that quantity.

TABLE 4 | Global mean and global root-mean-square (RMS) of annual mean differences between model and observations.

	Bias			RMSD		
	Control	**UA**	**COARE**	**Control**	**UA**	**COARE**
Precipitation ($mm\ day^{-1}$)	0.38	0.37	0.32	1.02	1.02	0.98
TOA net radiation ($W\ m^{-2}$)	–0.34	0.13	0.64	8.19	7.97	8.38
TOA net shortwave ($W\ m^{-2}$)	–1.43	–1.36	–1.05	9.63	9.70	9.77
TOA net longwave ($W\ m^{-2}$)	–0.96	–1.36	–1.55	5.71	6.20	6.07
Net cloud forcing ($W\ m^{-2}$)	–6.98	–6.84	–6.37	11.16	10.94	11.00
Shortwave cloud forcing ($W\ m^{-2}$)	–3.64	–3.57	-3.14	10.17	10.18	10.25
Longwave cloud forcing ($W\ m^{-2}$)	–3.34	–3.26	-3.23	6.51	6.75	6.55

Precipitation is compared to GPCP observations. TOA radiation quantities are compared to CERES-EBAF v4.1 observations.

TABLE 5 | Ocean simulation global mean statistics.

	Control	**UA**	**COARE**
SST ($^{\circ}C$)	18.23	18.28	18.42
SSS (*PSU*)	34.58	34.58	34.55
ΔSSH (cm)[a]	38.27	30.99	70.06
ΔOHC (10^{22} J)[b]	–10.51	–1.254	+3.763
$\lvert SSS\ restoring \rvert$ ($m\ PSU\ yr^{-1}$)	12.5	12.2	12.4
$\lvert u \rvert$ ($cm\ s^{-1}$)	7.87	8.30	8.21
$\lvert v \rvert$ ($cm\ s^{-1}$)	4.05	4.24	4.18

Statistics are long-term annual averages unless otherwise indicated. Variables are sea surface temperature SST; sea surface salinity SSS; sea surface height SSH; ocean heat content OHC; SSS restoring; eastward surface current component u; and northward surface current component v. For SSS restoring, u and v, the absolute value is taken before applying spatial and temporal averaging.

[a] *Average SSH over model year 10 relative to initial condition.*

[b] *OHC in December of model year 10 relative to initial condition.*

3.3. Ocean Model Sensitivity

Changes in the ocean model are, like changes in the atmosphere model, constrained by the forcing dataset. In fact, for the ocean model the forcing is a stronger constraint because the wind speed—arguably the biggest factor in the atmosphere model changes seen above—is prescribed. Nonetheless, we do see ocean model responses due to the subtle changes in net heat flux, evaporation and wind stress. These are described here.

The SST in the ocean simulations is able to vary, though it is strongly constrained by the air temperature in the forcing. The differences seen in **Table 5** are therefore reflecting the different algorithms' preferred ($T_{2m} - T_s$) values, shown in **Table 3**: COARE has the highest ($T_s - T_{2m}$) and therefore the highest T_s, followed by UA, then control. While the SST is not able to respond fully to the differences in net heat flux, the ocean heat content (OHC) is able to respond more. We therefore see that changes in OHC (denoted ΔOHC) over the course of the ocean simulations do reflect the differences in net heat flux: the algorithms are ranked control, then UA, then COARE, in increasing order for both SST and ΔOHC. It should be noted that the differences in ΔOHC between model runs are of a comparable magnitude to observed decadal variability and trends, and are therefore physically meaningful.

Changes in evaporation could, in principle, affect both ocean salinity and sea level. However, surface salinity is subject to salinity restoring (the model field is relaxed to observational climatology; see Petersen et al., 2019 for further details) and this effectively cuts any link between evaporation changes and ocean salinity changes. It is therefore not surprising that all three ocean simulations have very similar surface salinity (**Table 5**). We can however, look at the magnitude of salinity restoring that is required to stop the model drifting away from observations. The mean absolute values are similar for all three simulations: UA has the lowest value, followed by COARE.

The changes in sea surface height (ΔSSH in **Table 5**) over the course of each ocean simulation are all of unrealistically large magnitude, likely due to a systematic imbalance between precipitation in the forcing data set and evaporation calculated in the model. However, *differences* (between ocean simulations) in the sea level change (**Table 5**) do reflect the evaporation differences seen in **Table 2**: UA has the largest evaporation and therefore the smallest sea level rise, while COARE has the smallest evaporation and the largest sea level rise. The remainder of the sea surface height changes include thermosteric effects, i.e., the expansion of sea water as it warms. The thermosteric component is isolated by subtracting the global ocean mean change due to evaporation. Thus, the difference between two algorithms can be expressed as:

$$\Delta SSH^{A-B}_{thermosteric} = (SSH^{A}_{year10} - SSH^{A}_{initial}) - (SSH^{B}_{year10} - SSH^{B}_{initial}) + (\sum_{time}[\overline{E_A} - \overline{E_B}]) \quad (4)$$

where A and B denote the two algorithms being compared, $\overline{E_{A,B}}$ are the global mean evaporation rates and the summation gives the cumulative evaporation difference. The spatial patterns of differences (between different bulk flux algorithms) are shown in **Figure 8**. Relative to control, UA and COARE result in similar changes, albeit with larger magnitudes for COARE. The changes are fairly symmetric about the equator, with the following key features: small changes of both signs for most regions equatorward of 15°; larger negative changes in the tropical east Pacific; relatively large increases between 15° and 45°; and large decreases poleward of this, especially in the Southern Ocean. This all suggests that much of the extra heat content of the UA and COARE simulations, caused by the larger net heat flux with these algorithms compared to control, ends up being "stored" in the subtropics and midlatitudes.

Ocean surface velocity is strongly constrained by the wind field specified in the forcing data. However, differences in velocity component magnitudes do occur (**Table 5**). We see that UA has the highest velocities, followed closely by COARE, and control has the lowest by a considerable margin. Note that this is the reverse of the pattern seen in the atmosphere 10 metre wind speeds seen in **Table 3**. Both of these changes are consistent with the fact that, for a particular wind speed, UA gives the largest wind stress, followed by COARE then control. Such differences were also found (at least for moderate wind speeds) in Zeng et al. (1998; their Figure 3C). This means that, where wind speeds are specified (in the ocean simulations) UA gives the largest wind stress and therefore the highest ocean surface velocities. On the other hand, when the wind speed can vary but the surface velocity is fixed (in the atmosphere simulations), UA results in the lowest wind speeds while giving similar wind stress.

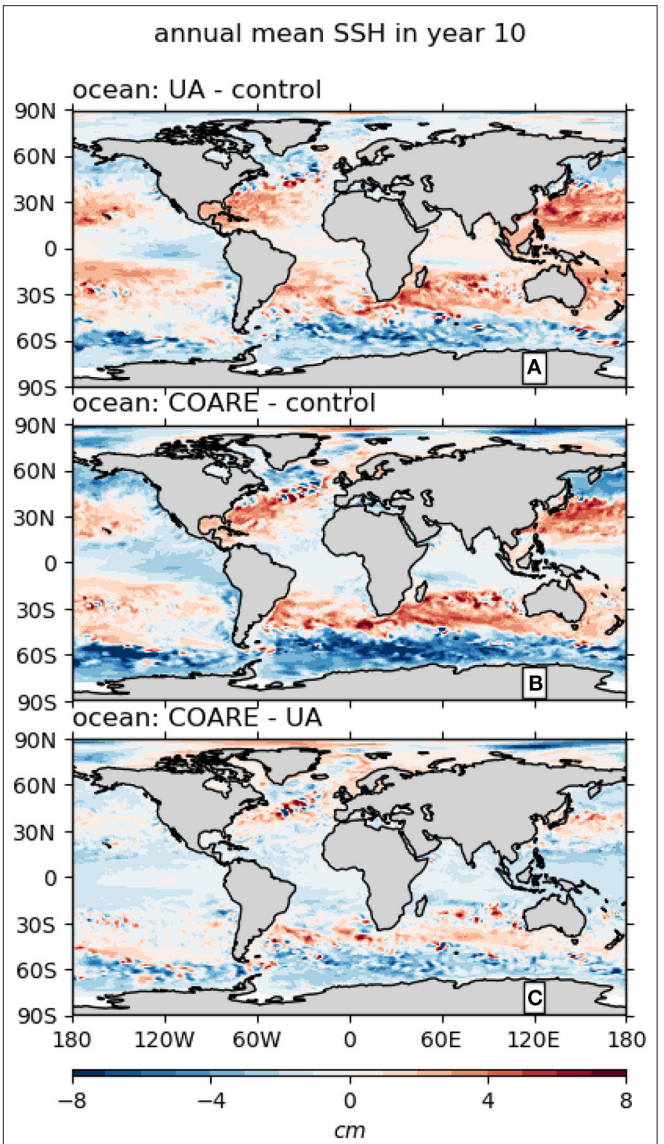

FIGURE 8 | Differences in model year 10 sea surface height between simulations with different ocean surface bulk flux parameterizations. The changes in sea surface height due to evaporation differences have been removed as in Equation (4).

A number of other variables are affected by the choice of bulk flux algorithm, though the changes are relatively minor. The Atlantic Meridional Atlantic Circulation (AMOC) is unrealistically weak in all three simulations (as has been noted in other E3SMv1 simulations; Golaz et al., 2019; Petersen et al., 2019) and there are only minor differences between them. However, AMOC is slightly stronger in UA and control than in COARE (**Supplementary Figure 7**). Possibly related to this

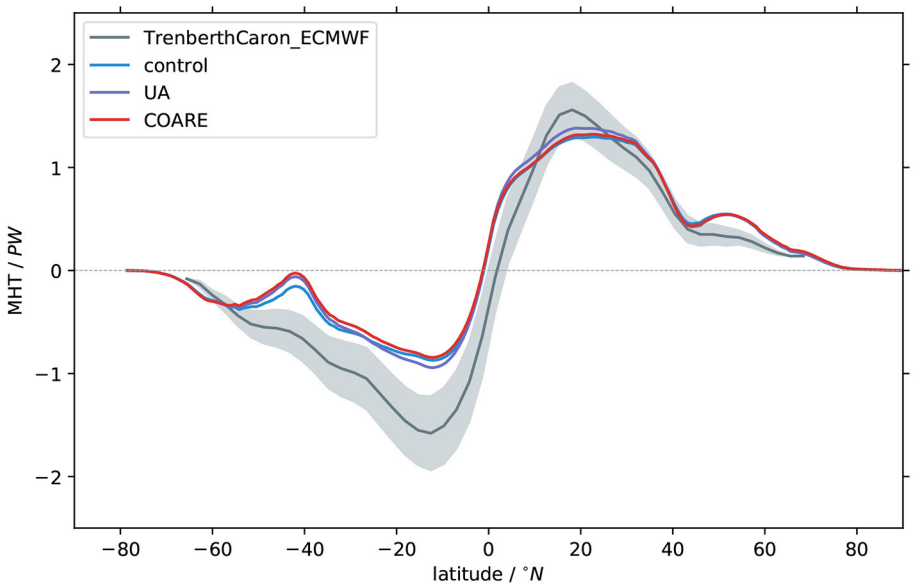

FIGURE 9 | Mean global meridional ocean heat transport (positive northwards) from ocean simulations. Also shown is a reanalysis-based observational estimate from Trenberth and Caron (2001): shading represents ±1 standard error, based on their error analysis using assumed uncertainties in derived surface fluxes.

are changes in wintertime ocean mixed layer depths in the North Atlantic Deep Water formation regions (not shown) and changes in the global meridional heat transport (MHT; **Figure 9**). However, global MHT integrates more processes than just the AMOC (e.g., Forget and Ferreira, 2019), and it is in fact the tropical maxima of MHT (shallower circulations more directly linked to surface fluxes) that are changed most—generally of slightly larger magnitude in UA than in control and COARE. As with the AMOC, the MHT differences do not have large enough impacts to significantly reduce the model's background biases. Even so, we suggest that the sensitivity of ocean circulation to algorithm choice deserves longer model runs and further study, beyond the more directly affected quantities discussed here.

4. CONCLUSIONS AND FURTHER DISCUSSION

We have performed sensitivity tests of three ocean surface flux parameterizations in the atmosphere and ocean components of E3SM. Spatial patterns of heat flux and wind stress sensitivity differ significantly between ocean and atmosphere simulations, with larger magnitudes of changes in the atmosphere simulations. This is not surprising given that wind speed—which strongly affects surface fluxes—can vary in the atmosphere simulations but is specified by the forcing data in ocean simulations. What is perhaps more surprising is the degree of consistency (between ocean and atmosphere simulations) of the global mean latent heat flux and net surface heat flux sensitivity.

The impact of wind speed-flux feedbacks on the atmosphere simulation sensitivity highlights the central role of wind speed in determining fluxes. Thus, the ocean simulations (with fixed wind speeds) tell us more about the theoretical aspects of algorithm design (e.g., the functional forms of stability and roughness formulae) while at the same time revealing how the ocean may respond to flux changes. On the other hand, the atmosphere simulations (where wind speed can vary) tell us about the combined effects of theoretical changes and resultant wind speed differences. Thus, our results show that, relative to the control algorithm, COARE has greater theoretical differences, but when wind speeds are allowed to vary, UA has a greater overall effect. A regional example of this is shown in **Figure 10** for the Gulf Stream, where both COARE and UA have lower magnitude of annual mean latent heat flux than control (**Figure 1**). **Figure 10** shows that, for wind speeds greater than about 12 $m\ s^{-1}$, both COARE and UA have lower magnitude latent heat fluxes than control. However, it is also clear that the distribution of wind speeds are shifted, with UA having the lowest speeds, followed by COARE and then control having the highest. Another illustration of the importance of wind speed changes in the atmosphere simulations is the degree of correspondence between the latent heat flux changes (**Figure 1**, left column) and the wind speed changes (**Figure 2**, left column): patterns of negative wind speed differences match closely with positive latent heat flux differences (i.e., due to the sign convention, negative flux *magnitude* differences).

An important caveat to this interpretation, however, is that some of the impacts of the UA algorithm are tempered by its use of temperature-dependent L_v (latent heat of vaporization). Thus, although UA has larger differences (relative to control) in latent heat flux and net heat flux, COARE has a larger difference in evaporation, and therefore a larger impact on precipitation. This can have other important consequences for modeled global energy and water cycles, as was seen in the ocean simulations: compared to control, UA simulates a sea level fall and OHC

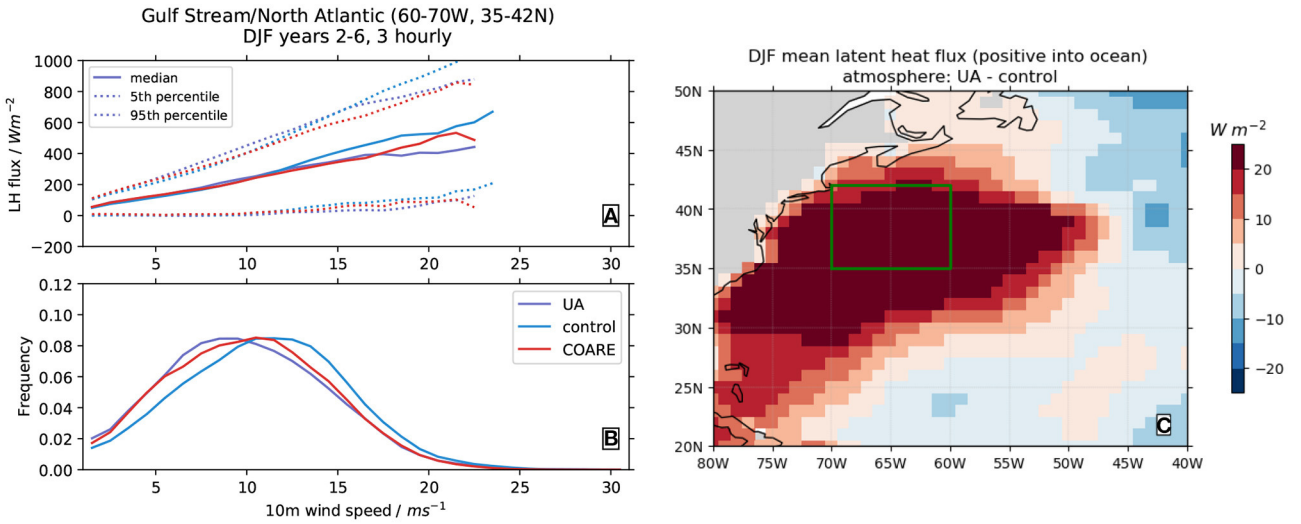

FIGURE 10 | (A) Latent heat flux quantiles, as functions of 10-m wind speed, and **(B)** 10-m wind speed distributions, for the three atmosphere simulations in a region around the Gulf Stream (60−70°W, 35−42°N). The quantiles and wind speed distribution are calculated from 3-hourly model output from the winter season (December, January, and February) over model years 2–6 of each simulation, binned into 1 $m\ s^{-1}$ bins. **(C)** December to February multi-year mean latent heat flux difference between UA and control atmosphere simulations, with the region used in **(A,B)** shown by the green box. Note that the heat flux sign convention in **(A)** is opposite to that used in **(C)**: positive values correspond to evaporation. The colors shown in the legend of **(B)** also apply to **(A)**.

increase, while COARE simulates sea level *rise* and OHC increase. Of course, the comparison with control is somewhat arbitrary and does not have any physical significance when interpreting any single model simulation. It does however, underscore that the algorithms give different portrayals of the links between global energy and water cycles. This point is particularly important for coupled Earth system modeling, where conservation of water and energy are important constraints in model realism. The effects of flux algorithm choice in this respect are the subject of ongoing coupled model development and testing within the E3SM project.

It is worth noting that the absolute values (from any single simulation) of quantities like ΔOHC are not physically meaningful. Instead, they are a product of the disequilibrium between the forcing data and initial conditions [see Strobach et al. (2018) for a thorough exploration of such disequilibrium conditions]. Nonetheless, the *differences* between algorithms in their responses to this disequilibrium are meaningful: these kind of differences are exactly what may yield variations in estimates of transient climate response to greenhouse gas and other anthropogenic climate forcing.

We finish by revisiting our aims for this study and summarizing the key results for each:

1. Our atmosphere sensitivity tests suggest that parts of the tropical Indo-Pacific region (∼20°N−20°S, 60°E−150°W), along with western boundary currents, are hotspots of algorithm differences, as might be expected from the fact that these regions are the continued focus of ocean-atmosphere interaction research (e.g., Edson et al., 2013). In addition, our ocean sensitivity tests highlight the tropical east Pacific and the Southern Ocean as regions of uncertainty, worthy of further study. It is interesting to note that these regions include a number of "edge cases" recognized in recent ocean-atmosphere interaction research. The Indo-Pacific warm pool can exhibit strong diurnal SST warming (Fairall et al., 1996a) and gusty winds in thunderstorm cold pools (Zeng et al., 2002). Western boundary currents and the eastern tropical Pacific are both domains of strong gradients with complex wind-wave-current interactions which are not well-understood (Villas Bôas et al., 2019). The Southern Ocean features consistently strong winds and extreme wave conditions. These cases lead to uncertainties in fluxes and differences between the algorithms, both by design and due to insufficient direct flux observations to constrain bulk algorithm formulation.
2. We find that the choice of test methodology seems to highlight different aspects of the algorithms' differences. Atmosphere simulations, by allowing a wind speed-flux feedback cycle, show the highest absolute magnitudes of flux differences between algorithms. This has the advantage of allowing investigation of changes in wind speed distribution due to differences in algorithms' surface roughness formulations. However, it has disadvantages in that changes in any particular location may be influenced by remotely forced atmospheric circulation changes (e.g., tropical forcing of midlatitude circulation), and that changes may be due to model internal variability (i.e., chaotic differences in weather patterns). Our significance testing is intended to address this, but the relatively short simulations used here are certainly a minor limitation of this study.
3. Finally, we have demonstrated that impacts of algorithm choice are seen throughout the atmosphere and ocean models. Of particular importance in the atmosphere simulations are

the systematic circulation changes and differences in global mean precipitation and TOA radiative effects. There are also important regional changes — for example in heat fluxes in the seas adjacent to the Asian Monsoon system, with associated precipitation changes over land. In the ocean, we see small but notable impacts on meridional overturning circulations and meridional heat transport. It is interesting to speculate that the changes seen in these quantities in a coupled model setup (where the larger magnitude flux changes seen in the atmosphere simulations might be imposed on the ocean) could be larger than seen in our ocean simulation results. This possibility, along with the differences in global energy and water cycle responses discussed above, are good reasons to pursue coupled Earth system model sensitivity testing in future studies. Indeed, such efforts are already underway in the E3SM project.

In the absence of a definitive observational basis to rank algorithms by flux biases, these other changes offer a way to inform algorithm choice. In particular, both UA and COARE improve on the control algorithm in global mean precipitation and TOA radiative metrics, though there are some important regional changes that should also be considered. In the ocean, UA seems to reduce biases slightly (in comparison to control) in the Atlantic meridional overturning circulation and meridional heat transport.

DATA AVAILABILITY STATEMENT

1. Model source code is available at https://github.com/E3SM-Project/E3SM/commit/121d1c99d1c8573dc9e57536a0819ec7f423e2ee. Raw model output is available at https://portal.nersc.gov/archive/home/j/jeyre/www/. Intermediate data used to create the figures and tables in this article are available at https://osf.io/4enh5/. Computer code used to create the figures and tables is available at https://bitbucket.org/jack_eyre/oceanfluxes_13apr2021. Some additional calculations were used from the MPAS-Analysis package (https://github.com/MPAS-Dev/MPAS-Analysis).
2. OAflux, CERES-EBAF and GPCP are publicly available from repositories given in the References section and cited in the text.

AUTHOR CONTRIBUTIONS

JRE implemented the UA algorithm in E3SM, performed the model runs and data analysis, and led the writing. XZ provided guidance on modeling strategy and analysis methods, and contributed to the writing. KZ implemented the COARE algorithm in E3SM and contributed to the writing. All authors contributed to the article and approved the submitted version.

FUNDING

This research was supported by the U.S. Department of Energy (DE-SC0016533, DE-AC52-07NA27344/B639244). KZ was supported by the Office of Science of the U.S. Department of Energy as part of the Earth System Modeling Program. The Pacific Northwest National Laboratory is operated for DOE by Battelle Memorial Institute under contract DE-AC05-76RL01830.

ACKNOWLEDGMENTS

We thank Thomas Tonazzio and Chris Fairall for providing the COARE algorithm code. We thank Luke Van Roekel and Po-Lun Ma for assistance in setting up the model runs. Michael Brunke, Joellen Russell, and Chris Castro provided much useful advice about details of the flux algorithms and interpretation of results. We thank the editor and reviewers for their constructive comments. This research used resources of the National Energy Research Scientific Computing Center (NERSC), a U.S. Department of Energy Office of Science User Facility operated under Contract No. DE-AC02-05CH11231. We gratefully acknowledge the computing resources provided on Blues, a high-performance computing cluster operated by the Laboratory Computing Resource Center at Argonne National Laboratory.

SUPPLEMENTARY MATERIAL

The Supplementary Material for this article can be found online at: https://www.frontiersin.org/articles/10.3389/fmars.2021.642804/full#supplementary-material

REFERENCES

Adler, R. F., Huffman, G. J., Chang, A., Ferraro, R., Xie, P.-P., Janowiak, J., et al. (2003). The version-2 global precipitation climatology project (GPCP) monthly precipitation analysis (1979–present). *J. Hydrometeorol.* 4, 1147–1167. doi: 10.1175/1525-7541(2003)004<1147:TVGPCP>2.0.CO;2

Adler, R. F., Huffman, G. J., Chang, A., Ferraro, R., Xie, P.-P., Janowiak, J., et al. (2018). *GPCP Version 2.3 Combined Precipitation Data Set (Updated Monthly)*. Available online at: https://psl.noaa.gov/data/gridded/data.gpcp.html (accessed February 07, 2020).

Beljaars, A. C. M., and Holtslag, A. A. M. (1991). Flux parameterization over land surfaces for atmospheric models. *J. Appl. Meteorol. Climatol.* 30, 327–341. doi: 10.1175/1520-0450(1991)030<0327:FPOLSF>2.0.CO;2

Brodeau, L., Barnier, B., Gulev, S. K., and Woods, C. (2016). Climatologically significant effects of some approximations in the bulk parameterizations of turbulent air–sea fluxes. *J. Phys. Oceanogr.* 47, 5–28. doi: 10.1175/JPO-D-16-0169.1

Brunke, M. A., Fairall, C. W., Zeng, X., Eymard, L., and Curry, J. A. (2003). Which bulk aerodynamic algorithms are least problematic in computing ocean surface turbulent fluxes? *J. Clim.* 16, 619–635. doi: 10.1175/1520-0442(2003)016<0619:WBAAAL>2.0.CO;2

Brunke, M. A., Wang, Z., Zeng, X., Bosilovich, M., and Shie, C.-L. (2011). An assessment of the uncertainties in ocean surface turbulent fluxes in 11 reanalysis, satellite-derived, and combined global datasets. *J. Clim.* 24, 5469–5493. doi: 10.1175/2011jcli4223.1

Brunke, M. A., Zeng, X., and Anderson, S. (2002). Uncertainties in sea surface turbulent flux algorithms and data sets. *J. Geophys. Res. Oceans* 107, 5–1–5–21. doi: 10.1029/2001JC000992

Brunke, M. A., Zeng, X., Misra, V., and Beljaars, A. (2008). Integration of a prognostic sea surface skin temperature scheme into weather

and climate models. *J. Geophys. Res.* 113. doi: 10.1029/2008jd010607

Brutsaert, W. (1982). *Evaporation into the Atmosphere: Theory, History and Applications*. Environmental Fluid Mechanics. Dordrecht: Springer.

Doelling, D. (2019). *CERES Energy Balanced and Filled (EBAF) TOA Monthly Means Data in netCDF Edition4.1*. Available online at: 10.5067/TERRA-AQUA/CERES/EBAF-TOA_L3B004.1 (accessed 23, June 2020).

Dyer, A. J. (1974). A review of flux-profile relationships. *Bound. Layer Meteorol.* 7, 363–372. doi: 10.1007/BF00240838

Edson, J. B., Hinton, A. A., Prada, K. E., Hare, J. E., and Fairall, C. W. (1998). Direct covariance flux estimates from mobile platforms at sea*. *J. Atmos. Ocean. Technol.* 15, 547–562. doi: 10.1175/1520-0426(1998)015<0547:DCFEFM>2.0.CO;2

Edson, J. B., Jampana, V., Weller, R. A., Bigorre, S. P., Plueddemann, A. J., Fairall, C. W., et al. (2013). On the exchange of momentum over the open ocean. *J. Phys. Oceanogr.* 43, 1589–1610. doi: 10.1175/JPO-D-12-0173.1

Fairall, C. W., Bradley, E. F., Godfrey, J. S., Wick, G. A., Edson, J. B., and Young, G. S. (1996a). Cool-skin and warm-layer effects on sea surface temperature. *J. Geophys. Res. Oceans* 101, 1295–1308. doi: 10.1029/95JC03190

Fairall, C. W., Bradley, E. F., Hare, J. E., Grachev, A. A., and Edson, J. B. (2003). Bulk parameterization of air–sea fluxes: updates and verification for the COARE Algorithm. *J. Clim.* 16, 571–591. doi: 10.1175/1520-0442(2003)016<0571:BPOASF>2.0.CO;2

Fairall, C. W., Bradley, E. F., Rogers, D. P., Edson, J. B., and Young, G. S. (1996b). Bulk parameterization of air-sea fluxes for tropical ocean-Global atmosphere coupled-Ocean atmosphere response experiment. *J. Geophys. Res. Oceans* 101, 3747–3764. doi: 10.1029/95JC03205

Forget, G., and Ferreira, D. (2019). Global ocean heat transport dominated by heat export from the tropical Pacific. *Nat. Geosci.* 12, 351–354. doi: 10.1038/s41561-019-0333-7

Găinuşă-Bogdan, A., Braconnot, P., and Servonnat, J. (2015). Using an ensemble data set of turbulent air-sea fluxes to evaluate the IPSL climate model in tropical regions. *J. Geophys. Res. Atmos.* 120, 4483–4505. doi: 10.1002/2014JD022985

Golaz, J.-C., Caldwell, P. M., Roekel, L. P. V., Petersen, M. R., Tang, Q., Wolfe, J. D., et al. (2019). The DOE E3SM coupled model version 1: overview and evaluation at standard resolution. *J. Adv. Model. Earth Syst.* 11, 2089–2129. doi: 10.1029/2018MS001603

Harrop, B. E., Ma, P.-L., Rasch, P. J., Neale, R. B., and Hannay, C. (2018). The role of convective gustiness in reducing seasonal precipitation biases in the Tropical West Pacific. *J. Adv. Model. Earth Syst.* 10, 961–970. doi: 10.1002/2017MS001157

Harrop, B. E., Ma, P.-L., Rasch, P. J., Qian, Y., Lin, G., and Hannay, C. (2019). Understanding monsoonal water cycle changes in a warmer climate in E3SMv1 using a normalized gross moist stability framework. *J. Geophys. Res. Atmos.* 124, 10826–10843. doi: 10.1029/2019JD031443

Holdsworth, A. M., and Myers, P. G. (2015). The influence of high-frequency atmospheric forcing on the circulation and deep convection of the Labrador Sea. *J. Clim.* 28, 4980–4996. doi: 10.1175/JCLI-D-14-00564.1

Holtslag, A. A. M., Bruijn, E. I. F. D., and Pan, H.-L. (1990). A high resolution air mass transformation model for short-range weather forecasting. *Mon. Weather Rev.* 118, 1561–1575. doi: 10.1175/1520-0493(1990)118<1561:AHRAMT>2.0.CO;2

Hu, Q., Jiang, D., Lang, X., and Yao, S. (2021). Moisture sources of summer precipitation over eastern China during 1979–2009: a Lagrangian transient simulation. *Int. J. Climatol.* 41, 1162–1178. doi: 10.1002/joc.6781

Kader, B. A., and Yaglom, A. M. (1990). Mean fields and fluctuation moments in unstably stratified turbulent boundary layers. *J. Fluid Mech.* 212, 637–662. doi: 10.1017/S0022112090002129

Kostov, Y., Johnson, H. L., and Marshall, D. P. (2019). AMOC sensitivity to surface buoyancy fluxes: the role of air-sea feedback mechanisms. *Clim. Dyn.* 53, 4521–4537. doi: 10.1007/s00382-019-04802-4

Large, W. G., and Caron, J. M. (2015). Diurnal cycling of sea surface temperature, salinity, and current in the CESM coupled climate model. *J. Geophys. Res. Oceans* 120, 3711–3729. doi: 10.1002/2014JC010691

Large, W. G., and Pond, S. (1981). Open ocean momentum flux measurements in moderate to strong winds. *J. Phys. Oceanogr.* 11, 324–336.

Large, W. G., and Pond, S. (1982). Sensible and latent heat flux measurements over the ocean. *J. Phys. Oceanogr.* 12, 464–482.

Large, W. G., and Yeager, S. G. (2004). *Diurnal to Decadal Global Forcing for Ocean and Sea-Ice Models: The Data Sets and Flux Climatologies*. NCAR Tech. Note NCAR/TN-460+STR, University Corporation for Atmospheric Research.

Large, W. G., and Yeager, S. G. (2009). The global climatology of an interannually varying air-sea flux data set. *Clim. Dyn.* 33, 341–364. doi: 10.1007/s00382-008-0441-3

L'Ecuyer, T. S., Beaudoing, H. K., Rodell, M., Olson, W., Lin, B., Kato, S., et al. (2015). The observed state of the energy budget in the early twenty-first century. *J. Clim.* 28, 8319–8346. doi: 10.1175/JCLI-D-14-00556.1

Lélé, M. I., Leslie, L. M., and Lamb, P. J. (2015). Analysis of low-level atmospheric moisture transport associated with the West African Monsoon. *J. Clim.* 28, 4414–4430. doi: 10.1175/JCLI-D-14-00746.1

Li, C., von Storch, J.-S., and Marotzke, J. (2013). Deep-ocean heat uptake and equilibrium climate response. *Clim. Dyn.* 40, 1071–1086. doi: 10.1007/s00382-012-1350-z

Liu, W., Cook, K. H., and Vizy, E. K. (2020). Role of the West African westerly jet in the seasonal and diurnal cycles of precipitation over West Africa. *Clim. Dyn.* 54, 843–861. doi: 10.1007/s00382-019-05035-1

Loeb, N. G., Doelling, D. R., Wang, H., Su, W., Nguyen, C., Corbett, J. G., et al. (2018). Clouds and the Earth's radiant energy system (CERES) energy balanced and filled (EBAF) top-of-atmosphere (TOA) Edition-4.0 data product. *J. Clim.* 31, 895–918. doi: 10.1175/JCLI-D-17-0208.1

Palter, J. B. (2015). The role of the Gulf stream in European climate. *Annu. Rev. Mar. Sci.* 7, 113–137. doi: 10.1146/annurev-marine-010814-015656

Pathak, A., Ghosh, S., Martinez, J. A., Dominguez, F., and Kumar, P. (2017). Role of oceanic and land moisture sources and transport in the seasonal and interannual variability of summer monsoon in India. *J. Clim.* 30, 1839–1859. doi: 10.1175/JCLI-D-16-0156.1

Petersen, M. R., Asay-Davis, X. S., Berres, A. S., Chen, Q., Feige, N., Hoffman, M. J., et al. (2019). An evaluation of the ocean and sea ice climate of E3SM using MPAS and interannual CORE-II forcing. *J. Adv. Model. Earth Syst.* 11, 1438–1458. doi: 10.1029/2018MS001373

Polichtchouk, I., and Shepherd, T. G. (2016). Zonal-mean circulation response to reduced air–sea momentum roughness. *Q. J. R. Meteorol. Soc.* 142, 2611–2622. doi: 10.1002/qj.2850

Rhein, M., Rintoul, S., Aoki, S., Campos, E., Chambers, D., Feely, R., et al. (2013). "Observations: ocean," in *Climate Change 2013: The Physical Science Basis. Contribution of Working Group I to the Fifth Assessment Report of the Intergovernmental Panel on Climate Change*, eds T. Stocker, D. Qin, G.-K. Plattner, M. Tignor, S. Allen, J. Boschung, A. Nauels, Y. Xia, V. Bex, and P. Midgley (Cambridge; New York, NY: Cambridge University Press, 255–316.

Smith, S. D. (1988). Coefficients for sea surface wind stress, heat flux, and wind profiles as a function of wind speed and temperature. *J. Geophys. Res. Oceans* 93, 15467–15472.

Strobach, E., Molod, A., Forget, G., Campin, J.-M., Hill, C., Menemenlis, D., et al. (2018). Consequences of different air-sea feedbacks on ocean using MITgcm and MERRA-2 forcing: implications for coupled data assimilation systems. *Ocean Model.* 132, 91–111. doi: 10.1016/j.ocemod.2018.10.006

Trenberth, K. E., and Caron, J. M. (2001). Estimates of meridional atmosphere and ocean heat transports. *J. Clim.* 14, 3433–3443. doi: 10.1175/1520-0442(2001)014<3433:EOMAAO>2.0.CO;2

Tsujino, H., Urakawa, S., Nakano, H., Small, R. J., Kim, W. M., Yeager, S. G., et al. (2018). JRA-55 based surface dataset for driving ocean–sea-ice models (JRA55-do). *Ocean Model.* 130, 79–139. doi: 10.1016/j.ocemod.2018.07.002

Villas Bôas, A. B., Ardhuin, F., Ayet, A., Bourassa, M. A., Brandt, P., Chapron, B., et al. (2019). Integrated observations of global surface winds, currents, and waves: requirements and challenges for the next decade. *Front. Mar. Sci.* 6:425. doi: 10.3389/fmars.2019.00425

Wills, S. M., and Thompson, D. W. J. (2018). On the observed relationships between wintertime variability in Kuroshio–Oyashio extension sea surface temperatures and the atmospheric circulation over the North Pacific. *J. Clim.* 31, 4669–4681. doi: 10.1175/JCLI-D-17-0343.1

Wills, S. M., Thompson, D. W. J., and Ciasto, L. M. (2016). On the observed relationships between variability in Gulf stream sea surface temperatures and the atmospheric circulation over the North Atlantic. *J. Clim.* 29, 3719–3730. doi: 10.1175/JCLI-D-15-0820.1

Yu, L. (2019). Global air–sea fluxes of heat, fresh water, and momentum: energy budget closure and unanswered questions. *Annu. Rev. Mar. Sci.* 11, 227–248. doi: 10.1146/annurev-marine-010816-060704

Yu, L., Jin, X., and Weller, R. A. (2006). *Objectively Analyzed Air-Sea Fluxes (OAFlux) For Global Oceans*. Available online at: ftp://ftp.whoi.edu/pub/science/oaflux/data_v3/monthly/evaporation/ (accessed March 28, 2020).

Yu, L., and Weller, R. A. (2007). Objectively analyzed air–sea heat fluxes for the global ice-free oceans (1981–2005). *Bull. Am. Meteorol. Soc.* 88, 527–540. doi: 10.1175/BAMS-88-4-527

Zender, C. (2020). *netCDF Operator (NCO) User Guide*. Technical report. Available online at: http://nco.sf.net/nco.pdf.

Zeng, X., and Beljaars, A. (2005). A prognostic scheme of sea surface skin temperature for modeling and data assimilation. *Geophys. Res. Lett.* 32:L14605. doi: 10.1029/2005GL023030

Zeng, X., Zhang, Q., Johnson, D., and Tao, W.-K. (2002). Parameterization of wind gustiness for the computation of ocean surface fluxes at different spatial scales. *Mon. Weather Rev.* 130, 2125–2133. doi: 10.1175/1520-0493(2002)130<2125:POWGFT>2.0.CO;2

Zeng, X., Zhao, M., and Dickinson, R. E. (1998). Intercomparison of bulk aerodynamic algorithms for the computation of sea surface fluxes using TOGA COARE and TAO data. *J. Clim.* 11, 2628–2644.

Zhang, X., Liu, H., and Zhang, M. (2015). Double ITCZ in coupled ocean-atmosphere models: from CMIP3 to CMIP5. *Geophys. Res. Lett.* 42:2015GL065973. doi: 10.1002/2015GL065973

Conflict of Interest: At time of article submission, JRE is a member of the research group of one of the topic editors for this Research Topic (Dr. Meghan F. Cronin).

The remaining authors declare that the research was conducted in the absence of any commercial or financial relationships that could be construed as a potential conflict of interest.

frontiers in Marine Science

ORIGINAL RESEARCH
published: 26 July 2021
doi: 10.3389/fmars.2021.598981

Low-Level Atmospheric Responses to the Sea Surface Temperature Fronts in the Chukchi and Bering Seas

*Yoshimi Kawai**

Research Institute for Global Change, Japan Agency for Marine-Earth Science and Technology, Yokosuka, Japan

OPEN ACCESS

Edited by:
Petra Heil,
Australian Antarctic Division, Australia

Reviewed by:
Katherine Hedstrom,
University of Alaska Fairbanks, United States
Ian Herbert Simmonds,
The University of Melbourne, Australia
Gary Wick,
National Oceanic and Atmospheric Administration (NOAA), United States

***Correspondence:**
Yoshimi Kawai
ykawai@jamstec.go.jp

Specialty section:
This article was submitted to Ocean Observation, a section of the journal Frontiers in Marine Science

Received: *26 August 2020*
Accepted: *01 July 2021*
Published: *26 July 2021*

Citation:
Kawai Y (2021) Low-Level Atmospheric Responses to the Sea Surface Temperature Fronts in the Chukchi and Bering Seas. Front. Mar. Sci. 8:598981. doi: 10.3389/fmars.2021.598981

Atmospheric responses to ocean surface temperature (ST) fronts related to western boundary currents have been extensively analyzed over the last two decades. However, the organized near-surface response to ST, which is defined as the temperature of open water and sea ice, excluding land surface, at higher latitudes where sea ice exists has been rarely investigated due to the difficulties of observations. Here, 32 years of high-resolution atmospheric reanalysis data are analyzed to determine the atmospheric responses to ST fronts in the Bering Sea and Chukchi Sea. In the Chukchi Sea, the convergence of 10-m-high wind increases in October and November, when the horizontal gradient and Laplacian of ST become noticeable. On the other hand, an ST contrast between the continental shelf and the southwestern deep basin develops in winter in the Bering Sea. In both seas, the spatial distribution of surface wind convergence and the Laplacians of ST and sea level pressure agree well with each other, demonstrating the pressure adjustment mechanism. The vertical mixing mechanism is also confirmed in both seas. Ascending motion and diabatic heating develop over the Chukchi Sea in late autumn, but are confined to the lower troposphere. Turbulent heat fluxes at the surface become especially large in this season, resulting in an increase of diabatic heating and low-level clouds. Low-level clouds and downward shortwave radiation exhibit contrasting behavior across the shelf break in the Bering Sea that corresponds to the ST distribution, which is regulated by the bottom topography.

Keywords: Bering Sea, Chukchi Sea, air-sea interaction, pressure adjustment, vertical mixing, sea surface temperature, sea ice, Climate Forecast System Reanalysis

INTRODUCTION

Air-sea interaction studies in recent decades have revealed that the mid-latitude marine atmosphere is significantly affected by ocean surface temperature (ST). Ocean ST fronts associated with warm western boundary currents such as the Gulf Stream and Kuroshio induce horizontal air temperature gradients, leading to low pressure anomalies, convergence, and ascending motion over the warm flank of the ST front (e.g.,Minobe et al., 2008; Tokinaga et al., 2009; Sasaki et al., 2012). This is referred to as the pressure adjustment mechanism (PAM) (e.g.,Takatama et al., 2015). On the other hand, winds in the marine atmospheric boundary layer (MABL) are strengthened over high ST areas due to intensified vertical mixing, which is referred to as the vertical mixing mechanism (VMM) (Wallace et al., 1989). This effect produces horizontal gradients of wind speed across ST fronts, resulting in wind stress curl or divergence anomalies immediately above the ST fronts (Chelton et al., 2004). These two mechanisms are not contradictory to each other, and their relative dominance depends on the background wind direction with respect to the ST front (Chelton and Xie, 2010; Takatama et al., 2015). The influence of a mid-latitude ocean ST front is not only found in mesoscale MABL properties, but can develop into large-scale phenomena, with a higher ST able to penetrate the middle and upper troposphere. The resultant diabatic heating over the Gulf Stream remotely affects circulation over the Barents Sea and Eurasia (Minobe et al., 2008; Sato et al., 2014). Luo et al. (2017) and Luo B. et al. (2019) furthermore revealed that the combination of the positive phase of the North Atlantic Oscillation (NAO) and the Ural blocking set up a pathway that effectively brings moisture from the Gulf Stream region to the Barents Sea, and resultant increase of downward longwave radiation enhanced the warming in the Barents Sea. ST anomaly around the Gulf Stream was related with the strengthening of the westerly wind that tended to make the Ural blocking last longer. Such remote effect from the mid latitudes to the polar region has been also confirmed in the Southern Hemisphere. Wintertime higher ST in the Tasman Sea modifies storm tracks, leading to warming over the Antarctic Peninsula (Sato et al., 2021).

The atmospheric responses to relatively cold ST fronts have also been investigated in recent studies. A prominent ST front exists in the subarctic region of the Northwestern Pacific Ocean, which is referred to as the Oyashio front. This front is formed at the southern edge of subarctic low-salinity water and corresponds closely to the ST contour of 4°C in winter (Yasuda, 2003). The ST and surface turbulent heat flux around the Oyashio front

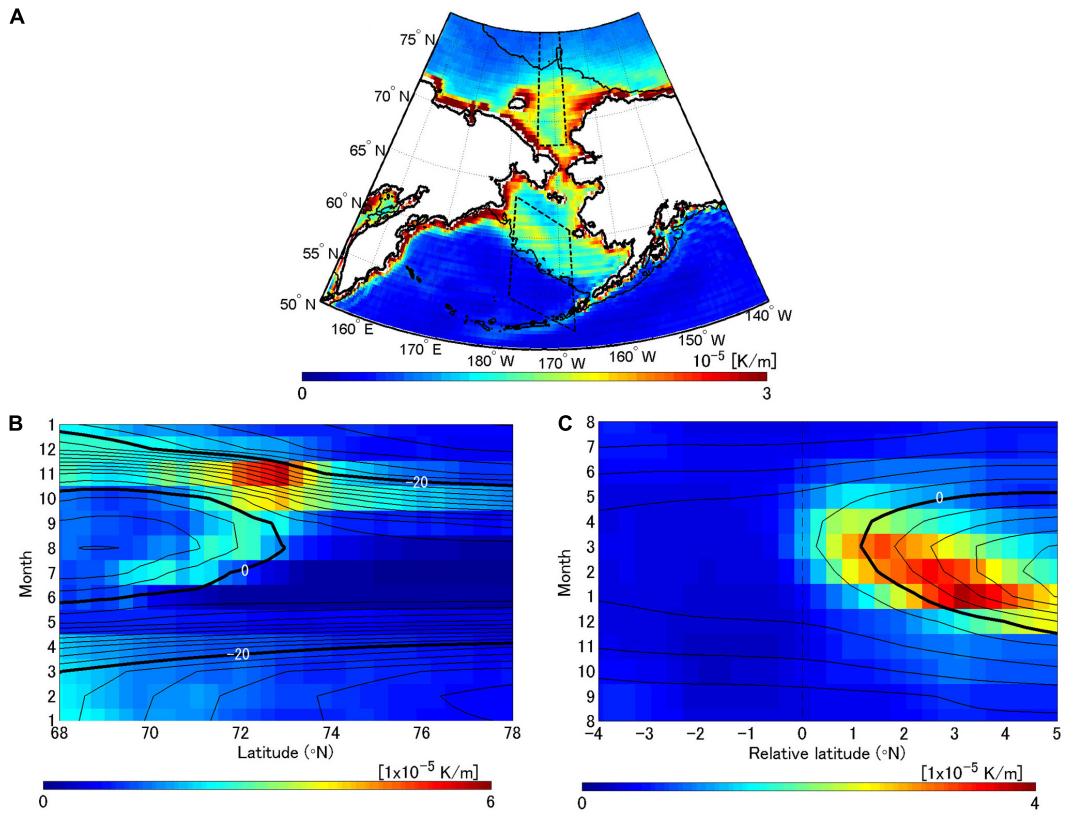

FIGURE 1 | (A) Annual-mean climatology of the Euclidean norm of horizontal gradient of ST, and latitude-time sections of monthly climatological data of the ST horizontal gradient in **(B)** the Chukchi Sea and **(C)** the Bering Sea. Black solid lines in **(A)** are depth contours of 200 m. The areas enclosed with black dashed lines in **(A)** are the domains for **(B,C)**. The middle dashed line near the 200-m-contour in the Bering Sea is the coordinate origin of latitude for **(C)**. Contours in **(B,C)** show ST, and the intervals indicated by thin and bold contours in **(B,C)** are 2 and 20°C, respectively.

are lower than those around the Kuroshio Extension, but the Oyashio front has clear effects on the subarctic atmosphere. Satellite data show that the Laplacian of MABL thickness is proportional to surface wind divergence and the Laplacian of ST, even around the Oyashio front (Shimada and Minobe, 2011), which indicates an effective PAM. Masunaga et al. (2015) confirmed the impact of the subarctic ST front using high-resolution atmospheric reanalysis data. Kawai et al. (2019) also showed evidence of the VMM across the Oyashio front from intensive *in situ* observations. Furthermore, numerical modeling and reanalysis data have indicated that the atmospheric response to the Oyashio front affects the wintertime Aleutian low on a decadal scale (Frankignoul et al., 2011; Taguchi et al., 2012).

For decades, the Arctic Ocean has been warming and the sea ice concentration has been decreasing significantly (e.g.,Vaughan et al., 2013). It has been demonstrated that the drastic change of the Arctic sea ice significantly affects the atmospheric circulation (e.g.,Honda et al., 2009; Mori et al., 2019), but some other studies have denied their relationship (e.g.,McCusker et al., 2016).This issue still remains controversial, but it has been recently pointed out that connections between the Arctic and mid latitudes becomes obvious only in brief periods and in conditions with weakened potential vorticity gradient, which may lead to the discrepancy between the previous studies (Luo D. et al., 2019; Rudeva and Simmonds, 2021). Another study demonstrated implications of the warming of the Bering and Chukchi Seas for the large-scale circulation. Tachibana et al. (2019) indicated that these seas warmed during the winter of 2017–2018 and played an important role in causing the poleward upglide motion of anomalous southerly over the seas, resulting in jet meanders.

Clarifying basic physical processes in the Arctic air-sea interaction is indispensable for climate research. Very large horizontal temperature gradients are produced across the marginal ice zone, and sea-breeze-like circulation is formed over ice edges (e.g.,Chu, 1987). Crawford and Serreze (2016) indicated that a narrow band of strong horizontal gradient along the Arctic coastline plays a role in intensifying cyclones that cross the coast in summer. Organized near-surface convergence/divergence in response to ST in high latitude areas where sea ice exists, however, has not been sufficiently investigated due to difficulties conducting observations.Seo and Yang (2013) indicated from model simulations that the PAM is effective even in the Chukchi Sea. Therefore, this study further analyzes atmospheric reanalysis data to investigate the climatological features of atmospheric responses to ST in the Bering Sea and Chukchi Sea. The study data are presented in sections "Data" and "Results" describes the PAM in both seas, See section "Discussion" discusses the effect on solar radiation at the sea surface, the VMM, and the temporal trends, and provides a summary of the study.

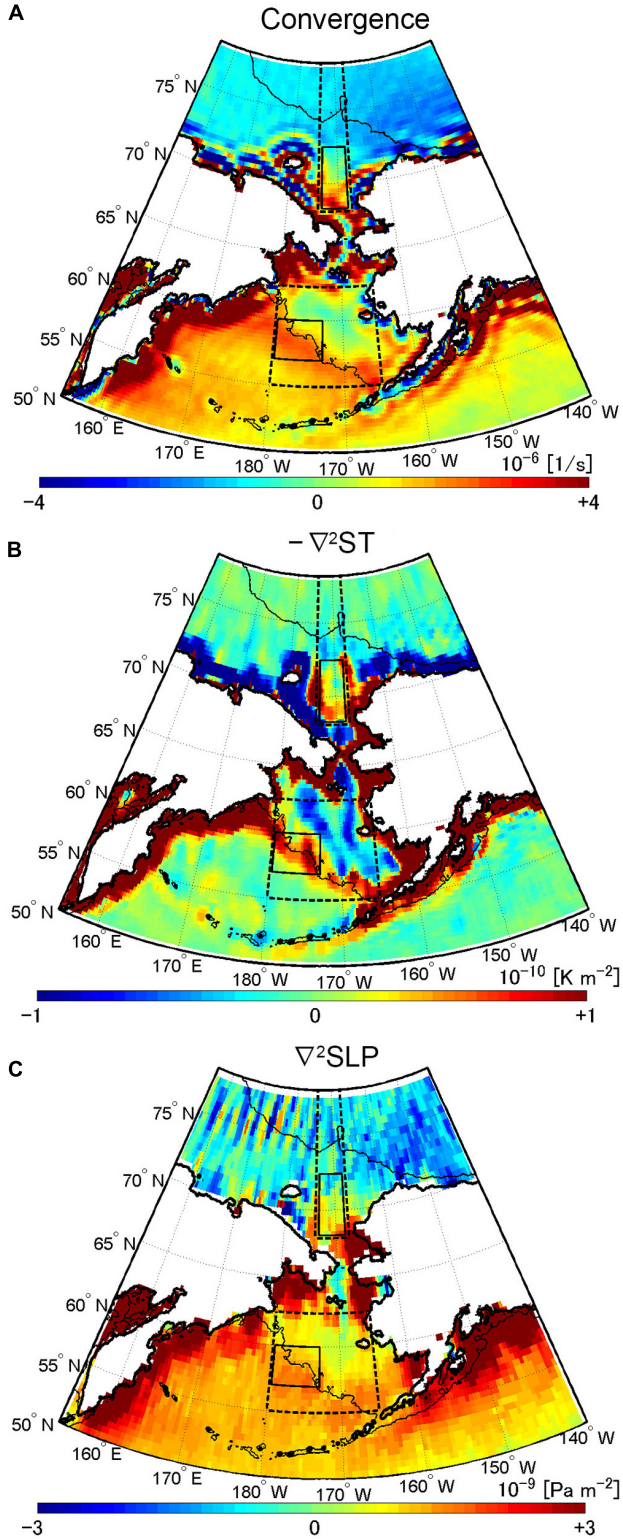

FIGURE 2 | Annual-mean climatologies of **(A)** 10-m-high wind convergence, **(B)** the sign-reversed Laplacian of ST, and **(C)** the Laplacian of SLP. Black solid lines are depth contours of 200 m. Black dashed and solid boxes denote analysis areas in **Figures 3**, **4**, respectively. A two-dimensional median filter of 5 × 5 is applied to the Laplacians of ST and SLP.

DATA

Monthly Climate Forecast System Reanalysis (CFSR) data were analyzed from 1979 to 2010, which were provided by the National

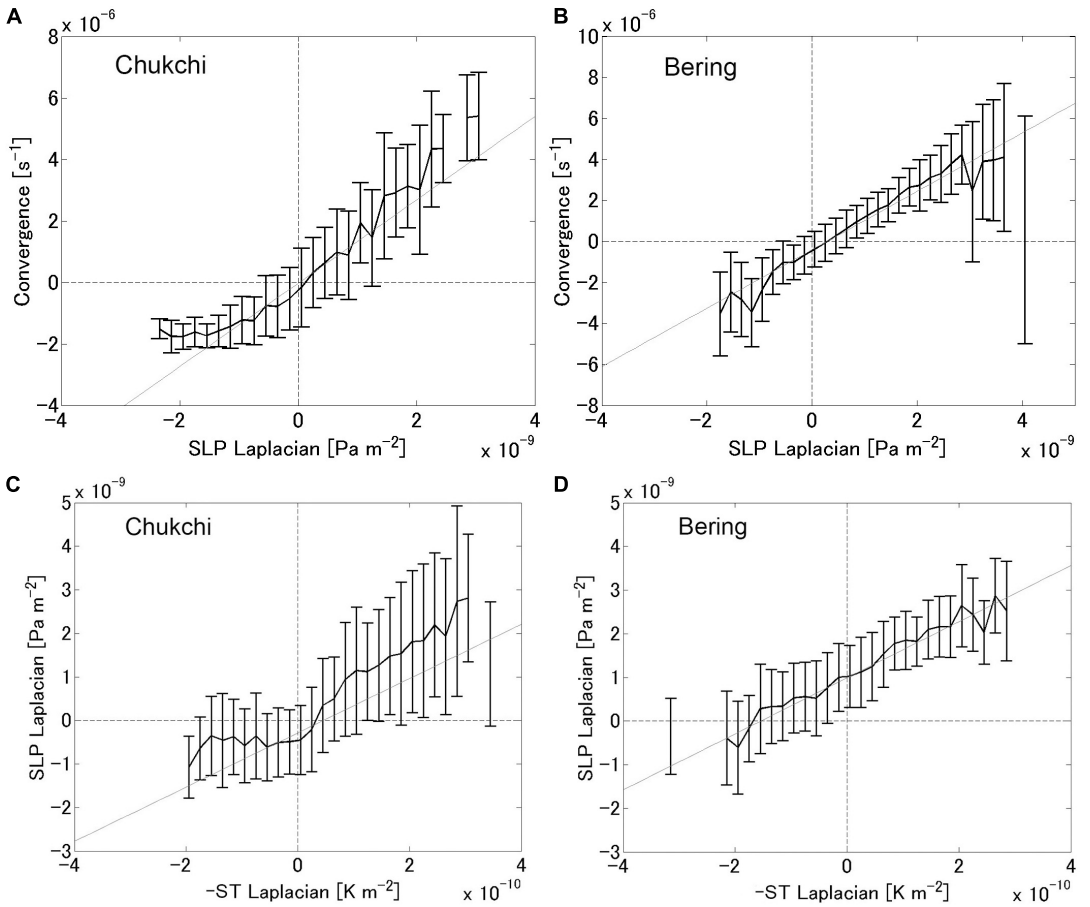

FIGURE 3 | Annual relationships (top) between the SLP Laplacian and surface wind convergence and (bottom) between the SLP and ST Laplacians averaged over the areas defined by the black dashed boxes in **Figure 2** in **(A,C)** the Chukchi Sea and **(B,D)** the Bering Sea based on monthly climatological data. Gray thin straight line is the linear regression line. Error bars denote ± 1 standard deviation. A two-dimensional median filter of 5 × 5 is applied to the Laplacians of ST and SLP.

Centers for Environmental Prediction (NCEP) (Saha et al., 2010). The atmospheric model adopted in the CFSR had a high horizontal resolution of approximately 38 km with 64 vertical levels (T382L64). Observations were assimilated with a three-dimensional variational method and CFSR data were produced by an atmosphere-ocean-land coupled assimilation system. Note that ocean STs were relaxed every 6 h to 0.25° daily mean optimum interpolation values based on observations in order to provide a stronger constraint on the sea surface. Sea ice concentration was predicted in the forecast guess and assimilated to obtain a realistic sea ice distribution. The CFSR successfully reproduced the trends of sea ice extent, which was slightly positive for the Antarctic and negative for the Arctic (Saha et al., 2010). The horizontal resolution of the CFSR data released to the public is 0.3125° for surface meteorological variables and heat fluxes, 0.5° for vertical velocity and cloud water, and 1.0° for diabatic heating rates. The author additionally used monthly data of the Climate Forecast System version 2 (CFSv2) operational analysis from April 2011 (Saha et al., 2014) to examine temporal trends in see section"Temporal Trends." Diabatic heating data after 2010 are not released, therefore climatological mean fields are investigated by using only the CFSR data until 2010.

RESULTS

Distribution of ST, Sea Level Pressure, and Surface Convergence

Here, the term "ST" refers to the surface temperature of water or sea ice that is directly in contact with the atmosphere. Thus, ST does not necessarily indicate the seawater temperature, but excludes land surface temperature. In the climatological mean, the Euclidean norm of the horizontal gradient of ST is the largest in the zone around 72°N east of Wrangel Island in the Chukchi Sea, and along the shelf break over the continental shelf in the Bering Sea (**Figure 1A**). (The Euclidean norm of gradient vector is referred to simply as "gradient" hereafter in this manuscript.) The ST gradient in the Chukchi Sea becomes obvious in July, reaches its maximum in November, and begins to diminish from December (**Figure 1B**). On the other hand, the ST over the continental shelf in the Bering Sea is consistently lower than that

in the southwestern basin (Aleutian Basin) (**Figure 1C**). The ST contrast between the shelf and basin is lowest in July and August, starts increasing from autumn, and reaches a peak in March, when sea ice extends the furthest toward the shelf break. The spatial distributions of the climatological means of surface wind convergence and the Laplacians of ST and sea level pressure (SLP) correspond well to each other (**Figure 2**). An intriguing feature is that their spatial patterns clearly reflect the bottom topography of the Bering Sea and their maxima lie along the shelf break. The annual scatter plots between $-\nabla^2$ST, ∇^2SLP, and convergence obtained from the monthly climatological data exhibit linear relationships in both the Chukchi and Bering Seas, although these relationships are slightly distorted and the dispersion is larger in the Chukchi Sea (**Figure 3**). The good spatial agreement and the linear relationship indicate that the PAM is effective (Minobe et al., 2008; Shimada and Minobe, 2011). The Chukchi and Bering Seas are discussed separately in the following subsections.

Chukchi Sea

In the Chukchi Sea, convergence of the 10-m-high wind increases in October and November, but is close to zero or even negative from January to September (**Figure 4A**). The seasonal cycles of ∇^2SLP and ∇^2ST agree well with the cycle of convergence. ST in the Chukchi Sea is highest in August, but its meridional gradient peaks in November (**Figure 4C**). The direction of the ST gradient vector in this region is northward in autumn. In November, sea ice is already increasing, but does not completely cover the surface, and the ST is still relatively high due to warm water coming from the Bering Sea. Conversely, ST in the region north of the Chukchi Sea drops below -20°C, which results in the largest gradient and Laplacian in November. From December, the Chukchi Sea is filled with sea ice and the ST substantially decreases.

Regarding the atmospheric responses to ST, the vertical velocity and diabatic heating in the lower troposphere show the same seasonal cycle as the surface convergence (**Figure 5**). Low-level upward motion and diabatic heating develop in October and November; however, these responses are restricted to the boundary layer, unlike those in the Kuroshio and the Gulf Stream. Sasaki et al. (2012) showed that the ascending motion due to large diabatic heating extended to the upper troposphere over the Kuroshio in the East China Sea in early summer. The diabatic heating in the CFSR product consists of six components: vertical diffusion, deep convection, shallow convection, large-scale condensation, and solar and longwave radiation. The diabatic heating over the Chukchi Sea shown in **Figure 5b** is dominated by vertical diffusion (see **Supplementary Figure 1**). Large-scale condensation is the second largest component, and peaks in October (**Figure 5c**), which corresponds well to the cloud water mixing ratio (**Figure 5e**). Condensation results in low-level clouds between 950 and 800 hPa and evaporation cools the near-surface air; longwave radiation also reflects this pattern (**Figure 5d**). The other three components of diabatic heating are negligible. Sensible and latent heat fluxes in the Chukchi Sea are less than $\pm$ 20 W m^{-2} except in autumn, and both exceed 60 W m^{-2} in October and November (**Figure 5f**), leading to large near-surface diabatic heating. Basically the highly stable atmosphere suppresses forcing from the sea surface. However, in October and November, when the sea surface begins to freeze, the supply of heat and water vapor from the surface increases drastically and the heat flux gradients become large. As a result, low-level ascent

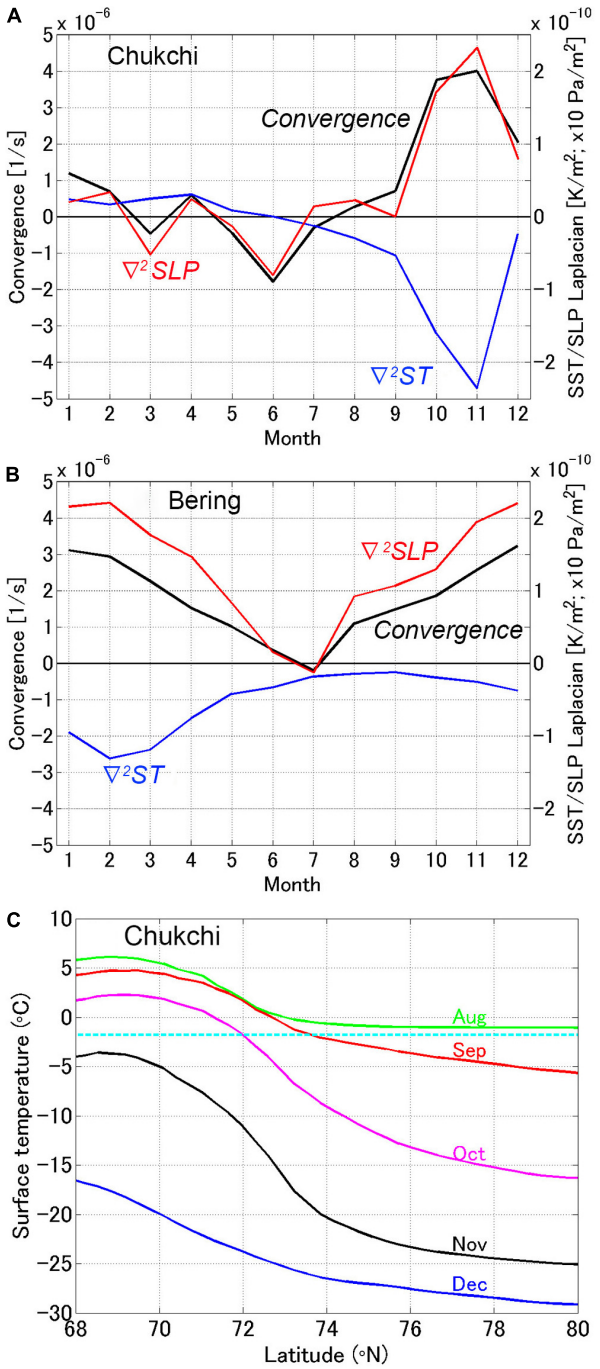

FIGURE 4 | Monthly climatology of 10-m-high wind convergence and the Laplacians of ST and SLP averaged over the black-solid box area in **Figure 2** in **(A)** the Chukchi Sea and **(B)** the Bering Sea. **(C)** Monthly climatological data of ST averaged between 167.5 and 174.0°W in the Chukchi Sea. Cyan dashed line represents a temperature of -1.8°C.

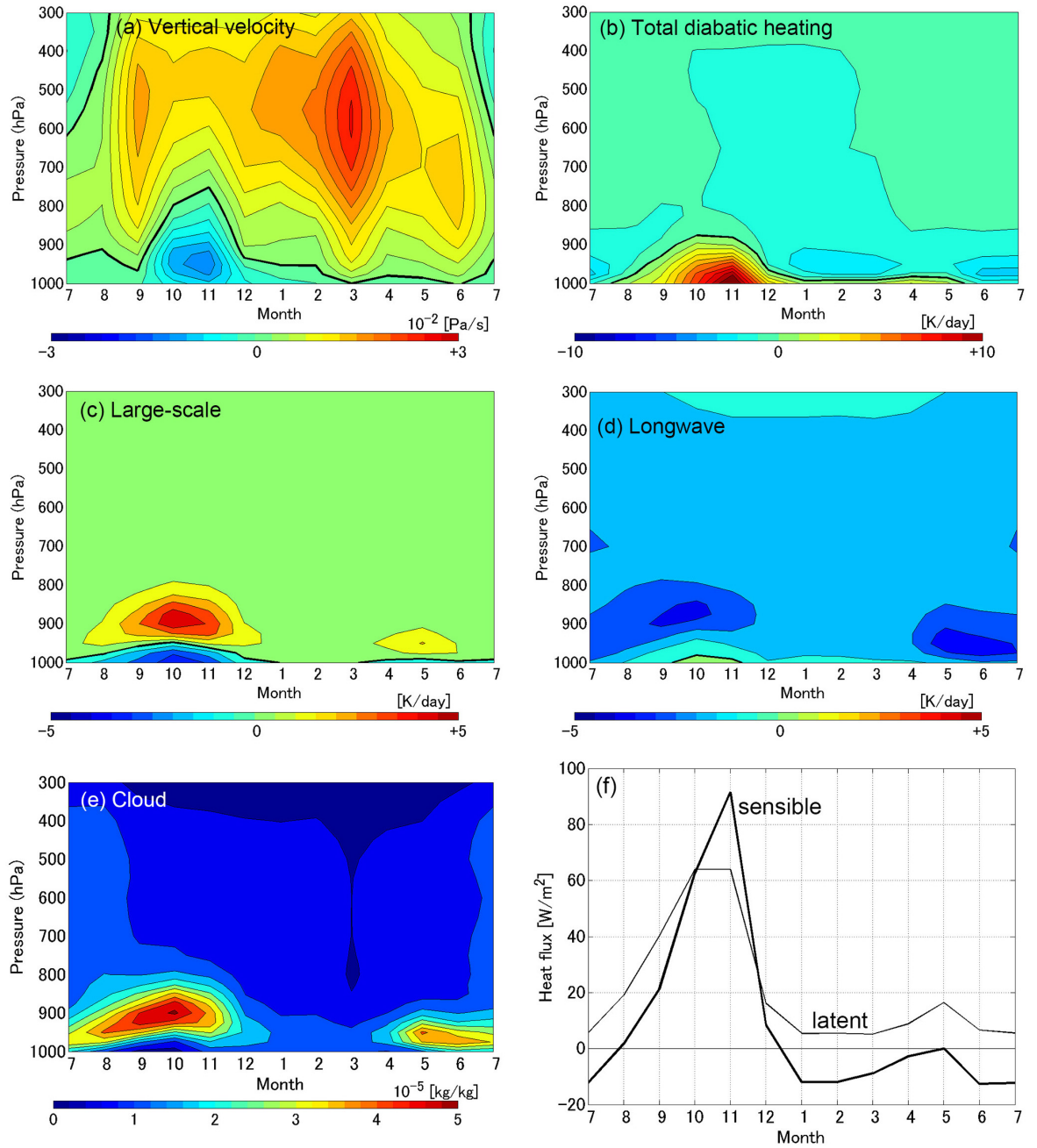

FIGURE 5 | Seasonal variations of **(a)** vertical velocity, **(b)** total diabatic heating rate, **(c)** large-scale condensation component, **(d)** longwave radiation component, **(e)** cloud water mixing ratio, and **(f)**surface turbulent heat fluxes averaged over the area of 68.0–72.5°N, 167.5–174.0°W (black solid box in **Figure 2**) in the Chukchi Sea. Negative values in **(a)** indicate ascending motion. Black bold lines in **(a–d)** are zero contours.

and diabatic heating are organized over the Chukchi Sea, but do not penetrate the stable polar atmosphere.

Bering Sea

According to the annual mean values, the surface convergence and ∇^2ST are largest over the shelf break. Surface winds diverge over the continental shelf region (**Figure 2A**). Over the shelf break region, the convergence and ∇^2SLP exhibit clear seasonality, being smaller in summer and larger in winter (**Figure 4B**). ∇^2ST over the shelf break is negative throughout the year and especially large from January to April due to sea ice extending over the continental shelf.

The convergence-divergence pattern across the ST front corresponds to ascending motion over the shelf break and descending motion on the northern side in the lower troposphere (**Figures 6a,c**). This ascent-descent pattern becomes obvious in

February and March (**Figure 6b**). The ascent that occurs in November and December extends throughout the troposphere across the shelf break, which is likely due to a synoptic-scale phenomenon rather than surface forcing. While the minimum of the climatological mean SLP is south off the Aleutian Islands, far away from the shelf break in February-March, it is located near the shelf break in November-December (see **Supplementary Figure 2**). This implies that the formation of the descending motion over the shelf tends to be suppressed by the ascending motion near cyclone centers in November-December. The mean meridional wind in winter is southward in the lower troposphere and northward in the middle and upper troposphere (**Figure 6c**). This spatial pattern of the meridional and vertical velocity implies the formation of horizontal convection over the continental shelf.

Diabatic heating is almost confined to the boundary layer (**Figure 7B**) and determined by vertical diffusion (see **Supplementary Figure 3**), similar to the Chukchi Sea. It peaks in January and February (**Figure 7A**). Although the latent heat flux is largest immediately above the shelf break, the sensible heat flux and low-level diabatic heating peak over the continental shelf approximately 200 km away, where the ice concentration is approximately 15%, at the southern edge of the marginal ice zone (**Figure 7E**). The contours of diabatic heating in the latitude-altitude diagram slant northward, and diabatic heating at the level of 900 hPa is largest over the shelf break (**Figure 7B**). Large-scale condensation and the cloud water mixing ratio are noticeable between 800 hPa and 900 hPa south of the shelf break (**Figures 7C,D**).

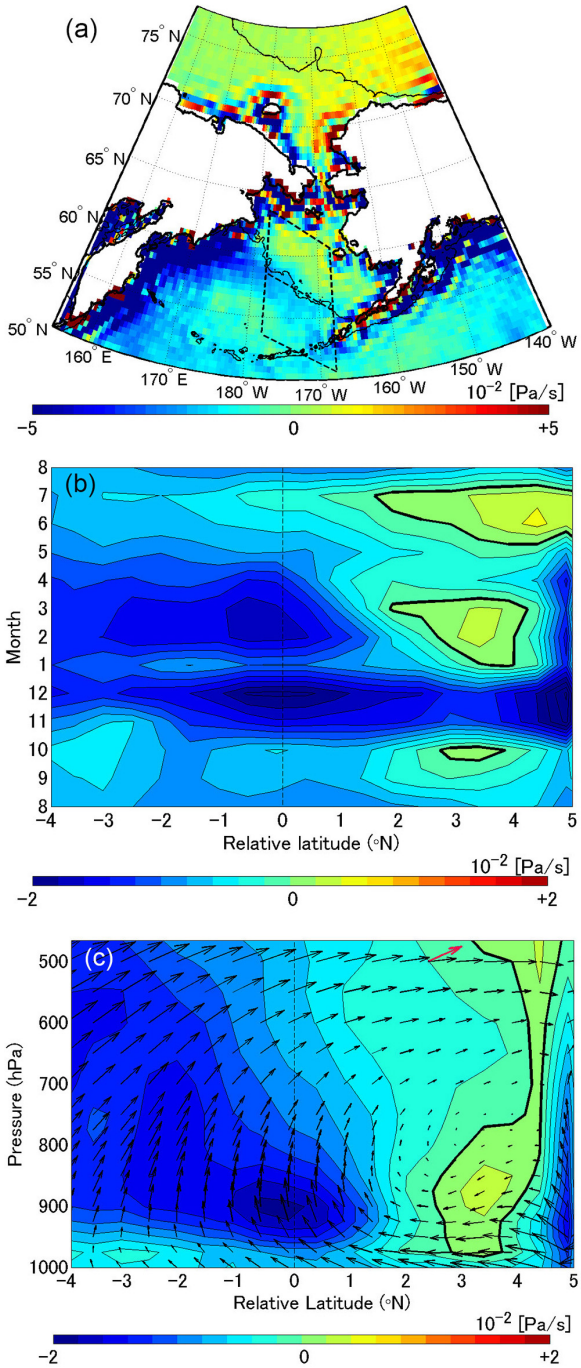

FIGURE 6 | (a) Annual-mean climatology and **(b)** latitude-time section of vertical velocity between 850 and 900 hPa. **(c)** Latitude-altitude section of vertical velocity (color) and two-dimensional wind vector for February to March. Scaling for the arrows is given near the upper-right corner in **(c)** (red arrow, meridional and vertical components of 3.0 m s^{-1} and 1.0 × 10^{-2} Pa s^{-1}). Black bold lines in **(b, c)** are zero contours. The black dashed box in **(a)** is the average domain for **(b,c)**.

DISCUSSION

Effect on Shortwave Radiation and Precipitation Into the Ocean

Cloud water concentrates in the lower troposphere and exhibits a clear contrast across the shelf break in the Bering Sea. Clouds significantly affect shortwave radiation into the ocean. **Figure 7D** suggests that the distribution of low-level clouds reflects that of ST, whereby the horizontal gradient of cloud water below 700 hPa is large along the shelf break from winter to summer (**Figure 8**), although the meridional contrast vanishes in September to December (**Figure 8C**). The spatial distribution of downward shortwave radiation at the sea surface clearly reflects that of the low-level cloud water mixing ratio (**Figures 9A,B**). As solar radiation also depends on latitude, it exhibits a trough on the southern side of the shelf break in the Aleutian Basin. The precipitation rate also shows a contrast between the shallow shelf region and the deep basin, and is slightly intensified over the shelf break (**Figures 9C,D**).

As the wintertime oceanic mixed layer reaches the bottom in the shallow continental shelf region (Kawai et al., 2018), the mixed layer in the shelf region is cooled more than that in the deep southwestern basin. In the Bering Sea, the bottom topography regulates the upper ocean temperature and the low-level atmosphere, as Xie et al. (2002) indicated for the Yellow and East China Seas. The spatial distribution of low-level clouds that reflects the bottom topography then controls the shortwave radiation entering the ocean. Photosynthetically active radiation (PAR) is proportional to the shortwave radiation, and

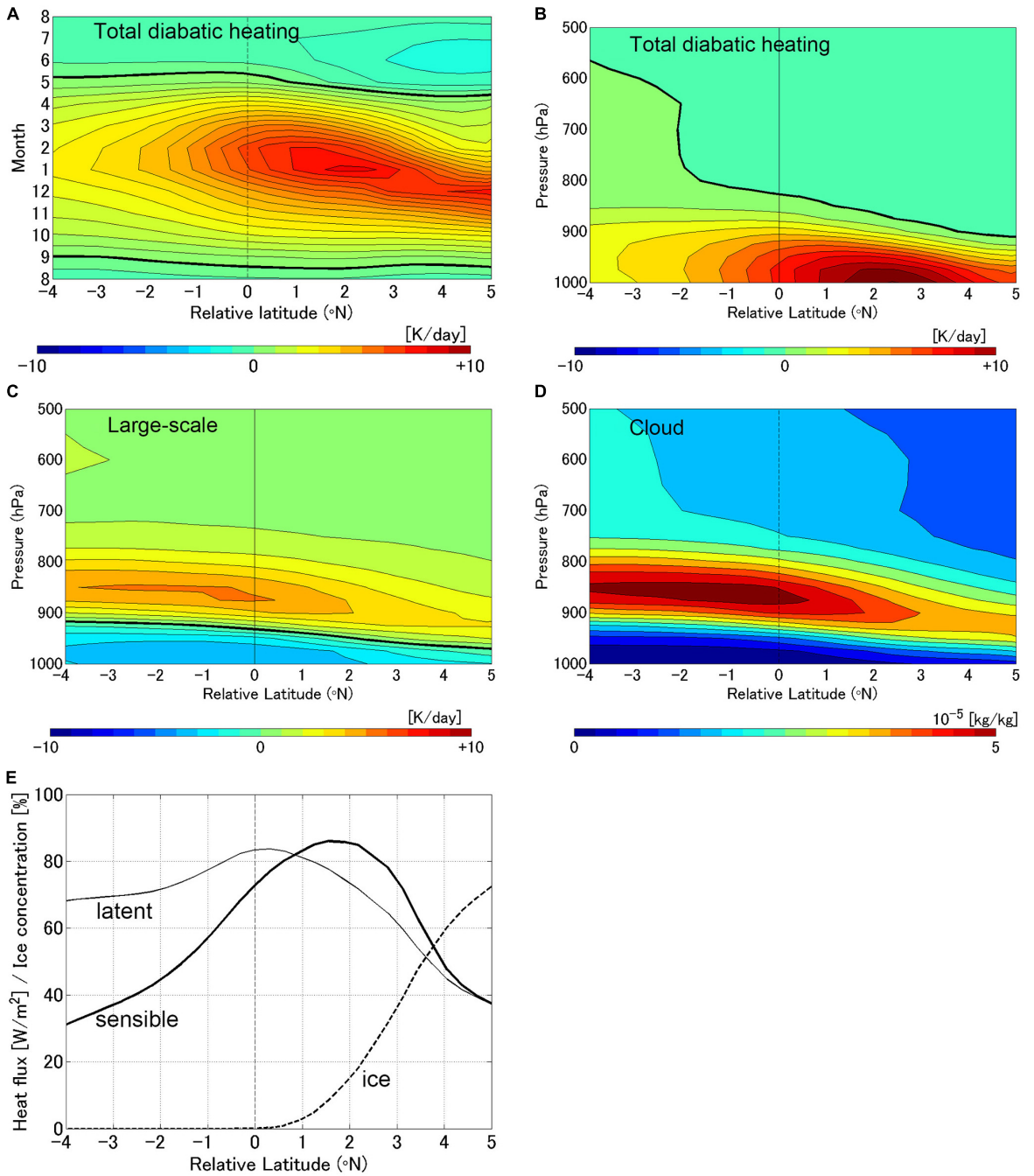

FIGURE 7 | (A) Latitude-time section of total diabatic heating averaged between 900 and 1,000 hPa, and altitude-latitude sections of **(B)** total diabatic heating, **(C)** large-scale condensation component, and **(D)** cloud water mixing ratio over the Bering Sea (black dashed box in **Figure 6A**) for January to February. Black bold lines in **(A–C)** are zero contours. **(E)** Sensible heat flux (bold line), latent heat flux (thin line), and sea ice concentration (dashed line) for January to February.

the characteristic pattern of incoming radiation will have an impact on the marine ecosystem in the Bering Sea.

Vertical Mixing

The previous subsection described the PAM, but the VMM is also effective. The spatial distribution of high-pass-filtered ST and 10-m-high wind speed shows good correspondence, albeit with some disagreement (**Figure 10**). The wind speed anomalies are positive over the shelf break and the southern Chukchi Sea, where ST exhibits warm anomalies.

According to the diagnostics of Takatama et al. (2015), although the PAM almost completely determines the surface convergence, the surface curl is mainly accounted for by the

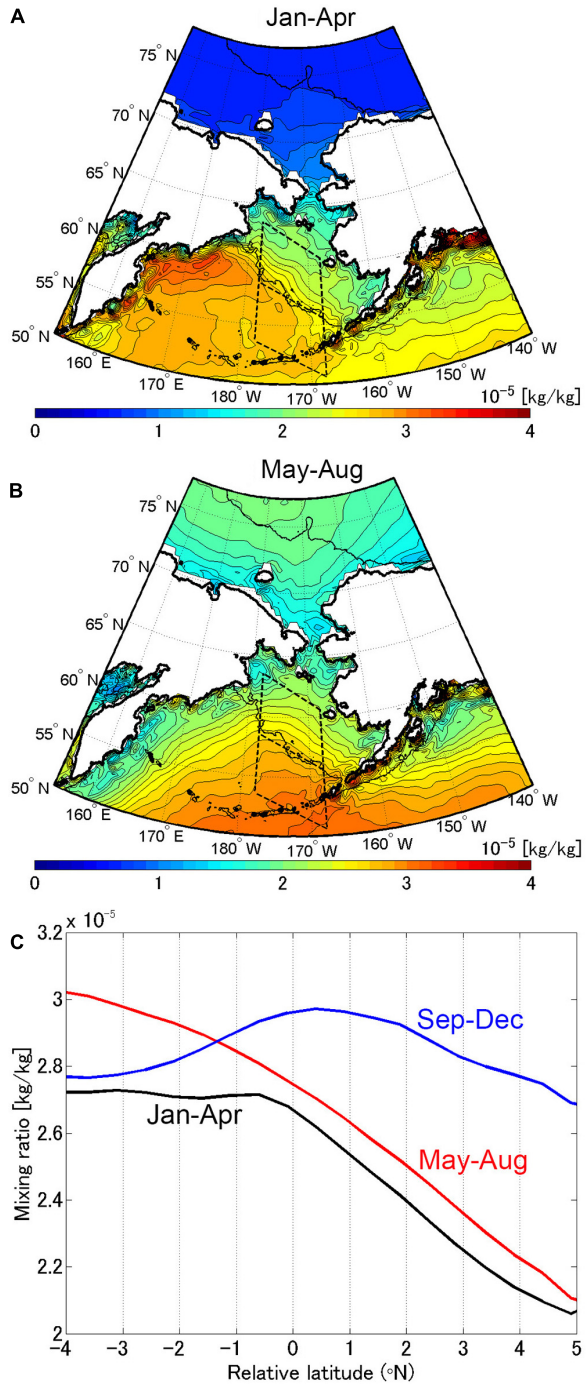

FIGURE 8 | Climatology of the cloud water mixing ratio averaged between 700 and 1,000 hPa for **(A)** January to April and **(B)** May to August. **(C)** Cloud water mixing ratio from 700 to 1,000 hPa averaged over the black dashed box in **(A,B)** for January to April (black), May to August (red), and September to December (blue).

VMM; this difference can be explained by the background wind direction with respect to the ST front. Along-front (cross-front) wind leads to wind stress curl (divergence) due to the VMM (Chelton et al., 2004), and the PAM is independent of the wind direction. Low-level geostrophic wind tends to blow parallel to the ST front in the Chukchi Sea, and perpendicular to the front in the Bering Sea (**Figure 11A**). A downwind ST gradient $-\mathbf{v}_{10}\cdot\nabla ST$ is observed over the continental shelf near the shelf break in the Bering Sea, and the crosswind ST gradient $-\mathbf{v}_{10} \times \nabla ST$ is larger than $-\mathbf{v}_{10}\cdot\nabla ST$ in the Chukchi Sea (**Figures 11B,C**). Thus, the contribution of downward momentum input to surface curl is expected to be relatively large in the Chukchi Sea. The convergence of downward momentum input by the VMM also reinforces surface convergence in the Bering Sea, but its relative contribution is small and the PAM dominates surface convergence.

In this study, the effect of sea ice roughness is not examined. A colder sea surface makes the atmosphere more stable and the surface wind weaker. Larger friction over sea ice has the same effect of reducing the near-surface wind speed. Hence, it is expected that the contrast in the near-surface friction across an ST front becomes much larger when sea ice exists on the cold side, which magnifies both the VMM and PAM. Sea ice roughness depends on factors such as the sea ice concentration and the thickness and age of ice; however, the effects of these factors on air-sea interactions are beyond the scope of this study.

Temporal Trends

Linear trends were calculated for the period from 1979 to 2020. The trend of ST in the Chukchi Sea is striking around 75°N in October and 72.5°N in November (**Figure 12A**). As a result, areas with a large ST gradient shifted northward in October and November, and the gradient around 72.5°N became larger in December due to the delay and retreat of sea ice formation (**Figure 12C**). In the Bering Sea, ST shows warming trends in summer and autumn, and no significant trend in winter and spring (**Figure 12B**). There is also no clear trend in sea ice concentration (**Figure 12D**). (In fact, cooling trend was seen in the northern shelf region in winter for the period until 2010, the warming in the 2010s obscured the trend.) Hereafter, the trend in the Chukchi Sea is discussed.

Remarkable trends of cloud water are observed in October and November (**Figure 13A**). Cloud water decreases near the surface but increases above 900 hPa, indicating an increase in the altitude of low-level clouds. This is consistent with the observational results of Sato et al. (2012), who showed that the base height of low-level clouds became higher as a result of the Arctic warming. A vertical velocity trend is observed near the surface in November and December, which is related to the delay of sea ice extension (**Figure 13B**). In October-November, the decrease of sensible heat flux in the southern Chukchi Sea (**Figure 14**) corresponds to the delay of freezing, suggesting that the atmospheric change led to the ocean warming. The increases of upward and downward longwave radiation at the surface balanced with each other south of 75°N. Downward shortwave radiation slightly decreased, maybe due to the change of low-level clouds. The positive trends

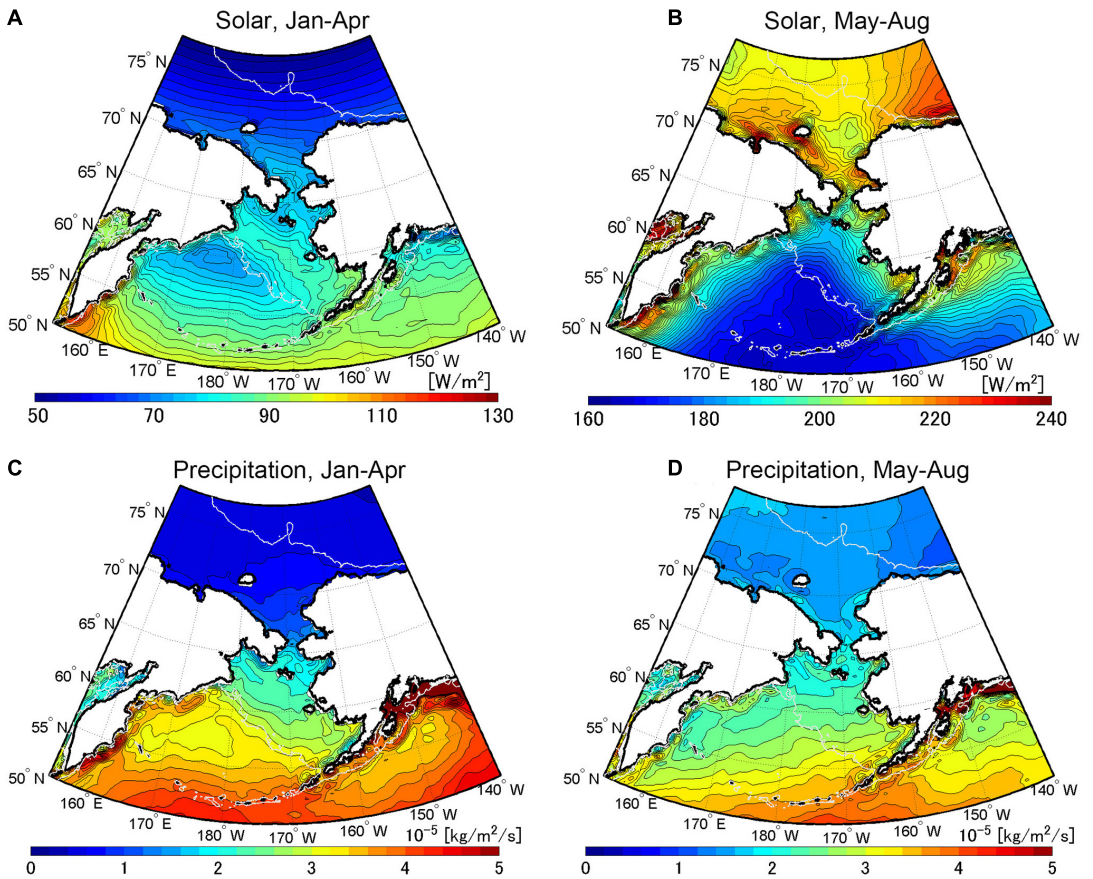

FIGURE 9 | Climatology of **(A,B)** solar radiation at the sea surface and **(C,D)** precipitation rate for **(A,C)** January to April and **(B,D)** May to August. White lines are depth contours of 200 m.

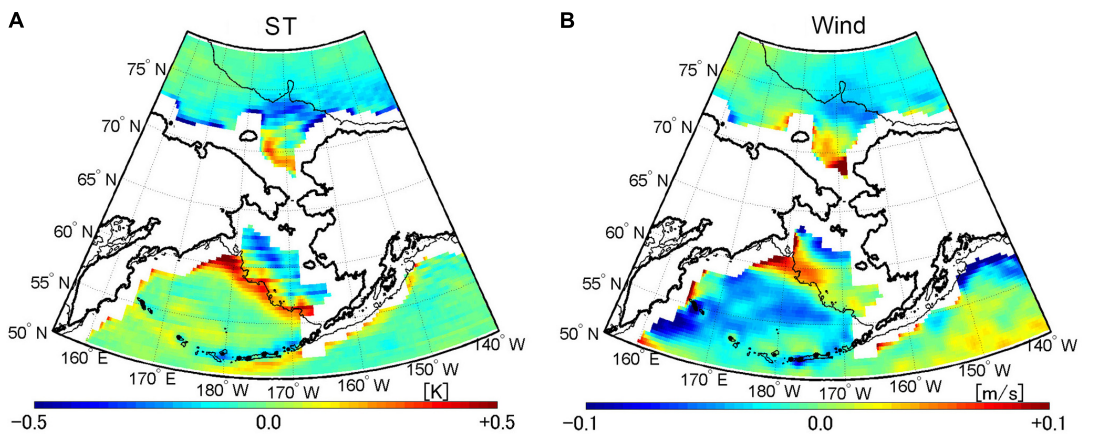

FIGURE 10 | Annual-mean climatology of spatially high-pass-filtered **(A)** ST and **(B)** 10-m-high wind speed. The high-pass-filtered anomaly is derived as the deviation from the 5 × 5 grid mean. Black thin lines are depth contours of 200 m.

of sensible and latent heat fluxes in 72–77°N, corresponding to the northward shift of marginal ice zone, mean that the warmed sea surface strengthened turbulent heat transfer to the atmosphere, and the warm water inflow from the Pacific Ocean (Shimada et al., 2006) would offset the surface heat loss. In the region north of 78°N, the changes of turbulent

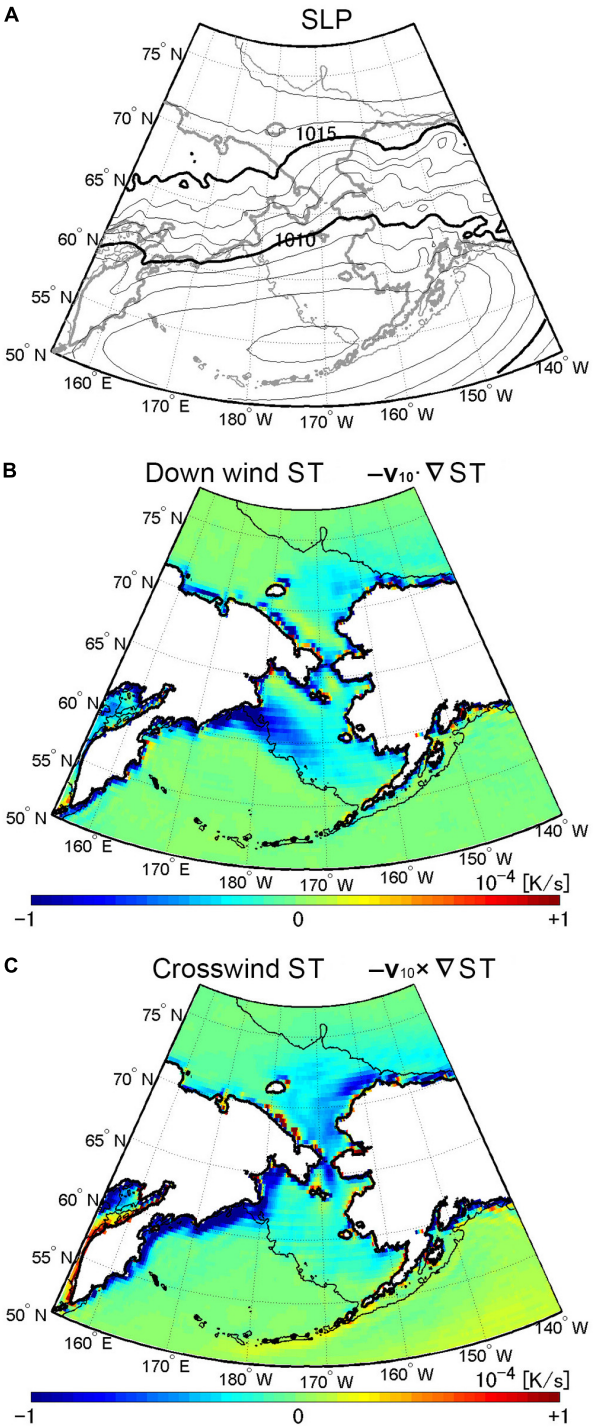

FIGURE 11 | Annual-mean climatology of **(A)** SLP, **(B)** sign-reversed downwind ST gradient, and **(C)** sign-reversed crosswind ST gradient. The intervals indicated by thin and bold contours in **(A)** are 1 and 5 hPa, respectively.

heat fluxes were negligible and the increase of downward longwave radiation was dominant. In summary, while the ocean warming increased the heat release to the atmosphere in the northern Chukchi Sea, downward radiation drove the ST rise near the polar, which is consistent with the indication of Lee et al. (2017).

Summary

It is expected that the horizontal temperature gradient will increase substantially over the border between open water and sea ice, similar to the ST fronts related to western boundary currents in the mid latitudes; however, air-sea interaction from the viewpoint of the ST front has seldom been investigated at high latitudes. Therefore, this study examined the atmospheric responses to ST in the Chukchi and Bering Seas, where sea ice develops in the cold season, using a high-resolution atmospheric reanalysis dataset. In the Chukchi Sea, ST peaks in August, but its horizontal gradient becomes largest in November. Convergence of 10-m-high wind is also large in October and November, and approximately zero or negative from January to September. On the other hand, there is a clear contrast in ST between the continental shelf and the southwestern deep basin of the Bering Sea throughout the year, which develops in winter. The ST front shifts southward as sea ice spreads over the shelf region, and the front is located immediately above the northern flank of the shelf break in March, when the marginal ice zone extends furthest south. In both the Chukchi and Bering Seas, the spatial distribution of surface wind convergence and the Laplacians of ST and SLP agree well with each other, which demonstrates an effective PAM. The VMM is also confirmed in both seas.

Ascending motion and diabatic heating develop over the Chukchi Sea in October and November, corresponding to surface wind convergence; however, this response is confined to the lower troposphere. Diabatic heating is dominated by the vertical diffusion component. Turbulent heat fluxes at the sea surface becomes especially large in late autumn, when sea ice is increasing, resulting in the intensification of heating and low-level clouds. Ascent is also strengthened over the shelf break and a circulation pattern similar to horizontal convection appears over the shelf in the Bering Sea in late winter. Low-level clouds show a clear contrast across the shelf break in the Bering Sea, and downward solar radiation at the surface reflects the spatial pattern of the clouds. The bottom topography regulates the ST and affects clouds and incoming radiation through the ST. During 1979–2020, the Arctic Ocean including the Chukchi Sea experienced drastic warming and retreat of sea ice in autumn, although the ST exhibited no clear trends in the Bering Sea in the cold season. Over the Chukchi Sea, there was a tendency for low-level clouds to rise in October and November, which corresponded to the warming trend. This is consistent with a previous study that analyzed*in situ* observation data. The analysis of surface heat fluxes supported the indication of previous study that while downward longwave radiation was responsible for the ST increase near the polar, the ocean warming increased turbulent heat fluxes in the northern Chukchi Sea.

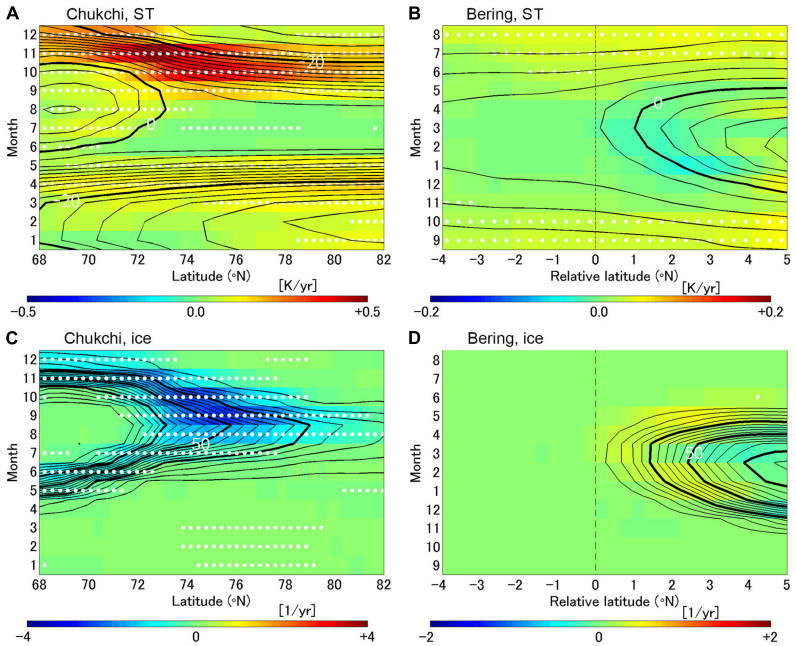

FIGURE 12 | Latitude-time sections of **(A,B)** ST and **(C,D)** sea ice concentration trends for 1979–2020 in **(A,C)** the Chukchi Sea and **(B,D)** the Bering Sea. White dots denote statistical significance at the 95% confidence level. Contours show climatologies of **(A,B)** ST and **(C,D)** sea ice concentration. The intervals indicated by thin and bold contours are 2 and 20°C in **(A,B)** and 5and 25% in **(C,D)**, respectively.

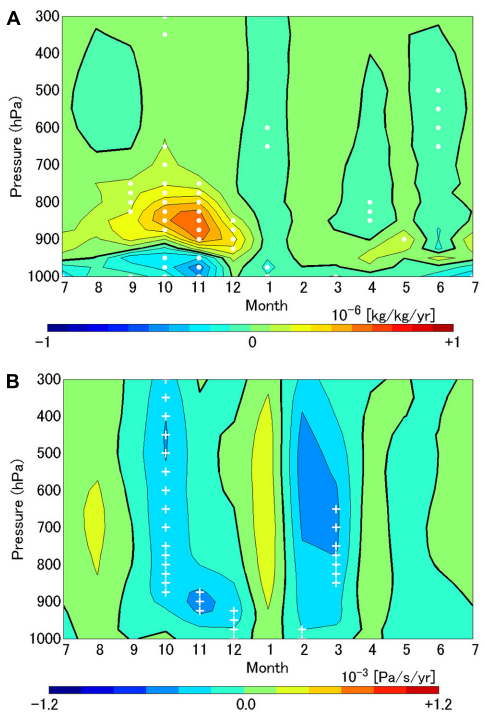

FIGURE 13 | Trends of **(A)** cloud water mixing ratio and **(B)** vertical velocity averaged over the area of 68.0–72.5°N and 167.5–174.0°W (black solid rectangle in **Figure 2A**) in the Chukchi Seafor 1979–2020. Black bold lines are zero contours. White dots in **(A)** and pluses in **(B)** denote statistical significance at the 95 and 90% confidence level, respectively.

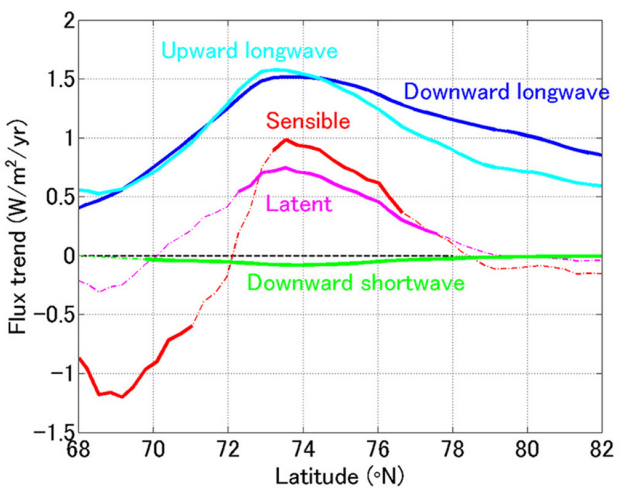

FIGURE 14 | Trends of surface heat fluxes averaged over the area of 167.5–174.0°W in October-November for 1979–2020. Thick solid lines denote statistical significance at the 95% confidence level, and thin chained lines show no significance.

In the Chukchi and Bering Seas, the development of an ST gradient and subsequent impacts on the atmosphere are regulated by the season and bottom topography. This study only focused on the local responses; their effects on a synoptic or larger scale and their modulation under the Arctic warming should be analyzed in future research.

DATA AVAILABILITY STATEMENT

Publicly available datasets were analyzed in this study. This data can be found here: https://www.ncei.noaa.gov/data/climate-forecast-system/access/reanalysis/monthly-means/, https://www.ncei.noaa.gov/data/climate-forecast-system/access/operational-analysis/monthly-means-flux/, and https://www.ncei.noaa.gov/data/climate-forecast-system/access/operational-analysis/monthly-means-by-pressure/.

AUTHOR CONTRIBUTIONS

YK designed the study, analyzed the data, and wrote the manuscript.

FUNDING

This work was supported by the Japan Society for the Promotion of Science (JSPS) Grants-in-Aid for Scientific Research (B), and (C) (KAKENHI) (16H04046 and 16K05563), and also by the Ministry of Education, Culture, Sports, Science and Technology (MEXT) of Japan, Grant-in-Aid for Scientific Research on Innovative Areas (19H05700).

ACKNOWLEDGMENTS

The CFSR and CFSv2 data used in this study were supplied by the NCEP.

SUPPLEMENTARY MATERIAL

The Supplementary Material for this article can be found online at: https://www.frontiersin.org/articles/10.3389/fmars.2021.598981/full#supplementary-material

REFERENCES

Chelton, D. B., Schlax, M. G., Frelich, M. H., and Milliff, R. F. (2004). Satellite measurements reveal persistent small-scale features in ocean winds. *Science*303, 978–983. doi: 10.1126/science.1091901

Chelton, D. B., and Xie, S.-P. (2010). Coupled ocean-atmosphere interaction at oceanic mesoscales. *Oceanography*23, 52–69. doi: 10.5670/oceanog.2010.05

Chu, P. C. (1987). An ice breeze mechanism for an ice divergence-convergence criterion in the marginal ice zone. *J. Phys. Oceanogr.*17, 1627–1632. doi: 10.1175/1520-0485(1987)017<1627:aibmfa>2.0.co;2

Crawford, A. D., and Serreze, M. C. (2016). Does the summer Arctic frontal zone influence Arctic Ocean cyclone activity. *J. Clim.*29, 4977–4993. doi: 10.1175/JCLI-D-15-0755.1

Frankignoul, C., Sennéchael, N., Kwon, Y.-O., and Alexander, M. A. (2011). Influence of the meridional shifts of the Kuroshio and the Oyashio extensions on the atmospheric circulation. *J. Clim.*24, 762–777. doi: 10.1175/2010JCLI3731.1

Honda, M., Inoue, J., and Yamane, S. (2009). Influence of low Arctic sea-ice minima on anomalously cold Eurasian winters. *Geophys. Res. Lett.*36:L08707.

Kawai, Y., Nishikawa, H., and Oka, E. (2019). In situ evidence of low-level atmospheric responses to the Oyashio front in early spring. *J. Meteor. Soc. Japan*97, 423–438. doi: 10.2151/jmsj.2019-024

Kawai, Y., Osafune, S., Masuda, S., and Komuro, Y. (2018). Relations between salinity in the northwestern Bering Sea, the bering Strait throughflow and sea surface height in the Arctic Ocean. *J. Oceanogr.*74, 239–261. doi: 10.1007/s10872-017-0453-x

Lee, S., Gong, T., Feldstein, S. B., Screen, J. A., and Simmonds, I. (2017). Revisiting the cause of the 1989-2009 Arctic surface warming using the surface energy budget: downward infrared radiation dominates the surface fluxes. *Geophys. Res. Lett.*44, 10654–10661. doi: 10.1002/2017GL075375

Luo, B., Luo, D., Wu, L., Zhong, L., and Simmonds, I. (2017). Atmospheric circulation patterns which promote winter Arctic sea ice decline. *Environ. Res. Lett.*12:054017. doi: 10.1088/1748-9326/aa69d0

Luo, B., Wu, L., Luo, D., Dai, A., and Simmonds, I. (2019). The winter midlatitude-Arctic interaction: effects of North Atlantic SST and high-latitude blocking on Arctic sea ice and Eurasian cooling. *Clim. Dyn.*52, 2981–3004. doi: 10.1007/s00382-018-4301-5

Luo, D., Chen, X., Overland, J., Simmonds, I., Wu, Y., and Zhang, P. (2019). Weakened potential vorticity barrier linked to recent winter Arctic sea ice loss and midlatitude cold extremes. *J. Clim.*32, 4235–4261. doi: 10.1175/JCLI-D-18-0449.1

Masunaga, R., Nakamura, H., Miyasaka, T., Nishii, K., and Tanimoto, Y. (2015). Separation of climatological imprints of the Kuroshio extension and Oyashio fronts on the wintertime atmospheric boundary layer: their sensitivity to SST resolution prescribed for atmospheric reanalysis. *J. Clim.*28, 1764–1787. doi: 10.1175/JCLI-D-14-00314.1

McCusker, K. E., Fyfe, J. C., and Sigmond, M. (2016). Twenty-five winters of unexpected Eurasian cooling unlikely due to Arctic sea-ice loss. *Nat. Geosci.*9, 838–842. doi: 10.1038/ngeo2820

Minobe, S., Kuwano-Yoshida, A., Komori, N., Xie, S. –P., and Small, R. J. (2008). Influence of the gulf stream on the troposphere. *Nature*452, 206–209. doi: 10.1038/nature06690

Mori, M., Kosaka, Y., Watanabe, M., Nakamura, H., and Kimoto, M. (2019). A reconciled estimate of the influence of Arctic sea-ice on recent Eurasian cooling. *Nat. Clim. Change*9, 123–129. doi: 10.1038/s41558-018-0379-3

Rudeva, I., and Simmonds, I. (2021). Midlatitude winter extreme temperature events and connections with anomalies in the Arctic and tropics. *J. Clim.*34, 1–47. doi: 10.1175/JCLI-D-20-0371.1

Saha, S., Moorthi, S., Pan, H. L., Wu, X. R., Wang, J. D., Nadiga, S., et al. (2010). The NCEP climate forecast system reanalysis. *Bull. Amer. Meteor. Soc.*91, 1015–1057. doi: 10.1175/2010BAMS3001.1

Saha, S., Moorthi, S., Wu, W., Wang, J., Nadiga, S., Tripp, P., et al. (2014). The NCEP climate forecast system version 2. *J. Clim.*27, 2185–2208. doi: 10.1175/JCLI-D-12.00823.1

Sasaki, Y. N., Minobe, S., Asai, T., and Inatsu, M. (2012). Influence of the Kuroshio in the East China Sea on the early summer (Baiu) rain. *J. Clim.*25, 6627–6645. doi: 10.1175/JCLI-D-11-00727.1

Sato, K., Inoue, J., Kodama, Y., and Overland, J. E. (2012). Impact of Arctic sea-ice retreat on the recent change in cloud-base height during autumn. *Geophys. Res. Lett.*39:L10503. doi: 10.1029/2012GL051850

Sato, K., Inoue, J., Simmonds, I., and Rudeva, I. (2021). Antarctic Peninsula warm winters influenced by Tasman Sea temperatures. *Nat. Commun.*12:1497. doi: 10.1038/s41467-021-21773-5

Sato, K., Inoue, J., and Watanabe, M. (2014). Influence of the gulf stream on the Barents sea ice retreat and Eurasian coldness during early winter. *Environ. Res. Lett.*9:084009. doi: 10.1088/1748-9326/9/8/084009

Seo, H., and Yang, J. (2013). Dynamical response of the Arctic boundary layer process to uncertainties in sea-ice concentration. *J. Geophys. Res. Atmos.*118, 12383–12402. doi: 10.1002/2013JD020312

Shimada, K., Kamoshida, T., Itoh, M., Nishino, S., Carmack, E., McLaughlin, F., et al. (2006). Pacifici Ocean inflow: influence on catastrophic reduction of

sea ice cover in the Arctic Ocean. *Geophys. Res. Lett.*33:L08605. doi: 10.1029/2005GL025624

Shimada, T., and Minobe, S. (2011). Global analysis of the pressure adjustment mechanism over sea surface temperature fronts using AIRS/Aqua data. *Geophys. Res. Lett.*38:L06704. doi: 10.1029/2010GL046625

Tachibana, Y., Komatsu, K. K., Alexeev, V. A., Cai, L., and Ando, Y. (2019). Warm hole in Pacific Arctic sea ice cover forced mid-latitude Northern Hemisphere cooling during winter 2017-18. *Sci. Rep.*9:5567. doi: 10.1038/s41598-019-41682-4

Taguchi, B., Nakamura, H., Nonaka, M., Komori, N., Kuwano-Yoshida, A., Takaya, K., et al. (2012). Seasonal evolutions of atmospheric response to decadal SST anomalies in the North Pacific subarctic frontal zone: observations and a coupled model simulation. *J. Clim.*25, 111–139. doi: 10.1175/JCLI-D-11-00046.1

Takatama, K., Minobe, S., Inatsu, M., and Small, R. J. (2015). Diagnostics for near-surface wind response to the gulf stream in a regional atmospheric model. *J. Clim.*28, 238–255. doi: 10.1175/JCLI-D-13-00668.1

Tokinaga, H., Tanimoto, Y., Xie, S.-P., Sampe, T., Tomita, H., and Ichikawa, H. (2009). Ocean frontal effects on the vertical development of clouds over the western north Pacific: in situ and satellite observations. *J. Clim.*22, 4241–4260. doi: 10.1175/2009JCLI2763.1

Vaughan, D. G., Comiso, J. C., Allison, I., Carrasco, J., Kaser, G., Kwok, R., et al. (2013). "Observations: cryosphere," in *Climate Change 2013: The Physics Science Basis. Contribution of Working Group I to the Fifth Assessment Report of the Intergovernmental Panel on Climate Change*, eds T. F.Stocker, et al. (Cambridge, NY: Cambridge University Press).

Wallace, J. M., Mitchell, T. P., and Deser, C. (1989). The influence of sea-surface temperature on surface wind in the eastern equatorial Pacific: seasonal and interannual variability. *J. Clim.*2, 1492–1499. doi: 10.1175/1520-0442(1989)002<1492:tiosst>2.0.co;2

Xie, S.-P., Hafner, J., Tanimoto, Y., Liu, W. T., Tokinaga, H., and Xu, H. (2002). Bathymetric effect on the winter sea surface temperature and climate of the Yellow and East China Seas. *Geophys. Res. Lett.*29:L2228. doi: 10.1029/2002GL015884

Yasuda, I. (2003). Hydrographic structure and variability in the Kuroshio-Oyashio transition area. *J. Oceanogr.*59, 389–402. doi: 10.1023/A:1025580313836

Conflict of Interest: The author declares that the research was conducted in the absence of any commercial or financial relationships that could be construed as a potential conflict of interest.

Publisher's Note: All claims expressed in this article are solely those of the authors and do not necessarily represent those of their affiliated organizations, or those of the publisher, the editors and the reviewers. Any product that may be evaluated in this article, or claim that may be made by its manufacturer, is not guaranteed or endorsed by the publisher.

frontiers in Environmental Science

ORIGINAL RESEARCH
published: 25 August 2021
doi: 10.3389/fenvs.2021.689301

On the Treatment of Soil Water Stress in GCM Simulations of Vegetation Physiology

P. L. Vidale[1,2]*, *G. Egea*[3], *P. C. McGuire*[1,2], *M. Todt*[1,2], *W. Peters*[4,5], *O. Müller*[6], *B. Balan-Sarojini*[7] and *A. Verhoef*[8]

[1]Department of Meteorology, University of Reading, Reading, United Kingdom, [2]National Centre for Atmospheric Science, University of Reading, Reading, United Kingdom, [3]Area of Agroforestry Engineering, Technical School of Agricultural Engineering, University of Seville, Seville, Spain, [4]Environmental Sciences Group, Wageningen University, Wageningen, Netherlands, [5]University of Groningen, Centre for Isotope Research, Groningen, Netherlands, [6]Facultad de Ing. y Cs. Hídricas, Universidad Nacional del Litoral and CONICET, Santa Fe, Argentina, [7]European Centre for Medium-Range Weather Forecasting (ECMWF), Reading, United Kingdom, [8]Department of Geography and Environmental Science, University of Reading, Reading, United Kingdom

Current land surface schemes in weather and climate models make use of the so-called coupled photosynthesis–stomatal conductance (A–g_s) models of plant function to determine the surface fluxes that govern the terrestrial energy, water and carbon budgets. Plant physiology is controlled by many environmental factors, and a number of complex feedbacks are involved, but soil moisture control on root water uptake is primary, particularly in sub-tropical to temperate ecosystems. Land surface models represent plant water stress in different ways, but most implement a water stress factor, β, which ranges linearly (more recently also curvilinearly) between $\beta = 1$ for unstressed vegetation and $\beta = 0$ at the wilting point, expressed in terms of volumetric water content (θ). β is most commonly used to either limit A or g_s, and hence carbon and water fluxes, and a pertinent research question is whether these treatments are in fact interchangeable. Following Egea et al. (Agricultural and Forest Meteorology, 2011, 151 (10), 1,370–1,384) and Verhoef et al. (Agricultural and Forest Meteorology, 2014, 191, 22–32), we have implemented new β treatments, reflecting higher levels of biophysical complexity in a state-of-the-art LSM, Joint UK Land Environment Simulator, by allowing root zone soil moisture to limit plant function non-linearly and via individual routes (carbon assimilation, stomatal conductance, or mesophyll conductance) as well as any (non-linear) combinations thereof. The treatment of β does matter to the prediction of water and carbon fluxes: this study demonstrates that it represents a key structural uncertainty in contemporary LSMs, in terms of predictions of gross primary productivity, energy fluxes and soil moisture evolution, both in terms of climate means and response to a number of European droughts, including the 2003 heat wave. Treatments allowing β to act on vegetation fluxes via stomatal and mesophyll routes are able to simulate the spatiotemporal variability in water use efficiency with higher fidelity during the growing season; they also support a broader range of ecosystem responses, e.g., those observed in regions that are radiation limited or water limited. We conclude that current practice in weather and climate modelling is inconsistent, as well as too simplistic, failing to credibly

OPEN ACCESS

Edited by:
Paul A Dirmeyer, George Mason University, United States

Reviewed by:
Guo-Yue Niu, University of Arizona, United States
Meg Fowler, National Center for Atmospheric Research (UCAR), United States

***Correspondence:**
P. L. Vidale
p.l.vidale@reading.ac.uk

Specialty section:
This article was submitted to Interdisciplinary Climate Studies, a section of the journal Frontiers in Environmental Science

Received: *05 April 2021*
Accepted: *23 July 2021*
Published: *25 August 2021*

Citation:
Vidale PL, Egea G, McGuire PC, Todt M, Peters W, Müller O, Balan-Sarojini B and Verhoef A (2021) On the Treatment of Soil Water Stress in GCM Simulations of Vegetation Physiology. Front. Environ. Sci. 9:689301. doi: 10.3389/fenvs.2021.689301

simulate vegetation response to soil water stress across the typical range of variability that is encountered for current European weather and climate conditions, including extremes of land surface temperature and soil moisture drought. A generalized approach performs better in current climate conditions and promises to be, based on responses to recently observed extremes, more trustworthy for predicting the impacts of climate change.

Keywords: photosyhthesis, soil moisture, stomatal conductance, internal CO_2 concentration, heatwave 2003

INTRODUCTION

Water availability exerts a major control on vegetation gross primary productivity (GPP), as well as on the land surface energy balance. It has been estimated that ~40% of the global vegetated land surface, particularly in sub-humid, semi-arid, and arid regions (Stocker et al., 2018; O'Sullivan et al., 2020), experiences plant activity/growth limitations caused by seasonal water deficits (Nemani et al., 2003; Beer et al., 2010). In the context of future projections of ecosystem response, soil moisture stress is predicted to increase over large regions (Berg et al., 2016; Ukkola et al., 2020). Consequently, there is a clear requirement to incorporate accurate, process-based models of plant response to soil moisture stress in coupled land-atmosphere climate models. However, the models currently used to represent biogeophysical and biogeochemical processes in Earth System Models, or even simpler GCMs, are often unable to properly capture observed responses to soil moisture stress (e.g., Beer et al., 2010; Powell et al., 2013; Medlyn et al., 2016; De Kauwe et al., 2017; Restrepo-Coupe et al., 2017; Peters et al., 2018; Paschalis et al., 2020).

Plants respond to reductions in soil moisture content (SMC) through a range of drought tolerance and prevention strategies; a thorough review of the state of our knowledge of these processes is provided in Harper et al. (2021). The immediate response is to reduce physiological activity, which has consequences for primary production and for transpiration. Land-atmosphere feedbacks involving anomalously high near-surface vapor pressure deficit and leaf boundary temperature (see e.g., Ball et al., 1987), further exacerbate concurrent soil drought and atmospheric aridity (Zhou et al., 2019). Such conditions are more likely when meteorological drought occurs, often as a result of stagnant atmospheric conditions (e.g., summertime blocking). Such events see a reduction in carbon uptake, with possible consequences for plant growth and below-ground carbon allocation, but also increase the Bowen ratio, raise surface temperature and can lead to further dessication of the soils, at a Clausius-Clapeyron rate (see for instance the review in Seneviratne et al., 2010 and Vargas Zeppetello et al., 2019).

Most land surface schemes do incorporate the process of downregulation of photosynthesis, or of stomatal conductance, but this is mostly done in a simplistic way and with a macroscale approach; a review of the range of complexity is available in Verhoef and Egea (2014). A typical LSM represents the regulation of stomatal conductance as a simple generic function of SMC, generally expressed in terms of volumetric water content (θ, $m^3\ m^{-3}$). This simple generic function is the so-called "beta" function, where β is a factor between zero and one that limits photosynthesis in some way (this depends on the LSM, see **Section 2**). Above a critical SMC, θ_c, there is no stress ($\beta = 1$), and below the critical threshold value, stress increases as SMC decreases, until the wilting point, θ_w, is reached ($\beta = 0$). Alternative, yet related, expressions are available whereby stomatal regulation occurs through changes in the soil matric potential, ψ (a measure of how tightly the water is held in the soil pores, thereby affecting water uptake by the roots), expressed in pressure units, such as MPa. θ and ψ are closely related, via the water retention curve, and some models emulate a ψ-type parametrization via a curvilinear dependence on θ (see more details in Verhoef and Egea, 2014). It is important to note, in this context, that the widely adopted linear relationship in most LSMs simulates unrealistically low plants resiliency to water stress in drought conditions (Niu et al., 2020, as well as the discussion in; Verhoef and Egea, 2014).

A recent survey of land surface schemes currently in use in the land surface processes community (available in Peters et al., 2018) has indicated that three strategies, or pathways, exist: 1) those that impose soil moisture stress by regulating stomatal conductance (e.g., LPJ-GUESS, LPJ-C13, CLM); 2) those that impose soil moisture stress by downregulating photosynthesis (e.g., SiB2, CLM, JULES); 3) those that employ some form of control on mesophyll conductance (e.g., SIBCASA, ORCHIDEE) and 4) those that employ all strategies at once (e.g., SIBCASA, ORCHIDEE). **Table 1** provides a summary of the above and suggests that there is currently no community consensus on what approach is to be used. At the same time, **Table 1** illustrates that individual research groups have chosen the plant water stress strategy that best suited their specific scientific objective (e.g., the simulation of GPP), rather than choosing an approach that considers land surface fluxes and processes in an interconnected way.

A different approach to modelling the stomatal response to drought in LSMs is that based on plant hydraulics modelling (Eller et al., 2020; Sabot et al., 2020). This approach offers a promising and mechanistic alternative to the empirical β function approach, but it still has some limitations for global and long-term modelling related to model parameterization and limited knowledge on plant traits plasticity and acclimation (Anderegg and Venturas, 2020).

The main research question in this paper is what impacts those a-priori decisions on the "β pathway" have on the concurrent prediction of the surface energy balance, of GPP and surface temperature. A secondary question is whether, via triggering feedbacks involving near-surface atmospheric conditions, the choice of β pathway can alter the simulation of weather and climate trajectories and, ultimately, have consequences for ESM projections of climate change, particularly with regards to extremes such as heatwaves.

TABLE 1 | different strategies for imposing soil moisture stress on plants, as used in a number of current Land Surface Models (adapted and expanded from Peters et al., 2018).

LSM	Stomatal	Biochemical	Mesophyll	References
JULES v4.4		X		Clark et al. (2011); Best et al. (2011)
LPJ-GUESS	X			Smith et al. (2001), Smith et al. (2014)
LPJ-C13	X			Gerten et al. (2004); Sitch et al. (2003)
ORCHIDEE-MICT	X	X	X	Guimberteau et al. (2018)
CLM v4.5	X	X		Oleson et al. (2013)
SiBCASA	X	X	X	Schaefer et al. (2008)
SiB4		X		Haynes et al. (2019)
NOAH-MP	X	X		Niu et al. (2020)
VIC	X			Liang et al. (1994)
JSBACH	X	X		Mäkelä et al. (2019)

This study aims therefore to comparatively evaluate the impact of the pathway between soil moisture stress and vegetation function on the simulation of GPP and latent heat flux (LE) for a range of biomes and climates in Europe, under controlled conditions, enabling a direct comparison of the different strategies. A further focus is the ratio of leaf-internal to ambient CO_2 (C_i/C_a, here denoted as χ), which relates the assimilation rate to stomatal conductance (see for instance Prentice et al., 2014; Dewar et al., 2018), as 1) it is observable, even at the large scale, via the measurement of various isotopes; 2) it can be used as a proxy for water use efficiency (see for instance Peters et al., 2018) to confront model predictions; and 3) it has been shown to be (weakly) dependent on atmospheric CO_2 concentration (e.g. Lavergne et al., 2020), so a more robust indicator of long-term vegetation function. For all these reasons, χ must thus be thoroughly considered as a key variable in the study of anthropogenic climate change, but instead, it has been shown to be poorly represented by current LSMs (see the discussion in Peters et al., 2018), particularly in terms of (continental-scale) interannual variability.

The approach to the investigation is to adopt a generalized, agnostic β approach in a state-of-the-art LSM, driven by observed meteorology over a large region, and to focus on simulation fidelity in terms of climate means and variability, including the response to recent heat waves, particularly the extreme heat wave of 2003. The study is organized as follows: *Introduction* re-visits the Egea et al. (2011) solutions for aspects that matter to coupling to a full Land Surface Model (LSM); *Methods* describes Methods and Data used in the modelling study; *Results* presents results for climate means (3.1), for a composite of European droughts in the 1979–2011 period (3.2) and for the extreme growing season of 2003 (3.3), to then move into Europe-wide water use efficiency, first at the large scale level (3.4), next a mechanistic analysis at the stomatal and PFT level (3.5–3.6), to re-emerge to a scaling up of the results at European level, based on the isotopic fractionation Δ metric from Peters et al. (2018) in 3.7. *Discussion* discusses the implications of this study for climate studies, revisits Peters et al. (2018) from the perspective of model development, and suggests further avenues for progress, particularly from the point of view of more efficient numerical solutions; *Summary and Conclusion* provides summary and conclusions.

Idealised Analytical Solutions

The study by Egea et al. 2011, (E11 hereafter) developed and exploited analytical solutions for the simultaneous equation set that governs the fast, dynamic evolution of assimilation (A), stomatal conductance (g_s) and leaf internal CO_2 concentration (C_i), the more dynamic component of χ, observed during the diurnal cycle. Numerical solutions were based on an approach by Baldocchi (1994), and eliminated the need for iteration, while enabling complete freedom in the treatment of β. In order to understand the results in this study, which moves beyond E11 in implementing the framework into a full land surface simulation scheme, offered by the JULES LSM, the E11 equations are first re-visited in a highly idealized manner. This is a useful exercise, because in coupling E11 to a land surface scheme such as JULES, some feedbacks with the canopy environment become possible, at least in part (when JULES is used offline, as driven by observed meteorology) or more completely (when JULES is within the parent HadGEM3-GC31 GCM), clouding our interpretation of the primary chain of mechanisms and of the feedback responses. This preliminary step is thus important, because it enables the reader to better appreciate the motivation of the study, as well as to build expectations for what understanding can be achieved at this stage, prior to coupling to a complex land surface scheme, or even to a GCM.

Figure 1 provides a conceptual-level prediction of the shape of the functional relationships between soil moisture availability and land surface prognostic variables, when applying the E11 framework to the coupled A-g_s model contained in an LSM such as JULES. The relative stomatal conductance, $g_s/g_s(\beta = 1)$, is shown on the *x*-axis, while relative assimilation, $A/A(\beta = 1)$, is shown on the *y* axis, where $g_s(\beta = 1)$ and $A(\beta = 1)$ are the unstressed stomatal conductance and assimilation, respectively. If no other stress, or any feedbacks, are imposed, the relationship should be linear, as in the typical Ball-Berry plot, and that linear relationship is indicated by the black straight line. The three panels in **Figure 1** show, instead, the responses obtained in the E11 framework: by imposing soil moisture stress (β) on the stomatal conductance pathway (left panel, blue curve), a curvilinear relationship is revealed, and this shape generally implies a higher water use efficiency (WUE) at intermediate β levels; the other two pathways (biochemical and mesophyll) show no deviation from the linear relationship. Adding an idealized

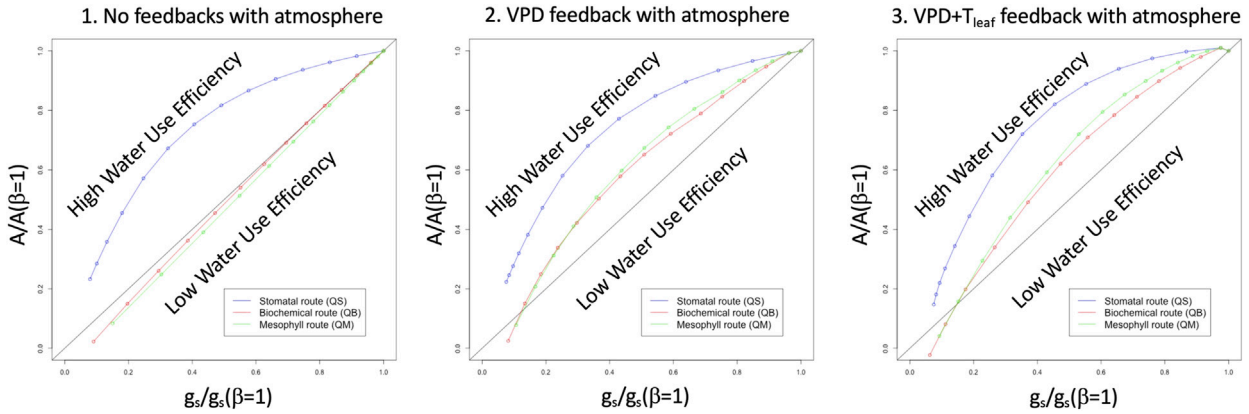

FIGURE 1 | Idealized solutions provided by the Egea et al. (2011) model: relative stomatal conductance (g_s/g_s ($\beta = 1$), *x* axis) versus relative assimilation (A/A ($\beta = 1$), *y* axis) for the three pathways and for zero feedback with the canopy air environment (left panel), VPD feedback with the canopy air environment (center panel) and VPD plus leaf temperature feedback with the canopy air environment (right panel).

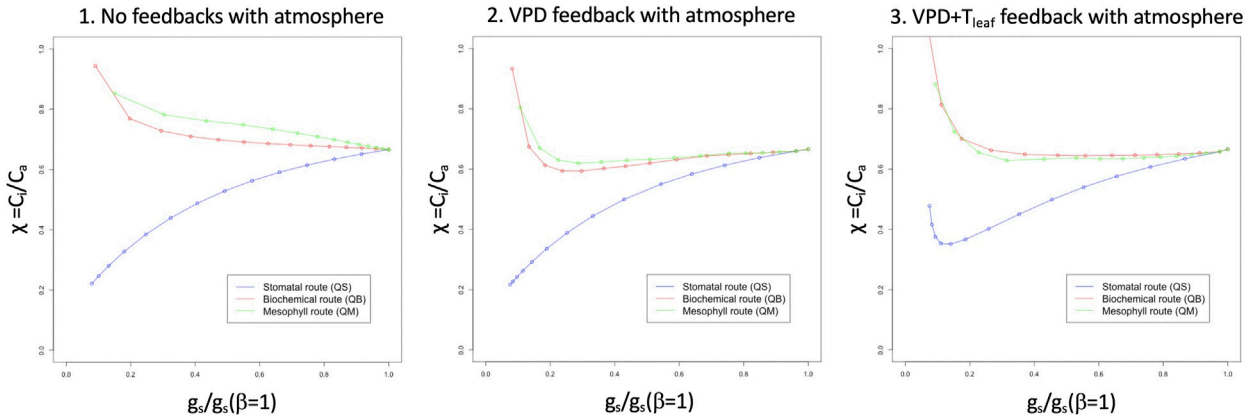

FIGURE 2 | Idealized solutions provided by the Egea et al. (2011) model: relative stomatal conductance (g_s/g_s ($\beta = 1$), *x* axis) versus internal CO_2 concentration, C_i (*y* axis, expressed as **Eq. 5**) for the three pathways and for zero feedback with the canopy air environment (left panel), VPD feedback with the canopy air environment (center panel) and VPD plus leaf temperature feedback with the canopy air environment (right panel).

vapor pressure deficit (VPD) feedback term to E11 (center panel, this is done by editing the leaf-level atmospheric input file to the E11 model that increases VPD in proportion to 1/β), causes no change in the stomatal pathway, but now causes the two non-stomatal pathways to also become curvilinear, and to partially emulate the stomatal pathway, with a higher WUE, maximized near the β mid-range. The addition of a term that emulates (leaf) temperature feedback (right panel, this is done by increasing leaf temperature linearly by a factor proportional to 1/β) further increases WUE (right panel) for all three pathways. The rightmost panel is the one that most resembles field observations under conditions of vegetation stress, e.g., what is shown in E11 for some agricultural crops in southern Spain.

Figure 2 shows the response of χ to relative stomatal aperture (as directly caused by the soil moisture stress) for the three pathways, under the same conditions imposed for **Figure 1**: when no feedback with the atmosphere is allowed (left panel), any of the non-stomatal routes show a very high value of χ under stressed conditions, which results from the suppression of assimilation, as directly caused by β. This is not observed in the stomatal pathway, because stomata close, but assimilation carries on unhindered by β, using CO_2 inside the stomatal chamber. The three pathways behave identically for unstressed vegetation. When a VPD feedback is allowed (center panel), the two non-stomatal pathways show a reduction of χ in the lower range of stomatal conductance, while the stomatal pathway solution resembles the one in the leftmost panel. The introduction of a leaf temperature feedback (right panel) has different effects on the biochemical and stomatal pathways: the former returns to higher levels of χ for low stomatal conductance conditions (strong soil moisture stress), while the latter shows a reversal at low stomatal conductance levels, with χ increasing. The latter is the response that most strongly resembles the field

observations in E11, as well as those presented in Yan et al. (2017).

These exploratory analyses strengthen the need for an investigation of the E11 under conditions that more closely resemble those of a GCM, albeit without incurring the additional complexity of GCM errors in the surface energy balance, which would hinder our understanding.

METHODS

The JULES Land Surface Component of HadGEM3-GC31

JULES (the Joint United Kingdom Land Environment Simulator) is based on the Hadley Centre land surface scheme MOSES2. Full descriptions of JULES are provided in Best et al., 2011; Clark et al., 2011. JULES simulates the exchange of water, momentum and energy between the soil, land surface, and atmosphere. It is driven by sub-daily (typically 3-hourly) time series of radiation, precipitation, temperature, humidity, wind speed and surface pressure. The soil is divided into layers, with the thermal and hydraulic characteristics defined for all layers. It is important for the interpretation of the experiments presented in this study to note that the soil column in each grid box is vertically resolved by four layers of increasing thickness, down to a total depth of 3 m. Land surface tiles share a single soil column, and soil moisture is thus shared across tiles in each grid box.

In its standard configuration, JULES divides the land-surface into nine surface types: broadleaf trees, needle leaf trees, C3 (temperate) grass, C4 (tropical) grass, shrubs, urban, inland water, bare soil, and ice. Crops are treated as grasses. Sub-grid heterogeneity is represented by tiling of land-surface types (for example, Essery et al., 2003). All land grid boxes can be made up of any mixture of the nine land-surface types, except ice. The surface fluxes of moisture and heat are computed individually for each tile, and the state of the grid box is prognosed via the aggregation of tiles fluxes.

The biophysical state of each vegetation tile is defined by its leaf area index (LAI), canopy height and rooting depth. In the JULES experiments presented in this study a seasonal vegetation phenology, based on a MODIS climatology, is imposed at each grid point, so that no aspect of dynamic vegetation is enabled; this conscious decision imposes a buffering effect on the perturbation experiments, but makes it easier to interpret the sensitivity to β pathway, also because the dynamic vegetation aspects of JULES have been tuned in the past for the biochemical β route.

The surface fluxes of moisture and heat in JULES depend on the atmospheric boundary conditions and the characteristics of the land surface. The fluxes are computed by a network of parameterizations including soil surface, stomatal and aerodynamic resistances. Stomatal resistance also controls the intake of CO_2, and is thus the link between the carbon, water and energy cycles. The stomatal resistance parameterization (Cox et al., 1998) depends on environmental conditions, including the ambient concentration of CO_2.

JULES calculates the photosynthesis rate using the method described in Collatz et al. (1991) for the C3 pathway and Collatz et al. (1992) for the C4 pathway. Potential photosynthesis takes place at the minimum of three limiting rates: light; enzyme kinematics (Rubisco); and the transport of photosynthetic products. The potential photosynthesis is reduced under water-stressed conditions by β, the soil moisture availability factor. Photosynthesis is scaled from the leaf to the grid box scale under the assumption that the rate of photosynthesis is a function of the LAI.

The Implementation of a Flexible Treatment of β Into JULES

The three equations that must be solved simultaneously in order to produce land surface prognostics for temperature, moisture, GPP, and relative fluxes to the atmosphere are:

$$A = \gamma \frac{(C_c - \Gamma^*)}{(C_c + \beta_A)} \quad (1)$$

$$g_{sc} = g_0 + m \frac{A}{(C_s - \Gamma)\left(1 + \frac{D_s}{D^*}\right)} \quad (2)$$

$$A = g_t (C_s - C_c) \quad (3)$$

In **Eq. 1**, for Rubisco-limited photosynthesis (A_c), $\gamma = V_{cmax}$ and $\beta_A = K_c(1 + O_i/K_o)$; for Light-limited photosynthesis (A_j), $\gamma = J/4$ and $\beta_A = 2\Gamma^*$, where V_{cmax} is the maximum carboxylation rate (μmol m^{-2} s^{-1}) and J is the electron transport rate (μmol m^{-2} s^{-1}), the $K_{c,o}$ are the Michaelis-Menton kinetic factors for carboxylation and oxygenation (Pa), Γ^* is the chloroplastic CO_2 photocompensation point in the absence of mitochondrial respiration (μmol mol^{-1}) and C_c is the chloroplastic CO_2 concentration (μmol mol^{-1}).

In **Eq. 2** g_{sc} (mol m^{-2} s^{-1}) is the stomatal conductance to CO_2, g_0 (mol m^{-2} s^{-1}) is the cuticular conductance, C_s (μmol mol^{-1}) is the CO_2 concentration at the leaf surface, Γ is the CO_2 compensation point (μmol mol^{-1}), D_s is the vapour pressure deficit at the leaf surface, m is equal to $1/(1\text{-}f_0)$ and D^* is $D_{max}/(m\text{-}1)$; f_0 and D_{max} are the parameters defined by Jacobs et al. (1996).

In **Eq. 3** g_t (mol m^{-2} s^{-1}) = $(g_{sc} \cdot g_m)/(g_{sc} + g_m)$, where g_m is the mesophyll conductance to CO_2 diffusion (mol m^{-2} s^{-1}).

In order to solve the simultaneous set above, the three equations that describe A, g_{sc} and g_m as a function of C_c were coupled together and solved for C_c, resulting in a cubic relationship, which was solved using the Baldocchi (1994) method. This approach is very flexible and removes the requirement for iteration, which is computationally inefficient. The mathematical details are fully explained in the Supplementary Material section. Similar to the approach in E11, the scheme was first tested at a small selection of FLUXNET sites (not shown), e.g., for accuracy and for numerical stability, but then applied to the regional distributed simulations shown here.

In order to find solutions for the A-g_s sub-model, enabling soil moisture stress to impact the biochemical pathway (assimilation) the conductance pathways (stomatal, mesophyll), or any combinations thereof, the functional relationships, as in E11, are:

$$A = A_p\beta_B;\ \ g_s = g_s\beta_S;\ \ g_m = g_m\beta_M$$

TABLE 2 | the configuration of the β_i functions enabling the four sensitivity experiments with JULES.

β pathway	QS	QB	QM	C6
Biochemical exponent $q_{j=B}$	0	1	0	0.25
Mesophyll exponent $q_{j=M}$	0	0	1	0.5
Stomatal exponent $q_{j=S}$	1	0	0	0.25

where β, as in E11, can be applied to any single pathway, or combinations, or to all, with different shapes (linear or curvilinear) and weights (see E11 for a large selection of tests). The subscripts i,j = B, S and M correspond to biochemical, stomatal, and mesophyll limitations, respectively (see **Table 2**).

The general expression for β, also enabling non-linear dependence, is, as in E11:

$$\beta_i = \begin{cases} 1 & \theta \geq \theta_c \\ \left[\dfrac{\theta - \theta_w}{\theta_c - \theta_w}\right]^{q_j} & \theta_w < \theta < \theta_c \\ 0 & \theta \leq \theta_w \end{cases} \quad (4)$$

where β_i is a soil moisture dependent function ranging from 1 to 0. The subscript j for the q_j exponent signifies that independent functional shapes can be adopted in the definition of each β_i, enabling complete freedom for each pathway (see **Table 2**); for further details, see the discussion, after Eq. 16, in E11.

Following E11, in order to test the relative influence of soil moisture stress on canopy-atmosphere exchange processes, we have set up Europe-wide JULES model experiments with the following four model configurations, constituting four sensitivity experiments.

Configuration QB fully corresponds in its design (application to photosynthetic capacity) to that of the original JULES, and could in principle be considered our control experiment. We have chosen, however, to include an unmodified JULES integration (CTL) in our analysis, as it was deemed useful in order to understand the impact of using the analytic solution method in E11 (see the full development in Additional Materials) and to quantify any uncertainty. Configuration QS applies soil moisture limitation stress to stomatal closure exclusively; configuration QM applies soil moisture limitation stress to the mesophyll conductance exclusively; C6, finally, applies soil moisture limitation stress to all three pathways, albeit with differing weights and functional shapes (see the motivation for these choices in E11).

Experimental Design

We have configured a Europe-wide (35N–65N, 10W to 40E) JULES (a full set was run with v2.2 initially, but for all results presented here we have re-run with v4.4, Clark et al., 2011), driven by meteorological data (net radiation, precipitation, wind, reference height temperature and humidity; WATCH, Weedon et al., 2011). The model grid configuration, in the horizontal and vertical, is identical to that in Clark et al. (2011); model parameters, in particular those controlling photosynthesis, are also standard. Each grid point comprises 9 "tiles", five of which are plant functional types (PFTs), the others are ice, bare soil, urban. The model is run continuously, at half-hourly time steps, for 33 years, from 1979 to 2011. We apply an initial spin-up to each simulation, to create 1979 balanced initial conditions for soil prognostics; spin-up completion is governed by convergence of soil moisture and soil temperature solution (to within 1% between spin-up cycles). Typically, each model goes through 30 spin-up cycles of 10 years each, until full convergence, for a maximum total of 300 years.

The E11 scheme was implemented as an alternative to the standard A-g_s scheme (see Cox et al., 1998), albeit only for C3 plants at this initial (developmental) stage. The abundance of C4 plants in the European domain chosen for this study is minimal (mostly less than 10%, with only a single grid point found to be dominant in Turkey) and any grid points containing a fraction of C4 plants above 15% are discarded from the analysis presented in this paper. This approach is fully consistent with our forcing of the model using observed meteorology, by which individual grid points are fully independent from each other (and tiles partially so, because of the shared within-soil solutions), so that any tiles potentially "contaminated" by C4 biophysics cannot contribute to the evolution of fluxes in any neighboring grid cells. This is because in the off-line setup there is no horizontal advection of air between grid points. Future applications with the coupled GCM, in which air can move freely between grid points, will require development of an equivalent β pathway treatment for C4 plants.

Atmospheric CO_2, thus C_a=C_s were fixed at 360 μmol mol^{-1} for the period.

Special High-Frequency Stomatal-Level Diagnostics

New stomatal level diagnostics for C_i (also for leaf-level VPD, not shown here), for each PFT, were introduced in JULES, in order to study the evolution of χ in high detail (time-step level), and to enable intrinsic Water Use Efficiency (iWUE) and isotopic discrimination metric (Δ, ‰) diagnostics, see 2.6, to be used for comparison with FLUXNET observations in the diurnal and seasonal cycle of $C_i\,(\chi)$. The C_i equation is:

$$C_i = C_s - \frac{A}{g_{sc}} \quad (5)$$

The equation used to estimate Δ from C_i is, as in Peters et al. (2018):

$$\Delta \approx \Delta_d + \left(\Delta_p - \Delta_d\right)\frac{C_i}{C_a} \quad (6)$$

where Δ_p (27‰) and Δ_d (4.4‰) are the isotopic discriminations during assimilation catalysed by the enzyme Rubisco in C3 photosynthesis and molecular diffusion of CO_2 through the stomata, respectively.

$$\text{iWUE} \approx \frac{c_a \cdot \left(1 - \frac{C_i}{C_a}\right)}{1.6} \quad (7)$$

These time-step level diagnostics of C_i and Δ, thus iWUE, were next resampled to 3-hourly frequency for each PFT (5 in total in this study), GPP-weighted as in observations, and for each grid box in the domain. As such, the output is large, and more detailed than what can be achieved in a GCM setting. The same high-frequency diagnostics, for simulation QB, were used in Peters et al. (2018). The ecosystem-level water use efficiency, eWUE, was computed using the ratio of NPP and evapotranspiration from grid-box daytime averages, as represented by 6-hourly model statistics, then projected onto monthly means.

Observational Datasets Used for Model Assessment

The FLUXCOM data were obtained from Jung et al. (2019) and are used as monthly means over 0.5° grid boxes. While we realize that FLUXCOM are not actually observations, it is often assumed, for evaluation purposes, to be a suitable extrapolation of the measured net ecosystem exchange from many eddy-covariance sites across Europe. This also enables the study to be verified with a relatively independent dataset (the version chosen upscales the FLUXNET observations by using neural networks to combine it with remote sensing and meteorological data, in this case also WFDEI). This is the best compromise achievable in bridging the field scale (FLUXNET towers) to the large scale used in this study, without direct use of re-analysis products, which are strongly model-dependent in terms of surface fluxes. The measurements used as reference for iWUE are derived from FLUXNET data, as described in Peters et al. (2018), Section S5, and summarized in their Table S3. To compare these two better, relative changes in ‰ from the baseline (years 2002–2006) are shown in *Results*. Averaging of C_i, thus iWUE, over time was also GPP-weighted, such that high-photosynthesis hours are represented the most.

Definition of JULES Soil Moisture Droughts for Masking of Regional Flux Averages

JULES soil moisture droughts are defined by the seasonal average (AMJJAS) of the linearly calculated β anomaly ($\Delta\beta$) at each grid point, as deviations from the 1979–2011 climatology in CTL (enabling a common comparison). A regional mask is constructed from these $\Delta\beta$ for each year through a three-step process, using a quantile approach. At first, drought thresholds were calculated for each grid cell and each month as the 20th percentile of daily β values using the CTL simulation. Subsequently, differences between monthly averages of β and monthly drought thresholds were summed up over the period April to September for each grid cell and each year, and grid cells were marked as dry for a particular year when this sum was negative. Integrating over the period April to September, which was selected based on GPP values, allows to capture droughts of different intensities and durations, i.e., short, intense droughts as well as prolonged, weaker droughts. Finally, drought masks were created by selecting the largest connected area identified as dry within the model domain for each year. These drought masks were applied to all simulations, to guarantee consistency in spatial averages across simulations.

RESULTS

All experiments (CTL, QB, QS, QM, C6) were spun-up individually and run for the full period. However, in terms of presentation, in order to reduce the number of plots and sub-plots, CTL is only shown in terms of long-term soil moisture memory, as QB is virtually identical to CTL in terms of land-atmosphere fluxes. First the climatological biases of some variables of interest will be shown, then the 2003 heat wave response will be used as a surrogate for future climate conditions, as suggested for instance in Schär et al. (2004), where it was shown how the 2003 event represents an outlier for current climate, but is, instead, compatible with a temperature probability distribution function (PDF) extracted from climate projections forced by a strong climate change scenario. For completeness, we have also included a more general assessment of all major droughts in the period.

Climatological Biases

All biases have been computed relative to FLUXCOM products (Jung et al., 2019). Similar plots have also been produced with alternative products in the ILAMB verification toolkit, but are not shown here, as they would not bring extra information. The focus for the fluxes is on the growing season (MAM + JJA), as autumn and wintertime responses to the perturbation experiments are of much smaller amplitude, but soil moisture will be shown over a more extended period, because of soil moisture memory effects, which are of interest.

Figure 3 shows the GPP climatological biases for experiments QB, QS, and C6, which are the most salient. Overall, the figure indicates that the QB model (nearly identical to CTL, not shown) tends to overestimate European GPP in spring, particularly in central Europe, which is made worse, and more widespread, by QS and C6. In summer, following an overactive use of soil moisture (mostly by vegetation) at the center of the domain, the GPP tends to be underestimated by QB, as well as, in the North and South of the domain, by QS and C6; there is a slight overestimation at the center of the domain, and over the Alps. The summer biases are sufficient to overwhelm the annual mean.

Figure 4 shows the LE response, which, to a large extent, reflects the transpiration response, given the high vegetation fraction for these large-scale experiments. For the three models, QB, QS, and C6, latent heat tends to be overestimated in Spring nearly everywhere in Europe, while for Summer a dipole emerges, with a slight overestimation in North and Central Europe, but a pronounced underestimation in Southern Europe, very likely due to soil dessication. No significant differences are seen, however, between QB and C6 in any of the seasons, which is an important result in view of what has been found for the GPP response. Model QS shows some indication of a bias reduction in the NE portion of the domain, but a worsening in the SE (over Greece and Turkey).

Figure 5 shows the sensible heat flux (SH) response, which is nearly insensitive to the model formulation in spring, and shows small regional responses in summer, which mirror the responses seen in the latent heat flux maps (**Figure 4**): this small response to model formulation is again rather expected (because the model was run with observed meteorology and is thus constrained) and

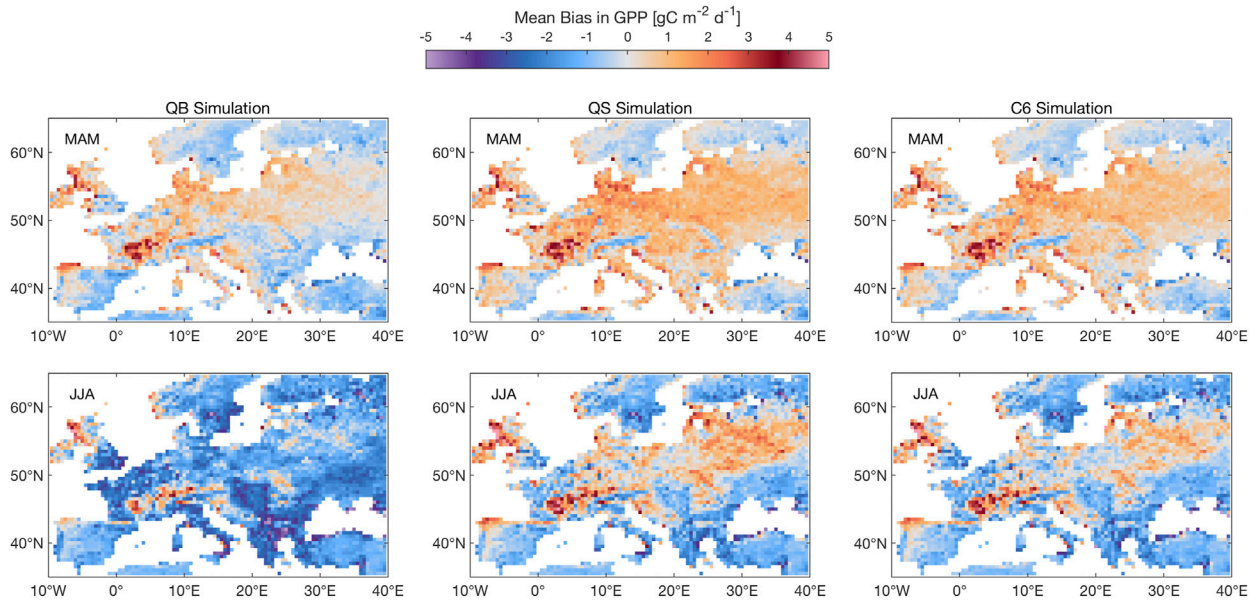

FIGURE 3 | Mean climatological bias for GPP in simulations QB, QS and C6 against FLUXCOM observations. MAM mean (top row) and JJA mean (bottom row). Units: gC m^{-2} d^{-1}.

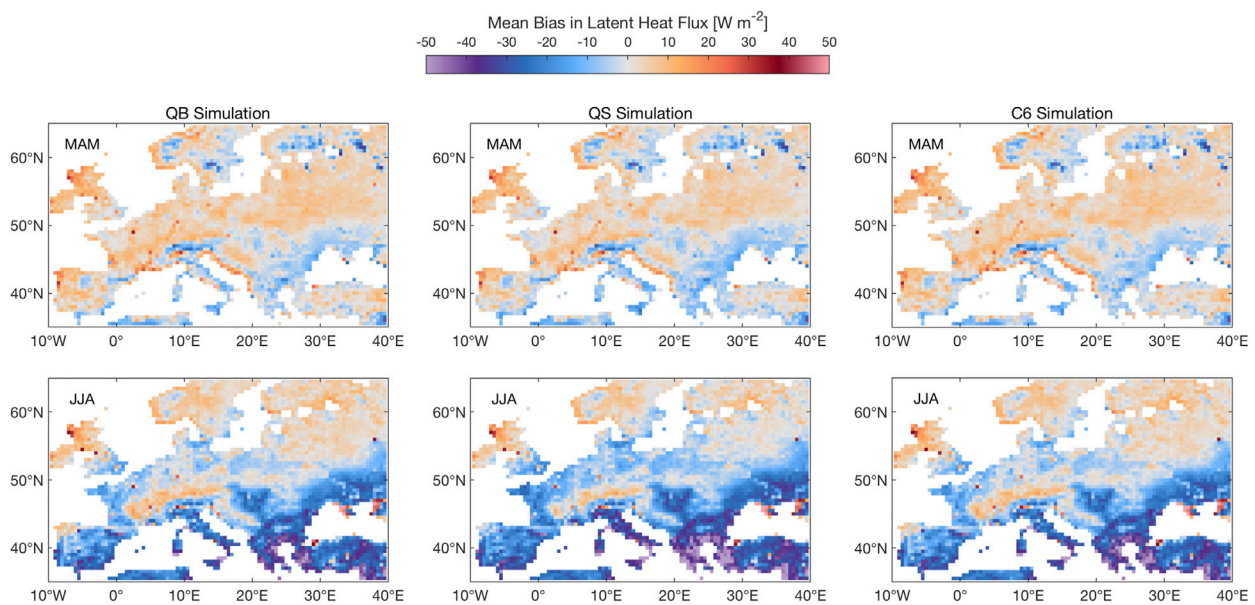

FIGURE 4 | Same as **Figure 3**, albeit for latent heat. Units: W m^{-2}.

rather reassuring, as in most years European plants are not water stressed for periods of time long enough to impact climate means.

Figure 6 shows the available soil moisture response in terms of the β factor in the soil: since it is a relative measure, and weighted by layer thickness, it reflects the effect on the bulk of the roots for the JULES vegetation (mostly forests and C3 grasses in this European domain), with a possible buffering effect from the deepest layer, which is more accessible to trees than grasses. The response of each model is quite strikingly different: while QB is virtually identical to CTL (some differences are expected, since these are long-term spun-up experiments, and any numerical residual would show strongly in a cumulative variable such as soil moisture), the QM response is mostly a strong drying, seen in all seasons, but with a strong North-West to South-East gradient. The response of QS is, instead, a moistening, again with a strong NW to SE gradient. The C6 response is, remarkably, nearly identical to the QB (CTL) response, indicating that this combined pathway for soil moisture impact on the surface

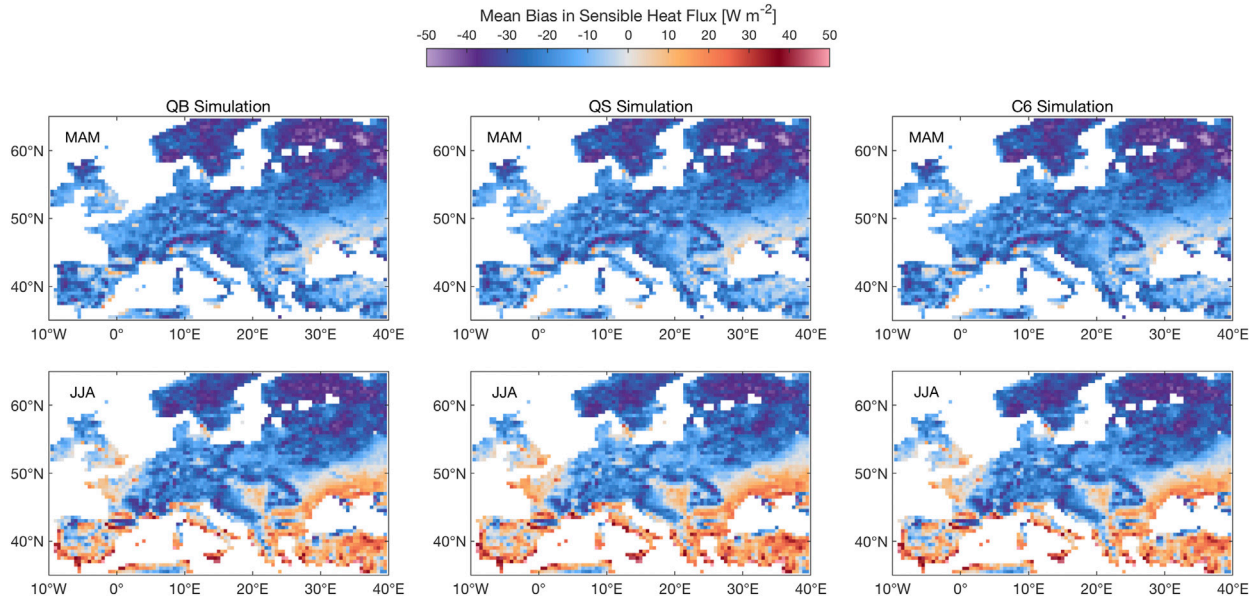

FIGURE 5 | Same as **Figure 3**, albeit for sensible heat. Units: W m^{-2}.

latent heat flux is nearly soil moisture neutral. These responses are consistent with, and do help to interpret, the LE and SH responses seen previously in **Figures 4**, **5**, both in terms of the N-S gradient and in terms of the seasonal evolution.

Response to Multiple Droughts in the 1979–2011 Period

Figure 7 shows a panoramic view of all droughts in Europe, with different severities, both in terms of intensity (going as far as a Δβ exceeding −0.3) and of spatial extent. Key drought years present characteristics that are spatially consistent, indicative of a large-scale atmospheric forcing, and often corresponding to heat waves, such as 2003 and 2010, as discussed in Fischer et al. (2008) and in Russo et al. (2015). Notable droughts in recent times are 1995 (United Kingdom and Spain), 1996 (North Europe), 2002 (Poland, Belarus), 2003 and 2011, over most of Western Europe, 2005 (Spain) and 2010 (Russia, mostly outside the domain). By using the mask constructed from **Figure 7**, it is next possible to produce a synthesis plot that presents the response to the treatment of β, for each year in which a significant drought has been identified.

Figure 8 provides a synthesis of model behavior for 20 soil moisture drought years, indicated by dots of different magnitude, according to spatial extent and intensity, expanding from the focus on the largest disturbance, 2003, which remains a prominent benchmark in terms of area extent and intensity. **Figure 8** shows the summary of model flux errors, averaged over each drought year, extracted from the data used for **Figures 3–5** (and defined as difference from identically processed FLUXCOM observations), against the annual AMMJAS Δβ.

Figure 8A shows that the majority of drought years correspond to years of (overly) depressed GPP; however, the depressed vegetation production response is strongly dependent on the treatment of β, which can be appreciated by how clustered the coloured dots are, and less dependent on the intensity of the drought, as the dots tend to be organized in horizontal bands, rather than on a diagonal. Simulations QS and C6 correspond to the data clusters with the least bias in GPP for those soil moisture drought years, independent of location.

Figure 8B shows the errors in the evaporative fraction (EF), which is included here to account for differences in the sum of SH and LE between simulations and FLUXCOM products. The errors are now aligned on a diagonal, with smaller values of Δβ mostly corresponding to a negative bias (caused by a positive error in SH and a negative error in LE, see **Figure 8C**, and **Figure 8D**), and larger values of Δβ leading to a positive bias in EF. Simulation QS is closest to EF observations for 2003, with C6 second-best, albeit similar to QB, and with QM displaying the largest bias. The small amplitude Δβ (negative EF bias) seem to correspond to points in the Northern portion of the domain.

For LE flux, **Figure 8C** shows that the error metric is now aligned on a diagonal (unlike GPP) and tends to be dominated by the southern portion of the domain, where JULES strongly underestimates LE in the climatology. As the drought severity increases, the LE flux bias is reduced, suggesting that the LE response to Δβ starts to plateau, and the model has an opportunity to "catch up" to observations. There are indications that QM, the most liberal treatment of β in terms of soil water usage, has the least error overall, while QS, the most conservative, is exaggerating the LE response, particularly at moderate Δβ levels. Relative advantages are not so clear for the other treatments (QB, C6), even for the largest events.

Figure 8D shows the error in SH as a function of Δβ, which is aligned on a diagonal with slope opposite to the one for LE: SH is strongly underestimated in severe drought cases, meaning that the observed heating from the anomalous 2003 soil dessication is not

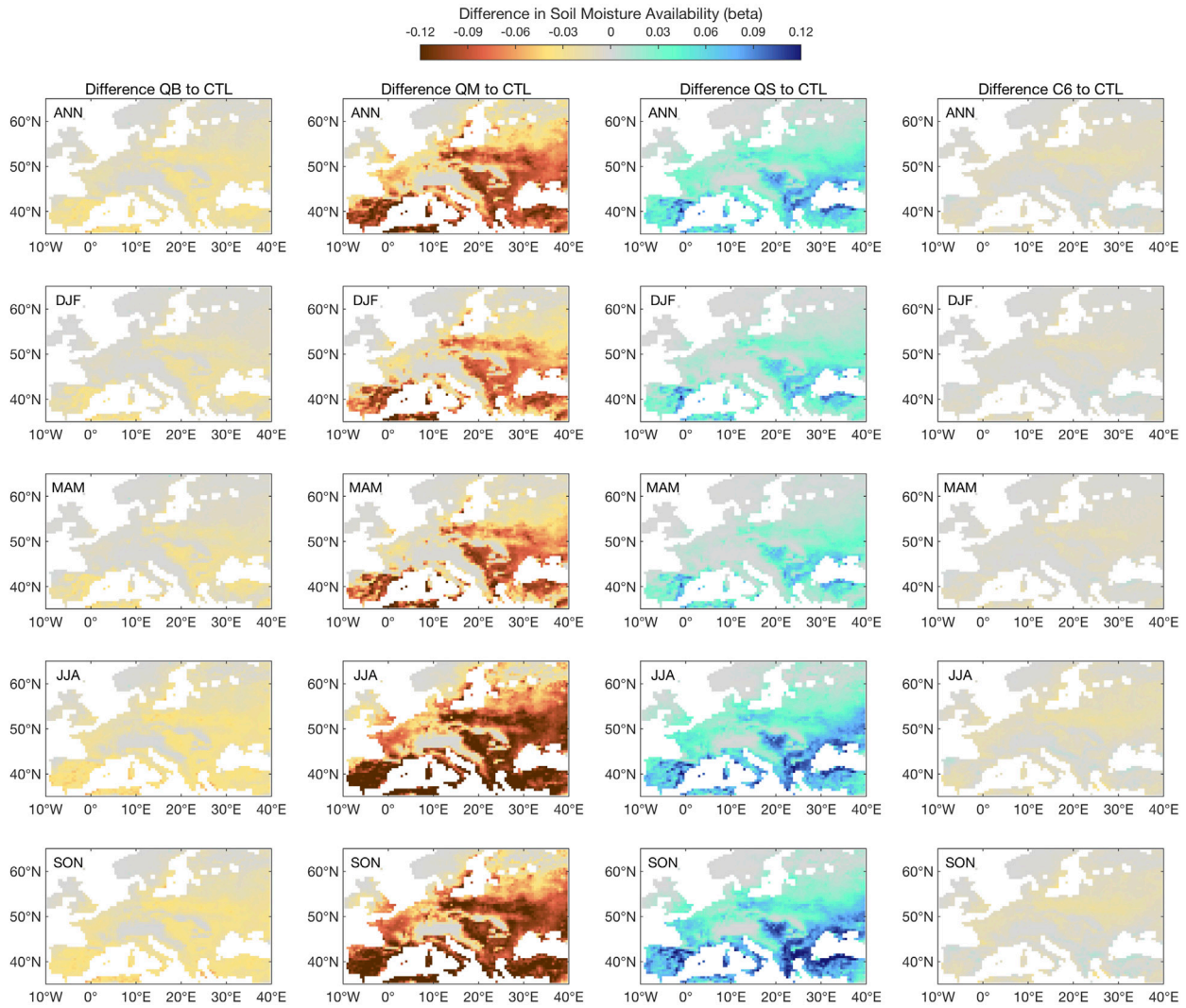

FIGURE 6 | Climatology of available soil moisture, as indicated by β in each simulation, as compared to the control simulation (CTL). All values apply to the full soil profile. β is unitless.

simulated faithfully, and slightly overestimated in moderate drought cases. For this variable, simulation QM seems to be slightly worse than the others for the most pronounced droughts (better skill for low intensity droughts), while QS seems to have a small advantage overall at medium $\Delta\beta$ levels; C6 is quite similar to QB in this respect.

The overall lesson is that, while GPP errors are affected systematically by the choice of β treatment, the errors in energy fluxes are shifted to different equilibria, reflecting climatological shifts in soil moisture, and could be interpreted as a near-neutral response.

Response to Extreme Atmospheric Forcing: The European Heat Wave of 2003

Figure 9 shows the evolution of GPP during the 2003 summer heat wave, as monthly means, from April to August, for simulations QB, QS, and C6, the most interesting ones, analyzed in terms of the evolution of model error (against FLUXCOM). While it is well-known that Spring 2003 saw clear skies and warmer conditions, leading to enhanced vegetation activity while there was still ample soil moisture availability, both QB and C6 exaggerate this response, particularly over France and Germany, with C6 showing the largest response in April, which implies a larger soil moisture usage. This deficit can then lead, via soil memory, to a suppressed GPP in each of the JJA months; in this respect, C6 is an improvement over QB, as it is apparently able to sustain a larger JJA GPP. Simulation QS is nearly identical to C6, albeit with a slightly smaller amplitude for the JJA signal for the Western Europe mean, therefore the smallest error overall, while simulation QM (not shown) has a far smaller response.

For latent heat flux during the Summer 2003 heat wave (**Figure 10**), simulation C6 hardly shows any difference to

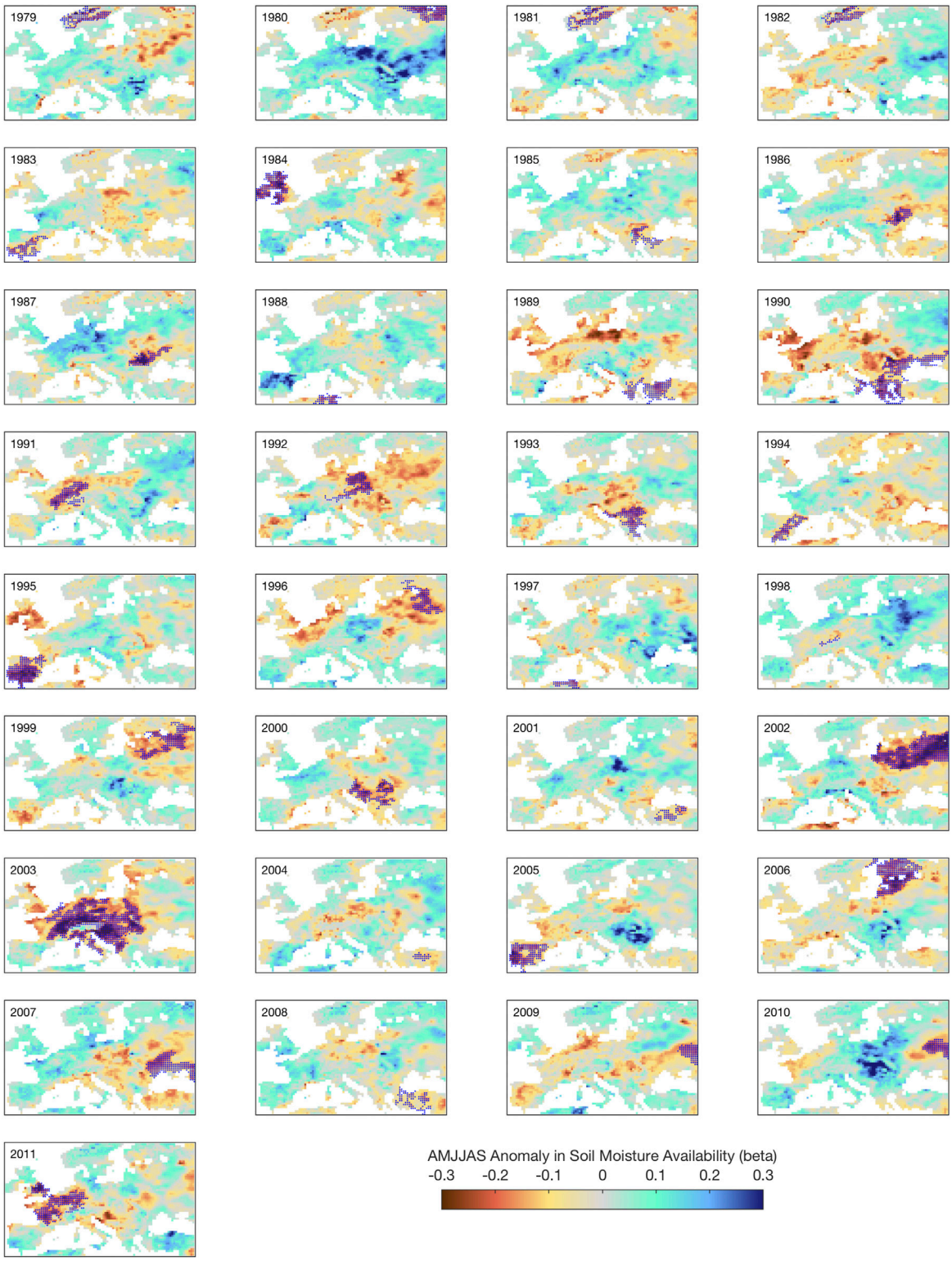

FIGURE 7 | Annual extent and intensity of drought anomalies across Europe in the period 1979–2011, as revealed by the β factor in the JULES land surface model (CTL experiment). β is unitless.

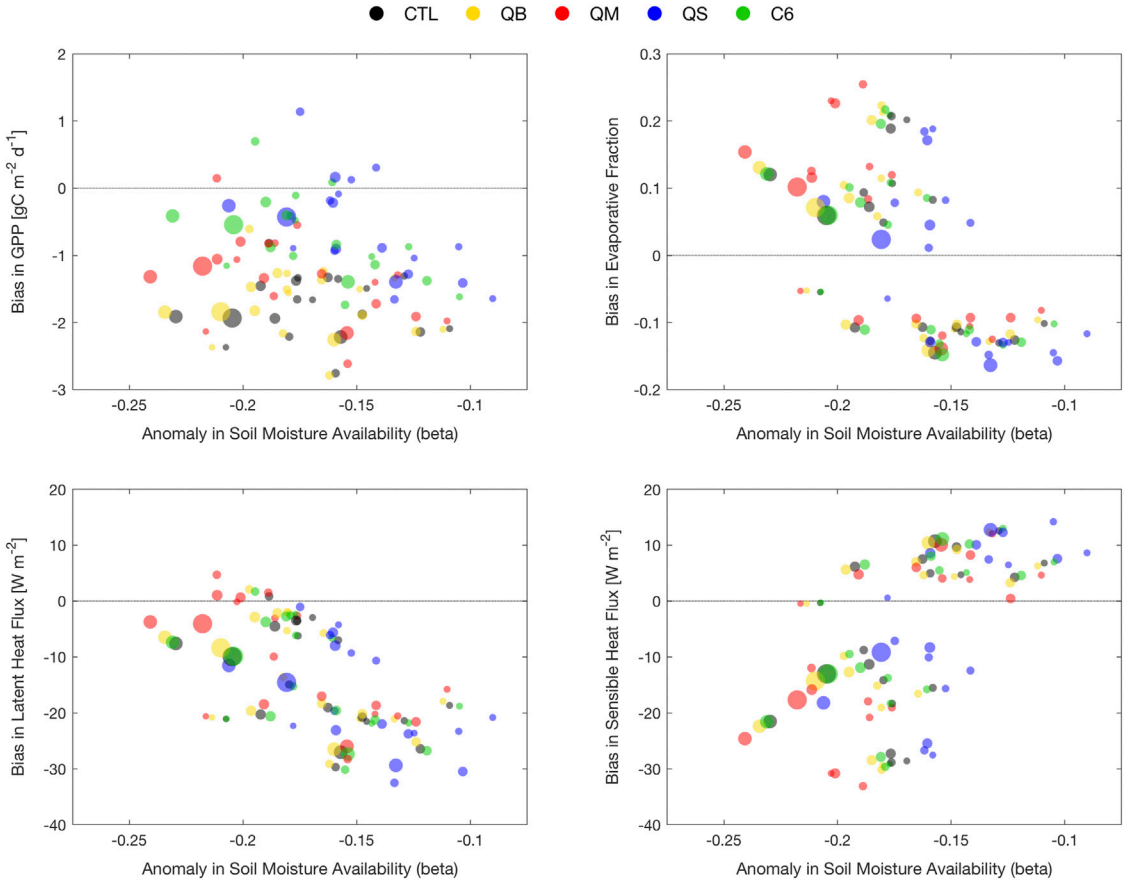

FIGURE 8 | Model errors in GPP (top left), evaporative fraction (top right), latent heat (bottom left) and sensible heat (bottom right) for the top ten droughts in Europe in the period 1979–2011 identified via the mask developed from **Figure 7**.

CTL (better evidenced in the soil moisture maps, **Figures 6**, **11**), while simulation QS displays a more interesting seasonal behavior, with a regional worsening of the dry bias in Spain and Eastern Europe (June), then in a region that covers France, Germany and Poland by August. This indicates that the enhanced GPP response in Spring has indeed consequences for the water cycle, via soil moisture memory, so that the errors in JJA are larger than for QB and C6. Simulation QM (not shown) shows a similar, albeit even more pronounced enhanced spring behavior, with a strong overestimation throughout, particularly from May to July, in most of central Europe, but then a relative reduction of the dry bias in August. These behaviors might amplify and lead to far worse summer conditions if the heat wave had been repeated in 2004 in this region.

Figure 11 reveals a soil moisture evolution for 2003 that mostly explains the above results for GPP and latent heat. Simulation QS is increasingly accumulating soil moisture in the soil, in a rather linear way, from April to August, but this is then reflected in too strong a limitation of transpiration, thus latent heat, as will be shown in **Figure 12**. Simulation C6 is closest to CTL, and demonstrates a neutral response to the soil moisture stress, despite having achieved the best performance in terms of the simulation of GPP in **Figure 9**. Simulation QM (not shown) responds as an enhanced QS: starting from already dry conditions, it develops a seasonally increasing drying in the soil, which is compatible with too liberal a use of soil moisture, e.g., for Eastern Europe in spring and summer.

Comparison of Ecosystem Water Use Efficiency

Figure 12 shows a comparison of ecosystem water use efficiency (eWUE, calculated here from NPP and evapotranspiration at grid-box level) for the year 2003, one of the key years identified in Peters et al. (2018), as a seasonal evolution. It is clear that, as early as April, a large area of Europe experienced high eWUE, as the atmosphere was clear and net radiation abundant, but springtime soil moisture was already starting to become depressed, as was seen in **Figure 11**. As the season evolved, and assimilation (A) dropped due to increased plant water stress, particularly for the southern part of the domain, differences start to become obvious for the treatments involving a stomatal conductance route: QS and C6 show a clear advantage over the entire 45–60 latitude band, from May to August. This is quite easy to explain for simulation QS, which

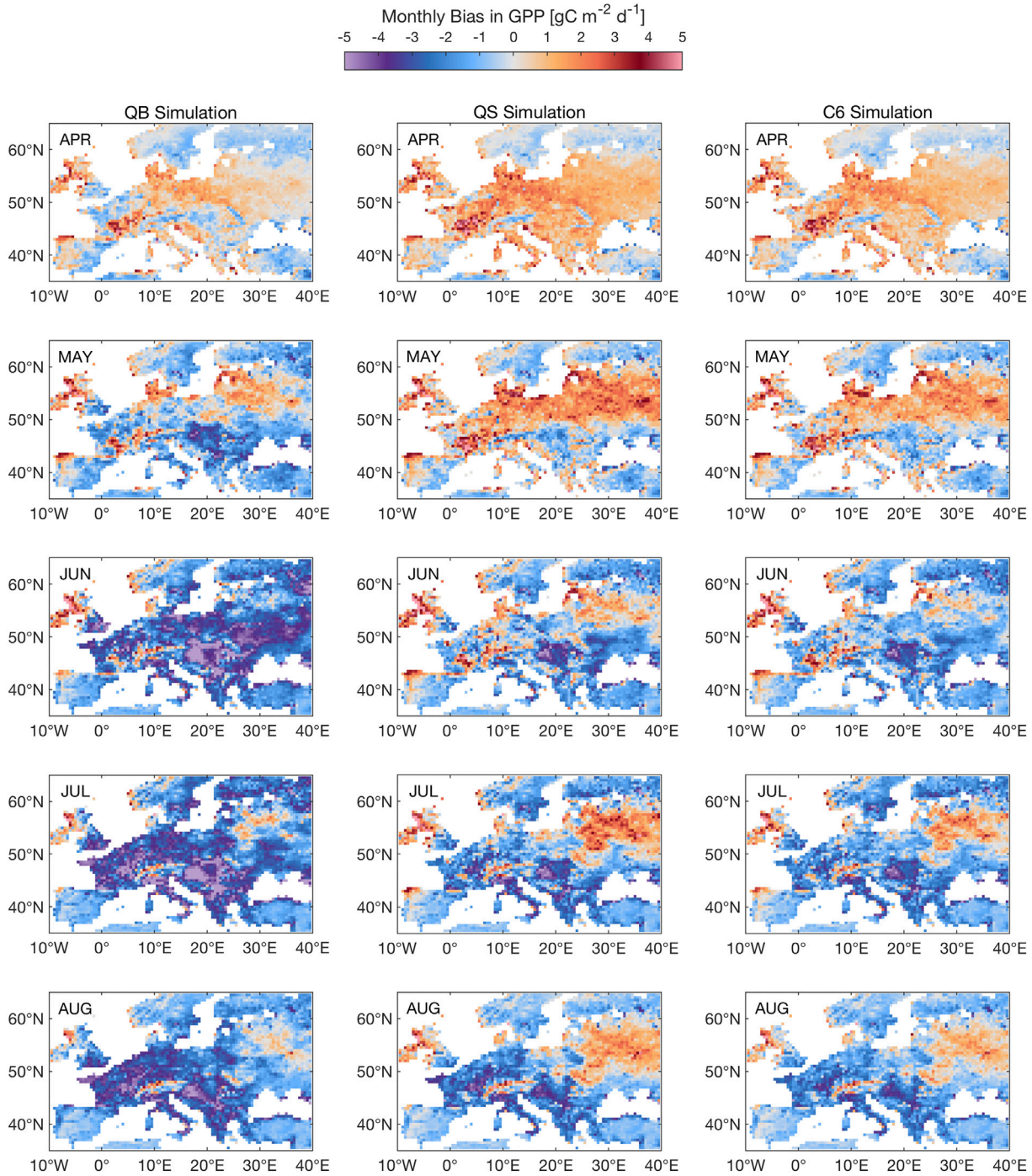

FIGURE 9 | Seasonal evolution of GPP response to the 2003 heat wave for simulation QB, QS, C6, as compared to FLUXCOM. The 2003 season starts at the top row, with the April 2003 monthly mean response, and ends in August 2003, with the monthly mean response. Units: gC m^{-2} d^{-1}.

showed a large 2003 soil moisture surplus when compared to the other simulations, but more subtle for simulation C6, which shows virtually no change in soil moisture when compared to CTL, and even to QB. The C6 response must then be explained by changes in carbon assimilation, which must have become more efficient. It remains to be seen whether this advantage represents a realistic response, by further verification against observations.

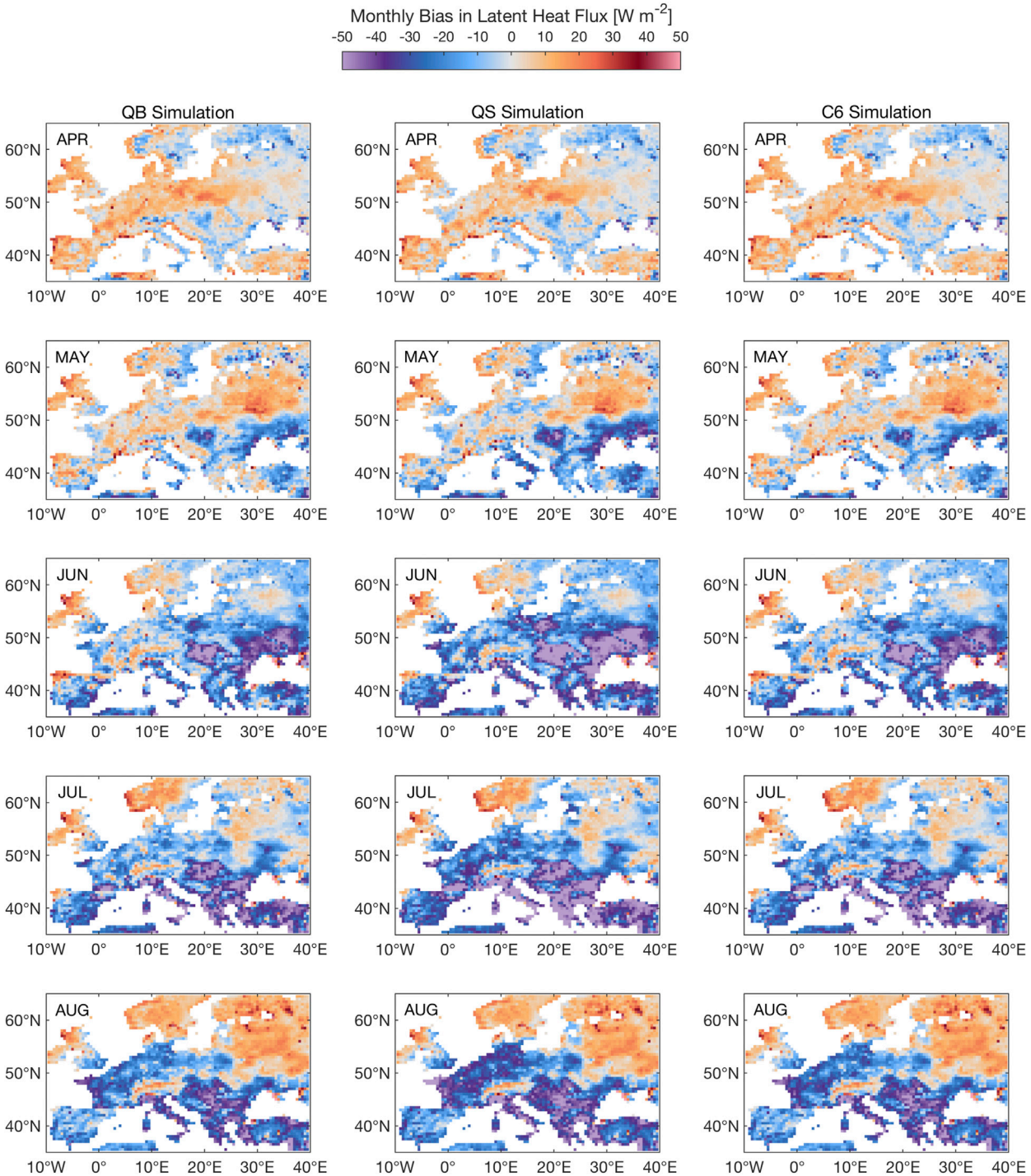

FIGURE 10 | Seasonal evolution of Latent Heat Flux (LE) response to the 2003 heat wave for simulations QB, QS, C6 (as compared to FLUXCOM). The 2003 season starts at the top row, with the April 2003 monthly mean response, and ends in August 2003, with the monthly mean response. Units: W m^{-2}.

The Diurnal and Seasonal Cycles of Stomatal Conductance

Figure 13 shows the diurnal and seasonal evolutions of stomatal conductance for water vapor (g_s) for a grid point in France nearest the location of maximum heating in summer 2003, and for the broadleaf land tile (the C3 grass response is very similar, albeit less sharp). Time runs from 2002, near the bottom, to 2006 near the top of each panel: 2002 was a relatively cold and wet summer in this region, while 2003 experienced one of the worst summer heat waves in recent times for this portion of Europe. By

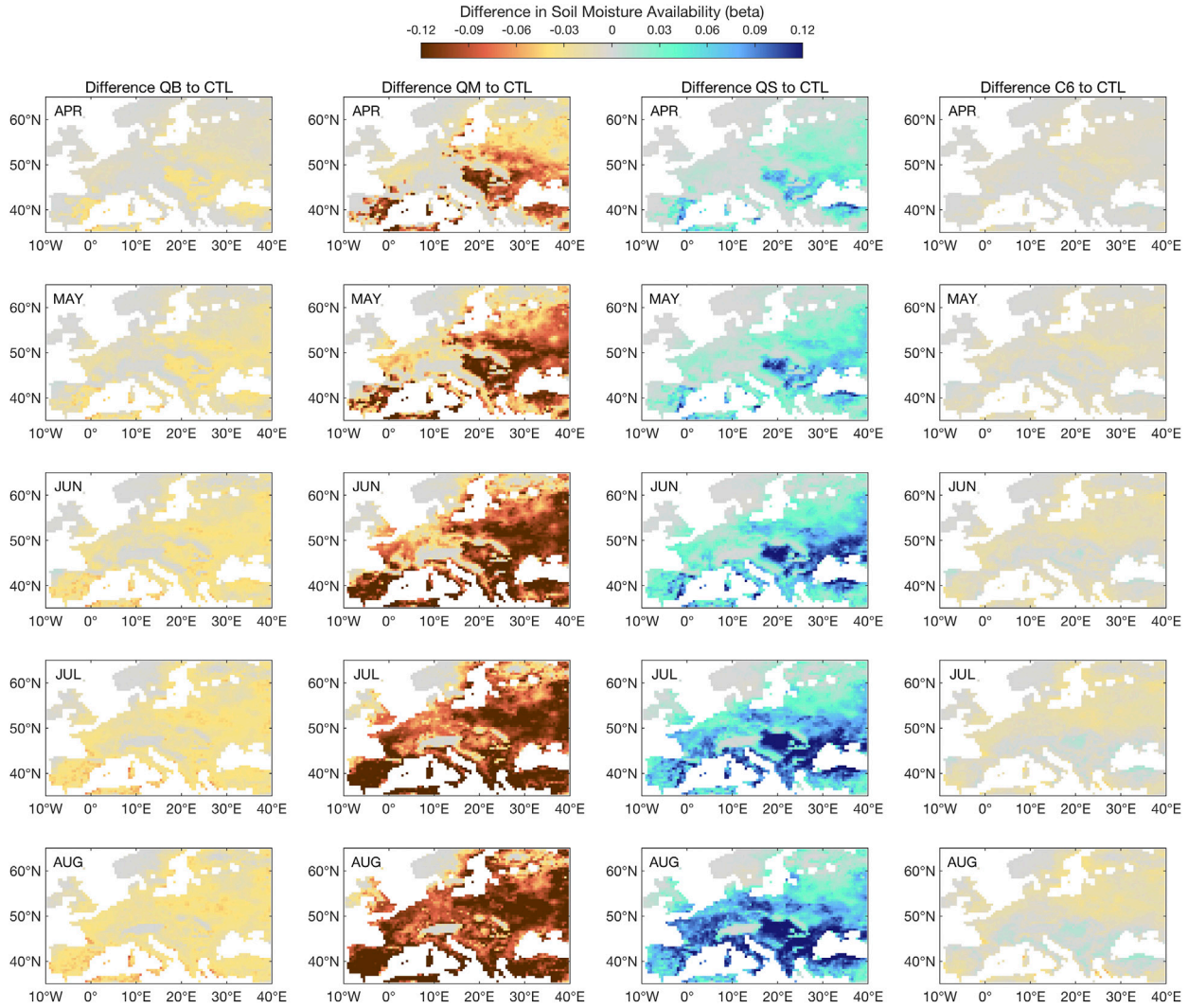

FIGURE 11 | Seasonal evolution of available soil moisture response to the 2003 heat wave in all simulations, as compared to CTL. The 2003 season starts at the top row, with the April 2003 monthly mean response, and ends in August 2003, with the monthly mean response. β is unitless.

comparing the different responses, from left to right, pathway QB sees a strong reduction in stomatal conductance in 2003, as compared to 2002 and later years, in which a vegetation recovery occurred. An even stronger response can be seen in the second column, corresponding to pathway QS, which is easy to understand from the point of view of the β (**Eq. 4**). The mesophyll pathway (QM) shows the least reduction of stomatal conduction in 2003, while C6 exhibits an interim response in comparison to QB and QM.

The Diurnal and Seasonal Cycles of C_i (χ)

Figure 14 shows the diurnal and seasonal evolution of C_i for the same grid point shown in **Figure 12**, which is fully indicative of χ evolution, since reference level CO_2 is prescribed in these simulations, due to the atmosphere being forced. The difference between the four different simulations is striking, particularly for years in which plants experienced strong environmental stress, such as 2003. Simulation QS exhibits the strongest response: by closing the stomata during periods of increased drying, such as early 2003, the C_i level drops dramatically, as had been anticipated in **Figure 2**. However, at the peak of the 2003 summer heat wave, during the late stage of the diurnal cycle, when the soil moisture stress (and the mounting temperature stress, which compounds the effect) starts to reach its peak, C_i returns towards the C_a value (in the early morning and late evening), because photosynthesis stops, also as seen previously in **Figure 2**, due to a compound stress effect. Simulation C6 shows a response that is qualitatively similar, albeit with smaller magnitude, while simulations QB and QM hardly drop the C_i level at all, also consistent with what had been seen in **Figure 2**.

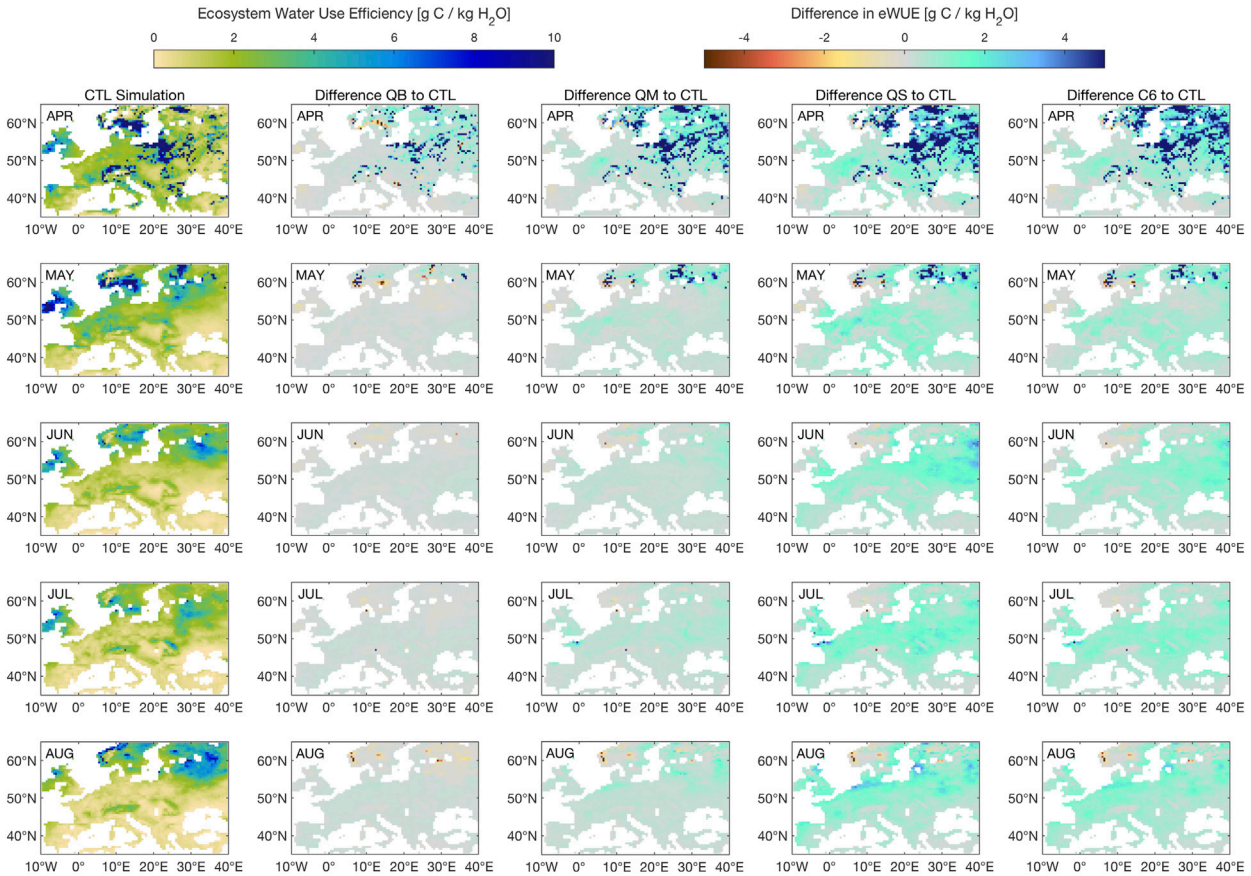

FIGURE 12 | Seasonal evolution of ecosystem Water Use Efficiency (eWUE) for simulation CTL, followed by the difference between each simulation (QB, QS, C6), and CTL. Units are g C per kg of H_20.

Comparison With Intrinsic Water Use Efficiency From FLUXNET Observations

It is expected that in years of drought vegetation stress will also be revealed by measurements of isotopic discrminination, which was the main topic of Peters et al. (2018). The mechanisms involved in the process of photosynthesis favor the lighter $^{12}CO_2$ molecule over the heavier $^{13}CO_2$ molecule, at several stages in the mechanistic chain. This leads to 'discrimination': stressed vegetation will present lower $\delta^{13}C = {}^{13}C/{}^{12}C$ values, relative to the atmosphere, and the difference is denoted by the symbol $\Delta = \delta^{13}C_a - \delta^{13}C_v$ (units of ‰). In JULES, Δ can be estimated approximately, by using in **Eq. 6**, *Methods*. **Supplementary Figure S1** shows the domain average behavior of the four C3 vegetation types in the JULES experiments, as annual anomalies for the year 2003. Because of drought stress, it is expected that NPP will be reduced compared to other years, and that Δ will be smaller, which is: see Figure S1 of Peters et al. for the curve of C_i/C_a vs Δ, what is shown by observations and by the model intercomparison in Peters et al. (2018). **Supplementary Figure S1** reveals that grasses suffer the most during the severe drought year of 2003, with NPP reductions of over 100 Tg C, while needleleaf trees are quite resilient (also because they are mostly located outside the area of drought, but a similar calculation with a drought mask shows the same qualitative behavior). Simulation C6 shows the least drop in NPP and the most realistic response in terms of the combined NPP/Δ metric, as compared to the data in Peters et al. (2018), with the anomaly in Δ reaching values of -0.15 for grasses, while simulation QB tends to have a Δ closer to 0 or above. It is next possible to plot the combined gridbox Δ data on a map and to compare with observations.

Figure 15 shows a superposition of iWUE in observations (Peters et al., 2018), and as produced by JULES, computed by using **Eq. 7**, and using 3-hourly C_i at PFT level. The four panels show the response (marked by dots and color-coded for change in iWUE, as originally presented in Peters et al., 2018) over the region mostly affected by the 2003 heat wave, namely Western Europe, where iWUE reached a maximum, indicated by the green color. The dots show data from point observations; the insets at the top right of each panel show the PDF of values in the domain. It is clear from the comparison of the four panels that the biochemical pathway for β fails to simulate the high level of iWUE reached by plants in Western Europe during the 2003 heat wave. The β pathways that retain some level of control via stomatal conductance are more realistic, with the C6

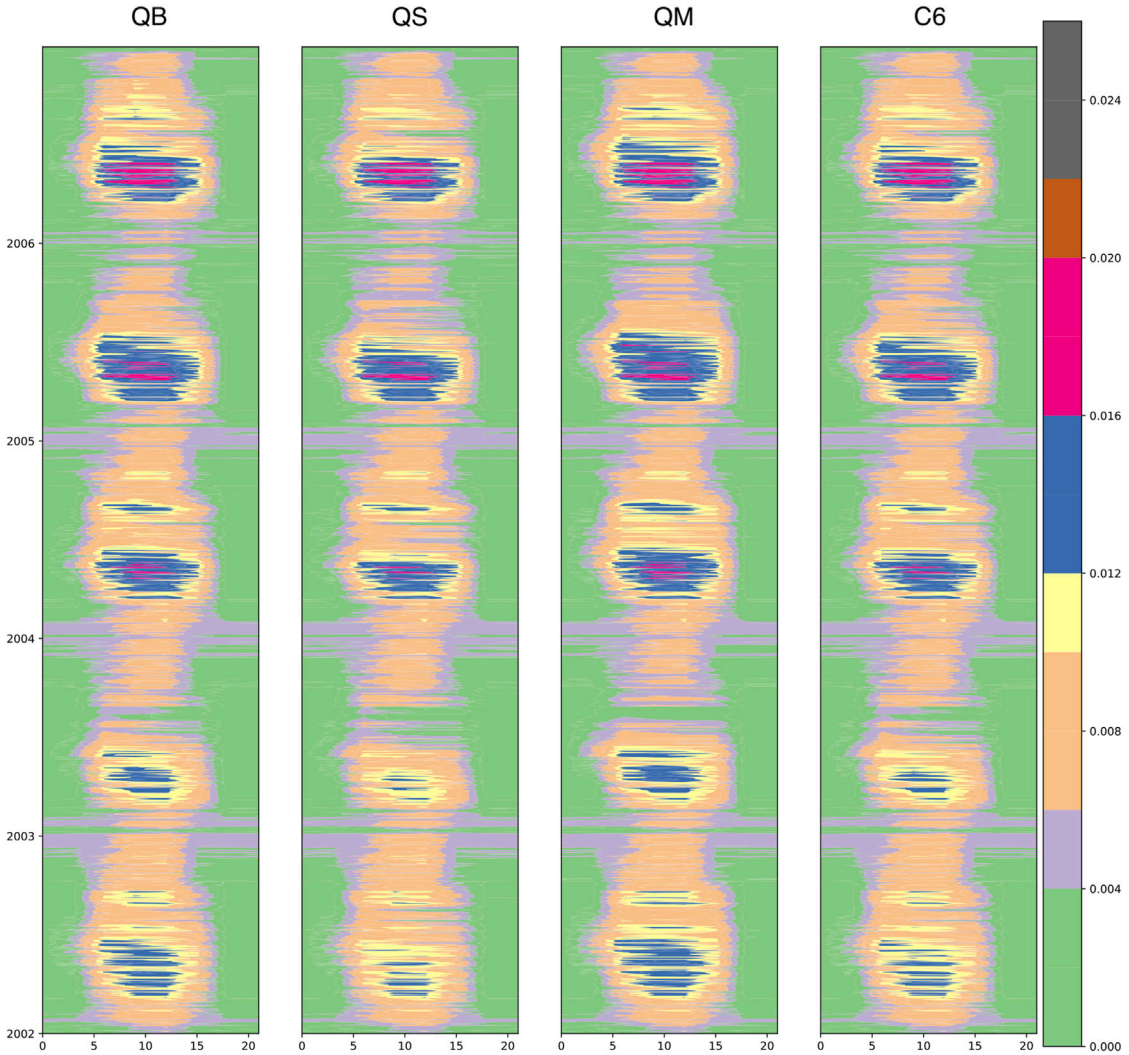

FIGURE 13 | The diurnal and seasonal evolution of stomatal conductance (g_s, m s^{-1}) as filled contours for the JULES Plant Functional Type 1 (Broadleaf Trees) at a grid point in France. The diurnal cycle (GMT hour) is shown on the *x* axis, while the seasonal cycle (indicated by years from 2002 to 2006, top) is shown on the *y* axis. The four experiments are QB, QS, QM, and C6 in each column.

(combined) pathway achieving the best match with observations, as had shown by other case studies in Southern Spain (see E11).

The original multi-model presentation of this figure (see Supplementary Material in Peters et al., 2018), indicated that most LSMs struggle to simulate the shift to higher iWUE (greener colors), which is summarized for the observation sites in the PDFs in each inset. The original JULES-CTL had in fact failed to capture both the magnitude and spatial extent of the impact, similar to the QB simulation developed for this study, which clearly missed the high level of iWUE reached by plants in Western Europe during the 2003 heat wave, so that it was replaced with configuration C6.

iWUE and eWUE originate at different scales in the model, the first stomatal, via the C_i route, and the second involving area averaging of carbon and water fluxes over each grid box, weighted by PFT abundance, and are thus compared against different types of observations. The consistency of the improvement, from iWUE to eWUE, over a coarser scale and over a larger domain, for well-observed events like 2003, gives us further confidence that our proposed pathways strongly improve the JULES drought response, not just for reductions in GPP and LE (achieved in all schemes) but especially for their relative ratio (captured best by the C6 configuration).

DISCUSSION

The E11 model was implemented in a state-of-the-art LSM, JULES, now with complete freedom in enabling soil moisture stress to limit photosynthesis (QB), stomatal conductance (QS) or mesophyll conductance (QM), independent of any a-priori

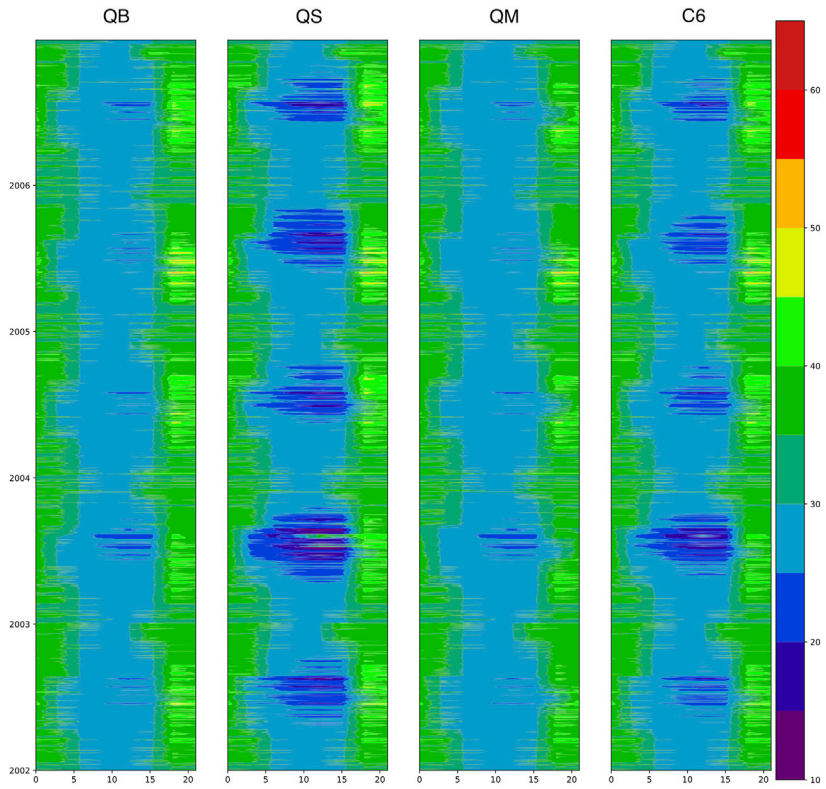

FIGURE 14 | The diurnal and seasonal evolution of internal CO_2 pressure (C_i, Pa) as filled contours for the JULES Plant Functional Type 1 (Broadleaf Trees) at a grid point in France. The diurnal cycle (GMT hour) is shown on the *x* axis, while the seasonal cycle (indicated by years from 2002 to 2006, top) is shown on the *y* axis. The four experiments are QB, QS, QM, and C6 in each column.

assumptions on what are the controlling mechanisms and pathways. A combined treatment (C6) was also tested, taken from the E11 recommendations. A conscious decision was made, at this stage, to choose a framework in which GCM biases in surface energy balance would not cloud the investigation, thus observed meteorology was used as a forcing. Additionally, the parsimonious requirements for computational resources enabled a broad set of experiments, including a lengthy LSM spin-up (cycles up to 300 years) for each, could be made feasible, unlike in a full GCM set-up. It has also to be remembered that, at this stage, the solution algorithm has yet to be made efficient, and these simulations, based on polynomial solutions, are slow, unsuitable for a GCM environment.

The primary purpose of this LSM development was indeed to answer the question of whether or not the a-priori decision of implementing the β limitation on just one of the model components, e.g., photosynthesis, as in models based on the Collatz et al. (1991) formulation, has consequences for our ability to credibly predict the future of land surface dynamics. There is strong demand for predicting the fate of feedbacks between the energy and water cycles (but including carbon over longer periods), as triggered by soil moisture deficits, but such an investigation must be carried out incrementally, with many of the feedbacks purposefully disabled, in order to enable clearer understanding.

The overall model sensitivity seems to be revealed more systematically on the GPP side than on the energy fluxes, as adjustments occur, as revealed by EF, also in response to long-term soil moisture memory. This flux adjustment can be seen as a reassuring result in this particularly constrained experimental setup. Because of non-linearities in the system, models in which β is applied to stomatal conductance tend to limit transpiration, thus to conserve soil moisture, while only partially affecting GPP, except perhaps in parts of Southern Europe at the end of summer. Models in which β is applied to mesophyll conductance tend to overuse soil moisture, creating a deficit, particularly evident in semi-arid regions, and causing stress (from drought and heating) at the end of summer, but this does not seem to have any effect on GPP, implying that water use efficiency is increased in Southern Europe.

Analysis focusing on the 2003 summer heat wave revealed that the environmental stress, as an earlier and more intensive use of soil moisture by evaporation across Europe, causes an even stronger sensitivity response in the four models that have been analyzed. While a negative bias in GPP is present in all models, the 2003 heat wave is most credibly simulated by applying the combined pathway (C6) for the months June, July and August, despite an earlier overestimation of GPP. The heat wave can, however, develop more severely (making the dry bias even worse) when using models with β applied

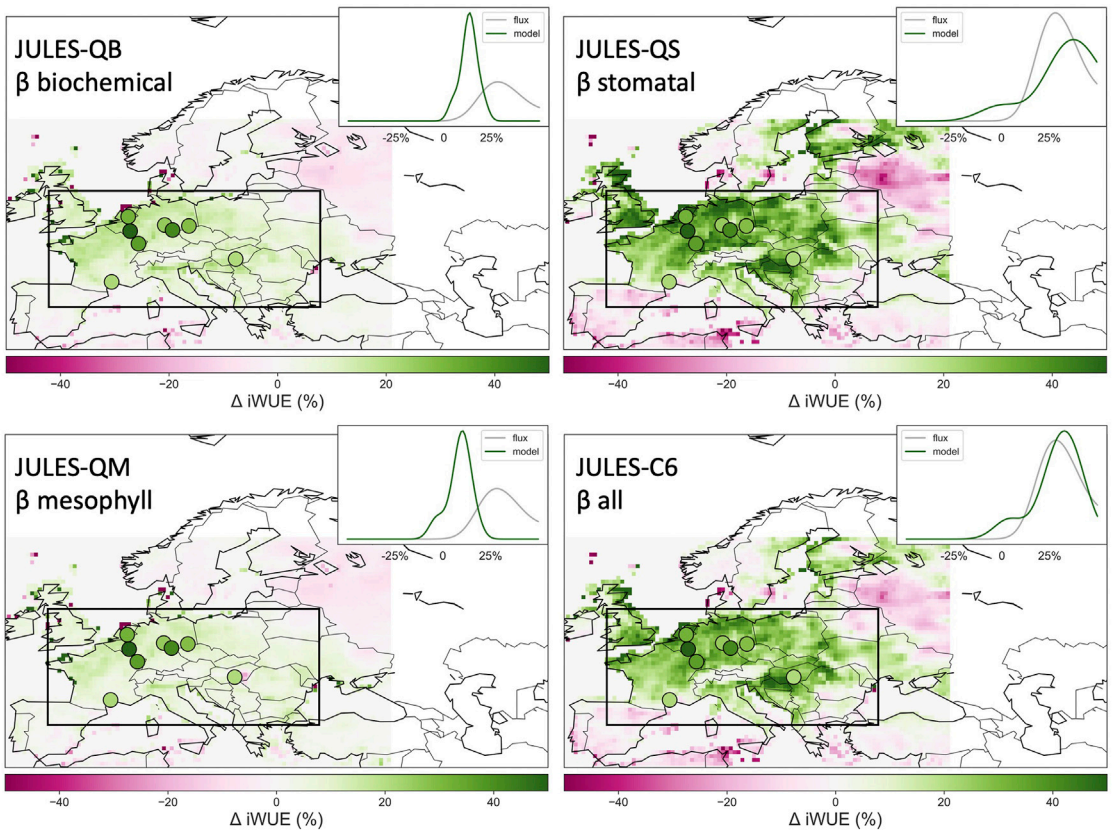

FIGURE 15 | Water Use Efficiency anomaly for 2003 (Δ iWUE, %), as revealed by the Peters et al. (2018) dataset and as simulated by JULES using the four different *β* pathways.

directly to stomatal control, particularly in Southern Europe, or be classified as less severe when using any models that involve mesophyll conductance (e.g., QM, or even the more moderate C6). It is unclear whether the more intensive water use incurred by models including the mesophyll pathway would be sustainable if the anomalously dry and warm conditions were to last for more than 1 year, unlike what happened in post-2003: for Europe winter precipitation is normally sufficient to recharge soil moisture on an interannual basis, but this is not true for other regions, e.g. for the Southern United States, which has been experiencing multi-year drought conditions in recent years.

For χ, the diurnal and seasonal behavior uncovered in the latter part of the study are fully consistent with the expectations raised by the idealized study in the introduction: during the heat wave, enhanced stress conditions (e.g., at noon and/or at the peak of summer) result in stomatal closure, which then results in a strong reduction of χ, but does not necessarily need imply a direct reduction of GPP, as caused instead by making the decisions, conscious or not, of imposing β on carbon assimilation, as is done in many second-generation LSMs. Comparisons provided in E11, and many references therein, indicate that low levels of χ, made possible in JULES with the new generalized analytical scheme, are credible, and indicative of a correct chain of mechanisms.

A strong confirmation of this interpretation is the fact that results of all experiments were now used to compute iWUE from C_i, and showed that the C6 formulation performs comparatively better against the data collected and analysed in Peters et al. (2018) study, revealing a very realistic response of the model to the 2003 perturbation, which seems governed by mechanisms at the stomatal level, and primarily by the fast evolution of C_i. The comparison of eWUE (performed on grid-scale variables) and iWUE (performed at stomatal and PFT level C_i every 3 h) show complete consistency and indicates that applying the β stress to photosynthesis alone is unable to reproduce a credible vegetation response to the large 2003 event, as well as, from the new analysis in this study, to the other European droughts in the simulated period.

It has also to be remembered that C_i can also be used to compute the isotopic discrimination metric, Δ, and that in the Peters et al. (2018) study JULES (in the C6 configuration) performed best when assessed against independent isotopic measurements, and against other models, some of which had been specifically developed to simulate isotopic discrimination. This further confirmation (and more analysis, see Supplementary Material), via the C_i chain of mechanisms, indicates that C_i dynamics is more credibly represented by allowing soil moisture stress to affect all plant function at once, which has

important implications for applications to studies of climate variability and change including the carbon cycle.

There are, however, shortcomings in the adopted methodology: it is impossible, with the current set of experiments, driven by observed meteorology, to estimate the full impact of the surface temperature feedback, because the experimental setup only allows feedback to the leaf-level temperature, but this is then nudged towards the value of the atmospheric near-surface temperature, for each JULES model time step in the 3-hourly meteorological forcing data intervals. If anything, because of the use of observed meteorology as drivers, the present results are indicative of a muted version of possible land-atmosphere feedbacks that can be unleashed by choosing one model configuration over another.

The impact of feedbacks would very likely be significantly larger in a free-running GCM experiment. This may result in more dramatic conclusions with respect to suitability for the CMIP-type climate predictions, particularly if any form of dynamic vegetation (e.g., dynamic phenology or phenology plus competition) is taken into account, as the present results indicate that soil moisture response is over large scales and long time periods, thus with the potential for altering important components of the terrestrial carbon cycle.

However, while the experiments in this study have demonstrated that the generalized β scheme is fully functional (and numerically stable), the solution scheme is more expensive (at least a factor 3x) than the original JULES scheme, because of the use of complex polynomials (see Supplementary Material), which are onerous and hard to optimize, even with modern compilers.

A Practical Proposal for Future Solution Schemes for the E11 Model

As discussed above, the new implementation of the E11 model, now inside a state-of-the-art land surface scheme, JULES, was successful, and the prognostics that are produced seem sound in all respects. The scheme is, however, more expensive than the original (iterative) scheme in JULES; this is currently untenable for use in GCMs, but this study suggests that the same set of experiments should now be run in a full GCM setting. In order to find viable configurations, **Supplementary Figure S2** in Supplementary Materials suggests possible future avenues for a more computationally parsimonious implementation. Starting from the top, the standard JULES scheme is summarized, then the E11 scheme implemented in this paper. Two further solution schemes are proposed. The first one is inspired by a classic forward-backward in time (FTBT) scheme, used in a variety of ocean and atmospheric models (e.g. in WRF), either A or g_s are diagnosed at the start of each time step, and then a quadratic equation for C_c is solved at each time step (depending on g_s or A on alternate time steps), which is cheaper than solving a cubic equation. A second additional scheme is proposed, in which g_s is initially estimated as a simple prognostic (as in Sellers et al., 1996, but also reminiscent of the modified Matsuno, 1966, scheme, in which an initial Euler step precedes an imitation of an implicit time scheme), leading again to a quadratic equation for the other two variables. This implementation was successful in SiB2 and also reduced fast time oscillations, which can potentially be incurred by FTBT-type schemes. This same approach could in the future be applied to the prediction of χ, or to C_c.

Once a suitable numerical implementation is found, with computational costs comparable to the standard JULES scheme, and once a C4 scheme for the β pathway is developed, it will be possible to run the same type of experiment in the HadGEM3-GC31 GCM, albeit only for the most promising configuration, C6, given the large computational costs involved.

SUMMARY AND CONCLUSION

We have implemented the generalized, analytical and simultaneous soil water stress scheme of Egea et al. (2011) into a state-of-the-art land surface model, JULES, which can be used at multiple scales, including global offline and coupled to the HadGEM3 GCM. In this study, we have chosen to focus on the European region, and to drive JULES with observed meteorology, in order to retain a degree of control on feedbacks and to enable comparison with the standard (CTL) JULES configuration. The implementation required the development of a new solution set for the three simultaneous equations that are used to prognose A, g_s, and C_c. A further development in Egea et al. (2011) that was implemented in JULES is the inclusion of mesophyll conductance. The new prognostic scheme was shown to be successful and to enable complete freedom in imposing soil water stress, β, via any pathways (stomatal, biochemical, mesophyll) or any combinations thereof, including non-linear relationships between soil moisture values and β.

Results show that the treatment of soil moisture stress matters to the simulation of land surface climate in Europe, particularly for summer, but even extending into Spring and Autumn. All land surface prognostics are affected by the choice of β pathway, but particularly those controlling water and carbon fluxes between the land and the atmosphere, as well as soil moisture dynamics, which shows a cumulative effect, with strong depletion if a mesophyll conductance pathway is chosen, and strong surplus (particularly in the Southern part of the domain) if a stomatal pathway is chosen. Seasonal and climatological feedbacks between soil moisture levels and land surface fluxes are then triggered.

Responses to the drought involved in the exceptional 2003 summer heat wave, also expanded to other droughts in the last 30 years, demonstrate how important vegetation function feedbacks, from intra-seasonal to interannual, can be initiated even in a modelling framework in which the atmospheric signal is imposed. Under such conditions, it has been shown that models including a stomatal pathway can reach very low levels of stomatal conductance, accompanied by very low, and realistic, χ levels, which result in more realistic simulation of intrinsic and ecosystem Water Use Efficiency, as well as, via a specific metric of isotopic fractionation (Δ), large scale anomalies in vegetation activity. This skill in representing the chain of mechanisms involved in drought response is not normally seen in LSMs, suggesting that the realistic prediction of the feedbacks involved in changes in the carbon cycle requires re-visiting some of the most fundamental assumptions in LSMs used for climate prediction.

DATA AVAILABILITY STATEMENT

The raw data supporting the conclusions of this article will be made available by the authors, without undue reservation.

AUTHOR CONTRIBUTIONS

PV, GE and AV designed the experiments. GE and PV implemented the E11 model into JULES, which required the development of new numerical solution methods (see Supplementary Materials), mostly accomplished by GE. PV and BB-S ran all experiments with JULES 2.2; PV then reported the E11 model to the more recent JULES 4.4 and ran initial quality assurance and stability experiments, but PM finally completed the full set of experiments presented in this article. MT and OM performed the analysis of climatological biases and variability; MT produced the analysis of drought years and the synthesis of annual GPP responses, as well as revised energy flux figures. PV conducted the idealised WUE and χ analyses at the start of the article and wrote the diagnostic code for C_i, VPD and T* at stomatal and PFT levels. WP helped with the water-use efficiency analysis and provided comments on the text.

FUNDING

This research has been supported by the Horizon 2020 programme: PRIMAVERA (grant no. 641727), the National Environmental Research Council (NERC), United Kingdom Earth System Modelling (grant no. NE/N017951/1) and by NERC grant IMPETUS (NE/L010488/1). WP acknowledges funding from the H2020 ERC project ASICA (grant no. 649087).

ACKNOWLEDGMENTS

PLV and PM acknowledge the NERC-Met Office HRCM research programme and the EU-Horizon2020 PRIMAVERA programme. MT and PM acknowledge the CSSP Porcelain grant. GE acknowledges the award of a postdoctoral fellowship from Fundación Ramón Areces (Madrid, Spain) and support from the University of Seville. We kindly acknowledge the contributions from Mr E. van Schaik to the research presented. This work used eddy covariance data acquired by the FLUXNET community. We acknowledge the financial support to the eddy covariance data harmonization provided by CarboEuropeIP, FAO-GTOS-TCO, iLEAPS, Max Planck Institute for Biogeochemistry, National Science Foundation, University of Tuscia, Université Laval and Environment Canada, and US Department of Energy and the database development and technical support from Berkeley Water Center, Lawrence Berkeley National Laboratory, Microsoft Research eScience, Oak Ridge National Laboratory, University of California Berkeley, University of Virginia.

SUPPLEMENTARY MATERIAL

The Supplementary Material for this article can be found online at: https://www.frontiersin.org/articles/10.3389/fenvs.2021.689301/full#supplementary-material

REFERENCES

Anderegg, W. R. L., and Venturas, M. D. (2020). Plant Hydraulics Play a Critical Role in Earth System Fluxes. *New Phytol.* 226, 1535–1538. doi:10.1111/nph.16548

Baldocchi, D. (1994). An Analytical Solution for Coupled Leaf Photosynthesis and Stomatal Conductance Models. *Tree Physiol.* 14, 1069–1079. doi:10.1093/treephys/14.7-8-9.1069

Ball, J. T., Woodrow, I. E., and Berry, J. A. (1987). "A Model Predicting Stomatal Conductance and its Contribution to the Control of Photosynthesis under Different Environmental Conditions," in *Progress in Photosynthesis Research*. Editor J. Biggens (Dordrecht: Martinus Nijhoff), IV, 221–224. doi:10.1007/978-94-017-0519-6_48

Beer, C., Reichstein, M., Tomelleri, E., Ciais, P., Jung, M., Carvalhais, N., et al. (2010). Terrestrial Gross Carbon Dioxide Uptake: Global Distribution and Covariation with Climate. *Science* 329, 834–838. doi:10.1126/science.1184984

Berg, A., Findell, K., Lintner, B., Giannini, A., Seneviratne, S. I., van den Hurk, B., et al. (2016). Land-atmosphere Feedbacks Amplify Aridity Increase over Land under Global Warming. *Nat. Clim Change* 6, 869–874. doi:10.1038/nclimate3029

Best, M. J., Pryor, M., Clark, D. B., Rooney, G. G., Essery, R. L. H., Ménard, C. B., et al. (2011). The Joint UK Land Environment Simulator (JULES), Model Description - Part 1: Energy and Water Fluxes. *Geosci. Model. Dev. Discuss.* 4, 595–640. doi:10.5194/gmdd-4-595-2011

Clark, D. B., Mercado, L. M., Sitch, S., Jones, C. D., Gedney, N., Best, M. J., et al. (2011). The Joint UK Land Environment Simulator (JULES), Model Description - Part 2: Carbon Fluxes and Vegetation Dynamics. *Geosci. Model. Dev.* 4, 701–722. doi:10.5194/gmd-4-701-2011

Collatz, G. J., Ball, J. T., Grivet, C., and Berry, J. A. (1991). Physiological and Environmental Regulation of Stomatal Conductance, Photosynthesis and Transpiration: a Model that Includes a Laminar Boundary Layer. *Agric. For. Meteorol.* 54, 107–136. doi:10.1016/0168-1923(91)90002-8

Collatz, G., Ribas-Carbo, M., and Berry, J. (1992). Coupled Photosynthesis-Stomatal Conductance Model for Leaves of C4 Plants. *Funct. Plant Biol.* 19, 519–538. doi:10.1071/pp9920519

Cox, P. M., Huntingford, C., and Harding, R. J. (1998). A Canopy Conductance and Photosynthesis Model for Use in a GCM Land Surface Scheme. *J. Hydrol.* 212-213, 79–94. doi:10.1016/S0022-1694(98)00203-0

De Kauwe, M. G., Medlyn, B. E., Walker, A. P., Zaehle, S., Asao, S., Guenet, B., et al. (2017). Challenging Terrestrial Biosphere Models with Data from the Long-Term Multifactor Prairie Heating and CO 2 Enrichment experiment. *Glob. Change Biol.* 23, 3623–3645. doi:10.1111/gcb.13643

Dewar, R., Mauranen, A., Mäkelä, A., Hölttä, T., Medlyn, B., and Vesala, T. (2018). New Insights into the Covariation of Stomatal, Mesophyll and Hydraulic Conductances from Optimization Models Incorporating Nonstomatal Limitations to Photosynthesis. *New Phytol.* 217, 571–585. doi:10.1111/nph.14848

Egea, G., Verhoef, A., and Vidale, P. L. (2011). Towards an Improved and More Flexible Representation of Water Stress in Coupled Photosynthesis-Stomatal Conductance Models. *Agric. For. Meteorol.* 151 (10), 1370–1384. doi:10.1016/j.agrformet.2011.05.019

Eller, C. B., Rowland, L., Mencuccini, M., Rosas, T., Williams, K., Harper, A., et al. (2020). Stomatal Optimization Based on Xylem Hydraulics (SOX) Improves

Land Surface Model Simulation of Vegetation Responses to Climate. *New Phytol.* 226, 1622–1637. doi:10.1111/nph.16419

Essery, R., Pomeroy, J., Parviainen, J., and Storck, P. (2003). Sublimation of Snow from Coniferous Forests in a Climate Model. *J. Clim.* 16 (11), 1855–1864. doi:10.1175/1520-0442(2003)016<1855:sosfcf>2.0.co;2

Farquhar, G. D., von Caemmerer, S., and Berry, J. A. (1980). A Biochemical Model of Photosynthetic CO2 Assimilation in Leaves of C3 Species. *Planta* 149, 78–90. doi:10.1007/bf00386231

Farquhar, G., and Wong, S. (1984). An Empirical Model of Stomatal Conductance. *Funct. Plant Biol.* 11, 191–209. doi:10.1071/pp9840191

Gerten, D., Schaphoff, S., Haberlandt, U., Lucht, W., and Sitch, S. (2004). Terrestrial Vegetation and Water Balance-Hydrological Evaluation of a Dynamic Global Vegetation Model. *J. Hydrol.* 286, 249–270. doi:10.1016/j.jhydrol.2003.09.029

Guimberteau, M., Zhu, D., Maignan, F., Huang, Y., Yue, C., Dantec-Nédélec, S., et al. (2018). ORCHIDEE-MICT (v8.4.1), a Land Surface Model for the High Latitudes: Model Description and Validation. *Geosci. Model. Dev.* 11, 121–163. doi:10.5194/gmd-11-121-2018

Harper, A. B., Williams, K. E., McGuire, P. C., Duran Rojas, M. C., Hemming, D., Verhoef, A., et al. (2021). Improvement of Modelling Plant Responses to Low Soil Moisture in JULESvn4.9 and Evaluation against Flux tower Measurements. *Geosci. Model. Dev.* 14 (6), 3269–3294. doi:10.5194/gmd-2020-273

Haynes, K. D., Baker, I. T., Denning, A. S., Stöckli, R., Schaefer, K., Lokupitiya, E. Y., et al. (2019). Representing Grasslands Using Dynamic Prognostic Phenology Based on Biological Growth Stages: 1. Implementation in the Simple Biosphere Model (SiB4). *J. Adv. Model. Earth Syst.* 11 (12), 4423–4439. doi:10.1029/2018ms001540

Jacobs, C. M. J., Van den Hurk, B. M. M., and de Bruin, H. A. R. (1996). Stomatal Behaviour and Photosynthetic Rate of Unstressed Grapevines in Semi-arid Conditions. *Agric. For. Meteorol.* 80, 111–134. doi:10.1016/0168-1923(95)02295-3

Jung, M., Koirala, S., Weber, U., Ichii, K., Gans, F., Camps-Valls, G., et al. (2019). The FLUXCOM Ensemble of Global Land-Atmosphere Energy Fluxes. *Sci. Data* 6, 74. doi:10.1038/s41597-019-0076-8

Liang, X., Lettenmaier, D. P., Wood, E. F., and Burges, S. J. (1994). A Simple Hydrologically Based Model of Land Surface Water and Energy Fluxes for General Circulation Models. *J. Geophys. Res.* 99 (D7), 14415–14428. doi:10.1029/94JD00483

Mäkelä, J., Knauer, J., Aurela, M., Black, A., Heimann, M., Kobayashi, H., et al. (2019). Parameter Calibration and Stomatal Conductance Formulation Comparison for Boreal Forests with Adaptive Population Importance Sampler in the Land Surface Model JSBACH. *Geosci. Model. Dev.* 12 (9), 4075–4098. doi:10.5194/gmd-12-4075-2019

Matsuno, T. (1966). Numerical Integrations of the Primitive Equations by a Simulated Backward Difference Method. *J. Meteorol. Soc. Jpn.* 44, 76–84. doi:10.2151/jmsj1965.44.1_76

Medlyn, B. E., De Kauwe, M. G., Zaehle, S., Walker, A. P., Duursma, R. A., Luus, K., et al. (2016). Using Models to Guide Field Experiments: A Priori Predictions for the CO 2 Response of a Nutrient and Water-Limited Native Eucalypt woodland. *Glob. Change Biol.* 22, 2834–2851. doi:10.1111/gcb.13268

Nemani, R. R., Keeling, C. D., Hashimoto, H., Jolly, W. M., Piper, S. C., Tucker, C. J., et al. (2003). Climate-Driven Increases in Global Terrestrial Net Primary Production from 1982 to 1999. *Science* 300, 1560–1563. doi:10.1126/science.1082750

Niu, G. Y., Fang, Y. H., Chang, L. L., Jin, J., Yuan, H., and Zeng, X. (2020). Enhancing the Noah-MP Ecosystem Response to Droughts with an Explicit Representation of Plant Water Storage Supplied by Dynamic Root Water Uptake. *J. Adv. Model. Earth Syst.* 12 (11), e2020MS002062. doi:10.1029/2020ms002062

Oleson, K., Lawrence, D. M., Bonan, G. B., Drewniak, B., Huang, M., Koven, C. D., et al. (2013). Technical Description of Version 4.5 of the Community Land Model (CLM), NCAR Earth System Laboratory – Climate and Global Dynamics Division. Technical Report. Boulder, Colorado, USA. TN-503+STR.

Paschalis, A., Fatichi, S., Zscheischler, J., Ciais, P., Bahn, M., Boysen, L., et al. (2020). Rainfall Manipulation Experiments as Simulated by Terrestrial Biosphere Models: Where Do We Stand? *Glob. Change Biol.* 26, 3336–3355. doi:10.1111/gcb.15024

Peters, W., van der Velde, I. R., van Schaik, E., Miller, J. B., Ciais, P., Duarte, H. F., et al. (2018). Increased Water-Use Efficiency and Reduced CO2 Uptake by Plants during Droughts at a continental Scale. *Nat. Geosci.* 11, 744–748. doi:10.1038/s41561-018-0212-7

Powell, T. L., Galbraith, D. R., Christoffersen, B. O., Harper, A., Imbuzeiro, H. M. A., Rowland, L., et al. (2013). Confronting Model Predictions of Carbon Fluxes with Measurements of Amazon Forests Subjected to Experimental Drought. *New Phytol.* 200, 350–365. doi:10.1111/nph.12390

Prentice, I. C., Dong, N., Gleason, S. M., Maire, V., and Wright, I. J. (2014). Balancing the Costs of Carbon Gain and Water Transport: Testing a New Theoretical Framework for Plant Functional Ecology. *Ecol. Lett.* 17, 82–91. doi:10.1111/ele.12211

Press, W. H., Flannery, B. P., Teukolsky, S. A., and Vetterling, W. T. (1989). *Numerical Recipes: The Art of Scientific Computing*. Cambridge, U.K.: Cambridge University Press, 992.

R Development Core Team (2010). *R: A Language and Environment for Statistical Computing*. Vienna, Austria: R Foundation for Statistical Computing. Available at: http://www.R-project.org (ISBN 3-900051-07-0.

Restrepo-Coupe, N., Levine, N. M., Christoffersen, B. O., Albert, L. P., Wu, J., Costa, M. H., et al. (2017). Do dynamic Global Vegetation Models Capture the Seasonality of Carbon Fluxes in the Amazon basin? A Data-Model Intercomparison. *Glob. Change Biol.* 23, 191–208. doi:10.1111/gcb.13442

Russo, S., Sillmann, J., and Fischer, E. M. (2015). Top Ten European Heatwaves since 1950 and Their Occurrence in the Coming Decades. *Environ. Res. Lett.* 10 (12), 124003. doi:10.1088/1748-9326/10/12/124003

Sabot, M. E. B., De Kauwe, M. G., Pitman, A. J., Medlyn, B. E., Verhoef, A., Ukkola, A. M., et al. (2020). Plant Profit Maximization Improves Predictions of European forest Responses to Drought. *New Phytol.* 226, 1638–1655. doi:10.1111/nph.16376

Schaefer, K., Collatz, G. J., Tans, P., Denning, A. S., Baker, I., Berry, J., et al. (2008). Combined Simple Biosphere/Carnegie-Ames-Stanford Approach Terrestrial Carbon Cycle Model. *J. Geophys. Res.* 113, G03034. doi:10.1029/2007JG000603

Schär, C., Vidale, P. L., Lüthi, D., Frei, C., Häberli, C., Liniger, M. A., et al. (2004). The Role of Increasing Temperature Variability in European Summer Heatwaves. *Nature* 427, 332–336. doi:10.1038/nature02300

Sellers, P. J., Randall, D. A., Collatz, G. J., Berry, J. A., Field, C. B., Dazlich, D. A., et al. (1996). A Revised Land Surface Parameterization (SiB2) for Atmospheric GCMS. Part I: Model Formulation. *J. Clim.* 9, 676–705. doi:10.1175/1520-0442(1996)009<0676:arlspf>2.0.co;2

Seneviratne, S. I., Corti, T., Davin, E. L., Hirschi, M., Jaeger, E. B., Lehner, I., et al. (2010). Investigating Soil Moisture-Climate Interactions in a Changing Climate: A Review. *Earth Sci. Rev.* 99, 125–161. doi:10.1016/j.earscirev.2010.02.004

Sitch, S., Smith, B., Prentice, I. C., Arneth, A., Bondeau, A., Cramer, W., et al. (2003). Evaluation of Ecosystem Dynamics, Plant Geography and Terrestrial Carbon Cycling in the LPJ Dynamic Global Vegetation Model. *Glob. Change Biol.* 9, 161–185. doi:10.1046/j.1365-2486.2003.00569.x

Smith, B., Prentice, I. C., and Sykes, M. T. (2001). Representation of Vegetation Dynamics in the Modelling of Terrestrial Ecosystems: Comparing Two Contrasting Approaches within European Climate Space. *Glob. Ecol Biogeogr.* 10, 621–637. doi:10.1046/j.1466-822x.2001.00256.x

Smith, B., Wårlind, D., Arneth, A., Hickler, T., Leadley, P., Siltberg, J., et al. (2014). Implications of Incorporating N Cycling and N Limitations on Primary Production in an Individual-Based Dynamic Vegetation Model. *Biogeosciences* 11, 2027–2054. doi:10.5194/bg-11-2027-2014

Stocker, B. D., Zscheischler, J., Keenan, T. F., Prentice, I. C., Peñuelas, J., and Seneviratne, S. I. (2018). Quantifying Soil Moisture Impacts on Light Use Efficiency across Biomes. *New Phytol.* 218, 1430–1449. doi:10.1111/nph.15123

Ukkola, A. M., De Kauwe, M. G., Roderick, M. L., Abramowitz, G., and Pitman, A. J. (2020). Robust Future Changes in Meteorological Drought in CMIP6 Projections Despite Uncertainty in Precipitation. *Geophys. Res. Lett.* 47, e2020GL087820. doi:10.1029/2020GL087820

Vargas Zeppetello, L. R., Battisti, D. S., and Baker, M. B. (2019). The Origin of Soil Moisture Evaporation "Regimes". *J. Clim.* 3232 (20), 6939–6960. Retrieved from: https://journals.ametsoc.org/view/journals/clim/32/20/jcli-d-19-0209.1.xml. doi:10.1175/jcli-d-19-0209.1

Verhoef, A., and Egea, G. (2014). Modeling Plant Transpiration under Limited Soil Water: Comparison of Different Plant and Soil Hydraulic Parameterizations and Preliminary Implications for Their Use in Land Surface Models. *Agric. For. Meteorol.* 191, 22–32. doi:10.1016/j.agrformet.2014.02.009

Weedon, G. P., Gomes, S., Viterbo, P., Shuttleworth, W. J., Blyth, E., Österle, H., et al. (2011). Creation of the WATCH Forcing Data and its Use to Assess Global and Regional Reference Crop Evaporation over Land during the Twentieth Century. *J. Hydrometeorol.* 12 (5), 823–848. doi:10.1175/2011jhm1369.1

Zhou, S., Williams, A. P., Berg, A. M., Cook, B. I., Zhang, Y., Hagemann, S., et al. (2019). Land-atmosphere Feedbacks Exacerbate Concurrent Soil Drought and Atmospheric Aridity. *Proc. Natl. Acad. Sci. USA* 116 (38), 18848–18853. doi:10.1073/pnas.1904955116

Conflict of Interest: The authors declare that the research was conducted in the absence of any commercial or financial relationships that could be construed as a potential conflict of interest.

frontiers in Marine Science

ORIGINAL RESEARCH
published: 06 September 2021
doi: 10.3389/fmars.2021.688299

Evaluation of Regional Surface Energy Budget Over Ocean Derived From Satellites

Seiji Kato[1], Fred G. Rose[2], Fu-Lung Chang[2], David Painemal[2] and William L. Smith[1]*

[1] NASA Langley Research Center, Hampton, VA, United States, [2] Science Systems and Applications Inc., Hampton, VA, United States

The energy balance equation of an atmospheric column indicates that two approaches are possible to compute regional net surface energy flux. The first approach is to use the sum of surface energy flux components $F_{net,c}$ and the second approach is to use net top-of-atmosphere (TOA) irradiance and horizontal energy transport by the atmosphere $F_{net,t}$. When regional net energy flux is averaged over the global ocean, $F_{net,c}$ and $F_{net,t}$ are, respectively, 16 and 2 Wm^{-2}, both larger than the ocean heating rate derived from ocean temperature measurements. The difference is larger than the estimated uncertainty of $F_{net,t}$ of 11 Wm^{-2}. Larger regional differences between $F_{net,c}$ and $F_{net,t}$ exist over tropical ocean. The seasonal variability of energy flux components averaged between 45°N and 45°S ocean reveals that the surface provides net energy to the atmosphere from May to July. These two examples demonstrates that the energy balance can be used to assess the quality of energy flux data products.

Keywords: energy budget, climatology, ocean surface, remote sensing, atmosphere-ocean coupling

OPEN ACCESS

Edited by:
Meghan F. Cronin, Pacific Marine Environmental Laboratory, National Oceanic and Atmospheric Administration (NOAA), United States

Reviewed by:
Samson Hagos, Pacific Northwest National Laboratory (DOE), United States
Chunlei Liu, Guangdong Ocean University, China

****Correspondence:***
Seiji Kato
seiji.kato@nasa.gov

Specialty section:
This article was submitted to Ocean Observation, a section of the journal Frontiers in Marine Science

Received: *30 March 2021*
Accepted: *16 August 2021*
Published: *06 September 2021*

Citation:
Kato S, Rose FG, Chang F-L, Painemal D and Smith WL (2021) Evaluation of Regional Surface Energy Budget Over Ocean Derived From Satellites. Front. Mar. Sci. 8:688299. doi: 10.3389/fmars.2021.688299

INTRODUCTION

Estimating the surface energy budget is one of the key components of understanding energy flow within the Earth system. Surface energy fluxes determine the energy input to the ocean and energy transfer through the ocean-atmosphere boundary. In addition, surface fluxes often drive processes occurring near the surface. For example, energy fluxes at the surface affect cloud processes occurring in the boundary layer (e.g., Betts, 1985; Betts and Ridgway, 1988; Albrecht et al., 1990; Bretherton and Wyant, 1997; Wood, 2012). In addition, surface radiative fluxes play a key role in determining sea ice melts (Hudson et al., 2013). Both low-level clouds (Soden et al., 2008; Loeb et al., 2018) and sea ice play a critical role determining climate feedback and Earth's energy budget (Hartmann and Ceppi, 2014).

Components of the surface energy flux are radiative flux (irradiance), turbulent flux, and flux associated with mass transfer. Surface irradiance is composed of shortwave and longwave irradiances. Downward surface shortwave irradiance is the solar irradiance transmitted through the atmosphere. Part of the irradiance that reaches the surface is reflected by the surface, which can be reflected back to the surface by the atmosphere, and the rest is absorbed by the surface. Broadband ocean surface albedo is about 0.05 (e.g., Kato et al., 2002) but the albedo depends on solar zenith angle and surface wind speed (Cox and Munk, 1955) and chlorophyll concentration (Jin et al., 2004). Downward surface longwave irradiance is the emitted irradiance by the atmosphere. Similar to the shortwave irradiance, a part of the downward longwave irradiance is reflected and

the rest is absorbed by the surface. The surface also emits longwave irradiance, with a magnitude depending on the temperature and emissivity, with the latter being a function of wind speed over ocean (Sidran, 1981; Masuda et al., 1988).

Turbulent heat fluxes consist of sensible and latent heat fluxes. These are enthalpy fluxes and depend on near surface and surface properties (e.g., Cronin et al., 2019). In addition to these enthalpy fluxes, the enthalpy is transferred through the atmosphere-ocean boundary when water is transported by precipitation and evaporation (Mayer et al., 2017; Trenberth and Fasullo, 2018; Kato et al., 2021).

From a regional ocean energy budget perspective, surface fluxes are needed to separate the energy input from that by horizontal energy transport by ocean, provided that the regional ocean temperature tendency is known (Trenberth and Solomon, 1994). Despite the importance of surface energy fluxes, there is a large uncertainty associated with surface fluxes derived from satellite observations. The uncertainty in the regional monthly mean net surface irradiance over ocean estimated by Kato et al. (2020) is 13 Wm^{-2}. Similarly, a typical error in a long-term mean net energy flux over ocean is 10 Wm^{-2} (Cronin et al., 2019). In addition, temperatures of raindrops and water vapor are needed to estimate the enthalpy transfer associated with water mass transfer (Mayer et al., 2017; Kato et al., 2021). As a consequence, when satellite derived surface flux data products are integrated to assess the surface energy balance, the residual of annual global surface energy balance is about 10–15 Wm^{-2} (Kato et al., 2011; Stephens et al., 2012; Loeb et al., 2014; L'Ecuyer et al., 2015; Wild et al., 2015). Therefore, annual net surface energy fluxes averaged over global ocean is one order of magnitude larger (Meyssignac et al., 2019) than the mean ocean heating rate of 0.8 Wm^{-2} (Johnson et al., 2016; Loeb et al., 2018; von Schuckmann et al., 2020).

Computed surface fluxes have been evaluated using observations. However, the spatial and temporal coverage of surface observations are limited. Comparisons of similar data products are useful to identify outliers and unphysical assumptions. Even though the regional energy budget bias in satellite-based data products is significant, the bias can be explained by the sum of uncertainties of all components (L'Ecuyer et al., 2015). A less explored approach for evaluating energy budget flux products is to use horizontal energy transport by the atmosphere and to compare the resulting net surface energy flux with the sum of surface energy flux components. In this study, we integrate surface energy data products and demonstrate the use of energy divergence in the atmosphere in evaluating surface energy flux data products. In addition, we examine regional water mass balance to understand whether the regional water mass balance residual can explain the energy balance residual. Furthermore, we analyze the seasonal variability of surface energy fluxes to test whether the variability can be used in the evaluation. If the physical processes are robust, the seasonal variability might be used to evaluate the quality of energy data products.

Section "Regional Water Mass and Atmosphere Energy Budget Equations" introduces regional energy and water mass budget equations that are used in this study. Data products used in this study are described in section "Data Products." Regional net surface energy flux and mass balance, as well as seasonal variability of surface energy fluxes are discussed in section "Results."

REGIONAL WATER MASS AND ATMOSPHERE ENERGY BUDGET EQUATIONS

One form of energy balance equations of an atmospheric column is the balance between energy tendency in the column and fluxes at boundaries, i.e., top-of-atmosphere (TOA), lateral boundaries, and at surface boundary (Trenberth, 1997). The energy flux at the top boundary is the net TOA irradiance R_{TOA}. R_{TOA} is the sum of absorbed shortwave irradiance, which is the insolation minus reflected shortwave irradiance and emitted longwave irradiance multiplied by −1 (because the net is defined downward positive in this study). Fluxes at the surface include net surface irradiance R_{sfc}, sensible heat flux F_{SH} and latent heat flux F_{LH}, and enthalpy flux associated with precipitation $F_{fallout}$ and evaporation F_v. The atmosphere can transport enthalpy, potential energy and kinetic energy through lateral boundaries. The energy budget equation of an atmospheric column is then expressed as (Mayer et al., 2017; Trenberth and Fasullo, 2018; Kato et al., 2021),

$$\begin{aligned}&\frac{1}{g}\frac{\partial}{\partial t}\int_0^{p_{sfc}}\left(c_pT+\Phi_s+k+l\right)\mathrm{dp}\\&+\frac{1}{g}\nabla\cdot\int_0^{p_{sfc}}\mathbf{U}_a\left(c_pT+\Phi+k+l\right)dp\\&=\left(R_{TOA}-R_{sfc}\right)+F_{SH}+F_{LH}+F_v+F_{fallout}-F_h\end{aligned}\quad(1)$$

where $\mathbf{U}_a$ is the dry air horizontal velocity, c_p is the specific heat capacity, T is the temperature, Φ is the geopotential, Φ_s is the surface geopotential, k is the kinetic energy, p is the pressure, p_{sfc} is the surface pressure, t is time, and g is the gravitation acceleration at sea level. All energy terms include contributions from dry air, water vapor and hydrometeors and they are added weighted by their respective mixing ratios r,

$$k=k_a+r_vk_v+r_lk_l+r_ik_i+r_rk_r+r_sk_s\quad(2)$$

$$c_p=c_{p_a}+r_vc_{p_v}+r_lc_l+r_ic_i+r_rc_r+r_sc_s\quad(3)$$

where $c_{p_a}$is the specific heat capacity of dry air at constant pressure, c_{p_v} is the specific heat capacity of water vapor at constant pressure, and c is the specific heat capacity of hydrometeors. Subscripts v, l, i, r, s are, respectively, water vapor, liquid and ice cloud particles, rain, and snow. The latent heat l is the sum of the enthalpy change when water vapor is condensed or hydrometeors are evaporated,

$$l=\sum_{j=v,l,i,r,s}l_jr_j=l_vr_v-l_l\left(r_l+r_r\right)-l_f\left(r_i+r_s\right)\quad(4)$$

l_v is the enthalpy of vaporization, l_f is enthalpy of fusion, r is the mixing ratio. The latent heat is determined by the enthalpy

release when water vapor is condensed or snow and ice crystals are melted. Therefore, l_l in this case is the specific heat capacity multiplied by the temperature difference between cloud particles or raindrops and the reference temperature. The F_h term on the right side of Eq. 1 represents the divergence of moist static and kinetic energy associated with hydrometeors moving at different velocities from the dry air velocity (Kato et al., 2021),

$$F_h = \frac{1}{g}\int_0^{p_{sfc}} \left[\sum_{j=v,l,i,r,s} \nabla \cdot \mathbf{v}_j r_j \left(c_j T + k_j + l_j + \Phi\right) \right] \mathrm{dp}. \quad (5)$$

Because F_h is not provided by data products used in this study, we assume that velocities of all hydrometeors are equal to the dry air velocity (i.e., $F_h = 0$). The enthalpy fluxes associated with water mass transfer F_m are the sum of,

$$F_{fallout} = -c_w \dot{P} \left(T_w - T_0\right) \quad (6)$$

$$F_v = c_{p_v} \dot{E} \left(T_{skin} - T_0\right) \quad (7)$$

and

$$F_m = F_{fallout} + F_v \quad (8)$$

where c_w is the specific heat capacity of either ice or liquid water, T_w is 2 m wet bulb temperature, T_{skin} is the ocean skin temperature, T_0 is 0°C (Mayer et al., 2017; Trenberth and Fasullo, 2018), $\dot{P}$ is the precipitation rate and $\dot{E}$ is the evaporation rate.

The energy balance Eq. 1 suggests two possible ways of computing net surface energy flux. One way is to use all the surface flux components,

$$F_{net,c} = R_{sfc} - F_{SH} - F_{LH} - F_m \quad (9)$$

where $F_{net,c}$ is positive downward (hereinafter the component approach). The second method for deriving the net surface flux suggested by Eq. 1 is to use TOA net irradiance, atmospheric divergence, and tendency terms (hereinafter the transport approach),

$$F_{net,t} = R_{TOA} - \frac{1}{g}\frac{\partial}{\partial t}\int_0^{p_{sfc}} \left(c_p T + \Phi_s + k + l\right) dp - \frac{1}{g}\nabla \cdot \int_0^{p_{sfc}} \mathbf{U}_a \left(c_p T + \Phi + k + l\right) dp. \quad (10)$$

This approach is used by, for example, Trenberth (1997); Trenberth et al. (2001), Trenberth and Stepaniak (2004); Liu et al. (2015), and Mayer et al. (2017); Trenberth and Fasullo (2018), and Liu et al. (2020). Similar to the energy balance Eq. 1, the water mass balance equation for an atmospheric column is (Trenberth, 1991),

$$\frac{1}{g}\frac{\partial}{\partial t}\int_0^{p_{sfc}} r dp + \frac{1}{g}\nabla \cdot \int_0^{p_{sfc}} \mathbf{U}_a r dp - F_r = \dot{E} - \dot{P} \quad (11)$$

where

$$F_r = \frac{1}{g}\int_0^{p_{sfc}} \sum_{j=v,l,i,r,s} \nabla \cdot \mathbf{v}_j r_j \mathrm{dp} \quad (12)$$

and the precipitation rate $\dot{P} = \dot{P}_r + \dot{P}_s$ is the sum of rain and snow rates. Eq. 11 states that the tendency and convergence of water mass is balanced with the difference of precipitation and evaporation rates at the surface. Because of the assumption of hydrometeors traveling with the dry air velocity, $F_r = 0$. The energy balance Eq. 1 and water mass balance Eq. 11 are related through the diabatic heating term in the total energy equation of the atmospheric column (e.g., Kato et al., 2021).

DATA PRODUCTS

The TOA and surface irradiance data product used in this study is the Edition 4.1 Clouds and the Earth's Radiant Energy System (CERES) Energy Balance and Filled (EBAF). Global net TOA irradiances averaged over 10 years from July 2005 to June 2015 is adjusted to 0.71 Wm^{-2} based on ocean heating rates, ice warming and melts, and atmospheric and lithospheric warming (Johnson et al., 2016; Loeb et al., 2018). A detailed description of the method to produce TOA and surface irradiances included in the product and their uncertainty are given, respectively, in Loeb et al. (2018) and Kato et al. (2018). Horizontal transport of moist static energy and water vapor, as well as surface turbulent fluxes are derived from the ERA-Interim reanalysis data product (Dee et al., 2011). Although mass is not conserved in the original data product (Mayer et al., 2017; Trenberth and Fasullo, 2018; Liu et al., 2020), it is conserved in the ERA-Interim data product used in this study. Mass correction procedures and the method to compute horizontal transport are discussed in Trenberth and Fasullo (2018). Two other sets of surface turbulence fluxes used in this study are Version 3 SeaFlux data product (Roberts et al., 2020) and the Version 3 of the Objectively Analyzed Air-sea Fluxes (OAFlux) (Yu et al., 2008). Precipitation rate data product used in this study is Version 2.3 Global Precipitation Climatology Project (GPCP) data product (Adler et al., 2012). EBAF irradiances, SeaFlux turbulent fluxes, and GPCP precipitation rates are derived using primarily satellite observations. The time period used in this study is from January 2001 to December 2016.

RESULTS

In this section, we investigate the consistency of regional surface energy budget derived by two different approaches (Eqs. 9, 10). Seasonal variabilities of surface net energy fluxes averaged over 45°N to 45°S ocean are compared to check the consistency of the temporal variability.

Regional Surface Energy Budget and Water Mass Balance

Figure 1 shows four surface energy flux components that appear on the right side of Eq. 1. The net irradiance R_{sfc} is primarily a function of latitude. A positive net irradiance over the tropical ocean is largely compensated by latent heat flux F_{LH}. Sensible heat flux F_{SH} is much smaller than F_{LH}. In addition, the meridional gradient of F_{SH} is much smaller than the meridional gradient of

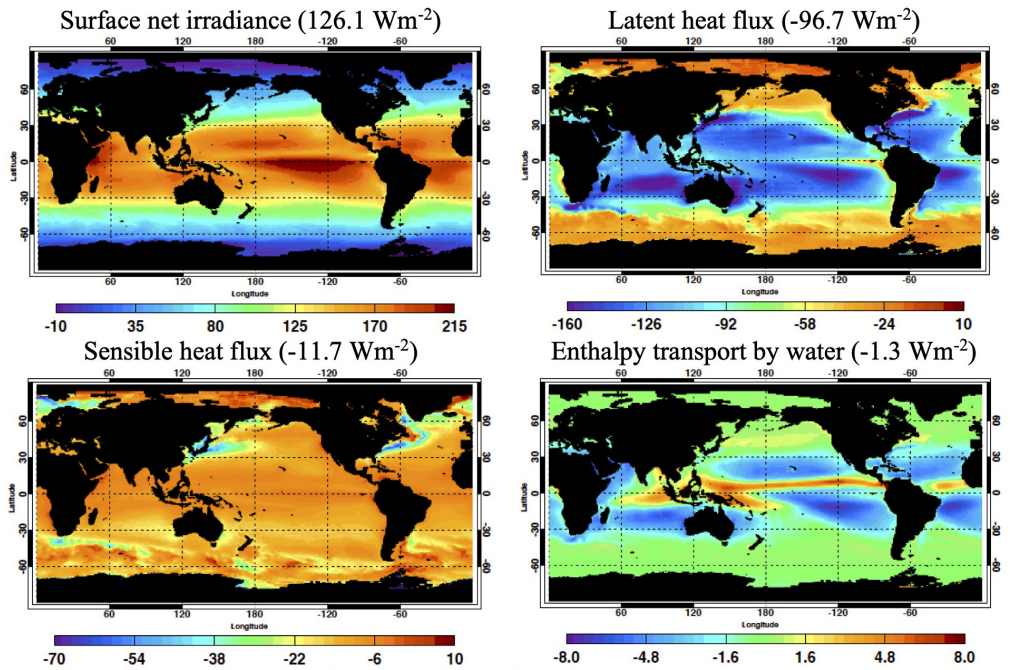

FIGURE 1 | (Top left) Surface net irradiance derived from Edition 4.1 Energy Balance and Filled (EBAF) product, **(top right)** latent heat flux derived from Version 3 SeaFlux product, **(bottom left)** SeaFlux sensible heat flux, and **(bottom right)** enthalpy flux associated with water mass transfer derived from Version 2.3 Global Precipitation Climatology Project (GPCP) and SeaFlux. All maps are climatological mean values from January 2001 to December 2016. Net irradiance and fluxes are defined positive downward. Units is Wm^{-2} for all plots. Mean values averaged over the global ocean are shown with titles.

R_{sfc} and F_{LH}. The spatial pattern of the enthalpy flux associated with water mass transfer F_m resembles the spatial pattern of precipitation rate. When these components are averaged over the global open water, R_{sfc}, F_{LH}, F_{SH}, and F_m are, respectively, 126, -97, -12, and -1 Wm^{-2}. The sum of these four components is 16 Wm^{-2}, which is one order of magnitude larger than the annual global mean ocean heating rates. Note that the annual global mean ocean heating rate given in Johnson et al. (2016) of 0.68 Wm^{-2} is averaged over the entire global area. Therefore, the ocean heating rate averaged over the global ocean is 0.93 Wm^{-2}, which is estimated as the product of 0.68 Wm^{-2} and the ratio of the global area to the ocean area of 1.37 (=0.510 / 0.372). We ignore enthalpy transported to the global ocean by river runoff, which is about 10% of water evaporated from the ocean (Rodell et al., 2015).

The regional energy budget computed by Eq. 9 $F_{net,c}$, expressed as the sum of R_{sfc}, F_{LH}, F_{SH}, and F_m, is shown in the left panel of **Figure 2**. A positive value indicates that net energy is transferred to the ocean. The right panel of **Figure 2** also shows the regional energy budget computed by Eq. 10 $F_{net,t}$. The net surface flux $F_{net,t}$ averaged over the global open water is 2.1 Wm^{-2}, whereas its $F_{net,c}$ counterpart is 16.3 Wm^{-2}. Mayer et al. (2021) who computed net surface energy flux over ocean with ECMWF ERA5 (Hersbach et al., 2018) by the transport approach report $F_{net,t}$ of 1.6 Wm^{-2}. Josey et al. (2013) who computed net surface energy flux over ocean with OAFlux turbulent fluxes (Yu and Weller, 2007) and International Satellite Cloud Climatology Project (ISCCP) irradiances (Zhang et al., 2004) by the component approach report $F_{net,c}$ of 29 Wm^{-2}. The difference between $F_{net,c}$ and $F_{net,t}$ is the atmospheric energy balance residual ε_E,

$$\varepsilon_E = F_{net,c} - F_{net,t}. \tag{13}$$

The difference between $F_{net,c}$ and $F_{net,t}$ exists over tropics (bottom left plot of **Figure 2**). Spatial distribution of $F_{net,t}$ is not necessarily correct, but a casual comparison for $F_{net,c}$ and $F_{net,t}$ showing large ε_E over the tropics leads us to conclude that the tropical region is largely responsible for the larger energy budget residual from the component approach. The standard deviation over the tropics (bottom right plot of **Figure 2**) is nearly equal to ε_E over the tropics while it is larger than ε_E over mid-latitude. This indicates that seasonal variability of ε_E is small over the tropics, but larger seasonal variability exists over mid-latitude. Note that the spatial pattern of ε_E shown in the bottom left plot of **Figure 2** differs from the spatial pattern of **Figure 3** of Kato et al. (2016) because different energy balance equations of an atmospheric column, hence different energy flux data products, are used.

Because F_{LH} is equal to $\dot{E} l_v$, Eqs. 9, and 11 suggest that a bias in the regional water mass balance can affect regional surface energy balance. In order to assess regional water mass balance, in **Figure 3** we plot the divergence of water vapor as a form of the latent heat plus the tendency term on the top left panel and $l_{v0}(\dot{P} - \dot{E})$ on the top right panel where l_{v0} is the enthalpy of vaporization at 0°C. In the tropics, water vapor converges toward the inter tropical convergence zone (ITCZ)

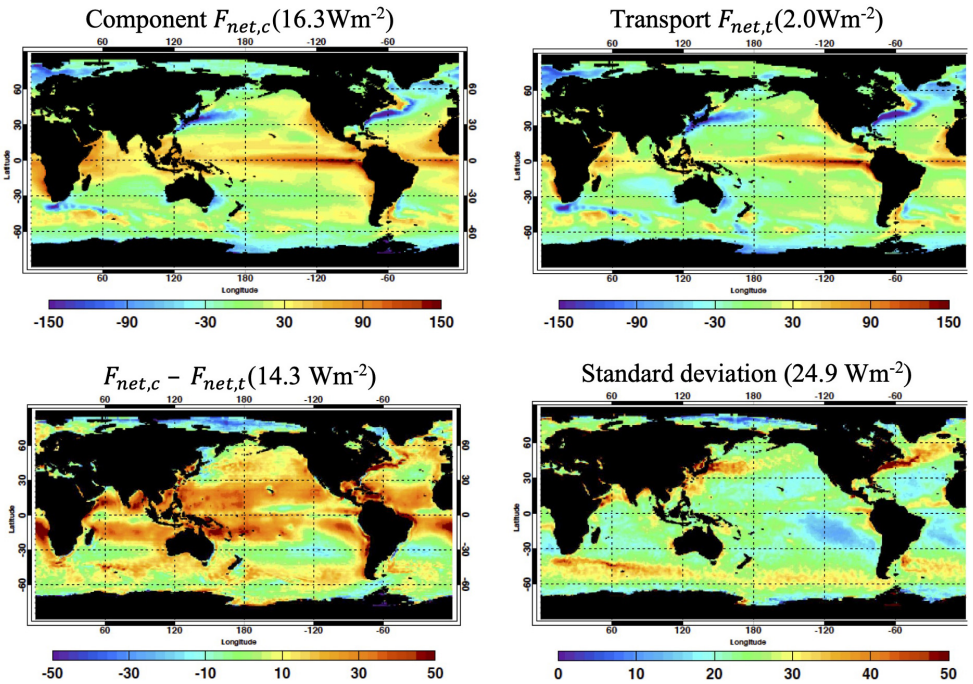

FIGURE 2 | (Top left) Regional net surface energy flux computed with net irradiance, sensible and latent heat fluxes, and enthalpy flux associated with water mass transfer (component approach $F_{net,c}$) **(Top right)** Regional net surface energy flux computed with top-of-atmosphere (TOA) net irradiance, moist static divergence, and moist static energy tendency (transport approach $F_{net,t}$). **(Bottom left)** Difference of regional net surface energy fluxes, $F_{net,c} - F_{net,t}$. **(Bottom right)** standard deviation of reginal monthly $F_{net,c} - F_{net,t}$ computed over 192 months. All maps are climatological mean values from January 2001 to December 2016. Net irradiance and fluxes are defined positive downward. Units is Wm^{-2} for all plots. Mean values averaged over global ocean are shown with titles.

where larger precipitation rates are present. For the atmosphere to balance water mass by Eq. 11 regionally, the sum of values shown in left and right plots needs to be 0. The bottom left plot of **Figure 3** shows the water mass balance residual expressed in Wm^{-2}. Regions with negative values are where convergence is too large, precipitation rate is too small, or evaporation rate is too large. Although the size is unknown, the F_h term defined by Eq. 5 that are neglected in this study can contribute to both energy and water mass balance residuals (Kato et al., 2021). While the standard deviation is relatively large over the tropics (bottom right plot of **Figure 3**), the spatial pattern of water mass residual differs from the spatial pattern of net surface energy flux (top left panel of **Figure 2**). This indicates that the bias is not limited to a common component, i.e., F_{LH} and $l_v\dot{E}$, which affect both balances, but also in other energy flux components likely play a role.

To understand the effect of water mass balance residual to surface net energy flux, however, we assume that all water mass residual is caused by one component of water mass fluxes. If the residual is caused by the bias in F_{LH}, the bias corrected $F_{net,c}$ is,

$$F_{net,c} - l_{v0}\varepsilon_M = R_{sfc} - F_{SH} - F_{LH} - F_m - l_{v0}\varepsilon_M \quad (14)$$

where the water mass balance residual ε_M is

$$\varepsilon_M = \frac{1}{g}\frac{\partial}{\partial t}\int_0^{p_{sfc}} r dp + \frac{1}{g}\nabla\cdot\int_0^{p_{sfc}} \mathbf{U}_a r dp + \dot{P} - \dot{E} \quad (15)$$

If the residual is caused by latent heat divergence then the bias corrected $F_{net,t}$ is,

$$F_{net,t} - l_{v0}\varepsilon_M = R_{TOA} - \frac{1}{g}\frac{\partial}{\partial t}\int_0^{p_{sfc}} \left(c_p T + \Phi_s + k + l\right) \mathrm{dp}$$
$$-\frac{1}{g}\nabla\cdot\int_0^{p_{sfc}} \mathbf{U}_a \left(c_p T + \Phi + k + l\right) dp - l_{v0}\varepsilon_M. \quad (16)$$

The water mass balanced surface net energy flux is $F_{net,c} - l_{v0}\varepsilon_M$ and $F_{net,t} - l_{v0}\varepsilon_M$, which are shown, respectively, on the left and right panel of **Figure 4**. The surface net energy flux shown in **Figure 4** is the flux if regional water mass were balanced. We can further combine surface net energy fluxed derived from two approaches and water mass correction to form the water mass corrected atmospheric energy balance residual,

$$F_{net,c} - F_{net,t} - l_{v0}\varepsilon_M = \varepsilon_E - l_{v0}\varepsilon_M \quad (17)$$

Figure 5 shows regional $\varepsilon_E - l_{v0}\varepsilon_M$. The bias can be associated with any of the energy flux components that appear in Eqs 9, and 10. The bias in F_{LH} can also contribute to $\varepsilon_E - l_{v0}\varepsilon_M$, provided that biases in water mass flux components are present in a way that the sum is not altering the regional water mass balance. Regions with a positive value need a larger upward surface energy flux or a smaller moist energy and kinetic energy divergence.

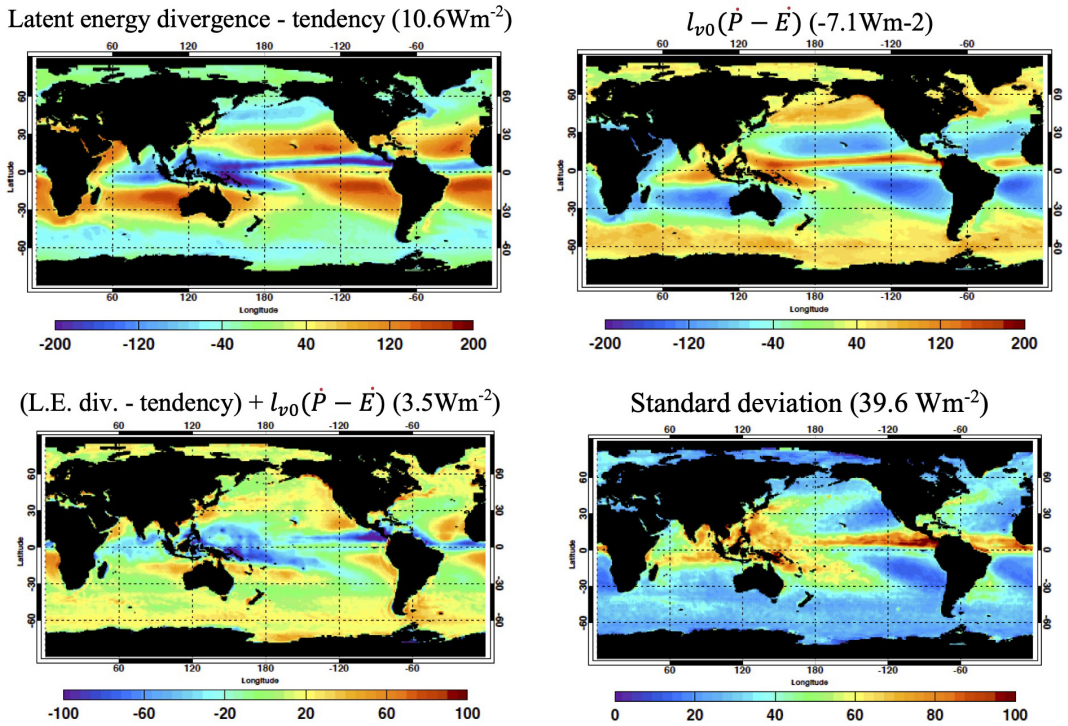

FIGURE 3 | (Top left) Latent heat divergence plus tendency derived from ERA-Interim. **(Top right)** Diabatic heating by precipitation minus surface latent heat flux derived from GPCP and SeaFlux. **(Bottom left)** Regional water mass balance computed as latent heat divergence, tendency, and diabatic heating by precipitation minus surface latent heat flux. **(Bottom right)** Standard deviation of the reginal monthly water mass balance computed over 192 months. Regional values are 16-year climatological mean (from January 2001 to December 2016). Units is in Wm^{-2} for all plots. Mean values averaged over the global ocean are shown with titles.

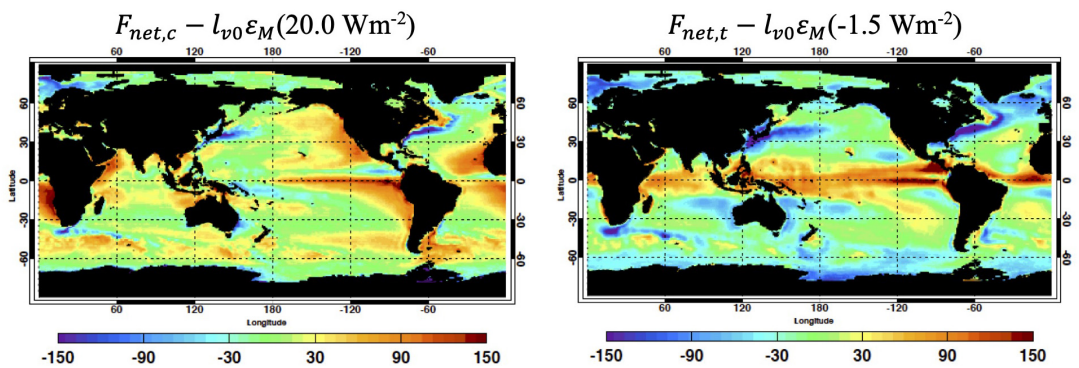

FIGURE 4 | Water mass balanced surface net energy flux $F_{net,c} - l_{v0}\varepsilon_M$ given by Eq. 11 on the panel left and $F_{net,t} - l_{v0}\varepsilon_M$ given by Eq. 13 on the panel right. Regional values are 16-year climatological mean (from January 2001 to December 2016). Units is in Wm^{-2} for all plots. Mean values averaged over the global ocean are shown with titles.

Seasonal Variability

Figure 6 shows climatological seasonal variability of energy flux components averaged between 45°N and 45°S over ocean. The net TOA irradiance (blue line in the top plot) seasonal variability is similar to the seasonal variability of the climatological global mean shown in Fasullo and Trenberth (2008). The seasonal variability is largely caused by insolation driven by the Earth-to-sun distance, which in turn affects absorbed shortwave irradiance. The energy divergence in the atmosphere averaged between 45°N and 45°S over ocean is relatively constant. During May through July, the atmosphere transports more energy than net TOA irradiance, indicating that additional net energy is provided from the surface during these months. The bottom plot of **Figure 6** shows the surface flux components separately. The net surface irradiance is indicated by the blue line and three estimates of turbulent flux from SeaFlux, OAFlux and ERA-Interim are indicated, respectively, by red, magenta, and green lines. In **Figure 6**, the net surface irradiance is positive downward and

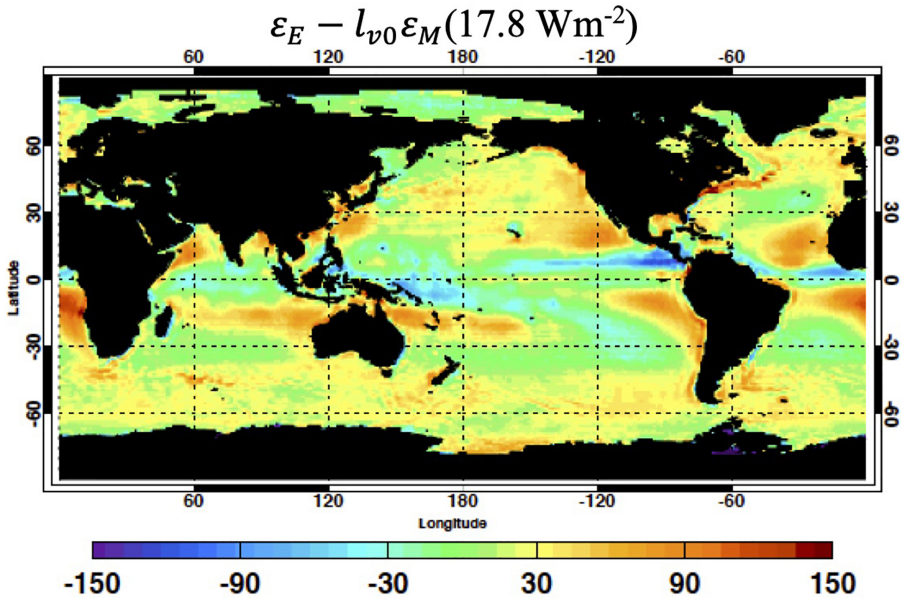

FIGURE 5 | Water mass corrected atmospheric energy balance residual $\varepsilon_E - l_{v0}\varepsilon_M$ defined by Eq. 14 in Wm^{-2}. Mean value averaged over the global ocean is 17.8 Wm^{-2}. Regional values are 16-year climatological mean (from January 2001 to December 2016).

the turbulent fluxes are positive upward. From May to July, ERA-Interim turbulent flux is larger than the net irradiance, while SeaFlux and OAFlux turbulent fluxes are smaller than the net irradiance throughout the year. The larger ERA-Interim turbulent flux than the net irradiance during May through July is interpreted as the surface providing net energy to the atmosphere, which is consistent with the top plot of **Figure 6**. This result suggests that SeaFlux and OAFlux turbulent fluxes are too small or both the net surface irradiance and divergence are too large during these 3 months. More importantly, annual mean turbulent fluxes averaged over 45°N to 45°S over ocean derived from three different products differ by nearly 20 Wm^{-2}, which is approximately 14% of the annual mean value. The 20 Wm^{-2} difference of turbulent fluxes is nearly equivalent to the difference between the net surface energy fluxes derived from two methods.

Although the net surface energy fluxes derived by the two methods differ by more than 10 Wm^{-2}, **Figure 6** indicates that differences of turbulent fluxes derived from ERA-Interim, SeaFlux, and OAFlux are nearly constant throughout the year. As a consequence, once respective annual mean values are subtracted, seasonal variabilities derived from two data products are similar (**Figure 7**, bottom plot). After the corresponding annual mean is subtracted, the difference in climatological monthly mean variability is less than ± 2 Wm^{-2}, which is approximately 10% of the amplitude of the seasonal cycle.

DISCUSSION AND SUMMARY

Energy flux data products were integrated by two different methods to assess the regional surface energy balance. The first method is to use all surface flux components and the resulting net surface flux is denoted by $F_{net,c}$. The second method is to use the TOA net irradiance, horizontal energy transport by the atmosphere, and tendency for which the resulting net surface flux is denoted by $F_{net,t}$. While the uncertainty in regional $F_{net,c}$ is larger than $F_{net,t}$, the advantage of the component approach is that it provides all components. The transport approach only provides the net surface energy flux. However, $F_{net,c}$ averaged over the global ocean is 16 Wm^{-2} while $F_{net,t}$ averaged over the global ocean is 2 Wm^{-2}. The comparisons of net surface energy fluxes derived from both approaches shed lights into the uncertainties of their components. For example, the net surface energy flux averaged over global ocean is nearly equal to the ocean heating rate provided that the enthalpy transported by river runoff is negligible. Because annual mean ocean heating rate is 0.93 Wm^{-2}, the size of combined biases from flux components used in estimating the net surface energy flux averaged over global ocean is nearly equal to $F_{net,c}$. Our results also indicate that the residual of energy balance (16–0.93 Wm^{-2}) is larger than the residual of mass balance (4 Wm^{-2}) when they are averaged over global ocean. It is not obvious why the energy balance residual is larger than the mass balance residual. One reason might be due to the components achieving energy and mass balances. The surface energy balance is achieved largely among R_{sfc}, F_{SH}, and F_{LH} while the mass balance is achieved among F_{LH}, precipitation rate, and horizontal transport of water.

The water mass residual indirectly affects energy budget residual. Kato et al. (2021) show that regional water mass is not conserved when multiple data products are integrated. This is also illustrated in **Figure 3**. Horizontal transport of water vapor derived from ERA-Interim is shown on the top left plot of **Figure 3**. The annual mean water vapor transport from ocean

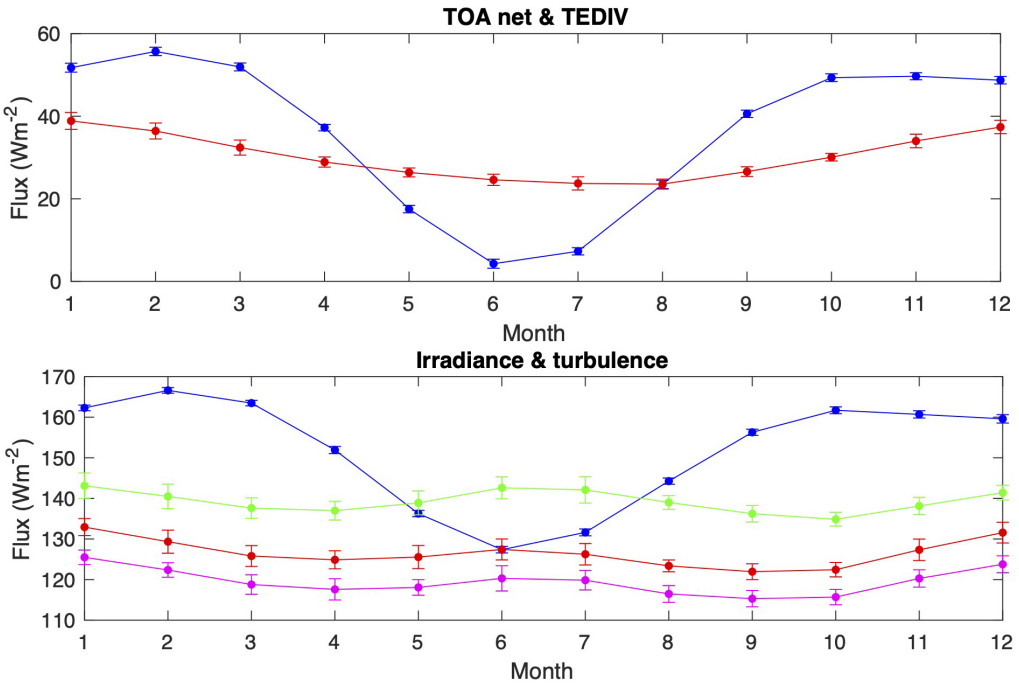

FIGURE 6 | (Top) Climatological monthly mean net TOA irradiance (blue line) defined as positive downward and divergence of moist static and kinetic energy (red line) averaged between 45°N and 45°S over ocean. **(Bottom)** Net surface irradiance (blue line), turbulent flux (i.e., the sum of sensible and latent heat fluxes) derived from SeaFlux (red line), ERA-Interim (green line), and Objectively Analyzed Air-sea Fluxes (OAFlux) (magenta line). Turbulent fluxes are positive upward. Climatological means are computed with 16 years of data (January 2001 to December 2016) and error bars indicate the standard deviation.

to land is 4×10^4 km^3 yr^{-1} in the units of volume, which is equivalent to 3.2 PW or approximately 10 Wm^{-2}. This is nearly the same size of the energy flux from ocean to land (Fasullo and Trenberth, 2008), indicating that the ocean to land energy transport is dominated by latent heat divergence. Our value of water mass divergence averaged over the global ocean in the units of energy flux of 11 Wm^{-2} is consistent with the value given in Trenberth and Fasullo (2013) and Rodell et al. (2015). At a regional scale, water vapor divergence plus tendency in the atmosphere should balance with $\dot{E} - \dot{P}$ (Eq. 3). This implies that $\dot{P} - \dot{E}$ averaged over the global ocean should be approximately -10 Wm^{-2}, provided that the tendency term is small. When GPCP precipitation rate and SeaFlux latent heat flux are used, $\dot{P} - \dot{E}$ averaged over global ocean is -7 Wm^{-2}. This suggests that biases in $\dot{P}$ and $\dot{E}$ are nearly the same size and partially cancels when $\dot{E}$ is subtracted from $\dot{P}$. This may be the reason for the smaller water mass balance residual than the energy balance residual averaged over the global ocean. Note that the annual mean latent heat flux form OAFlux averaged over global ocean is approximately 5.5 Wm^{-2} smaller than the SeaFlux counterpart value so that $\dot{P} - \dot{E}$ averaged over global ocean is -1.5 Wm^{-2}, which gives a larger ε_M than ε_M computed with SeaFlux.

The $\dot{E} - \dot{P}$ value also depends on precipitation data product. Generally, precipitation rate estimated over ocean is uncertain due to lack of ground-based direct observations compared to precipitation rate estimated over land (Sun et al., 2018). A study by Behrange and Song (2020) suggests that GPCP precipitation rate over global ocean is underestimated by 9%. Precipitation rates over the ITCZ regions estimated by GPCP are generally smaller than those estimated from a similar multiple observation merged global precipitation data product of the CPC Merged Analysis of Precipitation (CMAP; Xie and Arkin, 1997). In addition, GPCP precipitation over the tropics is smaller than TRMM 3B42 precipitation (Masunaga et al., 2019). In particular, heavy rain rates larger than 30 mm day^{-1} over ocean occur less frequent in GPCP precipitation than TRMM 3B42v7 precipitation (Masunaga et al., 2019). The spatial pattern of water mass residual (lower left of **Figure 3**) suggests that the residual is not limited over the ITCZ, indicating that the water mass balance residual is not entirely caused by our choice of data products.

The surface net energy flux $F_{net,c}$ averaged over the global ocean of 16 Wm^{-2} is smaller than the maximum standard deviation of regional net fluxes of approximately 30 Wm^{-2} derived from 12 data products shown in Yu (2019). Therefore, regional $F_{net,c}$ shown in **Figure 2** could change depending on the data product. Nevertheless, given the regional water vapor balance residual shown in **Figure 3**, the water mass balance residual contributes a large portion of the energy balance residual for some regions.

We showed that sums of latent heat and sensible heat fluxes from SeaFlux and OAFlux averaged between 45°N and 45°S over ocean during May through July are likely to be too small because the atmosphere transports energy more than energy input from the top and bottom boundary. If the moist static divergence is too large, the net surface irradiance is also too large. The difference between annual mean $F_{net,c}$ and $F_{net,t}$ averaged over 45°N to 45°S is 18 Wm^{-2}. The 20 Wm^{-2} difference of turbulent fluxes found between three products is nearly equivalent to the

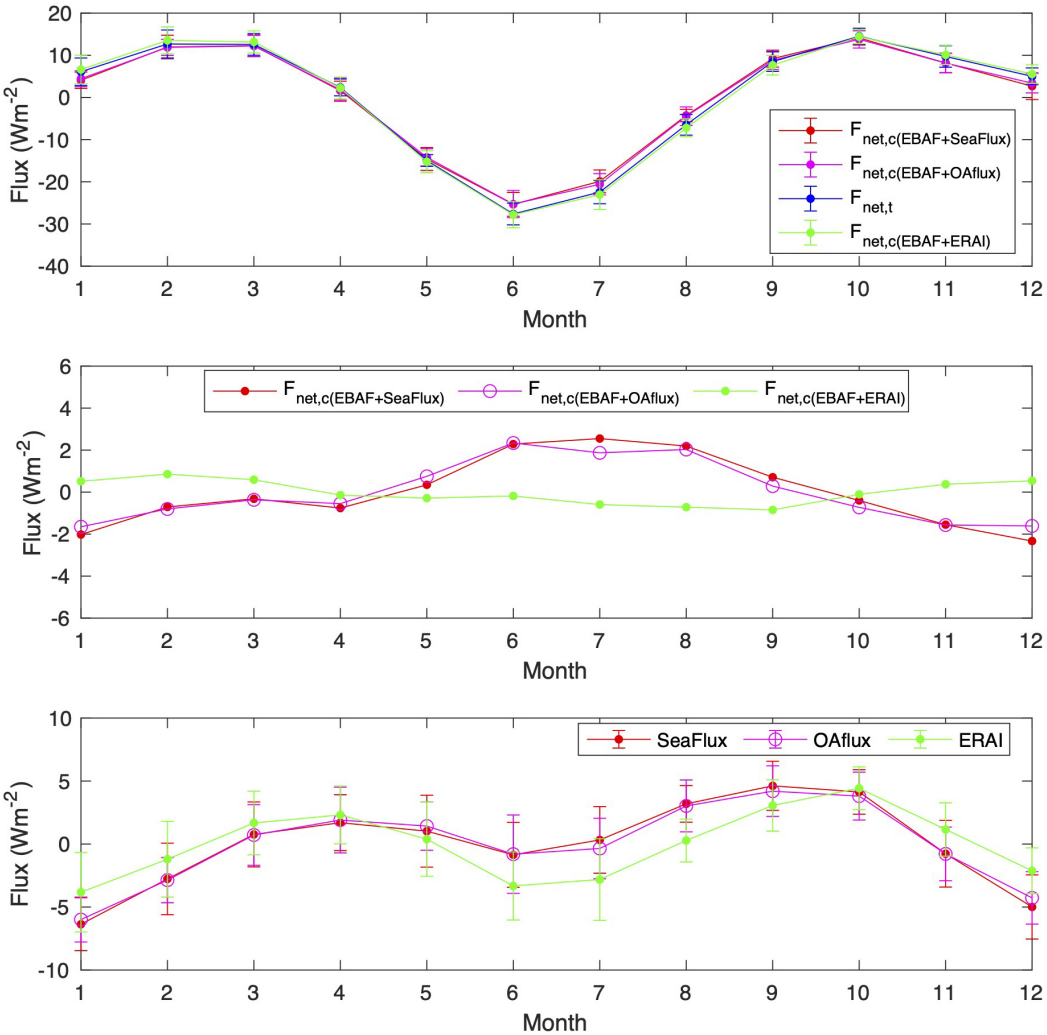

FIGURE 7 | (Top) Monthly climatological mean of net surface energy flux variability computed by the component approach ($F_{net,c}$) using the EBAF data product and SeaFlux (blue line), OAFLux (magenta line), and ERA-Interim (green line). Net surface energy flux computed by the transport approach ($F_{net,t}$) is shown with red line. All values are averaged between 45°N and 45°S over ocean. Corresponding annual mean is subtracted from monthly means. Means are average from January 2001 to December 2016 and error bars indicate the standard deviation. **(Middle)** Difference of monthly climatological mean variabilities $F_{net,c} - F_{net,t}$, i.e., the red, magenta, and green lines minus the blue line shown in the top plot. **(Bottom)** Monthly mean climatology minus annual mean of sensible and latent heat fluxes computed with SeaFLux, OAFlux, and ERA-Interim products.

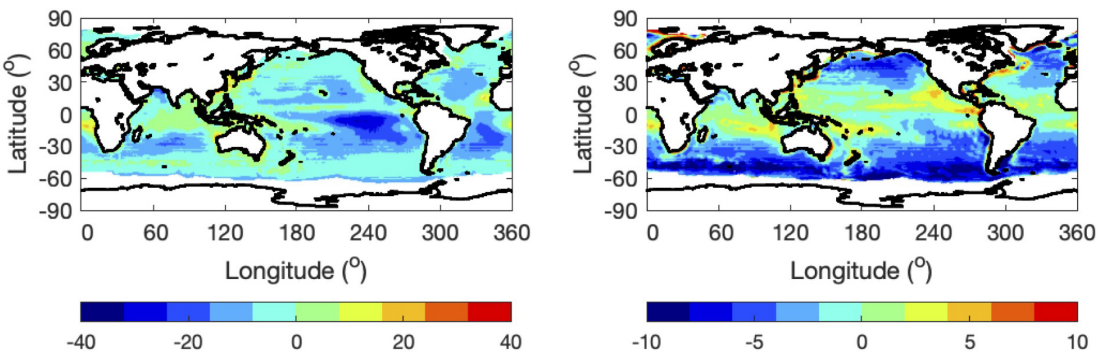

FIGURE 8 | Difference of surface **(left)** latent heat flux and **(right)** sensible heat flux derived from OAFlux and SeaFLux data products (OAFlux minus SeaFlux) averaged over 16 years (from January 2000 to December 2015) in Wm^{-2}. Fluxes are defined positive upward.

difference of $F_{net,c}$ and $F_{net,t}$. In addition, if we assume that the 2.5 Wm^{-2} uncertainty in regional outgoing TOA shortwave and longwave irradiances (Loeb et al., 2018) and the 10 Wm^{-2} uncertainty in horizontal transport (Trenberth and Fasullo, 2018) are independent, then the uncertainty in regional $F_{net,t}$ is 11 Wm^{-2} [$=(2.5^2+2.5^2+10^2)^{1/2}$]. Therefore, the 18 Wm^{-2} is likely to be larger than the uncertainty in TOA net irradiance and transport combined.

The root-mean-square (RMS) difference of monthly mean downward irradiances compared with observations at buoy sites that are mostly located in the tropics is 11 and 5 Wm^{-2}, respectively, for shortwave and longwave irradiances (Kato et al., 2018). The estimated uncertainty in the regional monthly mean net surface irradiance over ocean is 13 Wm^{-2} (Kato et al., 2020). The uncertainty in regional turbulent flux in $F_{net,c}$ is difficult to estimate. A casual comparison of latent heat flux shown in **Figure 1** with the latent heat flux from the Japanese Ocean Flux Data Set with Use of Remote-sensing Observations (J-OFURO) (**Figure 4** of Tomita et al., 2019) suggests that SeaFLux F_{LH} over tropics is smaller than Japanese ocean flux data set with use of remote-sensing observations (J-OFULO) F_{LH}. Comparisons of daily mean J-OFULO F_{LF} against buoy observations in Tomita et al. (2019) yield a typical RMS difference of less than 25 Wm^{-2}. If there is a random error contribution, the RMS difference in monthly means is expected to be smaller. In fact, climatological mean differences of regional F_{SH} and F_{LH} from SeaFLux and OAFlux are within 10 Wm^{-2} for most regions (**Figure 8**), although the differences of F_{SH} and F_{LH} over tropical regions have the same sign. All these results suggest that estimated uncertainties in monthly mean R_{sfc}, F_{SH}, and F_{LH} are of the order of 10 Wm^{-2}.

As mentioned in Cronin et al. (2019), the uncertainty in satellite derived gridded energy products is larger than the *in situ* observation uncertainty of ∼10 Wm^{-2} in a long-term averaged value (e.g., monthly mean) largely due to limitations in observing surface air temperature and humidity. Near surface temperature and humidity affect both downward longwave irradiance and sensible and latent heat fluxes. In addition, ocean skin temperature retrieved from satellite observations is the temperature of the thermal skin layer of about a 0.1 mm thick below ocean surface (Wong and Minnett, 2018). Furthermore, the ocean thermal skin layer temperature is generally lower than ocean temperature below the surface at a depth of ∼2 m because of evaporative cooling at the air-sea interface (Smith et al., 1996). Therefore, satellite derived skin temperature can be different from ocean surface temperature (Cronin et al., 2019).

In addition to these input variables, there is the uncertainty associated with the turbulent flux parametrizations and the use of bulk state variables (Cronin et al., 2019; Yu, 2019). Gustiness of wind speed can alter turbulent fluxes and needs to be taken into account. Wind speed dependent ocean surface roughness length and transfer coefficients need to be improved, and their dependence on the sea state might need to be incorporated into parameterizations. Furthermore, deriving latent heat flux from satellites is challenging because of their diurnal sampling and calibration stability (Robertson et al., 2020). Also, a larger footprint size and broad passive microwave channel weighting functions are not ideal for deriving near surface humidity with a required spatial resolution (Robertson et al., 2020).

Advances in remote sensing techniques to derive surface air temperature and humidity will help reduce errors in surface irradiance. In addition, better observations of ocean surface temperature, wind speed at a high temporal resolution, and sea state at a global scale are needed to improve turbulent fluxes. Some promising observations to improve surface fluxes are proposed in Cronin et al. (2019) and are expected to provide indispensable observations toward reducing uncertainties in estimating regional surface energy fluxes. Our results highlight the weakness of the component approach to estimate regional net surface energy flux and identify regions where larger issues remain. Our analysis indicates that large surface energy flux biases exist in the tropics, which is consistent with earlier studies (Loeb et al., 2014; Kato et al., 2016). Improving future observations need to target the regions with large residuals, which could lead to improved understanding and reduction of these biases. In addition, toward achieving the goal of improving surface energy flux, data product integration and physical processes demonstrated in this study can be used to assess the quality of individual data products. Reducing surface energy budget uncertainty needs coordinate efforts among surface radiation and turbulent flux data providers.

DATA AVAILABILITY STATEMENT

The datasets EBAF for this study can be found in the NASA Langley Atmospheric Science Data Center (https://ceres.larc.nasa.gov/data/), SeaFux can be found in the NASA Earthdata (https://ghrc.nsstc.nasa.gov/pub/seaflux/data/), OAFlux can be found in the Woods Hole Oceanographic Institution site (ftp://ftp.whoi.edu/pub/science/oaflux/data_v3), GPCP can be found in the University of Maryland site (http://gpcp.umd.edu/), and ERA-Interim can be found in the NCAR site (ftp://ftp.cgd.ucar.edu/archive/BUDGETS/ERAI).

AUTHOR CONTRIBUTIONS

SK wrote the first draft of the manuscript. DP contributed to the editing. FR generated the figures. SK, FR, F-LC, DP, and WS contributed to the analysis. All authors contributed to the article and approved the submitted version.

FUNDING

This work was supported by the NASA CERES and the NASA's Energy and Water cycle Study (NEWS) projects.

ACKNOWLEDGMENTS

We thank John Fasullo of NCAR for providing ERA-Interim energy transport data product and William Olson of UMBC and Brent Roberts of NASA MFSC for useful discussions.

REFERENCES

Adler, R. F., Gu, G., and Huffman, G. J. (2012). Estimating climatological bias errors for the Global Precipitation Climatology Project (GPCP). *J. Appl. Meteor. Climatol.* 51, 84–99. doi: 10.1175/JAMC-D-11-052.1

Albrecht, B. A., Fairall, C. W., Thomson, D. W., White, A. B., and Snider, J. B. (1990). Surface-based remote sensing of the observed and the adiabatic liquid water content of stratocumulus clouds. *Geophys. Res. Lett.* 17, 89–92.

Behrange, A., and Song, Y. (2020). A new estimate for oceanic precipitation amount and distribution using complementary precipitation observations from space and comparison with GPCP. *Environ. Res. Lett.* 15:124042.

Betts, A. K. (1985). Mixing line analysis of clouds and cloudy boundary layers. *J. Atmos. Sci.* 42, 2751–2763.

Betts, A. K., and Ridgway, W. (1988). Coupling of the radiative convective, and surface fluxes over the equatorial Pacific. *J. Atmos. Sci.* 45, 522–536.

Bretherton, C. S., and Wyant, M. C. (1997). Moisture transport, lower-tropospheric stability, and decoupling of cloud-topped boundary layers. *J. Atmos. Sci.* 54, 148–167.

Cox, C., and Munk, W. (1955). Some problems in optical oceanography. *J. Mar. Res.* 14, 63–78.

Cronin, M. F., Gentemann, C. L., Edson, J., Ueki, I., Bourassa, M., Brown, S., et al. (2019). Air-sea fluxes with a focus on heat and momentum. *Front. Mar. Sci.* 6:430. doi: 10.3389/fmars.2019.00430

Dee, D. P., Uppala, S. M., Simmons, A. J., Berrisford, P., Poli, P., Kobayashi, S., et al. (2011). The ERA- interim reanalysis: configuration and performance of the data assimilation system. *Q.J.R. Meteorol. Soc.* 137, 553–597.

Fasullo, J. T., and Trenberth, K. E. (2008). The annual cycle of the energy budget. Part I: global mean and land-ocean exchanges. *J. Climate* 21, 2297–2312. doi: 10.1175/2007JCLI1935.1

Hartmann, D. L., and Ceppi, P. (2014). Trends in the CERES dataset, 20000-13: the effects of sea ice and jet shifts and comparison to climate models. *J. Clim.* 27, 2444–2456. doi: 10.1175/JCLI-D-13-00411.1

Hersbach, H., de Rosnay, P., Bell, B., Schepers, D., Simmons, A., and Soci, C. (2018). Operational global reanalysis: progress, future directions and synergies with NWP. *ERA Rep. Ser.* 27:65. doi: 10.21957/tkic6g3wm

Hudson, S. R., Granskog, M. A., Sundfjord, A., Randelhoff, A., Renner, A. H. H., and Divine, D. V. (2013). Energy budget of first-year Arctic sea ice in advance stages of melt. *Geophys. Res. Lett.* 40, 2679–2683. doi: 10.1002/grl.50517

Jin, Z., Charlock, T. P., Smith, W. L., and Rutledge, K. (2004). A parameterization ocean surface albedo. *Geophys. Res. Lett.* 31:L22301. doi: 10.1029/2004GL021180

Johnson, G. C., Lyman, J. M., and Loeb, N. G. (2016). Improving estimates of Earth's energy imbalance. *Nat. Climate Change* 6, 639–640. doi: 10.1038/nclimate3043

Josey, S. A., Gulev, S., and Yu, L. (2013). "Exchange through the ocean surface," in *Ocean Circulation and Climate: A 21st Century Perspective, Int. Geophys. Ser*, Vol. 103, eds G. Siedler, et al. (Oxford: Academic Press), 115–140.

Kato, S., Rose, F. G., Rutan, D. A., Thorsen, T. J., Loeb, N. G., Doelling, D. R., et al. (2018). Surface irradiances of edition 4.0 clouds and the earth's radiant energy system (CERES) energy balanced and filled (EBAF) data product. *J. Climate* 31, 4501–4527. doi: 10.1175/JCLI-D-17-0523.1

Kato, S., Loeb, N. G., Fasullo, J. T., Trenberth, K. E., Lauritzen, P. H., Rose, F. G., et al. (2021). Regional energy and water budget of a precipitating atmosphere over ocean. *J. Clim.* 34, 4189–4205. doi: 10.1175/JCLI-D-20-0175.1

Kato, S., Loeb, N. G., and Rutledge, C. K. (2002). Estimate of top-of-atmosphere albedo for a molecular atmosphere over ocean using Clouds and the Earth's Radiant Energy System measurements. *J. Geophys. Res.* 107:4396. doi: 10.1029/2001JD001309

Kato, S., Rose, F. G., Sun-Mack, S., Miller, W. F., Chen, Y., Rutan, D. A., et al. (2011). Improvements of top-of-atmosphere and surface irradiance computations with CALIPSO-, CloudSat-, and MODIS-derived cloud and aerosol properties. *J. Geophys. Res.* 116:D19209. doi: 10.1029/2011JD016050

Kato, S., Rutan, D. A., Rose, F. G., Caldwell, T. E., Ham, S.-H., Radkevich, A., et al. (2020). Uncertainty in satellite-derived surface irradiances and challenges in producing surface radiation budget climate data record. *Remote Sens.* 12:1950. doi: 10.3390/rs12121950

Kato, S., Xu, K.-M., Wong, T., Loeb, N. G., Rose, F. G., Trenberth, K. E., et al. (2016). Investigation of the bias in column integrated atmospheric energy balance using cloud objects. *J. Clim.* 29:20. doi: 10.1175/JCLI-D-15-0782.1

L'Ecuyer, T., Tristan, S., Beaudoing, H. K., Rodell, M., Olson, W., Lin, B., et al. (2015). The observed state of the energy budget in the early twenty-first century. *J. Clim.* 28, 8319–8346. doi: 10.1175/JCLI-D-14-00556.1

Liu, C., Allan, R. P., Berrisford, P., Mayer, M., Hyder, P., Loeb, N., et al. (2015). Combining satellite observations and reanalysis energy transports to estimate global net surface energy fluxes 1985–2012. *J. Geophys. Res. Atmos.* 120, 9374–9389. doi: 10.1002/2015JD023264

Liu, C., Allan, R. P., Mayer, M., Hyder, P., Desbruyeres, D., Cheng, L., et al. (2020). Variability in the global energy budget and transports 1985-2017. *Clim. Dyn.* 55, 3381–3396. doi: 10.1007/s00382-020-05451-8

Loeb, G. L., Thorsen, T. J., Norris, J. R., Wang, H., and Su, W. (2018). Changes in Earth's energy budget during and after the "pause" in global warming: an observational perspective. *Climate* 6:62. doi: 10.3390/cli6030062

Loeb, N. G., Rutan, D. A., Kato, S., and Wang, W. (2014). Observing in- terannual variations in Hadley circulation atmospheric diabatic heating and circulation strength. *J. Clim.* 27, 4139–4158. doi: 10.1175/JCLI-D-13-00656.1

Masuda, K., Takashima, T., and Takayama, Y. (1988). Emissivity of pure and sea waters for the model sea surface in the infrared window regions. *Remote Sens. Environ.* 24, 313–329.

Masunaga, H., Schroder, M., Furuzawa, F. A., Kummerow, C., Rustemeier, E., and Schneider, U. (2019). Inter-product biases in global precipitation extremes. *Environ. Res. Lett.* 14:125016. doi: 10.1088/1748-9326/ab5da9

Mayer, L., Mayer, M., and Haimberger, L. (2021). Consistency and homogeneity of atmospheric energy, moisture, and mass budget in ERA5. *J. Clim.* 34, 3955–3974. doi: 10.1175/JCLI-D-20-0676.1

Mayer, M., Haimberger, L., Edwards, J. M., and Hyder, P. (2017). Toward consistent diagnostics of the coupled atmosphere and ocean energy budgets. *J. Clim.* 30, 9225–9246. doi: 10.1175/JCLI-D-17-0137.1

Meyssignac, B., Boyer, T., Zhao, Z., Hakuba, M. Z., Landerer, F. W., Stammer, D., et al. (2019). Measuring global ocean heat content to estimate the earth energy imbalance. *Front. Mar. Sci.* 6:432. doi: 10.3389/fmars.2019.00432

Roberts, J. B., Clayson, C. A., and Robertson, F. R. (2020). *SeaFlux Data Products Version 3. Dataset Available Online from the NASA Global Hydrology Resource Center DAAC*. Huntsville, AL. doi: 10.5067/SEAFLUX/DATA101

Robertson, F. R., Roberts, J. B., Bosilovich, M. G., Bentamy, A., Clayson, C. A., Fennig, K., et al. (2020). Uncertainties in ocean latent heat flux variations over recent decades in satellite-based estimates and reduced observation reanalyses. *J. Clim.* 33, 8415–8437. doi: 10.1175/JCLI-D-19-0954.1

Rodell, M., Beaudoing, H. K., L'Ecuyer, T. S., Olson, W. S., and Famiglietti, J. S. (2015). The observed state of the water cycle in the early twenty-first century. *J. Clim.* 28:8289. doi: 10.1175/JCLI-D-14-00555.1

Sidran, M. (1981). Broadband reflectance and emissivity of specular and rough water surfaces. *Appl. Opt.* 20, 3176–3183.

Smith, W. L., Knuteson, R. O., Revercomb, H. E., Feltz, W., Howell, H. B., Menzel, W. P., et al. (1996). Observations of the infrared radiative properties of the ocean–implications for the measurement of sea surface temperature via satellite remote sensing. *Bull. Am. Meteorol. Soc.* 77, 41–52.

Soden, B. J. I, Held, M., Colman, R., Shell, K. M., Kiehl, J. T., and Shields, C. A. (2008). Quantifying climate feedbacks using radiative kernels. *J. Clim.* 21, 3504–3520. doi: 10.1175/2007JCLI2110.1

Stephens, G. L., Li, J., Wild, M., Clayson, C. A., Loeb, N., and Kato, S. (2012). An update on Earth's energy balance in light of the latest global observations. *Nat. Geosci.* 5, 691–696. doi: 10.1038/NGEO1580

Sun, Q., Miao, C., Duan, Q., Ashouri, H., Sorooshian, S., and Hsu, K.-L. (2018). A review of global precipitation data sets: data sources, estimation, and inter-comparisons. *Rev. Geophys.* 56, 79–107. doi: 10.1002/2017RG000574

Tomita, H., Hihara, T., Kato, S., Kubota, M., and Kutsuwada, K. (2019). An introduction to J-OFURO3, a third-generation Japanese ocean flux data set using remote-sensing observations. *J. Oceanogr.* 75, 171–194. doi: 10.1007/s10872-018-0493-x

Trenberth, K. E., and Fasullo, J. T. (2013). Regional energy and water cycles: transports from ocean to land. *J. Climate* 26, 7838–7851. doi: 10.1175/JCLI-D-13-00008.1

Trenberth, K., and Fasullo, J. (2018). Applications of an updated atmospheric energetics formulation. *J. Clim.* 31, 6263–6279. doi: 10.1175/JCLI-D-17-0838.1

Trenberth, K. E. (1991). Climate diagnostics from global analysis: conservation of mass in ECMWF analysis. *J. Clim.* 4, 707–722.

Trenberth, K. E. (1997). Using atmospheric budgets as constraint on surface fluxes. *J. Clim.* 10, 2796–2809.

Trenberth, K. E., Caron, J. M., and Stepaniak, D. P. (2001). The atmospheric energy budget and implications for surface fluxes and ocean heat transports. *Clim. Dyn.* 17, 259–276.

Trenberth, K. E., and Solomon, A. (1994). The global heat balance: heat transport in the atmosphere and ocean. *Clim. Dyn.* 10, 107–134.

Trenberth, K. E., and Stepaniak, D. P. (2004). The flow of energy through the earth's climate system. *Q. J. R. Meteorol. Soc.* 130, 2677–2701.

von Schuckmann, K., Cheng, L., Palmer, M. D., Hansen, J., Tassone, C., Aich, V., et al. (2020). Heat stored in the earth system: where does the energy go? *Earth Syst. Sci. Data* 12, 2013–2041. doi: 10.5194/essd-12-2013-2020

Wild, M., Folini, D., Hakuba, M. Z., Schar, C., Seneviratne, S. I., Kato, S., et al. (2015). The energy balance over land and oceans: an assessment based on direct observations and CMIP5 climate models. *Clim. Dyn.* 44, 3393–3429.

Wong, E. W., and Minnett, P. J. (2018). The response of the ocean thermal skin layer to variations in incident infrared radiation. *J. Geophys. Res. Oceans* 123, 2475–2493.

Wood, R. (2012). Stratocumulus clouds. *Monthly Weather Rev.* 140, 2373–2423. doi: 10.1175/MWR-D-11-00121.1

Xie, P., and Arkin, P. A. (1997). Global precipitation: a 17-year monthly analysis based on gauge observations, satellite estimates, and numerical model outputs. *Bull. Am. Meteor. Soc.* 78, 2539–2558.

Yu, L. (2019). Global air–sea fluxes of heat, fresh water, and momentum: energy budget closure and unanswered questions. *Annu. Rev. Mar. Sci.* 11, 227–248. doi: 10.1146/annurev-marine-010816-060704

Yu, L., and Weller, R. A. (2007). Objectively analyzed air-sea heat Fluxes (OAFlux) for the global ocean. *Bull. Am. Meteorol. Soc.* 88, 527–539.

Yu, L., Jin, X., and Weller, R. A. (2008). *Multidecade Global Flux Datasets from the Objectively Analyzed Air-Sea Fluxes (OAFlux) Project: Latent and Sensible Heat Fluxes, Ocean Evaporation, and Related Surface Meteorological Variables. Woods Hole Oceanographic Institution, OAFlux Project Technical Report. OA-2008-01*. Massachusetts: Woods Hole, 64.

Zhang, Y.-C., Rossow, W. B., Lacis, A. A., Oinas, V., and Mishchenko, M. I. (2004). Calculation of radiative fluxes from the surface to top of atmosphere based on ISCCP and other global data sets: refinements of the radiative transfer model and the input data. *J. Geophys. Res.* 109:D19105.

Conflict of Interest: FR, F-LC, and DP are employed by the company Science Systems and Applications Inc.

The remaining authors declare that the research was conducted in the absence of any commercial or financial relationships that could be construed as a potential conflict of interest.

Publisher's Note: All claims expressed in this article are solely those of the authors and do not necessarily represent those of their affiliated organizations, or those of the publisher, the editors and the reviewers. Any product that may be evaluated in this article, or claim that may be made by its manufacturer, is not guaranteed or endorsed by the publisher.

frontiers in Marine Science

ORIGINAL RESEARCH
published: 23 February 2022
doi: 10.3389/fmars.2022.766810

Impact of Sea Ice Melting on Summer Air-Sea CO_2 Exchange in the East Siberian Sea

*Ahra Mo[1,2], Eun Jin Yang[2], Sung-Ho Kang[2], Dongseon Kim[3], Kitack Lee[4], Young Ho Ko[5], Kitae Kim[6] and Tae-Wook Kim[1,5]**

[1] Division of Environmental Science and Ecological Engineering, Korea University, Seoul, South Korea, [2] Division of Ocean Science, Korea Polar Research Institute, Incheon, South Korea, [3] Marine Environmental Research Center, Korea Institute of Ocean Science and Technology, Busan, South Korea, [4] Division of Environmental Science and Ecological Engineering, Pohang University and Science and Technology, Pohang, South Korea, [5] OJEong Resilience Institute, Korea University, Seoul, South Korea, [6] Research Unit of Cryogenic Novel Materia, Korea Polar Research Institute, Incheon, South Korea

The role of sea ice melting on the air-sea CO_2 flux was investigated at two ice camps in the East Siberian Sea of the Arctic Ocean. On average, sea ice samples from the two ice camps had a total alkalinity (TA) of ~108 and ~31 μmol kg^{-1} and a corresponding salinity of 1.39 and 0.36, respectively. A portion (18–23% as an average) of these sea ice TA values was estimated to exist in the sea ice with zero salinity, which indicates the excess TA was likely attributed to chemical ($CaCO_3$ formation and dissolution) and biological processes in the sea ice. The dilution by sea ice melting could increase the oceanic CO_2 uptake to 11–12 mmol m^{-2} d^{-1} over the next 21 days if the mixed layer depth and sea ice thickness were assumed to be 18.5 and 1.5 m, respectively. This role can be further enhanced by adding TA (including excess TA) from sea ice melting, but a simultaneous release of dissolved inorganic carbon (DIC) counteracts the effect of TA supply. In our study region, the additional impact of sea ice melting with close to unity TA:DIC ratio on air-sea CO_2 exchange was not significant.

Keywords: Arctic Ocean, East Siberian Sea, sea ice melting, ikaite, total alkalinity

OPEN ACCESS

Edited by:
Masao Ishii, Meteorological Research Institute (MRI), Japan

Reviewed by:
Kumiko Azetsu-Scott, Bedford Institute of Oceanography (BIO), Canada
Naohiro Kosugi, Meteorological Research Institute, Japan Meteorological Agency, Japan

****Correspondence:***
Tae-Wook Kim
kimtwk@korea.ac.kr

Specialty section:
This article was submitted to Ocean Observation, a section of the journal Frontiers in Marine Science

Received: *30 August 2021*
Accepted: *31 January 2022*
Published: *23 February 2022*

Citation:
Mo A, Yang EJ, Kang S-H, Kim D, Lee K, Ko YH, Kim K and Kim T-W (2022) Impact of Sea Ice Melting on Summer Air-Sea CO_2 Exchange in the East Siberian Sea. Front. Mar. Sci. 9:766810. doi: 10.3389/fmars.2022.766810

INTRODUCTION

The carbon dioxide concentration in the atmosphere has increased from ~280 ppm in the preindustrial era to the current ~410 ppm due to human activities, such as the use of fossil fuels, cement production, and land-use changes (Le Quéré et al., 2018). During this period of increasing atmospheric CO_2, more than a third of anthropogenic CO_2 has been absorbed by the ocean through the air-sea gas exchange (Sabine et al., 2004; Gruber et al., 2009, 2019). Specifically, it has been suggested that marginal seas bordering continents contribute disproportionately to storing anthropogenic CO_2 despite their small spatial coverage (~7%) (Cai et al., 2006; Chen and Borges, 2009; Lee et al., 2011). As of 2005, the Arctic Ocean had absorbed 2.5–3.5 Pg C of anthropogenic CO_2 (Tanhua et al., 2009), which is twice the amount expected for the area it covers. The absorption of CO_2 by the Arctic Ocean may be further enhanced by increasing surface area exposed to the atmosphere and reduced surface partial pressure of CO_2 (pCO_2) caused by mixing with ice melt waters (Bates et al., 2006; Sejr et al., 2011). However, opposing results were also reported (Cai et al., 2010; DeGrandpre et al., 2020). Oceanic CO_2 uptake can be suppressed

as a result of increasing temperature and decreasing nutrient availability, which reduces CO_2 solubility and biological CO_2 uptake, respectively (Cai et al., 2010; Land et al., 2013). According to the Intergovernmental Panel on Climate Change, sea ice coverage in September will be reduced by ∼50% in Representative Concentration Pathways (RCP) 2.6 scenario and by almost 100% in RCP8.5 scenario compared to observational sea ice extent from 1986 to 2005 (Pörtner et al., 2019). Based on the 2°C warming scenario, Niederdrenk and Notz (2018) suggested a ∼20% reduction of the sea ice extent in March and a ∼15% chance of near ice-free conditions during summer months by the end of this century. In this future scenario, contrary to the impact of the increasing ice-free surface on the air-sea CO_2 flux, Arctic Ocean warming will reduce the seawater solubility of CO_2 and may be capable of weakening the CO_2 absorption processes involved in the annual cycle of sea ice formation and melting (Manizza et al., 2013; Ouyang et al., 2020). The latter effect explained below is the main focus of this study.

Arctic sea ice begins to form during the fall season. During sea ice formation, impurities such as salt, gasses, and particles are partly rejected to the underlying seawater and partly trapped within the sea ice structure. As sea ice cools down and brine partly freezes, the salinity of the brine remaining in the brine pocket increases, causing a buildup of dissolved inorganic carbon (DIC) and total alkalinity (TA). In addition, the contraction of the brine volume in sea ice caused by low temperatures can make sea ice effectively impermeable to brine transport (Golden et al., 2007). Along with these processes, the crystallization of calcium carbonate minerals (Ikaite: $CaCO_3{\cdot}6H_2O$) can be facilitated in the sea ice (Papadimitriou et al., 2004; Dieckmann et al., 2008, 2010; Geilfus et al., 2013; Rysgaard et al., 2014; Obbard et al., 2016; Petrich and Eicken, 2017). As pCO_2 increases in response to $CaCO_3$ precipitation, the CO_2 efflux from the sea ice to the atmosphere is enhanced during the fall season when sea ice is formed (Geilfus et al., 2013). However, brine rejection during sea ice formation causes an increase in salinity (and density) of the surrounding seawater, and thus facilitates the sinking of surface water, sequestrating CO_2 at greater depths (Miller et al., 2011; König et al., 2018). During the melting season, the CO_2 flux from the atmosphere to the sea ice and seawater becomes dominant. In the sea ice, pCO_2 of the brine decrease due to the dissolution of $CaCO_3$ crystals and a dilution by snow and sea ice melt water with low DIC (Geilfus et al., 2012, 2015; Lannuzel et al., 2020). Furthermore, as water from sea ice melting is released at the ocean surface, DIC and pCO_2 in the seawater decrease, thereby increasing the uptake of CO_2 from the atmosphere to the ocean. $CaCO_3$ crystals are also released at the ocean surface during sea ice melting, supplying an excess TA that is not explained by a conservative linear relationship between salinity and TA (Nedashkovsky et al., 2009; Geilfus et al., 2012; Rysgaard et al., 2012; Chen et al., 2015). Geilfus et al. (2016) performed a sea ice-seawater mesocosm experiment to show the effect of $CaCO_3$ crystal export on water column carbonate chemistry during sea ice growth and degradation. The presence of $CaCO_3$-induced TA was reported more than 30 years ago in both Arctic and Antarctic seawaters (e.g., Jones et al., 1983; Chen, 1985). The brine rejection and $CaCO_3$ production involved in the seasonal waning and waxing of sea ice may serve as a natural CO_2 pump in polar regions (Rysgaard et al., 2007). However, the impact of these processes has not been fully explored despite increasing efforts to include inorganic carbon dynamics related to sea ice (e.g., Moreau et al., 2015, 2016; Fransson et al., 2017; DeGrandpre et al., 2019).

The East Siberian Sea (ESS) is one of the least studied subregions in the Arctic Ocean, although this region is experiencing the most rapid change in sea ice coverage, which could be partially attributed to recent Siberian heatwaves (Stroeve et al., 2012; Krumpen et al., 2019; Overland and Wang, 2020; Wang et al., 2020). In this perspective, we aim to quantify the effect of sea ice melting on the summertime CO_2 absorption capacity of the ESS, dependent on the degree of freshening and TA/DIC concentration and ratio of the sea ice. Following Chen (1985) and Nomura et al. (2013a), we also evaluated excess TA of sea ice, including the possible contribution of $CaCO_3$ using a conservative linear mixing relationship between salinity and TA, which only requires analytical systems for salinity and TA that are more easily accessible to research groups (e.g., chemical oceanographers) investigating this issue.

MATERIALS AND METHODS

This study was performed in August 2017 as part of the Arctic Cruise program (ARA08B) of the Korea Polar Research Institute, using the icebreaker ARAON. Two ice camps were established for sampling sea ice cores, snow, and melt pond water. The first ice camp sampling (IC1) was conducted on 13 August and the second (IC2) on 16 August (**Figure 1**). IC1 and IC2 were located at 77°35.8552′N, 179°19.4508′E and 75°22.0475′N, 176°14.0973′E, respectively, and were predicted to be covered by 1st-year ice (**Figure 1C**, obtained from the National Snow and Ice Data Center). Four sea ice cores were obtained from IC1, and three sea ice cores and five melt pond water samples were collected from IC2. One snow sample covering the sea ice core sites was collected from both ice camps. The sea ice cores had a diameter of 9 cm and were extracted using a MARK II coring system (Kovacs Enterprises, Roseburg, OR, United States) and stored in polyethylene (PE) bags at −20°C. All sea ice samples were transported to the laboratory for analyses of TA and DIC after the cruise (October, 2017). Melt ponds were not found at IC1, however, melt pond water was sampled at IC2 using a peristaltic pump. Samples were stored in 500 mL borosilicate bottles and immediately mixed with a 200 μL saturated mercury (II) chloride ($HgCl_2$) solution.

In the laboratory (January, 2018), the sea ice cores were cut into 20 cm-long segments, transferred to commercially available low-density polyethylene (LDPE) bags and then mixed with the saturated $HgCl_2$ solution in proportion to sea ice sample weight (0.04% by sample volume) to prevent biological activity. The LDPE bags were twice sealed with a vacuum sealer (FM-06, Eiffel, Seoul, South Korea) and a Nylon/polyethylene bag. The samples stored in gas-tight laminated plastic bags and the Nylon/polyethylene bag presented indistinguishable DIC concentrations (Hu et al., 2018). It was also shown that the use

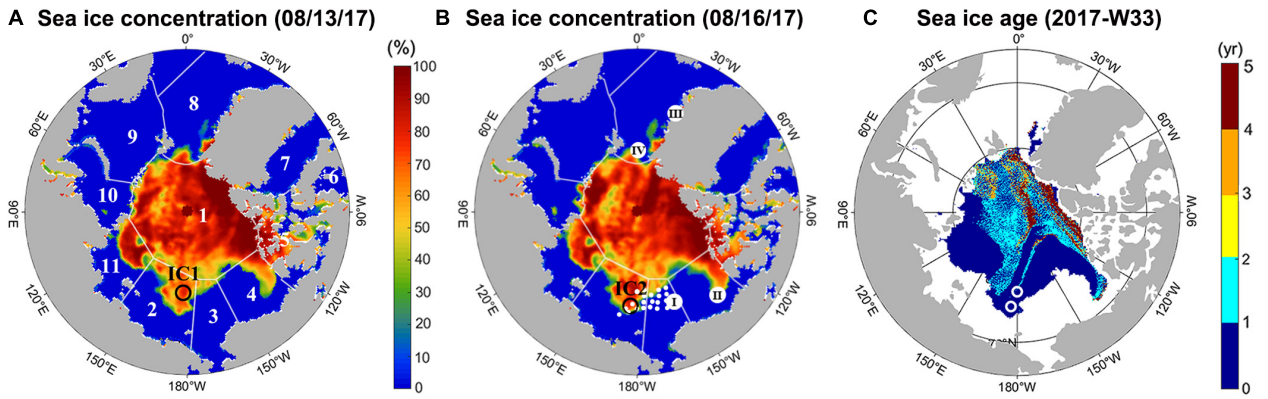

FIGURE 1 | Sea ice concentration of the Arctic Ocean on **(A)** 13 August 2017, and **(B)** 16 August 2017. Color shading indicates the percentage of sea ice obtained from the National Snow and Ice Data Center (NSIDC; Maslanik and Stroeve, 1999). **(A)** Location of the first ice camp (IC1; open circle) and the Sea Ice Index regions of the Arctic Ocean (numbers), corresponding to (1) Central Arctic, (2) East Siberian Sea, (3) Chukchi Sea, (4) Beaufort Sea, (5) Canadian Archipelago, (6) Hudson, (7) Baffin, (8) Greenland Sea, (9) Barents Sea, (10) Kara Sea, and (11) Laptev Sea. Data for the Sea Ice Index regions were taken from Meier et al. (2007). **(B)** Location of the second ice camp (IC2; open circle) and seawater sampling stations (closed circle). Roman numerals represent the locations of previous studies investigating the impact of sea ice melting on air-sea exchange of CO_2: (I) Cai et al. (2010), (II) Else et al. (2013), (III) Rysgaard et al. (2013), and (IV) Rysgaard et al. (2012). **(C)** Sea ice age in the 33rd week (08/14 to 08/20) of 2017, obtained from the NSIDC (Tschudi et al., 2019). The locations of the two ice camps are also shown (white circles).

of the Nylon/polyethylene bags and the vacuum sealer caused no significant changes in the properties of seawater samples (Hu et al., 2018). After the sea ice and snow samples were completely melted, meltwater samples were slowly transferred to 500 mL borosilicate bottles to prevent the formation of bubbles. The DIC in the transferred samples (DIC_{ICE}) was measured *via* coulometric titration using a Versatile Instrument for the Determination of Titration Alkalinity (VINDTA 3C, Marianda, Kiel, Germany) at room temperature.

Because of very low salinity (<3) and TA values (<220 μmol kg^{-1}), the sea ice samples were mixed with various volumes of $HgCl_2$-poisoned seawater collected in the East Sea (Sea of Japan) (salinity of 32 and TA of 2100 ± 2 μmol kg^{-1}), and the TA of the mixture (TA_{MIX}) was measured by potentiometric titration (Millero et al., 1993) using a VINDTA 3C instrument. The mixing (thus increasing salinity of samples) might reduce any potential problem caused by the difference in ionic strength in the TA samples and seawater certified reference material (CRM; prepared and distributed by Andrew Dickson, Scripps Institution of Oceanography) used to calibrate our analysis system. To validate this dilution method for TA measurement, we measured the TA value of the diluted seawater sample using CRM. In the salinity range of 15–32, measured TA values were consistent with the calculated TA values using a mixing ratio between CRM and deionized water (**Supplementary Table 1**). Prior to mixing, the ice meltwater sample and the seawater were, respectively filtered with syringe filter units of 0.45-μm pore size (ADVANTEC, 25HP045AN, Tokyo, Japan) and glass microfiber filters (GF/F; Whatman) at room temperature for the removal of phytoplankton and bacteria contribution on TA (Kim et al., 2006). It is noted that both ice meltwater and seawater are undersaturated with respect to ikaite at room temperature due to the high solubility of ikaite (Bischoff et al., 1993). Each empty borosilicate bottle was weighed, which was followed by weighing the bottle containing the seawater and the bottle containing the seawater and the sample. Based on weight changes, the mixing ratios of the sample and seawater were accurately determined. The salinity values of the seawater (S_{SW}) were measured using a portable salinometer (8410A), while a portable conductivity meter (Orion Star A222) was used to determine the salinity of the sea ice meltwater (S_{ICE}), snow (S_{SN}), and melt pond water (S_{MP}). All salinity values were reported as practical salinity unit in this study, and thus unit was not indicated. The salinity values (S_{MIX}) of the sample mixtures were determined based on the corresponding mixing ratios. Finally, a linear S_{MIX}-TA_{MIX} relationship was established for each sea ice segment sample and used to determine a TA value in the corresponding sea ice sample (i.e., TA_{ICE}) in combination with S_{ICE}. Confidence intervals at the 95% significance level for these TA measurements were determined from the uncertainties of the linear regressions.

Routine analyses using CRM ensured that the analytical precision for the DIC and TA measurements was approximately 1 and 2 μmol kg^{-1}, respectively. The DIC and TA of snow (DIC_{SN} and TA_{SN}, respectively) and melt pond water (DIC_{MP} and TA_{MP}, respectively) samples were determined using identical procedures as described above. Initial seawater conditions, which were required to examine the effect of sea ice melting on the air-sea CO_2 flux, were ascertained from the mean DIC and TA values of surface seawater samples taken between the latitudes 75 and 77°N (collection locations shown in **Figures 1A,B**). The seawater DIC and TA measurements were also done using the VINDTA 3C. Seawater pH was measured by a spectrophotometric method to evaluate a possible contribution of organic alkalinity to our results (Clayton and Byrne, 1993; Ko et al., 2016). We used the CO2SYS program (CO2SYS Excel Macro version 2.3, Lewis and Wallace, 1998) to calculate pCO_2 from the measured TA and DIC using measured sea surface temperature, and TA from the measured pH and DIC at the room temperature (**Table 1**),

TABLE 1 | Comparisons with the previous studies in polar regions.

Location	Latitude	Longitude	Season and date (DD/MM/YY)	S_{ICE}	Air temp.	SST	TA_{ICE}	DIC_{ICE}	Ikaite (μmol kg^{-1})		pCO_{2ICE}	Potential CO_2 flux*	References
				PSU	°C	°C	μmol kg^{-1}	μmol kg^{-1}	Min.	Max.	μatm	mmol m^{-2} d^{-1}	
East Siberian Sea	75.4~77.6°N	176.2~179.3°E	Summer (13/08/17 and 16/08/17)	0.05~2.88	−3~0	−1.5~0	3~220	16~209	>4 (IC2)	>10 (IC1)	0.6~4.2	11~12	This study
Fram strait	80~81°N	2~5°E	Summer (22/06/10 to 30/06/10)	0.2~6	0	0	210~680	80~435	81	121	0.2~0.5	10.6	Rysgaard et al. (2012)
East Antarctic	64~66°S	116~128°E	Austral spring (11/09/07 to 07/10/07	2~18	−20.1~−6.9	−1.8~−1.6**	–	–	1	47	–	–	Fischer et al. (2013)
Barrow, Alaska	71.2°N	156.5°W	Spring (06/04/09)	11.2~31.5	−14.2	−0.5**	492~863	418~488	15	25	–	–	Geilfus et al. (2013)
Svalbard	80~81°N	15~19°E	Spring (27/04/11 to 11/05/11)	0~7.1	−12.8~0.3	−0.7~0.7**	306~1239	–	27	54	–	–	Nomura et al. (2013a)
Eastern Greenland	74°N	20°W	Winter (Early 03/12)	4~12	−25~−20	1.4~2.8**	380~800	>250~600	100	900	<15	5.9	Rysgaard et al. (2013)

*Potential CO_2 flux was calculated under the assumption that the sea ice was completely melted and mixed with seawater in the MLD (20 m). Positive value means value indicates ocean uptake. ** Sea surface temperature (SST) values were not reported. Instead climatological values were provided from the NOAA High Resolution SST data produced by the NOAA/OAR/ESRL PSL, Boulder, Colorado, United States (https://psl.noaa.gov/data). Our estimate represents a lower limit of total ikaite in sea ice. It is a note that ikaite concentration is a half of TA_{EX} in our study because 1 mole of $CaCO_3$ equals 2 moles of TA.

the carbonate dissociation constants of Mehrbach et al. (1973) (the equations refitted by Dickson and Millero, 1987) and other ancillary thermodynamic constants tabulated in Millero (1995). We also used the boron to chlorinity ratio of Lee et al. (2010). This set of thermodynamic constants yielded the agreement (comparable to analytical precision; ∼2 μmol kg^{-1}) between measured CRM TA and calculated value from measured pH and DIC value of CRM, as previously demonstrated in a range of laboratory and field studies (McElligott et al., 1998; Lueker et al., 2000; Millero et al., 2006).

Finally, air-sea CO_2 flux (F) was estimated from an air-sea difference in pCO_2 (ΔpCO_2 = atmospheric pCO_2 − seawater pCO_2) and the following equation,

$$F = k \times K_0 \times \Delta pCO_2 \quad (1)$$

where, k represents the gas transfer velocity determined from Wanninkhof (2014), and K_0 is the solubility coefficient in seawater for CO_2 (Weiss, 1974). We used 400 μatm for the atmospheric pCO_2, which was reported in Barrow, Alaska (71.3 °N, 156.6 °W) by the Scripps CO_2 program.[1] The mixed layer depth used in this study was provided from the Monthly Isopycnal and Mixed-layer Ocean Climatology data (Schmidtko et al., 2013).

RESULTS AND DISCUSSION

Total Alkalinity and Dissolved Inorganic Carbon in the Ice Camp Samples and Factors Affecting Them

The average lengths (±1 standard deviation) of the sea ice cores were 110.3 (±35.9) cm at IC1, and 128.3 (±9.1) cm at IC2. At IC1, S_{ICE} ranged from 0.16 to 2.88, and TA_{ICE} and DIC_{ICE} ranged from 27 to 219 μmol kg^{-1} and from 25 to 209 μmol kg^{-1}, respectively (**Figures 2A–D**). In general, S_{ICE}, TA_{ICE}, and DIC_{ICE} increased with depth at IC1. A similar profile was reported in the sea ice samples collected in the Beaufort Sea at the beginning of summer (Scharien et al., 2010). At IC2, the top (shallower than 30 cm) ice layer of two samples had higher values of S_{ICE}, TA_{ICE} and DIC_{ICE} relative to the middle layer (**Figures 2E,F**). However, in common with IC1, the bottom (deeper than 50 cm) ice layer has the highest values of S_{ICE}, TA_{ICE}, and DIC_{ICE} in all samples at IC2. In addition, the salinity profile shown in Fransson et al. (2013) was similar to our results (**Figure 2F**). The overall values of these components were lower in IC2, with S_{ICE} in the range 0.05–1.23 and TA_{ICE} and DIC_{ICE} in the ranges of 3–87 and 16–77 μmol kg^{-1}, respectively. As expected, the primary factor controlling TA_{ICE} and DIC_{ICE} were salinity-related changes such as concentration and dilution during sea ice formation and degradation, respectively, which may be affected by weather conditions (e.g., air temperature above seas). In the snow and melt pond water, the TA and DIC distributions also increased with increasing salinity. The estimated TA_{SN} and DIC_{SN} values (± 95% confidence intervals) were -4 ± 4 and 17 ± 0 μmol kg^{-1}

[1]http://scrippsco2.ucsd.edu

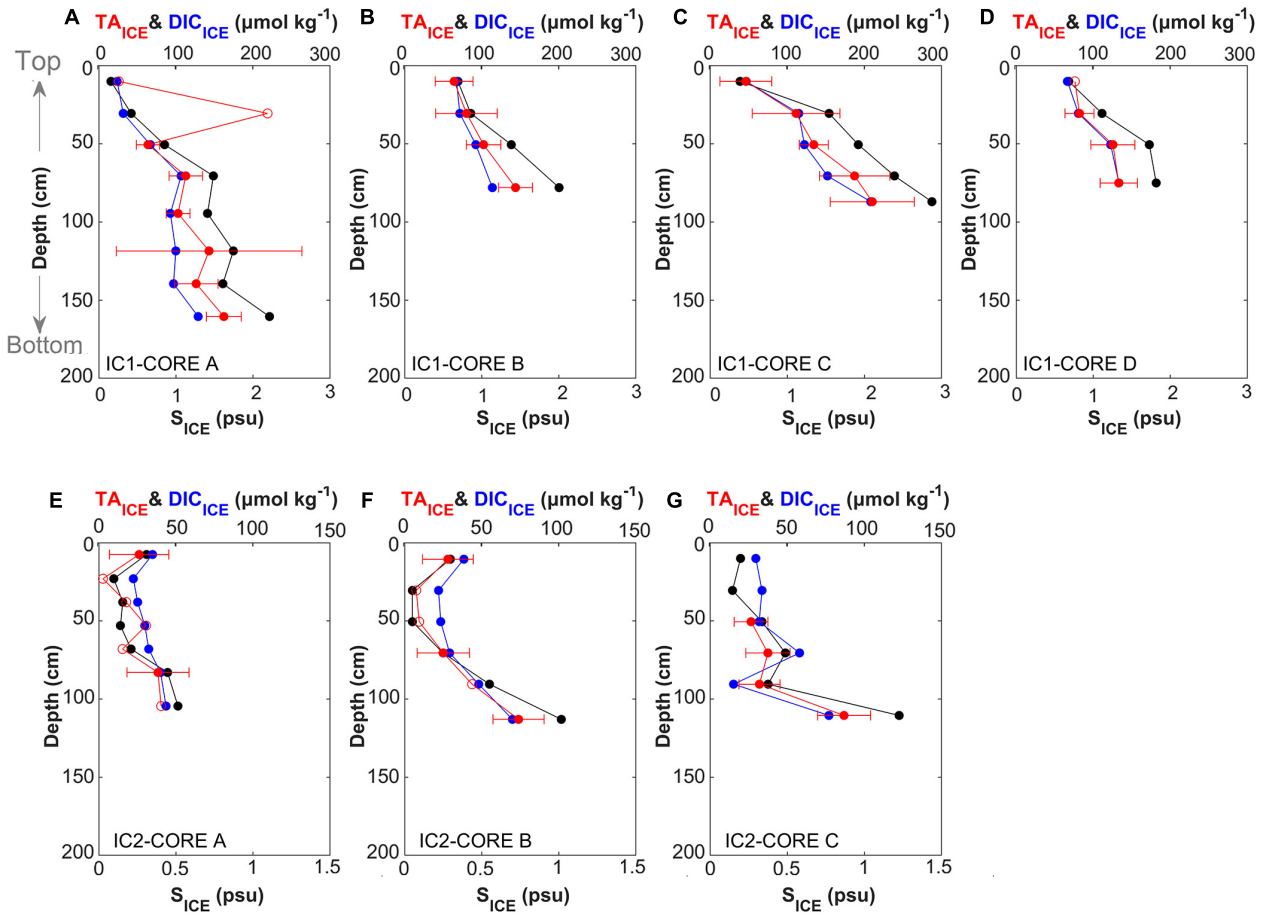

FIGURE 2 | Vertical distributions of salinity (S_{ICE}; black, *x*-axis on the bottom of each panel), dissolved inorganic carbon (DIC_{ICE}; blue, *x*-axis on the top of each panel), and total alkalinity (TA_{ICE}; red, *x*-axis on the top of each panel) with a 95% confidence interval. **(A–D)** represent results for Ice Camp 1 (IC1) and **(E–G)** for Ice Camp 2 (IC2). The TA_{ICE} values shown with an open circle were statistically insignificant at a 95% confidence interval.

at IC1, and 0 ± 4 and 18 ± 1 μmol kg^{-1} at IC2, respectively. The negative TA value of the snow sample may be attributed to acid (e.g., SO_4^{-2} and NO_3^-) deposition (Björkman et al., 2013; Macdonald et al., 2017).

The concentrations of S_{ICE}, TA_{ICE}, and DIC_{ICE} were lower at IC2 than at IC1 (**Figure 1A**), indicating that the volume of sea ice melting at IC2 was comparatively greater. These observations are also consistent with the formation of melt pond only at IC2. For the melt pond water, TA_{MP} and DIC_{MP} were in the ranges of 17–88 and 40–91 μmol kg^{-1}, respectively. S_{SN} (∼0.013) was found to be much lower than S_{MP} (0.20–0.95). Thus the melt ponds appear to be significantly affected by sea ice melting. However, additional evidence such as oxygen isotope is required to confirm source waters for melt pond. The sea ice meltwater likely diluted or washed out the salts from the sea ice (Fransson et al., 2011; Geilfus et al., 2015; Kotovitch et al., 2016), and TA and DIC accumulated at the boundary regions between the ice crystals. Fresh water is released as sea ice melts, and air gaps emerge inside the sea ice, increasing permeability and the air-ice gas exchange flow (Cox and Weeks, 1983). Enhanced permeability may partially compensate for such a loss in DIC, which could explain the occurrence of some sea ice samples with DIC_{ICE}:TA_{ICE} > 1 (**Figures 2E–G**). Previously, a laboratory sea ice chamber experiment reported an air-to-ice CO_2 flux during ice melt (Kotovitch et al., 2016).

Excess Total Alkalinity in Sea Ice

The regression equations between TA_{ICE} and S_{ICE} for both IC1 and IC2 show non-zero intercepts of 19 ± 8 μmol kg^{-1} (R^2 = 0.98, p < 0.005) and 7 ± 4 μmol kg^{-1} (R^2 = 0.95, p < 0.005), respectively (**Figures 3A,B**). These excess TA values at S = 0 (TA_{EX}) indicate that the sea ice samples were influenced by a process that shifted a conservative TA-S mixing line upward. We attribute the positive intercepts to the contribution of $CaCO_3$ (TA_{CC}) in the sea ice (i.e., TA_{EX} formed by TA_{CC}). However, an alternative explanation is the contribution of freshwater containing TA, as studies have reported that rivers discharging into the Arctic Ocean have an average TA of ∼1000 μmol kg^{-1} (Cooper et al., 2008). Pipko et al. (2011) reported lower values for the ESS (∼470 and ∼850 μmol kg^{-1} from the Kolyma and Lena rivers, respectively). We, therefore, tested the possibility that riverine TA produced the TA_{EX} in our sea ice samples. We

first assumed that the proportion of all chemical species rejected during the formation of sea ice was the same as that in seawater with no $CaCO_3$ precipitation. In other words, the TA value of any sea ice should fall on a linear relationship between two points representing pure ice (i.e., $S_{ICE} = 0$ and $TA_{ICE} = 0$ μmol kg^{-1}) and the source seawater that froze to generate the sampled sea ice (**Figure 3C**).

Two seawater endmembers were considered to investigate the effect of riverine water on our TA_{EX}: Pacific Winter Water in the Chukchi Sea (S = 32.99 and TA = 2269 μmol kg^{-1}; Qi et al., 2017) and the same seawater but diluted by 10% with river water (S = 0 and TA = 1048 μmol kg^{-1}). The 10% contribution of river waters was chosen based on Jung et al. (2021) conducted in the same cruise. Three points, including zero salinity and TA values, form a triangle zone between the two lines shown in **Figure 3C**. In principle, any data falling above this zone (or above the upper line; **Figures 3A,B**) cannot be explained by riverine TA only, and must include the effect of sea ice TA_{EX}. Thus almost all data with $S_{ICE} < 1$ could support the presence of TA_{EX} (formed by ikaite) in sea ice. The higher concentration of TA_{EX} in the upper layer is consistent with previous studies suggesting that ikaite concentration is related to the temperature of the sea ice (Fransson et al., 2013; Rysgaard et al., 2013, 2014). In contact with the cold atmosphere, the top of the sea ice is favorable (close or lower than freezing temperature) for ikaite precipitation (Bischoff et al., 1993), and a relatively large amount of ikaite can be preserved in summer (Nomura et al., 2013a). On the other hand, a lower concentration of ikaite in the middle and bottom layers suggested that ikaite was exported to underlying seawater in summer (Rysgaard et al., 2013). If no $CaCO_3$ precipitation was assumed to occur, any sea ice affected by a riverine contribution (<10%) should fall within the triangle zone with no exception. However, the converse is not always true. In other words, all the data located within the triangle zone were not only affected by riverine TA, allowing the contributions of other TA_{EX} sources to them. Therefore, it was required to assess the whole data together. If riverine TA was the only TA_{EX} source, the regression of all available data should approach a zero TA with decreasing salinity, as riverine TA (accumulated in the source seawater) mixed with sea ice meltwater with no TA_{EX}. To test this, we randomly selected the same number of data points within the same salinity ranges as IC1 and IC2, and calculated the intercept of the linear regression line. Repeated simulations (n = 50,000) showed that it was nearly impossible for the case of mixing with river water (<10%) to produce the observed TA_{EX} of 19 and 7 μmol kg^{-1} in IC1 and IC2, respectively (**Figures 3D,E**). The riverine TA could produce a TA_{EX} of ∼4 and ∼2 μmol kg^{-1} at IC1 and IC2 at best, respectively, which are values that lie within the uncertainties of our estimates.

Another factor capable of altering sea ice acid-base balance is organic acids (Yang et al., 2015; Ko et al., 2016), because high dissolved organic carbon concentrations (up to 600 μM) were reported in the Arctic sea ice (Thomas et al., 1995). However, according to the TA definition of Dickson (1981), organic acids with $pK_a \geq 4.5$ do not change TA because a dissociated conjugate base reacts with a proton of titrant, and thus cause no change in TA, whereas organic acids with $pK_a < 4.5$ reduce TA (Ko et al., 2016; Hu, 2020). The former is the same as the effect of CO_2 dissolution on TA. Therefore, our TA_{EX} estimates cannot be generated by organic bases originating from dissolved organic matter production or degradation of particulate organic matter. Rather, our results would be underestimated if there was a significant production of weak organic acids with $pK_a < 4.5$. As an exception, if the sea ice samples had precipitates consisting of metal ions and conjugate bases of organic acids with $pK_a \geq 4.5$, they would increase TA, whose effect is identical to that of $CaCO_3$ crystals (Hu, 2020). To our knowledge, such a precipitate was not reported in sea ice. Finally, phytoplankton uptake of nutrient increase TA. However, ocean climatology databases (World Ocean Atlas 2018 and Global Ocean Data Analysis Project version 2) showed depletions of NO_3^- in the surface layer of the study area (Garcia et al., 2019; Olsen et al., 2020).

Weak organic acids can introduce an error in calculating a carbonate variable from two measured ones (e.g., pCO_2 from TA and DIC), because organic acids proportionally change the contributions of other species (e.g., CO_3^{2-}, $B(OH)_4^-$) to TA (Ko et al., 2016). Thus we evaluated the effect of organic acids contained in Arctic seawater on the internal consistency among seawater carbonate parameters by comparing measured TA (TA_{MEAS}) and calculated one (TA_{CALC}) from measured pH and DIC. The difference ($\Delta TA_{M-C} = TA_{MEAS} - TA_{CALC}$) can be attributed to the effect of organic alkalinity (conjugate bases of weak acids) (e.g., Yang et al., 2015; Ko et al., 2016). The estimated ΔTA_{M-C} was ∼7 μmol kg^{-1} in seawaters, and thus the potential organic alkalinity contributions were estimated to be ∼0.3 and ∼0.1 μmol kg^{-1}, at IC1 and IC2, respectively, if taking into account a linear reduction of ΔTA_{M-C} with decreasing salinity. Thus we ignored the effect of organic alkalinity on estimating the impact of sea ice melting on air-sea exchange of CO_2 in the following section.

Previous studies showed that the ikaite concentration in sea ice samples varies considerably in time and space (Rysgaard et al., 2012, 2013; Fischer et al., 2013; Geilfus et al., 2013; Nomura et al., 2013a). Our estimates are much lower than most of those observed in previous studies (**Table 1**). It is a note that ikaite concentration is a half of TA_{EX} in our study because 1 mole of $CaCO_3$ equals 2 moles of TA. Factors affecting ikaite formation and dissolution include air and ice temperatures (controlling sea ice formation), salinity (affecting ion strength, crystal nucleation, and concentrations of CO_3^{2-} and Ca^{2+} ions), pH (affecting CO_3^{2-} concentration), CO_2 removal (by air-sea exchange or CO_2 assimilation; affecting pH and DIC), snow (affecting ice temperature), and other ion species (Mg^{2+}, PO_4^{3-}, and SO_4^{2-} as inhibitor or facilitator) (Papadimitriou et al., 2013, 2014; Rysgaard et al., 2013, 2014; Hu et al., 2014; Tollefsen et al., 2018). However, unfortunately, it was not possible to assess the effects of various ions, salts, and pH on the estimated ikaite concentrations of the previous studies (shown in **Table 1**), because temporal evolutions of these variables from winter to summer were not available. In general, previous estimates of higher ikaite concentration during winter than in summer indicate a seasonal reduction of ikaite concentration during the warming period (Rysgaard et al., 2013). Similarly, our summer sampling, and thus under conditions of enhanced

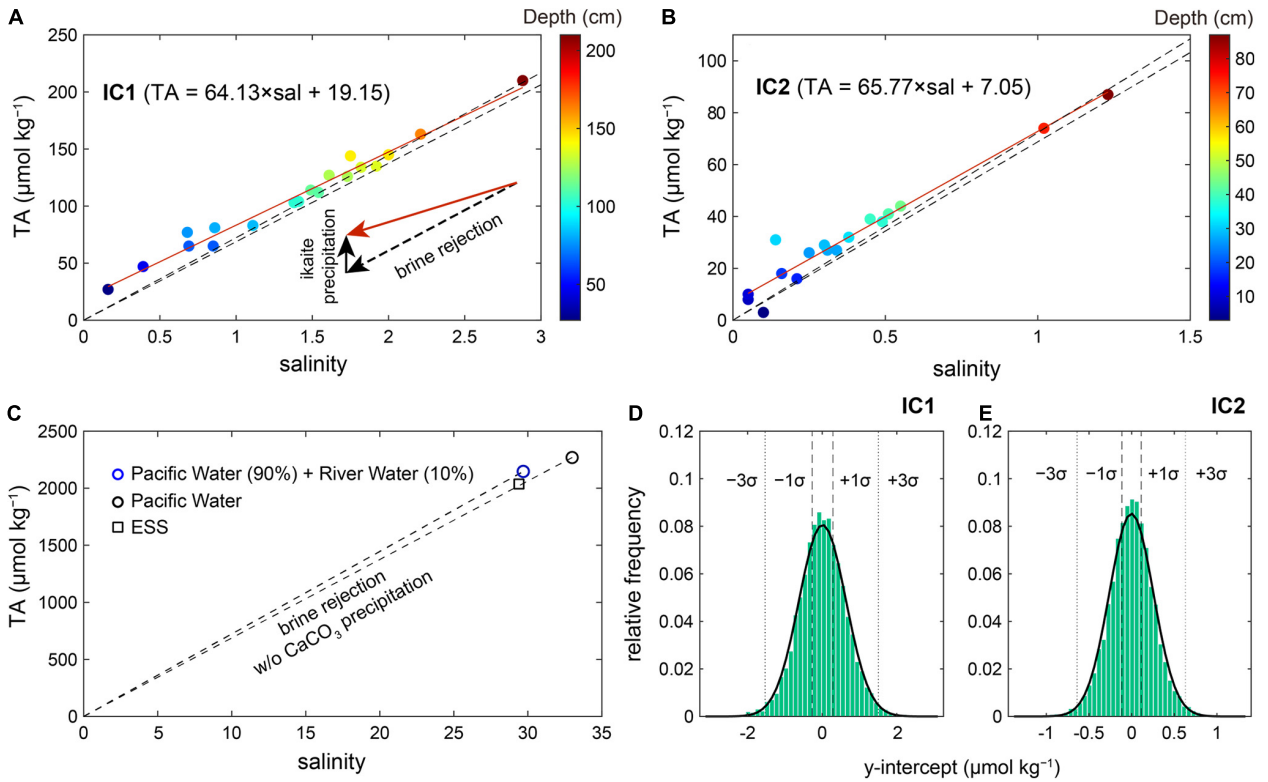

FIGURE 3 | Relationships between TA_{ICE} and S_{ICE} at IC1 **(A)** and IC2 **(B)**. Red lines indicate the linear regression lines. Positive intercepts suggest the existence of $CaCO_3$ crystals in sea ice samples. Color shading represents the depths for the sea ice segments. **(C)** Linear relationships representing conservative mixing between pure sea ice water (S = 0 and TA = 0 μmol kg^{-1}) and two seawater endmember values (open circles), with one representing Pacific Winter Water and the other representing the same seawater but diluted by 10% with river water with TA = 1048 μmol kg^{-1}. These lines are also shown in **(A,B)**. Note that S_{ICE} and TA_{ICE} in the winter season are likely to be located in the triangle (close to the bottom line) because river discharge in winter (67 km^3 $month^{-1}$) is ∼25% of summer (253 km^3 $month^{-1}$) in the Arctic Ocean (Holmes et al., 2012). In the winter, net community production, which can deviate the linear relationship between salinity and TA by raising TA, is limited by reduced solar radiation. The square symbol represents the mean seawater TA and S values in the East Siberian Sea (ESS). Probability distribution plots showing intercept values that could be produced from excess TA in river water with no $CaCO_3$ precipitation at IC1 **(D)** and IC2 **(E)**. An anomalously high TA_{ICE} value (=219 μmol kg^{-1}; **Figure 2A**) was excluded in this figure and calculating the linear regression. It is a note that including it increased the y-intercept (i.e., TA_{EX}).

sea ice degradation, was probably one of the factors accounting for the relatively low ikaite concentration observed in our study. In addition, ikaite could transform into calcite or vaterite when exposed to air at higher temperature (>10°C) (Sánchez-Pastor et al., 2016; Purgstaller et al., 2017). At room temperature, the transformation of ikaite in the melted sea ice sample could result in an underestimation of our calculated TA_{EX} if particulate calcite or vaterite were preserved and filtered. However, our sea ice meltwater with low salinity was undersaturated with respect to calcite (saturation state of calcite is <0.3), suggesting that the effect of transformation of ikaite was negligible on our TA_{EX} estimate.

Rysgaard et al. (2013) compared the TA-to-salinity (TA:S) ratios in sea ice and seawater. The TA:S ratios were greater in sea ice relative to those in the water column by ∼17 μmol kg^{-1} S^{-1} as TA (not ikaite). The same study also showed that ikaite concentrations measured by an image analysis technique fell within the same range of sea ice TA (i.e., TA_{ICE} = TA_{CC} and TA_{EX} < TA_{CC}), implying that a TA fraction (TA_{SAL}) explained by the conservative TA-salinity relationship existed as ikaite within their sea ice samples. Based on this result, it could be inferred that our approach attributing only TA_{EX} to ikaite could underestimate ikaite concentration in sea ice. If extrapolating the excess TA:S in sea ice of Rysgaard et al. (2013) to our study (i.e., assuming simultaneous removal of ikaite and solutes with decreasing salinity or increasing dilution by sea ice melt water), IC1 and IC2 with the mean salinity values of 1.39 and 0.36 could have the sea ice TA_{EX} of ∼27 and ∼6 μmol kg^{-1}, respectively, reducing the gap between Rysgaard et al. (2013) and our study. The effects of sea ice ikaite formation on air-sea exchange of CO_2 need to be separated because the effects of TA_{SAL} can be evaluated from the seawater TA-S relationship without an effort to measure ikaite.

Our TA_{EX} values are also substantially lower than estimates of 160–240 μmol kg^{-1} (ikaite contribution as TA) reported by Rysgaard et al. (2012), who sampled drifting ice floes in the Fram Strait during the summer of 2010. In addition, a study conducted in the Pacific sector in the Arctic Ocean suggested

large enhancements in seawater TA caused by dissolution of ikaite crystal in the marginal sea ice zone during summer (Chen et al., 2015), which was quantitatively consistent with the result of Rysgaard et al. (2012). However, an assumption that Rysgaard et al. (2012) made to estimate ikaite tended to overestimate ikaite concentration. They calculated ikaite concentration from the difference between TA and DIC in sea ice, although DIC is not a conservative parameter due to gas exchange and biological processes. In fact, Moreau et al. (2015) suggested that a TA:DIC ratio of ∼2 in sea ice could be caused by outgassing. If comparing the TA:S ratio in sea ice and seawater of Rysgaard et al. (2012), their sea ice samples had the sea ice TA_{EX} of ∼107 μmol kg^{-1} at salinity of 3.9, which could be further reduced to 15–55 μmol kg^{-1} when normalizing to our sea ice salinity values. Nomura et al. (2013a) measured TA after filtering sea ice meltwaters to remove ikaite crystal, and then estimated a loss of TA relative to salinity. Their result represents only TA_{SAL} in sea ice, thus underestimating total ikaite concentration. Overall, our TA_{EX} could not represent the whole ikaite concentration in sea ice despite a TA_{EX} production due to ikaite formation, but instead should be used to separate the effects of sea ice melting on seawater carbonate chemistry that is not explained by sea ice salinity. Combining our approach and that of Nomura et al. (2013a) can reveal both TA_{EX} and TA_{SAL} in sea ice, and thus total ikaite concentration.

Impact of Sea Ice Melting on Air-Sea Exchange of CO_2

Based on the characteristics of the sea ice samples, we examined the impact of sea ice melting by calculating the potential uptake of atmospheric CO_2 in the MLD of the ESS (**Table 2**). The ESS MLD was assumed to be ∼20 m in the study area in summer (Schmidtko et al., 2013) with an average thickness of sea ice of ∼1.5 m (Global Ice-Ocean Modeling and Assimilation System; Zhang and Rothrock, 2003). Daily air-sea CO_2 flux was estimated from the equation (1), and the required gas transfer velocity (k) was calculated using the mean wind speed of ∼7.0 m s^{-1} (measured during the survey) following the suggestion of Wanninkhof (2014). The enhancement in the total carbon content due to air-sea CO_2 exchange was calculated under the assumption that the sea ice located in the marginal ice zone was completely melted and mixed with seawater in the MLD. We also assumed that the pCO_2 of the seawater returned to an original condition (pCO_2^{iSW}) through the air-sea CO_2 exchange without considering further degradations of sea ice and biological processes in our study region. The original condition corresponded to approximately pCO_2 of 309 μatm determined based on our observations (TA^{iSW} = 2037 μmol kg^{-1}, DIC^{iSW} = 1932 μmol kg^{-1}, S^{iSW} = 29.4, and T^{iSW} = 0°C; where iSW indicates "initial seawater condition") conducted during our survey period. The mean TA_{ICE} values were estimated from the linear TA_{ICE}-S_{ICE} relationship (**Figure 3**) and the mean salinity at the two ice camps (1.39 at IC1 and 0.36 at IC2). Sea ice (1.5 m) melting at IC1 (TA_{ICE} = 108 μmol kg^{-1}, TA_{EX} = 19 μmol kg^{-1}, and DIC_{ICE} = 97 μmol kg^{-1}) caused seawater (18.5 m) pCO_2 value to be reduced to ∼277 μatm. If TA_{EX} is excluded, the resulting pCO_2 is ∼280 μatm. In the case of IC2 (TA_{ICE} = 31 μmol kg^{-1}, TA_{EX} = 7 μmol kg^{-1}, and DIC_{ICE} = 25 μmol kg^{-1}), seawater pCO_2 was reduced to ∼276 μatm after sea ice melting (∼278 μatm without considering TA_{EX}). These estimated pCO_2 drops were twice that found in the Amundsen Gulf, Arctic Ocean during the spring season (Fransson et al., 2013).

In the 1st day after the complete melting and mixing in the MLD (20 m), the estimated CO_2 uptake from the atmosphere was ∼13 mmol m^{-2} d^{-1}, increasing pCO_2 and DIC concentration in the MLD by ∼1.7 μatm and ∼0.66 μmol kg^{-1}, respectively, at both IC1 and IC2 without a TA change. This approach was repeated every day until the pCO_2^{iSW} was recovered, which took approximately 21 days, giving the mean CO_2 uptake rate of 11–12 mmol m^{-2} d^{-1}. However, achieving air-sea equilibrium in this way was impossible because more than 200 days were required, during which sea conditions could significantly vary (Woosley and Millero, 2020). As a result, the total oceanic uptake of CO_2 was approximately 246 and 251 mmol m^{-2} for 21 days in IC1 and IC2 samples, respectively. Our estimate (11–12 mmol m^{-2} d^{-1}) is broadly consistent with those estimated from other field observations of TA and DIC in the ESS (−0.3 to 10.9 mmol m^{-2} d^{-1}, where a positive value indicates ocean uptake) (Nitishinsky et al., 2007; Semiletov et al., 2007; Bates and Mathis, 2009), and are also similar to the effect of sea ice melting (CO_2 uptake of 2.4–10.6 mmol m^{-2} d^{-1}) in other areas (Chukchi Sea, Beaufort Sea, and Greenland Sea) of the Arctic Ocean (**Figure 1**; Cai et al., 2010; Rysgaard et al., 2012, 2013; Else et al., 2013). In the Arctic Ocean the thickness of MLD was temporarily reduced to ∼2 m due to strong stratification by ice melted water (Woosley et al., 2017). If the sea ice (IC1) meltwater is confined to the 2 m of MLD, surface pCO_2 could be reduced to 56.9 μatm but equilibrated with atmospheric CO_2 in 7 days. Because of rapid rise of pCO_2 in the shallower MLD, oceanic CO_2 uptake rate (∼4.8 mmol m^{-2} d^{-1}) over 21 days was lower than our estimate for 20 m of MLD.

The impact of sea ice melting on the oceanic CO_2 absorption capacity is affected by the degree of freshening and the amount of TA_{ICE}, and TA_{ICE}:DIC_{ICE} ratio. In our study region, the increase in the CO_2 uptake was mainly due to the dilution-induced pCO_2 decrease (∼30 μatm) by sea ice melting (**Table 2** and **Supplementary Figure 1**). The release of TA_{ICE} did not reduce seawater pCO_2 due to the effect of DIC_{ICE} (TA_{ICE}:DIC_{ICE} = ∼1.1), which can offset the pCO_2 decrease. The exclusion of TA_{EX} also did not significantly change the mean flux rate and time required to recover the pCO_2^{iSW}. Our estimate for increased CO_2 uptake rate driven by sea ice melt was not significantly different from that (∼12 mmol m^{-2} d^{-1} or 250 mmol m^{-2} in total) expected from a mixture with pure sea ice meltwater (zero TA_{ICE}, DIC_{ICE}, and S_{ICE}). Because our sea ice samples were collected late summer, the CO_2 absorption of the partially degraded sea ice may have canceled out the effect of TA_{EX} by reducing TA_{ICE}:DIC_{ICE} ratio. If TA_{ICE} and DIC_{ICE} of IC1 sample are mainly controlled by $CaCO_3$ formation and dissolution without a contribution of air-ice CO_2 exchange (TA_{ICE}:DIC_{ICE} = ∼2; Rysgaard et al., 2012), the CO_2 uptake from the atmosphere would be ∼19 mmol m^{-2} d^{-1}.

TABLE 2 | Properties of source waters and estimated potential CO_2 uptake rate in the mixed layer depth of the ESS.

Type		Station	TA	DIC	S	pCO_2	Flux
			(μmol kg^{-1})			(μatm)	(mmol m^{-1} d^{-1})
Source properties	Seawater		2037	1932	29.4	309	
	Sea ice melt water	IC1	108	97	1.4	5	
	Sea ice melt water	IC2	31	25	0.4	1	
Potential CO_2 uptake	Dilution only		1884	1787	27.2	277	11.9
	Dilution + DIC_{ICE} + TA_{ICE}	IC1	1892	1794	27.3	277	11.7
		IC2	1887	1789	27.2	276	12.0
	Dilution + TA_{ICE}	IC1	1892	1787	27.3	260	18.8
		IC2	1887	1787	27.2	272	13.8
	Dilution + TA_{ICE} – TA_{EX}	IC1	1891	1787	27.3	263	17.5
		IC2	1886	1787	27.2	273	13.3

In addition, if applying the summertime TA_{ICE} concentration (~533 μmol kg^{-1}) and TA_{ICE}:DIC_{ICE} ratio (~2) of Rysgaard et al. (2012) to our study region, the seawater pCO_2 could be reduced to ~241 μatm, thereby increasing CO_2 uptake to ~27 mmol m^{-2} d^{-1}.

Finally, based on the TA_{MP} and DIC_{MP} values determined at the sites, a pCO_2 of 234 ± 146 μatm (average ± 1 standard deviation) was expected in the melt pond water with a temperature of ~0°C. Previous studies suggested the CO_2 uptake from the atmosphere to melt pond water ranged from 0.13 to 38.6 mmol m^{-2} d^{-1} from spring to summer (Nomura et al., 2010, 2013b; Geilfus et al., 2012, 2015). As the melt ponds appear to be affected by sea ice melting, the absorption of CO_2 by the melt pond water should be included when assessing the role of sea ice melting on atmospheric CO_2 sequestration. In fact, a study estimated 5–15% contribution of melt ponds to Arctic Ocean CO_2 uptake (Geilfus et al., 2015). However, in this study, the data were insufficient to extrapolate, and we note the importance of investigating the role of melt ponds in future studies. Melt ponds in the Canada Bain and the Chuckchi Sea shelf showed the pCO_2 ranges of 36–381 and 139–625 μatm, respectively (Bates et al., 2014; Geilfus et al., 2015). The broad pCO_2 ranges found in three regions imply a large variation in time and space, and inconsistent sampling timing after melt water formation should be taken into account to properly assess the CO_2 absorptions by melt ponds (Geilfus et al., 2015).

CONCLUSION

We evaluated variations in the total carbon content due to sea ice melting and estimated the corresponding enhancements of the air-to-sea CO_2 flux in the East Siberian Sea. Of the two ice camps, IC2 was located at the edge of the sea ice, and thus the loss of sea ice meltwater and brine was greater than at IC1, resulting in a TA_{ICE} value four times higher at IC1 (~108 μmol kg^{-1}) than at IC2 (TA_{ICE} = ~31 μmol kg^{-1}). Moreover, the large positive intercepts in the S_{ICE}-TA_{ICE} regression could be attributed to ikaite remained in summer sea ice. The enhancements in the CO_2 uptake by sea ice melting were mainly due to the dilution (release of meltwater containing a low level of DIC), and the effect of the TA_{ICE} release (reducing pCO_2) was largely canceled out by DIC_{ICE}. Our sea ice samples showed relatively low salinity and TA_{ICE} compared to those in other regions. The regional difference might be caused by variations in environmental factors affecting sea ice and ikaite formations to some extent. In addition, the difference in methods used to determine sea ice ikaite might prevent a direct comparison among the past studies. The potential air-sea CO_2 flux determined in our study (i.e., ESS in summer) was similar to or slightly higher than those reported in other regions (**Table 1**).

Climate change-induced changes in environmental condition during sea ice formation and degradation may alter physical and chemical properties of sea ice including $CaCO_3$ formation. In addition, current understanding of sea ice carbon parameters is not sufficient to fully address its effects on ocean biogeochemistry despite the previous efforts made a decade ago (Rysgaard et al., 2012; Fischer et al., 2013; Geilfus et al., 2013). Therefore, it appears that continued monitoring studies are required. Nonetheless, to our knowledge, there was no previous sea ice TA data to compare with our results in the East Siberian Sea. Given large spatiotemporal variations in the Atlantic sector of the Arctic Ocean, further studies on this issue should be followed in the Pacific sector using various complementary methods for the determination of sea ice ikaite. It might also be needed to separate the ikaite effect on seawater inorganic chemistry into TA_{EX} and TA_{SAL} because the latter can be assessed easily by sea ice salinity. In parallel, to determine factors affecting the large variations in ikaite concentrations, laboratory experiments on ikaite formation and degradation should also be conducted in the conditions representing changing physical and biogeochemical environments in the Arctic Ocean.

DATA AVAILABILITY STATEMENT

The datasets presented in this study can be found in online repositories: (https://kpdc.kopri.re.kr) Korea Polar Data Center

Entry ID: KOPRI-KPDC-00001430 and https://dx.doi.org/10.22663/KOPRI-KPDC-00001430.1.

AUTHOR CONTRIBUTIONS

AM analyzed the data and wrote the original draft. All authors discussed the results and contributed to the writing the manuscript.

FUNDING

This work was supported by the Polar Academic Program (PE17900) funded by the Korea Polar Research Institute, and the project titled "Korea-Arctic Ocean Warming and Response of Ecosystem (K-AWARE)," the Korea Polar Research Institute (KOPRI) 1525011760, funded by the Ministry of Oceans and Fisheries, South Korea. KL was supported by National Research Foundation of Korea (NRF-2021R1A2C3008748).

ACKNOWLEDGMENTS

We thank all researchers and funding agencies. Also, we would like to thank the R/V Araon crews. This work was not possible without their valuable contribution to the collection of samples.

SUPPLEMENTARY MATERIAL

The Supplementary Material for this article can be found online at: https://www.frontiersin.org/articles/10.3389/fmars.2022.766810/full#supplementary-material

REFERENCES

Bates, N. R., and Mathis, J. T. (2009). The Arctic Ocean marine carbon cycle: evaluation of air-sea CO_2 exchanges, ocean acidification impacts and potential feedbacks. *Biogeosciences* 6, 2433–2459. doi: 10.5194/bg-6-2433-2009

Bates, N. R., Garley, R., Frey, K. E., Shake, K. L., and Mathis, J. T. (2014). Sea-ice melt CO_2-carbonate chemistry in the western Arctic Ocean: meltwater contributions to air-sea CO_2 gas exchange, mixed-layer properties and rates of net community production under sea ice. *Biogeosciences* 11, 6769–6789. doi: 10.5194/bg-11-6769-2014

Bates, N. R., Moran, S. B., Hansell, D. A., and Mathis, J. T. (2006). An increasing CO_2 sink in the Arctic Ocean due to sea-ice loss. *Geophys. Res. Lett.* 33:L23609. doi: 10.1029/2006GL027028

Bischoff, J. L., Stine, S., Rosenbauer, R. J., Fitzpatrick, J. A., and Stafford, T. W. Jr. (1993). Ikaite precipitation by mixing of shoreline springs and lake water, Mono Lake, California, USA. *Geochim. Cosmochim. Acta* 57, 3855–3865. doi: 10.1016/0016-7037(93)90339-X

Björkman, M., Kühnel, R., Partridge, D., Roberts, T., Aas, W., Mazzola, M., et al. (2013). Nitrate dry deposition in Svalbard. *Tellus B Chem. Phys. Meteorol.* 65:19071. doi: 10.3402/tellusb.v65i0.19071

Cai, W. J., Chen, L., Chen, B., Gao, Z., Lee, S. H., Chen, J., et al. (2010). Decrease in the CO_2 uptake capacity in an ice-free Arctic Ocean basin. *Science* 329, 556–559. doi: 10.1126/science.1189338

Cai, W. J., Dai, M., and Wang, Y. (2006). Air-sea exchange of carbon dioxide in ocean margins: a province-based synthesis. *Geophys. Res. Lett.* 33:L12603. doi: 10.1029/2006GL026219

Chen, B., Cai, W. J., and Chen, L. (2015). The marine carbonate system of the Arctic Ocean: assessment of internal consistency and sampling considerations, summer 2010. *Mar. Chem.* 176, 174–188. doi: 10.1016/j.marchem.2015.09.007

Chen, C. T. A. (1985). Salinity, alkalinity and calcium of the Weddell Sea ice. *Antarct. J. U.S.* 17, 102–103.

Chen, C. T. A., and Borges, A. V. (2009). Reconciling opposing views on carbon cycling in the coastal ocean: continental shelves as sinks and near-shore ecosystems as sources of atmospheric CO_2. *Deep Sea Res. Part II Top. Stud. Oceanogr.* 56, 578–590. doi: 10.1016/j.dsr2.2009.01.001

Clayton, T. D., and Byrne, R. H. (1993). Spectrophotometric seawater pH measurements: total hydrogen ion concentration scale calibration of m-cresol purple and at-sea results. *Deep Sea Res. Part I Oceanogr. Res. Pap.* 40, 2115–2129. doi: 10.1016/0967-0637(93)90048-8

Cooper, L. W., McClelland, J. W., Holmes, R. M., Raymond, P. A., Gibson, J. J., Guay, C. K., et al. (2008). Flow-weighted values of runoff tracers ($\delta^{18}O$, DOC, Ba, alkalinity) from the six largest Arctic rivers. *Geophys. Res. Lett.* 35:L18606. doi: 10.1029/2008GL035007

Cox, G. F., and Weeks, W. F. (1983). Equations for determining the gas and brine volumes in sea-ice samples. *J. Glaciol.* 29, 306–316. doi: 10.3189/S0022143000008364

DeGrandpre, M. D., Evans, W., Timmermans, M. L., Krishfield, R., Williams, B., and Steele, M. (2020). Changes in the Arctic Ocean carbon cycle with diminishing ice cover. *Geophys. Res. Lett* 47:e2020GL088051. doi: 10.1029/2020GL088051

DeGrandpre, M. D., Lai, C. Z., Timmermans, M. L., Krishfield, R. A., Proshutinsky, A., and Torres, D. (2019). Inorganic carbon and pCO_2 variability during ice formation in the Beaufort Gyre of the Canada Basin. *J. Geophys. Res. Oceans* 124, 4017–4028. doi: 10.1029/2019JC015109

Dickson, A. G. (1981). An exact definition of total alkalinity and a procedure for the estimation of alkalinity and total inorganic carbon from titration data. *Deep Sea Res. Part I Oceanogr. Res. Pap.* 28, 609–623. doi: 10.1016/0198-0149(81)90121-7

Dickson, A. G., and Millero, F. J. (1987). A comparison of the equilibrium constants for the dissociation of carbonic acid in seawater media. *Deep Sea Res. Part A Oceanogr. Res. Pap.* 34, 1733–1743. doi: 10.1016/0198-0149(87)90021-5

Dieckmann, G. S., Nehrke, G., Papadimitriou, S., Göttlicher, J., Steininger, R., Kennedy, H., et al. (2008). Calcium carbonate as ikaite crystals in Antarctic sea ice. *Geophys. Res. Lett.* 35:L08501. doi: 10.1029/2008GL033540

Dieckmann, G. S., Nehrke, G., Uhlig, C., Göttlicher, J., Gerland, S., Granskog, M. A., et al. (2010). Ikaite ($CaCO_3 \cdot 6H_2O$) discovered in Arctic sea ice. *Cryosphere* 4, 227–230. doi: 10.5194/tc-4-227-2010

Else, B. G., Galley, R. J., Lansard, B., Barber, D. G., Brown, K., Miller, L. A., et al. (2013). Further observations of a decreasing atmospheric CO_2 uptake capacity in the Canada Basin (Arctic Ocean) due to sea ice loss. *Geophys. Res. Lett.* 40, 1132–1137. doi: 10.1002/grl.50268

Fischer, M., Thomas, D. N., Krell, A., Nehrke, G., Göttlicher, J., Norman, L., et al. (2013). Quantification of ikaite in Antarctic sea ice. *Antarct. Sci.* 25, 421–432. doi: 10.1017/S0954102012001150

Fransson, A., Chierici, M., Miller, L. A., Carnat, G., Shadwick, E., Thomas, H., et al. (2013). Impact of sea-ice processes on the carbonate system and ocean acidification at the ice-water interface of the Amundsen Gulf. *Arctic Ocean. J. Geophys. Res. Oceans* 118, 7001–7023. doi: 10.1002/2013JC009164

Fransson, A., Chierici, M., Skjelvan, I., Olsen, A., Assmy, P., Peterson, A. K., et al. (2017). Effects of sea-ice and biogeochemical processes and storms on under-ice water fCO_2 during the winter-spring transition in the high Arctic Ocean: implications for sea-air CO_2 fluxes. *J. Geophys. Res. Oceans* 122, 5566–5587. doi: 10.1002/2016JC012478

Fransson, A., Chierici, M., Yager, P. L., and Smith, W. O. Jr. (2011). Antarctic sea ice carbon dioxide system and controls. *J. Geophys. Res. Oceans.* 116:C12. doi: 10.1029/2010JC006844

Garcia, H. E., Boyer, T. P., Baranova, O. K., Locarnini, R. A., Mishonov, A. V., Grodsky, A., et al. (2019). *World Ocean Atlas 2018: Product Documentation*, ed. A. Mishonov (Washington, DC: NOAA). doi: 10.13140/RG.2.2.34758.01602

Geilfus, N. X., Carnat, G., Dieckmann, G. S., Halden, N., Nehrke, G., Papakyriakou, T., et al. (2013). First estimates of the contribution of $CaCO_3$ precipitation to the release of CO_2 to the atmosphere during young sea ice growth. *J. Geophys. Res. Oceans* 118, 244–255. doi: 10.1029/2012JC007980

Geilfus, N. X., Carnat, G., Papakyriakou, T., Tison, J. L., Else, B., Thomas, H., et al. (2012). Dynamics of pCO_2 and related air-ice CO_2 fluxes in the Arctic coastal zone (Amundsen Gulf, Beaufort Sea). *J. Geophys. Res. Oceans* 117:C9. doi: 10.1029/2011JC007118

Geilfus, N. X., Galley, R. J., Crabeck, O., Papakyriakou, T., Landy, J., Tison, J. L., et al. (2015). Inorganic carbon dynamics of melt-pond-covered first-year sea ice in the Canadian Arctic. *Biogeosciences* 12, 2047–2061. doi: 10.5194/bg-12-2047-2015

Geilfus, N. X., Galley, R. J., Else, B. G., Campbell, K., Papakyriakou, T., Crabeck, O., et al. (2016). Estimates of ikaite export from sea ice to the underlying seawater in a sea ice–seawater mesocosm. *Cryosphere* 10, 2173–2189. doi: 10.5194/tc-10-2173-2016

Golden, K. M., Eicken, H., Heaton, A. L., Miner, J., Pringle, D. J., and Zhu, J. (2007). Thermal evolution of permeability and microstructure in sea ice. *Geophys. Res. Lett.* 34:L16501. doi: 10.1029/2007GL030447

Gruber, N., Clement, D., Carter, B. R., Feely, R. A., Van Heuven, S., Hoppema, M., et al. (2019). The oceanic sink for anthropogenic CO_2 from 1994 to 2007. *Science* 363, 1193–1199. doi: 10.1126/science.aau5153

Gruber, N., Gloor, M., Mikaloff Fletcher, S. E., Doney, S. C., Dutkiewicz, S., Follows, M. J., et al. (2009). Oceanic sources, sinks, and transport of atmospheric CO_2. *Global Biogeochem. Cycles* 23:GB1005. doi: 10.1029/2008GB003349

Holmes, R. M., McClelland, J. W., Peterson, B. J., Tank, S. E., Bulygina, E., Eglinton, T. I., et al. (2012). Seasonal and annual fluxes of nutrients and organic matter from large rivers to the Arctic Ocean and surrounding seas. *Estuaries Coast* 35, 369–382. doi: 10.1007/s12237-011-9386-6

Hu, X. (2020). Effect of organic alkalinity on seawater buffer capacity: a numerical exploration. *Aquat. Geochem.* 26, 161–178. doi: 10.1007/s10498-020-09375-x

Hu, Y. B., Wang, F., Boone, W., Barber, D., and Rysgaard, S. (2018). Assessment and improvement of the sea ice processing for dissolved inorganic carbon analysis. *Limnol. Oceanogr. Methods.* 16, 83–91. doi: 10.1002/lom3.10229

Hu, Y. B., Wolf-Gladrow, D. A., Dieckmann, G. S., Völker, C., and Nehrke, G. (2014). A laboratory study of ikaite ($CaCO_3{\cdot}6H_2O$) precipitation as a function of pH, salinity, temperature and phosphate concentration. *Mar. Chem.* 162, 10–18. doi: 10.1016/j.marchem.2014.02.003

Jones, E. P., Coote, A. R., and Levy, E. M. (1983). Effect of sea ice meltwater on the alkalinity of seawater. *J. Mar. Res.* 41, 43–52. doi: 10.1357/002224083788223063

Jung, J., Son, J. E., Lee, Y. K., Cho, K. H., Lee, Y., Yang, E. J., et al. (2021). Tracing riverine dissolved organic carbon and its transport to the halocline layer in the Chukchi Sea (western Arctic Ocean) using humic-like fluorescence fingerprinting. *Sci. Total Environ.* 772:145542. doi: 10.1016/j.scitotenv.2021.145542

Kim, H. C., Lee, K., and Choi, W. (2006). Contribution of phytoplankton and bacterial cells to the measured alkalinity of seawater. *Limnol. Oceanogr.* 51, 331–338. doi: 10.4319/lo.2006.51.1.0331

Ko, Y. H., Lee, K., Eom, K. H., and Han, I. S. (2016). Organic alkalinity produced by phytoplankton and its effect on the computation of ocean carbon parameters. *Limnol Oceanogr*. 61, 1462–1471. doi: 10.1002/lno.10309

König, D., Miller, L. A., Simpson, K. G., and Vagle, S. (2018). Carbon dynamics during the formation of sea ice at different growth rates. *Front. Earth Sci.* 6:234. doi: 10.3389/feart.2018.00234

Kotovitch, M., Moreau, S., Zhou, J., Vancoppenolle, M., Dieckmann, G. S., Evers, K. U., et al. (2016). Air-ice carbon pathways inferred from a sea ice tank experiment. *Element. Sci. Anth.* 4:000112. doi: 10.12952/journal.elementa.000112

Krumpen, T., Belter, H. J., Boetius, A., Damm, E., Haas, C., Hendricks, S., et al. (2019). Arctic warming interrupts the Transpolar Drift and affects long-range transport of sea ice and ice-rafted matter. *Sci. Rep.* 9:5459. doi: 10.1038/s41598-019-41456-y

Land, P. E., Shutler, J. D., Cowling, R. D., Woolf, D. K., Walker, P., Findlay, H. S., et al. (2013). Climate change impacts on sea–air fluxes of CO_2 in three Arctic seas: a sensitivity study using Earth observation. *Biogeosciences* 10, 8109–8128. doi: 10.5194/bg-10-8109-2013

Lannuzel, D., Tedesco, L., Van Leeuwe, M., Campbell, K., Flores, H., Delille, B., et al. (2020). The future of Arctic sea-ice biogeochemistry and ice-associated ecosystems. *Nat. Clim. Chang.* 10, 983–992. doi: 10.1038/s41558-020-00940-4

Le Quéré, C., Andrew, R. M., Friedlingstein, P., Sitch, S., Hauck, J., Pongratz, J., et al. (2018). Global carbon budget 2018. *Earth Syst. Sci. Data.* 10, 2141–2194. doi: 10.5194/essd-10-2141-2018

Lee, K., Kim, T. W., Byrne, R. H., Millero, F. J., Feely, R. A., and Liu, Y. M. (2010). The universal ratio of boron to chlorinity for the North Pacific and North Atlantic oceans. *Geochim. Cosmochim. Acta* 74, 1801–1811. doi: 10.1016/j.gca.2009.12.027

Lee, K., Sabine, C. L., Tanhua, T., Kim, T. W., Feely, R. A., and Kim, H. C. (2011). Roles of marginal seas in absorbing and storing fossil fuel CO_2. *Energy Environ. Sci.* 4, 1133–1146. doi: 10.1039/C0EE00663G

Lewis, E. R., and Wallace, D. W. R. (1998). *Data From: Program Developed for CO_2 System Calculations (No. Cdiac: CDIAC-105). Environmental System Science Data Infrastructure for a Virtual Ecosystem*. doi: 10.15485/1464255

Lueker, T. J., Dickson, A. G., and Keeling, C. D. (2000). Ocean pCO_2 calculated from dissolved inorganic carbon, alkalinity, and equations for K1 and K2: validation based on laboratory measurements of CO_2 in gas and seawater at equilibrium. *Mar. Chem.* 70, 105–119. doi: 10.1016/S0304-4203(00)00022-0

Macdonald, K. M., Sharma, S., Toom, D., Chivulescu, A., Hanna, S., Bertram, A. K., et al. (2017). Observations of atmospheric chemical deposition to high Arctic snow. *Atmos. Chem. Phys.* 17, 5775–5788. doi: 10.5194/acp-17-5775-2017

Manizza, M., Follows, M. J., Dutkiewicz, S., Menemenlis, D., Hill, C. N., and Key, R. M. (2013). Changes in the Arctic Ocean CO_2 sink (1996–2007): a regional model analysis. *Global Biogeochem. Cycles* 27, 1108–1118. doi: 10.1002/2012GB004491

Maslanik, J., and Stroeve, J. (1999). *Data from: Near-Real-Time DMSP SSM/I-SSMIS Daily Polar Gridded sea Ice Concentrations*. doi: 10.5067/U8C09DWVX9LM

McElligott, S., Byrne, R. H., Lee, K., Wanninkhof, R., Millero, F. J., and Feely, R. A. (1998). Discrete water column measurements of CO_2 fugacity and pH_T in seawater: a comparison of direct measurements and thermodynamic calculations. *Mar. Chem.* 60, 63–73. doi: 10.1016/S0304-4203(97)00080-7

Mehrbach, C., Culberson, C. H., Hawley, J. E., and Pytkowicx, R. M. (1973). Measurement of the apparent dissociation constants of carbonic acid in seawater at atmospheric pressure 1. *Limnol. Oceanogr.* 18, 897–907. doi: 10.4319/lo.1973.18.6.0897

Meier, W. N., Stroeve, J., and Fetterer, F. (2007). Whither Arctic sea ice? A clear signal of decline regionally, seasonally and extending beyond the satellite record. *Ann. Glaciol.* 46, 428–434. doi: 10.3189/172756407782871170

Miller, L. A., Papakyriakou, T. N., Collins, R. E., Deming, J. W., Ehn, J. K., Macdonald, R. W., et al. (2011). Carbon dynamics in sea ice: a winter flux time series. *J. Geophys. Res. Oceans* 116:C2. doi: 10.1029/2009JC006058

Millero, F. J. (1995). Thermodynamics of the carbon dioxide system in the oceans. *Geochim. Cosmochim. Acta* 59, 661–677. doi: 10.1016/0016-7037(94)00354-O

Millero, F. J., Graham, T. B., Huang, F., Bustos-Serrano, H., and Pierrot, D. (2006). Dissociation constants of carbonic acid in seawater as a function of salinity and temperature. *Mar. Chem.* 100, 80–94. doi: 10.1016/j.marchem.2005.12.001

Millero, F. J., Zhang, J. Z., Lee, K., and Campbell, D. M. (1993). Titration alkalinity of seawater. *Mar. Chem.* 44, 153–165. doi: 10.1016/0304-4203(93)90200-8

Moreau, S., Vancoppenolle, M., Bopp, L., Aumont, O., Madec, G., Delille, B., et al. (2016). Assessment of the sea-ice carbon pump: insights from a three-dimensional ocean-sea-ice biogeochemical model (NEMO-LIM-PISCES) Assessment of the sea-ice carbon pump. *Element. Sci. Anthrop*. 4:000122. doi: 10.12952/journal.elementa.000122

Moreau, S., Vancoppenolle, M., Delille, B., Tison, J. L., Zhou, J., Kotovitch, M., et al. (2015). Drivers of inorganic carbon dynamics in first-year sea ice: a model study. *J. Geophys. Res. Oceans* 120, 471–495. doi: 10.1002/2014JC010388

Nedashkovsky, A. P., Khvedynich, S. V., and Petrovsky, T. V. (2009). Alkalinity of sea ice in the high-latitudinal arctic according to the surveys performed at north pole drifting station 34 and characterization of the role of the arctic ice in the CO_2 exchange. *Oceanology* 49, 55–63. doi: 10.1134/S000143700901007X

Niederdrenk, A. L., and Notz, D. (2018). Arctic sea ice in a 1.5 °C warmer world. *Geophys. Res. Lett.* 45, 1963–1971. doi: 10.1002/2017GL076159

Nitishinsky, M., Anderson, L. G., and Hölemann, J. A. (2007). Inorganic carbon and nutrient fluxes on the Arctic Shelf. *Cont. Shelf Res.* 27, 1584–1599. doi: 10.1016/j.csr.2007.01.019

Nomura, D., Assmy, P., Nehrke, G., Granskog, M. A., Fischer, M., Dieckmann, G. S., et al. (2013a). Characterization of ikaite ($CaCO_3$·6HO) crystals in first-year Arctic sea ice north of Svalbard. *Ann. Glaciol.* 54, 125–131. doi: 10.3189/2013AoG62A034

Nomura, D., Granskog, M. A., Assmy, P., Simizu, D., and Hashida, G. (2013b). Arctic and Antarctic sea ice acts as a sink for atmospheric CO_2 during periods of snowmelt and surface flooding. *J. Geophys. Res. Oceans.* 118, 6511–6524. doi: 10.1002/2013JC009048

Nomura, D., Eicken, H., Gradinger, R., and Shirasawa, K. (2010). Rapid physically driven inversion of the air–sea ice CO2 flux in the seasonal landfast ice off Barrow, Alaska after onset of surface melt. *Cont. Shelf Res.* 30, 1998–2004.

Obbard, R. W., Lieb-Lappen, R. M., Nordick, K. V., Golden, E. J., Leonard, J. R., Lanzirotti, A., et al. (2016). Synchrotron X-ray fluorescence spectroscopy of salts in natural sea ice. *Earth. Space Sci.* 3, 463–479. doi: 10.1002/2016EA000172

Olsen, A., Lange, N., Key, R. M., Tanhua, T., Bittig, H. C., Kozyr, A., et al. (2020). An updated version of the global interior ocean biogeochemical data product, GLODAPv2. 2020. *Earth Syst. Sci. Data* 12, 3653–3678. doi: 10.5194/essd-12-3653-2020

Ouyang, Z., Qi, D., Chen, L., Takahashi, T., Zhong, W., DeGrandpre, M. D., et al. (2020). Sea-ice loss amplifies summertime decadal CO_2 increase in the western Arctic Ocean. *Nat. Clim. Chang.* 10, 678–684. doi: 10.1038/s41558-020-0784-2

Overland, J. E., and Wang, M. (2020). The 2020 Siberian heat wave. *Int. J. Climatol.* 41, E2341–E2346. doi: 10.1002/joc.6850

Papadimitriou, S., Kennedy, H., Kattner, G., Dieckmann, G. S., and Thomas, D. N. (2004). Experimental evidence for carbonate precipitation and CO_2 degassing during sea ice formation. *Geochim. Cosmochim. Acta* 68, 1749–1761. doi: 10.1016/j.gca.2003.07.004

Papadimitriou, S., Kennedy, H., Kennedy, P., and Thomas, D. N. (2013). Ikaite solubility in seawater-derived brines at 1 atm and sub-zero temperatures to 265 K. *Geochim. Cosmochim. Acta* 109, 241–253. doi: 10.1016/j.gca.2013.01.044

Papadimitriou, S., Kennedy, H., Kennedy, P., and Thomas, D. N. (2014). Kinetics of ikaite precipitation and dissolution in seawater-derived brines at sub-zero temperatures to 265 K. *Geochim. Cosmochim. Acta* 140, 199–211. doi: 10.1016/j.gca.2014.05.031

Petrich, C., and Eicken, H. (2017). "Overview of sea ice growth and properties," in *the Sea Ice*, ed. D. N. Thomas (Chichester: John Wiley & Sons), 1–41.

Pipko, I. I., Semiletov, I. P., Pugach, S. P., Wåhlström, I., and Anderson, L. G. (2011). Interannual variability of air-sea CO_2 fluxes and carbon system in the East Siberian Sea. *Biogeosciences* 8, 1987–2007. doi: 10.5194/bg-8-1987-2011

Pörtner, H. O., Roberts, D. C., Masson-Delmotte, V., Zhai, P., Poloczanska, E., Mintenbeck, K., et al. (2019). *IPCC, 2019: Technical Summary. In IPCC Special Report on the Ocean and Cryosphere in a Changing Climate*. Geneva: IPCC.

Purgstaller, B., Dietzel, M., Baldermann, A., and Mavromatis, V. (2017). Control of temperature and aqueous Mg^{2+}/Ca^{2+} ratio on the (trans-) formation of ikaite. *Geochim. Cosmochim. Acta* 217, 128–143. doi: 10.1016/j.gca.2017.08.016

Qi, D., Chen, L., Chen, B., Gao, Z., Zhong, W., Feely, R. A., et al. (2017). Increase in acidifying water in the western Arctic Ocean. *Nat. Clim.* 7, 195–199. doi: 10.1038/nclimate3228

Rysgaard, S., Glud, R. N., Lennert, K., Cooper, M., Halden, N., Leakey, R. J. G., et al. (2012). Ikaite crystals in melting sea ice-implications for pCO_2 and pH levels in Arctic surface waters. *Cryosphere* 6, 901–908. doi: 10.5194/tc-6-901-2012

Rysgaard, S., Glud, R. N., Sejr, M. K., Bendtsen, J., and Christensen, P. B. (2007). Inorganic carbon transport during sea ice growth and decay: a carbon pump in polar seas. *J. Geophys. Res. Oceans* 112:C3. doi: 10.1029/2006JC003572

Rysgaard, S., Søgaard, D. H., Cooper, M., Pućko, M., Lennert, K., Papakyriakou, T. N., et al. (2013). Ikaite crystal distribution in winter sea ice and implications for CO_2 system dynamics. *Cryosphere* 7, 707–718. doi: 10.5194/tc-7-707-2013

Rysgaard, S., Wang, F., Galley, R. J., Grimm, R., Notz, D., Lemes, M., et al. (2014). Temporal dynamics of ikaite in experimental sea ice. *Cryosphere* 8, 1469–1478. doi: 10.5194/tc-8-1469-2014

Sabine, C. L., Feely, R. A., Gruber, N., Key, R. M., Lee, K., Bullister, J. L., et al. (2004). The oceanic sink for anthropogenic CO_2. *Science* 305, 367–371. doi: 10.1126/science.1907403

Sánchez-Pastor, N., Oehlerich, M., Astilleros, J. M., Kaliwoda, M., Mayr, C. C., Fernández-Díaz, L., et al. (2016). Crystallization of ikaite and its pseudomorphic transformation into calcite: Raman spectroscopy evidence. *Geochim. Cosmochim. Acta* 175, 271–281. doi: 10.1016/j.gca.2015.12.006

Scharien, R. K., Geldsetzer, T., Barber, D. G., Yackel, J. J., and Langlois, A. (2010). Physical, dielectric, and C band microwave scattering properties of first-year sea ice during advanced melt. *J. Geophys. Res. Oceans* 115:C12026. doi: 10.1029/2010JC006257

Schmidtko, S., Johnson, G. C., and Lyman, J. M. (2013). MIMOC: a global monthly isopycnal upper-ocean climatology with mixed layers. *J. Geophys. Res. Oceans* 118, 1658–1672. doi: 10.1002/jgrc.20122

Sejr, M. K., Krause-Jensen, D., Rysgaard, S., Sørensen, L. L., Christensen, P. B., and Glud, R. N. (2011). Air—sea flux of CO_2 in arctic coastal waters influenced by glacial melt water and sea ice. *Tellus B Chem. Phys. Meteorol.* 63, 815–822. doi: 10.1111/j.1600-0889.2011.00540.x

Semiletov, I. P., Pipko, I. I., Repina, I., and Shakhova, N. E. (2007). Carbonate chemistry dynamics and carbon dioxide fluxes across the atmosphere–ice–water interfaces in the Arctic Ocean: Pacific sector of the Arctic. *J. Mar. Syst.* 66, 204–226. doi: 10.1016/j.jmarsys.2006.05.012

Stroeve, J. C., Serreze, M. C., Holland, M. M., Kay, J. E., Malanik, J., and Barrett, A. P. (2012). The Arctic's rapidly shrinking sea ice cover: a research synthesis. *Clim. Change* 110, 1005–1027. doi: 10.1007/s10584-011-0101-1

Tanhua, T., Jones, E. P., Jeansson, E., Jutterström, S., Smethie, W. M., Wallace, D. W., et al. (2009). Ventilation of the Arctic Ocean: mean ages and inventories of anthropogenic CO_2 and CFC-11. *J. Geophys. Res. Oceans* 114:C1. doi: 10.1029/2008JC004868

Thomas, D. N., Lara, R. J., Eicken, H., Kattner, G., and Skoog, A. (1995). Dissolved organic matter in Arctic multi-year sea ice during winter: major components and relationship to ice characteristics. *Polar Biol.* 15, 477–483. doi: 10.1007/BF00237461

Tollefsen, E., Stockmann, G., Skelton, A., Mörth, C. M., Dupraz, C., and Sturkell, E. (2018). Chemical controls on ikaite formationel. *Mineral. Mag.* 82, 1119–1129. doi: 10.1180/mgm.2018.110

Tschudi, M., Meier, W. N., Stewart, J. S., Fowler, C., and Maslanik, J. (2019). *Data from: EASE-Grid Sea Ice Age*. doi: 10.5067/UTAV7490FEPB

Wang, Z., Li, Z., Zeng, J., Liang, S., Zhang, P., Tang, F., et al. (2020). Spatial and temporal variations of Arctic Sea ice from 2002 to 2017. *Earth Space Sci.* 7:e2020EA001278. doi: 10.1029/2020EA001278

Wanninkhof, R. (2014). Relationship between wind speed and gas exchange over the ocean revisited. *Limnol. Oceanogr. Methods* 12, 351–362. doi: 10.4319/lom.2014.12.351

Weiss, R. F. (1974). Carbon dioxide in water and seawater: the solubility of a non-ideal gas. *Mar. Chem.* 2, 203–215. doi: 10.1016/0304-4203(74)90015-2

Woosley, R. J., and Millero, F. J. (2020). Freshening of the western Arctic negates anthropogenic carbon uptake potential. *Limnol. Oceanogr.* 65, 1834–1846. doi: 10.1002/lno.11421

Woosley, R. J., Millero, F. J., and Takahashi, T. (2017). Internal consistency of the inorganic carbon system in the Arctic Ocean. *Limnol. Oceanogr. Methods* 15, 887–896. doi: 10.1002/lom3.10208

Yang, B., Byrne, R. H., and Lindemuth, M. (2015). Contributions of organic alkalinity to total alkalinity in coastal waters: a spectrophotometric approach. *Mar. Chem.* 176, 199–207. doi: 10.1016/j.marchem.2015.09.008

Zhang, J., and Rothrock, D. A. (2003). Modeling global sea ice with a thickness and enthalpy distribution model in generalized curvilinear coordinates. *Mon. Weather Rev.* 131, 845–861. doi: 10.1175/1520-04932003131<0845:MGSIWA<2.0.CO;2

Conflict of Interest: The authors declare that the research was conducted in the absence of any commercial or financial relationships that could be construed as a potential conflict of interest.

Publisher's Note: All claims expressed in this article are solely those of the authors and do not necessarily represent those of their affiliated organizations, or those of the publisher, the editors and the reviewers. Any product that may be evaluated in this article, or claim that may be made by its manufacturer, is not guaranteed or endorsed by the publisher.

frontiers | Frontiers in Marine Science

ORIGINAL RESEARCH
published: 30 June 2022
doi: 10.3389/fmars.2022.826421

Global Synthesis of Air-Sea CO_2 Transfer Velocity Estimates From Ship-Based Eddy Covariance Measurements

Mingxi Yang[1], Thomas G. Bell[1], Jean-Raymond Bidlot[2], Byron W. Blomquist[3,4], Brian J. Butterworth[3,4], Yuanxu Dong[1,5], Christopher W. Fairall[4], Sebastian Landwehr[6], Christa A. Marandino[7], Scott D. Miller[8], Eric S. Saltzman[9] and Alexander Zavarsky[7]*

[1] Plymouth Marine Laboratory, Prospect Place, Plymouth, United Kingdom, [2] European Centre for Medium-Range Weather Forecasts, Shinfield Park, Reading, United Kingdom, [3] Cooperative Institute for Research in Environmental Sciences, University of Colorado, Boulder, CO, United States, [4] National Oceanic and Atmospheric Administration (NOAA) Physical Sciences Laboratory, 325 Broadway, Boulder, CO, United States, [5] Centre for Ocean and Atmospheric Sciences, School of Environmental Sciences, University of East Anglia, Norwich, United Kingdom, [6] Formerly at School of Physics and Ryan Institute, National University of Ireland Galway, Galway, Ireland, [7] GEOMAR Helmholtz Centre for Ocean Research Kiel, Wischhofstraße 1-3, Kiel, Germany, [8] University at Albany, State University of New York, Albany, NY, United States, [9] Department of Earth System Science, University of California, Irvine, Irvine, CA, United States

OPEN ACCESS

Edited by:
Laurent Coppola, UMR7093 Laboratoire d'océanographie de Villefranche (LOV), France

Reviewed by:
Daiki Nomura, Hokkaido University, Japan
Bernd Jähne, Heidelberg University, Germany

***Correspondence:**
Mingxi Yang
miya@pml.ac.uk

Specialty section:
This article was submitted to Ocean Observation, a section of the journal Frontiers in Marine Science

Received: *30 November 2021*
Accepted: *31 May 2022*
Published: *30 June 2022*

Citation:
Yang M, Bell TG, Bidlot J-R, Blomquist BW, Butterworth BJ, Dong Y, Fairall CW, Landwehr S, Marandino CA, Miller SD, Saltzman ES and Zavarsky A (2022) Global Synthesis of Air-Sea CO_2 Transfer Velocity Estimates From Ship-Based Eddy Covariance Measurements. Front. Mar. Sci. 9:826421. doi: 10.3389/fmars.2022.826421

The air-sea gas transfer velocity (K_{660}) is typically assessed as a function of the 10-m neutral wind speed (U_{10n}), but there remains substantial uncertainty in this relationship. Here K_{660} of CO_2 derived with the eddy covariance (EC) technique from eight datasets (11 research cruises) are reevaluated with consistent consideration of solubility and Schmidt number and inclusion of the ocean cool skin effect. K_{660} shows an approximately linear dependence with the friction velocity (u_*) in moderate winds, with an overall relative standard deviation (relative standard error) of about 20% (7%). The largest relative uncertainty in K_{660} occurs at low wind speeds, while the largest absolute uncertainty in K_{660} occurs at high wind speeds. There is an apparent regional variation in the steepness of the K_{660}-u_* relationships: North Atlantic ≥ Southern Ocean > other regions (Arctic, Tropics). Accounting for sea state helps to collapse some of this regional variability in K_{660} using the wave Reynolds number in very large seas and the mean squared slope of the waves in small to moderate seas. The grand average of EC-derived K_{660} ($-1.47 + 76.67u_* + 20.48u_*^2$ *or* $0.36 + 1.203U_{10n} + 0.167U_{10n}^2$) is similar at moderate to high winds to widely used dual tracer-based K_{660} parametrization, but consistently exceeds the dual tracer estimate in low winds, possibly in part due to the chemical enhancement in air-sea CO_2 exchange. Combining the grand average of EC-derived K_{660} with the global distribution of wind speed yields a global average transfer velocity that is comparable with the global radiocarbon (^{14}C) disequilibrium, but is ~20% higher than what is implied by dual tracer parametrizations. This analysis suggests that CO_2 fluxes computed using a U_{10n}^2 dependence with zero intercept (e.g., dual tracer) are likely underestimated at relatively low wind speeds.

Keywords: air-sea exchange, gas exchange, eddy covariance (EC), CO_2, transfer velocity, waves

1 INTRODUCTION

Approximately a quarter to a third of CO_2 emitted by human-related activities is absorbed annually by the global oceans (Khatiwala et al., 2013; Friedlingstein et al., 2020), which has mitigated its atmospheric greenhouse effect but led to ocean acidification. Air-sea gas flux is generally estimated with a bulk formula, i.e., as the air-sea concentration difference (ΔC) multiplied by the gas transfer velocity (K). K is typically parametrized as a function of the 10-m neutral wind speed (U_{10n}), but there is still considerable uncertainty in this relationship (Wanninkhof, 2014). More than half of the uncertainty in estimates of the net global air-sea CO_2 flux arises from errors in the parametrization of K (Woolf et al., 2019), which severely hinders our ability to quantify the current carbon cycle and forecast climate in the near future.

The micro-metrological eddy covariance (EC) method provides a direct measurement of CO_2 flux that is independent of seawater concentration. EC flux is derived from the correlation between rapid (typically 10 Hz) fluctuations in the vertical wind velocity (w) and in the dry mixing ratio of CO_2 in the atmosphere (X_{CO2}). The resultant CO_2 flux is converted to molar concentration units (e.g., mmol m^{-2} d^{-1}) using the mean dry air density (ρ_{dry}):

$$Flux_{CO_2} = \rho_{dry}\ \overline{w' X'_{CO_2}} \quad (1)$$

Here the primes denote fluctuations and the overbar indicates temporal averaging, typically over intervals of 10 minutes to an hour.

Combining the EC flux with concurrent measurement of ΔC, K can be independently determined by rearranging the bulk formula. In the case of seawater CO_2 measurement, the gas analyzer measures the fugacity of CO_2 in an equilibrator (fCO_{2w} in μatm, proportional to dissolved concentration by the gas solubility) and in the atmosphere (fCO_{2a} in μatm), which allows for the approximation (conversion from μatm to atm and from m s^{-1} to cm hr^{-1} not shown):

$$K = Flux_{CO2}/\Delta C \approx \rho_{dry}\ \overline{w' X'_{CO_2}}/Sol_{bulk}/(fCO_{2w} - fCO_{2a}) \quad (2)$$

On a ship, fCO_{2w} and fCO_{2a} are typically measured from ca. 5 m below and 15 m above the ocean surface, respectively. The bulk solubility Sol_{bulk} (in mol m^{-3} atm^{-1}) is computed from the underway water temperature and salinity at ca. 5m depth. To account for the temperature dependence in the gas transfer velocity and facilitate comparison between different measurements, K is further normalized to 20 °C *via* the Schmidt number (Sc), where the exponent n is typically assumed to be -1/2 over the open ocean:

$$K_{660} = K(660/Sc)^n \quad (3)$$

Building upon the works of Ward et al. (2004) and McGillis and Wanninkhof (2006), Woolf et al. (2016) identified two main ways in which near surface temperature gradients may impact the air-sea CO_2 concentration gradient: the presence of a cool skin and a diurnal warm layer. Driven by heat fluxes at the surface (latent heat, longwave radiation, and sensible heat, Saunders, 1967; Soloviev and Schluessel, 1994) and present ubiquitously over the ocean, the cool skin effect causes the temperature at the air-sea interface to be ~0.2°C cooler than water ca. 1 mm below (Donlon et al., 2002). The diurnal warm layer refers to heating of the top meters of the ocean due to incoming shortwave radiation, a phenomenon more important in tropical regions and at low wind speeds (e.g., Fairall et al., 1996).

Accounting for these near surface temperature gradients led to a substantial increase in the estimated global net CO_2 uptake (Woolf et al., 2016; Watson et al., 2020). However, these global flux estimates used a K_{660} parametrization that was derived from the dual tracer ($^3He/SF_6$) technique (e.g., Ho et al., 2006). ^3He and SF_6 differ from CO_2 from at least two perspectives: 1) they are much less soluble than CO_2, and solubility is important in bubble-mediated gas exchange (Woolf, 1997; Asher and Wanninkhof, 1998); 2) they are inert, whereas the air-sea exchange of CO_2 is affected by chemical enhancement due to the carbonate kinetics (Wanninkhof, 1992). In addition, the derivation of K_{660} from the $^3He/SF_6$ measurements is highly sensitive to the Schmidt number exponent n, which is thought to deviate from -1/2 at low wind speeds (e.g., Esters et al., 2017; Nagel et al., 2019). It is arguably more robust to use K_{660} directly derived from CO_2 measurements to estimate the global/regional CO_2 flux to avoid the aforementioned possible sources of uncertainty.

Eddy covariance measurements of air-sea CO_2 flux from ships have improved significantly since the maturation of the motion correction algorithms (Edson et al., 1998; Landwehr et al., 2015) and adoption of fast response, closed-path CO_2 analyzers with a dryer (Nafion) to eliminate the signal contamination due to fluctuations in water vapor (Miller et al., 2009; Blomquist et al., 2014; Landwehr et al., 2014). There have been about a dozen cruises since the late 2000s that used this method to derive K_{660} for CO_2 (following Eq. 2 and 3). The original analyses of these data were made on different averaging timescales, used outdated fits for the solubility and Schmidt number of CO_2 (Wanninkhof, 1992), and typically ignored near surface temperature gradients. This reevaluation addresses those inconsistencies and presents the first synthesis of shipboard EC CO_2 flux-derived K_{660} measurements. We assess the comparability and variability in the K_{660} measurements in Section 3, with an exploration of the impact of waves on gas exchange. We then compare the grand average of the EC-derived K_{660} measurements with the dual tracer estimate and global radiocarbon estimate in Section 4 and offer some outlooks in Section 5.

2 EXPERIMENTAL

2.1 Datasets

Table 1 and **Figure 1** summarize the eight datasets (11 cruises) reevaluated in this study (also see Supplementary **Figure 1**). Most cruises took place in mid/high latitudes (sea surface temperature, or SST, well below 20 °C), where CO_2 fluxes were

TABLE 1 | Shipboard eddy covariance CO_2 gas transfer measurements using closed-path infrared analyzers (LI-COR Li-7200 or modified LI-COR Li-7500) or cavity ringdown analyzers (Picarro G1301-f, G2311-f) with a physical dryer.

Cruise ID	Time	Ship	Region	CO_2 analyzer	N > 20 (30) µatm	Mean SST	Original reference
Knorr-07 (a/b)	Jun-Jul 2007	*Knorr*	North Atlantic	Modified LI-COR Li-7500	61 (61)	13	Miller et al., 2009
Knorr-11	Jun-Jul 2011	*Knorr*	North Atlantic	Modified LI-COR Li-7500	215 (215)	10	Bell et al., 2017
SOAP	Feb-Mar 2012	*Tangaroa*	Southern Ocean (temperate)	Modified LI-COR Li-7500	220 (220)	15	Landwehr et al., 2018
NBP-1210/1402	Jan-Feb 2013; Feb-Mar 2014	*Palmer*	Southern Ocean (polar)	LI-COR Li-7200	302 (302)	0	Butterworth & Miller, 2016
HiWinGS	Oct-Nov 2013	*Knorr*	North Atlantic	Picarro G1301-f (LI-COR Li-7200)	530 (467)	10	Blomquist et al., 2017
SO-234/235	Jul-Aug 2014	*Sonne*	Tropical Indian	LI-COR Li-7200	86 (44)	25	Zavarsky et al., 2018
ANDREXII	Feb-Apr 2019	*James Clark Ross*	Southern Ocean (subpolar)	Picarro G2311-f	289 (199)	1	Yang et al., 2021
JR18007	Aug 2019	*James Clark Ross*	Arctic	Picarro G2311-f	278 (278)	6	Dong et al., 2021

N indicates the hours of open water flux measurements with minimum $|\Delta fCO_2|$ of 20 (30) µatm. SST indicates underway water temperature (typically at a depth of ~5 m).

largely into the ocean. Only the tropical cruise SO-234/235 and the Southern Ocean cruise ANDREXII experienced periods of significant CO_2 evasion. Most of the observations were made at 10-m neutral wind speeds of 3-13 m s^{-1} (friction velocity u_* of approximately 0.1 to 0.5 m s^{-1}). The North Atlantic cruise HiWinGS had largest sample size and experienced the highest wind speed (up to 25 m s^{-1}), while SO-234/235 and the North Atlantic cruise Knorr-07 had the smallest sample sizes. NBP-1210/1402 in the Southern Ocean, JR18007 in the Arctic, and HiWinGS had the most hours of low wind measurements. The polar datasets of K_{660} here (NBP-1210/1402 and JR18007) do not include periods near sea ice.

All the cruises above used a closed-path CO_2 analyzer (LI-COR or Picarro cavity ringdown analyzers) with a Nafion dryer, effectively eliminating the issue of water vapor interference in the CO_2 signal and the need for a Webb correction (e.g., Landwehr et al., 2014; Blomquist et al., 2014). We do not consider data from the earlier GasEx studies in this reevaluation. The SO GasEx (Edson et al., 2011) cruise used an open-path LI-COR CO_2 analyzer with known water vapor interference (Landwehr et al., 2014; Blomquist et al., 2014). GasEx98 (Wanninkhof and McGillis, 1999; McGillis et al., 2001) and GasEx01 (McGillis et al., 2004) used a closed-path LI-COR CO_2 analyzer but without a dryer. Observations by Prytherch et al. (2017) near

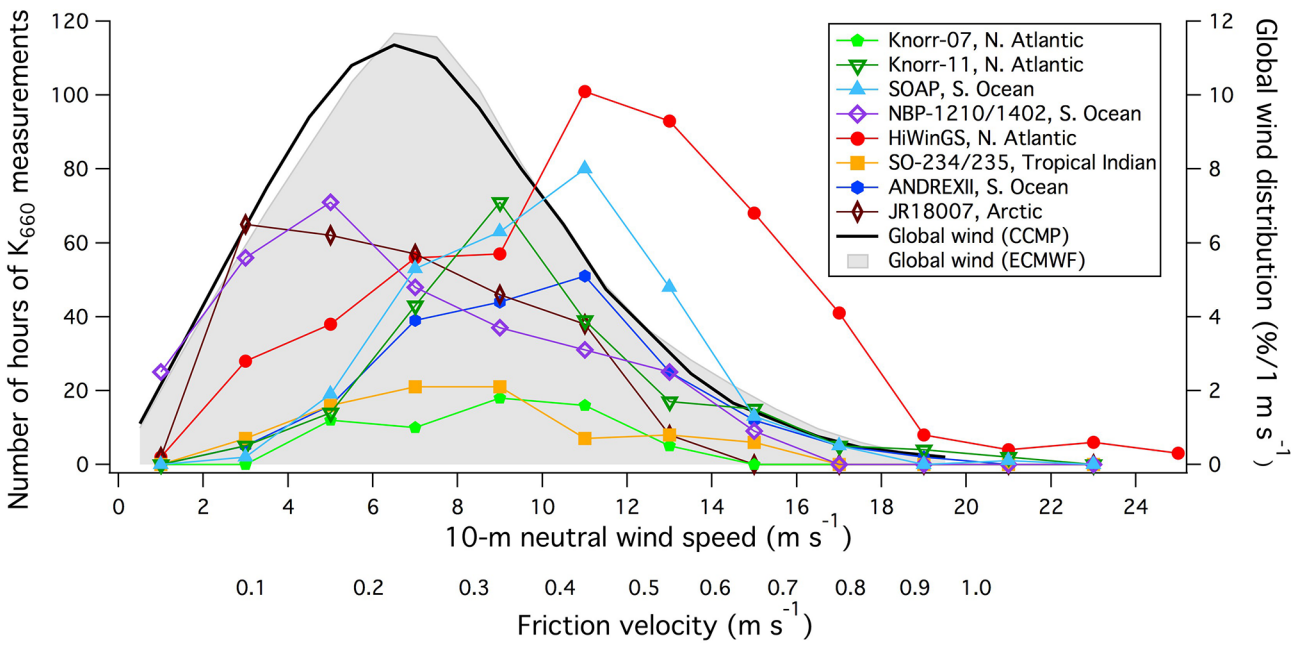

FIGURE 1 | Hours of K_{660} measurements from eight datasets (11 cruises) at different wind speeds and the global wind distributions. The approximate u_* values are shown on the bottom of the plot.

sea ice used a Fast Greenhouse Gas Analyzer (Los Gatos Research), which is substantially noisier than the closed-path LI-COR and Picarro cavity ringdown analyzers and thus resulted in a much greater flux uncertainty (Yang et al., 2016); those observations are also not considered in this analysis.

Cruise data were supplemented with model U_{10n} data provided by the ECMWF global reanalysis (ERA-5) and ocean wave data from a hindcast based on ERA-5 forcing (ERA-5H). The ERA-5 reanalysis provides a comprehensive record of the global atmosphere, land surface, and ocean waves from 1950 onwards. Compared with the previous reanalysis (ERA-Interim), ERA-5 benefits from over a decade of research and development in model physics, core dynamics, and data assimilation. The reanalysis also offers an increase in horizontal resolution (31 km) and time resolution (1 hour), as well as an increase in the vertical atmospheric model levels. The ERA-5 output was produced with ECMWF IFS Cy41r2, used for the operational forecast from March 8 to November 2016. For more details, please refer to Hersbach et al. (2020).

Even though ERA-5 has an ocean wave component, in this study we use wave data from an hindcast (ERA-5H). This hindcast is based on a more advanced version of ECMWF wave prediction system ecWAM (Cy47r1; ECMWF, 2020). The ERA-5H is a long global wave model simulation (1979-2020), forced by ERA-5 hourly 10-m neutral winds, surface air density, gustiness, and sea ice cover. The latter is used to prevent wave generation and propagation in all areas with the sea ice cover >30%. Like ERA-5, the output of ERA-5H is hourly, but it has finer spatial (~20 km) and spectral resolutions (ERA-5: 24 directions, 30 logarithmically spaced frequencies, last frequency ~0.56 Hz; ERA-5H: 14 km, 36 directions and 36 frequencies, last frequency ~1 Hz). The ERA-5H benefits from an updated wave physics for wind input and swell dissipation (based on the work of Ardhuin et al., 2010) and has been successfully incorporated into the operational ecWAM wave model component of IFS (Bidlot, 2019).

Model data are collocated with the cruise data using a bi-linear interpolation in space and a linear interpolation in time. For the purpose of this study, the total significant wave height (H_s) and the mean squared slope (MSS) of the waves from the model are used (see ECMWF, 2020 for further details). It is important to note that the MSS here is determined with the high frequency cut-off given by the model discretization (~1 Hz).

2.2 Reevaluation Methods

EC CO_2 flux data are reevaluated to ensure comparability. Significant changes to some of the original data include:

- CO_2 flux data averaged to hourly interval (minimum of 40 minutes required per hour) following recommendation by Dong et al. (2021)
- Solubility and Schmidt number computed following the equations given by Wanninkhof (2014)
- Air-sea CO_2 concentration difference computed with consideration of the skin temperature effect (see Eq. 4 below)

The cool skin effect is accounted for when computing the gas transfer velocity:

$$K_{660} = \rho_{dry}\ \overline{w'X'_{CO_2}}(\mathrm{fCO_{2w}}Sol_{bulk} - \mathrm{fCO_{2a}}Sol_{skin})^{-1}(660/Sc)^{-0.5} \quad (4)$$

The CO_2 solubility at the skin temperature (Sol_{skin}) is used to calculate the equilibrium atmospheric concentration. The skin temperature is estimated from the COARE3.5 model using underway water measurements and meteorological observations as inputs (see e.g., Fairall et al., 1996 and Zhang et al., 2020 for validation of the modeled cool skin temperature effect). Because Sol_{skin} is almost always greater than Sol_{bulk}, relative to the original analyses (Eq. 2) the inclusion of the cool skin effect reduces K_{660} slightly during CO_2 invasion, and increases K_{660} slightly during CO_2 evasion. For example, at a fCO_{2a} value of 400 µatm and a cool skin effect of 0.17°C, the difference between ΔC with consideration of cool skin (fCO_{2w} Sol_{bulk} – fCO_{2a} Sol_{skin}) and the 'traditional' ΔC (Sol_{bulk} (fCO_{2w} – fCO_{2a})) equates to about 2 µatm. If Sol_{bulk} (fCO_{2w} – fCO_{2a}) is –30 µatm, consideration of the cool skin reduces K_{660} by ~7%. Note that to ensure comparability with previous publications, *Sc* here is computed using the bulk, rather than skin, temperature. Using the skin temperature to compute the Schmidt number would generally increase K_{660} by ~0.5% (see Woolf et al., 2016 for further discussion on this detail).

Woolf et al. (2016) suggested that in the presence of a diurnal warm layer, the bulk underway temperature will be different from the temperature at the base of the thermal diffusive layer (i.e., subskin temperature at ca. 1 mm depth). We have assumed a negligible diurnal warm layer effect and assume that underway water temperature is equal to the subskin temperature for two reasons. First, *in-situ* skin (or subskin) temperature was rarely measured on these cruises, while match ups with satellite skin (or subskin) temperatures are very rare. Two, measurements of subskin temperature using a floating thermistor (aka the NOAA "sea snake") during HiWinGS and SO GasEx suggest that for open ocean at mid/high latitudes, the diurnal warm layer effect is small (see **Supplementary Figures 2**, **3**). Note that near surface temperature gradients might have been more important for the tropical cruises SO-234/235.

Original references for HiWinGS and for SO-234/235 included data where $|\Delta fCO_2|$ was as low as ~20 µatm. Selecting an appropriate $|\Delta fCO_2|$ threshold is important for minimizing random uncertainty as well as bias in K_{660}. As shown by Dong et al. (2021), the bottom-up uncertainty in K_{660} (derived from uncertainty in EC flux and dominated by random uncertainty) increases significantly when $|\Delta fCO_2| < 20$ µatm. At wind speeds < ~6 m s^{-1}, a more stringent threshold of 30 µatm is needed to maintain a reasonable signal:noise ratio. In addition, any bias in the air-sea CO_2 concentration difference (e.g., due to measurement uncertainty or unaccounted for near surface temperature gradients) would have a proportionally greater impact on K_{660} at low $|\Delta fCO_2|$ values. For example, uncertainty in fCO_{2w} from the Surface Ocean CO_2 Atlas (Bakker et al., 2016) is often taken to be ~2 µatm. A total uncertainty in air-sea CO_2 gradient of 3 µatm (considering similar contribution from errors due to fCO_2a and temperature) would contribute to a relative uncertainty in K_{660}

of ~15% at $|\Delta fCO_2|$ = 20 μatm. A more stringent $|\Delta fCO_2|$ threshold reduces the amount of data available, and so the reanalyzed HiWinGS and SO-234/235 data are presented with minimum $|\Delta fCO_2|$ of both 20 and 30 μatm.

For most cruises, we use the bulk u_* computed with the COARE3.5 model from the least distorted shipboard wind speed measurement. Note that this bulk u_* is largely a function of wind speed and atmospheric stability, and does not explicitly consider the impact of waves. For SOAP, the EC system was positioned lower and closer to ship's bow, which caused significant flow distortion (Landwehr et al., 2018). The authors estimated U_{10n} from the EC u_* using the COARE3.5 u_* vs. U_{10n} relationship, but the corrected U_{10n} still tends to be higher than the ECMWF data except at the highest wind speeds (see **Table 2**). For the SO-234/235 cruises, where the EC system was also positioned lower, the *in-situ* U_{10n} tends to be higher than the ECMWF data except at the lowest wind speeds. While the ECMWF U_{10n} estimates are not exempt from bias, this comparison implies that the K_{660} vs. u_* relationships for SOAP and SO-234/235 could be subject to an additional U_{10n}-driven uncertainty of ~10%.

3 RESULTS

To facilitate the interpretation of the large number of data points from all cruises (~2000 hours of K_{660} observations), this work focuses on the statistics (e.g., mean, standard deviation, standard error) of binned hourly K_{660} values. The standard deviation is used to illustrate variability, while the standard error reflects the accuracy in the measurement. The hourly data from each cruise are included in the supplement for interested readers.

3.1 Moderate Winds

We first look at K_{660} data at moderate wind speeds (u_* 0.1-0.5 m s^{-1}, or U_{10n} of approximately 3-13 m s^{-1}), which encompasses the majority of the measurements (**Figure 1**). We choose u_* as the default independent parameter for assessing the variability in K_{660}, in accordance with the custom of similarity theory. K_{660} scales approximately linearly with u_* within this range (**Figure 2**). We note that much of the HiWinGS data at intermediate wind speeds were collected during the decline of intense storms, when the waves were much larger than typically observed at those windspeeds. This probably led to enhanced transfer. See Section 3.3 for further discussion about waves.

The regression statistics, computed both from the bin-averaged K_{660} as well as from hourly K_{660} data, are shown in **Table 2**. The r^2 value in the hourly K_{660} fit to u_* tends to be higher for more localized cruises (e.g., SOAP and JR18007) and lower for cruises spanning a large spatial (e.g., NBP-1210/1402, ANDREXII) or temporal (e.g., HiWinGS) range. The mean in the K_{660} vs. u_* slopes in the moderate wind regime is about 93 (cm hr^{-1} (m $s^{-1})^{-1}$), with a relative standard deviation of ~15% and a range of ~40%. The steepness in the K_{660} vs. u_* slopes appears to follow a general trend of North Atlantic ≥ Southern Ocean > Arctic and tropical Indian. The K_{660}-U_{10n} relationships are similar to the K_{660}-u_* relationships in spatial distribution but are less linear (**Supplementary Figure 4**).

Any bias in the K_{660} vs. u_* (or U_{10n}) relationships could be due to biases in u_* (or U_{10n}), in the EC flux, or in the air-sea concentration difference. The slope between *in-situ* derived U_{10n} and U_{10n} from the ECMWF model is within 4% from unity (relative standard deviation of 2.5%), with the exception of SOAP and SO-234/235 (see *Reevaluation Methods*). The good agreement implies that any bias in the *in-situ* u_* (or U_{10n}) data (e.g., due to flow distortion) is generally small. Plotting K_{660} against U_{10n} from ECMWF does not substantially change the mean K_{660} vs. U_{10n} relationships (**Supplementary Figure 4**).

The quasi-linearity between K_{660} and u_* at moderate wind speeds allows us to assess possible biases in flux and in the air-sea concentration difference. Data at low $|\Delta fCO_2|$, typically discarded in the calculation of K_{660}, are particularly useful for evaluating such biases. Normalizing the measured EC flux for the kinetic forcing, here we define a new term:

$$\text{Akinetic flux} = Flux_{CO2}\, u_*^{-1} (660/Sc)^{-0.5} = \Delta C\, K_{660}\, u_*^{-1} \qquad (5)$$

The akinetic flux is plotted against ΔC (**Figure 3**), including the low $|\Delta fCO_2|$ data that are often-discarded. It is apparent that the akinetic flux from all cruises follow a broadly similar trend (slope = $K_{660}\, u_*^{-1}$, the dimensionless transfer coefficient; Jähne et al., 1987). For cruises with both positive and negative concentration differences (NBP1210/1402, ANDREXII, and SO-234/235), the akinetic flux approximately goes through the origin. The fact that the EC flux is roughly zero when the concentration difference is zero suggests that both the flux and

TABLE 2 | Regression analyses between CO_2 K_{660} (in cm hr^{-1}) and friction velocity (in m s^{-1}) between u_* values of 0.1 and 0.5 m s^{-1}.

Cruise ID	K_{660} fit to u_* (bin-averages)	K_{660} fit to u_* (hourly data)	r^2 of hourly fit	Min/median/max in ΔfCO_2	*In-situ* U_{10n} vs. ECMWF U_{10n}
Knorr-07(a/b)	-2.7 + 103.1u_*	-0.2 + 91.1u_*	0.48	-122/-51/-36	0.46 + 0.97 U_{10n}_ECMWF
Knorr-11	-4.3 + 105.8u_*	-5.7 + 112.2u_*	0.58	-110/-50/-35	0.96 + 0.96 U_{10n}_ECMWF
SOAP	-2.9 + 83.2u_*	-7.7 + 96.2u_*	0.72	-130/-54/-36	1.91 + 0.88 U_{10n}_ECMWF
NBP-1210/1402	-4.7 + 88.8u_*	-3.2 + 85.3u_*	0.51	-250/-55/24	0.43 + 0.99 U_{10n}_ECMWF
HiWinGS	-2.7 + 94.6u_* (-4.4 + 104.3u_*)	-4.3 + 99.8u_* (-6.8 + 111.9u_*)	0.40 (0.37)	-63/-41/-11	0.33 + 0.96 U_{10n}_ECMWF
SO-234/235	-0.3 + 58.2u_* (-3.3 + 77.1u_*)	-2.0 + 66.9u_* (-1.9 + 72.0u_*)	0.54 (0.67)	-49/9/40	-0.45 + 1.13 U_{10n}_ECMWF
ANDREXII	-2.0 + 94.0u_*	-4.8 + 100.0u_*	0.46	-87/-12/76	0.16 + 1.01 U_{10n}_ECMWF
JR18007	-4.5 + 79.0u_*	-3.8 + 78.1u_*	0.72	-183/-122/-64	0.50 + 0.97 U_{10n}_ECMWF

The mean K_{660} vs. u_* slope in the moderate wind regime is 93 (cm hr^{-1} (m $s^{-1})^{-1}$). The minimum $|\Delta fCO_2|$ threshold is generally 30 μatm (see main text for details). For HiWinGS and SO-234/235 cruises, additional statistics for $|\Delta fCO_2| > 20$ μatm are presented in parenthesis. Also shown are the minimum, median and maximum in ΔfCO_2 (μatm), including periods omitted from K_{660} calculation, and the relationship between in-situ U_{10n} and U_{10n} from the ECMWF model (both in m s^{-1}).

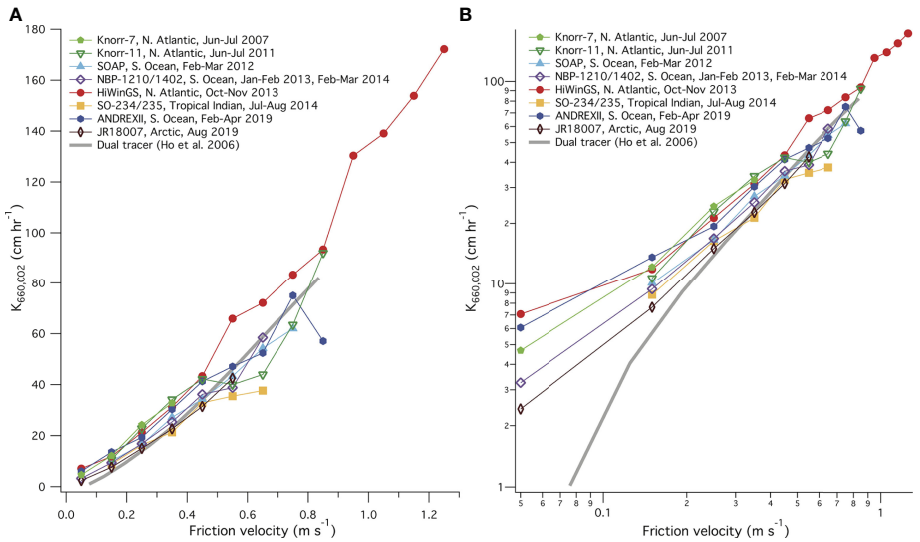

FIGURE 2 | **(A)** K_{660} averaged to friction velocity (u_*) bins in linear scale; **(B)** the same but in log-log scale. Also shown is the dual tracer relationship from Ho et al., 2006.

concentration measurements do not suffer from large bias. From this, we conclude that the variability in the mean K_{660} vs. u_* relationships among different cruises is not primarily due to measurement uncertainties.

Figure 4 shows the variability and uncertainty in K_{660} within this dataset. For individual cruises, standard deviation (standard error) is computed from hourly K_{660} data within u_* bins. Relative standard deviation (relative standard error) is the standard deviation (standard error) above divided by the bin-averaged K_{660}. Similar statistics are also computed from the bin-averaged K_{660} (black lines). While standard error in K_{660} tends to increase with u_* (as expected), the relative standard error is at its minimum in moderate winds (generally within 10%). The lowest and highest wind speed bins for each cruise have the smallest sample sizes, which contribute to larger relative standard error. The next sections will focus on K_{660} in the low and high wind speed regimes.

3.2 Low Wind Regime

Gas exchange at low wind speeds (u_* <0.25 m s^{-1}, or U_{10n} < 7 m s^{-1}) has received relatively little attention over the last decade. **Figure 4** shows that the relative uncertainty (both relative standard error and relative standard deviation) in K_{660} of CO_2 is the largest at low winds. This is partly caused by the increase in the turbulent integral time scale at low wind speed, which increases the EC sampling error. Large relative uncertainty at low wind speeds is observed in fluxes of CO_2 (Dong et al., 2021) as well as in momentum and heat (Blomquist et al., 2014). In addition, processes other than wind that affect gas exchange (e.g., chemical enhancement, surfactants, convection) probably contribute more significantly towards the variability in K_{660} at low winds.

The absolute uncertainty in K_{660} at low winds is small, and the bin-averaged K_{660} from all of the cruises significantly exceeds the dual tracer parametrization (Ho et al., 2006) by a few cm hr^{-1} at u_* below 0.25 m s^{-1} (**Figure 2**). This amounts to a mean difference of ~75% at u_* of 0.15 m s^{-1}. There are several possible reasons for this discrepancy between dual tracer and EC-derived K_{660}: a) very few dual tracer measurements of K_{660} over the ocean were made at low wind speeds, with only two points below a wind speed of 5 m s^{-1} in Ho et al., 2006; b) the quadratic fit of dual tracer K_{660} was forced through the origin; c) chemical enhancement, we discuss below. Physical considerations lead us to expect some gas transfer even at very low wind speeds. For example, Mackay and Yeun (1983) estimate the 'still air' K_{660} to be ~0.4 cm hr^{-1}. Convective turbulence related to heat fluxes may further enhance K_{660} under calm conditions, and the COARE3.0 model estimates this to contribute ~2 cm hr^{-1} at typical (slightly unstable) oceanic conditions (see e.g., Yang et al., 2011).

Furthermore, unlike the dual tracers ^{3}He and SF_6, the air-sea exchange of CO_2 is subject to chemical enhancement due to carbonate equilibrium kinetics (faster in warmer waters, e.g., Soli and Byrne, 2002). Based on the film model of Hoover and Berkshire (1969) and carbonate kinetics, Wanninkhof (1992) estimated the chemical enhancement of CO_2 to be on the order of 2 cm hr^{-1}. Jähne et al. (2010) derived a similar value for chemical enhancement by concurrently measuring the exchange of N_2O (no chemical enhancement) and CO_2 in a wind-wave tank. The enhancement was found to be well described by a surface renewal model that incorporates carbonate kinetics. Considering together the field and laboratory evidence as well as theoretical understanding, it is highly likely that using the dual tracer parametrization of K_{660} (e.g., Ho et al., 2006) will result in an underestimation of air-sea CO_2 exchange at low wind speeds.

The computed K_{660} from EC CO_2 fluxes could be even greater at low wind speeds if we assume a different Schmidt number scaling. Liss and Merlivat (1986) found that the wind speed dependence in K_{660} is weaker within the smooth surface regime (below U_{10n} of 3.6 m s^{-1} per their definition), where gas exchange

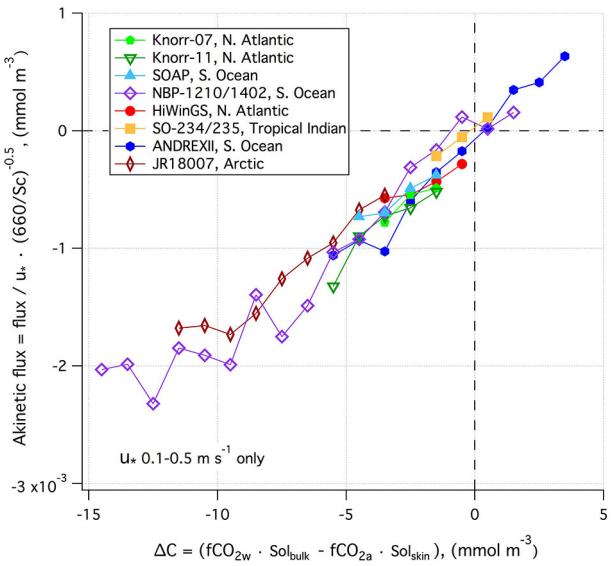

FIGURE 3 | Akinetic flux vs. the air-sea concentration difference in moderate winds.

is dominated by waterside diffusive processes. They suggested that K_{660} should be scaled with $Sc^{-2/3}$ within this smooth regime; then once waves appear the Schmidt number exponent transitions to -1/2. Recent laboratory (Nagel et al., 2019) and field (Esters et al., 2017) observations imply that there is a smooth transition in n between -2/3 and -1/2. The intercepts of the K_{660}-u_* fits (over u_* range of 0.1-0.5 m s^{-1}) are negative for all cruises (**Table 2**), which implies different physical processes occurring at low wind speeds. All cruises (except for SO-234/235) took place in waters less than 20 °C (the temperature where Sc of CO_2 = 660). Scaling to K_{660} from K with $Sc^{-2/3}$ instead of $Sc^{-1/2}$ would lead to an increase in K_{660} by ~10% (from SST = 10 °C) to ~20% (from SST = 0 °C), and bring the intercept in the K_{660}-u_* relationship closer to zero. In **Supplementary Figure 5**, K_{660} normalized using a variable Schmidt number exponent (Esters et al., 2017) is shown, which can be compared against **Figure 2**. We retain the $Sc^{-1/2}$ scaling for the rest of this work to ensure comparability with previous dual tracer and ^{14}C analyses and provide the K data at ambient SST in the supplement.

It is worth repeating that accounting for the cool skin effect (i.e., use of Eq. 4 instead of Eq. 2 and 3) increases the magnitude of ΔC and thus reduces the derived K_{660} of CO_2 in regions of CO_2 invasion. Vertical gradients in fCO_{2w} between the depth of water sampling (typically ~5 m) and the subskin due to diurnal warm layer formation may occur under calm conditions and strong solar irradiance. We have not explicitly considered warm layer in this analysis due to a paucity of near surface temperature observations, incomplete input variables needed for modeling the warm layer (e.g., solar flux missing for several cruises), and uncertainty in the model (Fairall et al., 1996). To illustrate an order of magnitude effect, the global mean daytime difference between the subskin and ~5 m depth is about 0.08°C at U_{10n} = 5 m s^{-1} based on NOAA's long-term shipboard measurements between 70°N and 60°S. This corresponds to an isochemical change (i.e., constant alkalinity and total dissolved inorganic carbon; Woolf et al., 2016) in fCO_{2w} of about 1.4 μatm. The effect of warm layer on ΔC is thus similar in magnitude to the cool skin effect at this wind speed, but in the opposite direction. Inclusion of any warm layer effect in regions of CO_2 invasion would thus increase the derived K_{660} of CO_2 by ~5% at $|\Delta fCO_2|$ = 30 μatm. Large swaths of the global oceans experience low wind speeds. Given the uncertainty surrounding the various concurrent physical processes, gas exchange under these

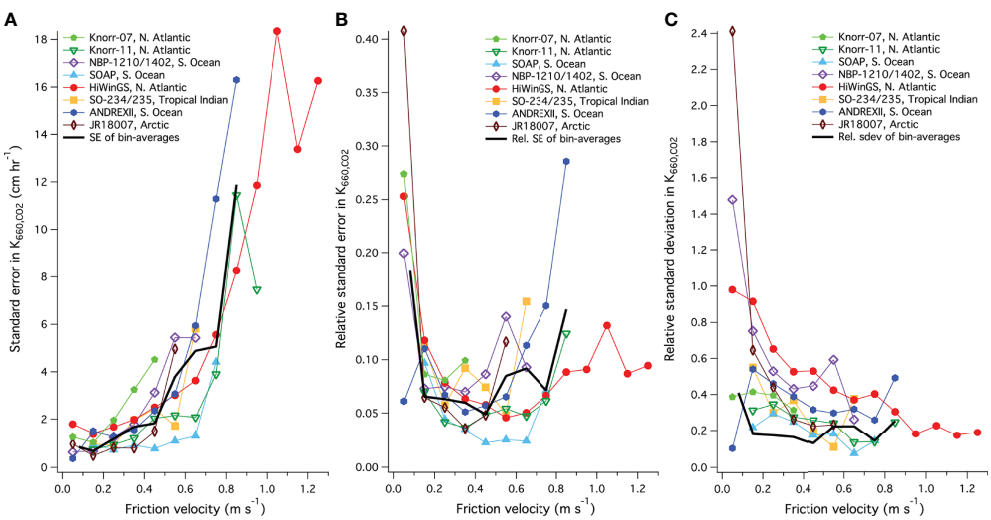

FIGURE 4 | **(A)** standard error in hourly K_{660} for each cruise (colored markers) and the standard error of the bin-averages for all the cruises (black line); **(B)** the same but showing the relative standard error in hourly K_{660}; **(C)** the same but showing the relative standard deviation in hourly K_{660}. Standard deviation here is approximately the root mean squared error, not mean absolute error.

conditions requires further investigation (e.g., a dedicated research campaign in calm conditions, similar to GasEx01 but with improved flux methodology and a thorough examination of the surface temperature profile).

3.3 High Wind Regime and Waves

A number of studies over the last decade have focused on gas exchange at high wind speeds (especially HiWinGS), where K_{660} is considered to be the most uncertain. As shown in **Figure 4**, at u_* above 0.5 m s^{-1} the standard errors in K_{660} (absolute and relative) for individual cruises as well as for bin-averages of all cruises do increase in high winds. In contrast, the relative standard deviation does not increase with wind speed. This is likely in part because the relative uncertainty in EC CO_2 flux tends to decrease with increasing wind speed, presumably due to better sampling statistics (i.e., more turbulent eddies blowing past the sensor within a given averaging time; see Dong et al., 2021). Thus, the perceived large uncertainty in K_{660} in high winds can at least be partly attributed to the paucity of observations. More measurements under those extreme conditions will improve the accuracy in K_{660}.

What does this large dataset tell us about the effect of wave breaking and bubble-mediated gas exchange on K_{660}? Following Woolf (1997) and the COARE model (Fairall et al., 2011), CO_2 gas transfer velocity is often thought to be the sum of diffusive (i.e., interfacial) gas exchange (scaled with u_*) and bubble-mediated gas exchange. Bubble-mediated exchange, scaled with the whitecap fraction, is judged to be the reason why CO_2 transfer is much faster than DMS transfer at high wind speeds (e.g., Bell et al., 2017) and has been estimated to be dominant exchange pathway for CO_2 in rough seas (e.g., Blomquist et al., 2017). The whitecap fraction is long thought to have a cubic wind speed dependence, but observations during HiWinGS at wind speeds up to ~ 24 m s^{-1} show an overall windspeed dependence in whitecap fraction that is much weaker than cubic (Brumer et al., 2017a). This might be one reason why the u_* (and U_{10n}) dependence in K_{660} of CO_2 is closer to linear than to cubic (**Figure 2** and **Supplementary Figure 4**).

Another possibility for the near linear dependence in K_{660} of CO_2 on u_* could be saturation in diffusive gas exchange at very high wind speeds. This phenomenon has sometimes been observed in the more soluble gas dimethyl sulfide (DMS), e.g., during SO GasEx as described by Blomquist et al. (2017) and during Knorr-11 as described by Bell et al. (2013), and it could partly compensate for the rapid increase in bubble-mediated gas exchange with wind. In the following, we explore the use of wave parameters, rather than whitecap fraction, to represent the effects of wave breaking and bubbles on K_{660}.

Figure 5 shows the distribution of significant wave height (H_s) for all the cruises. HiWinGS in the North Atlantic and ANDREXII in the sub-polar Southern Ocean (two cruises with high K_{660}:u_*; see **Table 2**) experienced some of the largest waves at moderate to high wind speeds (also see **Supplementary Figure 6**). In contrast, NBP-1210/1402 in the polar Southern Ocean and JR18007 in the Arctic (two cruises with low K_{660}:u_*; see **Table 2**) often encountered small waves, possibly due to the close proximity of sea ice and thus shorter fetch. For context, **Figure 5** also shows the global distribution in H_s from ECMWF ERA5 (0.5° hourly resolution data; Hersbach et al., 2018), here approximated from 12 evenly spaced days in year 2020 (e.g., 1st January, 1st February, 1st March…). H_s data from the individual cruises span from below to above the global distribution.

Brumer et al. (2017b) suggested the K_{660} is better parameterized as a function of the wave Reynolds number ($R_{Hw} = H_s\ u_* \nu^{-1}$) than as a function of wind speed, where ν is the viscosity of seawater. K_{660} is plotted against the wave Reynolds number (R_{Hw}) in **Figure 6**. Here H_s from the ECMWF model and seawater viscosity at 20°C (rather than ambient temperature) are used to compute R_{Hw} for all cruises. Using ambient water viscosity substantially increases the discrepancy in the K_{660}-R_{Hw} relationships between polar and temperate cruises.

It appears that R_{Hw} does help to collapse the variability in K_{660} among the different cruises in very heavy seas (i.e., $R_{Hw} > 10^6$). For example, the relative standard deviation in K_{660} among HiWinGS, SOAP, ANDREXII, and Knorr-11 at R_{Hw} between $2 \bullet 10^6$ and $3 \bullet 10^6$ is 12-14%. In comparison, the relative standard deviation at u_* above 0.5 m s^{-1} is about 20% for these cruises (**Figure 4**). Note that the K_{660} data from all cruises fall below the Brumer et al. (2017b) parametrization ($K_{660} = 2.04 \cdot 10^{-4} R_{Hw}^{0.88}$) in heavy seas because that parametrization was largely developed from the original HiWinGS K_{660} data. Those data were overestimates due to an incorrect treatment of CO_2 solubility.

In less extreme seas (i.e., $R_{Hw} < 10^6$), R_{Hw} explains less of the variability in K_{660} than u_*. For example, the relative standard deviation in bin-averaged K_{660} among all cruises at R_{Hw} of $3.8 \bullet 10^5$ is 38%. Possible explanations for this include a) R_{Hw} is an imperfect descriptor of wave breaking, especially for small scale waves, and b) breaking of large-scale waves and bubble-mediated processes become dominant for CO_2 gas exchange only in very heavy seas, whereas gas exchange at lower wind speeds is dominated by diffusive transfer.

The mean squared slope (MSS) of the waves incorporates to an extent the combined effect of wind and smaller-scale waves. Frew et al. (2004) observed that K_{660} consistently correlates better with MSS than with wind speed at a coastal location at fairly low wind speeds. **Figure 7** shows the CO_2 K_{660} vs. MSS from the ECMWF model (integrated up to 1 Hz) as well as vs. the ECMWF U_{10n}. In small to moderate seas, MSS explains slightly more variance in K_{660} than U_{10n}. For example, between MSS of 0.025 to 0.04, the relative standard deviation in K_{660} averaged in MSS bins among all cruises is ~15%. In comparison, the relative standard deviation as a function of ECMWF U_{10n} is close to 20% at moderate wind speeds of ~10 m s^{-1}. In rougher seas, the advantage of using MSS over U_{10n}, u_*, or R_{Hw} to parametrize is K_{660} less obvious.

The regional variability in the K_{660}-u_* relationships is less apparent in the K_{660}-R_{Hw} and K_{660}-MSS relationships, which implies that variations in waves in different ocean basins contribute towards the regional variability in K_{660}. A logical future step for extrapolating the K_{660} data to the global oceans may be to develop a wind/wave-dependent parametrization of K_{660} (e.g., as a function of R_{Hw} and MSS). However, in the next section we take the

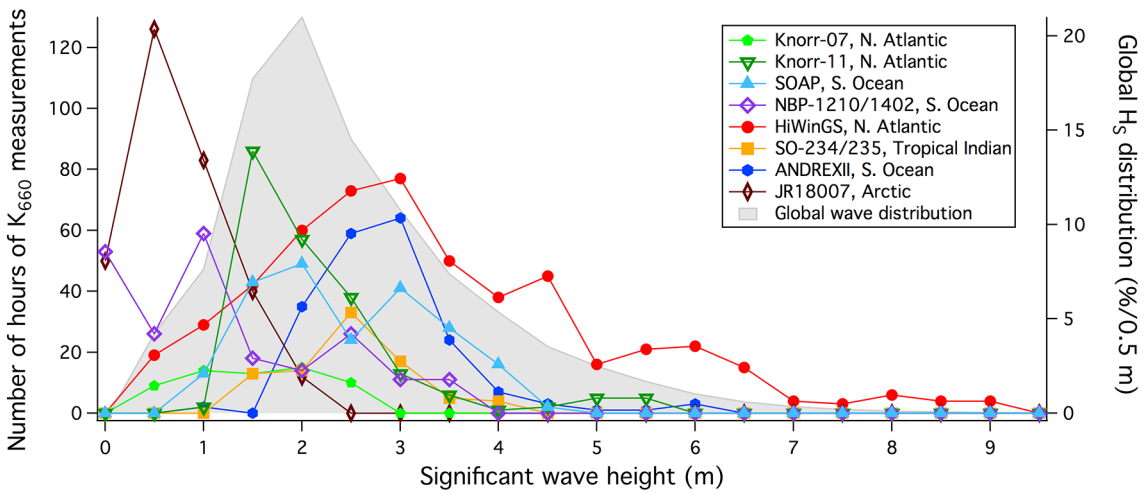

FIGURE 5 | Hours of K_{660} measurements at different significant wave heights and the global distribution of significant wave height from ECMWF.

simpler approach of computing the grand average K_{660}-u_* relationship and combining it with the global wind speed distribution. The resultant global average K_{660} implied from EC CO_2 flux measurements is then compared against tracer-based estimates.

4 COMPARISON TO TRACER-BASED ESTIMATES AND IMPLICATIONS ON THE GLOBAL CO_2 FLUX

A fairly robust constraint for global average air-sea CO_2 exchange is the ^{14}C disequilibrium. Wanninkhof (1992) combined an estimate of this value with the global mean wind speed and assumed a quadratic wind speed dependence (with no gas exchange at U_{10n} = 0) to develop a widely used K_{660} parametrization. The ^{14}C-based global average K_{660} value has since been reassessed by Naegler et al. (2006); Krakauer et al. (2006); Sweeney et al. (2007), and Müller et al. (2008). Accordingly, the ^{14}C tracer based K_{660} parametrization has been updated by Wanninkhof (2014). Naegler (2009) further corrected the global average K_{660} estimates upwards by accounting for the changing oceanic radiocarbon inventory due to CO_2 uptake and using realistic reconstructions of sea surface ^{14}C disequilibrium.

Our study incorporates over 2000 hours of EC K_{660} data from 11 cruises around different parts of the global oceans. Is the overall

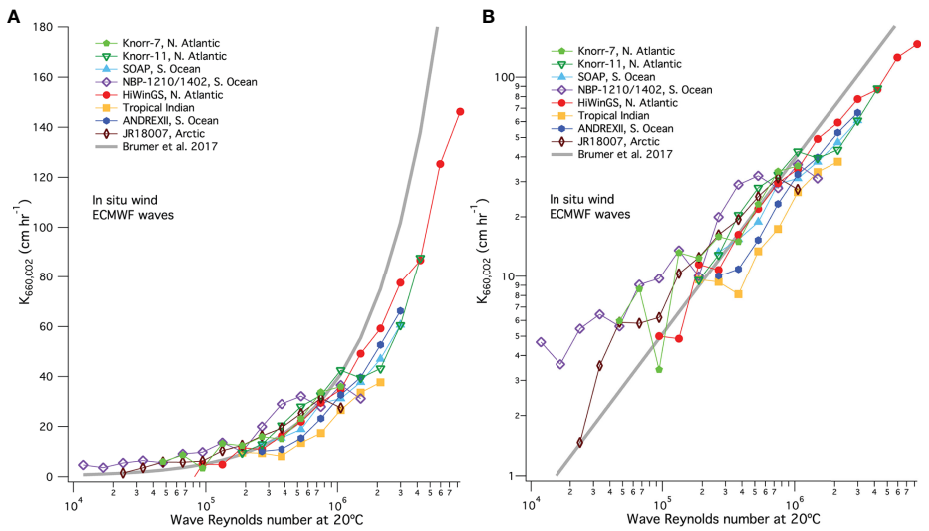

FIGURE 6 | K_{660} averaged into bins of R_{Hw} (20 °C) in semi-log scale **(A)** and log-log scale **(B)**.

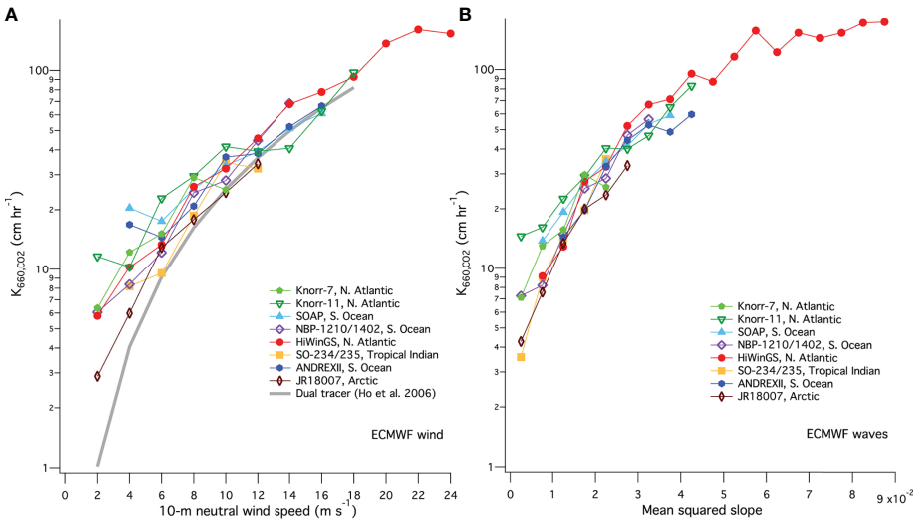

FIGURE 7 | **(A)** K_{660} averaged into bins of ECMWF U_{10n}; **(B)** K_{660} averaged into bins of ECMWF mean squared slope (MSS).

mean of these observations representative of the global average and how does that compare to the tracer data? The grand average of EC K_{660} data (average of the bin averages) from all cruises is shown in **Figure 8**. The polynomial fits of this data to u_* and to U_{10n}, weighted by the standard error in each bin, are $K_{660} = -1.47 + 76.67u_* + 20.48u_*^2$ and $K_{660} = 0.36 + 1.203U_{10n} + 0.167U_{10n}^2$, respectively ($K_{660}$ in cm hr^{-1}; u_* and U_{10n} in m s^{-1}). A power fit of the grand average as a function of wind speed yields an exponent that is less than two: $K_{660} = 1.92 + 0.57U_{10n}^{1.68}$. The relative standard error is ~7% and the relative standard deviation of our grand average is ~19% at moderate wind speeds. We note that for users who wish to apply the above equations to estimate CO_2 fluxes, the cool skin effect should be taken into account in the calculation of ΔC and the Schmidt number should be computed at the subskin, rather than skin, temperature.

To compute a global average K_{660} from EC observations, we primarily utilize the global Cross-Calibrated Multi-Platform (CCMP) wind speed distribution (0.25°, 6-h resolution; Atlas et al., 2011), which was used by Wanninkhof (2014) to develop the ^{14}C-based K_{660} parametrization. Combining the grand average of EC K_{660} as a function of u_* with the CCMP wind speed distribution (transformed to u_* according to the COARE 3.5 stress relationship), we get a global average K_{660} implied from EC observations of 20.6 cm hr^{-1}, with a standard error (standard deviation) of 1.5 (3.9) cm hr^{-1}. This global average is well within the range and uncertainties of the corrected global average values (18.2 ± 3.6 cm hr^{-1}) reported by Naegler (2009) based on ^{14}C disequilibrium (**Figure 9**). Using the ECMWF ERA5 global wind speed distribution (0.25°, 1-h resolution; Hersbach et al., 2020) instead, we get a slightly lower global average, EC-implied K_{660} of 19.7 cm hr^{-1}. This was estimated by applying the coefficients provided in by Fay et al. (2021, Table A2) to the CCMP-based K_{660}.

Some regions of the global oceans are missing (e.g., most of the Pacific Ocean) from or underrepresented (e.g., tropics) in this analysis. We have chosen to omit coastal measurements from stationary sites, which may be more affected by spatial heterogeneity in the flux footprint (e.g., Yang et al., 2019), fetch (e.g., Prytherch and Yelland, 2021), and different wave breaking characteristics compared to the open ocean. Furthermore, there are some differences between the grand average H_s from all the cruises and the global average H_s in high winds (see **Supplementary Figure 6**). Nevertheless, **Figures 8**, **9** suggest that the grand average of EC K_{660} from the 11 cruises is a reasonable representation of the global average air-sea CO_2 exchange.

The tracer-based K_{660} parametrizations (Wanninkhof, 2014 and Ho et al., 2006) are noticeably lower (i.e., below the 95% confidence bands) than the grand average of EC K_{660} data at low wind speeds (**Figure 8**). As discussed in Section 3.2, this discrepancy likely relates to the early assumption of no gas exchange at $U_{10n} = 0$. In moderate to high winds, the tracer-based estimates are within the confidence bands of the EC K_{660} grand average.

Based on the CCMP global wind distribution, the implied global average K_{660} from EC CO_2 measurements is about 20% higher than the dual tracer estimate from Ho et al. (2006). Adjusting K_{660} upwards at low wind speeds but not at high wind speeds will affect the spatial and temporal variability in estimated CO_2 fluxes. The lower latitude oceans are typically regions of net CO_2 emission and tend to have fairly low wind speeds. Meanwhile, in temperate/high latitudes, the spring phytoplankton bloom usually coincides with shoaling of the ocean mixed layer that is in part aided by a seasonal reduction in wind speed. Our results suggest that previous estimates of CO_2 emission and uptake in such instances could be underestimated.

5 LOOKING FORWARD

Overall, the relative uncertainty in K_{660} is largest at very low wind speeds (Section 3.2), while the absolute uncertainty is

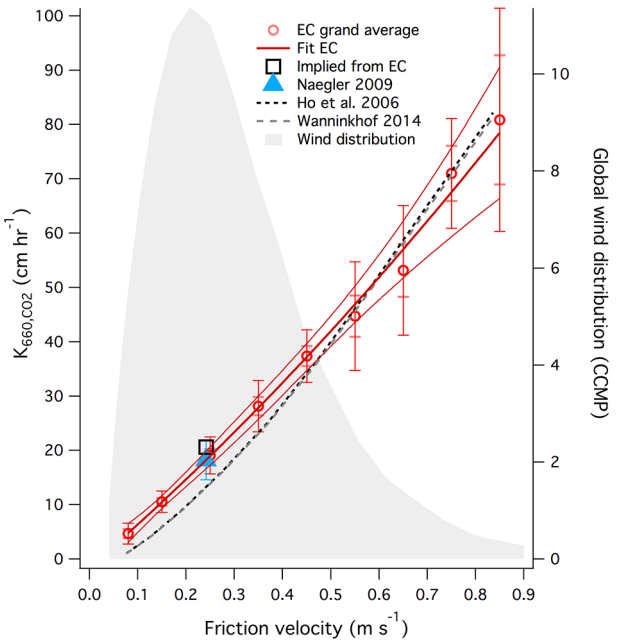

FIGURE 8 | Grand average of EC K_{660} from all cruises vs. friction velocity, with the smaller (larger) error bars indicating standard error (standard deviation). The thick red line indicates the weighted polynomial fit to this data ($K_{660} = -1.47 + 76.67u_* + 20.48u_*^2$), while the thin red lines are the 95% confidence bands for the fit. Combining the grand average of EC K_{660} with the CCMP wind distribution yields a global average K_{660}, which is shown along with the Naegler (2009) estimate. Also shown are previous K_{660} relationships from Wanninkhof (2014) based on ^{14}C disequilibrium and from Ho et al. (2006) based on the dual tracer ($^3He/SF_6$) method.

largest at very high wind speeds (*High Wind Regime and Waves*). Despite combining 11 cruises, data during these extreme conditions remain scarce (**Figure 1**) and should be the foci of future field projects. Future measurements in the tropics and in the Pacific Ocean should further improve the representativeness of the grand average EC K_{660} and aid the development of a wind/wave-dependent parametrization of K_{660}.

One of the key advantages of the EC technique is the ability to capture variability in K_{660} on much shorter timescales (one to a few hours; see Dong et al., 2021) than tracer-based approaches (days to years). EC is thus well suited for studying the more ephemeral processes that affect air-sea exchange. The analysis presented here has taken the approach of bin-averaging K_{660} data in various parameter spaces (e.g., u_*, U_{10n}, R_{Hw}, and MSS). This approach is useful for reducing measurement noise but could have the undesirable effect of averaging out the processes of interest. Hourly data from all the cruises are included in the supplement. Future analysis of this dataset (plus any additional datasets) on shorter timescales (e.g., without bin-averaging) may illuminate further process-level insights.

Consideration of waves helps to explain some of the variability that is not accounted for by U_{10n} (or by a U_{10n} dependent formulation of u_*). Future EC K_{660} measurements should clearly be accompanied by high resolution wave measurements (such as during Knorr-11 and HiWinGS). At low to moderate wind speeds, given the fact that K_{660} is more scattered vs. ECMWF U_{10n} (**Figure 7**) than vs. *in-situ* U_{10n} (**Supplementary Figure 4**), it is plausible that an *in-situ* observation of surface roughness or MSS would be superior to the current model MSS for parametrizing K_{660}. Such a measurement possibly also helps to account for the dampening of smaller-scale waves by surfactants (Frew et al., 2004). Further model development (e.g., Janssen and Bidlot, 2021) extending the MSS estimate to higher frequencies (i.e., including micro-breaking) may also be fruitful. At high wind speeds, the current use of R_{Hw} ignores any directional difference between wind and wave, which has been proposed to have some influence on gas exchange (Zavarsky and Marandino, 2019). Following Blomquist et al. (2017) and Brumer et al. (2017b), this work only considers H_s of the total waves in the calculation of R_{Hw}. The supplement of this paper includes hindcast wave data for both wind-sea and swell, permitting a more thorough investigation into the effects of wind-wave directional offset as well as the different influences from wind-sea and swell on gas exchange.

Partitioning the total gas transfer velocity into diffusive and wave-dependent bubble components (following the approaches of e.g., Blomquist et al., 2017; Deike and Melville, 2018), constrained by multiple gases of different solubility, is necessary to further improve process-level understanding in gas exchange. In addition to CO_2 and DMS, concurrent K measurement of another gas (preferably with solubility less than or similar to CO_2) would be particularly useful. Such an approach applied in two different wind-wave facilities at high wind speeds with many tracers spanning a wide range of solubilities suggests that bubble-mediated gas transfer is not significant for gases with similar solubility to CO_2 (Krall et al., 2019). This discrepancy between field and laboratory data needs further investigations. Active thermography (e.g., Frew et al., 2004) represents an alternative method to investigate K (especially diffusive exchange) on a short temporal scale. Though given the low Schmidt number of heat (~9), derivation of K_{660} using this method is very sensitive to the assumption of the Schmidt number exponent.

Our discussion so far has not explicitly considered the impact of surfactants. Recent observations (Sabbaghzadeh et al., 2017; Mustaffa et al., 2020) show large spatial variability in sea surface surfactant concentrations, which in turn affect the rate of gas transfer (Pereira et al., 2018; Yang et al., 2021). Yang et al. (2021) used a novel measurement of the gas transfer efficiency to show that the effect of surfactants on CO_2 K_{660} could be on the order of 30% at a global mean wind speed of 7 m s^{-1}, with even greater effects at lower wind speeds. Future cruises with EC CO_2 fluxes would benefit from concurrent observations of such controlling factors.

6 CONCLUSION

In this work, we reevaluate eddy covariance (EC)-derived CO_2 gas transfer velocity (K_{660}) estimates from eight datasets (11

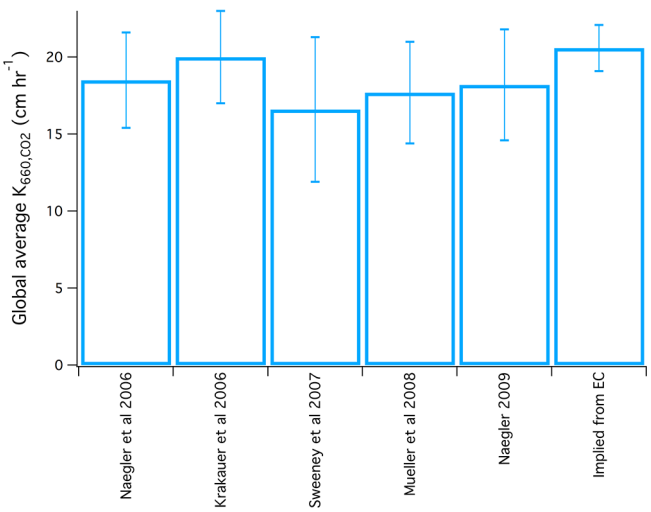

FIGURE 9 | Global average K_{660} estimates from ^{14}C (see Naegler, 2009) and implied from EC measurements, the latter based on CCMP wind distribution. The error bar on the EC estimate represents standard error.

research cruises). The reevaluation process unified flux averaging times, applied consistent and updated calculations of solubility and Schmidt number, and considered the ocean cool skin effect. Measurement biases in wind, flux, and ΔC were found to be minor. K_{660} scales approximately linearly with the friction velocity (u_*) in moderate winds, with a relative standard deviation (relative standard error) of about 20% (7%).

EC-derived K_{660} at low wind speeds is relatively uncertain, but consistently exceeds the dual tracer estimate, perhaps due to chemical enhancement in CO_2 exchange and the assumptions of the tracer model. The relative standard error (but not the relative standard deviation) in K_{660} increases substantially as wind speed becomes higher. This suggests the perceived large uncertainty in K_{660} in high winds is at least in part due to a paucity of observations.

The steepness in the K_{660}-u_* slope demonstrates some regional variability (North Atlantic ≥ Southern Ocean > Arctic, Tropics), and this variability was not primarily due to measurement uncertainties. Compared to wind speed or u_*, the modeled wave Reynolds number (R_{Hw}, a proxy for breaking of largescale waves) helps to collapse some of the variability in K_{660} in very heavy seas, while the modeled wave mean squared slope (MSS, a proxy for breaking of smaller waves) may capture more of the variability in K_{660} in calmer seas. The K_{660}-R_{Hw} and K_{660}-MSS relationships also show less regional variability than the K_{660}-u_* relationships, further illustrating the value of accounting for waves when parameterizing K_{660}.

Combining the grand average of EC-derived K_{660} from 11 cruises with the global distribution of wind speed yields a global average transfer velocity that is comparable with the most recent estimates based on global radiocarbon (^{14}C) disequilibrium. The EC-implied global average K_{660} is however ~20% higher than what is implied by the widely used K_{660} parametrizations based on dual tracer (Ho et al., 2006), with the largest difference at low wind speeds. Our analysis suggests that estimates of CO_2 fluxes using a U^2_{10n} dependence with zero intercept (e.g., dual tracer) are likely biased when wind speeds are low.

DATA AVAILABILITY STATEMENT

The original contributions presented in the study are included in the article/**Supplementary Material**. Further inquiries can be directed to the corresponding author.

AUTHOR CONTRIBUTIONS

The original collectors of EC data for this synthesis are MY, TB, BWB, BJB, YD, CF, SL, CM, SM, ES, and AZ. J-RB supplied the ECMWF data. MY performed the data reevaluation and wrote the paper with contributions from all coauthors. All authors contributed to the article and approved the submitted version.

FUNDING

This work, and the contributions of MY and TB, is supported by the UK Natural Environment Research Council's ORCHESTRA (Grant No. NE/N018095/1) and PICCOLO (Grant No. NE/P021409/1) projects, and by the European Space Agency's AMT4OceanSatFlux project (Grant No. 4000125730/18/NL/FF/gp). YD was supported by the China Scholarship Council (CSC/201906330072). CF and BWB are funded by the NOAA's Global Ocean Monitoring and Observing program (http://data.crossref.org/fundingdata/funder/10.13039/100018302). Funding for HiWinGS was provided by the US National Science Foundation grant AGS-1036062. The Knorr-07, Knorr-11 and SOAP campaigns were supported by the NSF Atmospheric Chemistry Program (Grant No. ATM-0426314, AGS-

08568, -0851472, -0851407 and -1143709). Observations on the *Sonne* were carried out under the Helmholtz Young Investigator Group of CAM, TRASE-EC (VH-NG819), from the Helmholtz Association. The cruise 234-2/235 was financed by the BMBF, 03G0235A. The Nathaniel B. Palmer measurements were supported by NSF Office of Polar Programs Award 1043623.

ACKNOWLEDGMENTS

This paper attempts to synthesize the enormous efforts in the area of direct air-sea CO_2 exchange measurements over more than a decade. The author list here consists primarily of main data originators and does not include everyone who contributed towards the observations. Please refer to the original paper for each cruise for the full list of contributors. The first author thanks B. Huebert (University of Hawaii), P. Liss (University of East Anglia), and J. Shutler (University of Exeter) for their inspirations and helpful questions during the paper writing. Brian Butterworth was additionally supported by the NOAA Physical Sciences Laboratory. This work represents a contribution towards the international Surface Lower Atmosphere Studies (SOLAS).

SUPPLEMENTARY MATERIAL

The Supplementary Material for this article can be found online at: https://www.frontiersin.org/articles/10.3389/fmars.2022.826421/full#supplementary-material

REFERENCES

Ardhuin, F., Rogers, E., Babanin, A. V., Filipot, J. F., Magne, R., Roland, A., et al. (2010). Semiempirical Dissipation Source Functions for Ocean Waves. Part I: Definition, Calibration, and Validation. *J. Phys. Oceanogr.* 40 (9), 1917–1941. doi: 10.1175/2010JPO4324.1

Asher, W. E., and Wanninkhof, R. (1998). The Effect of Bubble-Mediated Gas Transfer on Purposeful Dual-Gaseous Tracer Experiments. *J. Geophys. Res.: Ocean.* 103 (C5), 10555–10560. doi: 10.1029/98JC00245

Atlas, R., Hoffman, R. N., Ardizzone, J., Leidner, S. M., Jusem, J. C., Smith, D. K., et al. (2011). A Cross-Calibrated, Multiplatform Ocean Surface Wind Velocity Product for Meteorological and Oceanographic Applications. *Bull. Am. Meteorol. Soc.* 92 (2), 157–174. doi: 10.1175/2010BAMS2946.1

Bakker, D. C., Pfeil, B., Landa, C. S., Metzl, N., O'brien, K. M., Olsen, A., et al. (2016). A Multi-Decade Record of High-Quality fCO_2 Data in Version 3 of the Surface Ocean CO_2 Atlas (SOCAT). *Earth Sys. Sci. Data* 8 (2), 383–413. doi: 10.5194/essd-8-383-2016

Bell, T. G., De Bruyn, W., Miller, S. D., Ward, B., Christensen, K. H., and Saltzman, E. S. (2013). Air–sea Dimethylsulfide (DMS) Gas Transfer in the North Atlantic: Evidence for Limited Interfacial Gas Exchange at High Wind Speed. *Atmos. Chem. Phys.* 13 (21), 11073–11087. doi: 10.5194/acp-13-11073-2013

Bell, T. G., Landwehr, S., Miller, S. D., De Bruyn, W. J., Callaghan, A. H., Scanlon, B., et al. (2017). Estimation of Bubble-Mediated Air–Sea Gas Exchange From Concurrent DMS and CO_2 Transfer Velocities at Intermediate–High Wind Speeds. *Atmos. Chem. Phys.* 17 (14), 9019–9033. doi: 10.5194/acp-17-9019-2017

Bidlot, J.-R. (2019). *Model Upgrade Improves Ocean Wave Forecasts* Vol. 159 (ECMWF newsletter), 10–10. Available at: https://www.ecmwf.int/en/newsletter/159/news/model-upgrade-improves-ocean-wave-forecasts.

Blomquist, B. W., Brumer, S. E., Fairall, C. W., Huebert, B. J., Zappa, C. J., Brooks, I. M., et al. (2017). Wind Speed and Sea State Dependencies of Air-Sea Gas Transfer: Results From the High Wind Speed Gas Exchange Study (HiWinGS). *J. Geophys. Res.: Ocean.* 122 (10), 8034–8062. doi: 10.1002/2017JC01318110.1002/ 2017JC013181

Blomquist, B. W., Huebert, B. J., Fairall, C. W., Bariteau, L., Edson, J. B., Hare, J. E., et al. (2014). Advances in Air–Sea $$\Hbox {CO} _2 $$ CO_2 Flux Measurement by Eddy Correlation. *Bound.-Lay. Meteorol.* 152 (3), 245–276. doi: 10.1007/s10546-014-9926-2

Brumer, S. E., Zappa, C. J., Blomquist, B. W., Fairall, C. W., Cifuentes-Lorenzen, A., Edson, J. B., et al. (2017b). Wave-Related Reynolds Number Parametrization of CO_2 and DMS Transfer Velocities. *Geophys. Res. Lett.* 44 (19), 9865–9875. doi: 10.1002/2017GL074979

Brumer, S. E., Zappa, C. J., Brooks, I. M., Tamura, H., Brown, S. M., Blomquist, B. W., et al. (2017a). Whitecap Coverage Dependence on Wind and Wave Statistics as Observed During SO GasEx and HiWinGS. *J. Phys. Oceanogr.* 47 (9), 2211–2235. doi: 10.1175/JPO-D-17-0005.1

Butterworth, B. J., and Miller, S. D. (2016). Air-Sea Exchange of Carbon Dioxide in the Southern Ocean and Antarctic Marginal Ice Zone. *Geophys. Res. Lett.* 43 (13), 7223–7230. doi: 10.1002/2016GL069581

Deike, L., and Melville, W. K. (2018). Gas Transfer by Breaking Waves. *Geophys. Res. Lett.* 45, 482– 10,492. doi: 10.1029/2018GL078758

Dong, Y., Yang, M., Bakker, D. C., Kitidis, V., and Bell, T. G. (2021). Uncertainties in Eddy Covariance Air–Sea CO_2 Flux Measurements and Implications for Gas Transfer Velocity Parameterisations. *Atmos. Chem. Phys.* 21 (10), 8089–8110. doi: 10.5194/acp-21-8089-2021

Donlon, C. J., Minnett, P. J., Gentemann, C., Nightingale, T. J., Barton, I. J., Ward, B., et al (2002). Toward Improved Validation of Satellite Sea Surface Skin Temperature Measurements for Climate Research. *Journal of Climate*, 15 (4):353–69. doi: 10.1175/1520-0442(2002)015<0353:TIVOSS>2.0.CO;2

ECMWF (2020). "Part VII: ECMWF Wave Model," in *IFS Documentation CY47R1, (Reading: Shinfield Park)*. Available at: https://www.ecmwf.int/en/elibrary/19311-part-vii-ecmwf-wave-model. doi: 10.21957/21g1hoiuo

Edson, J. B., Fairall, C. W., Bariteau, L., Zappa, C. J., Cifuentes-Lorenzen, A., McGillis, W. R., et al. (2011). Direct Covariance Measurement of CO_2 Gas Transfer Velocity During the 2008 Southern Ocean Gas Exchange Experiment: Wind Speed Dependency. *J. Geophys. Res.: Ocean.* 116 (C4).C00F10

Edson, J. B., Hinton, A. A., Prada, K. E., Hare, J. E., and Fairall, C. W. (1998). Direct Covariance Flux Estimates From Mobile Platforms at Sea. *J. Atmos. Ocean. Technol.* 15 (2), 547–562. doi: 10.1175/1520-0426(1998)015<0547:DCFEFM>2.0.CO;2

Esters, L., Landwehr, S., Sutherland, G., Bell, T. G., Christensen, K. H., Saltzman, E. S., et al. (2017). Parameterizing Air-Sea Gas Transfer Velocity With Dissipation. *J. Geophys. Res.: Ocean.* 122 (4), 3041–3056. doi: 10.1002/2016JC012088

Fairall, C. W., Bradley, E. F., Godfrey, J. S., Wick, G. A., Edson, J. B., and Young, G. S. (1996). Cool-Skin and Warm-Layer Effects on Sea Surface Temperature. *J. Geophys. Res.: Ocean.* 101 (C1), 1295–1308. doi: 10.1029/95JC03190

Fairall, C. W., Yang, M., Bariteau, L., Edson, J. B., Helmig, D., McGillis, W., et al. (2011). Implementation of the Coupled Ocean-Atmosphere Response Experiment Flux Algorithm With CO_2, Dimethyl Sulfide, and O3. *J. Geophys. Res.: Ocean.* 116 (C4):C00F09. doi: 10.1029/2010JC006884

Fay, A. R., Gregor, L., Landschützer, P., McKinley, G. A., Gruber, N., Gehlen, M., et al. (2021). SeaFlux: Harmonization of Air–Sea CO_2 Fluxes From Surface pCO_2 Data Products Using a Standardized Approach. *Earth Sys. Sci. Data* 13 (10), 4693–4710. doi: 10.5194/essd-13-4693-2021

Frew, N. M., Bock, E. J., Schimpf, U., Hara, T., Haussecker, H., Edson, J. B., et al. (2004). Air-Sea Gas Transfer: Its Dependence on Wind Stress, Small-Scale Roughness, and Surface Films. *J. Geophys. Res.* 109, C08S17. doi: 10.1029/2003JC002131

Friedlingstein, P., O'sullivan, M., Jones, M. W., Andrew, R. M., Hauck, J., Olsen, A., et al. (2020). Global Carbon Budget 2020. *Earth Sys. Sci. Data* 12 (4), 3269–3340. doi: 10.5194/essd-12-3269-2020

Hersbach, H., Bell, B., Berrisford, P., Biavati, G., Horányi, A., Muñoz Sabater, J., et al. (2018). "ERA5 Hourly Data on Single Levels From 1979 to Present," in

Copernicus Climate Change Service (C3S) Climate Data Store (CDS), 10. doi: 10.24381/cds.adbb2d47

Hersbach, H., Bell, B., Berrisford, P., Hirahara, S., Horányi, A., Muñoz-Sabater, J., et al. (2020). The ERA5 Global Reanalysis. *Q. J. R. Meteorol. Soc.* 146 (730), 1999–2049. doi: 10.1002/qj.3803

Ho, D. T., Law, C. S., Smith, M. J., Schlosser, P., Harvey, M., and Hill, P. (2006). Measurements of Air-Sea Gas Exchange at High Wind Speeds in the Southern Ocean: Implications for Global Parametrizations. *Geophys. Res. Lett.* 33 (16): L16611. doi: 10.1029/2006GL026817

Hoover, T. E., and Berkshire, D. C. (1969). Effects of Hydration on Carbon Dioxide Exchange Across an Air-Water Interface. *J. Geophys. Res.* 74 (2), 456–464. doi: 10.1029/JB074i002p00456

Jähne, B., Degreif, K., and Kuss, J. (2010). "Wind/wave-Tunnel Measurements of Chemical Enhancement of the Carbon Dioxide Gas Exchange," *Gas Transfer at Water Surfaces*. Kyoto, Japan. doi: 10.5281/zenodo.14928

Jähne, B., Münnich, K. O., Bösinger, R., Dutzi, A., Huber, W., and Libner, P. (1987). On the Parameters Influencing Air-Water Gas Exchange. *J. Geophys. Res.* 92, 1937–1949. doi: 10.1029/JC092iC02p01937

Janssen, P. A. E. M., and Bidlot, J.-R. (2021). "On the Consequences of Nonlinearity and Gravity-Capillary Waves on Wind-Wave Interaction," in *ECMWF Tech. Memo. 882* (Reading, United Kingdom: ECMWF), 42pp.

Khatiwala, S., Tanhua, T., Mikaloff Fletcher, S., Gerber, M., Doney, S. C., Graven, H. D., et al. (2013). Global Ocean Storage of Anthropogenic Carbon. *Biogeosciences* 10 (4), 2169–2191. doi: 10.5194/bg-10-2169-2013

Krakauer, N. Y., Randerson, J. T., Primeau, F. W., Gruber, N., and Menemenlis, D. (2006). Carbon Isotope Evidence for the Latitudinal Distribution and Wind Speed Dependence of the Air–Sea Gas Transfer Velocity. *Tell. B.: Chem. Phys. Meteorol.* 58 (5), 390–417. doi: 10.1111/j.1600-0889.2006.00223.x

Krall, K. E., Smith, A. W., Takagaki, N., and Jähne, B. (2019). Air–sea Gas Exchange at Wind Speeds Up to 85 m s-1. *Ocean. Sci.* 15 (6), 1783–1799. doi: 10.5194/os-15-1783-2019

Landwehr, S., Miller, S. D., Smith, M. J., Bell, T. G., Saltzman, E. S., and Ward, B. (2018). Using Eddy Covariance to Measure the Dependence of Air–Sea CO_2 Exchange Rate on Friction Velocity. *Atmos. Chem. Phys.* 18 (6), 4297–4315. doi: 10.5194/acp-18-4297-2018

Landwehr, S., Miller, S. D., Smith, M. J., Saltzman, E. S., and Ward, B. (2014). Analysis of the PKT Correction for Direct CO_2 Flux Measurements Over the Ocean. *Atmos. Chem. Phys.* 14 (7), 3361–3372. doi: 10.5194/acp-14-3361-2014

Landwehr, S., O'Sullivan, N., and Ward, B. (2015). Direct Flux Measurements From Mobile Platforms at Sea: Motion and Airflow Distortion Corrections Revisited. *J. Atmos. Ocean. Technol.* 32 (6), 1163–1178. doi: 10.1175/JTECH-D-14-00137.1

Liss, P. S., and Merlivat, L. (1986). "Air-Sea Gas Exchange Rates: Introduction and Synthesis," in *The Role of Air-Sea Exchange in Geochemical Cycling* (Dordrecht: Springer), 113–127.

Mackay, D., and Yeun, A. T. (1983). Mass Transfer Coefficient Correlations for Volatilization of Organic Solutes From Water. *Environ. Sci. Technol.* 17 (4), 211–217. doi: 10.1021/es00110a006

McGillis, W. R., Edson, J. B., Hare, J. E., and Fairall, C. W. (2001). Direct Covariance Air-Sea CO_2 Fluxes. *J. Geophys. Res.: Ocean.* 106 (C8), 16729–16745. doi: 10.1029/2000JC000506

McGillis, W. R., Edson, J. B., Zappa, C. J., Ware, J. D., McKenna, S. P., Terray, E. A., et al. (2004). Air-Sea CO_2 Exchange in the Equatorial Pacific. *J. Geophys. Res.: Ocean.* 109 (C8):C08S02. doi: 10.1029/2003JC002256

McGillis, W. R., and Wanninkhof, R. (2006). Aqueous CO_2 Gradients for Air-Sea Flux Estimates. *Mar. Chem.* 98, 100–108. doi: 10.1016/j.marchem.2005.09.003

Miller, S., Marandino, C., De Bruyn, W., and Saltzman, E. S. (2009). Air-Sea Gas Exchange of CO_2 and DMS in the North Atlantic by Eddy Covariance. *Geophys. Res. Lett.* 36 (15):L15816. doi: 10.1029/2009GL038907

Müller, S. A., Joos, F., Plattner, G. K., Edwards, N. R., and Stocker, T. F. (2008). Modeled Natural and Excess Radiocarbon: Sensitivities to the Gas Exchange Formulation and Ocean Transport Strength. *Global Biogeochem. Cycle.* 22 (3): GB3011. doi: 10.1029/2007GB003065

Mustaffa, N. I. H., Ribas-Ribas, M., Banko-Kubis, H. M., and Wurl, O. (2020). Global Reduction of *in Situ* CO_2 Transfer Velocity by Natural Surfactants in the Sea-Surface Microlayer. *Proc. R. Soc. A.* 476 (2234), 20190763. doi: 10.1098/rspa.2019.0763

Naegler, T. (2009). Reconciliation of Excess ^{14}C-Constrained Global CO_2 Piston Velocity Estimates. *Tell. B.* 61, 372–384. doi: 10.1111/j.1600-0889.2008.00408.x

Naegler, T., Ciais, P., Rodgers, K., and Levin, I. (2006). Excess Radiocarbon Constraints on Air-Sea Gas Exchange and the Uptake of CO_2 by the Oceans. *Geophys. Res. Lett.* 33 (11):L11802. doi: 10.1029/2005GL025408

Nagel, L., Krall, K. E., and Jähne, B. (2019). Measurements of Air–Sea Gas Transfer Velocities in the Baltic Sea. *Ocean. Sci.* 15 (2), 235–247. doi: 10.5194/os-15-235-2019

Pereira, R., Ashton, I., Sabbaghzadeh, B., Shutler, J. D., and Upstill-Goddard, R. C. (2018). Reduced Air–Sea CO_2 Exchange in the Atlantic Ocean Due to Biological Surfactants. *Nature Geoscience*, 11(7):492–6. doi: 10.1038/s41561-018-0136-2

Prytherch, J., Brooks, I. M., Crill, P. M., Thornton, B. F., Salisbury, D. J., Tjernström, M., et al. (2017). Direct Determination of the Air-Sea CO_2 Gas Transfer Velocity in Arctic Sea Ice Regions. *Geophys. Res. Lett.* 44 (8), 3770–3778. doi: 10.1002/2017GL073593

Prytherch, J., and Yelland, M. J. (2021). Wind, Convection and Fetch Dependence of Gas Transfer Velocity in an Arctic Sea-Ice Lead Determined From Eddy Covariance CO_2 Flux Measurements. *Global Biogeochem. Cycle.* 35 (2), e2020GB006633. doi: 10.1029/2020GB006633

Sabbaghzadeh, B., Upstill-Goddard, R. C., Beale, R., Pereira, R., and Nightingale, P. D. (2017). The Atlantic Ocean Surface Microlayer From 50 N to 50 S is Ubiquitously Enriched in Surfactants at Wind Speeds Up to 13 m s-1. *Geophys. Res. Lett.* 44 (6), 2852–2858. doi: 10.1002/2017GL072988

Saunders, P. M. (1967). The Temperature at the Ocean-Air Interface. *J. Atmos. Sci.* 24 (3), 269–273. doi: 10.1175/1520-0469(1967)024<0269:TTATOA>2.0.CO;2

Soli, A. L., and Byrne, R. H. (2002). CO_2 System Hydration and Dehydration Kinetics and the Equilibrium CO_2/H_2CO_3 Ratio in Aqueous NaCl Solution. *Mar. Chem.* 78 (2-3), 65–73. doi: 10.1016/S0304-4203(02)00010-5

Soloviev, A. V., and Schluessel, P. (1994). Parametrization of the Cool Skin of the Ocean and of the Air-Ocean Gas Transfer on the Basis of Modeling Surface Renewal. *J. Phys. Oceanogr.* 2, 1339–1346. doi: 10.1175/1520-0485(1994)024<1339:POTCSO>2.0.CO;2

Sweeney, C., Gloor, E., Jacobson, A. R., Key, R. M., McKinley, G., Sarmiento, J. L., et al. (2007). Constraining Global Air-Sea Gas Exchange for CO_2 With Recent Bomb ^{14}C Measurements. *Global Biogeochem. Cycle.* 21 (2):GB2015. doi: 10.1029/2006GB002784

Wanninkhof, R. (1992). Relationship Between Wind Speed and Gas Exchange Over the Ocean. *J. Geophys. Res.* 97 (C5), 7373 – 7382. doi: 10.1029/92JC00188

Wanninkhof, R. (2014). Relationship Between Wind Speed and Gas Exchange Over the Ocean Revisited. *Limnol. Oceanogr.: Methods* 12 (6), 351–362. doi: 10.4319/lom.2014.12.351

Wanninkhof, R., and McGillis, W. R. (1999). A Cubic Relationship Between Air-Sea CO_2 Exchange and Wind Speed. *Geophys. Res. Lett.* 26 (13), 1889–1892. doi: 10.1029/1999GL900363

Ward, B., Wanninkhof, R., McGillis, W. R., Jessup, A. T., DeGrandpre, M. D., Hare, J. E., et al. (2004). Biases in the Air-Sea Flux of CO_2 Resulting From Ocean Surface Temperature Gradients. *J. Geophys. Res.: Ocean.* 109 (C8): C08S08. doi: 10.1029/2003JC001800

Watson, A. J., Schuster, U., Shutler, J. D., Holding, T., Ashton, I. G., Landschützer, P., et al. (2020). Revised Estimates of Ocean-Atmosphere CO_2 Flux are Consistent With Ocean Carbon Inventory. *Nat. Commun.* 11 (1), 1–6. doi: 10.1038/s41467-020-18203-3

Woolf, D. K. (1997). "Bubbles and Their Role in Gas Exchange," in *The Sea Surface and Global Change*. Eds. R. Duce and P. Liss (New York: Cambridge Univ. Press), 173–205.

Woolf, D. K., Land, P. E., Shutler, J. D., Goddijn-Murphy, L. M., and Donlon, C. J. (2016). On the Calculation of Air-Sea Fluxes of CO_2 in the Presence of Temperature and Salinity Gradients. *J. Geophys. Res.: Ocean.* 121 (2), 1229–1248. doi: 10.1002/2015JC011427

Woolf, D. K., Shutler, J. D., Goddijn-Murphy, L., Watson, A. J., Chapron, B., Nightingale, P. D., et al. (2019). Key Uncertainties in the Recent Air-Sea Flux of CO_2. *Global Biogeochem. Cycle.* 33 (12), 1548–1563. doi: 10.1029/2018GB006041

Yang, M., Bell, T. G., Brown, I. J., Fishwick, J. R., Kitidis, V., Nightingale, P. D., et al. (2019). Insights From Year-Long Measurements of Air–Water CH_4 and CO_2 Exchange in a Coastal Environment. *Biogeosciences* 16 (5), 961–978. doi: 10.5194/bg-16-961-2019

Yang, M., Blomquist, B. W., Fairall, C. W., Archer, S. D., and Huebert, B. J. (2011). Air-Sea Exchange of Dimethylsulfide in the Southern Ocean: Measurements From SO GasEx Compared to Temperate and Tropical Regions. *J. Geophys. Res.: Ocean.* 116 (C4). doi: 10.1029/2010JC006526

Yang, M., Prytherch, J., Kozlova, E., Yelland, M. J., Parenkat Mony, D., and Bell, T. G. (2016). Comparison of Two Closed-Path Cavity-Based Spectrometers for Measuring Air–Water CO_2 and CH_4 Fluxes by Eddy Covariance. *Atmos. Measure. Techniq.* 9 (11), 5509–5522. doi: 10.5194/amt-9-5509-2016

Yang, M., Smyth, T. J., Kitidis, V., Brown, I. J., Wohl, C., Yelland, M. J., et al. (2021). Natural Variability in Air–Sea Gas Transfer Efficiency of CO_2. *Sci. Rep.* 11 (1), 1–9. doi: 10.1038/s41598-021-92947-w

Zavarsky, A., Goddijn-Murphy, L., Steinhoff, T., and Marandino, C. A. (2019). Bubble-Mediated Gas Transfer and Gas Transfer Suppression of DMS and CO_2. *J. Geophys. Res.: Atmos.* 123 (12), 6624–6647. doi: 10.1029/2017JD028071

Zavarsky, A., and Marandino, C. A. (2019). The Influence of Transformed Reynolds Number Suppression on Gas Transfer Parametrization and Global DMS and CO_2 Fluxes. *Atmos. Chem. Phys.* 19 (3), 1819–1834. doi: 10.5194/acp-19-1819-2019

Zhang, H., Beggs, H., Ignatov, A., and Babanin, A. V. (2020). Nighttime Cool Skin Effect Observed From Infrared SST Autonomous Radiometer (ISAR) and Depth Temperatures. *J. Atmos. Ocean. Technol.* 37 (1), 33–46. doi: 10.1175/JTECH-D-19-0161.1

Conflict of Interest: The authors declare that the research was conducted in the absence of any commercial or financial relationships that could be construed as a potential conflict of interest.

Publisher's Note: All claims expressed in this article are solely those of the authors and do not necessarily represent those of their affiliated organizations, or those of the publisher, the editors and the reviewers. Any product that may be evaluated in this article, or claim that may be made by its manufacturer, is not guaranteed or endorsed by the publisher.

frontiers | Frontiers in Marine Science

ORIGINAL RESEARCH
published: 29 July 2022
doi: 10.3389/fmars.2022.826606

Air-Sea Trace Gas Fluxes: Direct and Indirect Measurements

Christopher W. Fairall[1], Mingxi Yang[2], Sophia E. Brumer[3], Byron W. Blomquist[1,4], James B. Edson[5], Christopher J. Zappa[6], Ludovic Bariteau[1,4], Sergio Pezoa[1], Thomas G. Bell[2] and Eric S. Saltzman[7]*

[1] National Oceanic and Atmospheric (NOAA) Administration, Department: Physical Science Laboratory, Boulder, CO, United States, [2] Plymouth Marine Laboratory; Department: Marine Biogeochemistry and Observations, Plymouth, United Kingdom, [3] Laboratoire d'Océanographie Physique et Spatiale, UMR 6523, CNRS-IFREMER-IRD-UBO, IUEM, Plouzané, France, [4] Cooperative Institute for Research in Environmental Sciences, University of Colorado Boulder, Boulder, CO, United States, [5] Applied Ocean Physics & Engineering, Woods Hole Oceanographic Institution, Woods Hole, MA, United States, [6] Lamont-Doherty Earth Observatory of Columbia University, Pallisades, NY, United States, [7] Department of Earth System Science, University of California, Irvine, CA, United States

The past decade has seen significant technological advance in the observation of trace gas fluxes over the open ocean, most notably CO_2, but also an impressive list of other gases. Here we will emphasize flux observations from the air-side of the interface including both turbulent covariance (direct) and surface-layer similarity-based (indirect) bulk transfer velocity methods. Most applications of direct covariance observations have been from ships but recently work has intensified on buoy-based implementation. The principal use of direct methods is to quantify empirical coefficients in bulk estimates of the gas transfer velocity. Advances in direct measurements and some recent field programs that capture a considerable range of conditions with wind speeds exceeding 20 ms^{-1} are discussed. We use coincident direct flux measurements of CO_2 and dimethylsulfide (DMS) to infer the scaling of interfacial viscous and bubble-mediated (whitecap driven) gas transfer mechanisms. This analysis suggests modest chemical enhancement of CO_2 flux at low wind speed. We include some updates to the theoretical structure of bulk parameterizations (including chemical enhancement) as framed in the COAREG gas transfer algorithm.

Keywords: gas transfer velocity, chemical enhancement, bubble mediated transfer, COARE gas flux parameterization, Dimethylsufide (DMS), cardon dioxide (CO_2), bulk algorithm, direct observation

OPEN ACCESS

Edited by:
Petra Heil,
Australian Antarctic Division, Australia

Reviewed by:
Sohiko Kameyama,
Hokkaido University, Japan
Ivan Mammarella,
University of Helsinki, Finland

****Correspondence:***
Christopher W. Fairall
chris.fairall@noaa.gov

Specialty section:
This article was submitted to Ocean Observation, a section of the journal Frontiers in Marine Science

Received: *01 December 2021*
Accepted: *24 May 2022*
Published: *29 July 2022*

Citation:
Fairall CW, Yang M, Brumer SE, Blomquist BW, Edson JB, Zappa CJ, Bariteau L, Pezoa S, Bell TG and Saltzman ES (2022) Air-Sea Trace Gas Fluxes: Direct and Indirect Measurements. Front. Mar. Sci. 9:826606. doi: 10.3389/fmars.2022.826606

1 INTRODUCTION

The exchange of gases between the atmosphere and ocean is an important process in global budgets of many gases with significant implications in climate, biogeochemical cycles, oceanic ecosystems, and pollution. Because of its importance to global carbon budgets, biology, and climate, carbon dioxide (CO_2) tends to dominate our interest in the subject but many gases including oxygen (O_2), carbon monoxide (CO), dimethylsulfide (DMS), ozone (O_3), and sulfur dioxide (SO_2) to name a few, are also relevant - see Johnson (2010) for a list of 79 gases. The exchange of non-reactive gases are usually expressed as vertical fluxes which are principally driven by wind speed and the sea-air concentration difference of the gas. Gas fluxes may be measured directly from ships with bow-

mounted eddy correlation systems or estimated from mean concentrations using so-called bulk flux relationships (Fairall et al., 2000; Wanninkhof et al., 2009). Arrays of *in situ* measurements are not practical for global or regional budget closure, so some combination of satellite, reanalysis, and data assimilation synthesis is needed (Cronin et al., 2019; Shutler et al., 2020). These approaches rely on the bulk relationships. Thus, the principal application of direct measurements [including deliberate dual tracer techniques, Ho et al. (2011)] is in determining the appropriate bulk scaling variables and coefficients. It turns out this is a complex issue that involves similarity theory, chemistry, laboratory studies, process models such as direct numerical and large eddy simulations (DNS and LES), and a variety of experimental approaches in the field (see Garbe et al., 2014, for an overview).

The mass flux of some scalar variable, x, can be directly estimated from measurements of turbulent correlations in the near-surface atmosphere with the direct covariance (a.k.a. eddy correlation) technique:

$$F_x = \rho_{ad}\ \overline{w' r_x{}'} \cong \overline{w'x'} \tag{1}$$

Here ρ_{ad} is the density of dry air, r_x the mixing ratio of x (mass of x per dry mass of air), w' and x' are turbulent fluctuations of vertical velocity and dry air mole fraction of x, respectively. More often though, the air-sea flux is computed using the bulk method:

$$\overline{w'x'} = C_x S_z (X_s - X_z) = c_x^{1/2} u_\star (X_s - X_z) \tag{2}$$

where X is the mean concentration of x and the subscripts s and z refer to the value at the air-ocean interface and height z, respectively. S is the mean wind speed, C_x is the transfer coefficient for the mass flux of x, $c_x^{1/2}$ is the scalar transfer component specific to x and $u_* = \sqrt{C_d}\star U_{10}$ is the friction velocity where C_d is the drag coefficient and $U_{10} = \sqrt{U^2 + V^2}$ is the vector average wind speed for mean components U and V at reference height z = 10 m. Note mean wind *speed* is distinct from the mean vector wind components and is defined as $S^2 = \overline{(U + u')^2 + (V + v')^2}$, where the capitals and primes denote of the mean and turbulent fluctuations of the horizontal wind components. Differences between the mean wind speed, and vector-averaged winds are associated with gustiness (Fairall et al., 1996; Fairall et al., 2003).

The essence of bulk parametrizations is captured in specification of the transfer coefficient, C_x, which is obtained directly by measuring $\overline{w'x'}$, S_z, X_s, and X_z and applying (2). Note C_x will depend on z and buoyancy forcing as defined in Monin-Obukhov similarity theory (MOST – see e.g., Fairall et al. (1996)). Bulk algorithms have a long and successful history in meteorology; in this paper we will focus principally on the COARE family of flux codes (Fairall et al., 2011) where COAREG defines codes for gas transfer. There are certainly other products to choose from for gas transfer purposes, e.g., FluxEngine (Goddijn-Murphy et al., 2016; Shutler et al., 2016) or FuGas (Vieira et al., 2020).

While (2) is commonly used to estimate fluxes of sensible heat and moisture, the gas transfer community more often uses a formulation based on a transfer velocity, k_x,

$$F_x = \alpha_x k_x\ (X_w/\alpha_x - X_a) = \alpha_x k_x \Delta X \tag{3}$$

where α_x is the dimensionless solubility of the gas x in seawater, k_x the transfer velocity for the gas X, X_w and X_a the mean concentrations of x at some depth in water and some height in air, and we use ΔX to denote the sea-air difference in X taking solubility into account. Note that, compared to (2), expression (3) has the additional complexity of solubility. Superficially, k_x is equivalent to $C_x S_z = c_x^{1/2} u_*$ in (2). Because C_x for heat and moisture is approximately constant with the friction velocity or wind speed, we might infer that k_x is roughly proportional to wind speed. Would that it was so simple. To illustrate the variability in transfer with the properties of trace gases, Fairall et al. (2011) recast (3) as

$$F_x = \alpha_x k_x \Delta X = \left[\frac{\alpha_x k_x}{u_\star}\right]\left[u_\star \Delta X\right] = \mathrm{CP}_x\left[u_\star \Delta X\right] \tag{4}$$

with CP being interpreted as characterizing the chemical variability and $u_*\Delta X$ characterizing the physical forcing. Figure 1 in Fairall et al. (2011) shows CP varying by 4 orders of magnitude with small values (2×10^{-6}) for the highly insoluble gas neon, increasing with solubility to about 0.03 for α_x = 100 (e.g., ethanol) and then leveling off with increasing solubility. This leveling off for highly soluble gases is well understood to be the limit imposed by transfer in the atmosphere – i.e., similar to water vapor, which is unconstrained by transfer resistance on the ocean side, $\mathrm{CP}_v = c_v^{1/2} \approx 0.035$. Both CO_2 (solubility on the order of 0.5) and DMS (solubility on the order of 15) are intermediate to these extremes.

Early wind tunnel measurements (Liss and Merlivat, 1986) and analysis of ^{14}C in the ocean (Wanninkhof, 1992) found the transfer velocity of CO_2 (i.e., k_{co2}) to be non-linear in wind speed. Woolf (1993) argued that the stronger wind speed dependence of CO_2 was due to enhancement by bubbles generated by breaking waves. Because the enhancement was solubility dependent, Woolf predicted that more soluble gases would have a more linear wind speed dependence – a prediction that has been borne out by observations of DMS transfer velocity (e.g., Blomquist et al., 2006).

Ocean surface waves are an essential component in air-sea fluxes. The fluxes of momentum and kinetic energy from the atmosphere to the ocean are driven by a direct input to the ocean currents *via* viscous stress and input to waves *via* the pressure-wave slope correlation known as *form drag*. Viscous stress dominates the exchange at low wind speeds. As the winds increase, the dominant mechanism for exchange transfers to the form drag imposed primarily by wind waves with some modulation due to longer waves and swell. The action of the form drag grows waves which transfer their momentum and energy to ocean currents and turbulence initially through micro-breaking (Edson et al., 2013). The transition is complete once the waves become fully rough; a condition often associated with the onset of visible wave breaking around 7 m s^{-1}. At this point, bubble-mediated processes begin to gain importance (Woolf,

1993) and breaking of longer waves plays an increasingly important role in momentum and, particularly, energy exchange (Melville, 1996).

The simplicity of bulk flux relations (2) and (3) is somewhat misleading because complexity may be hidden in the transfer coefficients. The simplest forms contain little complexity, with power law dependence on wind speed at some reference height, typically 10m.

$$k_x = c_{1x} U_{10}^2 \tag{5}$$

where the coefficient c_{1x} depends on the gas and U in m s^{-1} (k_x in cm hr^{-1}). For CO_2 c_{1x} is on the order of 0.25 (Wanninkhof, 2014). However, there is debate about the power law with up to 3rd-order polynomials in wind speed being used (Wanninkhof et al., 2009). The temperature dependence of k_x is usually captured through a temperature-dependent Schmidt number $Sc_x = \nu/D_x$, where D_x is the oceanic molecular diffusivity and 660 is the reference value of Sc_{co2} at 20°C (although the 1/2 exponent may not hold in all conditions).

$$k_{660x} = c_{1x} U_{10}^2 (Sc_x/660)^{1/2} \tag{6}$$

Since the bulk gas and water concentrations are measured well away from the interface, mixing processes in both media must be considered. This has led to the development of physically-based parameterizations that attempt to capture the relevant processes in a unified mathematical structure (e.g. Liss and Slater, 1974; Fairall et al., 2011; Goddijn-Murphy et al., 2016). If this is successful, it is not necessary to measure c_{1x} for each gas of interest. This is the approach for the COAREG gas flux parameterizations where both atmospheric and oceanic interfacial forcing are framed within surface-layer turbulent scaling theory. In the ocean, turbo-molecular mixing and bubble mediated transfer are treated as parallel processes.

While wave processes are important in almost all aspects of air-sea interactions, it is interesting that many very successful parameterizations do not explicitly include wave properties. This is because wave properties are highly correlated with wind speed. Thus, simple representations in the drag coefficient, C_d, or k_x are done with wind speed alone. Ironically, decades of experimental and theoretical effort (see Brumer et al., 2017a) have yet to yield wave-based parameterizations for C_d, or k_x that give significantly better RMS fits to direct observations over the open ocean. This is partly due to the large sampling noise of the observations and partly the noisy and uncertain nature of characterizations of the wave field. However, that is not the complete story because wind-only parameterizations essentially characterize transfer for a mean wave climatology associated with that wind speed. We expect that when the waves depart significantly from that mean, then air-sea fluxes may be affected. For example, in a coastal region offshore winds may yield quite different fluxes compared to onshore winds at the same wind speed, as has been observed for sea spray (Yang et al., 2019). Regardless of our ability to explicitly include wave variables in a parameterization, separating near-surface turbulent and bubble-mediated processes in physically-based treatments of gas transfer is useful.

In this paper we will further discuss air-sea fluxes – principally gas transfer and its forcing mechanisms – in the context of the COARE algorithms. We will not attempt a detailed attack on all issues (e.g., discussion in Johnson et al., 2011; Woolf et al., 2019), but focus on specific topics where significant progress has been made through observations, theory, or numerical modeling. The principal scaling variables for k_x are solubility, Schmidt number, friction velocity, and whitecap fraction. The last two variables may be estimated with wind-only formulae or with formulae that add some wave information. We begin with a discussion of theoretical background, then sketch the formulation of COARE [taking from detail provided in Fairall et al. (2011)]. We will briefly describe direct observations and focus on three recent field programs. We will discuss wave-based parameterizations and the difficulty of determining them with observations alone. Because of their more than one order of magnitude solubility differences, simultaneous DMS and CO_2 observations can be analyzed to separate the turbo-molecular and bubble-mediated components. To do this, we will also have to deal with chemical enhancement of CO_2 flux (Wanninkhof, 1992; Luhar et al., 2018; Jørgensen et al., 2020). The turbo-molecular transfer is found to be quite linear with the *tangential* component of the stress. The bubble component is approximately linear with either whitecap fraction or air-entrainment rate of breaking waves but there is still some uncertainty in characterizing those quantities which will be discussed.

2 THEORETICAL BACKGROUND

In this section we describe a simple 1-dimensional theoretical framework for describing the flux-profile relationships for trace gas transport between the atmosphere and ocean. The approach has its roots in observations from wind tunnels and flat Kansas plains, so application over the ocean requires a certain skepticism. It is known that wind speed does not strictly obey the conventional log-layer behavior within the wavy boundary layer. Furthermore, distortions by wave motions on the ocean side occur on scales that are greater than the normal '10% of the mixed layer depth' usually ascribed to the surface layer where 'law of the wall' scaling is appropriate. Our justification for using this approach for gas transfer applications is based on the small scale of the molecular sublayer and the transition to the turbulent sublayer – this occurs at mm scales where local dominant wave-induced slopes are negligible. This theoretical approach allows us to conceptualize the balance of the processes and to create a scaling structure that can be tuned to observations with only a few universal parameters.

2.1 Fluxes, Solubility, Similarity and Turbo-Molecular Transport

In the absence of significant *in situ* sources or sinks, the vertical flux of some scalar variable, x, in either fluid can be defined as the sum of molecular and turbulent diffusivities

$$F_x = -D_x \frac{\partial X}{\partial z} + \overline{w'x'} \tag{7}$$

In the case where z is height or depth, the flux is positive directed away from the interface. Near the surface the turbulent flux can be represented in terms of the local gradient and a turbulent eddy diffusivity, $K(z)$, so that

$$F_x = -[D_x + K(z)] \frac{\partial X}{\partial z} \tag{8}$$

We can integrate (8) from the surface to some reference height (depth), z_r, to obtain the total change of X between the surface (subscript s) and z_r,

$$(X_s - X_r) = \Delta X_r = \int_0^{z_r} \frac{F_x dz}{[D + K(z)]} = F_x \int_0^{z_r} \frac{dz}{[D + K(z)]} \tag{9}$$

If we define an air-side transfer velocity of x, k_{xa}, as acting between the surface and some reference height in the atmosphere, z_{ra}, then

$$F_{xa} = k_{xa}(X_{sa} - X_{zra}) = k_{xa}\Delta X_{ra} \tag{10}$$

Thus, (9) and (10) imply

$$k_{xa}^{-1} = \int_0^{z_{ra}} \frac{dz}{[D + K(z)]} \tag{11}$$

Similarly, we can define a turbo-molecular flux on the water side

$$F_{xw} = k_{xw}(X_{sw} - X_{zrw}) = k_{xw}\Delta X_{rw} \tag{12}$$

While temperature is continuous across the interface, gas concentrations are not so we must account for the discontinuity by defining the solubility, α_x as

$$\alpha_x = X_{sw}/X_{sa} \tag{13}$$

If we assume the atmospheric flux is continuous with the oceanic flux (applicable to a gas not undergoing rapid chemical reactions), then we can derive (4) where

$$k_x^{-1} = k_{xw}^{-1} + \alpha_x k_{xa}^{-1} \tag{14}$$

We use Monin-Obukhov Similarity (MOS) to describe the turbulent diffusivity (Fairall et al., 2000, hereafter F00): MOS defines surface turbulent flux scaling parameters u_* and x_* in terms of turbulent conditions sufficiently far from the interface that fluxes of momentum or of a scalar x (i.e. trace gases) are completely carried by turbulent covariance

$$\overline{w'u'} = -u_*^2 \tag{15a}$$

$$\overline{w'x'} = -u_* x_* \tag{15b}$$

The profile of a dynamical variable can be described *via* a dimensionally consistent combination of the scaling parameters, z, and a dimensionless function of z/L, where L is the MOS buoyancy length scale. This leads to a simple specification of turbulent diffusivity

$$K(z) = \kappa z u_* / \phi(z/L) \approx \kappa z u_* \tag{16}$$

where ϕ is an empirical function that characterizes the enhancement of diffusion in convective conditions or suppression in stratified conditions and κ is the von Karman constant, $\kappa \approx 0.4$. Stability effects may be substantial but for dealing with near-surface and interfacial aspects of gas transfer, we can assume $\phi = 1$.

F00 discuss solutions to (9) and (11) using an approximation for $K(z)$ that accounts for the suppression of turbulence near the interface which occurs in the sublayer

$$z < \delta_u = \lambda \nu / u_* \tag{17}$$

Where λ is a coefficient on the order of 10. This is done by expressing $K(z)$ as

$$K(z) = \kappa z u_* / (1 + \delta_u / z) \tag{18}$$

The form of (18) produces a smooth transition from molecular-dominated diffusion to turbulent diffusion and has the effect of extending the depth of the molecular layer. The analytical solution to (9) produces a near-surface linear profile (molecular sublayer) that transitions to a logarithmic profile (turbulent sublayer)

$$\frac{\Delta X_s(z)}{F_{xs}} = \frac{1}{2c} \log (G/a) + \frac{2\left[\delta_u - \frac{b}{2c}\right]}{d} \left[\arctan \left(\frac{b + 2cz}{d} \right) - \arctan \left(\frac{b}{d} \right) \right] \tag{19}$$

where $a = D_x\ \delta_u$, $b = D_x$, $c = \kappa u_{*w}$, $d = [4D_x \delta_u \kappa u_{*w} - D_x^2]^{1/2}$ $G = a + bz + cz^2$.

In principle, this solution applies to vertical transfer of dissolved gas within the ocean in the absence of chemical reactions. The analytical profile in the turbulent layer can be approximated

$$\frac{\Delta X}{F_x} = \frac{\Delta X_m}{F_x} + \frac{1}{\kappa\ u_*} \log \left(\frac{z}{5\ \delta_u} \right) \tag{20}$$

where $5\delta_u$ is the maximum extent of the molecular sublayer (Zülicke, 2005) and ΔX_m characterizes the total change in X over that layer. Using $\lambda = 10$, the analytical solution gives

$$\frac{u_*\ \Delta X_m}{F_x} = \frac{1}{\kappa} \left[\frac{\pi}{2} (\lambda\ \kappa\ Sc_x)^{1/2} + \log \left(5 \left(\lambda\ \kappa\ Sc_x \right)^{1/2} \right) \right] = 7.8\ Sc_x^{1/2} + 2.5\ \log (10\ Sc_x^{1/2}) \tag{21}$$

The logarithmic form is an idealization because of the distortions of the wave motions. At heights well above the significant wave height, atmospheric logarithmic profiles are observed over the ocean (e.g. Edson et al., 2004). In the ocean, wave induced displacements are a significant fraction of the mixed layer depth and an idealized log-layer may not exist (Zheng et al., 2021). However, we still expect the idealized solution to reasonably describe the main aspects of the profile at cm scales.

2.2 The Wavy Boundary Layer - Viscous Stress Versus Wave Stress

Waves add another complication because of their role in the momentum transfer and the friction velocity. The fluxes of momentum and kinetic energy from the atmosphere to the ocean are, except in light winds, dominated by input to waves *via* the pressure-wave slope correlation – the so called form drag. The action of the wind grows waves which, when they break, transfer their momentum and energy to ocean currents and turbulence. The wind is also subject to a viscous drag which directly drives surface currents and near-surface turbulence. Far from the interface, (but still within the surface layer of the marine boundary layer), the momentum flux from the atmosphere (surface stress) can be expressed as the covariance of atmospheric turbulent velocity fluctuations similar to (1)

$$\tau = \rho_a \ \overline{w'u'} = -\rho_a \ u_{*\mathrm{a}}^2 \tag{22}$$

where u' represents fluctuations of wind speed in the in the mean wind direction (for simplicity, we ignore the crosswind stress component). Near the air-sea interface (even within the influence of surface wave disturbances) the momentum flux is the sum of viscous, turbulent, and wave-pressure components τ_v, τ_t, τ_g. Thus, while the total stress may be assumed to be approximately constant in height, the turbulent τ_t, component is not constant in the wave boundary layer (Ortiz-Suslow et al., 2021). At the interface, turbulence is negligible, and so the momentum flux delivered to the ocean is the sum of viscous (subscript *v*) and gravity wave drag (subscript *g*)

$$\tau = \tau_v + \tau_t + \tau_g = \tau_{vs} + \tau_{gs} = -\rho_a \nu_a \left[\frac{\partial U}{\partial z}\right]_s + \left[\overline{p' \ \frac{\partial \eta}{\partial x_u}}\right]_s$$

$$= -\rho_a \left(u_{*\mathrm{av}}^2 + u_{*\mathrm{ag}}^2\right) \tag{23}$$

Viscous (tangential) drag is the product of the air kinematic viscosity with the wind gradient at the surface (subscript *s*), while the gravity wave drag is the correlation of ' pressure fluctuations, p', and the wave slope' rho is the symbol for density, p the symbol for pressure (η is the vertical displacement of the surface by waves) and x_u is the horizontal coordinate in the mean wind direction. Soloviev (2007) and Fairall et al. (2011) argue that, at scales less than 1 m near the interface, u_{*av} should scale with the turbulent diffusion because the wave-pressure correlation has reduced the turbulent momentum flux. This has been discussed in more detail by Cifuentes-Lorenzen et al. (2018) who suggest the wave stress component decays exponentially with a height scale of about 1 m. The portioning suggested by (23) can be written

$$u_{*\mathrm{a}}^2 = c_d U_{10}^2 = \left(c_{dv} + c_{dg}\right) U_{10}^2 = u_{*\mathrm{av}}^2 + u_{*\mathrm{ag}}^2 = u_{*\mathrm{av}}^2 + \alpha_g u_{*\mathrm{a}}^2 \tag{24}$$

Cifuentes-Lorenzen et al. (2018) use the parameter α_g which is the fraction of wave stress to total stress so that

$$u_{*\mathrm{av}} = u_{*\mathrm{a}} \ \sqrt{1 - \alpha_g} \tag{25}$$

Fairall et al. (2011)) give an estimate of the ratio of viscous to total stress as

$$u_{*\mathrm{av}} = u_{*\mathrm{a}} \ \sqrt{c_{dv}/c_d} \tag{26}$$

and provide a simple formulation [see Figure B1 in Fairall et al. (2011)]. **Figure 1** shows estimates of α_g as a function of 10-m wind speed and wave age, c_p/U_{10} where c_p is the phase speed of the waves with frequency corresponding to the peak of the wave energy spectrum. α_g is small at low winds and increases with wind speed; viscous and wave components of stress are comparable at wind speeds on the order of 12 m s^{-1} (see **Figure 1**). Friction velocity on the ocean side is computed assuming the atmospheric viscous stress drives the oceanic viscous stress:

$$u_{*\mathrm{wv}} = \sqrt{\frac{\rho_a}{\rho_w}} \ u_{*\mathrm{av}} \tag{27}$$

2.3 Atmospheric and Ocean Side Turbulent-Molecular Diffusion and Bubbles

On the atmospheric side of the interface, the behavior of k_{xa} is well-constrained by direct covariance flux measurements of water vapor [see **Figure 4** in Fairall et al. (2000)] and other trace gases of high solubility/reactivity (Yang et al., 2014; Yang et al., 2016; Porter et al., 2020). While (11) implies a sensitivity of k_{xa} to molecular diffusivity, it turns out that the variation of atmospheric diffusivity amongst trace gases of interest is not significant (Rowe et al., 2011). Direct flux measurements of soluble trace gases to date (Yang et al., 2016; Porter et al., 2020) have shown some departures from water vapor or heat, but the measurement techniques are probably not sufficiently accurate to reject a simple water vapor analogy representation. The importance of air-side transfer declines as solubility declines. For DMS (solubility on the order of 15) k_{xa} contributes about 5% to (14) while for CO_2 (solubility on the order of 0.5) it contributes about 0.2%. For solubility greater than 100, k_{xa} dominates (14) and $k_x/u_{*\mathrm{a}} \approx k_{xa}/u_{*\mathrm{a}} \approx 0.03$.

On the ocean side of the interface the total transfer is assumed to be the sum of turbo-molecular, k_v, and bubble-mediated, k_b, processes:

$$k_w = k_v + k_b \tag{28}$$

The turbo-molecular part can be computed *via* (11) and (18) with the molecular sublayer part given by (21). The much smaller molecular diffusion coefficients in the ocean (Sc_x on the order of 1000 compared to 1 in the atmosphere) imply that most of the change in trace gas concentration on the ocean side occurs in the molecular transport sublayer. **Figure 2** contrasts the oceanic profiles for temperature (Sc_t = 5.9) and CO_2 (Sc_w = 660) at a water temperature of 20°C. The analytical solution is shown by the solid line and the log-layer portion by the dashed line. In this normalized form the log-layer slopes are the same but the offset caused by the molecular sublayer portion is relatively much

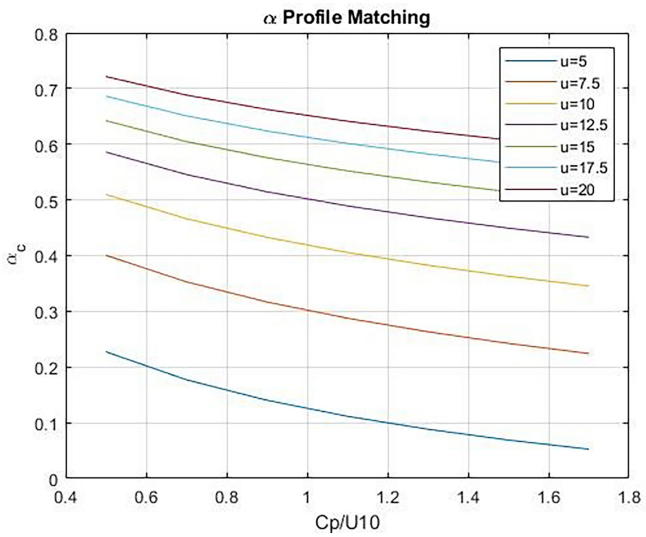

FIGURE 1 | Wave stress fraction, α_g, vs wave age, Cp/U_{10}, at different values of $u = U_{10}$. The lower curves correspond to lower wind speeds.

larger for CO_2 – implying the computation of the flux for CO_2 is much less sensitive to specification of the depth of the ocean side concentration measurement.

Bubble-mediated transfer is associated with air entrained by breaking waves. Wave breaking that entrains air rarely occurs in lighter wind regimes with a crude threshold of $U_{10} \approx$ 5-8 m s^{-1}. Gas transfer enhancement by bubbles has been studied in laboratory experiments (Woolf, 1993; Rhee et al., 2007; Krall et al., 2019) and with numerical models (Woolf and Thorpe, 1991; Liang et al., 2013; Deike et al., 2017). The laboratory studies quoted here conflict somewhat on the importance of bubbles. The numerical model approach is based on injecting into the ocean a numerical plume of bubbles with a spectrum of sizes. Gas transfer from the bubbles is computed for each bubble size as the plume rises and is vertically transported; total transfer is computed by integrating over the size spectrum. Turbulent mixing of the bubble plume may be neglected or can be very sophisticated (e.g., Liang et al. (2013) use a Large Eddy Simulation model). The variety of assumptions (injection depth, rise rate, bubble spectrum, bubble transfer rates, clean vs. dirty bubble, plume density, etc) lead to a variety of outcomes. Laboratory (Callaghan, 2013; Callaghan et al., 2016; Callaghan, 2018) and numerical modeling (Deike et al., 2016; Deike and Melville, 2018) have also advanced understanding of the

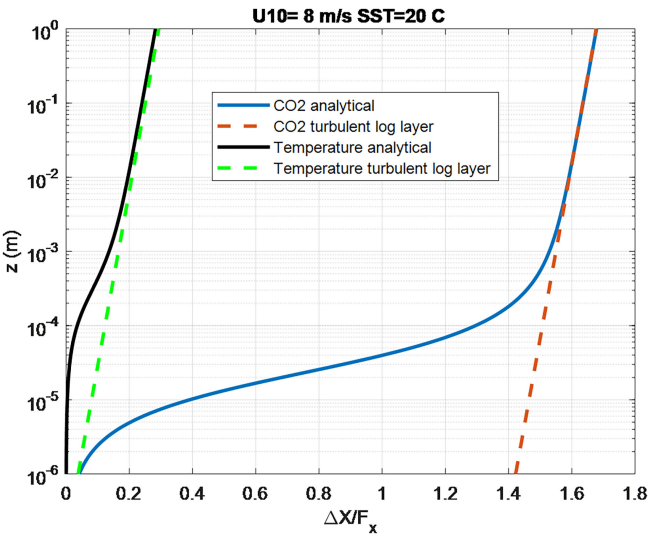

FIGURE 2 | Normalized profiles of ocean temperature and CO_2 concentration computed from the analytical solution (solid lines) $K(z) = \kappa z u_* / (1+\delta_\mu / z)$. The dashed lines are using (21) to represent the turbulent log-layer part of the profile.

connection between wave breaking and dissipation, air entrainment, bubble populations, and whitecap coverage.

An example of a parameterization developed for bubble transfer can be found in Woolf (1993),

$$k_{xb} = BV_0 f_{wh} \alpha_x^1 [1 + (e\alpha_x Sc_{xw}^{1/2})^{-1/n}]^{-n} \quad (29)$$

where B is an empirical constant tuned to observations, V_0 = 2450 cm hr^{-1} is the air volume entrainment flux per unit whitecap fraction, f_{wh} is the whitecap fraction, e = 14, and n =1.2. This form is chosen so that the transfer velocity obeys the expected limits for low solubility (bubble mediated flux depends on the diffusion, but not on solubility) and high solubility (bubble mediated flux scales inversely with solubility). There is some debate about the scaling of the forcing in (29): should it be whitecap fraction, actively breaking fraction, air entrainment velocity (V), or dissipation of wave breaking energy? The Woolf form assumes the scaling is $V = V_0 f_{wh}$ with whitecap fraction scaling as $U_{10}^{3.41}$ based on a fit to whitecap observations by Monahan (1971). Recent observations (Brumer et al., 2017b; Anguelova and Bettenhausen, 2019) have shown the Monahan formulation overestimates the wind-speed dependence which leads to overly large gas transfer estimates in high winds. Gas transfer versions of the COARE bulk transfer model, COAREG (Fairall et al., 2011), use (29) but Liang et al. (2013); Goddijn-Murphy et al. (2016), and Deike et al. (2017) offer viable alternatives to (29).

2.4 Chemical Enhancement

The COAREG models treat various gases with the assumption that they are conservatively transported. However, transfer of CO_2 is complicated by carbonate chemical reactions on the water side – a phenomenon referred to as chemical enhancement. Hoover and Berkshire (1969) (hereafrter HB69) express the chemical enhancement of CO_2, CE, as

$$\mathrm{CE}(T) = \mathrm{TT}/[(\mathrm{TT} - 1) + \tanh(Q\delta)/(Q\delta)] \quad (30)$$

where, adapting the notation of Wanninkhof and Knox (1996), TT and Q depend on CO_2–carbonate reaction rate constants and diffusivity (D_{co2}), and $\delta = D_{co2}/k$ is diffusion layer thickness. Temperature dependence is explicit in TT and Q. Wind speed dependence is implied in δ but no explicit functional form is given.

Wanninkhof (1992) (hereafter W92) considered this effect in the analysis of passive tracers to derive a formula for the enhanced transfer velocity for CO_2 k_{en660}. He uses a temperature-dependent but wind speed independent form for CE given by a polynomial fit, $p(T)$, to CE(T) at a constant k of 1 cm hr^{-1}.

$$k_{en\ 660} = p(T) + 0.31\ \ U_{10}^2 (Sc/660)^{1/2} \quad (31)$$

W92's formula gives $p(T)$ = 3 cm hr^{-1} in the tropics and 2 cm hr^{-1} for conditions relevant to the HiWinGS experiment (see Section 3.2). Wanninkhof and Knox (1996) define CE = k_{en}/k and examine the HB69 model with observations from several alkaline lakes and also estimate CE for the equatorial Pacific Ocean. Note, this implies that as k_{en}/k approaches 1.0 with increasing winds, CE becomes small.

More recently, Fairall et al. (2007), hereafter F07, investigated air-sea transfer of ozone by considering the 1-dimensional conservation equation with a simple chemical reaction

$$-\frac{\partial}{\partial z}\left[-D_x \frac{\partial X}{\partial z} + \overline{w'x'}\right] - a_r X = 0 \quad (32)$$

where flux is positive downward, X is the mean mass concentration and $a_r = C_{xy}Y$ is the reactivity coefficient for the reaction of constituent X and constituent Y with a reaction rate constant of C_{xy}. F07 assumed ozone was completely destroyed in seawater and that the reactions are with unspecified oceanic chemicals in significantly large concentration such that the reaction is pseudo first-order in X and a_r is equivalent to a rate constant (s^{-1}).

Here, we adapt this approach to CO_2. Following McGillis and Wanninkhof (2006), we assume the ocean mixed layer CO_2 concentration, X_e, is in near equilibrium with carbonate chemistry. We assume that X_e is the result of a balance with total carbonate and alkalinity so that in the absence of significant temperature gradients it is essentially independent of depth. This is a more complex case than for ozone, but we again make the simplifying assumption that the reaction is pseudo first order in X_e and reactivity can be represented by a simple reactivity coefficient a_r (s^{-1}) or time constant $\tau_r = 1/a_r$ (s). The time constant is unknown but can be estimated from measurements. Thus, for a reactive gas in equilibrium like CO_2, (32) can be written

$$-\frac{\partial}{\partial z}\left[-D_x \frac{\partial (X - X_e)}{\partial z} + \overline{w'x'}\right] - a_r (X - X_e) = 0 \quad (33)$$

The turbulent flux is represented in terms of turbulent diffusivity coefficient, $K(z)$, so that

$$-\frac{\partial}{\partial z}\left[-(D_x + K(z))\frac{\partial X'}{\partial z}\right] - a_r X' = 0 \quad (34)$$

where X'=X–X_e. Following F07, we can use (34) to define a general flux variable, F_x, as

$$F_x = -[D_x + K(z)]\frac{\partial X'}{\partial z} - a_r \int_0^z X'(z')dz' \quad (35)$$

The gradient term expresses the sum of molecular and turbulent diffusion and the second term the gain or loss of X *via* chemical reaction. In steady state as expressed by (35), F_x is independent of depth and equal to the flux at the interface, $F_x(0) = F_{xs}$. For non-reactive gases, we can use (35) with a_r = 0 to characterize the transport through the water

$$\frac{X_s' - X'(z)}{F_{xs}} = \frac{\Delta X_s(z)}{F_{xs}} = \int_0^z \frac{1}{D_x + K(z')}dz' = \frac{1}{k_{xw}} \quad (36)$$

Using the analytical solution (19) for the non-reactive case, k_{xw} represents the transfer velocity of x on the water side to some reference depth, z, on the order of 1 m. For $a_r > 0$ an analytical solution corresponding to (34) with (18) does not exist.

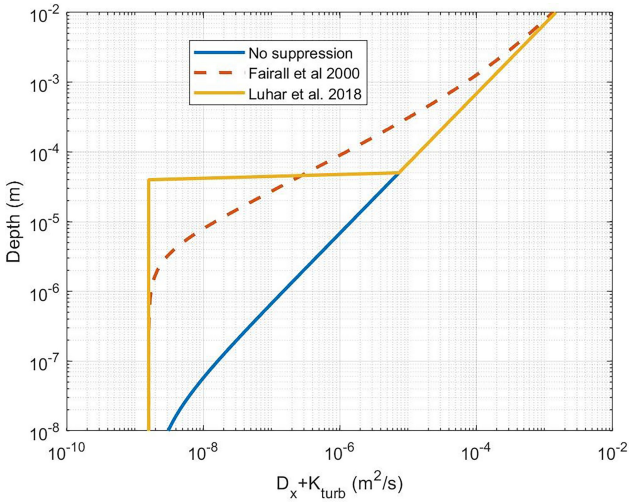

FIGURE 3 | Near-surface profile of the sum of molecular and turbulent diffusivities. The blue line is for $K(z)$ without near-surface dissipative suppression (Eq. (18) with $\delta_u = 0$). The dashed line is (41). The yellow line is the Luhar et al. (2018) approximation using (41).

Jørgensen et al. (2020) found solutions for (34) without the near-surface turbulence suppression. Another approach was developed by Luhar et al. (2018) who solved this problem by assuming that (18) could be approximated by setting the turbulent eddy diffusion coefficient to zero within some scale δ_m of the surface (see **Figure 3**) and $K(z) = \kappa z u_{*w}$ for z greater than δ_m. Thus within a scalar molecular layer a stagnant (non-turbulent) film is assumed. If $K(z)$ is set to 0 for $z < \delta_m$, the solutions of (34) with $K(z) = 0$. are exponentials. So the complete profile is given by

$$X = \begin{cases} A_1 \exp\left(\sqrt{\frac{a_r}{D_x}}\right) + B_1 \exp\left(-\sqrt{\frac{a_r}{D_x}}\right), & z <= \delta_m \\ B_2 K_0(\xi), & z > \delta_m \end{cases} \quad (37a, 37b)$$

where A_1, B_1, B_2 are constants and K_0 is a modified Bessel function of order 0. Luhar et al. (2018) give an analytical expression for transfer velocity over some depth where chemical reactions become negligible

$$\frac{1}{k_{xw}} = \frac{1}{\sqrt{a_r D_x}} \left[\frac{\psi K_1(\xi_\delta) sinh(\lambda_m) + K_0(\xi_\delta) cosh(\lambda_m)}{\psi K_1(\xi_\delta) cosh(\lambda_m) + K_0(\xi_\delta) sinh(\lambda_m)} \right] \quad (38)$$

where K_n are modified Bessel functions of order n, $\psi = [1+\kappa\, u_{*w}\, \delta_m/D_x]^{1/2}$, $\lambda_m = \delta_m (a_r/D_x)^{1/2}$, and ξ_δ is computed from

$$\xi^2 = \frac{4}{\kappa} \frac{a_r}{u_{*w}} \left(z + \frac{D_x}{\kappa\, u_{*w}} \right) \quad (39)$$

where $z = \delta_m$ corresponds to the depth where the turbulent transport starts. Luhar et al. (2018) examined temperature dependent specifications for reactivity, a_r, and several candidates for δ_m. Their final selections captured the modest temperature and weak wind speed dependencies of observed ozone deposition velocity, but because ozone has very high reactivity they did not clearly delineate a value for δ_m.

In order to choose the optimum value for δ_m, we integrate (36) with the specified 2-layer $K(z)$ profile with $a_r = 0$ and select δ_m to match the asymptotic form of the non-reactive analytical solution (21). This leads to

$$\delta_m = \delta_x = \frac{\pi}{2} \frac{\delta_u}{\sqrt{\lambda_u\ \kappa\ Sc}} = 0.79\ \ \delta_u / Sc^{1/2} \quad (40)$$

In our view, this is a rigorous choice because it guarantees the same transfer velocity in the absence of chemical reactions.

We can use the 2-layer model to evaluate CE for CO_2. However, a more rigorous approach is a brute-force numerical solution to (34) with (18). One advantage of this approach is we can check and/or tune the 2-layer analytical model, which can give us an analytical function for CE in terms of the forcing and a_r. The numerical solutions are computed using MATLAB® differential equation solvers. With a_r=0, the numerical solutions agreed with the non-reactive analytical solution (F00). Results for selected values of τ_r are shown in **Figure 4** where we compute the enhancement ratio *via*

$$\frac{k_{en}}{k} = \frac{k(a_r)}{k(a_r = 0)} \quad (41)$$

The use of the ratio reduces the sensitivity to the calibration of $k = k(a_r = 0)$. We then compute CE as

$$CE = \left(\frac{k_{en}}{k} - 1 \right) k_{c31x} \quad (42)$$

which is shown in **Figure 5**, where the COAREG 3.1 transfer velocity for gas x, k_{c31x}, is the estimate for transfer without CE. The Luhar et al. (2018) analytical approximation is a good match with the numerical solution with our choice for δ_m. This solution also works well for ozone. These calculations suggest CE of 3-5 cm hr^{-1} for CO_2 corresponding to a time constant, τ_r, on the order of 3 s.

3 DIRECT OBSERVATIONS

3.1 Advances in DMS and CO_2 Flux Measurement

In this paper, we tune the latest revision of the model (COAREG 3.6) to direct gas exchange observations made with the eddy covariance (EC) method. The application of the EC method for measuring gas fluxes at sea requires high temporal resolution measurements of 1) vertical wind velocity, and 2) gas mixing ratio. The advent of the motion-correction method in late 1990s (Edson et al., 1998) enabled the derivation of the ambient vertical wind velocity from a moving platform. This method is subsequently refined by Miller et al. (2010); Landwehr et al. (2015), and Blomquist et al. (2017). Comparisons of momentum and heat fluxes between a buoy and a nearby fixed tower demonstrate that the bias due to the motion correction is within 6% (Flügge et al., 2016). For CO_2, we utilize fluxes

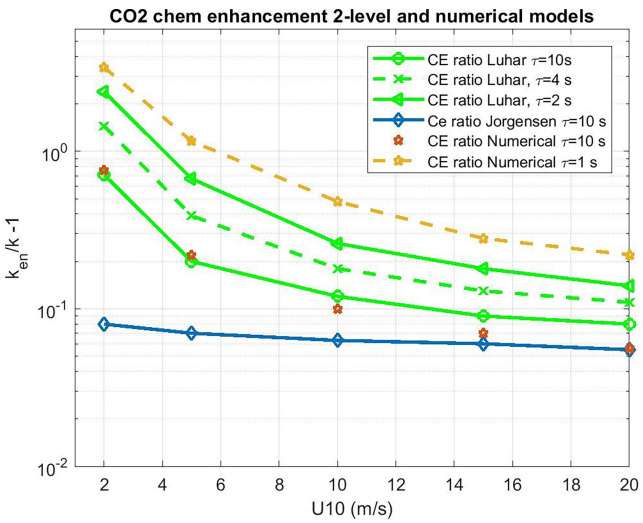

FIGURE 4 | Water side transfer velocity (normalized to *Sc* = 660) ratio of chemical enhanced to background value as a function of 10-m wind speed. Estimates of chemical enhancement (CE) *via* (42) for CO_2 are shown with star symbols using a numerical integration of (34) and (19) and the analytical model (38) as green lines for different values of the CO_2 carbonate reaction time constant, τ_r. The results of the Jørgensen et al. (2020) are shown as diamonds.

measured using a closed-path instrument with a dryer. Deemed the best practice by Landwehr et al. (2014) and Blomquist et al. (2014), this approach avoids the water vapor cross-sensitivity in the CO_2 measurement that likely confounded earlier flux measurements, especially using an open-path infrared analyzer [e.g., Edson et al. (2011)]. In particular, cavity ringdown analyzers (e.g., Picarro G2311-f) and closed-path infrared analyzers (e.g. Licor7200) are both well suited for measurements of air-sea CO_2 flux. Recent works by Dong et al. (2021) demonstrate that the random uncertainty in hourly CO_2 flux is typically 30-50% (mostly a function of the flux magnitude), with sensor noise from both Picarro G2311-f and Licor7200 only contributing a minor fraction of the total flux uncertainty. Air-sea DMS flux measurement is made with a chemical ionization mass spectrometer operating at near atmospheric pressure. Hourly random uncertainty in DMS flux is on the order of 20-30% (Blomquist et al., 2010), thanks to the high signal-to-noise ratio in the DMS flux measurement.

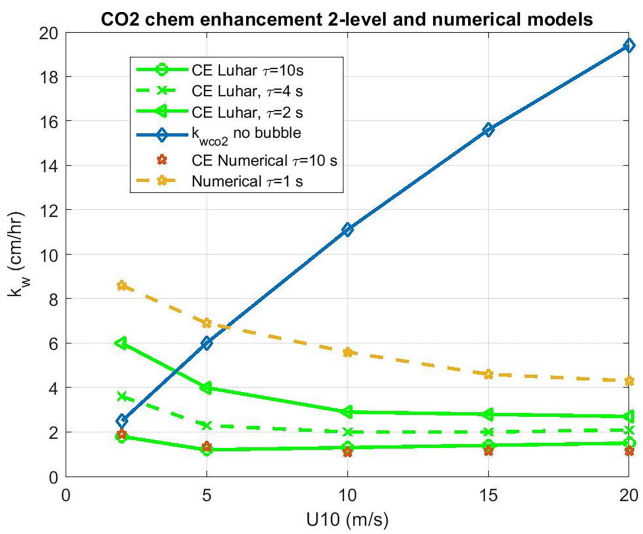

FIGURE 5 | Water side transfer velocity (normalized to *Sc* = 660) as a function of 10-m wind speed. The basic COAREG non-bubble relationship for neutral conditions is shown in the blue diamonds. Estimates of chemical enhancement (CE) for CO_2 are shown using a numerical model (stars) an and an analytical model (green lines) for different values of the CO_2 carbonate reaction time constant, τ_r.

3.2 Recent Field Programs

The last decade has seen over a dozen field programs dedicated to EC gas flux measurements, with at least eight cruises and several near shore deployments. Long term EC measurements have been undertaken at two coastal sites. Östergarnsholm station is located in the Baltic Sea (57°27'N, 18°59'E) and has been providing CO_2 fluxes since 1995 (Rutgersson et al., 2020). Penlee Point Atmospheric Observatory (PPAO) was established in 2014 by the Plymouth Marine Laboratory in the Plymouth Sound on the south-west coast of the United Kingdom (50°19.08'N, 4° 11.35'W). It provides CO_2, CH_4 fluxes (https://www.westernchannelobservatory.org.uk/penlee,Yang et al. (2016)). A list of all recently collected and analysed EC field measurements is given in **Table 1** along with references to relevant publications.

In this paper we focus on results from three recent campaigns (Knorr11 in 2011, SOAP in 2012, HiWinGS in 2013), where simultaneous air-sea exchange measurements of CO_2 and DMS are available. Some published direct measurements of DMS k_{660} have shown unexpected decreases at higher wind speeds: GasEx08 (Blomquist et al., 2017), Knorr11 (Bell et al., 2013; Bell et al., 2017), and Sonne-234/235 (Zavarsky and Marandino, 2019). This was discussed in depth by Zavarsky and Marandino (2019) and explained in terms of flow separation using a wave reference Reynolds number, Re_{tr}. The argument is that flow separation (which occurs when Re_{tr} < 6.5E6) suppresses the direct viscous transfer component and this affects DMS relatively more than CO_2 because the much larger bubble transfer for CO_2 masks the decrease. The basic idea has some logic, although Zavarsky et al. (2018) Figure 13 shows no dramatic decrease in DMS k_{660} for HiWinGS despite a large fraction of suppressed conditions for $U10 > 12$ m s^{-1}. In our own analysis of HiWinGS data, using their Re_{tr} criterion, we find no significant difference in k_{660} for DMS in suppressed vs. non-suppressed conditions, but CO_2 k_{660} is reduced by about 10 cm h^{-1} during 'suppressed' conditions. It seems the sudden decrease in k_{660} DMS in strong winds observed in some field programs remains puzzling.

4 ANALYSIS OF OBSERVATIONS IN A COARE CONTEXT

4.1 Turbo-Molecular and Bubble-Mediated Drivers

The last public release of the COAREG algorithm, version 3.1 (Fairall et al., 2011), does not include CE and gives a simple form for the transfer velocity (14) which captures the net transfer across water (w) and atmospheric (a) surface layers We can separate the oceanic and atmospheric components as follows

$$k_w = \left(1 + \frac{\alpha_x k_w}{k_a}\right) k = k_v + k_b \tag{43}$$

From measurements of k, we can compute the oceanside value, k_w, which is made up of a turbulent-molecular term, k_v, and a bubble-mediated term, k_b. For HiWinGS the term multiplying k in (43) is an average of 1.054 for DMS and 1.008 for CO_2. Following Appendix A of Fairall et al. (2011), we can convert k_w to k_{660} and write (43) as

$$k_{w\ 660} \cong k_{v\ 660} + k_{b\ 660}$$
$$= 37.5\ \ A\ \ u_{*v} + \frac{B\ \ V_0\ \ f_{wh}}{\alpha_x(20)}\ \ \gamma(T)\ \ G(T) \tag{44}$$

TABLE 1 | Recent field campaigns.

Year	Program	Region	Gas Measured	Platform	References
2011-2012	FINO-2 tower	western Baltic	CO_2	T	Ghobadian and Stammer (2019)
2011	Knorr11	North Atlantic	CO_2, DMS	S	Bell et al. (2013, 2017); Esters et al. (2017)
2012	SOAP	southwest Pacific/Southern Ocean	CO_2, DMS	S	Landwehr et al. (2018)
2013	HiWinGS	North Atlantic	CO_2, DMS, methanol, acetone	S	Yang et al. (2014); Blomquist et al. (2017); Brumer et al. (2017a)
	Arctic fjords	Adventfjorden (flux tower)	CO_2	T	Andersson et al. (2017)
	NBP-1210	MIZ, Southern Ocean (Punta Arenas to McMurdo)	CO_2	S	Butterworth and Miller (2016)
2014	ACSE (SWERUS-C3)	(2 legs) Arctic MIZ at edge of the Siberian shelf: Kara, Laptev, East Siberian, and Chukchi Seas	CO_2	S	Prytherch et al. (2017)
	NBP-1402	MIZ, Southern Ocean	CO_2	S	Butterworth and Miller (2016)
	PPAO	south-west coast of the United Kingdom	CO_2, CH4	T	Yang et al. (2016)
	SPACES-OASIS (SO234-2/235)	western tropical Indian Ocean	CO_2, DMS	S	Zavarsky et al. (2018); Zavarsky and Marandino (2019)
		Scripps Pier, La Jolla, California	SO_2	P	Porter et al. (2018)
2014-2015		Östergarnsholm + SAMI–CO_2	CO_2	T	Vieira et al. (2020)
2015		Duck USACE-FRF pier, North Carolina	SO_2	P	Porter et al. (2020)
2017-2018	Östergarnsholm station	Baltic Sea	CO_2, CH4	T	Gutiérrez-Loza et al. (2019)
2018-2019	AMT4OceanSatFlux	Atlantic Meridional Transect	CO_2	S	
2018-2019	ice camp Arctic Ocean 2018	open lead close to North Pole	CO_2	T	Prytherch and Yelland (2021)

Platforms: ship (S), tower (T), pier (P).

Here the first term on the right hand side represents tangential (interfacial) transfer, while the second term indicates bubble-mediated gas exchange (see Eq. 29). A and B are parameters tuned to fit the observations and the temperature- and gas-dependent factors are

$$\gamma(T) = \left[\frac{Sc_w}{660}\right]^{1/2} \frac{\alpha_x(20)}{\alpha_x(T)} \tag{45a}$$

$$G(T) = \left[1 + (14 \;\; \alpha_x / Sc_w^{1/2})^{-1/n}\right]^{-n} \tag{45b}$$

with $n = 1.2$. In (44) we have neglected buoyancy effects on the first term, which become more important at wind speeds less than 5 m s^{-1}. Note that in COAREG, k_v is scaled by *viscous*, rather than total, friction velocity.

We can now consider the form of (44) for both CO_2 (subscript c) and DMS (subscript d) with the temperature dependent factors in k_b, V_0 and $\alpha(20)$ combined into the single factors b_c and b_d

$$k_{c\ 660} = 37.5 \;\; A \;\; u_{*v} + B \;\; b_c \;\; f_{wh} \tag{46a}$$

$$\begin{aligned} k_{d\ 660} &= 37.5 \;\; A \;\; u_{*v} + B \;\; b_d \;\; f_{wh} \\ &= 37.5 \;\; A \;\; u_{*v} + B \;\; r_{dc} \;\; b_c \;\; f_{wh} \end{aligned} \tag{46b}$$

If k values are expressed in cm hr^{-1}, then the factor $b_c \cong 830$, while $b_d = 130 + 2.6T$ where T is in °C. Thus, the ratio between bubble-mediated gas exchange of DMS and that of CO_2, $r_{dc} = b_d/b_c$, in (46b) varies from 0.16 to 0.22 with an average of 0.18 for HiWinGS. The relationships in (46) can be applied to observations of k for CO_2 and DMS to estimate the constants A and B:

$$A = \frac{(k_{w660d} - r_{dc} k_{w660c})}{37.5 \;\; u_{*v}(1 - r_{dc})} \tag{47a}$$

$$B = \frac{(k_{w660c} - k_{w660d})}{830 \;\; f_{wh}(1 - r_{dc})} \tag{47b}$$

Note (47) is approximate because it uses mean values for T-dependent factors, but if (47) is applied to k_w values computed with the COAREG algorithm, then for a 10-m wind speed adjusted to neutral conditions, $U_{10n} > 5$ $m\ s^{-1}$, the values for A and B assumed in the algorithm will be recovered within 10%. Also, note that the value of A depends on the form of the friction velocity factor and B depends on choice of whitecap formulation. If the model and the measurements are consistent, then the values of A and B should be independent of wind speed.

Figure 6 shows values of A and B extracted from HiWinGS observations averaged in wind speed bins. To reduce the effects of flux sampling uncertainty, values of CO_2 transfer velocities were only used if the absolute value of sea-air partial pressure difference Δp_{co2} exceeded 20 µatm. Two retrievals have been done: 1) with bin averages of measured k_{w660} and 2) using power-law fits of k_{w660} to wind speed in the form

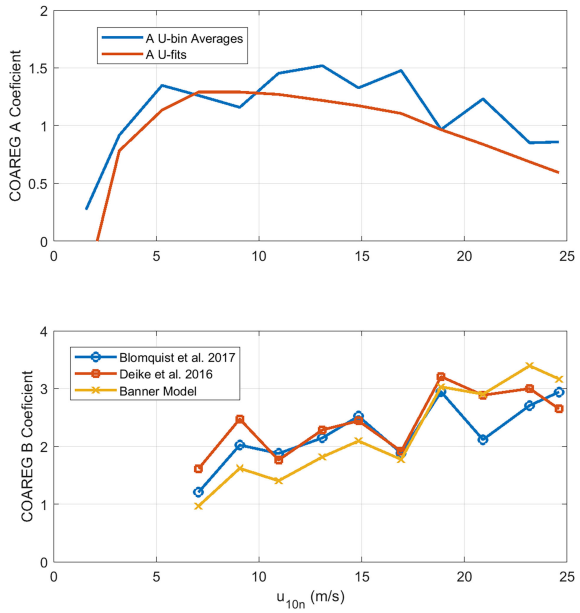

FIGURE 6 | Retrieved values of COAREG constants, A (upper panel) and B (lower panel), as a function of wind speed. For A, retrievals are based on mean values of observed k_{w660} averaged in wind speed bins plus values of k_{w660} computed from wind-speed power law fits. For B , only the wind speed bin results are shown. There are curves for three possible choices of f_{wh}. Data for $U_{10n} < 6$ are not shown because no whitecaps were observed.

$$k_{w\ 660} = c_0 + c_1 \;\; U_{10n}^m \tag{48}$$

We have used $c_0 = 6.0$, $c_1 = 0.41$, and $m = 1.9$ for CO_2; $c_0 = 0.6$, $c1 = 1.09$, and $m = 1.2$ for DMS. To compute B (47b), both retrievals used bin-averaged estimates of whitecap fraction computed from Brumer et al. (2017b)

$$f_{wh} = 5.0 \times 10^{-6} \left[\frac{H_s u_{*a}}{\nu_w}\right]^{0.9} \tag{49}$$

Averaging both retrieval methods yields $A = 1.25$ and $B = 2.3$, using (49) for whitecap fraction. We have also used bin-averaged values of observed f_{wh}; that yields noisier results but does not significantly change the final estimates of A and B.

In **Figure 7** we show a comparison of transfer velocities averaged in wind speed bins from the three calculation methods: linear+bubble (46); wind speed power law (48); and a new version of COAREG using these values of A and B and the Brumer et al. (2017b) whitecap formulation – we are referring to this as COAREG36. A summary of the mean and RMS statistics is given in **Table 2**. Since the power law is fit directly to the mean observations, it gives the best overall fit.

So far our specification of total gas transfer velocity (46) requires the turbo-molecular term to scale with u_{*v} and the bubble-mediated term to scale with f_{wh}. It is insightful to reevaluate the turbo-molecular and bubble terms separately without specifying the nature of the forcing. So we recast (47) without the u_{*v} and f_{wh} factors but assume the forcing will have some wind speed dependence:

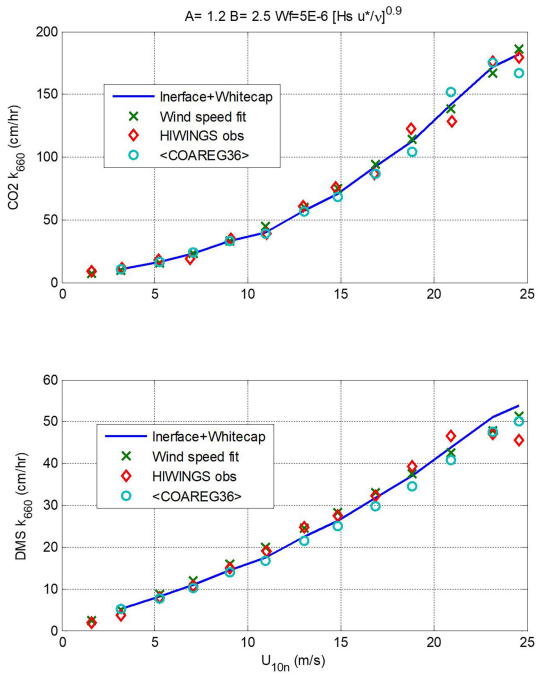

FIGURE 7 | Values of k_{w660} (upper panel, CO_2; lower panel, DMS) averaged in wind speed bins vs. 10-m neutral wind speed. The red diamonds are mean observed values, the x's are from the wind speed power-law fits (48), the blue line is from (46) using A = 1.2 and B = 2.5, and the circles are means of values computed using COAREG36.

$$A\ f(U) = \frac{(k_{w660d} - r_{dc}\ \ k_{w660c})}{37.5\ \ (1 - r_{dc})} \tag{50a}$$

$$B\ \ g(U) = \frac{(k_{w660c} - k_{w660d})}{830\ \ (1 - r_{dc})} \tag{50b}$$

The results are shown in **Figure 8** as a function of 10-m wind speed. Also shown on the graphs are the COAREG forms for the forcing: $f(U) = u_{*v}$ and $g(U) = f_{wh}$. We can see that the turbo-molecular term is nearly linear with the viscous stress and showing a hint of saturation at higher winds speeds. This could imply that our parametrization of viscous stress is too high and our parameterization underestimates the importance of the wave stress component at high winds speeds. The bubble-mediated term has a much stronger wind speed dependence and is well represented by the whitecap parameterization.

TABLE 2 | Summary of mean k_{660} (cm hr^{-1}) and RMS difference from mean HiWinGS measurements.

	CO_2		DMS	
	Mean	**RMS**	**Mean**	**RMS**
Observation	73.9	0	24.7	0
Interface + Whitecap	80.6	6.2	28.2	3.3
Power-law	74.4	6.5	25.3	2.2
COAREG36	75.2	10.1	24.8	2.8

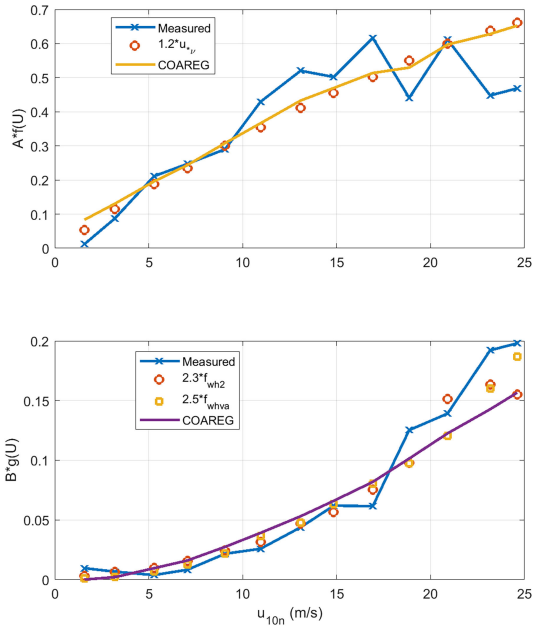

FIGURE 8 | Extraction of wind speed dependence of the turbo-molecular (upper panel) and bubble-mediated (lower panel) water-side transfer velocity terms using wind speed bin averages to the HiWinGS data. Two different whitecap formulations are used for the B term: f_{wh2} is (49). and f_{whva} is Deike et al. (2016). The solid lines are values extracted by applying the analysis to COAREG36 outputs.

4.2 Chemical Enhancement

We can use observations of CO_2 and DMS transfer velocity to estimate CE if the difference between CO_2 and dual tracer is due to chemical enhancement only by adding a term to (46)

$$k_{c660} = \mathrm{CE} + 37.5Au_{*v} + Bb_c f_{wh} \tag{51}$$

$$k_{d660} = 37.5Au_{*v} + Br_{dc} b_c f_{wh} \tag{52}$$

Taking the difference gives

$$k_{c660} - k_{d660} = \Delta k = \mathrm{CE} + B\ \ (1 - r_{dc})\ \ b_c f_{wh} \tag{53}$$

We can solve (53) for CE but we expect the values of CE will be the difference between two large numbers except at low wind speeds. In order to reduce the effect of sampling uncertainty, we have added data from four additional field programs – CO_2 from GasEx98, SOAP, and Knorr11 and DMS from SO-GasEx, SOAP, and Knorr11 – to the ensemble of data and produced a grand average for CO_2 and DMS transfer velocities (see **Figure 9**). In the case of GasEx98, CO_2 fluxes were determined with a closed path system that lacked a drier but used a long inlet. This tends to eliminate water vapor concentration variance and may be less affected by flux cross-talk than open path sensors. For $U_{10} < 10m$ s^{-1}, the uncertainty in these averages is ±2.0 cm hr^{-1} for CO_2 and ±0.4 cm hr^{-1} for DMS. The uncertainty in Δk is essentially that of CO_2. In **Figure 10** we show Δk as a function of U_{10} with separate curves for mean and medians of the four-experiment ensemble;

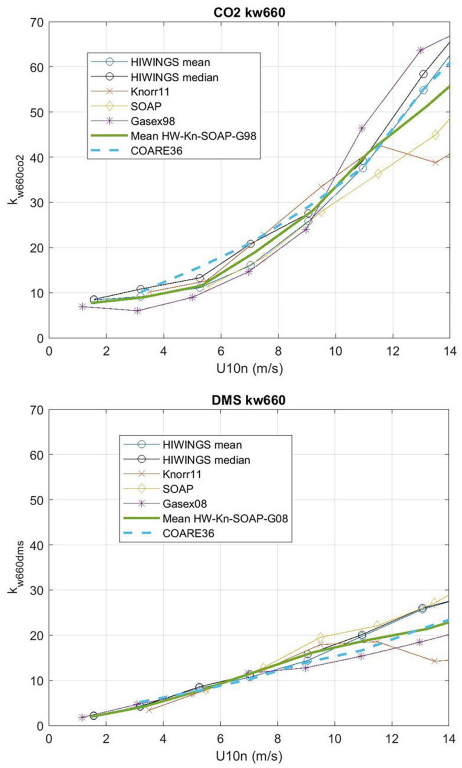

FIGURE 9 | Wind speed bin-averaged k_{w660} from HiWinGS, Knorr11, SOAP, GasEx98 and GasEx08 field programs: upper panel for CO_2 and lower panel for DMS. Both mean and median are shown for HiWinGS. The heavy green line is the mean of the five estimates. The dashed line is the COARE36 relationship.

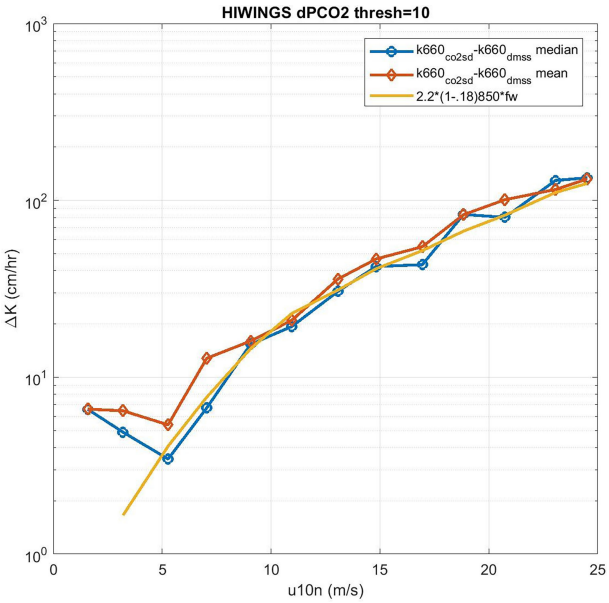

FIGURE 10 | Difference in CO_2 and DMS transfer velocities (normalized to Sc = 660) as a function of 10-m wind speed: blue –median and red –mean. The difference of either the red or blue curves from the COAREG estimate of the residual bubble component is hypothesized to be chemical enhancement.

we also show the bubble driven component [second term on RHS of (53)]. The data clearly imply values of CE on the order 4-6 cm hr^{-1} at the lowest wind speeds but even at U_{10} = 5 ms^{-1} it is doubtful the difference between observations of Δk and the estimates of the bubble component are significant. This result is similar to (Yang et al., 2022) who computed a grand-averaged k_{c660} from eight field programs (including the ones used here) and estimate CE by differencing their average with dual tracer estimates of k_{c660} (Ho et al., 2006). Because the dual tracer studies are done with non-reactive gases, the argument is that they do not include CO_2 CE. Yang et al. (2022) found CE values of about 4 cm hr^{-1} for $U_{10} < 10m$ s^{-1}. These results suggest τ_r on the order of 3 s (a_r = 0.33) should be used in (38) to estimate CE if the difference between CO_2 and dual tracer is due to chemical enhancement only.

5 DISCUSSION AND CONCLUSIONS

In this paper we analyze concurrent observations of CO_2 and DMS fluxes and ocean-side transfer velocity from three recent field programs. We emphasize the HiWinGS program because it has the broadest range of wind speeds and multiple systems of high quality covariance flux instrumentation. We frame our analysis in terms of the COAREG gas flux algorithm, which treats the ocean-side transfer as the sum of direct interfacial and bubble-mediated transfer mechanisms. We assume the interfacial transfer component scales as the square root of the Schmidt number and is driven linearly by the viscous friction velocity. The total surface stress is partitioned into viscous and wave contributions with the fraction going to viscous stress decreasing with increasing wind speed. COAREG scales the bubble-mediated component with whitecap fraction (Woolf, 1993) with additional temperature-dependent sensitivity to Schmidt number and solubility. Whitecap fraction is difficult to measure so parametrizations are uncertain, but whitecap fraction is only one of several possible choices to characterize the wave breaking contribution to bubble-mediated exchange (other possibilities include air entrainment rate or wave energy dissipated by breaking).

The analysis focuses on determination of the tuning constants A and B, which scale with the viscous and bubble-mediated terms. We use (47) to compute values of A and B in wind-speed bins. Note the value of A obtained from (47a) is independent of the formulation of whitecap scaling and B obtained *via* (47b) is independent of the formulation of the forcing of the viscous term. The wind speed dependence of A and B depends on the wind speed dependence of the forcing terms. The values of A and B determined from these data are essentially independent of wind speed for the chosen forcing: linear with u_{*_w} and with a particular whitecap formulation. At low wind speeds, there are departures for both A and B that we associate with the effects of chemical enhancement of CO_2 transfer, which are not captured in (47). CE is discussed theoretically in section 2.4 and a

parameterization is presented. In section 4.2 we exploit the difference in CO_2 and DMS transfer velocities to estimate CE – the result is noisy (**Figure 10**) but values are comparable to Wanninkhof (1992) and (Zheng et al., 2021).

The product of this effort is version 3.6 of the COARE flux algorithm – COAREG 3.6 which is available at https://downloads.psl.noaa.gov/BLO/Air-Sea/bulkalg/cor3_6/gasflux36/ (See the Supplement to this paper for more detail on the update). The algorithm incorporates a modern whitecap formulation that allows either pure wind speed or wave-dependent scaling. Chemical enhancement for CO_2 *via* (38) is included as an option. Wave dependence of the stress has also been updated.

DATA AVAILABILITY STATEMENT

Publicly available datasets were analyzed in this study. This data can be found here: https://downloads.psl.noaa.gov/psd3/cruises/HIWINGS_2013/Fairall_etal_2022_Frontiers_Paper/. Version 3.6 of the COARE flux algorithm (COAREG 3.6) is available at: https://downloads.psl.noaa.gov/BLO/Air-Sea/bulkalg/cor3_6/gasflux36/.

AUTHOR CONTRIBUTIONS

CWF wrote the first draft of the manuscript, MY and SEB each contributed a subsection. CWF, BWB, and MY revised the manuscript following the peer review process. JBE, CJZ, TGB, ESS, and SEB participated in discussions and provided edits. CWF, BWB, MY, SEB, LB, and CJZ participated in the HiWinGS experiment. TGB and ESS participated in the Knorr11 and SOAP experiment. JBE, CWF, and CJZ participated in the GasEx98 experiment. BB, LB, JBE, and CJZ participated in the SO-GasEx experiment. LB performed the numerical simulations with DE equation solver. SP and LB provided technical support for instrumentation, data collection, and analysis. All authors read and approved the finalized version.

FUNDING

This work, and the contributions of MY and TB, is supported by the UK Natural Environment Research Council's ORCHESTRA (Grant No. NE/N018095/1) and PICCOLO (Grant No. NE/P021409/1) projects, and by the European Space Agency's AMT4OceanSatFlux project (Grant No. 4000125730/18/NL/FF/gp). CF and BB are funded by the National Oceanic and Atmospheric Administration's Global Ocean Monitoring and Observing program (http://data.crossref.org/fundingdata/funder/10.13039/100018302). CZ was funded by the National Science Foundation (CJZ: OCE-2049579, Grants OCE-1537890 and OCE-1923935). Funding for HiWinGS was provided by the US National Science Foundation grant AGS-1036062. The Knorr-11 and SOAP campaigns were supported by the NSF Atmospheric Chemistry Program (Grant No. ATM-0426314, AGS-08568, -0851472, -0851407 and -1143709).

ACKNOWLEDGMENTS

SB was supported by a postdoctoral grant from the Centre National d'Études Spatiales (CNES).

SUPPLEMENTARY MATERIAL

The Supplementary Material for this article can be found online at: https://www.frontiersin.org/articles/10.3389/fmars.2022.826606/full#supplementary-material

REFERENCES

Andersson, A., Falck, E., Sjöblom, A., Kljun, N., Sahlée, E., Omar, A. M., et al. (2017). Air-Sea Gas Transfer in High Arctic Fjords. *Geophysical Res. Lett.* 44, 2519–2526. doi: 10.1002/2016GL072373

Anguelova, M. D., and Bettenhausen, M. H. (2019). Whitecap Fraction From Satellite Measurements: Algorithm Description. *J. Geophysical Research: Oceans* 124, 1827–1857. doi: 10.1029/2018JC014630

Bell, T. G., De Bruyn, W., Miller, S. D., Ward, B., Christensen, K., and Saltzman, E. S. (2013). Air-Sea Dimethylsulfide (DMS) Gas Transfer in the North Atlantic: Evidence for Limited Interfacial Gas Exchange at High Wind Speed. *Atmospheric Chem. Phys.* 13, 11073–11087. doi: 10.5194/acp-13-11073-2013

Bell, T. G., Landwehr, S., Miller, S. D., de Bruyn, W. J., Callaghan, A., Scanlon, B., et al. (2017). Estimation of Bubbled-Mediated Air/Sea Gas Exchange From Concurrent DMS and CO_2 Transfer Velocities at Intermediate-High Wind Speeds. *Atmos. Chem. Phys. Discuss.* 2017, 1–29. doi: 10.5194/acp-2017-85

Blomquist, B. W., Brumer, S. E., Fairall, C. W., Huebert, B. J., Zappa, C. J., Brooks, I. M., et al. (2017). Wind Speed and Sea State Dependencies of Air-Sea Gas Transfer: Results From the High Wind Speed Gas Exchange Study (HiWinGS). *J. Geophysical Research: Oceans* 122, 8034–8062. doi: 10.1002/2017JC013181

Blomquist, B. W., Fairall, C. W., Huebert, B. J., Kieber, D. J., and Westby, G. R. (2006). Dms Sea-Air Transfer Velocity: Direct Measurements by Eddy Covariance and Parameterization Based on the NOAA/COARE Gas Transfer Model. *Geophysical Res. Lett.* 33, L07601. doi: 10.1029/2006GL025735

Blomquist, B. W., Huebert, B. J., Fairall, C. W., Bariteau, L., Edson, J. B., Hare, J. E., et al. (2014). Advances in Air-Sea CO_2 Flux Measurement by Eddy Correlation. *Boundary-Layer Meteorology* 152, 245–276. doi: 10.1007/s10546-014-9926-2

Blomquist, B. W., Huebert, B. J., Fairall, C. W., and Faloona, I. C. (2010). Determining the Sea-Air Flux of Dimethylsulfide by Eddy Correlation Using Mass Spectrometry. *Atmospheric Measurement Techniques* 3, 1–20. doi: 10.5194/amt-3-1-2010

Brumer, S. E., Zappa, C. J., Blomquist, B. W., Fairall, C. W., Cifuentes-Lorenzen, A., Edson, J. B., et al. (2017a). Wave-Related Reynolds Number Parameterizations of CO_2 and DMS Transfer Velocities. *Geophysical Res. Lett.* 44, 9865–9875. doi: 10.1002/2017GL074979

Brumer, S. E., Zappa, C. J., Brooks, I. M., Tamura, H., Brown, S. M., Blomquist, B., et al. (2017b). Whitecap Coverage Dependence on Wind and Wave Statistics as Observed During SO-GasEx and HiWinGS. *J. Phys. Oceanography* 47(9); 2211–2235. doi: 10.1175/JPO-D-17-0005.1

Butterworth, B. J., and Miller, S. D. (2016). Air-Sea Exchange of Carbon Dioxide in the Southern Ocean and Antarctic Marginal Ice Zone. *Geophysical Res. Lett.* 43, 7223–7230. doi: 10.1002/2016GL069581

Callaghan, A. H. (2013). An Improved Whitecap Timescale for Sea Spray Aerosol Production Flux Modeling Using the Discrete Whitecap Method. *J. Geophysical Research: Atmospheres* 118, 9997–10010. doi: 10.1002/jgrd.50768

Callaghan, A. H. (2018). On the Relationship Between the Energy Dissipation Rate of Surface-Breaking Waves and Oceanic Whitecap Coverage. *J. Phys. Oceanography* 48, 2609 –2626. doi: 10.1175/JPO-D-17-0124.1

Callaghan, A. H., Deane, G. B., and Stokes, M. D. (2016). Laboratory Air-Entraining Breaking Waves: Imaging Visible Foam Signatures to Estimate Energy Dissipation. *Geophysical Res. Lett.* 43 (11), 320–11,328. doi: 10.1002/2016GL071226

Cifuentes-Lorenzen, A., Edson, J. B., and Zappa, C. J. (2018). Air-Sea Interaction in the Southern Ocean: Exploring the Height of the Wave Boundary Layer at the Air-Sea Interface. *Boundary-Layer Meteorology* 169, 461–482. doi: 10.1007/s10546-018-0376-0

Cronin, M. F., Gentemann, C. L., Edson, J., Ueki, I., Bourassa, M., Brown, S., et al. (2019). Air-Sea Fluxes With a Focus on Heat and Momentum. *Front. Mar. Sci.* 6. doi: 10.3389/fmars.2019.00430

Deike, L., Lenain, L., and Melville, W. K. (2017). Air Entrainment by Breaking Waves. *Geophysical Res. Lett.* 44, 3779–3787. doi: 10.1002/2017GL072883

Deike, L., and Melville, W. K. (2018). Gas Transfer by Breaking Waves. *Geophysical Res. Lett.* 45 (10), 482–10,492. doi: 10.1029/2018GL078758

Deike, L., Melville, W. K., and Popinet, S. (2016). Air Entrainment and Bubble Statistics in Breaking Waves. *J. Fluid Mechanics* 801, 91–129. doi: 10.1017/jfm.2016.372

Dong, Y., Yang, M., Bakker, D. C. E., Kitidis, V., and Bell, T. G. (2021). Uncertainties in Eddy Covariance Air–Sea CO_2 Flux Measurements and Implications for Gas Transfer Velocity Parameterisations. *Atmospheric Chem. Phys.* 21, 8089–8110. doi: 10.5194/acp-21-8089-2021

Edson, J. B., Fairall, C. W., Bariteau, L., Zappa, C. J., Cifuentes-Lorenzen, A., McGillis, W. R., et al. (2011). Direct Covariance Measurement of CO_2 Gas Transfer Velocity During the 2008 Southern Ocean Gas Exchange Experiment: Wind Speed Dependency. *J. Geophysical Res. - Oceans* 116, C00F. doi: 10.1029/2011JC007022

Edson, J. B., Hinton, A. A., Prada, K. E., Hare, J. E., and Fairall, C. W. (1998). Direct Covariance Flux Estimates From Mobile Platforms at Sea. *J. Atmospheric Oceanic Technol.* 15, 547–562. doi: 10.1175/1520-0426(1998)015<0547:DCFEFM>2.0.CO;2

Edson, J. B., Jampana, V., Weller, R. A., Bigorre, S. P., Plueddemann, A. J., and Fairall, C. W. (2013). On the Exchange of Momentum Over the Open Ocean. *J. Phys. Oceanography* 43, 1589–1610. doi: 10.1175/JPO-D-12-0173.1

Edson, J. B., Zappa, C. J., Ware, J., McGillis, W. R., and Hare, J. E. (2004). Scalar Flux Profile Relationships Over the Open Ocean. *J. Geophys. Res.* 109, C08S09. doi: 10.1029/2003JC001960

Esters, L., Landwehr, S., Sutherland, G., Bell, T. G., Christensen, K. H., Saltzman, E. S., et al. (2017). Parameterizing Air-Sea Gas Transfer Velocity With Dissipation. *J. Geophysical Research: Oceans* 122, 3041–3056. doi: 10.1002/2016JC012088

Fairall, C. W., Bradley, E. F., Hare, J. E., Grachev, A. A., and Edson, J. B. (2003). Bulk Parameterization of Air-Sea Fluxes: Updates and Verification for the Coare Algorithm. *J. Climate* 16, 571–591. doi: 10.1175/1520-0442(2003)016<0571:BPOASF>2.0.CO;2

Fairall, C. W., Bradley, E. F., Rogers, D. P., Edson, J. B., and Young, G. S. (1996). Bulk Parameterization of Air-Sea Fluxes for Tropical Ocean Global Atmosphere Coupled Ocean Atmosphere Response Experiment. *J. Of Geophysical Res.* 101, 3747–3764. doi: 10.1029/95JC03205

Fairall, C. W., Hare, J., Edson, J., and McGillis, W. (2000). Parameterization and Micrometeorological Measurement of Air-Sea Gas Transfer. *Bound.-Layer Meteor.* 96, 63–105. doi: 10.1023/A:1002662826020

Fairall, C. W., Helmig, D., Ganzeveld, L., and Hare, J. (2007). Water-Side Turbulence Enhancement of Ozone Deposition to the Ocean. *Atmospheric Chem. Phys.* 7, 443–451. doi: 10.5194/acp-7-443-2007

Fairall, C. W., Yang, M., Bariteau, L., Edson, J. B., Helmig, D., McGillis, W., et al. (2011). Implementation of the Coupled Ocean-Atmosphere Response Experiment Flux Algorithm With CO_2, Dimethyl Sulfide, and O_2. *J. Geophysical Res.* 116, C00F09. doi: 10.1029/2010JC006884

Flügge, M., Paskyabi, M. B., Reuder, J., Edson, J. B., and Plueddemann, A. J. (2016). Comparison of Direct Covariance Flux Measurements From an Offshore Tower and a Buoy. *J. Atmospheric Oceanic Technol.* 33, 873–890. doi: 10.1175/JTECH-D-15-0109.1

Garbe, C. S., Rutgersson, A., Boutin, J., Leeuw, G., Delille, B., Fairall, C. W., et al. (2014). *Transfer Across the Air-Sea Interface (Springer Berlin, Heidelberg, New York: Springer Earth System Sciences)*. 55–112. doi: 10.1007/978-3-642-25643-1

Ghobadian, M., and Stammer, D. (2019). Inferring Air-Sea Carbon Dioxide Transfer Velocities From Sea Surface Scatterometer Measurements. *J. Geophysical Research: Oceans* 124, 7974–7988. doi: 10.1029/2019JC014982

Goddijn-Murphy, L., Woolf, D. K., Callaghan, A. H., Nightingale, P. D., and Shutler, J. D. (2016). A Reconciliation of Empirical and Mechanistic Models of the Air-Sea Gas Transfer Velocity. *J. Geophysical Research: Oceans* 121, 818–835. doi: 10.1002/2015JC011096

Gutiérrez-Loza, L., Wallin, M. B., Sahlée, E., Nilsson, E., Bange, H. W., Kock, A., et al. (2019). Measurement of Air-Sea Methane Fluxes in the Baltic Sea Using the Eddy Covariance Method. *Front. Earth Sci.* 7. doi: 10.3389/feart.2019.00093

Ho, D. T., Law, C. S., Smith, M. J., Schlosser, P., Harvey, M., and Hill, P. (2006). Measurements of Air-Sea Gas Exchange at High Wind Speeds in the Southern Ocean: Implications for Global Parameterizations. *Geophys. Res. Lett.* 33, L16611. doi: 10.1029/2006GL026817

Hoover, T. E., and Berkshire, D. C. (1969). Effects of Hydration on Carbon Dioxide Exchange Across an Air-Water Interface. *J. Geophysical Res.* 74, 456–464. doi: 10.1029/JB074i002p00456

Ho, D., Sabine, C. L., Hebert, D., Ullman, D. S., Wanninkhof, R., Hamme, R. C., et al. (2011). Southern Ocean Gas Exchange Experiment: Setting the Stage. *J. Geophysical Res. - Oceans* 116, C00F08. doi: 10.1029/2010JC006852

Jørgensen, H. E., Sørensen, L. L., and Larsen, S. E. (2020). A Simple Model of Chemistry Effects on the Air-Sea CO_2 Exchange Coefficient. *J. Geophysical Research: Oceans* 125, e2018JC014808. doi: 10.1029/2018JC014808

Johnson, M. T. (2010). A Numerical Scheme to Calculate Temperature and Salinity Dependent Air-Water Transfer Velocities for Any Gas. *Ocean Sci.* 6, 913–932. doi: 10.5194/os-6-913-2010

Johnson, K. S., Barry, J. P., Coletti, L. J., Fitzwater, S. E., Jannasch, H. W., and Lovera, C. F. (2011). Nitrate and Oxygen Flux Across the Sediment-Water Interface Observed by Eddy Correlation Measurements on the Open Continental Shelf. *Limnology Oceanography: Methods* 9, 543–553. doi: 10.4319/lom.2011.9.543

Krall, K. E., Smith, A. W., Takagaki, N., and Jähne, B. (2019). Air–sea Gas Exchange at Wind Speeds Up to 85 ms^{-1}. *Ocean Sci.* 15, 1783–1799. doi: 10.5194/os-15-1783-2019

Landwehr, S., Miller, S. D., Smith, M. J., Bell, T. G., Saltzman, E. S., and Ward, B. (2018). Using Eddy Covariance to Measure the Dependence of Air–Sea CO_2 Exchange Rate on Friction Velocity. *Atmospheric Chem. Phys.* 18, 4297–4315. doi: 10.5194/acp-18-4297-2018

Landwehr, S., Miller, S. D., Smith, M. J., Saltzman, E. S., and Ward, B. (2014). Analysis of the PKT Correction for Direct CO_2 Flux Measurements Over the Ocean. *Atmospheric Chem. Phys.* 14, 3361–3372. doi: 10.5194/acp-14-3361-2014

Landwehr, S., O'Sullivan, N., and Ward, B. (2015). Direct Flux Measurements From Mobile Platforms at Sea: Motion and Air-Flow Distortion Corrections Revisited. *J. Atmospheric Oceanic Technol* 32(6); 1163–1178. doi: 10.1175/JTECH-D-14-00137.1

Liang, J.-H., Deutsch, C., McWilliams, J. C., Baschek, B., Sullivan, P. P., and Chiba, D. (2013). Parameterizing Bubble-Mediated Air-Sea Gas Exchange and its Effect on Ocean Ventilation. *Global Biogeochemical Cycles* 27, 894–905. doi: 10.1002/gbc.20080

Liss, P. S., and Merlivat, L. (1986). *Air-Sea Gas Exchange Rates: Introduction and Synthesis* (Dordrecht, Holland: D. Reidel), 113–127.

Liss, P. S., and Slater, P. G. (1974). Flux of Gases Across the Air-Sea Interface. *Nature* 247, 181–184. doi: 10.1038/247181a0

Luhar, A. K., Woodhouse, M. T., and Galbally, I. E. (2018). A Revised Global Ozone Dry Deposition Estimate Based on a New Two-Layer Parameterisation for Air–Sea Exchange and the Multi-Year Macc Composition Reanalysis. *Atmospheric Chem. Phys.* 18, 4329–4348. doi: 10.5194/acp-18-4329-2018

McGillis, W. R., and Wanninkhof, R. (2006). Aqueous CO_2 Gradients for Air-Sea Flux Estimates. *Mar. Chem.* 98, 100–108. doi: 10.1016/j.marchem.2005.09.003

Melville, W. K. (1996). The Role of Surface-Wave Breaking in Air-Sea Interaction. *Annu. Rev. Fluid Mechanics* 28, 279–321. doi: 10.1146/annurev.fl.28.010196.001431

Miller, S. D., Marandino, C., and Saltzman, E. S. (2010). Ship-Based Measurement of Air-Sea CO_2 Exchange by Eddy Covariance. *J. Geophysical Research: Atmospheres* 115, D02304. doi: 10.1029/2009JD012193

Monahan, E. C. (1971). Oceanic Whitecaps. *J. Phys. Oceanography* 1, 139–144. doi: 10.1175/1520-0485(1971)001<0139:OW>2.0.CO;2

Ortiz-Suslow, D. G., Kalogiros, J., Yamaguchi, R., and Wang, Q. (2021). An Evaluation of the Constant Flux Layer in the Atmospheric Flow Above the Wavy Air-Sea Interface. *J. Geophysical Research: Atmospheres* 126, e2020JD032834. doi: 10.1029/2020JD032834

Porter, J. G., de Bruyn, W. J., Miller, S. D., and Saltzman, E. S. (2020). Air/sea Transfer of Highly Soluble Gases Over Coastal Waters. *Geophysical Res. Lett.* 47, e2019GL085286. doi: 10.1029/2019GL085286

Porter, J. G., De Bruyn, W., and Saltzman, E. S. (2018). Eddy Flux Measurements of Sulfur Dioxide Deposition to the Sea Surface. *Atmospheric Chem. Phys.* 18, 15291–15305. doi: 10.5194/acp-18-15291-2018

Prytherch, J., Brooks, I. M., Crill, P. M., Thornton, B. F., Salisbury, D. J., Tjernström, M., et al. (2017). Direct Determination of the Air-Sea CO_2 Gas Transfer Velocity in Arctic Sea Ice Regions. *Geophysical Res. Lett.* 44, 3770–3778. doi: 10.1002/2017GL073593

Prytherch, J., and Yelland, M. (2021). Wind, Convection and Fetch Dependence of Gas Transfer Velocity in an Arctic Sea-Ice Lead Determined From Eddy Covariance CO_2 Flux Measurements. *Global Biogeochemical Cycles* 35, e2020GB006633. doi: 10.1029/2020GB006633

Rhee, T. S., Nightingale, P. D., Woolf, D. K., Caulliez, G., Bowyer, P., and Andreae, M. O. (2007). Influence of Energetic Wind and Waves on Gas Transfer in a Large Wind-Wave Tunnel Facility. *J. Geophysical Res.* 112, C05027. doi: 10.1029/2005JC003358

Rowe, M. D., Fairall, C. W., and Perlinger, J. A. (2011). Chemical Sensor Resolution Requirements for Near-Surface Measurements of Turbulent Fluxes. *Atmos. Chem. Phys.* 11, 5263–5275. doi: 10.5194/acp-11-5263-2011

Rutgersson, A., Pettersson, H., Nilsson, E., Bergström, H., Wallin, M. B., Nilsson, E. D., et al. (2020). Using Land-Based Stations for Air-Sea Interaction Studies. *Tellus A: Dynamic Meteorology Oceanography* 72, 1–23. doi: 10.1080/16000870.2019.1697601

Shutler, J. D., Land, P. E., Piolle, J.-F., Woolf, D. K., Goddijn-Murphy, L., Paul, F., et al. (2016). FluxEngine: A Flexible Processing System for Calculating Atmosphere-Ocean Carbon Dioxide Gas Fluxes and Climatologies. *J. Atmospheric Oceanic Technol.* 33, 741–756. doi: 10.1175/JTECH-D-14-00204.1

Shutler, J. D., Wanninkhof, R., Nightingale, P. D., Woolf, D. K., Bakker, D. C. E., Watson, A., et al. (2020). Satellites Will Address Critical Science Priorities for Quantifying Ocean Carbon. *Front. Ecol. Environ.* 18, 27–35. doi: 10.1002/fee.2129

Soloviev, A. V. (2007). Coupled Renewal Model of Ocean Viscous Sublayer, Thermal Skin Effect and Interfacial Gas Transfer Velocity. *J. Mar. Syst.* 66, 19–27. doi: 10.1016/j.jmarsys.2006.03.024

Vieira, V., Mateus, M., Canelas, R., and Leitão, F. (2020). The Fugas 2.5 Updated for the Effects of Surface Turbulence on the Transfer Velocity of Gases at the Atmosphere-Ocean Interface. *J. Mar. Sci. Eng.* 8, 435. doi: 10.3390/jmse8060435

Wanninkhof, R. (1992). Relationship Between Wind Speed and Gas Exchange Over the Ocean. *J. Geophysical Res.* 97, 7373–7382. doi: 10.1029/92JC00188

Wanninkhof, R. (2014). Relationship Between Wind Speed and Gas Exchange Over the Ocean Revisited. *Limnology Oceanography: Methods* 12, 351–362. doi: 10.4319/lom.2014.12.351

Wanninkhof, R., Asher, W. E., Ho, D., Sweeney, C., and McGillis, W. (2009). Advances in Quantifying Air-Sea Gas Exchange and Environmental Forcing. *Annu. Rev. Mar. Sci.* 1, 213–244. doi: 10.1146/annurev.marine.010908.163742

Wanninkhof, R., and Knox, M. (1996). Chemical Enhancement of CO_2 Exchange in Natural Waters. *Limnol. Oceanogr.* 41, 689–697. doi: 10.4319/lo.1996.41.4.0689

Woolf, D. K. (1993). Bubbles and the Air-Sea Transfer Velocity of Gases. *Atmos. Ocean* 31, 517–540. doi: 10.1080/07055900.1993.9649484

Woolf, D., Shutler, J., Goddijn-Murphy, L., Watson, A., Chapron, B., Nightingale, P., et al. (2019). Key Uncertainties in the Recent Air-Sea Flux of CO_2. *Global Biogeochemical Cycles* 33, 1548–1563. doi: 10.1029/2018GB006041

Woolf, D. K., and Thorpe, S. A. (1991). Bubbles and the Air-Sea Exchange of Gases in Near Saturation Conditions. *J. Mar. Res.* 49, 435–466. doi: 10.1357/002224091784995765

Yang, M., Bell, T. G., Bidlot, J., Blomquist, B. W., Butterworth, B. J., Dong, Y., et al. (2022). Global Synthesis of Air-Sea CO_2 Transfer Velocity Estimates From Ship-Based Eddy Covariance Measurements. *Front. Mar. Sci. Sec. Ocean Observation*. doi: 10.3389/fmars.2022.826421

Yang, M., Bell, T. G., Hopkins, F. E., Kitidis, V., Cazenave, P. W., Nightingale, P. D., et al. (2016). Air–sea Fluxes of CO_2 and CH_4 From the Penlee Point Atmospheric Observatory on the South-West Coast of the UK. *Atmospheric Chem. Phys.* 16, 5745–5761. doi: 10.5194/acp-16-5745-2016

Yang, M., Blomquist, B., and Nightingale, P. D. (2014). Air-Sea Exchange of Methanol and Acetone During Hiwings: Estimation of Air Phase, Water Phase Gas Transfer Velocities. *J. Geophysical Research: Oceans* 119, 7308–7323. doi: 10.1002/2014JC010227

Yang, M., Norris, S. J., Bell, T. G., and Brooks, I. M. (2019). Sea Spray Fluxes From the Southwest Coast of the United Kingdom–Dependence on Wind Speed and Wave Height. *Atmospheric Chem. Phys.* 19, 15271–15284. doi: 10.5194/acp-19-15271-2019

Zavarsky, A., Goddijn-Murphy, L., Steinhoff, T., and Marandino, C. A. (2018). Bubble-Mediated Gas Transfer and Gas Transfer Suppression of DMS and CO_2. *J. Geophysical Research: Atmospheres* 123, 6624–6647. doi: 10.1029/2017JD028071

Zavarsky, A., and Marandino, C. A. (2019). The Influence of Transformed Reynolds Number Suppression on Gas Transfer Parameterizations and Global DMS and CO_2 Fluxes. *Atmospheric Chem. Phys.* 19, 1819–1834. doi: 10.5194/acp-19-1819-2019

Zheng, T., Feng, S., Davis, K. J., Pal, S., and Morguí, J.-A. (2021). Development and Evaluation of CO_2 Transport in Mpas-a V6.3. *Geoscientific Model. Dev.* 14, 3037–3066. doi: 10.5194/gmd-14-3037-2021

Zülicke, C. (2005). Air-Sea Fluxes Including the Effect of the Molecular Skin Layer. *Deep Sea Res. Part II: Topical Stud. Oceanography* 52, 1220–1245. doi: 10.1016/j.dsr2.2005.01.008

Conflict of Interest: The authors declare that the research was conducted in the absence of any commercial or financial relationships that could be construed as a potential conflict of interest.

Publisher's Note: All claims expressed in this article are solely those of the authors and do not necessarily represent those of their affiliated organizations, or those of the publisher, the editors and the reviewers. Any product that may be evaluated in this article, or claim that may be made by its manufacturer, is not guaranteed or endorsed by the publisher.

Advantages of publishing in Frontiers

OPEN ACCESS
Articles are free to read for greatest visibility and readership

FAST PUBLICATION
Around 90 days from submission to decision

HIGH QUALITY PEER-REVIEW
Rigorous, collaborative, and constructive peer-review

TRANSPARENT PEER-REVIEW
Editors and reviewers acknowledged by name on published articles

Frontiers
Avenue du Tribunal-Fédéral 34
1005 Lausanne | Switzerland

Visit us: www.frontiersin.org
Contact us: frontiersin.org/about/contact

REPRODUCIBILITY OF RESEARCH
Support open data and methods to enhance research reproducibility

DIGITAL PUBLISHING
Articles designed for optimal readership across devices

FOLLOW US
@frontiersin

IMPACT METRICS
Advanced article metrics track visibility across digital media

EXTENSIVE PROMOTION
Marketing and promotion of impactful research

LOOP RESEARCH NETWORK
Our network increases your article's readership